Tunable Laser Applications

Second Edition

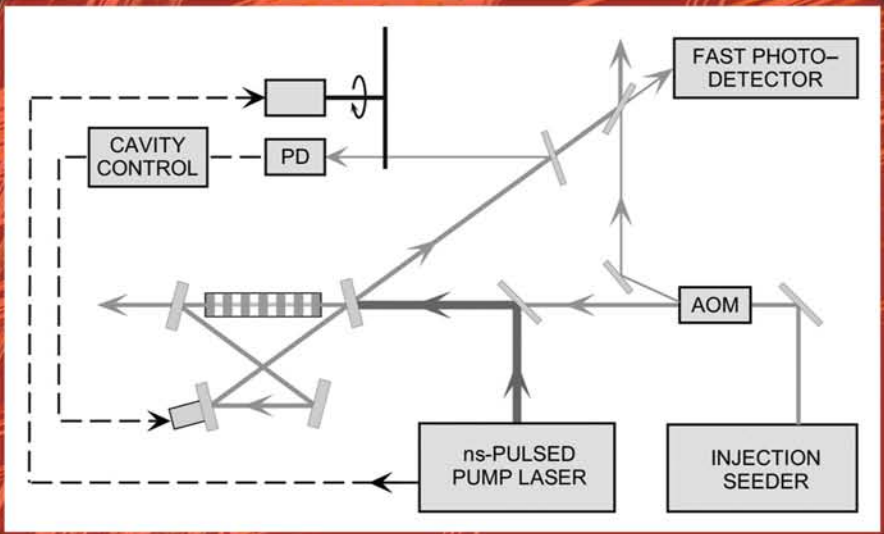

Edited by
F. J. Duarte

CRC Press
Taylor & Francis Group

Tunable Laser Applications

Second Edition

OPTICAL SCIENCE AND ENGINEERING

Founding Editor
Brian J. Thompson
University of Rochester
Rochester, New York

1. Electron and Ion Microscopy and Microanalysis: Principles and Applications, *Lawrence E. Murr*
2. Acousto-Optic Signal Processing: Theory and Implementation, *edited by Norman J. Berg and John N. Lee*
3. Electro-Optic and Acousto-Optic Scanning and Deflection, *Milton Gottlieb, Clive L. M. Ireland, and John Martin Ley*
4. Single-Mode Fiber Optics: Principles and Applications, *Luc B. Jeunhomme*
5. Pulse Code Formats for Fiber Optical Data Communication: Basic Principles and Applications, *David J. Morris*
6. Optical Materials: An Introduction to Selection and Application, *Solomon Musikant*
7. Infrared Methods for Gaseous Measurements: Theory and Practice, *edited by Joda Wormhoudt*
8. Laser Beam Scanning: Opto-Mechanical Devices, Systems, and Data Storage Optics, *edited by Gerald F. Marshall*
9. Opto-Mechanical Systems Design, *Paul R. Yoder, Jr.*
10. Optical Fiber Splices and Connectors: Theory and Methods, *Calvin M. Miller with Stephen C. Mettler and Ian A. White*
11. Laser Spectroscopy and Its Applications, *edited by Leon J. Radziemski, Richard W. Solarz, and Jeffrey A. Paisner*
12. Infrared Optoelectronics: Devices and Applications, *William Nunley and J. Scott Bechtel*
13. Integrated Optical Circuits and Components: Design and Applications, *edited by Lynn D. Hutcheson*
14. Handbook of Molecular Lasers, *edited by Peter K. Cheo*
15. Handbook of Optical Fibers and Cables, *Hiroshi Murata*
16. Acousto-Optics, *Adrian Korpel*
17. Procedures in Applied Optics, *John Strong*
18. Handbook of Solid-State Lasers, *edited by Peter K. Cheo*
19. Optical Computing: Digital and Symbolic, *edited by Raymond Arrathoon*
20. Laser Applications in Physical Chemistry, *edited by D. K. Evans*
21. Laser-Induced Plasmas and Applications, *edited by Leon J. Radziemski and David A. Cremers*
22. Infrared Technology Fundamentals, *Irving J. Spiro and Monroe Schlessinger*

23. Single-Mode Fiber Optics: Principles and Applications, Second Edition, Revised and Expanded, *Luc B. Jeunhomme*
24. Image Analysis Applications, *edited by Rangachar Kasturi and Mohan M. Trivedi*
25. Photoconductivity: Art, Science, and Technology, *N. V. Joshi*
26. Principles of Optical Circuit Engineering, *Mark A. Mentzer*
27. Lens Design, *Milton Laikin*
28. Optical Components, Systems, and Measurement Techniques, *Rajpal S. Sirohi and M. P. Kothiyal*
29. Electron and Ion Microscopy and Microanalysis: Principles and Applications, Second Edition, Revised and Expanded, *Lawrence E. Murr*
30. Handbook of Infrared Optical Materials, *edited by Paul Klocek*
31. Optical Scanning, *edited by Gerald F. Marshall*
32. Polymers for Lightwave and Integrated Optics: Technology and Applications, *edited by Lawrence A. Hornak*
33. Electro-Optical Displays, *edited by Mohammad A. Karim*
34. Mathematical Morphology in Image Processing, *edited by Edward R. Dougherty*
35. Opto-Mechanical Systems Design: Second Edition, Revised and Expanded, *Paul R. Yoder, Jr.*
36. Polarized Light: Fundamentals and Applications, *Edward Collett*
37. Rare Earth Doped Fiber Lasers and Amplifiers, *edited by Michel J. F. Digonnet*
38. Speckle Metrology, *edited by Rajpal S. Sirohi*
39. Organic Photoreceptors for Imaging Systems, *Paul M. Borsenberger and David S. Weiss*
40. Photonic Switching and Interconnects, *edited by Abdellatif Marrakchi*
41. Design and Fabrication of Acousto-Optic Devices, *edited by Akis P. Goutzoulis and Dennis R. Pape*
42. Digital Image Processing Methods, *edited by Edward R. Dougherty*
43. Visual Science and Engineering: Models and Applications, *edited by D. H. Kelly*
44. Handbook of Lens Design, *Daniel Malacara and Zacarias Malacara*
45. Photonic Devices and Systems, *edited by Robert G. Hunsberger*
46. Infrared Technology Fundamentals: Second Edition, Revised and Expanded, *edited by Monroe Schlessinger*
47. Spatial Light Modulator Technology: Materials, Devices, and Applications, *edited by Uzi Efron*
48. Lens Design: Second Edition, Revised and Expanded, *Milton Laikin*
49. Thin Films for Optical Systems, *edited by Francoise R. Flory*
50. Tunable Laser Applications, *edited by F. J. Duarte*
51. Acousto-Optic Signal Processing: Theory and Implementation, Second Edition, *edited by Norman J. Berg and John M. Pellegrino*
52. Handbook of Nonlinear Optics, *Richard L. Sutherland*

53. Handbook of Optical Fibers and Cables: Second Edition, *Hiroshi Murata*
54. Optical Storage and Retrieval: Memory, Neural Networks, and Fractals, *edited by Francis T. S. Yu and Suganda Jutamulia*
55. Devices for Optoelectronics, *Wallace B. Leigh*
56. Practical Design and Production of Optical Thin Films, *Ronald R. Willey*
57. Acousto-Optics: Second Edition, *Adrian Korpel*
58. Diffraction Gratings and Applications, *Erwin G. Loewen and Evgeny Popov*
59. Organic Photoreceptors for Xerography, *Paul M. Borsenberger and David S. Weiss*
60. Characterization Techniques and Tabulations for Organic Nonlinear Optical Materials, *edited by Mark G. Kuzyk and Carl W. Dirk*
61. Interferogram Analysis for Optical Testing, *Daniel Malacara, Manuel Servin, and Zacarias Malacara*
62. Computational Modeling of Vision: The Role of Combination, *William R. Uttal, Ramakrishna Kakarala, Spiram Dayanand, Thomas Shepherd, Jagadeesh Kalki, Charles F. Lunskis, Jr., and Ning Liu*
63. Microoptics Technology: Fabrication and Applications of Lens Arrays and Devices, *Nicholas Borrelli*
64. Visual Information Representation, Communication, and Image Processing, *edited by Chang Wen Chen and Ya-Qin Zhang*
65. Optical Methods of Measurement, *Rajpal S. Sirohi and F. S. Chau*
66. Integrated Optical Circuits and Components: Design and Applications, *edited by Edmond J. Murphy*
67. Adaptive Optics Engineering Handbook, *edited by Robert K. Tyson*
68. Entropy and Information Optics, *Francis T. S. Yu*
69. Computational Methods for Electromagnetic and Optical Systems, *John M. Jarem and Partha P. Banerjee*
70. Laser Beam Shaping, *Fred M. Dickey and Scott C. Holswade*
71. Rare-Earth-Doped Fiber Lasers and Amplifiers: Second Edition, Revised and Expanded, *edited by Michel J. F. Digonnet*
72. Lens Design: Third Edition, Revised and Expanded, *Milton Laikin*
73. Handbook of Optical Engineering, *edited by Daniel Malacara and Brian J. Thompson*
74. Handbook of Imaging Materials: Second Edition, Revised and Expanded, *edited by Arthur S. Diamond and David S. Weiss*
75. Handbook of Image Quality: Characterization and Prediction, *Brian W. Keelan*
76. Fiber Optic Sensors, *edited by Francis T. S. Yu and Shizhuo Yin*
77. Optical Switching/Networking and Computing for Multimedia Systems, *edited by Mohsen Guizani and Abdella Battou*
78. Image Recognition and Classification: Algorithms, Systems, and Applications, *edited by Bahram Javidi*
79. Practical Design and Production of Optical Thin Films: Second Edition, Revised and Expanded, *Ronald R. Willey*

80. Ultrafast Lasers: Technology and Applications, *edited by Martin E. Fermann, Almantas Galvanauskas, and Gregg Sucha*
81. Light Propagation in Periodic Media: Differential Theory and Design, *Michel Nevière and Evgeny Popov*
82. Handbook of Nonlinear Optics, Second Edition, Revised and Expanded, *Richard L. Sutherland*
83. Polarized Light: Second Edition, Revised and Expanded, *Dennis Goldstein*
84. Optical Remote Sensing: Science and Technology, *Walter Egan*
85. Handbook of Optical Design: Second Edition, *Daniel Malacara and Zacarias Malacara*
86. Nonlinear Optics: Theory, Numerical Modeling, and Applications, *Partha P. Banerjee*
87. Semiconductor and Metal Nanocrystals: Synthesis and Electronic and Optical Properties, edited by *Victor I. Klimov*
88. High-Performance Backbone Network Technology, *edited by Naoaki Yamanaka*
89. Semiconductor Laser Fundamentals, *Toshiaki Suhara*
90. Handbook of Optical and Laser Scanning, *edited by Gerald F. Marshall*
91. Organic Light-Emitting Diodes: Principles, Characteristics, and Processes, *Jan Kalinowski*
92. Micro-Optomechatronics, *Hiroshi Hosaka, Yoshitada Katagiri, Terunao Hirota, and Kiyoshi Itao*
93. Microoptics Technology: Second Edition, *Nicholas F. Borrelli*
94. Organic Electroluminescence, *edited by Zakya Kafafi*
95. Engineering Thin Films and Nanostructures with Ion Beams, *Emile Knystautas*
96. Interferogram Analysis for Optical Testing, Second Edition, *Daniel Malacara, Manuel Sercin, and Zacarias Malacara*
97. Laser Remote Sensing, *edited by Takashi Fujii and Tetsuo Fukuchi*
98. Passive Micro-Optical Alignment Methods, *edited by Robert A. Boudreau and Sharon M. Boudreau*
99. Organic Photovoltaics: Mechanism, Materials, and Devices, *edited by Sam-Shajing Sun and Niyazi Serdar Saracftci*
100. Handbook of Optical Interconnects, *edited by Shigeru Kawai*
101. GMPLS Technologies: Broadband Backbone Networks and Systems, *Naoaki Yamanaka, Kohei Shiomoto, and Eiji Oki*
102. Laser Beam Shaping Applications, *edited by Fred M. Dickey, Scott C. Holswade and David L. Shealy*
103. Electromagnetic Theory and Applications for Photonic Crystals, *Kiyotoshi Yasumoto*
104. Physics of Optoelectronics, *Michael A. Parker*
105. Opto-Mechanical Systems Design: Third Edition, *Paul R. Yoder, Jr.*
106. Color Desktop Printer Technology, *edited by Mitchell Rosen and Noboru Ohta*
107. Laser Safety Management, *Ken Barat*
108. Optics in Magnetic Multilayers and Nanostructures, *Štefan Višňovský*
109. Optical Inspection of Microsystems, *edited by Wolfgang Osten*

110. Applied Microphotonics, *edited by Wes R. Jamroz, Roman Kruzelecky, and Emile I. Haddad*
111. Organic Light-Emitting Materials and Devices, *edited by Zhigang Li and Hong Meng*
112. Silicon Nanoelectronics, *edited by Shunri Oda and David Ferry*
113. Image Sensors and Signal Processor for Digital Still Cameras, *Junichi Nakamura*
114. Encyclopedic Handbook of Integrated Circuits, *edited by Kenichi Iga and Yasuo Kokubun*
115. Quantum Communications and Cryptography, *edited by Alexander V. Sergienko*
116. Optical Code Division Multiple Access: Fundamentals and Applications, *edited by Paul R. Prucnal*
117. Polymer Fiber Optics: Materials, Physics, and Applications, *Mark G. Kuzyk*
118. Smart Biosensor Technology, *edited by George K. Knopf and Amarjeet S. Bassi*
119. Solid-State Lasers and Applications, *edited by Alphan Sennaroglu*
120. Optical Waveguides: From Theory to Applied Technologies, *edited by Maria L. Calvo and Vasudevan Lakshiminarayanan*
121. Gas Lasers, *edited by Masamori Endo and Robert F. Walker*
122. Lens Design, Fourth Edition, *Milton Laikin*
123. Photonics: Principles and Practices, *Abdul Al-Azzawi*
124. Microwave Photonics, *edited by Chi H. Lee*
125. Physical Properties and Data of Optical Materials, *Moriaki Wakaki, Keiei Kudo, and Takehisa Shibuya*
126. Microlithography: Science and Technology, Second Edition, *edited by Kazuaki Suzuki and Bruce W. Smith*
127. Coarse Wavelength Division Multiplexing: Technologies and Applications, *edited by Hans Joerg Thiele and Marcus Nebeling*
128. Organic Field-Effect Transistors, *Zhenan Bao and Jason Locklin*
129. Smart CMOS Image Sensors and Applications, *Jun Ohta*
130. Photonic Signal Processing: Techniques and Applications, *Le Nguyen Binh*
131. Terahertz Spectroscopy: Principles and Applications, *edited by Susan L. Dexheimer*
132. Fiber Optic Sensors, Second Edition, *edited by Shizhuo Yin, Paul B. Ruffin, and Francis T. S. Yu*
133. Introduction to Organic Electronic and Optoelectronic Materials and Devices, *edited by Sam-Shajing Sun and Larry R. Dalton*
134. Introduction to Nonimaging Optics, *Julio Chaves*
135. The Nature of Light: What Is a Photon?, *edited by Chandrasekhar Roychoudhuri, A. F. Kracklauer, and Katherine Creath*
136. Optical and Photonic MEMS Devices: Design, Fabrication and Control, *edited by Ai-Qun Liu*
137. Tunable Laser Applications, Second Edition, *edited by F. J. Duarte*

Tunable Laser Applications

Second Edition

Edited by

F. J. Duarte

CRC Press
Taylor & Francis Group
Boca Raton London New York

CRC Press is an imprint of the
Taylor & Francis Group, an **informa** business

CRC Press
Taylor & Francis Group
6000 Broken Sound Parkway NW, Suite 300
Boca Raton, FL 33487-2742

© 2009 by Taylor & Francis Group, LLC
CRC Press is an imprint of Taylor & Francis Group, an Informa business

No claim to original U.S. Government works
Printed in the United States of America on acid-free paper
10 9 8 7 6 5 4 3 2 1

International Standard Book Number-13: 978-1-4200-6009-6 (Hardcover)

This book contains information obtained from authentic and highly regarded sources Reasonable efforts have been made to publish reliable data and information, but the author and publisher cannot assume responsibility for the validity of all materials or the consequences of their use. The Authors and Publishers have attempted to trace the copyright holders of all material reproduced in this publication and apologize to copyright holders if permission to publish in this form has not been obtained. If any copyright material has not been acknowledged please write and let us know so we may rectify in any future reprint

Except as permitted under U.S. Copyright Law, no part of this book may be reprinted, reproduced, transmitted, or utilized in any form by any electronic, mechanical, or other means, now known or hereafter invented, including photocopying, microfilming, and recording, or in any information storage or retrieval system, without written permission from the publishers.

For permission to photocopy or use material electronically from this work, please access www.copyright.com (http://www.copyright.com/) or contact the Copyright Clearance Center, Inc. (CCC) 222 Rosewood Drive, Danvers, MA 01923, 978-750-8400. CCC is a not-for-profit organization that provides licenses and registration for a variety of users. For organizations that have been granted a photocopy license by the CCC, a separate system of payment has been arranged.

Trademark Notice: Product or corporate names may be trademarks or registered trademarks, and are used only for identification and explanation without intent to infringe.

Library of Congress Cataloging-in-Publication Data

Tunable laser applications / by Frank Duarte [editor]. --2nd ed.
p. cm.
Includes bibliographical references and index.
ISBN-13: 978-1-4200-6009-6
ISBN-10: 1-4200-6009-0
1. Tunable lasers. I. Duarte, F. J. (Frank J.) II. Title.

TA1706.T82 2008
621.36'6--dc22 2008008266

Visit the Taylor & Francis Web site at
http://www.taylorandfrancis.com

and the CRC Press Web site at
http://www.crcpress.com

Dedicated to the explorers that created the field of broadly tunable lasers . . . discovering new gain media, resonators . . . oscillators.

Contents

List of Figures xiii
List of Tables xxiii
Note to the First Edition from the Series Editor xxv
Preface to the Second Edition xxvii
About the Editor xxix
Contributors xxxi

Chapter 1 Introduction 1
F. J. Duarte

Chapter 2 Spectroscopic Applications of Tunable Optical Parametric Oscillators 15
B. J. Orr, Y. He, and R. T. White

Chapter 3 Solid-State Dye Lasers 97
A. Costela, I. García-Moreno, and R. Sastre

Chapter 4 Tunable Lasers Based on Dye-Doped Polymer Gain Media Incorporating Homogeneous Distributions of Functional Nanoparticles 121
F. J. Duarte and R. O. James

Chapter 5 Broadly Tunable External-Cavity Semiconductor Lasers 143
F. J. Duarte

Chapter 6 Tunable Fiber Lasers 179
T. M. Shay and F. J. Duarte

Chapter 7 Fiber Laser Overview and Medical Applications 197
S. Popov

Chapter 8 Medical Applications of Dye Lasers 227
A. Costela, I. García-Moreno, and R. Sastre

Chapter 9 Biological Microscopy with Ultrashort Laser Pulses 245
J. L. Thomas and W. Rudolph

Chapter 10 Pulsed, Tunable, Monochromatic X-Rays: Medical and Nonmedical Applications 281

F. E. Carroll

Chapter 11 Lithium Spectroscopy Using Tunable Diode Lasers 311

I. E. Olivares

Chapter 12 Interferometric Imaging 341

F. J. Duarte

Chapter 13 Multiple-Prism Arrays and Multiple-Prism Beam Expanders: Laser Optics and Scientific Applications 375

F. J. Duarte

Chapter 14 Coherent Electrically Excited Organic Semiconductors 389

F. J. Duarte

Chapter 15 Appendix on Optical Quantities and Conversions of Units 405

F. J. Duarte

Index 409

List of Figures

Figure 2.1 Schematic diagrams of three forms of optical parametric device: (a) optical parametric generator; (b) optical parametric amplifier; (c) optical parametric oscillator. 18
Figure 2.2 Schematic diagrams of three forms of optical parametric oscillator: (a) free-running OPO (with no active wavelength control), similar to Figure 2.1(c); (b) OPO with an intracavity tuning element (T); (c) injection-seeded OPO. 35
Figure 2.3 Schematic diagram of an injection-seeded tunable ns-pulsed OPO system, based on a multigrating PPLN chip with active intensity-dip cavity control. 43
Figure 2.4 Schematic diagram of a narrowband OPO, pumped by a ns-pulsed laser at wavelength λ_P and tuned by injection seeding a SAT optical cavity. 45
Figure 2.5 Injection-seeded, ns-pulsed tunable OPO with an OH detection system that is able to log the chirp and other instantaneous-frequency characteristics of each signal output pulse. 46
Figure 2.6 Illustration of the Fourier-transform chirp analysis procedure applied to signal output from a long-pulse injection-seeded PPKTP OPO. 48
Figure 3.1 Schematic energy level diagram for a typical dye molecule. 98
Figure 3.2 UV/VIS absorption and fluorescence spectra of the laser dye pyrromethene 567 in methanol solution. 99
Figure 3.3 Molecular structures of some commercial dipyrromethene. BF_2 complexes. 102
Figure 3.4 Molecular structures of some monomers used in solid-state dye lasers: methyl methacrylate (MMA), 2-hydroxyethyl methacrylate (HEMA), 2,2,2,-trifluoroethyl methacrylate (TFMA), trimethylolpropane trimethacrylate (TMPTMA), pentaerythritol triacrylate (PETA), and pentaerythritol tetraacrylate (PETRA). 103
Figure 3.5 Normalized laser output as a function of the number of pump pulses for PM567 dissolved in copolymers of MMA and PETRA. 104

Figure 3.6 Molecular structures of modified dipyrromethene. BF_2 complexes. 105
Figure 3.7 Percent intensity (referred to as initial intensity) of the laser output from a number of newly synthesized dipyrromethene. BF_2 dyes incorporated into linear and cross-linked copolymers of MMA, after 60,000 pump pulses at the same position of the sample. 106
Figure 3.8 Evolution of the normalized laser output of monomer dye P5MA linked covalently to polymer matrix with composition MMA-PETRA 95:5, model dye P5Ac dissolved in the same matrix, and dye PM567 dissolved in PMMA. 107
Figure 3.9 Evolution of the normalized laser output of PM597 in copolymers of MMA with fluorinated monomers at 30 Hz repetition rate. 108
Figure 3.10 Evolution of the output power as a function of time of PM567 and Rh6G in different polymeric media when pumped with a copper-vapor laser at 1 kHz repetition rate. 109
Figure 3.11 Evolution of the output power as a function of time of PM567 and Rh6G in different polymeric media when pumped with a Nd:YLF (second harmonic) laser at 10 kHz repetition rate. 109
Figure 3.12 Molecular structure of inorganic alkoxides TEOS, TMOS, TRIEOS, and DEOS. 112
Figure 3.13 Normalized laser output as a function of the number of pump pulses for PM567 (1.5×10^{-3} M) in hybrid matrices. 113
Figure 3.14 Normalized laser output as a function of the number of pump pulses for PM597 (6×10^{-4} M) in hybrid matrices of P(HEMA-MMA 1:1) with different wt% proportions of TRIEOS: (a) 15% and 10 Hz; (b) 15% and 30 Hz; and (c) 5% and 30 Hz. 114
Figure 3.15 Normalized laser output as a function of the number of pump pulses for PM567 (1.5×10^{-3} M) incorporated into (a) silica aerogel filled with the copolymer COP(MMA:TFMA 7:3), and (b) organic matrix, without silica aerogel. 115
Figure 3.16 Molecular structure of monomer 3-TMSPMA. 116
Figure 3.17 Normalized laser output as a function of the number of pump pulses for dye PM567 in (a) COP(MMA:TMSPMA 3:7) and (b) COP(HEMA:TMSPMA 7:3), and for dye PM597 in (c) COP(HEMA:TMSPMA 7:3) and (d) TERP(MMA:HEMA:TMSPMA 5:5:10). 116
Figure 3.18 Normalized laser output as a function of the number of pump pulses in the same position of the sample for dye PM597 in silicon-modified organic matrix. 117
Figure 4.1 Solid-state HMPGI grating laser oscillator. 123
Figure 4.2 Optimized solid-state MPL grating laser oscillator. 124
Figure 4.3 Long-pulse MPL grating laser oscillator. 125
Figure 4.4 Synthesis-manufacturing process for DDPN gain media. 127

Figure 4.5 Distorted beam profile, following propagation through an inhomogeneous dye-doped organic-inorganic gain medium. 129
Figure 4.6 Preservation of laser beam profile, following propagation through a homogeneous dye-doped polymer gain medium. 130
Figure 4.7 Mirror-grating cavity used in the DDPN gain media experiments. 130
Figure 4.8 Conservation of TEM_{00} beam profile following propagation through a DDPN gain media at 30% w/w SiO_2. 131
Figure 4.9 Laser beam profile generated with a mirror-grating resonator incorporating a Rhodamine 6G DPN gain medium. 132
Figure 4.10 Nanograph of the Rhodamine 6G DDPN solid-state laser matrix. 134
Figure 4.11 Nanograph of the coumarin 500 DDPN solid-state laser medium. 135
Figure 4.12 Simple diagram of a core-shell particle depicting the various parameters included in Equation 4.16. 137
Figure 5.1 Open-cavity configurations: (a) mirror-grating cavity incorporating intracavity étalons; (b) single-prism grating cavity; and (c) grazing-incidence grating cavity. 146
Figure 5.2 Closed-cavity configurations: (a) mirror-grating cavity and (b) mirror-grating cavity incorporating intracavity étalons. 147
Figure 5.3 MPL grating oscillator configurations: (a) the multiple-prism expander can be deployed in a (+, +, +, −) configuration or (b) a (+, −, +, −) configuration. 148
Figure 5.4 HMPGI grating laser oscillator. 149
Figure 5.5 Circular-beam close-cavity MPL grating laser oscillators: (a) moderate beam expansion corrects the asymmetry of the vertically elongated beam and enhances the dispersion of the cavity via the expanded illumination of a transmission diffraction grating; (b) beam expansion at both ends of the cavity. 149
Figure 5.6 Generalized multiple-prism array deployed in (a) an additive configuration and (b) a compensating configuration. 152
Figure 5.7 Wavelength tuning using the displacement of one of the mirrors of the resonator thus effectively changing the length of the cavity *L*. 162
Figure 5.8 Ultrashort-pulse ECS laser using a six-prism array to control the value of the GVD. 167
Figure 5.9 Dependence of pulse shape as a function of intracavity prism separation in the six-prism ECS laser. 168
Figure 5.10 Grating tuned passively modelocked MQW laser using grating-pair compressor. 168
Figure 6.1 Dual-clad gain fiber configuration. 181
Figure 6.2 Littrow diffraction grating tuned rare-earth-doped fiber laser. 183

Figure 6.3 Grazing-incidence (GI) diffraction grating tuned rare-earth-doped fiber laser. 183
Figure 6.4 (a) Flexible beam of thickness d with fiber Bragg grating glued to the beam. (b) Flexible beam bent at radius of curvature R with compressed fiber Bragg grating. 185
Figure 6.5 Generic linear cavity all-fiber tunable rare-earth-doped fiber laser. 186
Figure 6.6 Generic unidirectional ring cavity all-fiber tunable rare-earth-doped fiber laser. 186
Figure 6.7 Multiple-prism Littrow (MPL) grating configuration for narrow-linewidth tunable fiber lasers. 189
Figure 6.8 A multiring cavity all-fiber tunable Er-doped fiber laser. 192
Figure 7.1 General applications of lasers in medicine and life sciences. 200
Figure 7.2 Classical design of fiber laser using SESAM as a back mirror. 204
Figure 7.3 Modelocked fiber laser with loop-mirror cavity design with nonlinear fiber to obtain fs-pulse generation. 204
Figure 7.4 Schematic overview of most typical PCF cross-sections. 205
Figure 7.5 Examples of crystal fibers designed for double-cladding pumping schemes and supercontinuum fiber laser sources. 205
Figure 7.6 Energy levels of thulium (Tm^{3+}) ions, showing how multiphoton excitation with 1123 nm wavelength results in blue fluorescence through upconversion. 206
Figure 7.7 Double-clad PCF providing high NA acceptance of the pumping beam. 208
Figure 7.8 Different shapes of the double-clad fibers to improve pump-lasing modes overlapping. 208
Figure 7.9 Energy levels of erbium (Er^{3+}) ions and main transitions (in units of nm) in silica-based fibers used to get amplification and lasing. 210
Figure 7.10 The simplified fiber scheme for OCT. 211
Figure 7.11 Two-level transition structure for Yb^{3+} ions. 213
Figure 7.12 Selected set of energy levels of thulium (Tm^{3+}) in silica-fiber with pumping, absorption, and lasing transitions. 214
Figure 7.13 Simplified energy levels of Holmium (Ho^{3+}) in silica fiber. 216
Figure 7.14 Energy levels of co-doped Er^{3+}:Pr^{3+}:ZBLAN glass fiber. 217
Figure 7.15 Multimode fiber with zero-dispersion at the visible wavelength. 218
Figure 7.16 Comparison of supercontinuum spectra generated by different sources. 219
Figure 7.17 Air-cooled compact system SC450 generating supercontinuum radiation within 450–2000 nm bandwidth. 220
Figure 9.1 (a) Schematic diagram of scanning microscopy with short-pulse illumination producing an imaging signal P_{im} while either the focused laser beam or the sample is raster-scanned. (b) A laser beam focused into a sample. 247

Figure 9.2 (a) Pulse duration at the sample location as a function of the pulse duration out of the laser for different lengths of BK7 glass paths. (b) Normalized image signal for $n = 2$ as a function of the pulse duration produced by the laser for different BK7 glass paths. 251
Figure 9.3 (a) Excitation geometry of surface plasmons at the interfaces of an Au film and air. (b) Duration of the excitation relative to the incident pulse duration as a function of the incident pulse duration for different spot sizes at sample location A. 252
Figure 9.4 (a) Distribution of fluorescence emission for increasing intensities of spatially sinusoidal illumination, $I(x) = I_0 \sin(kx)$. (b) A Gaussian illumination profile (black line) will give a fluorescence distribution that is equally broad, in the absence of saturation. 254
Figure 9.5 (a) Imaging through scattering layers with short-pulse illumination. (b) Schematic diagram of confocal gating. (c) Parameter space (numerical aperture versus thickness of the scattering layer μd) in which imaging is possible (contrast $C > 1$) with confocal microscopy with and without fs time gating of the detection. 255
Figure 9.6 The essential part of a fs oscillator is an element or process that represents loss that decreases with intensity. 258
Figure 9.7 Deep tissue imaging using two-photon fluorescence and pulses from a Ti:sapphire regenerative amplifier. 261
Figure 9.8 Second harmonic generation *is* possible in centrosymmetric systems, such as liposomes. 266
Figure 9.9 Second harmonic generation (top) and two-photon excited fluorescence (bottom) from two adherent liposomes labeled in their outer leaflets with the dye di-6-ASPBS. 267
Figure 9.10 Energy level diagrams illustrating how certain terms in the perturbation expansion for $\chi^{(3)}$ are enhanced by resonance with molecular energy eigenstates. 270
Figure 9.11 A comparison of collinear CARS (F-CARS) and epi-CARS microscopy on unstained epithelial cells, with $\omega_p - \omega_s$ tuned to the fingerprint region for biomolecules (~1570 cm^{-1}). 274
Figure 9.12 Two-photon excited fluorescence and SPF images. 275
Figure 10.1 On the FEL, the electron beam entered from the left and the IR beam entered the beamline from the bottom. 282
Figure 10.2 The head-on collision accomplished in the Generation 2 device. 284
Figure 10.3 This machine (Generation 2) currently operates at the W. M. Keck Free-Electron Laser facility at Vanderbilt University. 285
Figure 10.4 In this embodiment, the laser sits atop the accelerator and the beamline is markedly shorter than that on the earlier devices. 289
Figure 10.5 Schematic difference between random events versus specifically targeting the DNA. 291

Figure 10.6 A photon tuned to the k-shell binding energy of the platinum atom will displace the electron from that orbit, while extinguishing the photon itself. 292
Figure 10.7 When the k-shell electron is displaced there is a cascade of outer shell electrons to replace the inner shell electrons, the Auger cascade. 292
Figure 10.8 Graphic representation of the percentage of lethal dose delivered to a tumor using a single rotating 50 keV monochromatic beam. 295
Figure 10.9 This shows the distribution of the dosage of radiation to the tumor and satellite lesion with a 7 MeV rotating beam. 296
Figure 10.10 Since the radiation in an Auger cascade is delivered within nanometers of the location of the target atom, it tends to break both DNA strands. 297
Figure 10.11 Side-by-side comparison of monochromatic and polychromatic images of a breast phantom showing simulated cancerous lesions seen to greatest advantage on the monochromatic image. 300
Figure 10.12 Sixty views, each performed with three degrees of rotation from the last were used to reconstruct a CT (3D) image of a breast phantom. 300
Figure 10.13 Standard x-ray absorption image of a mimosa blossom and twig using 10 keV monochromatic x-rays from a synchrotron. 303
Figure 10.14 Phase contrast image of the same mimosa blossom and twig demonstrating the marked improvement in visibility of structural detail. 303
Figure 11.1 Basic setup for saturation absorption spectroscopy. 312
Figure 11.2 Absorption (a) with and (b) without pump laser, Lamb dip. 313
Figure 11.3 Values of $N_{ifq} = |\langle i|D_q|f\rangle|^2/\|D\|^2$ for each transition of Li. 317
Figure 11.4 Doppler-free experimental setup. 320
Figure 11.5 (a) Doppler-limited ^{7}Li only and for the sum of ^{6}Li and ^{7}Li. (b) Optically thick Doppler-limited Li lines. 321
Figure 11.6 (a) Doppler-free spectrum at low Ar pressure: $P_{Ar} = 0.0018$ Torr, $I_P = 21$ W/m^2, n(Li) = 5×10^9 cm^{-3}, T = 375 °C. (b) Doppler-free spectrum at high Ar pressure: $P_{Ar} = 4.46$ Torr, $I_P = 79$ W/m^2, n(Li) = 5×10^9 cm^{-3}, $T = 375$ °C. 322
Figure 11.7 Energy level diagram for the two-step photoionization of lithium isotopes. 323
Figure 11.8 Apparatus diagram for the resonance ionization spectroscopy of lithium isotopes. 327
Figure 11.9 Typical RIS trace for the ^{6}Li and ^{7}Li isotopes. 328
Figure 11.10 Saturation curve for the absorption of the ^{7}Li D_2 line at 670.7764 nm. 329

Figure 11.11 Diagram of the mass separator. 331
Figure 11.12 Mass spectrum of mixed ^{7}Li/^{6}Li beta-eucryptite source. 334
Figure 11.13 Resonance ionization mass hyperfine spectrum recorded at the FC1. 334
Figure 11.14 Resonance ionization mass hyperfine spectrum recorded at the FC2. 335
Figure 12.1 Schematic of the interferometer. 345
Figure 12.2 (a) Generalized one-dimensional geometrical representation of the interferometric measurement. (b) Two-dimensional representation showing the zy plane that is orthogonal to the plane of propagation. 349
Figure 12.3 (a) Measurement of classical double slit interference. (b) Predicted interference pattern for the double-slit experiment using 50-μm-wide slits separated by 50 μm. 353
Figure 12.4 (a) Measured interferogram originating from a grating with 23 slits each 100 μm wide separated by 100 μm (center-to-center distance of 200 μm). (b) Theoretical reconstruction using the generalized interference equation. 354
Figure 12.5 (a) Measured interferogram originating from a grating with 25 slits each 100 μm wide separated by 100 μm (center-to-center distance of 200 μm). (b) Theoretical reconstruction using the generalized interference equation. 355
Figure 12.6 (a) Measured interferogram originating from a grating with 100 slits 30 μm wide separated by 30 μm (center-to-center distance of 60 μm). (b) Corresponding theoretical reconstruction using the generalized interference equation. 356
Figure 12.7 Theoretical interferogram for the grating composed of 100 slits 30 μm wide separated by 30 μm (center-to-center distance of 60 μm) and assuming a ≤2% uncertainty in the width of the slits. 357
Figure 12.8 Theoretical diffraction near-field pattern originating from a 4-mm-wide aperture. 358
Figure 12.9 Theoretical interference patterns for the (a) grating with 25 slits 100 μm wide (at a grating-to-screen distance of 25 cm) and (b) the grating with 100 slits 30 μm wide (at a grating-to-slit distance of 75 cm). 359
Figure 12.10 (a) Intensity profile, as a function of radial distance along the expanded axis, of the elongated Gaussian beam following propagation in air. (b) Intensity profile of the elongated Gaussian beam following propagation via a thin microscope slide. 360
Figure 12.11 (a) Intensity profile of the elongated Gaussian beam following propagation via a thin microscope slide with some dust particles deposited on it. (b) Intensity profile of a neutral density filter with an optical density of 4. 361

Figure 12.12 (a) Elongated Gaussian beam profile transmitted via a smooth thin glass substrate. (b) Interferometric profile of a high-quality clear polymeric film substrate. (c) Interferometric profile of a lesser-quality clear polymeric film substrate showing the effect of surface irregularities. 362
Figure 12.13 Schematics of the polarizer multiple-prism multiple laser (PMPML) printer. 365
Figure 12.14 Interferometric character "c" generated by the interaction of an expanded TEM_{00} laser beam with four equidistant slits. 367
Figure 12.15 Severe spatial distortions induced in the interferometric character c by introducing a thin beam splitter at an angle near the Brewster angle relative to the axis of propagation. 368
Figure 12.16 Spatial distortions in the interferometric character c with the thin beam splitter in place. 368
Figure 12.17 Removal of the beam splitter restores the original interferometric character c. 369
Figure 12.18 Cumulative spatial distortions in the interferometric character "c" caused by turbulence in the propagation air generated by a thermal source. 369
Figure 12.19 Single-layered textile 25×25 mm approximately. 370
Figure 12.20 Interferometric signature of single-layered textile. 370
Figure 13.1 Generalized multiple-prism array deployed in (a) an additive configuration and (b) a compensating configuration. 377
Figure 13.2 Multiple-prism expander, $r = 3$, designed for orthogonal beam exit. 379
Figure 13.3 The plane of the slits (j) illustrating incidence above the normal $+\Theta_m$ and diffraction below the normal $-\Phi_m$. 381
Figure 13.4 The plane of the slits (j) illustrating incidence below the normal $-\Theta_m$ and diffraction below the normal $-\Phi_m$. 381
Figure 14.1 Optimized multiple-prism grating tunable laser oscillator incorporating an organic dye-doped polymer gain medium. 390
Figure 14.2 Smooth near-Gaussian temporal profile of the single-longitudinal-mode emission. 391
Figure 14.3 Silver-halide photograph of a Fabry–Perot interferogram showing single-longitudinal-mode emission at a laser linewidth of $\Delta\nu \approx 350$ MHz. 391
Figure 14.4 Molecular structure for the coumarin 545 tetramethyl (C545T) dye. 393
Figure 14.5 Transversely excited C545T dye laser. 394
Figure 14.6 Laser tuning curve of the C545T laser at a concentration of 2 mM in ethanol. 394
Figure 14.7 Schematics of the electrically excited DICOS emitter powered by a submicron cavity with a length of $l \approx 300$ nm. 395
Figure 14.8 Beam profile recorded using black-and-white photographic film at a distance of $z \approx 340$ mm. 396

Figure 14.9 Beam profile from the DICOS emitter while under the excitation of nanosecond pulses at an amplitude of ~10 kV. 397
Figure 14.10 Interferogram of the radiation from the DICOS emitter, at $\lambda \approx$ 540 nm, for $z \approx 50$ mm. 398
Figure 14.11 Interferogram using the identical interferometer of radiation from a He–Ne laser, at $\lambda \approx 543.3$ nm, for $z \approx 50$ mm. 398
Figure 14.12 Interferometric comparison of the emission from the high-power C545T dye laser (a) and the emission from the DICOS emitter (b). 399

List of Tables

Table 1.1 Wavelength Range of Broadly Tunable Coherent Sources in the Pulsed Regime 2

Table 1.2 Short Pulse Emission Characteristics of Broadly Tunable Coherent Sources 2

Table 1.3 Energetic Characteristics of Broadly Tunable Coherent Sources in the Pulsed Regime 3

Table 1.4 Emission Characteristics Available from Broadly Tunable Sources of Coherent Radiation in the CW Regime 3

Table 1.5 Spectral Emission Characteristics of Discretely Tunable High-Power Pulsed Lasers 4

Table 2.1 Characteristics of Selected NLO Crystals Commonly Used in Near-IR and Mid-IR Optical Parametric Devices 26

Table 2.2 Typical Operating Regimes for Different Classes (Labeled A–D) of Single-Pass Optical Parametric Gain Process 28

Table 2.3 Operational Strategies for OPOs Applied to Spectroscopy 33

Table 2.4 Performance Characteristics of Various ns-Pulsed and CW Tunable Optical-Parametric Systems That Are Spectroscopically Measured under Doppler-Limited Experimental Conditions 52

Table 2.5 Performance Characteristics of Various ns-Pulsed and CW Tunable Optical-Parametric Systems That Are Spectroscopically Measured under Sub-Doppler Experimental Conditions 55

Table 3.1 Laser Parameters for Dye PM567 Dissolved in Homopolymer PMMA and Cross-Linked Copolymers (COP) 104

Table 3.2 Laser Parameters for Model (P*n*Ac, PAr*n*Ac) and Monomeric (P*n*MA, PAr*n*MA) Dyes in COP and Terpolymers (TERP) 106

Table 4.1 Performance of Narrow-Linewidth Solid-State Dye Laser Oscillators 124

Table 4.2 Mass Balances for Starting Components in Solid-State DDPN Gain Media 128
Table 4.3 Performance of Solid-State Lasers Incorporating DDP and DDPN Gain Matrices Using Rhodamine 6G Dye 132
Table 4.4 $\partial n/\partial T$ in DDP and PN Matrices 133
Table 4.5 Dimensions of the Silicate Structure in the DDPN Matrices 135
Table 5.1 Approximate Wavelength Ranges Covered by Broadly Tunable Semiconductor Lasers 144
Table 5.2 Performance of External-Cavity Semiconductor Lasers 165
Table 5.3 Performance of External-Cavity Semiconductor Lasers Using Alternative Tuning Methods 166
Table 5.4 Performance of Ultrashort-Pulse External-Cavity Semiconductor Lasers 169
Table 5.5 Brief Survey of ECS Laser Applications 171
Table 6.1 Characteristics of Er-Doped Tunable Fiber Lasers 191
Table 6.2 Characteristics of Tunable Yb- and Tm-Doped Fiber Lasers 191
Table 7.1 Main Laser Types and Fields of Applications in Medicine 199
Table 7.2 Rare-Earth Metal Ions Commonly Used in Fiber Lasers and Laser Applications in Medicine 210
Table 9.1 Laser Sources Used as Illumination Sources for Nonlinear Microscopy and Their Typical Parameters 257
Table 10.1 Machine Specifications: Generation 3 Tunable, Monochromatic X-Ray Source 288
Table 12.1 Line-Tunable CW Lasers 343
Table 12.2 Broadly Tunable Dye Lasers in the Yellow-Orange-Red Region of the Spectrum 344
Table 12.3 Broadly Tunable External-Cavity Semiconductor Lasers 344
Table 15.1 Physical Constants 406
Table 15.2 Linewidth Equivalence for $\Delta\lambda \approx 0.000406$ nm at $\lambda \approx 590$ nm 406
Table 15.3 Photon-Energy Wavelength Equivalence 407

Note to the First Edition from the Series Editor

Even though Einstein set forth the basic idea of the process of stimulated emission about 90 years ago, it was not until the 1950s that the concept was used to propose and then develop the first laser. The first laser was not a reality until 1960. Today, of course, lasers are in wide use in all sorts of systems with all sorts of powers and a wide variety of wavelengths. It is not surprising that a considerable body of literature exists. We add to that literature with this important work on tunable lasers and their applications. Tunability has added an important dimension to a variety of laser devices and led to new systems and applications. The concept of tunability and specific applications are described in this work by a group of experienced technicians, scientists, and leaders of the field, including F. J. Duarte, who also edits the volume.

Brian J. Thompson
University of Rochester
Rochester, New York

Preface to the Second Edition

Broadly tunable lasers have had a tremendous impact in many and diverse fields of science and technology. From a renaissance in laser spectroscopy, to Bose–Einstein condensation, the one nexus is the tunable laser. In this regard, numerous applications from physics, to isotope separation, and all the way to medicine, depend on the tunable laser. It is indeed a pleasure to offer, to the scientific community, this updated and enlarged second edition of *Tunable Laser Applications.* As editor, I remain indebted to all the contributing authors.

F. J. Duarte
Rochester, New York

About the Editor

F. J. Duarte is a research physicist with Interferometric Optics, Rochester, New York, and adjunct professor at the Electrical and Computer Engineering Department, University of New Mexico. He graduated with first-class honors in physics from Macquarie University (Sydney, Australia), where he was also awarded a PhD in physics for his research on optically pumped molecular lasers. He is the author of the generalized multiple-prism dispersion theory, has made various unique contributions to the physics and architecture of tunable laser oscillators, and has pioneered the use of Dirac's notation in classical optics. These contributions have found applications in the design of laser resonators, laser pulse compression, imaging, medicine, spectroscopy, and the nuclear industry. He is author and editor of *Dye Laser Principles*, *High-Power Dye Lasers*, *Selected Papers on Dye Lasers*, and *Tunable Lasers Handbook*. He is also the author of *Tunable Laser Optics*. Dr. Duarte received the Engineering Excellence Award from the Optical Society of America and is a fellow of both the Australian Institute of Physics and the Optical Society of America.

Contributors

F. E. Carroll
MXISystems
Fairview, Tennessee and
Vanderbilt University Medical Center
Nashville, Tennessee

A. Costela
Instituto de Química Física "Rocasolano"
CSIC
Madrid, Spain

F. J. Duarte
Interferometric Optics
Rochester, New York and
The University of New Mexico
Albuquerque, New Mexico

I. García-Moreno
Instituto de Química Física "Rocasolano"
CSIC
Madrid, Spain

Y. He
MQ Photonics Research Centre
Macquarie University
Sydney, Australia

R. O. James
QED Technologies
Rochester, New York

I. E. Olivares
Universidad de Santiago
Santiago, Chile

B. J. Orr
MQ Photonics Research Centre
Macquarie University
Sydney, Australia

S. Popov
Royal Institute of Technology
Stockholm, Sweden

W. Rudolph
The University of New Mexico
Albuquerque, New Mexico

R. Sastre
Instituto de Ciencia y Tecnología de Polímeros
CSIC
Madrid, Spain

T. M. Shay
Air Force Research Laboratory
Kirtland Air Force Base, New Mexico

J. L. Thomas
The University of New Mexico
Albuquerque, New Mexico

R. T. White
MQ Photonics Research Centre
Macquarie University
Sydney, Australia

1 Introduction

F. J. Duarte

CONTENTS

1.1 Introduction 1
1.2 Tunable Laser Complementarity 4
1.3 Tunable Laser Applications 5
1.4 Tunable Laser Applications: First Edition 6
1.5 Focus of This Book 6
Acknowledgments 9
References 9

1.1 INTRODUCTION

The ability to yield tunable coherent radiation enhances the applicability of a given laser substantially. Indeed, tunable lasers are among the most studied and successful lasers. For instance, the first broadly tunable laser, the *organic dye laser*, introduced circa 1966 [1–4], has enjoyed a significant amount of attention directed toward the study of its inherent physical properties and technology [5–12]. At the same time, these organic lasers have had a profound impact on a plethora of fields, including physics, spectroscopy, laser isotope separation, medicine, and astronomy [6, 13–16].

Today, the field of broadly tunable lasers includes an array of lasers, which has extended their applicability domain even further. In addition to the class of broadly tunable lasers there is a group of discretely tunable and/or line-tunable lasers. This latter class of laser, besides being able to shift emission frequency from transition to transition, can also be fine-tuned within the emission spectrum of a given transition. In the next few tables, basic tuning ranges and energetic properties of tunable sources of coherent radiation are provided to facilitate familiarity with their emission characteristics.

Table 1.1 lists the wavelength coverage published for various broadly tunable pulsed sources of coherent radiation, including the optical parametric oscillator (OPO) and the free electron laser (FEL). Table 1.2 lists reported short pulse durations demonstrated in several types of broadly tunable lasers, and Table 1.3 includes the energetic and power characteristics capabilities for tunable pulsed lasers.

Table 1.4 lists the emission characteristics from broadly tunable lasers in the continuous wave (CW) regime, including wavelength range and reported laser power. Although some types of lasers have been reported with higher-power figures,

TABLE 1.1
Wavelength Range of Broadly Tunable Coherent Sources in the Pulsed Regime

Tunable source	Spectral range
Dye laser	320 nm ≤ λ ≤ 1200 nm[a] [17]
$Ti^{3+}:Al_2O_3$ laser	660 nm ≤ λ ≤ 986 nm [18]
$Cr^{3+}:BeAl_2O_4$ laser	701 nm ≤ λ ≤ 818 nm [19]
Fiber laser[b]	980 nm ≤ λ ≤ 1070 nm [20]
OPO (BBO)	0.3 μm ≤ λ ≤ 3.0 μm [21]
OPO (KTP)	0.7 μm ≤ λ ≤ 4.0 μm [21]
Free electron laser	0.9 μm ≤ λ ≤ 10 μm[c] [22]
	830 nm ≤ λ ≤ 940 nm[d] [23]
	31 nm ≤ λ ≤ 32 nm [24]

[a] Tuning range resulting from the use of several dyes.
[b] Yb-doped fiber.
[c] The combined tuning range from various FEL facilities extends into the mm range.
[d] Large bandwidth.

at a single emission wavelength, these are not included given the emphasis on broad wavelength tunability. Extension of the tuning ranges cited in these tables can be established via nonlinear optical techniques [6, 11].

Spectral information on discretely tunable pulsed lasers is given in Table 1.5; line-tunable CW lasers such as Ar^+, Kr^+, He–Ne, and He–Cd are listed in Table 12.1 of Chapter 12. An interesting laser listed in Table 1.5 is XeF, as it can be classified as discretely tunable given the characteristics of its $B \rightarrow X$ transitions. However, the wide tunability of its $C \rightarrow A$ transition qualifies it as a broadly tunable laser. Notably, a distinct feature of the gas lasers listed in Table 1.5 is their ability to yield high-pulse energies and, in some cases, very high-average powers [16].

TABLE 1.2
Short Pulse Emission Characteristics of Broadly Tunable Coherent Sources

Tunable source	Δt
Dye laser	6 fs[a] [25]
$Ti^{3+}:Al_2O_3$ laser	5 fs[b] [26]
ECS[c] laser (AlGaAs)	200 fs[a] [27]
Fiber laser	24 fs [28]
OPO (BBO)	4 fs [29]
Free electron laser	25 fs [30]

[a] Using prismatic intracavity pulse compression.
[b] Using extracavity in addition to intracavity pulse compression.
[c] External-cavity semiconductor.

TABLE 1.3
Energetic Characteristics of Broadly Tunable Coherent Sources in the Pulsed Regime[a]

Tunable source	Pulse energy	Average power
Dye laser	400 J[b] [31]	2.5 kW[c] [16]
Ti^{3+}:Al_2O_3 laser	6.5 J[d] [32]	5.5 W[e] [33]
Cr^{3+}:$BeAl_2O_4$ laser	100 J [34]	
Fiber laser[f]	31 nJ [35]	3 W [35]
OPO (BBO)	>100 mJ [36]	5.4 W [37]
Free electron laser		100 W[g] [22]

[a] Energy and average power figures are from unrelated experiments.
[b] From a flashlamp-pumped dye laser.
[c] CVL-laser-pumped dye laser operating at a pulse repetition frequency (prf) of 13.2 kHz.
[d] Under flashlamp excitation.
[e] Under CVL excitation at a prf of 6.5 kHz.
[f] Oscillator amplifier configuration using a Tm-doped amplifier. System is tunable in the 1900–2040 nm region [35].
[g] Under broadly tunable conditions at the FEL of the Thomas Jefferson National Accelerator Facility. The average power can increase to over 10 kW at selected individual wavelengths [22].

TABLE 1.4
Emission Characteristics Available from Broadly Tunable Sources of Coherent Radiation in the CW Regime

Tunable source	Spectral range	CW power
Dye laser	365 nm ≤ λ ≤ 1000 nm[a] [38]	43 W[b] [39]
Ti^{3+}:Al_2O_3 laser	710 nm ≤ λ ≤ 870 nm[c] [40]	43 W[b,d] [41]
Cr^{3+}:$BeAl_2O_4$ laser	744 nm ≤ λ ≤ 788 nm [42]	6.5 W [42]
ECS laser (InGaAsP/InP)	1255 nm ≤ λ ≤ 1335 nm[e] [43]	≥1 mW [43]
ECS laser (GaAlAs)	815 nm ≤ λ ≤ 825 nm [44]	5 mW [44]
ECS laser array	750 nm ≤ λ ≤ 758 nm [45]	13.5 W [45]
OPO (PPLN)	3.3 μm ≤ λ ≤ 3.9 μm [46]	>1 W [46]
Fiber laser	1532 nm ≤ λ ≤ 1568 nm [47]	>100 W [47]

[a] Tuning range resulting from the use of several dyes.
[b] Under Ar^+ laser excitation.
[c] Tuning range of single-longitudinal-mode emission.
[d] Uses liquid-nitrogen cooling.
[e] Measured laser linewidth is $\Delta\nu \leq 100$ kHz [43].

TABLE 1.5
Spectral Emission Characteristics of Discretely Tunable High-Power Pulsed Lasers

Laser	Transition	Bandwidth (GHz)	Wavelength (nm)
ArF		~17,000[a] [48]	193
KrF	$B^2\Sigma^+_{1/2} - X^2\,\Sigma^+_{1/2}$	~10,500[a] [48]	248
XeCl	$B^2\Sigma^+_{1/2} - X^2\,\Sigma^+_{1/2}$	374 [49]	308
		397 [49]	308.2
XeF	B–X	187 [50]	351
		330 [50]	353
	C–A		466–514[a] [51]
N_2	$C^3\Pi_u$–$B^3\Pi_g$	203 [52]	337.1
HgBr		918 [53]	502
		1,012 [53]	504
Ca	$5^2S_{1/2}$–$4^2P_{3/2}$		373.7
Sr	$6^2S_{1/2}$–$5^2P_{3/2}$	2–12[b] [54]	430.5
Cd	$4^2F_{5/2}$–$5^2D_{3/2}$		533.7
Cu	$^2P_{3/2}$–$^2D_{5/2}$	7 [55]	510.5
	$^2P_{1/2}$–$^2D_{3/2}$	11 [55]	578.2
Au	$^2P_{1/2}$–$^2D_{3/2}$	1.5 [56]	627.8
Nd: YAG	$^4F_{3/2}$–$^4I_{11/2}$	15–32	1,064
CO_2	P14(00°1–10°0)[c]		10,532.09
	P16(00°1–10°0)		10,551.40
	P18(00°1–10°0)		10,571.05
	P20(00°1–10°0)	3–4[d] [57, 58]	10,591.04

[a] Tuning range.

[b] Variable-linewidth range.

[c] Emission transitions obtained in a hybrid CO_2 laser [58]. For a comprehensive listing of CO_2 laser transitions, see [59].

[d] Observed bandwidth in a transversely excited atmospheric pressure CO_2 laser in the absence of intracavity linewidth narrowing optics or injection from a CW CO_2 laser. Tunable narrow-linewidth emission, at $\Delta\nu \approx 107$ MHz, has been reported for this transition [60].

1.2 TUNABLE LASER COMPLEMENTARITY

The information in Tables 1.1 through 1.5 suggests that the field offers a wide variety of sources of tunable coherent radiation that have distinct optimal modes of operation. Hence, a useful generalized approach to the field should be from a perspective of complementarity. This principle of *tunable laser complementarity* [61, 62] offers a dual advantage, as it encourages the use of the most efficient and apt type of laser, for a given application, and the integration of different lasers into a single system if necessary. This latter approach has been fairly well demonstrated in hybrid laser systems using one class of laser at the oscillator stage and a different type of laser at the amplifier stage. Examples of these systems involve the use of a dye

laser oscillator and an XeF laser amplifier [51], a semiconductor laser oscillator in conjunction with a dye laser amplifier [63], and a solid-state dye laser oscillator [64] with an optical parametric oscillator (OPO) as amplifier [65]. A more well-known example of complementarity is the excitation of one class of laser by a different type of laser. Recent versions of this synergy are the fiber laser excitation of an optical parametric amplifier (OPA) [66], and the fiber laser excitation of tunable mid-IR solid-state lasers [67].

However, more fundamental than the skillful integration of hybrid systems is the appropriate, and most efficient, use of a laser system for a given application. For instance, if an application requires high-average powers, in the 580 nm $\leq \lambda \leq$ 590 nm region, the choice should still be a copper-vapor-laser (CVL)-pumped dye laser. If large pulsed energies, tens or hundreds of Joules per pulse, were necessary in the same spectral region, then a flashlamp-pumped dye laser would have to be considered. On the other hand, for an application requiring very narrow linewidth CW emission in the near infrared, an ECS laser should be preferred. Further still, for spectroscopic applications demanding considerable wavelength agility, throughout the visible, then an OPO system would be a most attractive option. In this context, at present, tunable fiber lasers appear best suited for applications requiring high-CW powers in the near infrared. This perspective of complementarity is compatible with the rationale that, under ideal conditions, *it should be the application that determines the use of a particular laser* [68, 69]. Note that under this utilitarian rationale, complementarity does not marginalize competition.

The logic to determine the usefulness of a given laser for an application of interest should follow the criteria of providing tunable coherent radiation, at a given spectral region, within specified emission parameters, using the simplest and most efficient means. However, in practice this approach can be complicated by extraneous issues such as existing managerial guidelines or cost constraints.

In the absence of extraneous constraints, parameters that should determine the suitability of a laser to a given application include required spectral region of emission, tuning range, output power or energy, emission linewidth, and ASE level. In the case of pulsed lasers, pulse duration and prf can often be considered important parameters.

At this juncture, it should be mentioned that although the word *laser* has been used throughout this chapter, an important source of coherent tunable radiation, the OPO, does not involve the process of population inversion. Nevertheless, what is important is that this source emits tunable coherent radiation that is indistinguishable from laser radiation. Hence, the title of the book and the ample use of the word *laser* are justified.

1.3 TUNABLE LASER APPLICATIONS

Applications for tunable lasers are extraordinarily widespread and varied so that only a few highlights can be mentioned in this introduction. For instance, the dye laser alone has been applied to physics [70–72], astronomy [16], spectroscopy [15, 73–76], laser isotope separation [16, 77–92], material diagnostics [93], material processing [93, 94], remote sensing [93, 95, 96], defense [17, 84, 97], and medicine [98].

Tunable solid-state coherent sources have found numerous applications, including spectroscopy [21, 99, 100] and remote sensing [101]. A remarkable application of short pulse solid-state lasers has been their use in the generation of frequency combs for optical clockworks [102, 103], which has led to a revolution in high-precision optical measurements.

Tunable semiconductor lasers are particularly well suited for applications to atomic physics [104–106] and spectroscopy [107, 108]. These sources are also useful in metrology, interferometry, and imaging. Furthermore, simple, compact external-cavity tunable semiconductor lasers have made essential contributions to studies in laser cooling [105, 107] and Bose–Einstein condensation [109]. They have also been applied to laser isotope separation [110] and have become a central component in the field of optical communications [111].

1.4 TUNABLE LASER APPLICATIONS: FIRST EDITION

The first edition of *Tunable Laser Applications* [112], published in 1995, included the following chapters:

1. "Introduction," by F. J. Duarte
2. "Spectroscopic Applications of Pulsed Tunable Optical Parametric Oscillators," by B. J. Orr, M. J. Johnson, and J. G. Haub
3. "Dispersive External Cavity Semiconductor Lasers," by F. J. Duarte
4. "Applications of Ultrashort Pulses," by X. M. Zhao, S. Diddams, and J. C. Diels
5. "Interferometric Imaging," by F. J. Duarte
6. "Medical Applications of the Free Electron Laser," by F. E. Carroll and C. A. Brau
7. "Lidar for Atmospheric and Hydrospheric Studies," by W. B. Grant

In fairness to the readers it was decided not to reproduce a chapter unless this was updated at least by one of the original authors. Thus, Chapters 1, 2, 3, and 5 are included in the second edition of *Tunable Laser Applications* [113] in an expanded and updated format. In addition, nine new chapters extend considerably the scope and coverage of this second edition, which is introduced and explained in the next section.

1.5 FOCUS OF THIS BOOK

The purpose of this book is to focus on some topics that highlight the utilitarian ethos of tunable lasers. Hence, although some emphasis in this book is given to issues of current interest in tunable laser development, the underlying thread is *applications*. In this regard, the topics selected focus on applications judged to be of broad interest, historical significance, and sustained value: spectroscopy, selective laser excitation, biology, medicine, imaging, and interferometry. Among these, the most prevalent theme of interest in this second edition of *Tunable Laser Applications* is medicine and biomedical applications.

Although there is no predetermined order of presentation and each chapter can be read independently, Chapters 2 to 7 deal with issues of gain media, device physics, and technology. Chapter 2, written by B. J. Orr, Y. He, and R. T. White, is entitled "Spectroscopic Applications of Tunable Optical Parametric Oscillators" and leads given its wider spectral coverage and its extensive, and authoritative, discussion on spectroscopy, perhaps the most recognized and widespread application of sources of tunable coherent radiation. Environmental and biomedical applications are also considered. Chapter 3, authored by A. Costela, I. García-Moreno, and R. Sastre, is entitled "Solid-State Dye Lasers" and focuses on solid-state dye lasers with a thorough emphasis on organic and organic-inorganic gain media. Chapter 4, by F. J. Duarte and R. O. James, is entitled "Tunable Lasers Based on Dye-Doped Polymer Gain Media Incorporating Homogeneous Distributions of Functional Nanoparticles" and provides a performance survey of tunable narrow-linewidth solid-state dye lasers and describes the characteristics of new dye-doped polymer gain media incorporating homogeneous nanoparticle distributions. Chapter 5, by F. J. Duarte, entitled "Broadly Tunable External-Cavity Semiconductor Lasers," focuses on the performance of dispersive external-cavity semiconductor lasers and describes intracavity optics and tuning methods, which are also relevant to other tunable sources of coherent radiation discussed in this book. Both Chapters 4 and 5 include a brief survey of biomedical applications. Chapter 6, written by T. M. Shay and F. J. Duarte, is entitled "Tunable Fiber Lasers" and focuses on the main approaches currently used to achieve tunability in these lasers. This is followed by Chapter 7, by S. Popov, which is entitled "Fiber Laser Overview and Medical Applications." This chapter provides a survey of fiber laser gain media and introduces the reader to the medical applications of these lasers. This chapter signals the shift in emphasis in the book toward biomedical applications.

The emphasis on medical and biomedical applications becomes a central theme in Chapter 8. This chapter is authored by A. Costela, I. García-Moreno, and R. Sastre, and is entitled "Medical Applications of Dye Lasers." This work provides an extensive survey of the applications of tunable dye lasers to medicine, including subjects such as dermatology, photodynamic therapy, and lithotripsy. Chapter 9, written by J. L. Thomas and W. Rudolph, is entitled "Biological Microscopy with Ultrashort Laser Pulses" and provides a thorough description of modern microscopy techniques, including coherent microscopy, nonlinear microscopy, and harmonic microscopy. The biomedical emphasis is concluded in Chapter 10, which is authored by F. E. Carroll and is entitled "Pulsed, Tunable, Monochromatic X-Rays: Medical and Nonmedical Applications." This work is based on tunable x-rays produced by laser-induced plasmas.

The remaining three chapters extend the utilitarian scope of this book by including an array of laser-based applications. Chapter 11, by I. E. Olivares, is entitled "Lithium Spectroscopy Using Tunable Diode Lasers" and discusses the use of external-cavity tunable narrow-linewidth semiconductor, or diode, lasers in the spectroscopy and selective sequential excitation of lithium isotopes. Chapter 12, by F. J. Duarte, is entitled "Interferometric Imaging" and discusses the use of lasers and tunable lasers in *N*-slit interferometry. These interferometric applications include imaging, coherent microscopy, free-space optical

communications, and biomedical applications. Chapter 13, by F. J. Duarte, is entitled "Multiple-Prism Arrays and Multiple-Prism Beam Expanders: Laser Optics and Scientific Applications" and provides a brief referenced survey of numerous fields of applications that use multiple-prism arrays deployed either directly, within a narrow-linewidth tunable laser, or within an ultrashort pulse laser. A description of recent experiments on electrically excited pulsed organic semiconductors entitled "Coherent Electrically Excited Organic Semiconductors," by F. J. Duarte, is given in Chapter 14. The book concludes with an appendix (Chapter 15) listing useful optical quantities and explaining the linewidth equivalence.

Although the emphasis in this new edition of *Tunable Laser Applications* is on biomedical and medical applications of tunable lasers, a plethora of other applications are mentioned in various degrees of detail. In alphabetical order the applications mentioned are:

Astronomy
Atmospheric sensing
Atomic physics
Atomic spectroscopy
Characterization of textiles
Coherent anti-Stokes Raman scattering (CARS) microscopy
Coherent microscopy
Communications
Densitometry
Digital imaging
Digital microscopy
Environmental monitoring
Harmonic microscopy
Interferometric communications
Interferometric imaging
Interferometry
Laser cooling
Laser isotope separation
Laser printing
Lidar
Medical applications of dye lasers
Medical applications of fiber lasers
Medical applications of tunable x-ray sources
Microdensitometry
Molecular imaging
Molecular spectroscopy
Nanoparticle transparency
Nonlinear microscopy
Optical coherence tomography (OCT)
Optical metrology
Ultrashort pulse microscopy

Those applications simply included in this list are just referenced. Applications highlighted in *italics* are described in some detail, and those highlighted in ***bold italics*** are treated in greater depth.

ACKNOWLEDGMENTS

This second edition of *Tunable Laser Applications* has been made possible by the support of *Interferometric Optics* and the integrated effort of the contributing authors. In addition to discussions of laser physics and technology they have provided an up-to-date and vibrant description of an enormous variety of applications of tunable sources of coherent radiation. For various comments and criticisms, during the composition of this introduction, the author is grateful to Dr. R. O. James and Dr. S. Y. Popov.

REFERENCES

1. Sorokin, P. P., and J. R. Lankard, Stimulated emission observed from an organic dye, chloroaluminum phthalocyanine, *IBM J. Res. Dev.* 10: 162–163 (1966).
2. Schäfer, F. P., W. Schmidt, and J. Volze, Organic dye solution laser, *Appl. Phys. Lett.* 9: 306–309 (1966).
3. Soffer, B. H., and B. B. McFarland, Continuously tunable narrow-band organic dye lasers, *Appl. Phys. Lett.* 10: 266–267 (1967).
4. Stepanov, B. I., A. N. Rubinov, and V. A. Mostovnikov, Optic generation in solutions of complex molecules, *JETP Lett.* 5: 117–119 (1967).
5. Schäfer, F. P. (Ed.), *Dye Lasers*, Springer-Verlag, Berlin, 1990.
6. Duarte, F. J., and L. W. Hillman (Eds.), *Dye Laser Principles*, Academic, New York, 1990.
7. Duarte, F. J. (Ed.), *High Power Dye Lasers*, Springer-Verlag, Berlin, 1991.
8. Stuke, M. (Ed.), *Dye Lasers: 25 Years*, Springer-Verlag, Berlin, 1992.
9. Duarte, F. J. (Ed.), *Selected Papers on Dye Lasers*, SPIE Optical Engineering Press, Bellingham, WA, 1992.
10. Duarte, F. J. (Ed.), *Tunable Lasers Handbook*, Academic, New York, 1995.
11. Duarte, F. J., *Tunable Laser Optics*, Elsevier-Academic, New York, 2003.
12. Maeda, M., *Laser Dyes*, Academic, New York, 1984.
13. Radziemski, L. J., R. W. Solarz, and J. A. Paisner (Eds.), *Laser Spectroscopy and Its Applications*, Marcel Dekker, New York, 1987.
14. Duarte, F. J., J. A. Paisner, and A. Penzkofer, Dye lasers: introduction by the feature editors, *Appl. Opt.* 31: 6977–6878 (1992).
15. Demtröder, W., *Laser Spectroscopy*, 3rd ed., Springer, Berlin, 2003.
16. Bass, I. L., R. E. Bonanno, R. P. Hackel, and P. R. Hammond, High-average-power dye laser at Lawrence Livermore National Laboratory, *Appl. Opt.* 31: 6993–7006 (1992).
17. Duarte, F. J., and L. W. Hillman, Introduction, in *Dye Laser Principles*, edited by F. J. Duarte and L. W. Hillman, Academic, New York, 1990, Chap. 1.
18. Moulton, P. F., Spectroscopic and laser characteristics of Ti:Al_2O_3, *J. Opt. Soc. Am. B* 3: 125–132 (1986).
19. Walling, J. C., O. G. Peterson, H. P. Jenssen, R. C. Morris, and E. W. O'Dell, Tunable alexandrite lasers, *IEEE J. Quantum Electron*. QE-16: 1302–1315 (1980).
20. Okhonikov, O. G., L. Gomes, N. Xiang, T. Jouhti, and A. B. Grudinin, Mode-locked ytterbium fiber laser tunable in the 980–1070 nm spectral range, *Opt. Lett.* 28: 1522–1524 (2003).

21. Orr, B. J., M. J. Johnson, and J. B. Haub, Spectroscopic applications of pulsed tunable optical parametric oscillators, in *Tunable Laser Applications*, 1st ed., edited by F. J. Duarte, Marcel Dekker, New York, 1995, Chap. 2.
22. Benson, S. V., Private communication (2007).
23. Andonian, G., A. Murokh, J. B. Rosenzweig, R. Agustsson, M. Babzien, I. Ben-Zvi, P. Frigola, J. Y. Huang, L. Palumbo, C. Pellegrini, S. Reiche, G. Travish, C. Vicario, and V. Yakimenko, Observations of anomalously large spectral bandwidth in a high-gain self-amplified spontaneous emission free electron laser, *Phys. Rev. Lett.* 95: (2005), doi:10.1103/PhysRevLett.95.054801.
24. Düsterer, S., P. Radcliffe, G. Geloni, U. Jastrow, M. Kuhlmann, E. Plönjes, K. Tiedke, P. Nicolosi, L. Poletto, P. Yeates, H. Luna, J. T. Costello, and P. Orr, Spectroscopic characterization of vacuum ultraviolet free electron laser pulses, *Opt. Lett.* 31: 1150–1152 (2006).
25. Fork, R. L., C. H. Brito-Cruz, P. C. Becker, and C. V. Shank, Compression of optical pulses to six femtoseconds by using cubic phase compensation, *Opt. Lett.* 12: 483–485 (1987).
26. Ell, R., U. Morgner, F. X. Kärtner, J. G. Fujimoto, E. P. Ippen, V. Scheuer, G. Angelow, T. Tschudi, M. J. Lederev, A. Boiko, and B. Luther-Davis, Generation of 5-fs pulses and octave-spanning spectra directly from a Ti:sapphire laser, *Opt. Lett.* 26: 373–375 (2001).
27. Delfyett, P. J., L. Florez, N. Stoffel, T. Gmitter, N. Andreadakis, G. Alphonse, and W. Ceislik, 200 fs optical pulse generation and intracavity pulse evolution in a hybrid mode-locked semiconductor diode-laser/amplifier system, *Opt. Lett.* 17: 670–672 (1992).
28. Tauser, F., F. Adler, and A. Leitenstorfer, Widely tunable sub-30-fs pulses from a compact erbium-doped fiber source, *Opt. Lett.* 29: 516–518 (2004).
29. Baltuska, A., T. Fuji, T. Kobayashi, Visible pulse compression to 4 fs by optical parametric amplification and programmable dispersion control, *Opt. Lett.* 27: 306–308 (2002).
30. Chalupsky, J., et al., Characteristics of focused soft X-ray free-electron laser beam determined by ablation of organic molecular solids, *Opt. Ex.* 15: 6036–6043 (2007).
31. Baltakov, F. N., B. A. Garikhin, and L. V. Sukhanov, 400-J pulsed laser using a solution of rhodamine 6G in ethanol, *JETP Let.* 19: 174–175 (1974).
32. Brown, A. J. W., and C. H. Fisher, A. 6.5-J flashlamp-pumped Ti:Al_2O_3 laser, *IEEE J. Quantum Electron.* 29: 2513–2518 (1993).
33. Knowles, M. R. H., and C. E. Webb, Efficient high-power copper-vapor-laser-pumped Ti:Al_2O_3 laser, *Opt. Lett.* 18: 607–609 (1993).
34. Walling, J. C., High energy pulsed alexandrite lasers, in *Technical Digest International Conference on Lasers '90*, San Diego, CA, 1990, paper MH.3.
35. Imeshev, G., and M. E. Fermann, 230 kW peak power femtosecond pulses from a high-power tunable source based from amplification in Tm-doped fiber, *Opt. Ex.* 13: 7424–7231 (2005).
36. Fix, A., T. Schröder, R. Wallenstein, J. G. Haub, M. J. Johnson, and B. J. Orr, Tunable β-barium borate optical parametric oscillator: operating characteristics with and without injection seeding, *J. Opt. Soc. Am. B* 10: 1744–1750 (1993).
37. Maruyama, Y., 0.5-kHz, 5-W optical parametric oscillator pumped by the second harmonic of a Nd:YAG laser, *Opt. Eng.* 44: 094202 (2005).
38. Hollberg, L., CW dye lasers, in *Dye Laser Principles*, edited by F. J. Duarte and L. W. Hillman, Academic, New York, 1990, Chap. 5.
39. Baving, H. J., H. Muuss, and W. Skolaut, CW dye laser operation at 200 W pump power, *Appl. Phys. B* 29: 19–21 (1982).
40. Adams, C. S., and A. I. Ferguson, Frequency doubling of a single frequency Ti:Al_2O_3 laser using an external enhancement cavity, *Opt. Commun.* 79: 219–223 (1990).

41. Erbert, G., I. Bass, R. Hackel, S. Jenkins, K. Kanz, and J. Paisner, 43-W, CW Ti:sapphire laser, in *Conference on Lasers and Electro-Optics*, Optical Society of America, Washington, DC, 1991, pp. 390–393.
42. Walling, J. C., O. G. Peterson, and R. C. Morris, Tunable CW alexandrite laser, *IEEE J. Quantum Electron*. QE-16: 120–121 (1980).
43. Zorabedian, P., Characteristics of a grating-external-cavity semiconductor laser containing intracavity prism beam expanders, *J. Lightwave Technol*. 10: 330–335 (1992).
44. Fleming, M. W., and A. Moorodian, Spectral characteristics of external-cavity controlled semiconductor lasers, *IEEE J. Quantum Electron*. QE-17: 44–59 (1981).
45. Meng, L. S., B. Nizamov, P. Nadasami, J. K. Brasseur, T. Henshaw, and D. K. Newmann, High-power 7-GHz bandwidth external-cavity diode laser array and its use in optically pumping singlet delta oxygen, *Opt. Ex.* 14: 10469–10474 (2006).
46. Bosenberg, W. R., A. Drobshoff, J. I. Alexander, L. E. Myers, and R. L. Byer, 93% pump depletion, 3.5 W continuous-wave, singly resonant optical parametric oscillator, *Opt. Lett.* 21: 1336–1338 (1996).
47. Shen, D. Y., J. K. Sahu, and W. A. Clarkson, Highly efficient Er, Yb-doped fiber laser with 188 W free running and >100 W tunable output power, *Opt. Ex.* 13: 4916–4921 (2005).
48. Loree, T. R., K. B. Butterfield, and D. L. Barker, Spectral tuning of ArF and KrF discharge lasers, *Appl. Phys. Lett.* 32: 171–173 (1978).
49. Lyutskanov, V. L., K. G. Khristov, and I. V. Tomov, Tuning the emission frequency of a gas-discharge XeCl laser, *Sov. J. Quantum Electron*. 10: 1456–1457 (1980).
50. Yang, T. T., D. H. Burde, G. A. Merry, D. G. Harris, L. A. Pugh, J. H. Tillotson, C. E. Turner, and D. A. Copeland, Spectra of electron beam pumped XeF laser, *Appl. Opt*. 27: 49–57 (1988).
51. Hofmann, T., and F. K. Tittel, Wideband-tunable high-power radiation by SRS of a XeF($C \rightarrow^{+} A$) excimer laser, *IEEE J. Quantum Electron*. 29: 970–974 (1993).
52. Woodward, B. W., V. J. Ehlers, and W. C. Lineberger, A reliable repetitively pulsed, high-power nitrogen laser, *Rev. Sci. Instrum*. 44: 882–887 (1973).
53. Shay, T. M., F. E. Hanson, D. Gookin, and E. J. Schimitscheck, Line narrowing and enhanced efficiency of an HgBr laser by injection locking, *Appl. Phys. Lett*. 39: 783–785 (1981).
54. Bukshpun, L. M., V. V. Zhukov, E. L. Latush, and M. F. Sem, Frequency tuning and mode self locking in He-Sr recombination laser, *Sov. J. Quantum Electron*. 11: 804–805 (1981).
55. Tenenbaum, J., I. Smilanski, S. Gabay, L. A. Levin, G. Erez, and S. Lavi, Structure of 510.6 and 578.2 nm copper laser lines, *Opt. Commun*. 32: 473–477 (1980).
56. Wang, Y., B. Lin, and Y. Qian, Spectral structure of the 627.8 nm gold vapor laser line. *Appl. Phys. B* 49: 149–153 (1989).
57. Duarte, F. J., Variable linewidth high-power TEA CO_2 laser, *Appl. Opt*. 24: 34–37 (1985).
58. Mehendale, S. C., D. J. Biswas, and R. G. Harrison, Single mode multiline emission from a hybrid CO_2 laser, *Opt. Commun*. 55: 427–429 (1985).
59. Chang, T. Y., Vibrational transition lasers, in *Handbook of Laser Science and Technology*, edited by M. J. Weber, CRC, Boca Raton, FL, 1991, Chap. 3.3.2.
60. Duarte, F. J., Multiple-prism Littrow and grazing-incidence pulsed CO_2 lasers, *Appl. Opt*. 24: 1244–1245 (1985).
61. Duarte, F. J., Introduction, in *Tunable Laser Applications*, 1st ed., edited by F. J. Duarte, Marcel Dekker, New York, 1995, Chap. 1.
62. Duarte, F. J., Introduction, in *Tunable Lasers Handbook*, edited by F. J. Duarte, Academic, New York, 1995, Chap. 1.
63. Farkas, A. M., and J. G. Eden, Pulsed dye amplification and frequency doubling of single longitudinal mode semiconductor, *IEEE J. Quantum Electron*. 29: 2923–2927 (1993).

64. Duarte, F. J., Solid-state multiple-prism grating dye-laser oscillators, *Appl. Opt.* 33: 3857–3860 (1994).
65. Orr, B. J., Private communication (1995).
66. Andersen, T. V., O. Schmidt, C. Bruchmann, J. Limpert, C. Aguergaray, E. Cormier, and A. Tünnermann, High repetition rate tunable femtosecond pulses and broadband amplification from fiber laser pumped parametric amplifier, *Opt. Ex.* 14: 4765–4773 (2006).
67. Eichhorn, M., Development of a high-pulse-energy Q-switched Tm-doped double-clad fluoride fiber laser and its application to the pumping of mid-IR lasers, *Opt. Lett.* 32: 1056–1058 (2007).
68. Duarte, F. J., Letter, *Laser Focus World* 27(5): 25 (1991).
69. Duarte, F. J., Letter, *Lasers Optron.* 10(5): 8 (1991).
70. Drell, P. S., and E. D. Commins, Parity nonconservation in atomic thallium, *Phys. Rev. A* 32: 2196–2210 (1985).
71. Gould, P. L., G. A. Ruff, and D. E. Pritchard, Diffraction of atoms by light: the near resonant Kapitza–Dirac effect, *Phys. Rev. Lett.* 56: 827–830 (1986).
72. Letokhov, V. S., Atomic optics with tunable dye lasers, in *Dye Lasers: 25 Years*, edited by M. Stuke, Springer-Verlag, Berlin, 1992, Chap. 11.
73. Hall, R. J., and A. C. Eckbreth, Coherent anti-Stokes Raman spectroscopy (CARS): application to combustion diagnostics, in *Laser Applications*, edited by J. F. Ready and R. K. Erf, Academic, New York, 1984, Vol. 5, Chap. 4.
74. Majewski, W. A., J. F. Pfanstiel, D. F. Plusquellic, and W. D. Pratt, High resolution optical spectroscopy in the ultraviolet, in *Laser Techniques in Chemistry*, edited by A. B. Myers and T. R. Rizzo, Wiley, New York, 1995, Chap. 4.
75. Sneddon, J., T. L. Thiem, and Y-I. Lee (Eds.), *Lasers in Analytical Atomic Spectroscopy*, Wiley-VCH, New York, 1996.
76. Demtröder, W., *Laserspektroscopie: Grundlagen und Techniken*, Springer, Berlin, 2007.
77. Pease, A. A., and W. M. Pearson, Axial-mode structure of a copper vapor pumped dye laser, *Appl. Opt.* 16: 57–60 (1977).
78. Hargrove, R. S., and T. Kan, High power efficient dye amplifier pumped by copper vapor lasers, *IEEE J. Quantum Electron.* QE 16: 1108–1113 (1980).
79. Duarte, F. J., and J. A. Piper, Comparison of prism-expander and grazing-incidence grating cavities for copper laser pumped dye lasers, *Appl. Opt.* 21: 2782–2786 (1982).
80. Duarte, F. J., and J. A. Piper, Narrow-linewidth, high-prf copper laser-pumped dye-laser oscillators, *Appl. Opt.* 23: 1391–1394 (1984).
81. Broyer, M., and J. Chevaleyre, CVL-pumped dye laser for spectroscopic applications, *Appl. Phys. B* 35: 31–36 (1984).
82. Paisner, J. A., and R. W. Solarz, Resonance photoionization spectroscopy, in *Laser Spectroscopy and Its Applications*, edited by L. J. Radziemski, R. W. Solarz, and J. A. Paisner, Marcel Dekker, New York, 1987, Chap. 3.
83. Paisner, J. A., Atomic vapor laser isotope separation, *Appl. Phys. B* 46: 253–260 (1988).
84. Duarte, F. J., H. R. Aldag, R. W. Conrad, P. N. Everett, J. A. Paisner, T. G. Pavlopoulos, and C. R. Tallman, High power dye laser technology, in *Proceedings of the International Conference on Lasers '88,* edited by R. C. Sze and F. J. Duarte, STS, McLean, VA, 1989, pp. 773–790.
85. Akerman, M. A., Dye-laser isotope separation, in *Dye Laser Principles*, edited by F. J. Duarte and L. W. Hillman, Academic, New York, 1990, Chap. 9.
86. Duarte, F. J., Dispersive dye lasers, in *High Power Dye Lasers*, edited by F. J. Duarte, Springer, Berlin, 1991, Chap. 2.
87. Tallman, C., and Tennant, R., Large-scale excimer-laser-pumped dye lasers, in *High Power Dye Lasers*, edited by F. J. Duarte, Springer, Berlin, 1991, Chap. 4.

88. Webb, C. E., High-power dye lasers pumped by copper-vapor lasers, in *High Power Dye Lasers*, edited by F. J. Duarte, Springer, Berlin, 1991, Chap. 5.
89. Singh, S., K. Dasgupta, S. Kumar, K. G. Manohar, L. G. Nair, and U. K. Chatterjee, High-power high-repetition-rate copper-vapor-pumped dye laser, *Opt. Eng.* 33: 1894–1904 (1994).
90. Sugiyama, A., T. Nakayama, M. Kato, Y. Maruyama, T. Arisawa, Characteristics of a pressure-tuned single-mode dye laser oscillator pumped by a copper vapor laser, *Opt. Eng.* 35: 1093–1097 (1996).
91. Ready, J. F., *Industrial Laser Applications*, Academic, New York, 1997.
92. Bokhan, P. A., V. V. Buchanov, N. V. Fateev, M. M. Kalugin, M. A. Kazaryan, A. M. Prokhorov, and D. E. Kakrevskii, *Laser Isotope Separation in Atomic Vapor*, Wiley-VCH, Weinheim, 2006.
93. Klick, D., Industrial applications of dye lasers, in *Dye Laser Principles*, edited by F. J. Duarte and L. W. Hillman, Academic, New York, 1990, Chap. 8.
94. Hargrove, R. S. Industrial applications of high power lasers, in *Technical Digest International Conference on Lasers '91*, San Diego, CA, 1991, paper THA.2.
95. Browell, E. V., Ozone and aerosol measurements with an airborne lidar system, *Opt. Photon. News* 2 (10): 8–11 (1991).
96. Grant, W. B., Lidar for atmospheric and hydrospheric studies, in *Tunable Laser Applications*, 1st ed., edited by F. J. Duarte, Marcel Dekker, New York, 1995, Chap. 7.
97. Duarte, F. J., Organic dye lasers: brief history and recent developments, *Opt. Photon. News* 14 (10): 20–25 (2003).
98. Goldman, L., Dye lasers in medicine, in *Dye Laser Principles*, edited by F. J. Duarte and L. W. Hillman, Academic, New York, 1990, Chap. 10.
99. Vassen, W., C. Zimmermann, R. Kallenbach, and T. W. Hänsch, A frequency-stabilized titanium sapphire laser for high-resolution spectroscopy, *Opt. Commun.* 75: 435–440 (1990).
100. Gilmore, D. A., P. V. Cvijin, and G. H. Atkinson, Intracavity absorption spectroscopy with a titanium:sapphire laser, *Opt. Commun.* 77: 385–389 (1990).
101. Bruneau, D., T. Arnaud des Lions, P. Quaglia, and J. Pelon, Injection-seeded pulsed alexandrite laser for differential absorption lidar application, *Appl. Opt.* 33: 3941–3950 (1994).
102. Diddams, S. A., D. J. Jones, J. Ye, S. T. Cundiff, J. L. Hall, J. K. Ranka, R. S. Windeler, R. Holzwarth, T. Udem, and T. W. Hänsch, Direct link between microwave and optical frequencies with 300 THz femtosecond laser comb, *Phys. Rev. Lett.* 84: 5102–5105 (2000).
103. Holzwarth, R., Th. Udem, T. W. Hänsch, J. C. Knight, W. J. Wadsworth, and P. S. J. Russell, Optical frequency synthesizer for precision spectroscopy, *Phys. Rev. Lett.* 85: 2264–2267 (2000).
104. Camparo, J. C., The diode laser in atomic physics, *Contemp. Phys.* 26: 443–477 (1985).
105. Wieman, C. E., and L. Hollberg, Using diode lasers in atomic physics, *Rev. Sci. Instrum.* 62: 1–20 (1991).
106. Camparo, J., The rubidium atomic clock and basic research, *Physics Today* 60 (11): 33–39 (2007).
107. Weidemüller, M., C. Gabbanini, J. Hare, M. Gross, and S. Haroche, A. beam of laser-cooled lithium Rydberg atoms for precision microwave spectroscopy, *Opt. Commun.* 101: 342–346 (1993).
108. Atutov, S. N., E. Mariotti, M. Meuchi, C. Marinelli, and L. Moi, 670 nm external-cavity single mode diode laser continuously tunable over 18 GHz range, *Opt. Commun.* 107: 83–87 (1994).
109. Myatt, C. J., N. R. Newbury, R. W. Ghrist, S. Loutzenhizer, and C. E. Wieman, Multiply loaded magneto-optical trap, *Opt. Lett.* 21: 290–292 (1996).

110. Olivares, I. E., A. E. Duarte, E. A. Saravia, and F. J. Duarte, Lithium isotope separation with tunable diode lasers, *Appl. Opt.* 41: 2973–2977 (2002).
111. Berger, J. D., and D. Anthon, Tunable MEMS devices for optical networks, *Opt. Photon. News* 14 (3): 43–49 (2003).
112. Duarte, F. J. (Ed.), *Tunable Laser Applications*, 1st ed., Marcel Dekker, New York, 1995.
113. Duarte, F. J. (Ed.), *Tunable Laser Applications*, 2nd ed., CRC, Boca Raton, 2008.

2 Spectroscopic Applications of Tunable Optical Parametric Oscillators

B. J. Orr, Y. He, and R. T. White

CONTENTS

2.1 Introduction: "Good-Bye to Ti: and Dye"? 16
2.2 Optical Parametric Devices: How They Operate 17
2.2.1 Optical Parametric Processes 17
2.2.2 $\chi^{(2)}$-Based Optical Parametric Gain and Amplification 22
2.2.3 Choice of Optical Parametric Gain Medium 25
2.2.4 Operating Regimes for Optical Parametric Processes 27
2.3 Elements of Optical Parametric Oscillator Design 28
2.3.1 Nanosecond-Pulsed Optical Parametric Oscillators 29
2.3.2 Continuous-Wave Optical Parametric Oscillators 30
2.3.3 Ultrafast Optical Parametric Oscillators 31
2.3.4 Optical Parametric Devices for Spectroscopic Applications 33
2.4 Optical Bandwidth Control in Nanosecond-Pulsed OPO_s 34
2.4.1 Factors Influencing Optical Bandwidth and Tunability 35
2.4.2 Injection-Seeded Pulsed OPOs: Early Days 38
2.4.2.1 Historical Overview 38
2.4.2.2 Mechanism of Injection-Seeded OPOs 39
2.4.2.3 Passively Seeded OPO Cavities 40
2.4.2.4 Multiplex and Multiwavelength Seeded OPOs 41
2.4.3 Injection-Seeded Pulsed OPOs: Recent Progress 42
2.4.3.1 Actively Seeded OPO Cavities 42
2.4.3.2 Intensity-Dip OPO Cavity Control 44
2.4.3.3 Self-Adaptive Tunable OPO 44
2.4.3.4 Chirp-Controlled, Injection-Seeded OPOs 46
2.4.3.5 Dynamics of SLM Pulsed OPO Operation 49
2.5 Spectroscopic Measurements Using OPOs 50
2.5.1 Spectroscopic Verification of OPO Performance 50

2.5.2 OPO-Spectroscopic Sensing of Atoms and Molecules 57
2.5.2.1 Fundamental OPO Spectroscopy of Atoms, Molecules, and Ions 57
2.5.2.2 OPO Applications in Atmospheric Sensing 59
2.5.2.3 OPO Applications in Industrial and Environmental Monitoring 61
2.5.3 CARS Microscopy: A Biomedical Application of OPOs 65
2.5.3.1 Background to CARS Microscopy 65
2.5.3.2 Instrumentation for CARS Microscopy 66
2.5.3.3 Challenges for CARS Microscopy 66
2.5.3.4 OPO Systems for CARS Microscopy 68
2.6 Concluding Remarks: New Frontiers for OPO Spectroscopy 70
2.6.1 Prospects for Orientation-Patterned GaAs 70
2.6.2 Backward (Mirrorless) OPOs 70
2.6.3 Terahertz Waves from OPGs and OPOs 71
2.6.4 Photonic Crystals Meet OPOs 72
2.6.5 Epilogue: A Selective View of OPOs and Spectroscopy 73
Acknowledgments 74
References 74

2.1 INTRODUCTION: "GOOD-BYE TO TI: AND DYE"?

The corresponding chapter in the first edition of this book [1] was written at a time when a prominent scientific laser manufacturer had advertised its latest optical parametric oscillator (OPO) with the motto "Good-bye to Ti: and Dye," signaling the possible demise of tunable dye lasers [2, 3] that had served laser spectroscopists and others well for at least 20 years. At that time, a book review [4] speculated that solid-state tunable lasers "might relegate the dye laser to the pages of the history book," counterpoised by a view that "the dye laser in its many incarnations looks set to be with us for quite some time yet." Some 15 years later, Ti:sapphire and dye lasers continue to occupy a significant place in the tunable laser market alongside many others (such as diode and quantum cascade lasers). However, solid-state nonlinear-optical (NLO) devices, such as OPOs, are now preferred as tunable coherent light sources for many spectroscopic purposes in the ultraviolet, visible, near-infrared, and mid-infrared [5, 6].

This chapter focuses on developments in the design, operation, and spectroscopic applications of tunable OPOs, as well as closely related optical parametric generators (OPGs) and optical parametric amplifiers (OPAs). Such optical parametric devices have now been available for almost four decades [7, 8], but it is only in the last 20 years that OPOs have become sufficiently reliable for routine, trouble-free operation. Pulsed OPO devices had long been recognized [6–11] as potentially useful sources of broadly tunable, coherent radiation for spectroscopic purposes, typically yielding high peak and average powers in the nanosecond regime. Their solid-state character and high efficiency offer substantial advantages in some respects over the ubiquitous dye laser. Moreover, the wide tuning range of many OPOs has opened up prospects for laser spectroscopy in otherwise inaccessible spectral regions, such as the near- and mid-infrared [5, 6], on which much of this chapter will concentrate.

The precursor of this chapter [1] reproduced a remarkably fine infrared absorption spectrum of the 2.35-μm 2–0 band of carbon monoxide gas that was recorded as early as 1972 by means of a pulsed, singly resonant $LiNbO_3$ OPO [12]. This particular spectrum spanned a 180-cm^{-1} range with an instrument-limited linewidth of ~0.5 cm^{-1} and was accompanied by the prophecy [9] that "the use of parametric oscillator sources for molecular spectroscopy should increase rapidly as the frequency range is extended further into the infrared and the bandwidth is reduced." However, despite some significant early progress [8–10, 13, 14], the spectroscopic potential of pulsed OPOs was not readily realized. Many research laboratories had dark recesses to which their early pulsed OPO systems had been relegated, either optically damaged or used occasionally as "one-wavelength-at-a-time" instruments, rather than the continuously scannable spectroscopic workhorses they were intended to be. This shortcoming was attributable to several critical factors:

- Low optical damage limits and high oscillation thresholds in available OPO gain materials
- The relative complexity of early pulsed OPO cavity designs [5, 8, 9, 15–21] (including phase-matching schemes and line-narrowing strategies) necessary to achieve narrowband, continuously tunable operation
- The need for intense, pulsed lasers with adequate temporal and spatial coherence as OPO pump sources

Within the last 20 years, these problems have diminished appreciably with the availability of new OPO materials [22–24] and high-quality pump sources [25]. A variety of pulsed tunable OPO systems has become commercially available and the spectroscopic community, sections of which had in earlier days been disappointed by the difficulty of implementing OPO technology, is now attracted to the cost-effectiveness and practical potential of such systems.

Since the first edition of this book [1], tunable OPOs, their applications, and relevant aspects of nonlinear optics have matured considerably. There have been numerous review articles, both by our research group at Macquarie University, Sydney [26–29], and by others [30–43], as well as relevant feature issues of topical journals on OPOs [44–48] and related spectroscopic techniques [49–51]. In this chapter, therefore, we do not intend to provide a comprehensive coverage of the field, but rather to address a number of issues concerning the design and operation of tunable OPOs (including continuous-wave and ultrafast-pulsed systems, as well as the nanosecond (ns)-pulsed devices on which our original chapter and our ongoing research focus) and a variety of their spectroscopic applications. Our approach here is essentially that of a "scrapbook," sampling assorted representative examples of progress in this area.

2.2 OPTICAL PARAMETRIC DEVICES: HOW THEY OPERATE

2.2.1 Optical Parametric Processes

Optical parametric devices are useful sources of coherent, laser-like radiation that is typically intense and tunable over a wide range of wavelengths. They invariably

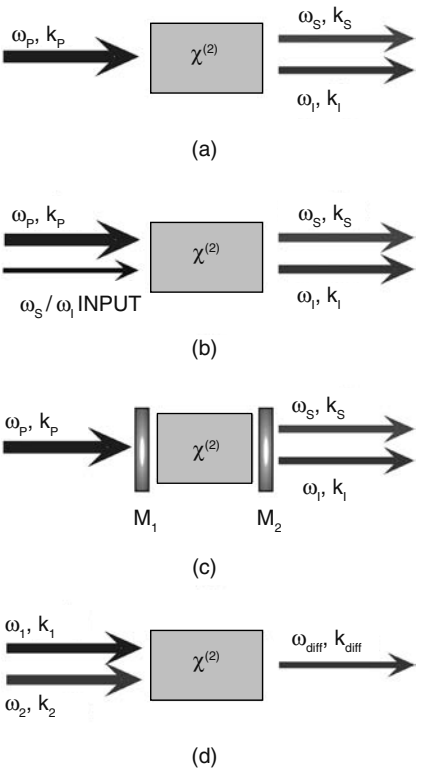

FIGURE 2.1 Schematic diagrams of three forms of optical parametric device: (a) optical parametric generator; (b) optical parametric amplifier; (c) optical parametric oscillator. Note that, by convention, optical frequencies of the signal (S) and idler (I) output waves are defined such that $\omega_S \geq \omega_I$. Also shown is a fourth closely related device: (d) difference-frequency generator. Nonlinear-optical media are denoted by their susceptibility $\chi^{(2)}$. Arrows represent input and output waves, together with their optical frequencies ω_j and wave vectors k_j. An OPO requires an optical resonator, comprising at least two aligned reflectors (M_1, M_2).

arise via nonlinear optics [52–55], most frequently through a three-wave mixing process mediated by the NLO susceptibility $\chi^{(2)}$ in a noncentrosymmetric crystalline medium. Three forms of optical parametric device are illustrated in Figure 2.1, namely: (a) optical parametric generator (OPG), (b) optical parametric amplifier (OPA), and (c) optical parametric oscillator (OPO). Also illustrated is a closely related (but distinct) NLO device: (d) difference-frequency generator (DFG). Coherent light waves are represented by arrows, with their associated optical angular frequency ω_j and wave vector $\mathbf{k}_j$ (as defined below). In Figure 2.1, input and output waves are shown as arrows on the left and right, respectively, with their breadth indicating typical relative intensities.

An OPG is the simplest form of optical parametric device. As depicted in Figure 2.1a, it entails a single input wave (pump P, at frequency ω_P) and two output waves: signal S (at ω_S) and idler I (at ω_I), where $\omega_S \geq \omega_I$. The NLO process itself

is initiated by spontaneous parametric processes that comprise naturally occurring emission/noise/fluorescence at low intensity, effectively "splitting" a pump photon into two new photons. Once a signal and/or idler wave has been generated, it can be coherently amplified by passing it through an OPA together with input pump radiation, as depicted in Figure 2.1b. A further order of sophistication is reached in an OPO, as depicted in Figure 2.1c, where the functions of an OPG and an OPA are combined by multipassing one or more of the optical waves involved inside a resonant optical cavity, formed by two or more appropriately aligned reflectors (M_1, M_2).

A DFG, as depicted in Figure 2.1d, is *not* an optical parametric device, although the DFG source term is central to the NLO mechanism of OPGs, OPAs, and OPOs. In a DFG [10, 56], two intense input waves (with frequencies ω_1 and ω_2) interact coherently to generate a third output wave (with frequency ω_{diff}) at the difference frequency of the two input waves. There are now two relatively high-power driving waves (rather than one) and the frequencies of these waves are subtracted from each other (rather than effectively splitting a single incident frequency in two, as in an optical parametric process). Nevertheless, the outcome and utility of a DFG can be similar to that of an optical parametric device. For instance, if coherent radiation is required at a particular infrared (IR) wavelength, it can be generated *either* as the idler wave of an optical parametric device, with frequency $\omega_I = (\omega_P - \omega_S)$ *or* as the output wave of a DFG, with frequency $\omega_{diff} = |\omega_1 - \omega_2|$. Moreover, the NLO source term for a DFG entails a form of susceptibility $\chi^{(2)}$ that is very similar to that for an OPG, OPA, or OPO.

Many desirable attributes of optical parametric devices in general, and tunable OPOs in particular, arise from the fact that any such instrument is derived from nonlinear optics [52–55] and is therefore distinctively different from a laser. This yields flexible, versatile design features, such as modes of temporal and wavelength control to which lasers are not amenable. Lasers generally depend on population inversion of an optical gain medium, with associated optical lifetime and saturation limitations. On the other hand, optical parametric gain, oscillation, and amplification facilitate modular system design because they entail NLO coefficients and phase-matching conditions, as explained below.

In nonlinear optics, a number ($\sigma, > 2$) of optical waves interact in a medium with NLO susceptibility tensor $\chi^{(\sigma-1)}$. For inelastic optical processes, these waves (with angular frequencies $\omega_1, \omega_2, \ldots, \omega_\sigma$) obey two conservation conditions, one for energy (or frequency):

$$\omega_1 + \omega_2 + \cdots + \omega_\sigma = 0. \tag{2.1}$$

The other conservation condition is effectively for momentum; this is expressed in terms of wave vectors $\mathbf{k}_j$ (with $j = 1, 2, \ldots, \sigma$) that have magnitudes $k_j = n_j\, \omega_j/c = 2\pi\, n_j/\lambda_j$, where n_j is the refractive index at vacuum wavelength λ_j and c is the speed of light:

$$\mathbf{k}_1 + \mathbf{k}_2 + \cdots + \mathbf{k}_\sigma + \Delta\mathbf{k} = 0, \tag{2.2}$$

where $\mathbf{\Delta k}$ is the phase-mismatch vector between the σ interacting waves. Each frequency component and wave vector is ascribed a positive or negative sign, according to their phase relationships. Equation 2.2 defines a phase-matching condition in

which $\Delta\mathbf{k}$ must be minimized in order to optimize the efficiency of the NLO process of interest.

Two specific three-wave NLO processes that are relevant to this chapter are those for *either* an optical parametric device (i.e., OPG, OPA, or OPO) *or* a DFG. Each of these is mediated by the second-order NLO susceptibility tensor $\chi^{(2)}$, which is nonzero in a crystalline medium only if that medium is noncentrosymmetric. Many such crystals are available [22, 23]. For example, lithium niobate ($LiNbO_3$) has been popular since the early days of pulsed tunable OPOs. Subsequent interest and activity in optical parametric device technology have been stimulated by the availability of NLO materials such as BBO (β-barium borate, BaB_2O_4) and KTP (potassium titanyl phosphate, $KTiOPO_4$). Recent impetus has come from quasi-phase-matched (QPM) NLO media, such as periodically poled lithium niobate (PPLN) and PPKTP, tailored for specific wavelengths by periodic structuring of ferroelectric domains. QPM media offer compact, efficient, low-threshold alternatives to conventional birefringently phase-matched (BPM) media. Characteristics of many BPM and QPM NLO crystalline media are accessible, both in books [22, 23] and via the versatile SNLO software package [24].

For a three-wave optical parametric device, which is of principal interest in this chapter, the energy and momentum conservation conditions of Equations 2.1 and 2.2 become:

$$\omega_P - \omega_S - \omega_I = 0;\ \mathbf{k}_P - \mathbf{k}_S - \mathbf{k}_I - \Delta\mathbf{k} = 0, \tag{2.3}$$

where a laser input wave ("pump," frequency ω_P, wave vector $\mathbf{k}_P$) yields two coherent output waves ("signal," ω_S, $\mathbf{k}_S$; "idler," ω_I, $\mathbf{k}_I$), such that $\omega_P > \omega_S \geq \omega_I$. Note that the idler frequency ω_I equals the difference $(\omega_P - \omega_S)$ between pump and signal frequencies. Equation 2.3 should be viewed in the context of Figure 2.1a to c.

Equation 2.2 and the second half of Equation 2.3 apply strictly only to the conventional case of BPM media. In such media, the phase-matching condition $\Delta\mathbf{k} \approx 0$ is attained by adjusting its ordinary- and extraordinary-ray refractive indices via the angle and/or temperature of a birefringent NLO crystal. Such adjustments are used to optimize parametric conversion efficiency for a particular set of frequencies $(\omega_P, \omega_S, \omega_I)$ and thereby control the output signal and idler wavelengths, λ_S and λ_I. If it is assumed that the three waves are collinear and $\Delta\mathbf{k}$ is exactly zero, then the signal frequency/wavelength is given simply in terms of the pump frequency/wavelength and the refractive indices n_j (j = P, S, I) as:

$$\omega_S = \omega_P\,(n_P - n_I)/(n_S - n_I);\ \lambda_S = \lambda_P\,(n_S - n_I)/(n_P - n_I). \tag{2.4}$$

Various angle-dependent index-matching schemes are applicable in the case of OPOs based on BPM crystals: for example, Type I (eeo/ooe) and Type II (oeo/eoe) in positive/negative uniaxial birefringent crystals, where "o" and "e" denote the ordinary and extraordinary waves listed in the order "I S P" [22, 56]. Many BPM optical parametric devices (especially those in the ns-pulsed regime) employ so-called critical phase matching (CPM, which may be either collinear or noncollinear) that depends on the orientation of the optical-wave propagation directions relative to the optic axis of the NLO crystal [9, 10, 22, 38, 41, 42, 56].

An alternative approach is so-called noncritical phase matching (NCPM, also known as 90-degree phase matching), where the propagation direction is normal to the optic axis of the NLO crystal and the ordinary- and extraordinary-wave refractive indices n_o and n_e have a zero first-order dependence on the orientation of the crystal [9, 10, 22, 38, 41, 42, 56]. NCPM enables the phase-matched interaction to be along a principal optical axis of the NLO material with no spatial walkoff. This also has the advantage that the effective interaction length is determined by the length of the crystal and is not reduced by spatial walkoff. For a fixed pump wavelength, the output signal and idler wavelengths of an NCPM OPO can then be tuned by varying the temperature (and hence the refractive indices) of the crystal at a fixed (90°) orientation. Alternatively, NCPM OPO output can be tuned by varying the pump wavelength (e.g., from a tunable dye or Ti:sapphire laser—so much for "Good-bye to Ti: and Dye," as proclaimed in Section 2.1), while maintaining fixed crystal temperature and orientation. Such an NCPM approach was popular in the early days of OPO spectroscopy [9, 10, 14, 15] and has since become resurgent, particularly for CW OPOs or for ultrafast OPOs where the absence of beam walkoff facilitates tight focusing of the (relatively low-power) CW or ultrafast pump beam to exceed the threshold of the OPO (as discussed in Sections 2.3.2 and 2.3.3).

The QPM approach was first recognized by pioneers of nonlinear optics in 1962 [57–59] as an alternative to birefringent phase matching. However, this QPM approach was not realized practically until approximately 30 years later [43, 60–64] via NLO media such as PPLN. For a QPM device, grating contributions, arising from the engineered microscale structure of the crystal, need to be included in phase-matching conditions. For instance, the z-component Δk of the wave-vector mismatch $\Delta\mathbf{k}$ in the second half of Equation 2.3 needs to be replaced by $\Delta k = [\Delta k_{QPM} + (2\pi\, m/\Lambda)]$, where m is the QPM order (an odd-numbered integer), Λ is the QPM grating period, and a collinear interaction along the z-axis is assumed.

In the corresponding case of a DFG (which, we repeat, is *not* an optical parametric device), two coherent input waves (frequencies ω_1, ω_2; wave vectors $\mathbf{k}_1$, $\mathbf{k}_2$) yield a single coherent output wave at the difference frequency $\omega_{diff} = |\omega_1 - \omega_2|$ (with wave vector $\mathbf{k}_{diff}$). The energy and momentum conservation conditions of Equations 2.1 and 2.2 then become:

$$|\omega_1 - \omega_2| - \omega_{diff} = 0;\ \mathbf{k}_1 - \mathbf{k}_2 - \mathbf{k}_{diff} - \Delta\mathbf{k} = 0, \tag{2.5}$$

as depicted in Figure 2.1d. Again, phase matching is defined by $\Delta\mathbf{k} \approx 0$ for BPM media. In the case of QPM media, there is an additional grating contribution in the second half of Equation 2.5, in which the z-component Δk of the vector $\Delta\mathbf{k}$ in the second half of Equation 2.3 needs to be replaced by $\Delta k = [\Delta k_{QPM} + (2\pi\, m/\Lambda)]$.

In a more general sense (which is only incidental to this chapter), other important forms of coherent wavelength conversion arise from four-wave mixing processes that are mediated by the third-order NLO susceptibility tensor $\chi^{(3)}$, which can be nonzero even in isotropic or centrosymmetric media such as gases, liquids, optical fibers, and all classes of crystal. Optical parametric processes of this type contribute to stimulated Raman scattering (SRS), involving an optical medium with Raman-active resonance frequencies ω_R that coincide with the difference between two optical

frequencies. This can provide a relatively straightforward source of coherent radiation, Raman-shifted at discrete intervals from the frequency ω_L of an input pump laser (either tunable or fixed-wavelength). These Raman-shifted intervals, both added to (anti-Stokes) and subtracted from (Stokes) the laser frequency ω_L, are integer multiples of ω_R. Other NLO Raman parametric processes give rise to various forms of nonlinear Raman spectroscopy, such as coherent anti-Stokes Raman scattering (CARS), and to Raman fiber-optical amplifiers, used in optical telecommunications. Another developing area of optical parametric device technology entails OPGs, OPAs, and OPOs based on $\chi^{(3)}$ nonlinearities in highly nonlinear optical fibers, with either pulsed or continuous-wave pump lasers. Such processes typically use two pump waves (P) to generate tunable signal (S) and idler (I) output waves, so that $\omega_I = 2\omega_P - \omega_S$.

2.2.2 $\chi^{(2)}$-Based Optical Parametric Gain and Amplification

The central theme of this chapter concerns $\chi^{(2)}$-based OPGs, OPAs, and OPOs, for which we can consider the intrinsic NLO process semiclassically in terms of three complex plane-wave radiation fields and the corresponding polarizations in the medium of interest, as follows:

$$\mathbf{E}_j(t) = \tfrac{1}{2}\,\mathbf{E}_j \exp[i\,(\mathbf{k}_j \cdot \mathbf{r} - \omega_j\, t)] + \tfrac{1}{2}\,\mathbf{E}_j^{*} \exp[-i\,(\mathbf{k}_j \cdot \mathbf{r} - \omega_j\, t)]; \tag{2.6}$$

$$\mathbf{P}_j(t) = \tfrac{1}{2}\,\mathbf{P}_j \exp[i\,(\mathbf{k}_j \cdot \mathbf{r} - \omega_j\, t)] + \tfrac{1}{2}\,\mathbf{P}_j^{*} \exp[-i\,(\mathbf{k}_j \cdot \mathbf{r} - \omega_j\, t)], \tag{2.7}$$

where the suffix j = P, S, or I. Interaction with the NLO susceptibility tensor $\chi^{(2)}$ of a noncentrosymmetric medium then causes these to be interrelated as follows:

$$\mathbf{P}_S^{(2)} = \varepsilon_0\, \chi^{(2)}\, \mathbf{E}_P\, \mathbf{E}_I^{*};\ \mathbf{P}_I^{(2)} = \varepsilon_0\, \chi^{(2)}\, \mathbf{E}_P\, \mathbf{E}_S^{*};\ \mathbf{P}_P^{(2)} = \varepsilon_0\, \chi^{(2)}\, \mathbf{E}_S\, \mathbf{E}_I, \tag{2.8}$$

where ε_0 is the vacuum permittivity (8.854×10^{-12} C^2 J^{-1} m^{-1}). Here, only the second-order polarizations $\mathbf{P}_j^{(2)}$ need to be considered and, in the interest of simplicity, the functional dependence of $\chi^{(2)}$ on optical frequencies ω_S, ω_I, ω_P has been suppressed.

It is customary at this stage to introduce a suitably defined effective nonlinear-optical coefficient d_{eff} (units: m V^{-1} or, more typically, pm V^{-1}) to yield [1]:

$$P_S^{(2)} = 2\,\varepsilon_0\, d_{eff}\, E_P\, E_I^{*};\ P_I^{(2)} = 2\,\varepsilon_0\, d_{eff}\, E_P\, E_S^{*};\ P_P^{(2)} = 2\,\varepsilon_0\, d_{eff}\, E_S\, E_I, \tag{2.9}$$

where d_{eff} is a linear combination of elements of the NLO susceptibility tensor $\chi^{(2)}$ for the medium of interest. For a particular BPM crystal, d_{eff} depends on its (noncentrosymmetric) crystal class and its cut and orientation relative to propagation and polarization directions of the incident light waves. The vector/tensor notation used in Equation 2.8 is not needed in Equation 2.9 for a specific experimental configuration.

By combining Equations 2.6, 2.7, and 2.9 with Maxwell's equations, our algebraic treatment of optical parametric amplification yields a set of relevant coupled wave equations for plane waves propagating in the z-direction. These are common to various forms of three-wave NLO processes, but are specified here for OPGs, OPAs, and OPOs [1]:

$$(dE_S/dz) + \alpha_S E_S = i\,(k_S/n_S^2)\, d_{eff}\, E_P\, E_I^{*} \exp(i\,\Delta k\, z); \tag{2.10}$$

$$(dE_I/dz) + \alpha_I E_I = i\,(k_I/n_I^2)\, d_{eff}\, E_P\, E_S^{*} \exp(i\,\Delta k\, z); \tag{2.11}$$

$$(dE_P/dz) = i\,(k_P/n_P^2)\, d_{eff}\, E_S\, E_I \exp(-\,i\,\Delta k\, z), \tag{2.12}$$

where α_j (j = S, I, P) are loss factors and the wave-vector mismatch Δk is the z-component of $\Delta\mathbf{k}$, as before. Equation 2.12 corresponds to the customary limit of negligible pump-field losses ($\alpha_P = 0$). In addition, the pump wave may be treated as undepleted ($dE_P/dz = 0$) when it is substantially more intense than the other two waves, thereby leaving only a pair of coupled differential equations.

In parametric generation, the pump field E_P is assumed to be relatively strong, whereas the signal and idler fields E_S and E_I grow from a low level. In the zero-loss limit (with all $\alpha_j = 0$), it can be shown that Equations 2.10 through 2.12 yield what is effectively a photon conservation condition:

$$\omega_S^{-1}\,(dI_S/dz) = \omega_I^{-1}\,(dI_I/dz) = -\,\omega_P^{-1}\,(dI_P/dz);$$

$$\lambda_S\,(dI_S/dz) = \lambda_I\,(dI_I/dz) = -\,\lambda_P\,(dI_P/dz), \tag{2.13}$$

where $I_j = \tfrac{1}{2}\, c\, \varepsilon_0\, n_j\, |E_j|^2$ (with j = S, I, or P) is the optical intensity or flux (units: W m^{-2}). Conversion of each photon from the pump field (P) is then seen to generate two photons, one in the signal field (S) and the other in the idler field (I).

A situation that is more realistic than this zero-loss limit is that with finite but equal signal and idler losses ($\alpha_S = \alpha_I = \alpha$). This yields a tractable general solution describing evolution of the signal and idler fields. In the case where a single-frequency idler field $E_I(z)$ is incident on a pumped medium of length L, it experiences a single-pass power gain of the form:

$$G_I\,(L) = [|E_I(z = L)|^2/|E_I(z = 0)|^2] - 1 = \Gamma^2\, L^2\, (g\, L)^{-2} \sinh^2(g\, L), \tag{2.14}$$

where g and Γ are the total and parametric gain coefficients, respectively, defined by:

$$\Gamma = (k_S\, k_I)^{1/2}\, |\, d_{eff}\, |\, |E_P^0|/(n_S\, n_I); \tag{2.15}$$

$$g = [|\Gamma^2 - (\Delta k/2)^2|]^{1/2}, \tag{2.16}$$

where, in the limit of zero pump depletion, $E_P^0 \equiv E_P(z = 0)$ is taken to be constant over the range $0 \le z \le L$ and the incident signal field $E_S(z = 0)$ is zero. The relatively simple functional form of Equations 2.14 through 2.16 applies only to the case of an effectively monochromatic incident idler wave. If more than one frequency is present, then the solutions become critically dependent on the phases of those incident waves relative to that of the pump radiation field.

In the high-gain limit, where $\Gamma^2 >> (\Delta k/2)^2$, the single-pass power gain corresponds to the extreme case of superfluorescent parametric emission:

$$G_I\,(L) = \tfrac{1}{4} \exp(2\,\Gamma\, L) \tag{2.17}$$

where zero loss has again been assumed. This situation arises when the medium is pumped by a high-intensity pulsed laser source, as in pulsed OPGs and OPOs.

Alternatively, pumping by a continuous-wave (CW) or low-/moderate-peak-power pulsed laser corresponds to the low-gain limit of parametric generation, with $\Gamma L < 1$ or $\Gamma^2 < (\Delta k/2)^2$:

$$G_I(L) = \Gamma^2 L^2 \operatorname{sinc}^2\{[\,|\,(\Delta k/2)^2 - \Gamma^2\,|\,]^{1/2} L\} \tag{2.18}$$

where $\operatorname{sinc} x = (\sin x)/x$. When $\Gamma^2 << (\Delta k/2)^2$, the argument of the sinc^2 function is $(\Delta k\, L/2)$, with the phase mismatch Δk exerting a dominant influence on the single-pass gain. Near phase matching $\Delta k \approx 0$ and $\Gamma\, L << 1$, the single-pass power gain $G_I(L) \approx \Gamma^2 L^2$.

An alternative form of Equation 2.15 can be derived in terms of the intensity or flux $I_P^0 \equiv I_P(z = 0)$ of the incident pump radiation, yielding the square of the total gain coefficient Γ:

$$\Gamma^2 = \left[8\,\pi^2\, d_{eff}^2/(c\,\varepsilon_0\, n_P\, n_S\, n_I\, \lambda_S\, \lambda_I)\right] I_P^0 = \left[2\, d_{eff}^2\, \omega_S\, \omega_I/(c^3\, \varepsilon_0\, n_P\, n_S\, n_I)\right] I_P^0, \tag{2.19}$$

where pump depletion is assumed to be zero.

Another useful transformation [7, 38, 41] is to introduce a parameter $\delta = [2(\omega_S/\omega_P) - 1] = [2(\lambda_P/\lambda_S) - 1]$, such that $\omega_S = ½\,\omega_P\,(1 + \delta)$ and $\omega_I = ½\,\omega_P\,(1 - \delta)$ and Equations 2.15 and 2.19 become:

$$\Gamma = k_0\, n_0^{-2}\,|\,d_{eff}\,|\,|E_P^0|\,(1 - \delta^2)^{1/2}; \tag{2.20}$$

$$\begin{aligned}\Gamma^2 &= \left[8\,\pi^2\, d_{eff}^2/(c\,\varepsilon_0\, n_P\, n_0^2\, \lambda_0^2)\right](1 - \delta^2)\, I_P^0 \\ &= \left[2\, d_{eff}^2\, \omega_0^2/(c^3\, \varepsilon_0\, n_P\, n_0^2)\right](1 - \delta^2)\, I_P^0,\end{aligned} \tag{2.21}$$

where the zero subscript denotes the degeneracy point such that $\omega_0 = ½\,\omega_P$, $\lambda_0 = 2\,\lambda_P$, and $n_0 \approx n_S \approx n_I$. The so-called degeneracy factor $(1 - \delta^2)^{1/2}$ is a measure of the reduction in parametric gain as ω_S and ω_I (or λ_S and λ_I) move away from the degeneracy point ω_0 (or λ_0).

In view of the functional forms of Γ and Γ^2 in Equations 2.15 and 2.19 through 2.21, it is useful to define an NLO figure of merit (FOM), as follows:

$$\text{FOM} = d_{eff}^2/n_P\, n_S\, n_I = d_{eff}^2\, n_{eff}^{-3}, \tag{2.22}$$

where $n_{eff} = (n_P\, n_S\, n_I)^{1/3}$ is a geometric mean of refractive indices. This arbitrary definition is consistent with that of Vodopyanov [40], although other (equally arbitrary) definitions of the FOM are in current usage [41, 56]. Whatever definition is chosen for the FOM, it incorporates NLO properties that are critical in determining the optical-parametric gain and hence the relative efficiencies of OPGs, OPAs, and OPOs based on different NLO media and operating regimes.

The FOM has an intrinsic wavelength dependence, not only from the dispersion of n_{eff} but also from the dispersion of $\chi^{(2)}$ and hence $d_{eff,}$ which, using Miller's

rule [65], can be predicted empirically to vary as $(n_{\text{eff}}^2 - 1)^3$; the net effect is that the FOM as defined in Equation 2.22 is expected to be approximately proportional to n_{eff}^9 [41]. One outcome is that, for a given pump intensity I_P^0 and crystal length L, normal dispersion causes the optical parametric gain to decline markedly as one moves from the visible and near-IR regions to longer wavelengths in the mid-IR and far-IR regions; this is aggravated by the dependence of Γ^2 on $(\lambda_S\ \lambda_I)^{-1}$, as in Equations 2.19 and 2.21. Optical parametric devices operating at longer wavelengths (e.g., in the mid-IR and far-IR regions) therefore continue to pose instrumental challenges.

2.2.3 Choice of Optical Parametric Gain Medium

The choice of NLO crystal for optical parametric devices depends on various well-established factors [7–10, 20–24, 31, 40, 41, 56]. In the traditional BPM case, these include:

- Symmetry class of the crystal, as only noncentrosymmetric crystals (also capable of piezoelectric response) can have nonzero $\chi^{(2)}$ tensor components (or values of d_{eff})
- Magnitude of $\chi^{(2)}$ (or d_{eff}), to ensure sufficient optical nonlinearity
- Form of phase matching used (e.g., Type I or Type II, CPM or NCPM)
- Capability of growing large crystals of high optical quality, to maximize path length in a wide-aperture, blemish-free NLO medium
- Transparency of the material at all three wavelengths (λ_S, λ_I, and λ_P) to enable the device to operate over as wide a tuning range as possible
- Optical damage threshold, particularly at the nominated pump wavelength, but also at signal and idler wavelengths in high-gain devices
- Handling ease of the crystal (e.g., hygroscopic properties, durability, hardness)
- Refractive indices, dispersion, and birefringent properties of the crystal, which need to be suitable for phase matching to be established
- Thermal coefficients of refractive index, either to enhance temperature tuning or to minimize temperature sensitivity

The choice of a particular NLO material is also influenced by the affordability and availability of suitable crystals. In the corresponding chapter in the first edition of this book [1], it was feasible to tabulate on two facing pages key properties of most of the BPM crystals that were in common use. Such a task is now impractical, in view of the improved availability and quality of BPM crystals, together with the advent of QPM media that are in high demand for OPG, OPA, and OPO applications over a wide range in the infrared and ultraviolet regions.

Table 2.1 lists a representative selection of uniaxial (*ua*) and biaxial (*ba*) NLO crystals that are used in near-IR and mid-IR optical parametric devices; their relevant characteristics include FOM values that scale as previously discussed. Also crucial, but not listed in Table 2.1, are estimates of optical damage thresholds, which limit the pump laser intensity, fluence, pulse duration, and repetition rate that can reliably be used for a given NLO material [22, 23]. A diversity of NLO materials is available for use in optical parametric devices, but surveying them comprehensively

TABLE 2.1
Characteristics of Selected NLO Crystals Commonly Used in Near-IR and Mid-IR Optical Parametric Devices[a]

NLO crystal (biaxial, *ba*/ uniaxial, *ua*)	Transparency range (μm)	$\lvert d_{eff} \rvert$ (pm V^{-1})	$n_{eff} = (n_P n_S n_I)^{1/3}$	FOM, $d_{eff}^2 n_{eff}^{-3}$ (pm^2 V^{-2})
	BPM materials			
$AgGaS_2$ (*ua*)	0.47 – 13	12	2.40	10.4
$AgGaSe_2$[b] (*ua*)	0.71 – 19	33	2.65	2.8
β-BaB_2O_4 (BBO)[c] (*ua*)	0.20 – 2.6	2.2	1.7	1.0
$KTiOAsO_4$ (KTA) (*ba*)	0.35 – 5.3	4	1.8	1.4
$KTiOPO_4$ (KTP) (*ba*)	0.35 – 4.3	4	1.8	1.4
LiB_3O_5 (LBO)[c] (*ba*)	0.16 – 2.6	0.9	1.6	0.2
$LiNbO_3$ (LN) (*ua*)	0.33 – 5.5	5	2.13	2.6
$RbTiOAsO_4$ (RTA) (*ba*)	0.35 – 5.3	4	1.8	2.7
$ZnGeP_2$ (ZGP)[b] (*ua*)	0.74 – 12	75	3.13	8.8
	QPM materials[d]			
PP $KTiOAsO_4$ (PPKTA) (*ba*)	0.35 – 5.3	10.3	1.8	18
PP $KTiOPO_4$ (PPKTP) (*ba*)	0.35 – 4.3	10.8	1.8	20
PP $LiNbO_3$ (PPLN) (*ua*)	0.40 – 5.5	14.2	2.13	20.9
PP $RbTiOAsO_4$ (PPRTA) (*ba*)	0.35 – 5.3	10.1	1.8	17.5
OP GaAs (orientation-patterned)	0.9 – 17	60	3.3	100

Source: Derived and adapted from Tables 1–3 of Vodopyanov, K. L., in *Solid-State Mid-Infrared Sources,* Springer, Berlin, 2003, 141–178; Table 2 of Ebrahimzadeh, M., in *Solid-State Mid-Infrared Sources,* Springer, Berlin, 2003, 179–218 [41]; Table 2 of Fischer, C., and M. W. Sigrist, in *Solid-State Mid-Infrared Sources,* Springer, Berlin, 2003, 97–140 [56]; Dmitriev, V. G., G. G. Gurzayan, and D. N. Nikogosyan, *Handbook of Nonlinear Optical Crystals*, Springer, New York, 3rd edition, 1999 [22]; and Smith, A. V., *SNLO Nonlinear Optics Code*, freeware downloadable from http://www.as-photonics.com/?q=SNLO [24].

[a] Typical operating conditions are: $\lambda_P = 1.06$ μm, $\lambda_S \approx 1.6$ μm, $\lambda_I \approx 3.2$ μm.

[b] Because of transparency and/or phase matching, it is not feasible to have $\lambda_P < \sim 2$ μm.

[c] Because of low IR transparency, typical operating conditions are taken to be: $\lambda_P = 0.35$ μm, $\lambda_S \approx 0.46$ μm, $\lambda_I \approx 1.5$ μm.

[d] Values of $\lvert d_{eff} \rvert$ for QPM materials correspond to $2\,\lvert d_{33} \rvert / \pi$. Ferroelectric media, such as KTA, KTP, LN, and RTA, can be periodically poled but GaAs, which is cubic and therefore not birefringent, must be used as an orientation-patterned NLO medium [40].

is beyond the scope of this chapter [22, 23], as is balancing the many design considerations [24] that arise when selecting such a material.

The QPM materials listed in the lower half of Table 2.1 are seen to have relatively high FOMs, primarily because it is then possible to take advantage of the largest NLO tensor element (e.g., d_{33} in various periodically poled materials) rather than smaller d_{ij} values (with $i \neq j$) for BPM devices. For instance, the widely used QPM medium PPLN (periodically poled $LiNbO_3$) with all waves z-polarized, offers an NLO gain enhancement of $(2\,d_{33}/\pi\,d_{31})^2 \approx 16$, relative to its BPM counterpart, bulk

$LiNbO_3$ [40]. The availability of PPLN and other QPM materials has revolutionized the design of optical parametric wavelength-conversion techniques (such as OPG, OPA, OPO, and DFG). However, applications such as high-power NLO devices and generation of coherent mid-IR radiation continue to rely on bulk crystalline BPM materials [40, 41, 56, 66].

As indicated in Table 2.1, orientation-patterned (OP) GaAs has a remarkable FOM advantage, owing to its enormous d_{eff} value of $(2\ d_{14}/\pi) = 60$ pm V^{-1}, 6.2 times that of PPLN [40, 67]. However, GaAs is a cubic crystal with zincblende structure, so that it is neither birefringent (i.e., a BPM device is not feasible) nor ferroelectric (i.e., it cannot be periodically poled). The availability of OP GaAs is still very limited, owing to the complicated fabrication processes (e.g., epitaxial growth [43, 66, 69–72]) that are needed to produce it. Nevertheless, OP GaAs is an extremely promising medium for NLO wavelength conversion, given its large NLO coefficient [40, 43, 67], its dispersion relationships that influence phase matching [68], its low absorption and high transparency over a wide IR wavelength range (0.9–17 μm), its high laser damage threshold, and its high thermal conductivity. Moreover, GaAs is a widely used semiconductor with well-tried material technology. Key NLO wavelength-conversion applications of OP GaAs include second harmonic generation [67], DFG-based spectroscopy at ~7–9 μm [73–75], pulsed tunable OPO operation at ~2–9 μm [76], a mid-IR continuum OPG spanning ~5–10 μm [77], and generation of terahertz (THz) waves in the range ~0.9–3 THz (~0.3–0.1 mm) [78, 79].

2.2.4 Operating Regimes for Optical Parametric Processes

Typical operating regimes for different classes (A–D) of single-pass optical parametric gain processes are examined in Table 2.2 under phase-matched conditions ($\Delta k = 0$) and near-degenerate operation with $\lambda_S \approx \lambda_I \approx 2$ μm, as previously reported by Ebrahim-Zadeh [41]. In terms of Equations 2.14 through 2.21, the parametric gain factor ΓL (which equals $g L$ when $\Delta k = 0$) is calculated and yields the single-pass power gain $G_I(L)$, which equals $\sinh^2 \Gamma L$. Typical NLO material parameters (e.g., $|d_{eff}| \approx 3$ pm V^{-1} and $n_{eff} \approx 1.5$, FOM ≈ 2.7) are assumed, and the four operating regimes are distinguished by choice of pump power, focal geometry, crystal length L, and (for pulsed cases B–D) pump pulse duration. The resulting values of $G_I(L)$ range over 33 orders of magnitude, from low-power CW operation (A) to high-energy ultrafast pulsed operation (D).

Usually, the signal and idler output power from an optical parametric device must build up from spontaneous parametric emission, so that only the high-energy ultrafast pulsed case (D) has sufficiently high single-pass power gain $G_I(L)$ to enable practical operation as an OPG or an OPA, as in Figures 2.1a and 2.1b, respectively. In such a situation, the parametric gain in the other three operating regimes (CW, Q-switched, and modelocked; cases A, B, and C, respectively) is typically too small to build up to a significant output power from spontaneous parametric emission. It is then necessary to adopt the OPO strategy, as in Figure 2.1c, with the NLO medium enclosed in an optical cavity to provide resonant optical feedback at the signal and/or idler wavelengths. On the other hand, if a sufficiently intense second input wave at the signal or idler frequency can be injected into the NLO medium together with

TABLE 2.2
Typical Operating Regimes for Different Classes (Labeled A–D) of Single-Pass Optical Parametric Gain Process[a]

Class of single-pass optical parametric gain:	Class A continuous-wave	Class B ns-pulsed	Class C modelocked	Class D modelocked and amplified
Pump pulse energy:	–	10 mJ	15 nJ	10 μJ
Pump pulse duration:	–	10 ns	100 fs	200 fs
Peak pump power:	5 W	1 MW	150 kW	50 MW
Focused waist radius (w_0):	20 μm	1 mm	15 μm	15 μm
Peak pump intensity I_P:	0.4 MW cm^{-2}	30 MW cm^{-2}	20 GW cm^{-2}	7 TW cm^{-2}
Crystal length L:	10 mm	10 mm	1 mm	1 mm
ΓL ($\equiv g L$ if $\Delta k = 0$):	0.09	0.77	1.99	37
$G_1(L)$, as in Eq. (14):	0.008	0.72	13	3.4×10^{31}
Relevant optical parametric device(s): [b]	OPO	OPO	OPO	OPO, OPG, OPA

Source: Adapted from Table 1 of Ebrahimzadeh, M., in *Solid-State Mid-Infrared Sources,* Springer, Berlin, 2003, 179–218 [41].

[a] The table is based on typical experimental values for pump laser and NLO material parameters (e.g., $|d_{eff}| \approx 3$ pm V^{-1} and $n_{eff} \approx 1.5$, so that FOM = 2.7) in each operating regime [41]. The parametric gain factor ΓL [$\equiv g L$, assuming phase-matched interaction ($\Delta k = 0$)], as in Equations 2.15 and 2.19 through 2.21, and single-pass power gain $G_1(L)$ [$\equiv \sinh^2 \Gamma L$], as in Equation 2.14, are calculated on the basis of near-degenerate operation with $\lambda_S \approx \lambda_I \approx 2$ μm.

[b] Operational option(s) if output power must build up from spontaneous parametric emission.

the pump, then these three lower-power regimes (A–C) are still amenable to OPA or DFG operation, as in Figures 2.2b and 2.2d, respectively.

2.3 ELEMENTS OF OPTICAL PARAMETRIC OSCILLATOR DESIGN

As already explained, we are primarily concerned in this chapter with tunable OPOs as coherent light sources for spectroscopic applications. Moreover, because such devices correspond inevitably to downconversion of input pump radiation (and are particularly well suited to that task), much interest is concentrated on the spectroscopic applications of tunable OPOs generating coherent light in the near-IR and mid-IR regions [40, 41]. Most of the arbitrarily chosen examples that are considered in later sections of this chapter are therefore more relevant to the IR region than to the visible and ultraviolet (UV) regions, as are the selected NLO materials surveyed in Table 2.1. Meanwhile, we consider a few specific examples of tunable OPO designs, many based on the ubiquitous QPM NLO material, PPLN.

There are many ways to design an OPO, depending on whether it is CW, ns-pulsed, or modelocked (i.e., corresponding to classes A, B, or C, respectively) and what its end use is intended to be [6, 37–42]. A key objective is invariably to ensure that the OPO has sufficiently high gain to overcome parasitic losses in the cavity.

One of the primary considerations concerns the extent to which the OPO's optical cavity is resonant with one or both of the signal and idler output waves and with the pump wave, and whether the pump source itself is in some way coupled to the OPO cavity. Assorted OPO design strategies have been reviewed elsewhere; for instance, Figure 2 of [37], Figure 3 of [38], Figure 1 of [39], and Figure 3 of [40] each provide a useful pictorial compilation. Likewise, as discussed in Sections 2.4 and 2.5 of this chapter, control of the OPO output wavelengths (and their optical bandwidth) is critical to spectroscopic applications. This generally depends on tuning of the OPO cavity itself (e.g., by varying the cavity length or by incorporating a suitable intracavity wavelength-selective element), or by tuning the pump laser wavelength, or (in the case of class B OPOs) by injection seeding of control radiation from an independent tunable low-power source.

Another means of using an OPO as a spectroscopic source is to take advantage of the intrinsically broad bandwidth of a free-running OPO and to use its signal or idler output for multiplex spectroscopy, with collection of the dispersed radiation by an optical-array detector. This approach has been demonstrated in various forms of OPO-based multiplex spectroscopy. The multiplex option (as discussed in Section 2.4) is able to use an extremely simple OPO cavity design, with much of the instrumental complexity transferred to the optical multichannel detection electronics. It is therefore attractive for various industrial laser-based monitoring applications where coherent light sources (e.g., OPOs) need to be as rugged, compact, and simple to control as possible.

The amenability of pulsed OPO radiation to NLO processes also enables it to be used in various NLO wavelength-extension schemes, such as sum-frequency generation (SFG), difference-frequency generation (DFG), second harmonic generation (SHG), and stimulated Raman scattering (SRS). These have been investigated [1, 27, 28] as ways to extend the fundamental tuning range of pulsed OPOs further into the ultraviolet and infrared regions.

2.3.1 Nanosecond-Pulsed Optical Parametric Oscillators

The initially reported PPLN-based OPO of Myers et al. [63] provides a useful example of typical operating conditions for a ns-pulsed OPO, as follows. A PPLN crystal (L = 5 mm, 0.5 mm thick) with a 31-μm QPM grating period was pumped at 1.064 μm by a pulsed, diode-pumped Nd:YAG laser (repetition rate, 100 Hz; pulse duration, 7 ns) with a focal spot diameter of 177 μm. A linear OPO cavity was formed by two carefully aligned reflectors (one 6.7-cm radius of curvature, the other flat) separated by 2.2 cm, each reflective (99% and 70% in this preliminary study [63]) and therefore resonant at the signal wavelength and transmissive at the pump and idler wavelengths. By varying the temperature of the PPLN crystal between room temperature and 180 °C, this OPO was continuously tunable from 1.66 μm to 2.95 μm. At 145 °C and λ_S = 1.83 μm, it was measured to have a pump threshold of 135 μJ, enabling damage-free pumping of the OPO as far as 10 times above threshold.

Subsequently [80], Myers et al. demonstrated an extended tuning range of 1.36 μm to 4.83 μm by implementing a multigrating PPLN chip (26 mm long, 0.5 mm thick), accommodating 25 gratings (each 0.5 mm wide) with QPM grating periods ranging from 26 μm to 32 μm in 0.25-μm steps. With this longer multigrating PPLN crystal and with

a higher-quality OPO cavity, an oscillation threshold of only 6 μJ was achieved, using a 7-ns pump pulse with a fluence of 0.09 J cm^{-2}. The average output power at an idler wavelength of 4 μm was 6 mW (with an average pump power of 100 mW at a repetition rate of 1 kHz).

These examples [63, 80] represent a relatively straightforward approach to ns-pulsed OPO operation, namely, in the form of a singly resonant oscillator (SRO), with *either* the signal wave *or* the idler wave (but not both) resonated in the cavity. Some other OPO designs [18, 19] incorporate a nonresonant oscillator (NRO) stage, which comprises an OPA-type medium in an optical cavity that is resonant at neither ω_S nor ω_I. Many additional examples of wavelength-control strategies for ns-pulsed OPOs will be presented in Section 2.4 of this chapter. Meanwhile, we briefly consider CW and ultrafast OPOs.

2.3.2 Continuous-Wave Optical Parametric Oscillators

While the SRO approach is often used in ns-pulsed (class B) OPO designs, realization of continuous-wave (CW) OPOs (i.e., class A) has presented much greater challenges [37, 38, 41, 48]. A doubly resonant oscillator (DRO), in which *both* signal *and* idler waves are resonated in the cavity, is intrinsically more complicated than an SRO but yields a lower oscillation threshold and has therefore been favored in many CW OPO designs [37, 38, 41]. Various multiparameter tuning approaches [38, 81, 82] have been devised to overcome mode- and cluster-hopping effects that complicate continuously tunable, single-longitudinal-mode operation of CW DROs. In one early example [82], a CW KTP DRO with a 40-mW oscillation threshold was pumped at ~1.047 μm near the signal/idler degeneracy point by a continuously tunable Nd:YLF laser, while maintaining resonance for a signal/idler pair at a discrete cavity length (stabilized to <0.4 nm) and tuning the OPO output frequencies over a range of ~4.5 GHz by tuning the pump laser frequency over a range of ~9 GHz. In another example [82], a CW KTP DRO with an oscillation threshold of <50 mW was pumped at ~0.769 μm by a single-stripe GaAlAs diode laser. Furthermore, by making the OPO cavity triply resonant (with the pump wave as well as the signal and idler waves), a pump-enhanced DRO attained an oscillation threshold as low as ~6 mW and yielded a 1.1-μm signal output power of ~10 mW with a diode-laser pump power of ~80 mW [83]. A CW PPLN DRO pumped at 0.810 μm by a 100-mW single-mode laser diode realized oscillation thresholds down to 16 mW, with quasicontinuous signal and idler tuning ranges of 1.15–1.25 μm and 2.31–2.66 μm, respectively, by variation of crystal temperature, pump wavelength, and grating period [84].

Singly resonant CW OPO operation can also be attained by pump enhancement [37, 38, 41, 85], with the OPO cavity resonant to the pump wave as well as signal or idler. In an early (but complicated) example of a CW pump-enhanced SRO [86], a KTP OPO was pumped at 532 nm by frequency-doubling an injection-locked single-frequency Nd:YAG laser and operated at ~2 times above threshold by double-passing both idler and pump waves and maintaining optimal phase relationships between all three waves in the standing-wave OPO cavity; with an oscillation theshold of 1.4 W, a CW pump power of 3.2 W yielded 1.07-W, 1.09-μm idler output. Schiller and

coworkers have reported CW pump-enhanced SROs based on PPLN [87] and MgO-doped $LiNbO_3$ (MgO:$LiNbO_3$) [88], with theoretical analysis [85].

Another way to achieve singly resonant CW OPO operation is to locate the NLO medium inside the cavity of the pump laser itself, comprising an intracavity SRO [37, 38, 41, 89–91]. For example, an early CW intracavity SRO comprised a KTP OPO located inside the cavity of a Ti:sapphire laser yielded idler output tunable from 2.53 μm to 2.87 μm with a maximum output power of ~0.4 W [92]. Corresponding Ti:sapphire-pumped intracavity SROs based on QPM NLO media such as PPLN (with signal and idler tuning ranges of 1.07–1.28 μm and 2.30–3.33 μm) [93] and PPKTP (with signal and idler tuning ranges of 1.14–1.27 μm and 2.23–2.73 μm) [91] have also been developed. A compact PPLN SRO sharing a dual cavity with a 1.064-μm Nd:YVO_4 mini-laser, pumped at 0.810 μm by a 1-W diode laser, yielded a diode-pump threshold of 310 mW; its quasicontinuous signal and idler tuning ranges were 1.45–1.60 μm and 3.16–4.02 μm, respectively [91, 94].

The availability of QPM NLO materials such as PPLN has greatly enhanced the feasibility of CW SROs, which are much more readily tunable than CW DROs [38]. This was first demonstrated by Bosenberg et al., using either standing-wave [95, 96] or ring [96] cavities. The ring OPO operated on a single longitudinal mode when pumped at 1.064 μm by a 13.5-W diode-pumped multiple-axial-mode CW Nd:YAG laser; by using a multigrating PPLN chip, combined with intracavity étalon and temperature tuning, the idler output could be tuned quasicontinuously from 3.95 μm to 3.25 μm with an optical bandwidth $\Delta\nu < 6$ GHz and a 3.6-W maximum power.

This PPLN SRO approach was extended [97] by replacing the multigrating PPLN chip by a "fan-out" grating on a 5-cm-long, 2-cm-wide PPLN crystal across which the QPM period changed continuously from 29.3 μm to 30.1 μm; single-frequency tuning of signal and idler outputs was achieved coarsely by translating the fan-out grating laterally, with finer tuning by rotating an intracavity étalon and varying the OPO cavity length at constant temperature.

Subsequent advances in PPLN-based CW SRO technology include: a singly resonant OPO ring cavity pumped at 0.925 μm by a 2.5-W diode laser (generating up to 0.48 W of idler output with a tuning range of 2.0–2.3 μm) [98]; a CW PPLN SRO pumped at 1.03–1.10 μm by a tunable 8-W Yb-doped CW fiber laser (generating up to 1.9 W of idler output with a tuning range of 3.0–3.7 μm) [99]; extended mode-hop-free tuning of a dual-cavity, pump-enhanced CW PPLN SRO (with idler tuning ranges of 2.71–3.26 μm and 4.07–5.26 μm) [100]; a pump-enhanced CW PPLN SRO pumped at ~0.81 μm by a tunable extended-cavity diode laser (generating up to 4 mW of idler output with a tuning range of 2.58–3.44 μm) [101]; a CW PPLN OPO, pumped at 1.064 μm by a CW Nd:YAG laser, for near-IR spectroscopic sensing by cavity-ringdown [102] and photoacoustic absorption [103] techniques; a critical comparison of the performance of CW QPM OPOs based on PPLN and PPRTA [104].

2.3.3 Ultrafast Optical Parametric Oscillators

We now turn from CW OPOs to ultrafast OPOs (classes C and D of Table 2.2). Despite the relatively high peak power of very short (sub-ns) pulses of coherent laser light, it is far from trivial to use such light to pump the NLO medium of an OPO

and to exceed its oscillation threshold [37, 38, 41]. This is because an ultrafast light pulse, on the timescale of picoseconds (ps, 10^{-12} s) or femtoseconds (fs, 10^{-15} s), does not have a sufficiently wide temporal window to enable a coherent parametric wave to build up coherent signal and idler waves in the NLO medium. Light travels only ~0.3 mm in 1 ps, which does not allow it to make multiple traversals of the NLO medium. Moreover, in contrast with the storage of population inversion in a laser, the NLO polarization in an OPO depends on the instantaneous optical field strength.

This significant problem is overcome by synchronous pumping (also used in some ultrafast lasers), in which a train of many consecutive ultrafast pulses from a pump laser interact sequentially with a single signal or idler pulse circulating within the OPO cavity. The modelocking interval of the pump laser (essentially the round-trip transit time in the laser cavity) must therefore equal the round-trip time of the downconverted (signal or idler) pulse in the OPO cavity. The situation is aggravated when sub-ps (e.g., ~100 fs) pump pulses are used, because the pump and signal (or idler) waves have sufficiently different group velocities that they undergo "temporal walk-off," becoming separated in space after traversing a relatively short distance (typically 1–10 mm for 100-fs pulses) in the NLO medium.

Practical ultrafast OPOs were introduced around 1990 and their utility grew as improved pump lasers, NLO materials (e.g., KTP, PPLN), and OPO cavity designs became available [37, 38, 41, 42, 45–48]. Research on ps- and fs-OPOs remains extremely active, and numerous broadly tunable commercial ultrafast optical parametric systems (not only OPOs, but also OPGs and OPAs) are now on the market. This is driven, at least in part, by the key role that ultrafast OPG/OPA/OPO-based spectroscopy and imaging plays in applications to biology and medicine, where many key processes occur on ps and fs timescales.

It is customary [38, 41] to classify synchronously pumped optical parametric systems as *either* CW ultrafast OPOs (i.e., pumped by a continuous train of ultrashort pulses) *or* quasi-CW/pulsed ultrafast OPOs (i.e., pumped by a burst of ultrashort pulses, contained in a ns or μs envelope). Because the former are effectively steady-state devices, the output is a genuinely continuous train of identical pulses, whereas output from the latter comprises groups of ultrashort pulses in which the duration and amplitude of any pulse can vary across the pulse envelope. Nevertheless, quasi-CW/pulsed ultrafast OPOs tend to yield significantly higher peak powers than their more stable CW ultrafast counterpart and have in the past therefore been more readily realized. In recent years, the advent of CW ultrafast OPOs has been promoted by the availability of high-power CW modelocked lasers and improved NLO materials, which enable CW ultrafast OPOs to be operated in the (highly desirable) SRO format.

Specific operational aspects of some ps-pulsed tunable OPOs are discussed in Section 2.5.3. Additional technical intricacies of ultrafast optical parametric devices (corresponding to classes C and D of Table 2.2) are beyond the scope of this chapter. The reader is directed to relevant review articles [37, 38, 41, 42, 45–48, 105] (particularly those concerning near- or mid-IR OPOs) and to various examples of tunable OPOs operating on ps and fs timescales [105–127], as well as work on ultrafast traveling-wave OPGs and OPAs [128–131].

2.3.4 Optical Parametric Devices for Spectroscopic Applications

Spectroscopic measurement is an area of laser-based science and technology in which optical parametric devices such as OPOs play a significant role as versatile NLO sources of tunable coherent light. Some key elements of the spectroscopic applications of tunable OPOs, on which this chapter focuses, are listed in Table 2.3.

Practical laser-spectroscopic measurements usually require a source of coherent light (e.g., a tunable OPO) that is narrowband, continuously tunable (without

TABLE 2.3
Operational Strategies for OPOs Applied to Spectroscopy

Objectives	Operational strategies	Comments on instrument/technique
Wavelength range: what spectra are to be measured?	UV/visible (0.2–0.7 μm); near infrared (0.7–4.0 μm); longwave infrared (>4.0 μm)	Many nonlinear-optical OPO materials are available, but less well-developed for the longwave IR. The UV/visible region is not considered thoroughly here.
Phase matching: BPM or QPM?	BPM, angle- or *T*-tuned; QPM in periodic NLO materials	BPM is well established and preferred for high-power operation, also mid-IR. Low-threshold QPM media are available for both pulsed and cw OPOs.
Temporal: pulsed or continuous-wave?	Pulsed for power and timing; Cw for narrowest bandwidth	Ultrafast (ps, fs) OPO output pulses are relatively broadband—considered only marginally here.
Optical bandwidth: narrowband or broadband?	Broadband (e.g., free-running); single longitudinal mode	The Fourier-transform limit is 44 MHz (0.0015 cm^{-1}) for an ideal 10-ns pulse. Cw OPOs enable even lower $\Delta\nu$.
Mode of recording spectra: multiplex or continuously tunable?	Scan narrowband signal/idler OPO output wavelength; free-running OPOs operate broadband in multiplex cases	Wavelength control gives continuously tuned narrowband spectra. Multiplex spectroscopy with dispersed detection or multiwavelength tailored.
Output wavelength control: via cavity length and/or intracavity tuning elements or variation of pump wavelength or injection seeding?	Cavity length control + intracavity grating or étalon; tuned pump with fixed cavity Injection seeding of signal or idler by a tunable low-power coherent light source	Intracavity-element designs yield broad tunability but can be complicated. Pump tuning is particularly useful for cw OPOs. Injection seeding enables narrowband, mode-hop-free spectroscopy and tailored multiwavelength studies.

The operational strategies offer ways to use OPOs for spectroscopic applications, such as:

Linear absorption (e.g., with multipass cell)	Nonlinear-optical (e.g., coherent Raman)
CRD absorption spectra	Atmospheric remote sensing (e.g., DIAL)
High-resolution spectra ($\Delta\nu \approx$ MHz/kHz/Hz)	Fast (μs, ns) and ultrafast (ps, fs) processes

Source: Adapted from He, Y., P. Wang, R. T. White, and B. J. Orr, *Optics and Photonics News*, 13 (5), 56–60, 76, 2002 [28]; and Orr, B. J., in *Encyclopedia of Modern Optics*, Elsevier Physics, 2004, "Nonlinear optics – applications" section, 43–51 [29].

mode-hops or other discontinuities), and sufficiently stable and powerful to yield high signal-to-noise ratios in recorded spectra. The intensity of coherent radiation is a key factor in the case of NLO spectroscopic measurements. Much developmental effort on tunable OPOs and other optical parametric devices for spectroscopic purposes (as reviewed in Sections 2.3.1 through 2.3.3 and Section 2.4) has aimed to meet such performance criteria. Moreover, particular applications (e.g., field-based spectroscopic sensing) impose additional constraints concerning system cost, compactness, ruggedness, portability, and ease of operation.

The optical bandwidth of tunable OPO radiation will often limit the attainable spectroscopic resolution. The FWHM linewidth arising in a particular spectroscopic application will usually determine the optimal optical bandwidth of OPO output light needed: typically a few cm^{-1} ($1\ cm^{-1} = 30$ GHz) for condensed phases or complicated biomolecular species, ~0.2 cm^{-1} (~60 GHz) for pressure-broadened gas-phase samples, and less than ~0.02 cm^{-1} (~0.7 GHz) for sub-Doppler spectra of atoms and molecules (e.g., with mass ~30 g mol^{-1} detected at 300 K and an absorption wavelength of 1 μm). High-resolution laser spectroscopy therefore requires narrowband radiation, preferably on a single-longitudinal-mode (SLM) basis.

There is an inherent limitation on the minimum optical bandwidth attainable in the case of pulsed light. A coherent light pulse with a full-width-at-half-maximum (FWHM) duration Δt, can have an FWHM optical bandwidth $\Delta\nu$ no finer than the associated Fourier-transform (FT) limit. For example, the FT limit for an idealized light pulse with pure Gaussian temporal and power-spectrum profiles is defined in terms of the time–bandwidth product [132]:

$$\Delta\nu \cdot \Delta t = (2 \ln 2/\pi) = 0.441. \tag{2.23}$$

An illustrative consequence of this relationship is that a Gaussian light pulse with $\Delta t =$ 10 ns will have an FT-limited optical bandwidth $\Delta\nu = 44$ MHz (i.e., 0.0015 cm^{-1}), whereas the corresponding FT limits for shorter Gaussian pulses with $\Delta t = 10$ ps and 10 fs are $\Delta\nu = 44$ GHz and 44 THz (i.e., 1.5 cm^{-1} and 1500 cm^{-1}), respectively. It is evident that CW (or at least long-pulse) coherent light sources are more amenable to high-resolution spectroscopy.

Aspects of Table 2.3 are relevant to Section 2.4, which considers in more detail ways to control and enhance the optical bandwidth and tunability of ns-pulsed OPOs.

2.4 OPTICAL BANDWIDTH CONTROL IN NANOSECOND-PULSED OPOs

In this section, we consider pulsed tunable OPOs that operate on nanosecond (10^{-9} s) timescales, and design features that make them fit for spectroscopy, which is one of the principal areas of application for optical parametric devices. Some design and wavelength-control features used in ns-pulsed OPOs are depicted schematically in Figure 2.2.

Our research group at Macquarie University has made some substantial contributions to this area of instrumental development. The first edition of this book

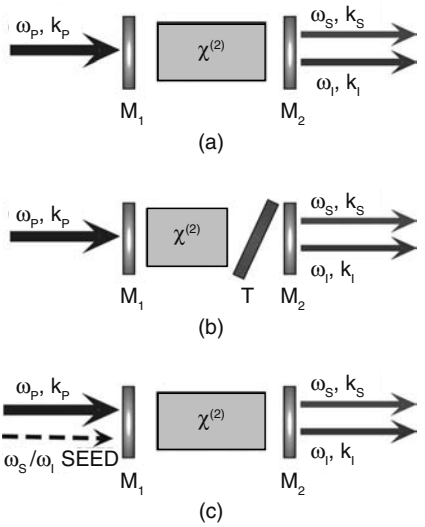

FIGURE 2.2 Schematic diagrams of three forms of optical parametric oscillator: (a) free-running OPO (with no active wavelength control), similar to Figure 2.1(c); (b) OPO with an intracavity tuning element (T); (c) injection-seeded OPO.

[1] reviewed much of our foundation work on injection-seeded, ns-pulsed tunable OPOs based on the popular NLO medium β-BaB_2O_4 (BBO), pumped at 355 nm, operating in the visible and near-IR regions (~0.4–2.7 μm) [133–141] and upconverted by NLO techniques to the near UV [27, 135]. Since then, our interest has shifted to injection-seeded, ns-pulsed tunable OPOs based on $LiNbO_3$ and its QPM counterpart PPLN [27, 28, 142–146], and, more recently, PPKTP [147–154]. Recent outcomes of research on injection-seeded tunable OPOs are surveyed in Section 2.4.2, preceded in Section 2.4.1 by a discussion of other methods of OPO wavelength control.

2.4.1 Factors Influencing Optical Bandwidth and Tunability

The first OPO, demonstrated by Giordmaine and Miller in 1965 [155], was ns pulsed; it was based on $LiNbO_3$, tunable over the range ~0.96–1.16 μm, spanning a signal- and idler-wavelength range of ±0.1 μm on either side of the degeneracy point defined by the 529-nm pump radiation (from a frequency-doubled, Q-switched Nd:$CaWO_4$ laser). This advance occurred soon after lasers were discovered and the potential of nonlinear optics had been realized through harmonic-generation processes such as frequency doubling [57, 58]. As already outlined in Section 2.1, ns-pulsed OPOs were soon established as practical sources of tunable coherent light for significant applications, such as spectroscopic sensing of chemical processes, in industrial or environmental diagnostics, and in basic science. Nevertheless, subsequent progress has been both laborious and sporadic toward being able to control the optical bandwidth and tunability of OPO output sufficiently well for OPOs to be a convenient form of spectroscopic instrumentation.

In a typical ns-pulsed OPO, the pump laser delivers sufficient power for parametric gain to build up from noise during the pump pulse, thereby exceeding the threshold for oscillation. To maximize gain, the parametric (signal and/or idler) waves are amplified by multipassing them during the pump pulse in an optical resonator, as depicted in Figures 2.1c and 2.2. Light travels ~3 m during a 10-ns pump pulse, so that the parametric waves can then make ~15 round-trips of a 10-cm linear OPO cavity. Multiple passes in the OPO cavity also tend to reduce the optical bandwidth of light emerging from a simple free-running pulsed OPO [11].

Such a free-running OPO, comprising simply an optical cavity with input and output mirrors M_1 and M_2 but with no wavelength-selective elements, is depicted in Figure 2.2a. The output radiation from such an OPO generally has a relatively broad optical bandwidth, typically ~5 cm^{-1} (~150 GHz) or more.

It is reasonably straightforward to predict the single-pass gain bandwidth of an idealized OPO in the low-gain, plane-wave limit [8–11, 156], as is shown in Equations 2.14 through 2.21 and borne out by some early experimental demonstrations [8, 9]. However, this idealized gain bandwidth does not necessarily correspond closely to the actual spectroscopic bandwidth of the OPO output radiation under operating conditions well above the oscillation threshold and in a multipass optical resonator [138, 139, 156]. In fact, it is the spectroscopic bandwidth, rather than the single-pass gain bandwidth, that is required to assess the practical utility of a free-running pulsed OPO in a given spectroscopic application.

The spectroscopic bandwidth of output radiation from a free-running, pulsed OPO is influenced by many factors, such as: dispersion and absorption of the OPO medium; wavelengths λ_P, λ_S, and λ_I; type of phase matching (BPM or QPM, CPM or NCPM, whether collinear or not); crystal dimensions and orientation; characteristics of the optical resonator such as the cavity reflectivity and the effective number of passes of the resonated wave; beam quality, optical bandwidth, divergence, pulse duration, and pulse energy of the pump radiation; the OPO's oscillation threshold; and NLO conversion efficiency [1, 8–11, 20, 21, 27, 31, 138, 139]. The collective outcome of most of these effects can be modeled by means of the versatile SNLO software package [24]. There is scope for control of these various factors in devising simple, free-running pulsed OPO devices with output bandwidths adequate for certain spectroscopic applications requiring moderate resolution (i.e., ~1 cm^{-1}).

As already indicated in Section 2.3.1 [63, 80], there is much interest in ns-pulsed tunable OPOs based on QPM NLO media such as PPLN, PPKTP, PPKTA, and PPRTA. Operation of pulsed QPM OPOs has been realized with much lower pump pulse energies than for pulsed BPM OPOs, in view of the higher FOM of QPM media (see Table 2.1) as well as their NCPM amenability and long interaction lengths. Diode-laser pump sources with low peak powers can therefore be used to drive efficient ns-pulsed OPOs based on PPLN [157, 158] and PPKTP [159]. Moreover, there have been several recent reports of intracavity ns-pulsed OPOs based on PPLN [160–162] and MgO-doped PPLN (MgO:PPLN) [163]. We note also a recent report of a cascaded PPLN OPO [164], in which the signal field of a primary OPO internally pumps a secondary OPO, with multiple output wavelengths controlled by temperature tuning and a dual fan-out grating structure. There are numerous additional representative examples of free-running ns-pulsed QPM OPOs [165–177].

Free-running pulsed OPOs represent one extreme of operational simplicity, yielding relatively broadband output radiation suitable for low-resolution or multiplex spectroscopy. Additional OPO wavelength-control measures are usually necessary for higher-resolution spectroscopic applications.

At the other extreme of operational complexity, intracavity wavelength-selective elements, such as gratings and/or étalons, provide a traditional way to control the output wavelength of a ns-pulsed OPO and to attain a narrow optical bandwidth. One such approach is depicted schematically in Figure 2.2b, where a tuning element T (in this case, a tilted étalon or filter; in other designs, an intracavity diffraction grating replacing the output cavity mirror M_2) is inserted in the cavity. Such approaches were used in early pulsed $LiNbO_3$ OPOs that were continuously tunable in the near IR with an optical bandwidth of ~0.1 cm^{-1} (~3 GHz) [1, 9–11, 14, 178–181]. However, these tended to be difficult to operate and to be damage-prone (with intracavity losses from gratings and étalons causing the oscillation threshold to approach the damage threshold of OPO NLO materials such as $LiNbO_3$). Many of these problems had been addressed by the mid-1980s, and assorted designs now abound for grating-tuned ns-pulsed OPOs, both BPM [15–19, 27, 28, 182–184] and QPM [185–190]. Other novel tuning strategies for QPM OPOs include use of a photorefractive distributed-feedback grating written by UV light into the PPLN NLO element [191] and electro-optic tuning by means of a three-segment PPLN crystal [192]. Specialized cavity designs that are appropriate for CW and ultrafast tunable OPOs have been outlined in Sections 2.3.2 and 2.3.3, respectively.

As explained in Section 2.3.4, continuous narrowband (preferably SLM) tunability is a performance characteristic of ns-pulsed OPOs that makes them amenable to high-resolution spectroscopy. The pre-1980 initiatives of Brosnan and Byer [11] laid the foundation for this objective. A commercially viable approach to this ideal is the advanced KTP OPO/NRO/OPA system of Bosenberg and Guyer [18, 19], which is continuously tunable under computer control in the near IR (1.3–4 μm) with narrow optical bandwidth (~0.02 cm^{-1} or better). We note that Scherer and colleagues [193, 194] have used tunable SLM IR radiation from such an OPO system to record high-quality rovibrational cavity ringdown (CRD) spectra of molecules (e.g., in combustion media [194]). CRD spectroscopy [195, 196] uses the temporal decay of light traversing a high-finesse optical cavity to enhance resolution, sensitivity, and photometric precision.

Another grating-tuned OPO [188–190] is a ns-pulsed PPLN OPO, tuned by a grazing-incidence intracavity grating (optical bandwidth ≈ 0.3 cm^{-1}). This has been used to record photoacoustic absorption spectra of methane (CH_4) in nitrogen (N_2) gas with a trace-level sensitivity approaching 1 ppbV (1 part in 10^9 by volume).

Vodopyanov has provided informative reviews [39, 40] of various ns-pulsed mid-IR tunable OPOs, of which a few can generate output radiation that is sufficiently narrowband (with sub-cm^{-1} optical bandwidth) to enable rotationally resolved spectroscopic sensing of molecules in the gas phase.

Richman et al. [197] developed a ns-pulsed SLM tunable OPO system, comprising a three-mirror signal-resonant ring cavity with a fan-out PPLN grating and an electronically tunable intracavity étalon (free spectral range = 420 GHz; finesse = 60; insertion loss = 30%); it was pumped at a 1-kHz repetition rate by 200-μJ pulses

from an SLM Nd:YAG laser. Its signal and idler tuning ranges were 1.45–1.8 μm and 2.6–4 μm with maximum pulse energies of 18 μJ and 15 μJ, respectively; continuous SLM tuning was feasible over ~10 cm^{-1} (~300 GHz) with ~0.005-cm^{-1} (~150-MHz) optical bandwidth. The output wavelengths and optical bandwidth of an earlier ns-pulsed tunable $LiNbO_3$ OPO, pumped at 930 nm by a Ti:sapphire laser, were controlled by an electronically tunable intracavity Fabry–Perot étalon [198].

A representative longer-wavelength ns-pulsed narrowband tunable coherent light source [199] used the NLO medium $ZnGeP_2$ (ZGP), pumped by the 2.55-μm idler output of a $LiNbO_3$ OPO, which was itself pumped at 1.064 μm by a Q-switched Nd:YAG laser. The signal-resonant ZGP OPO cavity incorporated a Littrow diffraction grating and a tiltable Si-plate étalon as tuning elements, yielding mid-IR output with 0.1-cm^{-1} (3-GHz) optical bandwidth.

A further development by Aniolek et al. comprised narrowband PPLN-based OPG/OPA tunable coherent light sources [200, 201], in which broadband (~15 cm^{-1} FWHM) output from a PPLN OPG was spectrally filtered before being amplified by a PPLN OPA. In the later development [201], both OPG and OPA stages were pumped at 1.064 μm by a 120-Hz Nd:YAG microlaser incorporating a Cr^{4+}:YAG passive Q switch. After pre-OPA spectral filtering via a high-finesse air-spaced étalon, the idler output of the OPG/OPA system was continuously tunable in 15 cm^{-1} (450 GHz) segments and had an optical bandwidth of ~0.05 cm^{-1} (~1.5 GHz) FWHM.

A closely related development [202] comprises an injection-seeded ns-pulsed OPG/OPA system based on diode-laser-pumped BBO (β-barium borate, BaB_2O_4) that combines relatively low thresholds with good conversion efficiencies. Because there is no need for active control of the optical properties of an OPO cavity, so that it matches the injected radiation field, external seeding over wide ranges by CW SLM lasers is straightforward. The signal (~0.628 μm) and idler (~0.815 μm) outputs of this OPG/OPA system had an optical bandwidth of ~0.07 cm^{-1} (~2.1 GHz) FWHM and were continuously tunable over a range of 20–30 cm^{-1} (600–900 THz).

The associated subject of injection-seeded, ns-pulsed tunable OPOs will be dealt with in greater detail in Sections 2.4.2 and 2.4.3.

2.4.2 Injection-Seeded Pulsed OPOs: Early Days

Injection seeding, by a low-power tunable coherent source such as a tunable diode laser (TDL), is a popular alternative approach to OPO wavelength control. This approach is depicted in Figure 2.3c; in practice, a ring cavity is often used to avoid feedback from the OPO to the seed laser. A significant advantage of injection seeding is that OPO construction is simplified by putting the wavelength-control function into a module that is effectively separate from the optical generation and amplification functions.

2.4.2.1 Historical Overview

Injection seeding of an OPO is not a recent innovation, having been first demonstrated and qualitatively explained by Bjorkholm and Danielmeyer [203], who used pulsed, single-mode ruby and Nd:YAG lasers as pump and seed, respectively, for a $LiNbO_3$ OPO. Their work was reported in 1969, a short while before Kreuzer first used an intracavity étalon to achieve single-mode operation of an OPO [204].

An early rate-equation model was developed by Cassedy and Jain [205], to provide a realistic qualitative model of such an injection-seeded pulsed OPO. Subsequent studies of ns-pulsed OPOs have used a variety of sources for injection seeding, as reviewed elsewhere [1, 27–29].

Many of the early (pre-1995) investigations of injection-seeded OPOs were performed with fixed seed laser wavelength and therefore appear to have focused primarily on attaining lower OPO oscillation threshold, higher efficiency, and narrower linewidth, rather than on continuous tunability [1, 20, 203, 206]. Subsequent research, both at Macquarie University [133–154] and elsewhere [207–226], has aimed to transfer the continuous tunability of a low-power seed laser to the signal and idler outputs of a higher-power ns-pulsed tunable OPO. Even so, reported demonstrations [27, 28, 143–145, 211, 214, 219–221] of injection-seeded ns-pulsed OPO systems used for high-resolution spectroscopy were relatively slow to emerge. Such applications require a narrow optical bandwidth (close to the Fourier-transform limit), high spatial beam quality, and continuously tunable single-longitudinal-mode operation.

Our own early work in this area (which was initiated in collaboration with Wallenstein, Fix, and others at Universität Kaiserslautern [133–154]) showed that a singly resonant BBO OPO, injection-seeded at the signal wavelength by narrowband radiation from a low-intensity tunable dye laser, could be continuously tuned in a spectroscopically useful fashion. This OPO yielded narrowband (~0.1 cm^{-1}) signal and idler outputs, continuously tunable over a wide range (>100 cm^{-1}) and with sufficient intensity and spatial coherence to enable applications to coherent Raman spectroscopy, as further discussed in later parts of this chapter.

2.4.2.2 Mechanism of Injection-Seeded OPOs

The mechanism of pulsed OPO wavelength control by injection seeding was well explained in qualitative terms from the outset [203]. It is understood that when a singly resonant OPO is switched on by a pulse of pump radiation exceeding the oscillation threshold, the various resonant cavity modes falling within its gain bandwidth build up exponentially from noise at different rates, which depend on the extent of their phase mismatch Δk. When the pump intensity is very close to the oscillation threshold, the output of an ideal OPO is expected to build up to a steady state in which only the cavity mode with $\Delta k \approx 0$ is oscillating. In reality, however, an OPO pumped at any practical margin above oscillation threshold tends to oscillate on more than one cavity mode, so that the output of a free-running pulsed OPO is intrinsically multimode and broadband. This can be overcome by injecting narrowband radiation coinciding with the frequency of one (or more) of the OPO cavity modes: If this injected radiation is significantly more intense than the noise level, the OPO will tend to oscillate predominantly on the injection-seeded resonant OPO cavity mode(s), which need not correspond to $\Delta k \approx 0$. It has been verified that the exact OPO resonant output frequency is determined by the optical cavity length, but not the seed frequency [144, 145]. If the duration of pumping is sustained, noise-generated oscillations will eventually build up and compete with the seeded mode(s) (e.g., as in CW OPOs, which do not respond markedly to injection seeding). However, this does not occur if the pump pulse is sufficiently short (or is terminated by pump depletion in the OPO gain process).

The theory of Cassedy and Jain [205] is consistent with this injection-seeding mechanism for a pulsed OPO. Moreover, this mechanism is borne out by the experiments of Fix and coworkers [210, 218, 223] with a pulsed BBO OPO operating close to its oscillation threshold; these reveal a halving of threshold pump energy as the seed radiation (from a pulsed dye laser) is increased in intensity 1000-fold (ranging from a pump threshold of 14 mJ per pulse with seed energies around 0.1 nJ per pulse to a 7-mJ threshold with 100-nJ seeding).

If the seed radiation is of sufficiently narrow bandwidth (as in several early instances of injection-seeded OPOs [20, 134, 203, 206–210]), then it is possible to match the narrowband seed frequency to that of a single cavity resonance and thereby to attain SLM OPO wavelength control. To achieve continuous tuning of the resonant OPO output without mode hopping, it is then necessary to vary the OPO cavity length synchronously with the seed-frequency scan. For scans over moderate frequency ranges, in the case of a BPM OPO, it is also necessary to vary the angular setting of the NLO gain medium, to keep the seeded mode near the $\Delta k \approx 0$ peak of the gain profile. Further experiments by Fix and Wallenstein [218], on an injection-seeded ns-pulsed BBO OPO with a very short (3.5-mm) optical cavity, were able to resolve discrete longitudinal mode structure and to examine its SLM dependence and fluctuations in output power on pump pulse energy and times-above-threshold factor.

2.4.2.3 Passively Seeded OPO Cavities

Passive OPO cavity control is a distinctive approach to injection-seeded tuning of ns-pulsed OPOs of an OPO for spectroscopic purposes [1, 26–29, 133–135, 140, 142]. This has been used at Macquarie University in the context of BPM media such as BBO and $LiNbO_3$. Our initial work [133–135] sought continuous tuning with moderate spectral bandwidth, rather than SLM operation. The tunable source used for injection seeding at the signal wavelength of our BBO OPO was a multimode dye laser, which is still sufficiently narrowband to generate rotationally resolved molecular spectra with linewidths approaching Doppler- and pressure-broadened limits. By continuously scanning the seed wavelength (and, on occasions, detuning the OPO cavity), it was possible for the OPO signal wavelength to be scanned smoothly over several cm^{-1}, without adjusting the phase-matching angle of the BBO crystal.

This approach was similar in some respects to a report by Abdullin et al. in 1984 [228], in which a multimode Nd:YAG laser pumped two ns-pulsed SROs, one an étalon-narrowed OPO based on $Ba_2NaNb_5O_{15}$ (popularly known as "banana") used to seed the other, a $LiNbO_3$ OPO. It was reported [228] that the output of the latter OPO could be tuned over a range of ~10 cm^{-1} (~300 GHz) by varying only the injection-seeding wavelength from the former. However, it is not clear that the output wavelengths from this injection-seeded OPO system could actually be continuously scanned (e.g., as required to record spectra).

At that stage approximately 15 years ago, it was evident [1] that injection seeding could play a key role in OPO technology, as a way to control and continuously tune signal and idler outputs of a pulsed, tunable OPO (instead of intracavity gratings and étalons), and that it was becoming increasingly well understood. By transferring wavelength-control complexities from the OPO cavity to the tunable seed source, it is possible for an injection-seeded OPO to be extremely small and simple: just two

mirrors and an NLO crystal, all on appropriate optical mounts that do not need to be adjusted during moderate wavelength scans over several cm^{-1}.

In our distinctive approach to passive OPO cavity control, one or more of the cavity reflectors is slightly misaligned to facilitate continuous tuning of the injection-seeded OPO signal and idler outputs. This measure decreases the effective finesse of the OPO cavity, so that it is not necessary to lock the OPO cavity length to the seed wavelength and effectively dispenses with active control of the OPO cavity and is therefore simpler optically and electronically. The method depends on the OPO cavity having a high Fresnel number, so that a series of high-order transverse modes can smooth out the sharp, widely separated resonances that occur when the OPO cavity is well aligned; a resulting disadvantage is that the multiple transverse modes tend to cause some degradation of output beam quality. Nevertheless, this approach has proved useful for many applications of tunable OPOs, with seeding by either pulsed dye lasers or CW tunable diode lasers (TDLs) [1, 26–29, 140, 142].

2.4.2.4 Multiplex and Multiwavelength Seeded OPOs

The above passive, misaligned-cavity approach to injection seeding of ns-pulsed BPM OPOs is well suited for multiline spectroscopic applications requiring a coherent light source that simultaneously generates two or more adjustable output wavelengths. This has previously been verified by OPO CARS experiments in our laboratory [140]. Dual-wavelength, pulsed OPO signal output at ~607 nm was generated by a passive-cavity BBO OPO, pumped at 355 nm by a pulsed, SLM Nd:YAG laser and injection-seeded at two separate 855-nm idler wavelengths by a pair of SLM TDLs. The 607-nm signal output served as the Raman Stokes beams in an NLO CARS process, with monochromatic 532-nm radiation (from the same SLM Nd:YAG laser) serving as the Raman pump beam. In this way, single-shot coherent-Raman thermometric spectra were recorded for nitrogen (N_2) in furnace air [140], by tuning the two signal/Stokes wavelengths to different rotational-state features in the *Q* branch of the Raman spectrum. This is an example of so-called spectroscopic tailoring of OPO output radiation to match spectral features of interest. By turning the injection seeding off, multiplex broadband OPO CARS measurements were also made [140] of a portion of the same Raman spectrum, but these were less sensitive than the dual-line Raman spectra recorded with the dual-wavelength injection-seeded OPO.

Incidentally, this dual-wavelength approach to injection seeding of a ns-pulsed OPO [140] had a useful mechanistic outcome in the context of NLO backconversion effects in the OPO itself [141]. By injection-seeding a ns-pulsed passive-cavity BBO OPO at two distinct idler wavelengths (separated by a frequency interval Δ falling within the 350-GHz free-running OPO bandwidth), above-threshold operation was found [141] to yield sidebands at multiples of Δ in the signal-output spectrum and extending well beyond the regular free-running OPO gain profile. The sideband spacing varied smoothly as Δ was tuned and corresponding sidebands were observed on the transmitted pump radiation. This provides direct evidence of backconversion of signal and idler waves in the pulsed OPO, consistent with temporal observations and other aspects of OPO performance such as the phase-matching conditions for the various OPO pump and idler (seed) frequencies that are involved.

Dual-wavelength injection seeding of ns-pulsed OPOs is particularly relevant to atmospheric remote-sensing techniques such as DIAL (differential absorption lidar) [26]. This has been borne out in two OPO-based IR DIAL demonstrations [221, 225, 226]. In one case [221], narrowband TDL-seeded OPO output was switched between on- and off-resonance wavelengths on alternate ns-pulsed pump laser shots, to make range-resolved measurements of atmospheric CH_4. Alternatively, in a system designed for airborne H_2O-vapor DIAL [225, 226], the ns-pulsed OPO output was switched rapidly from narrowband, TDL-seeded, on-resonance, to broadband, unseeded, (predominantly) off-resonance.

More recently, a novel spectroscopic tailoring concept, capable of extension from dual- to multiwavelength remote-sensing applications, has been proposed [26, 28, 29]. This requires a source of coherent, pulsed radiation to simultaneously generate a structured set of discrete wavelengths, each of which is set to be on- or off-resonance with characteristic features in DIAL or long-path absorption spectra of molecular target species of interest. Such an approach to remote sensing requires a multiplex system that employs a set of single-mode TDLs and a fiber-optic switch to injection-seed a multiwavelength passive-cavity-pulsed OPO. Modulation and demodulation sequences would decode resulting spectroscopic signals, with a multiplex advantage for sensitivity and specificity.

Multiwavelength spectroscopic tailoring of OPO output by injection seeding is readily implemented with a BPM medium in a passive cavity [26, 28, 29, 140], but a similar approach is also possible in QPM media with grating channels wide enough to allow different noncollinear phase-matching angles for each of the OPO output wavelengths [229, 230]. Such an approach has been used by Yang and Velsko [187] in a wavelength-agile PPLN OPO DIAL sensing system, pumped by a 1-kHz pulsed Nd:YAG laser and injection-seeded by two 1.5-μm TDLs; its 3-μm idler output is rapidly tunable over 400 cm^{-1} (12 THz) by using an acousto-optic deflector to vary the pump-beam angle.

2.4.3 Injection-Seeded Pulsed OPOs: Recent Progress

2.4.3.1 Actively Seeded OPO Cavities

As already explained in Sections 2.3.1, 2.3.4, and 2.4.1, narrowband operation (preferably SLM, with mode-hop-free continuous tunability) of a ns-pulsed OPO is traditionally achieved by means of wavelength-selective elements, such as intracavity gratings and/or étalons, as sketched in Figure 2.2b. Within the last 20 years, accompanying the revival in OPO technology, it has been recognized that injection seeding (by means of narrowband, tunable radiation from a low-power external light source) is an especially efficient way to control the output wavelengths and optical bandwidth of ns-pulsed OPOs intended for spectroscopic applications [1, 27, 28], as sketched in Figure 2.2c. Early progress in this regard has been surveyed in Section 2.4.2. In the current section, more recent progress on injection-seeded ns-pulsed OPOs is examined, with emphasis on high-performance instruments of this type that are closely associated with our own research at Macquarie University.

Injection seeding simplifies the design of a ns-pulsed OPO, by separating its wavelength-control function from that of power amplification. In this context, we

have exploited an SLM TDL for continuously tunable, mode-hop-free injection seeding of ns-pulsed near-IR OPOs based on $LiNbO_3$ in either its bulk [142] or QPM (PPLN) [143–146] forms, pumped at 1.064 μm by a high-performance Q-switched SLM Nd:YAG laser. This yields optical bandwidths that have been spectroscopically verified to be as low as ~0.005 cm^{-1} (~150 MHz) or better, approaching the FT limit of the pulsed radiation as defined in Equation 2.23 [132].

Applications of injection-seeded ns-pulsed OPO systems to high-resolution spectroscopy require narrow optical bandwidth (close to the FT limit), high spatial beam quality, and continuously tunable SLM operation. The performance criteria of such a spectroscopic OPO system therefore typically include the following three design features:

- A ns-pulsed pump laser, typically a 1.064-μm flashlamp-pumped, Q-switched Nd:YAG oscillator/amplifier system, usually with an injection seeder for SLM operation [25]
- Tunable low-power CW laser (usually an SLM TDL) to be injection seeder for the OPO
- Control of the injection-seeded OPO cavity length, usually achieved by actively varying the OPO cavity length synchronously with the wavelength scan of the seed source, employing some form of stabilization by optoelectronic feedback

A modular tunable OPO spectroscopic system, which relies on these design features, is illustrated schematically in Figure 2.3 [27, 143–146]. This representative example is based on the QPM NLO medium PPLN, with a multigrating design [80] to provide a broad tuning range.

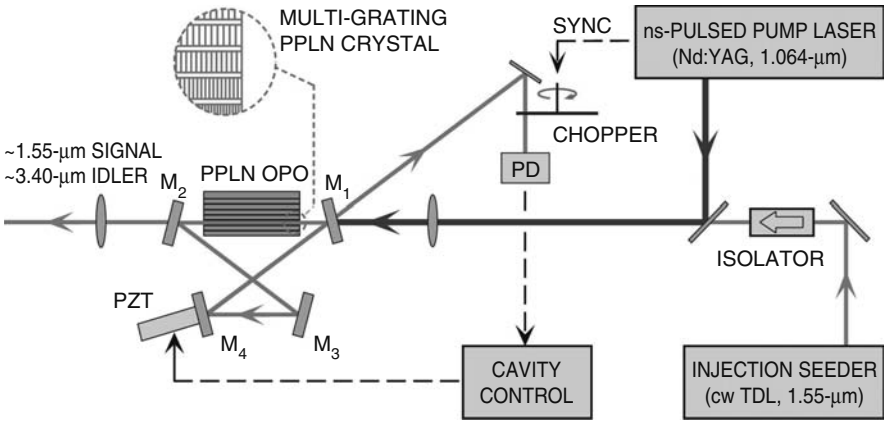

FIGURE 2.3 Schematic diagram of an injection-seeded tunable ns-pulsed OPO system, based on a multigrating PPLN chip with active intensity-dip cavity control [27–29, 143–145]. The OPO comprises a four-mirror ring cavity that is pumped at 1.064 μm by a ns-pulsed Nd:YAG laser and seeded (typically at ~1.55 μm) by a CW TDL. The resulting signal and idler outputs at wavelengths λ_S and λ_I (typically ~1.55 μm and ~3.4 μm), respectively, are continuously tunable on a single longitudinal mode. PD = photodetector; PZT = piezoelectric translator; $M_{1–4}$ = cavity reflectors; the inset shows the QPM multigrating structure of the PPLN nonlinear-optical crystal.

2.4.3.2 Intensity-Dip OPO Cavity Control

The TDL-seeded, ns-pulsed PPLN OPO system uses an actively controlled ring cavity and depends on our distinctive intensity-dip feedback scheme [143–145], in which CW TDL seed light reflected off the four-mirror OPO ring cavity is monitored by a photodetector (PD) and used to optimize the cavity length by means of a piezoelectric translator (PZT) in the interval (typically 100 ms) between successive pulses from the ns-pulsed 1.064-μm Nd:YAG pump laser. Typical signal and idler output wavelengths generated by this OPO system are $\lambda_S \approx 1.55$ μm (equal to the wavelength λ_{seed} of the CW TDL injection seeder) and $\lambda_I \approx 3.40$ μm. Using a pump pulse energy of ~1 mJ (delivered to the PPLN crystal with a beam waist of ~0.1 mm FWHM), the total output power is typically ~0.1 mJ (of which ~70% is signal radiation), but this OPO output can be pulse-amplified to a total output pulse energy of ~2 mJ by using an additional OPA stage based on a bulk BPM $LiNbO_3$ crystal [27, 143–145].

Such a high-performance narrowband tunable PPLN OPO system can be pumped at 1.064 μm and 10 Hz (with a pulse energy of ~1 mJ, delivered to the PPLN crystal within a beam waist of ~0.1 mm FWHM) *either* by an elaborate injection-seeded SLM Nd:YAG laser [143, 144] *or* by a more compact and economical multimode (MM) Nd:YAG laser [145]. In the former (SLM-pumped) case, both signal and idler output beams are narrowband, with $\Delta\nu \approx 130$ MHz (~0.0045 cm^{-1}) FWHM, approaching the FT limit [143, 144]. The latter (MM-pumped) version generates coherent near-IR (~1.55 μm) signal radiation that is continuously tunable, narrowband (sub-0.005 cm^{-1}), pulsed (~5 ns duration), and moderate energy (~0.1 mJ/pulse); the accompanying idler radiation is broader-band (MM) [145].

The less elaborate MM-pumped PPLN OPO [27, 145, 146] relies only on the second and third of the above design features. It does not need an elaborate, costly SLM pump laser as in the first design feature and is pumped instead by a compact, inexpensive MM Nd:YAG laser. A MM-pumped OPO system is more readily transportable than an SLM-pumped OPO and is therefore more amenable to operation in field settings for industrial or environmental monitoring applications requiring coherent tunable near-IR pulses.

The resonance properties of the actively controlled, TDL-seeded PPLN OPO ring cavity are used in the MM-pumped OPO to constrain the resonated wave (in this instance, the signal wave) to a single longitudinal mode of the OPO cavity and to tune it continuously without mode hops. The accompanying nonresonated wave (the idler in this case) carries all of the broadband character of the MM pump radiation. In this way, we are able to employ a multimode pump laser and still attain single-mode tunability of signal (or idler, if that is be the resonated wave) output radiation. We note that this property is associated with the intrinsic energy-conservation condition of OPOs. Such a possibility was recognized from the outset of their development [7], but rarely implemented.

2.4.3.3 Self-Adaptive Tunable OPO

A novel advance in injection-seeded OPO wavelength control [154] is a self-adaptive tunable (SAT) OPO design for a ns-pulsed tunable OPO system that needs no active

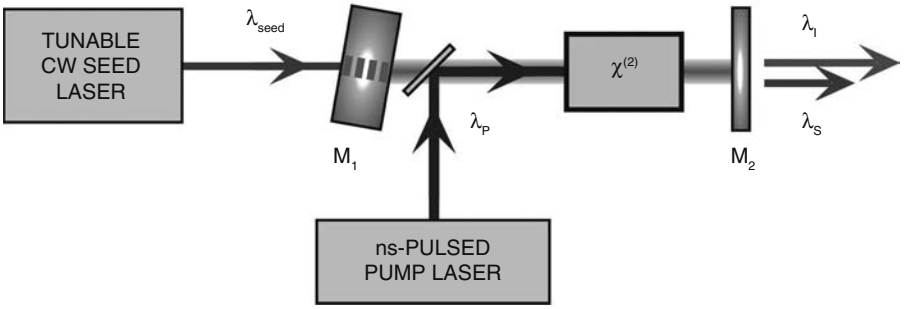

FIGURE 2.4 Schematic diagram of a narrowband OPO, pumped by a ns-pulsed laser at wavelength λ_P and tuned by injection seeding a SAT optical cavity. The SAT OPO cavity includes a photorefractive crystal M_1 (e.g., Rh:$BaTiO_3$), in which a phase-conjugate Bragg grating is written by interfering CW tunable seed laser light (at wavelength λ_{seed}) with its own back-reflection from cavity mirror M_2. The central wavelength of the induced reflective grating tracks λ_{seed} as it is scanned, such that the injection-seeded OPO cavity stays resonant at λ_{seed} and is automatically controlled to yield continuously tunable SLM signal and idler output beams at wavelengths λ_S and λ_I, respectively. This novel SAT approach to narrowband, mechanical-adjustment-free control of OPO output wavelength and optical bandwidth has been demonstrated in the form of a compact, rugged OPO system that is based on PPKTP, injection-seeded (typically in the range 820–850 nm) by a CW tunable diode laser, and pumped at 532 nm by a ns-pulsed Nd:YAG laser [154].

variation of the cavity length or other mechanical adjustment as the wavelength λ_{seed} of the injection seeder is scanned. As depicted schematically in Figure 2.4, this SAT OPO employs a photorefractive crystal [231] to serve as a phase-conjugate cavity mirror (M_1). A phase-conjugate Bragg grating mirror is formed within a few seconds in a Rh:$BaTiO_3$ crystal by photorefractive interaction with the forward-propagating and retro-reflected CW seed beams. Its reflectivity is centered at the wavelength λ_{seed} of the tunable CW seed laser and it adapts automatically to remain wavelength-selective as λ_{seed} is scanned.

This SAT approach has been realized with an OPO system pumped at 532 nm by a frequency-doubled SLM Nd:YAG laser (~8-ns pulse duration at 10 Hz), a PPKTP NLO medium, and a CW SLM TDL as injection seeder (~5 mW CW at 820–855 nm). This injection-seeded, self-adaptive ns-pulsed OPO cavity stays resonant at λ_{seed} and generates continuously tunable SLM output beams at signal and idler wavelengths λ_S and λ_I. Étalon measurements confirm that they are SLM, with optical bandwidth close to the FT limit, and continuously tunable without mode-hopping. This adjustment-free SAT OPO approach [154] is potentially useful for high-resolution time-resolved laser spectroscopy close to the FT limit. It is particularly promising for applications that require a stable, continuously tunable SLM source of coherent, narrowband, ns-pulsed near-IR radiation without any active wavelength-selective feedback or mechanically adjustable elements in the OPO cavity.

This robust, simple design provides a remarkably simple way to achieve reliable narrowband (SLM) tuning of OPO signal and idler output. It takes advantage of the high photorefractive efficiency of Rh:$BaTiO_3$ [231], which can be used with seed

radiation at near-IR wavelengths (0.6–1.1 μm). Other photorefractive materials may be suitable for SAT OPOs that are injection-seeded at longer IR wavelengths, such as the 1.55-μm optical telecommunications band. For example, vanadium-doped cadmium telluride (V:CdTe) [232] has been used as an adaptive intracavity filter to facilitate SLM tuning of an external-cavity diode laser operating at ~1.55 μm [233]. We note that a photorefractive grating, permanently written in PPLN by UV light, has been used for distributed-feedback operation of a pulsed PPLN OPO [191]: a less dynamic and adaptable arrangement than in our SAT OPO [154].

2.4.3.4 Chirp-Controlled, Injection-Seeded OPOs

Ongoing collaboration between Macquarie University and the Australian National University is directed toward optical-heterodyne measurement and control of frequency chirp in the output of a high-performance ns-pulsed injection-seeded OPO system intended for advanced high-resolution atomic and molecular spectroscopic applications [147–153]. As shown in Figure 2.5, this chirp-controlled OPO system is based on PPKTP (periodically poled $KTiOPO_4$), pumped at 532 nm by the second harmonic of a long-pulse SLM Nd:YAG laser, and injection-seeded by a CW SLM TDL at a signal wavelength λ_{seed} of ~842 nm. The Nd:YAG pump radiation employed in our

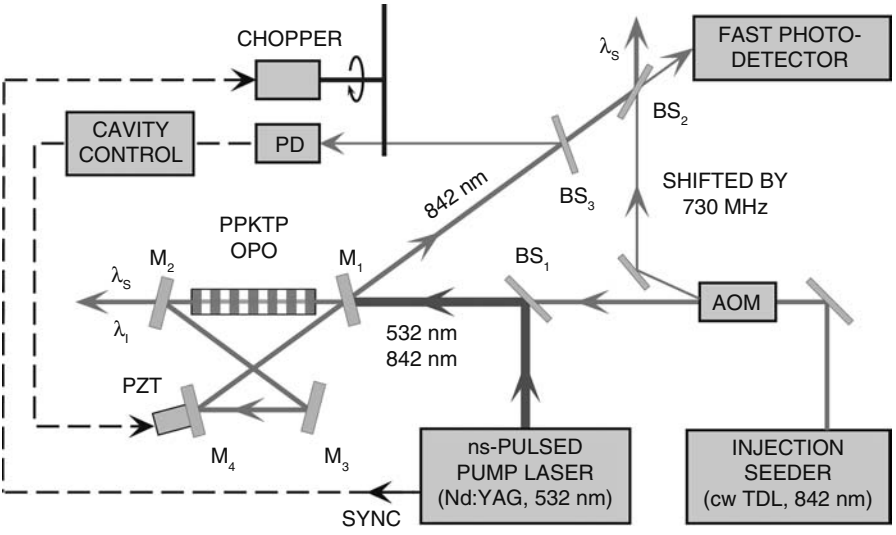

FIGURE 2.5 Injection-seeded, ns-pulsed tunable OPO with an OH detection system that is able to log the chirp and other instantaneous-frequency characteristics of each signal output pulse [147–153]. The OPO system comprises a four-mirror ring cavity based on PPKTP, is controlled by intensity-dip feedback to a PZT, is injection-seeded (typically at ~842 nm) by a CW TDL, and is pumped at 532 nm by a ns-pulsed SLM Nd:YAG laser. The pulsed OPO signal output beam (typically at ~842 nm) is combined at BS_2 with frequency-shifted sideband light from the CW seed source via an acousto-optic modulator (typically driven at ~730 MHz). The resulting beats are detected by a fast photodetector and analyzed by the OH method. Legend: M_1–M_4, OPO cavity mirrors; BS_1–BS_3, beam splitters; SYNC, synchronization circuit.

most recent work [149–153] has a relatively long pulse duration of ~27 ns FWHM (3.5 times that used to pump a previously reported 8-ns pulsed OPO system [147, 148]). According to Equation 2.23 [132], the corresponding FT-limited optical bandwidth of the resulting 842-nm OPO signal output pulses (duration ≈ 25 ns FWHM) is reduced to ~17.5 MHz (~0.0006 cm^{-1}) FWHM. The chirp-controlled OPO system generates SLM-pulsed coherent signal and idler output radiation that is continuously tunable with narrow optical bandwidth (<20 MHz), and low-frequency chirp (<10 MHz).

The chirp-control module of the OPO system shown in Figure 2.5 is able to measure the optical phase properties of its pulsed coherent output radiation by means of optical heterodyne (OH) techniques [234–236], in which OPO output pulses beat against CW TDL-seed radiation that is frequency shifted by an acousto-optic modulator (AOM). Of central importance in such considerations is the instantaneous-frequency profile, $f_{inst}(t)$, of the pulse, which is expressed [148, 235] in terms of the time-derivative of the optical phase $\phi(t)$:

$$f_{inst}(t) = (2\pi)^{-1} \, d\,\phi(t)/d\,t, \tag{2.24}$$

where any phase perturbations during an optical pulse are assigned to $\phi(t)$; $f_{inst}(t)$ is defined relative to the time-independent central frequency ($<\omega>/2\pi$) of the pulsed optical field. The phenomenon of frequency chirp can then be understood in terms of an approximately linear or monotonic change in $f_{inst}(t)$, which may include quadratic and other higher-order chirp terms.

A representative set of temporal and frequency profiles, extracted from typical observed output for a single pulse from the long-pulse OPO, is depicted in Figure 2.6. The successive FT analysis steps [148, 235] needed to process such measurements are indicated by arrows. The beat waveform in panel b contains intrinsic information about the instantaneous frequency and the frequency chirp. An FT algorithm is used to extract from these beats the temporal profile of the narrowband OPO pulse amplitude (which is used to reconstruct the pulse intensity profile in panel d for comparison with the raw intensity profile in panel a) and to determine the associated instantaneous frequency profile $f_{inst}(t)$ (panel e). A key step (panel c) entails isolation of one of the two OH sidebands (each displaced from the central peak in the power spectrum by the AOM frequency of ~730 MHz) by means of a suitable numerical filter prior to the second FT step. Vertical dashed lines in panels d and e denote 10%-intensity points of the OPO pulse's temporal profile, indicating the range of signal output amplitude over which frequency chirp can be conservatively estimated. In this particular example (in which the OPO operating conditions are chosen to ensure that phase mismatch $\Delta k \approx 0$), the frequency chirp is very small (less than 10 MHz) on the basis of *either* the spread of $f_{inst}(t)$ values *or* a straight-line fit slope of the $f_{inst}(t)$ in panel e of Figure 2.6.

The PPKTP OPO and the OH detection system used to measure the instantaneous-frequency characteristics of its signal output are depicted schematically in Figure 2.5. The essential features of this instrument [149, 150] are as follows:

- High-performance Q-switched, injection-seeded SLM Nd:YAG laser system [149, 150], custom-built to deliver spatially and temporally smooth 1064-nm pump pulses with relatively long durations (e.g., ~27-ns FWHM at 10-Hz pulse repetition rate) that minimize their FT-limited optical bandwidth

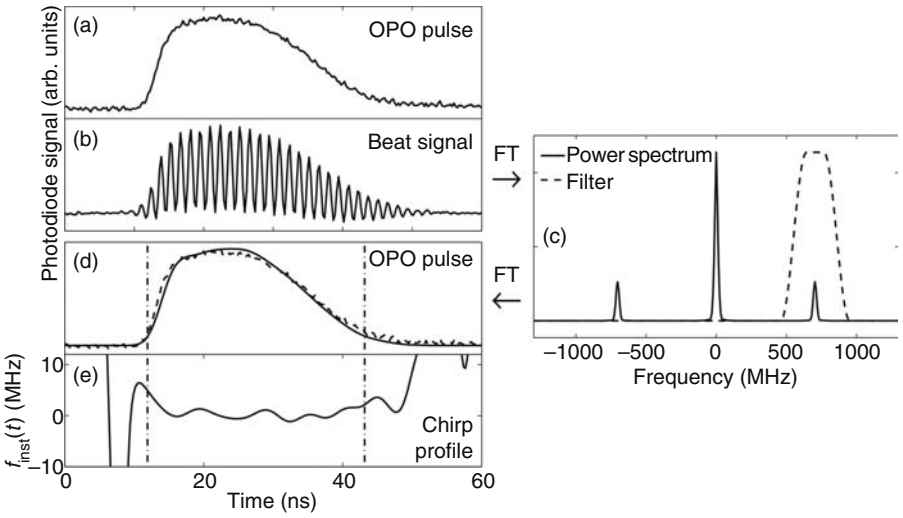

FIGURE 2.6 Illustration of the Fourier-transform chirp analysis procedure applied to signal output from a long-pulse injection-seeded PPKTP OPO [147–153]. Panels a and b depict the measured temporal profiles for amplitude and OH beat waveform, respectively, as measured for an actual OPO signal pulse. The FT algorithm converts panel b into the power spectrum in panel c, where two OH sidebands are displaced from a central peak by the AOM frequency (~730 MHz), then one OH sideband is numerically filtered and FT-analyzed to yield the temporal profiles of reconstructed OPO pulse amplitude and instantaneous frequency $f_{inst}(t)$ in panels d and e, respectively. Vertical dashed lines indicate 10%-intensity points of the OPO pulse, indicating the range over which frequency chirp can be conservatively estimated. The pump-pulse energy (64 μJ) is twice the unseeded threshold level and the PPKTP temperature is T_{PPKTP} = 125.0 °C, so that the signal wavelength of the free-running PPKTP OPO is λ_{free} = 841.75 ± 0.02 nm. The TDL-seeded signal wavelength λ_s (841.76 ± 0.01 nm) is virtually identical to λ_{free}; this minimizes phase mismatch and attains a frequency chirp of less than 10 MHz, as is evident from the f_{inst} profile in panel e.

- Four-mirror signal-resonant OPO ring cavity containing a temperature-controlled PPKTP crystal (e.g., with grating period Λ = 9.35 μm yielding free-running OPO signal output wavelengths λ_{free} that range from 815 nm to 877 nm at T_{PPKTP} = 200 °C and 20 °C, respectively [147])
- TDL injection seeder delivering continuously tunable CW SLM radiation at ~842 nm (e.g., with OPO signal seed wavelengths λ_{seed} that are tunable over 834–851 nm [147]) via an optical isolator and spatial filter or a single-mode optical fiber
- Piezoelectrically controlled intensity-dip cavity locking system [143–145] that maintains the OPO cavity in resonance at a signal wavelength λ_S that coincides with the TDL injection-seeder wavelength λ_{seed}
- AOM (e.g., driven at ~730 MHz), with the undiffracted CW seed beam directed into the OPO cavity while the diffracted, frequency-shifted CW beam is combined with output from the OPO system to generate OH beats on a fast square-law photodetector (e.g., with 1-GHz bandwidth) [147–150]

Additional pulsed optical amplifier stages (either OPA [151, 152] or Ti:sapphire) can be added for higher-power applications.

This injection-seeded long-pulse PPKTP OPO system exhibits stable SLM operation, with frequency chirp that is minimal when the phase mismatch Δk is close to zero, which is attained by minimizing the wavelength difference $|\lambda_S - \lambda_{free}|$. The OH module of this OPO system allows us to monitor the frequency chirp and central-frequency fluctuations in the SLM signal output on a real-time, pulse-by-pulse capability basis. This capability to log instantaneous-frequency data for each OPO output pulse has resulted in a new form of sub-Doppler spectroscopy: CHAPS (coherent heterodyne-assisted pulsed spectroscopy) [151, 152], as will be discussed in Sections 2.5.1 and 2.5.3.

Under certain conditions (excessive pump-pulse intensity and/or Δk), seeding is found [149, 150] to fail partway through the output pulse, such that operation on multiple longitudinal modes ensues, as observed via irregularities in temporal profiles of the injection-seeded long-pulse PPKTP OPO signal output at higher pump-laser energies (e.g., ~3 times unseeded OPO threshold) and with phase mismatch $|\Delta k| >> 0$ (e.g., at large values of $|\lambda_S - \lambda_{free}| \approx 0.2$ nm) [149, 150, 153]. The buildup of multimode operation becomes a significant problem in OPOs when longer pump-pulse durations (e.g., ~27 ns [149, 150]) are used to produce a narrower FT-limited optical bandwidth, particularly when pump-laser intensities are high. However, reliable SLM operation is feasible throughout each pulse when the buildup time for free-running modes exceeds the pump-pulse duration; this holds if phase mismatch $\Delta k \approx 0$ (i.e., if $|\lambda_S - \lambda_{free}| \approx 0$) for moderate pump-laser intensities, approaching the PPKTP damage threshold.

2.4.3.5 Dynamics of SLM Pulsed OPO Operation

There has been much recent fundamental interest in the temporal, spatial, and spectral performance of ns-pulsed OPOs, both within our own research group [147–153] and elsewhere [237–244]. Effects such as frequency chirp, the breakdown of seeding during signal and idler pulse generation, reduced backconversion, spatial beam quality, and spectro-temporal dynamics have been measured and modeled under various operating conditions [153, 212, 213, 237–244], for both BPM and QPM NLO media. Numerical simulation studies of such processes, in and beyond the range in which they are observed, offer insight into mechanisms that are at work in injection-seeded ns-pulsed OPOs and thereby enable their design and performance to be improved.

In particular, we have employed the SNLO code [24] to perform numerical simulations in order to reveal mechanisms of spectro-temporal dynamics and to model the performance characteristics of our injection-seeded long-pulse PPKTP OPO system [149, 150]. These simulations [153] are in satisfactory agreement with our OH measurements of instantaneous-frequency profiles and frequency chirp in the narrowband signal output from this OPO.

Frequency chirp in narrowband signal output pulses from such an OPO system has previously been observed to depend on phase mismatch between the pump, signal, and idler waves, and also on the pump pulse energy. Our simulations accurately predict the observed dependence of the frequency chirp on phase mismatch between the pump, signal, and idler waves, and also on the pump pulse energy. They yield realistic estimates of the frequency chirp, optical bandwidth, and spectral purity of the signal output pulse as it evolves, including effects that are not readily observed directly. For instance, rapid walk-off oscillations, which are predicted [238, 243] to be

associated with breakdown in backconversion and injection seeding owing to group-velocity mismatch, are evident in our simulations [153]; these oscillations are too rapid to observe with the photodetectors regularly used in our OH detection system. The combination of our experiments [149, 150] and simulations [153] provides a dynamic, time-resolved view of the partial failure of injection seeding and the transition from SLM to multimode OPO operation.

Our simulations [153] explore instrumental conditions that facilitate continuously tunable SLM operation of our injection-seeded long-pulse PPKTP OPO [149, 150], with optical bandwidth as close as possible to the FT limit. The excellent agreement between the simulations and experiment confirms that this OPO system is a well-characterized, reliable source of tunable, narrowband, coherent radiation for high-resolution spectroscopy on a nanosecond timescale.

It is expected that, after addition of amplification stages, our injection-seeded PPKTP OPO system will serve as a ns-pulsed, tunable, SLM coherent light source for high-resolution laser spectroscopy requiring high peak power and narrow optical bandwidth. Such sources are particularly useful in the vacuum ultraviolet (VUV) region where NLO upconversion is needed to generate the required wavelengths. For instance, the 1 ^{1}S–2 ^{1}S two-photon absorption transition of helium (He) has been measured with narrowband 120-nm VUV radiation generated by pulsed dye amplification of a CW tunable Ti:sapphire laser, followed by NLO upconversion [245]. However, the precision of these VUV spectroscopic studies was limited by degradation of near-infrared optical bandwidth arising from the pulsed dye amplification processes; this arose from shot-to-shot fluctuations in the frequency of the dye laser pulse (e.g., due to thermal lensing and dye flow inhomogeneities), as well as frequency chirp attributable to changes in population inversion during the laser pulse itself.

To circumvent such bandwidth limitations, we aim to employ our injection-seeded long-pulse PPKTP OPO [149, 150] to generate narrowband tunable light pulses at ~842 nm. In this NLO approach, with its OH-characterized shot-to-shot frequency stability, the frequency chirp cannot be adversely affected by population inversion as in dye amplification. Our next steps will therefore be to upconvert the amplified OPO output from ~842 nm to ~210 nm and, ultimately, to ~120 nm, to access the He 1 ^{1}S–2 ^{1}S two-photon transition [245].

2.5 SPECTROSCOPIC MEASUREMENTS USING OPOs

2.5.1 Spectroscopic Verification of OPO Performance

It is evident (e.g., from the operational strategies listed in Table 2.2) that, in many of its applications, an OPO is primarily used as a spectroscopic instrument. The utility of OPOs in this regard depends on a variety of distinctive properties, including:

- *Continuous tunability*, particularly in spectroscopic regions that are inaccessible to other tunable coherent light sources
- *Narrow optical bandwidth* (narrowest in the case of CW OPOs, FT-limited in the case of pulsed OPOs), for high-resolution spectroscopy
- *High optical intensity*, enabling assorted forms of NLO spectroscopy and up- or downconversion to more remote regions of the spectrum (e.g., VUV, mid-IR, or far-IR)

- *Laser-like beam quality*, comprising sufficiently high spatial coherence, collimation, and directionality to facilitate long-path absorption for high sensitivity, remote sensing of distant targets, fine focusing for microimaging, etc.
- *Pulsed capability* (e.g., ns, ps, or fs), enabling time-resolved spectroscopy
- *Broadband capability*, as an option that may be useful for multiplex spectroscopy

Within this spectroscopic context, the ultimate test of OPO performance characteristics may entail a spectroscopic measurement itself, rather than relying solely on optical diagnostic instruments such as étalons, spectrum analyzers, wavemeters, spatial beam profilers, and so on. For instance, spectra recorded by tuning the signal or idler output wavelength of an OPO may reveal scanning irregularities or discontinuities (such as mode hops) that are difficult to detect in practice by analyzing Fabry–Perot étalon fringes. Moreover, the finesse of such an étalon may be insufficient to resolve the optical bandwidth of a narrowband SLM tunable OPO.

This approach, in which actual spectra are used to confirm spectroscopic performance, was evident in the early OPO literature, as exemplified by the OPO-recorded 2.35-μm 2–0 band of CO cited in Section 2.1 [1, 9, 12] and by other early investigations [10, 13, 14, 178–181, 246]. Nevertheless, of the many reports of "tunable" OPOs over the last 30 years, it is relatively rare to find convincing demonstrations of continuously tunable operation, suitable for convenient spectroscopic scanning. It is more usual for OPO performance characteristics such as optical bandwidth to be reported at a single, fixed wavelength with little or no evidence that the OPO can be continuously tuned on an SLM basis, or at least reliably stepped from one longitudinal mode to another at which spectroscopic data can be collected.

The Bosenberg–Guyer KTP OPO/NRO/OPA system [18, 19] is an instance of spectroscopic verification of the narrow optical bandwith, SLM character, and continuous tunability of output OPO radiation. A sub-Doppler degenerate four-wave mixing (DFWM) spectrum, continuously scanned over a 30-GHz (1-cm^{-1}) range at ~2963.5 cm^{-1} (~3.3745 μm), shows the $R(3)$ line in the 1–0 absorption band of $H^{35}Cl$ with an FWHM width of 0.45 GHz (0.015-cm^{-1}), indicating that the OPO has an SLM optical bandwidth of ~0.42 GHz (~0.014 cm^{-1}).

A central theme of our own research on injection-seeded ns-pulsed OPOs [1, 27, 28, 142–154] has been to confirm performance by using the generated OPO radiation in actual spectroscopic applications. In Tables 2.4 and 2.5, we present chronologically ordered summaries of these investigations, together with a noncomprehensive selection of examples from other research groups. Table 2.4 is devoted to gas-phase spectroscopic measurements with moderate resolution, in which linewidths are limited by inhomogeneous broadening due to the Doppler effect. Table 2.5 concerns higher-resolution spectroscopy, designated "sub-Doppler," in which inhomogeneous broadening is circumvented in various ways.

The survey in Tables 2.4 and 2.5 refers predominantly to ns-pulsed OPOs; the few instances of spectroscopically characterized continuous-wave OPOs are designated "cw" (in bold). Likewise, the emphasis is primarily on near-IR tunable OPO sources, with a few examples of UV [27], visible [135, 136, 138, 139, 214, 257, 259], and mid-IR [199, 246] sources. Tables 2.4 and 2.5 focus on continuous tunability and

TABLE 2.4
Performance Characteristics of Various ns-Pulsed and CW Tunable Optical-Parametric Systems That Are Spectroscopically Measured under Doppler-Limited Experimental Conditions

Type of OPO system[a] [Ref(s)]	Description of spectrum and Doppler-limited technique[b]	$\Delta\nu_{spectrum}$[c] (cm^{-1})	$\Delta\nu_{OPO}$[d] (cm^{-1})
Grating/étalon-controlled BPM $LiNbO_3$ OPO (Byer et al., 1972–1975) [9, 12]	Absorption of CO gas in a 3-cm cell at 3 atm; continuous 180-cm^{-1} scan over the 2.35-μm 2–0 band of CO; reproduced in Figure 1 of Ref. [1].	~0.5 (OPO-limited)	~0.5 (~15 GHz)
Grating/étalon-controlled BPM $LiNbO_3$ OPO (Byer et al., 1975–1977) [10, 246]	CARS spectrum of H2 gas @ 325 Torr; 50-cm^{-1} scan in 0.25-cm^{-1} steps of the signal @ ~1.9 μm, with 1.064-μm Raman pump, in the *Q* branch, with 4155-cm^{-1} $J = 1$ peak.	2 (grating only)	2 (grating only); 0.1 (with étalon)
Dye-laser-seeded passive-cavity BBO OPO (Haub et al., 1991–1993) [133, 135]	PA spectra of C_2H_2 gas @ 100 Torr; continuous scans of idler @ ~965 nm in the C_2H_2 ($\nu_1 + 2\nu_3 + \nu_5$) band: an 8.5-cm^{-1} scan of the *Q* branch and four 1-cm^{-1} scans of the 10382.3-cm^{-1} *R*(7) line.	0.12 (pressure-broadened)	~0.1 (~3 GHz)
$LiNbO_3$ OPO, injection-seeded by SFG in $LiIO_3$ (Huisken et al., 1992) [208]	IR spectra of HCl vapor @ 19 Torr; continuous 60-cm^{-1} scan of idler @ ~2.7 μm over the *P*(1), *P*(2), and *P*(3) lines in the HCl 1–0 band.	2.3-cm^{-1} H35Cl/H37Cl splittings resolved	~0.1 (seeded by narrowband dye laser)
Dye-laser-seeded passive-cavity BBO OPO (Fix et al., 1993) [134]	PA spectrum of C_2H_2 gas @ 80 Torr; continuous 135-cm^{-1} scan of idler @ ~1.04 μm in the *P* and *R* branches of the C_2H_2 $3\nu_3$ band.	0.25 (~7.5 GHz)	<0.25 (<7.5 GHz)
Dye-laser-seeded passive-cavity BBO OPO (Haub et al., 1993) [135, 136]	CARS spectra of N_2 in air @ 1 atm; continuous 5-cm^{-1} signal scan @ ~607 nm with 532-nm Raman pump, in the 2330-cm^{-1} *Q* branch.	0.2 (pressure-broadened)	~0.1 (~3 GHz)
TDL-seeded passive ring-cavity BBO OPO (Johnson et al., 1995) [137, 139]	PA spectrum of C_2H_2 gas @ 14 Torr; continuous 1.1-cm^{-1} scan of idler @ ~865.5 nm covering part of the C_2H_2 ($\nu_2 + 3\nu_3$) band.	0.03 (Doppler-broadened)	≤0.008 (≤250 MHz) from TPE
Aperture-selected free-running BBO OPO (Haub et al., 1995) [138, 139]	DFWM spectrum of Na in an air-acetylene flame; continuous 17-cm^{-1} scan of signal over the 589.0- and 589.6-nm Na *D*-lines.	~4 (aperture-limited)	~4 (full beam: ~20 cm^{-1})

TABLE 2.4 ***(continued)***

Type of OPO system[a] [Ref(s)]	Description of spectrum and Doppler-limited technique[b]	$\Delta\nu_{spectrum}$[c] (cm^{-1})	$\Delta\nu_{OPO}$[d] (cm^{-1})
TDL-seeded passive ring-cavity BBO OPO (Baxter et al., 1996) [140]	CARS spectra of N_2 gas @ 75 Torr; continuous 1.6-cm^{-1} signal scan @ ~607 nm with 532-nm Raman pump, in 2330-cm^{-1} *Q* branch of N_2.	0.018 (0.54 GHz)	~0.01 (~0.3 GHz)
Dual-wavelength passive ring-cavity $LiNbO_3$ OPO seeded by 2 TDLs (Baxter et al., 1996) [140]	Dual-wavelength CARS spectra of N_2 gas in furnace air @ 300–1200 K, enabling instantaneous single-shot OPO CARS thermometry.	0.4 (12 GHz), diode-array limited	~0.01 (~0.3 GHz) for each wavelength
Dual-wavelength passive ring-cavity $LiNbO_3$ OPO seeded by 2 TDLs (Baxter et al., 1997) [141]	Dual-wavelength signal output spectra display sidebands due to backconversion when OPO is operated above threshold.	0.4 (12 GHz), diode-array limited	~0.01 (~0.3 GHz) for each wavelength
TDL-seeded $LiNbO_3$ OPO (Milton et al., 1997) [221]	Absorption of 2% CH_4 in 1 atm of air; stepwise scan over a 1.2-cm^{-1} range @ ~3.428 μm over several lines @ 2916.5–2918.0 cm^{-1} near the 3019-cm^{-1} ν_3 band of CH_4.	0.02 (pressure-broadened)	0.005 (135 MHz) estimated
TDL-seeded passive ring-cavity $LiNbO_3$ OPO (Baxter et al., 1998) [142]	PA & CARS spectra of CH_4 gas @ 10 Torr; continuous scans of idler & signal in 3019-cm^{-1} ν_3 & 2916.5-cm^{-1} ν_1 *Q* branches, respectively.	≤0.02 (≤0.6 GHz)	~0.01 (~0.3 GHz)
Single-frequency **CW** PPLN OPO system (Kühnemann et al., 1998) [251]	PA detection of C_2H_6 (83 ppm in N_2 @ 1 atm) at a single frequency at ~3.3 μm of ^rQ sub-branches in the 2985.4-cm^{-1} C_2H_6 ν_7 band.	~0.4 (multiline, pressure-broadened)	Not specified (probably <1 MHz)
Grazing-incidence grating-tuned PPLN OPO system (Yu and Kung, 1999) [188]	PA spectra of CH_4 gas @ 16 Torr; continuous 40- and 60-cm^{-1} scans of signal and idler @ ~1.645 and ~3.28 μm, in the ν_3 and $(\nu_1 + \nu_3)$ bands of CH_4, respectively.	0.3 (signal) and 0.9 (idler)	0.3 (signal) and 0.9 (idler)
BPM-angle-scanned $AgGaS_2$ OPO with wide tuning range (4–11 μm) (Vodopyanov et al., 1999) [246]	Absorption spectrum of CO gas @ 630 Torr; continuous 200-cm^{-1} scan of resonated signal over the ~4.65-μm 1–0 band of CO.	~1 (30 GHz)	~1 (30 GHz)
TDL-seeded passive-cavity BBO OPO/SFG system (Baxter et al., 2000) [27]	LIF-detected spectrum of NO gas @ 0.25 Torr; continuous 2.1-cm^{-1} scan within the NO $A\ ^2\Sigma+ \leftarrow X\ ^2\Pi$ 0–0 band @ ~226 nm.	0.115 (3.45 GHz)	0.06 (1.8 GHz)
TDL-seeded PPLN OPO with intensity-dip control, MM-pumped (He and Orr, 2001) [145]	CRD spectra of C_2H_2 gas @ 100 Torr; continuous 1-cm^{-1} scan of 1.528-μm TDL-seeded signal over weak lines @ 6543.3–6544.0 cm^{-1} near the $(\nu_1 + \nu_3)$ *P* branch of C_2H_2.	0.016 (Doppler-broadened)	<0.004 (<120 MHz)

continued

TABLE 2.4 ***(continued)***

Type of OPO system[a] [Ref(s)]	Description of spectrum and Doppler-limited technique[b]	$\Delta\nu_{spectrum}$[c] (cm^{-1})	$\Delta\nu_{OPO}$[d] (cm^{-1})
TDL-seeded PPLN OPO, MM- & SLM-pumped with intensity-dip control (He and Orr, 2001) [145, 146]	CRD spectra of CO_2 gas @ 1 atm; continuous 120-cm^{-1} scans of TDL-seeded signal @ 1.54 μm over the 6503-cm^{-1} CO_2 $(3\nu_1 + \nu_3)_I$ band.	0.0065 (195 MHz)	<0.004 (<120 MHz)
Grating/étalon-controlled mid-IR $ZnGeP_2$ OPO (Ganikhanov et al., 2001) [199]	Absorption spectra of H_2O vapor @ 60°C; continuous 2- and 7-cm^{-1} scans of resonated signal within the range 1615–1630 cm^{-1}.	0.3–0.4 (9–12 GHz)	0.1–0.15 (3–4.5 GHz) estimated
TDL-seeded PPKTP OPO, with photorefractive SAT control (He and Orr, 2001) [154]	CRD spectrum of CO_2 gas @ 20 Torr; continuous 0.15-cm^{-1} scan of 1.44-μm idler over the 6948.76-cm^{-1} CO_2 $3\nu_3$ $P(24)$ line.	0.017 (507 MHz)	≤0.0033 (≤100 MHz)
Nd:YAG-laser-pumped **CW** fan-grating PPLN OPO (Bisson et al., 2001) [252]	PA spectroscopy of CH_4 @ 1 atm; a 9-cm^{-1} idler mode-hop scan in the 3019-cm^{-1} Q branch of the CH_4 ν_3 band.	~0.1 (pressure-broadened)	Sub-MHz (mode-hop scanned)
Nd:YAG-laser-pumped **CW** fan-grating PPLN OPO (van Herpen et al., 2002) [253–255]	PA spectroscopy of C_2H_6 (0.4 ppb in N_2 @ 1 atm); a continuous 0.6-cm^{-1} idler scan over the 2996.85-cm^{-1} Q branch of the C_2H_6 ν_7 band.	~0.15 (pressure-broadened)	Sub-MHz (pump-frequency scanned)
Nd:YAG-laser-pumped **CW** PPLN OPO system (Popp et al., 2002) [102]	CRD detection of C_2H_6 @ 77 Torr at a single frequency (2990.096 cm^{-1}) in the 3.34-μm ${}^rQ_1$ sub-branch of the C_2H_6 ν_7 band, yielding 0.3-ppb detection limit.	~0.5 (multiline, pressure-broadened)	Sub-MHz (fixed single frequency)
Nd:YAG-laser-pumped **CW** dual-cavity PPLN OPO system (Müller et al., 2003) [103]	PA spectroscopy of C_2H_6 (1 ppm in N_2 @ 1 atm); a 1-cm^{-1} idler mode-hop scan in 2983.4-cm^{-1} pQ_1 sub-branch of the C_2H_6 ν_7 band, yielding 0.11-ppb detection limit.	~0.13 (multiline, pressure-broadened)	Sub-MHz (± 30-MHz stability in 45 min)
Diode-laser-pumped **CW** PP $MgO:LiNbO_3$ OPO system (Ngai et al., 2007) [256]	Quartz-enhanced PA spectroscopy (QEPAS) of trace-level CH_4, C_2H_6, H_2O, … in 0.2 atm of laboratory air; continuous scan over 15-cm^{-1} range @ ~3.35 μm.	0.03 (pressure-broadened)	Sub-MHz

[a] OPOs are ns-pulsed unless otherwise specified (e.g., continuous-wave designated "**CW**").

[b] Acronyms for spectroscopic techniques (CARS, PA, DFWM, CRD) are defined in the text; ppb = parts per billion (by volume).

[c] $\Delta_{\nu spectrum}$ is the FWHM spectroscopic linewidth (in units of cm^{-1}; also GHz or MHz).

[d] $\Delta_{\nu OPO}$ is the FWHM optical bandwidth of the OPO output radiation, inferred from the spectrum (unless otherwise specified), allowing for Doppler and/or pressure broadening.

TABLE 2.5
Performance Characteristics of Various ns-Pulsed and CW Tunable Optical-Parametric Systems That Are Spectroscopically Measured under Sub-Doppler Experimental Conditions

Type of OPO system[a] [Ref(s)]	Description of spectrum and sub-Doppler technique[b]	$\Delta\nu_{spectrum}$[c] (cm^{-1})	$\Delta\nu_{OPO}$[d] (cm^{-1})
Grating/étalon-tuned KTP OPO/NRO/OPA (Bosenberg and Guyer, 1993) [19]	DFWM, continuous 1-cm^{-1} scan @ ~3.374 μm of $R(3)$ line in 1–0 band of $H^{35}Cl$ (pressure not specified).	0.015 (450 MHz)	~0.014 (~420 MHz)
TDL-seeded passive-cavity BBO OPO (Johnson et al., 1995) [137, 139]	LIF-detected TPE of Rb vapor @ ~90°C; continuous scan of idler @ ~778.1 nm over the 25703.5-cm^{-1} $5d\ ^2S_{½} \leftarrow 5s\ ^2S_{½}$ 85Rb ($F = 3$) line.	0.01 (315 MHz)	≤0.008 (≤250 MHz)
TDL-seeded BBO OPO system (Boon-Engering et al., 1995) [214]	Ionization-detected TPE in beam of Ba metastables; 0.8-cm^{-1} continuous scan @ ~620.6 nm over 16112.864-cm^{-1} $6s\ 5d\ ^3P_0 \leftarrow 5d\ 7d\ ^3D_2$ Ba line.	0.02 (600 MHz)	0.012 (~400 MHz)
TDL-seeded passive ring-cavity $LiNbO_3$ OPO (Baxter et al., 1998) [142]	CARS of a CH_4 supersonic free jet with $T_{rot} = 10$–20 K; continuous 0.2-cm^{-1} scans of signal @ ~1.54 μm (with 1064-nm Raman pump) in 2330-cm^{-1} ν_1 Q branch.	0.008 (240 GHz)	0.007 (210 MHz)
TDL-seeded PPLN OPO with intensity-dip control (Baxter et al., 1998) [143]	CARS of a CH_4 supersonic free jet with $T_{rot} = 15$ K; continuous 0.15-cm^{-1} scan of signal @ ~1.54 μm (with 1064-nm Raman pump) in 2330-cm^{-1} ν_1 Q branch.	0.0065 (195 MHz)	~0.0045 (135 MHz)
TDL-seeded PPLN OPO with intensity-dip control, SLM- or MM-pumped (He and Orr, 1999) [145]	CRD spectra of a C_2H_2 supersonic free jet with $T_{rot} \approx 20$ K; continuous 0.03-cm^{-1} scans of 1.528-μm TDL-seeded signal over the $P(5)$ line @ 6544.442 cm^{-1} in the $\nu_1 + \nu_3$ band of C_2H_2.	SLM pump: 0.0037 (110 MHz) MM pump: 0.0042 (125 MHz)	<0.004 (<120 MHz)
Multistage Nd:YAG/SHG-pumped **CW** MgO:$LiNbO_3$ DRO system with SHG stage (Petelski et al., 2001) [257]	Hyperfine spectral hole-burning spectrum of $^7F_0 \leftarrow {}^5D_0$ transition in Eu^{3+}:Y_2SiO_5 @ 4 K; continuous 6.7-cm^{-1} scan @ ~580 nm.	≤0.1 (≤3 GHz) inhomogeneous width	<3.3 × 10–5 (<1 MHz) *ex* hole-burning

continued

TABLE 2.5 ***(continued)***

Type of OPO system[a] [Ref(s)]	Description of spectrum and sub-Doppler technique[b]	$\Delta\nu_{spectrum}$[c] (cm^{-1})	$\Delta\nu_{OPO}$[d] (cm^{-1})
Étalon- and pump-frequency-scanned **CW** SLM PPLN OPO system (Kovalchuk et al., 2001) [258]	High-resolution Doppler-free FM saturation spectroscopy in 6 mTorr of CH_4 @ 3.39 μm; 1.8-GHz (0.06- cm^{-1}) continuous tuning range.	1.7×10–5 (0.5 MHz), pressure-broadened	0.1 MHz (with ~0.2–0.4 MHz jitter)
TDL-seeded BBO OPG/OPA system (Kulatilaka et al., 2005) [259]	LIF-detected TPE spectra of 0.3% NO in 2 Torr of N_2; continuous 0.5-cm^{-1} scan within the NO $A\ ^2\Sigma^+ \leftarrow X\ ^2\Pi$ 0–0 band @ ~452 nm.	~0.01 (~300 MHz)	0.007 (220 MHz) *ex* spectrum analyzer
TDL-seeded PPKTP OPO with intensity-dip and OH chirp control (Kono et al., 2005–2006) [151, 152]	LIF-detected TPE CHAPS of Cs vapor @ ~90°C; signal-pulse histogram sampled @ ~822.47-nm on a 2-MHz grid at the $8s\ ^2S_{½} \leftarrow 6s\ ^2S_{½}$ ($F = 4$) 2-photon transition of Cs.	0.0006 (18 MHz) from TPE histogram	0.0006 (18 MHz), with jitter suppressed by CHAPS.

[a] OPOs are ns-pulsed unless otherwise specified (e.g., continuous-wave designated "**CW**").

[b] Acronyms for spectroscopic techniques (DFWM, LIF, TPE, CARS, CRD, CHAPS, FM) are defined in the text.

[c] $\Delta\nu_{spectrum}$ is the FWHM spectroscopic linewidth (in units of cm^{-1}; also GHz or MHz).

[d] $\Delta\nu_{OPO}$ is the FWHM optical bandwidth of the OPO output radiation, inferred from the spectrum (unless otherwise specified), allowing for Doppler and/or pressure broadening.

optical bandwidth, although other characteristics are implicated indirectly (e.g., optical intensity and beam quality in the case of NLO spectroscopic methods).

It is evident from Tables 2.4 and 2.5 that a diverse range of laser-spectroscopic techniques [247–250] is available for OPO performance characterization. These can be subdivided somewhat arbitrarily into "linear" optical absorption spectroscopy and nonlinear-optical spectroscopy. The former include the following linear spectroscopic techniques:

- *Simple absorption*, in which direct transmission of an absorbing medium is measured [9, 12, 199, 221, 246]
- *Photoacoustic (PA)* spectroscopy, in which optically absorbed energy is detected as sound waves generated by thermal relaxation [103, 133, 135, 137, 139, 142, 188, 251–256]
- *Laser-induced fluorescence (LIF)*, entailing luminescence excited by optical absorption [27, 137, 139, 151, 152, 259]
- *CRD* spectroscopy [195, 196], in which temporal decay of light in an optical cavity is measured rather than transmitted intensity [102, 145, 146, 154]

The latter include the following nonlinear spectroscopic techniques:

- *CARS*, a form of coherent Raman spectroscopy [260–261] depending on the third-order NLO susceptibility $\chi^{(3)}$, in which molecules are excited by

two coherent light waves (Raman pump and Raman Stokes; frequencies ω_{pump} and ω_{Stokes}) and a third coherent anti-Stokes wave is generated (at $2\omega_{pump} - \omega_{Stokes}$) when $(\omega_{pump} - \omega_{Stokes})$ matches a Raman frequency of the molecules [10, 135, 136, 140, 142, 143]

- *DFWM* spectroscopy [264], another $\chi^{(3)}$-dependent NLO technique in which three coherent input waves (all at frequency ω) generate a fourth coherent wave (also at ω) [19, 138, 139, 264–267]
- *Two-photon excitation (TPE)* spectroscopy, detected either by ionization [214] or LIF [137, 139, 151, 152, 259]

Sub-Doppler spectra can be obtained in the gas or vapor phase by two of the above nonlinear spectroscopic techniques: DFWM [19, 138, 139, 265–267] and TPE (with counterpropagating beams) [137, 139, 151, 152, 214, 259]. CHAPS (coherent heterodyne-assisted pulsed spectroscopy) [137, 139] is a new form of high-precision spectroscopy with sub-Doppler resolution that relies on our OH-based capability to make shot-to-shot instantaneous frequency measurements on the output of our injection-seeded long-pulse PPKTP OPO [149, 150]. Sub-Doppler CARS [142, 143] and CRD [145] spectra can be detected in supersonic molecular beams or jets, with the optical path(s) carefully aligned to be transverse to the direction of the beam or jet. Narrow homogeneously broadened spectral features can also be extracted from inhomogeneously broadened spectra by various forms of saturation or hole-burning spectroscopy [247, 248, 257, 258]. Moreover, CARS spectroscopy (with counterpropagating beams) is able to provide some reduction, by a factor of at least $(\omega_{pump} - \omega_{Stokes})/\omega_{Stokes}$, of the inhomogeneous line-broadening in the case of gas-phase molecules, given that the relevant Doppler width is proportional to $(\omega_{pump} - \omega_{Stokes})$, rather than the tunable OPO frequency ω_{Stokes} itself; such reduction effects are evident in Table 2.4.

2.5.2 OPO-Spectroscopic Sensing of Atoms and Molecules

Tables 2.4 and 2.5 provide ample evidence of a wide range of spectroscopic measurements to which tunable OPOs may be applied. However, most of the spectra involved are of little intrinsic spectroscopic interest or novelty, given that they are already well known and may be recorded routinely in less elaborate ways, such as FTIR or linear Raman spectrometry. In this section, we consider spectroscopic applications in which the spectra themselves provide *not only* a way to characterize OPO performance *but also* a fresh source of information about fundamental atomic and molecular processes, or highly sensitive analytical methodologies, or spectroscopic sensing strategies for atmospheric and other industrial, environmental, or biological media. This section comprises only a selective, representative sample of a wide range of the many spectroscopic applications of optical parametric devices.

2.5.2.1 Fundamental OPO Spectroscopy of Atoms, Molecules, and Ions

Sub-Doppler OPO spectroscopy, as outlined in Section 2.5.1 (including Table 2.5), is now established as a source of fundamental spectroscopic information. For instance, Kovalchuk et al. [258] have reported a CW OPO system that is based on multigrating PPLN and is SLM-tuned by a combination of tilting an intracavity étalon and

scanning the frequency of the CW Nd:YAG pump laser; the OPO idler output has a continuous, mode-hop-free tuning range of 1.8 GHz (0.06 cm^{-1}) and an optical bandwidth of ~0.1 MHz (with 0.5-ms integration time and typical idler-frequency drift of 0.5 MHz min^{-1}), measured by beating the OPO idler at 3.39 μm against a CH_4-stabilized He–Ne laser. The sub-Doppler spectroscopic performance of this OPO system has been demonstrated [258] by recording frequency-modulation (FM) saturation spectra of the classic 3.39-μm resonance in CH_4 gas, with counterpropagating saturating (10-mW) and probe (2-mW) beams in a 2-m-long cell at pressures of 6–54 mTorr; the observed sub-Doppler linewidth at 6 Torr is ~0.5 MHz (1.7×10^{-5} cm^{-1}), which is attributable to a combination of pressure broadening (~0.2 MHz) and medium-term OPO frequency jitter (~0.2–0.4 MHz).

Another relevant example (although not strictly "sub-Doppler") is that of Petelski et al. [257], who have used a frequency-doubled CW MgO:$LiNbO_3$ tunable OPO system to measure hyperfine hole-burning spectra of the 580-nm $^7F_0 \leftarrow {}^5D_0$ transition in Eu^{3+}:Y_2SiO_5 at 4 K. The inhomogeneously broadened two-site spectrum of this low-temperature crystalline medium has a linewidth of ≤3 GHz (0.1 cm^{-1}) FWHM; after 40 min of spectral hole-burning, its 580.070-nm peak is found to have a homogeneous linewidth of <1 MHz (<3.3×10^{-5} cm^{-1}) and a decay time of ~15 hours.

As outlined in Section 2.4.3.5, our injection-seeded long-pulse PPKTP OPO/OPA system [149, 150] with its OH chirp-control system has been designed as the primary stage of an all-solid-state narrowband SLM-tunable source of coherent VUV radiation for fundamental spectroscopic experiments in atomic and molecular physics. Our CHAPS spectroscopic technique [151, 152], as mentioned in Section 2.5.1 and in Table 2.5, is a preliminary stage in this program, yielding sub-Doppler LIF-detected TPE spectra of the 822.47-nm $8s\ ^2S_{½} \leftarrow 6s\ ^2S_{½}$ ($F = 4$) two-photon transition of atomic cesium (Cs). It is next proposed to carefully characterize subsequent amplification and upconversion stages (from ~842 nm to ~210 nm and, ultimately, to ~120 nm) that are required to access the quantum-electrodynamically significant He $1\ ^1S–2\ ^1S$ two-photon transition [245].

As mentioned in earlier sections, Rakestraw and coworkers have used a commercial Bosenberg–Guyer-type KTP OPO/NRO/OPA system [18, 19] to record high-resolution rovibrational DFWM spectra, realizing a spectroscopic bandwidth of ≤450 MHz (≤0.015 cm^{-1}) in the 3-μm region. High-quality spectra of this type have been published, for the 3.37-μm 1–0 band of HCl (near the $R(3)$ line) [19], for the 3.30-μm ν_3 band of CH_4 [266, 267], and for the 3.05-μm $\nu_3/(\nu_2 + \nu_4 + \nu_5)^0$ Fermi-dyad bands of C_2H_2 [266, 267].

Such a high-performance, computer-controlled SLM-tunable coherent IR source [18, 19] has been used for various forms of laser spectroscopy (CRD, DFWM, long-path absorption, etc.), including investigations of chemically reactive media, combustion diagnostics, and studies of processes in molecular beams. For instance, Bieske and coworkers have used a similar OPO/NRO/OPA system to record mechanistically significant IR spectra of mass-selected complexes of a halide ion with various molecules, such as acetylene (C_2H_2): $Cl^–$–$(C_2H_2)n$ (n = 1–9) [268], $Br^–$–$(C_2H_2)n$ (n = 1–8) [269,270], and $I^–$–$(C_2H_2)n$ (n = 1–4) [271]. Such gas-phase IR-spectroscopic studies, which have recently been reviewed [272], explore the nature of hydrogen bonds between "solute" atomic or molecular anions and neutral "solvent" molecules.

The alternative injection-seeding approach to narrowband OPO tuning has been used by Huisken and colleagues [208] in a 1.064-μm pumped BPM $LiNbO_3$ OPO seeded at its idler wavelength by a $LiIO_3$ DFG stage that mixes 532-nm Nd:YAG and tunable visible dye laser radiation; continuous tuning over ranges of at least 50 cm^{-1} is achieved by "look-up table" computer-based control of NLO phase-matching angles as the dye-laser diffraction grating is rotated. This DFG-seeded $LiNbO_3$ OPO system has been used to record vibrational spectra of small water complexes embedded in large liquid He clusters [216] and to measure gas- and supersonic-jet-phase DFWM and resonance-enhanced stimulated Raman scattering (SRS) spectra of C_2H_2, carbon dioxide (CO_2), and nitrous oxide (N_2O) [222].

Nesbitt and coworkers have also developed a high-performance injection-seeded tunable OPO system with peak output energies ≥ 10 mJ and optical bandwidth (160 ± 20 MHz) close to the FT limit [219]. They have applied it to high-resolution vibrational overtone studies of HOD and H_2O in the $3\nu_{OH}$ and $4\nu_{OH}$ regions, to high-resolution LIF Doppler spectroscopy of OH radicals, and to IR-UV multiple resonance spectroscopy of H–OH bond breaking in quantum-state-selected Ar-H_2O molecular clusters [220, 273, 274].

In another example of fundamental molecular spectroscopy, Ashworth, Western, and coworkers have used an injection-seeded narrowband ns-pulsed SLM tunable OPO to record sub-Doppler LIF spectra displaying hyperfine structure in the A $^3\Pi$ electronic states of the molecular radicals PF [275, 276] and PH [277] in a supersonic jet expansion.

At Macquarie University, an early objective of our OPO-related research was to devise convenient tunable, narrowband coherent sources of ns-pulsed IR and UV radiation for time-resolved, LIF-detected IR-UV (IR-UV DR) spectroscopy to probe energy-transfer dynamics of small gas-phase polyatomic molecules such as C_2H_2 [278]. At the outset, UV-scanned IR-UV DR spectra of the "$3\nu_{CH}$" manifold at ~9600 cm^{-1} in the electronic ground-state $\tilde{X}$of C_2H_2, were recorded using an injection-seeded passive-cavity BBO OPO as IR source (e.g., pumping the 9567.36-cm^{-1} $3\nu_3$ $R(7)$ rovibrational transition) to reveal interesting anomalies in the resulting collision-induced IR-UV DR spectra [1, 135]. Our subsequent OPO-based IR-UV DR research has focused on the "$4\nu_{CH}$" manifold at ~12700 cm^{-1} in the electronic ground-state $\tilde{X}$of C_2H_2, where discrete rovibrational structure is known [278–280] to be complicated by an underlying collision-induced quasicontinuous background (CIQCB). We therefore introduced two tunable OPO systems to attain higher spectroscopic resolution (relative to that of the tunable dye lasers regularly used for our IR-UV DR experiments [278–280]): as continuously tunable narrowband IR pump source, a Bosenberg–Guyer-type KTP OPO/NRO/OPA system [18, 19]; as UV probe source, an injection-seeded passive-cavity BBO OPO with additional BBO SFG upconversion stage tuned to a characteristic rovibronic transition of C_2H_2 (e.g., by probing the $\nu_1 + 3\nu_3$, $J = 19$ rovibrational level). It was of particular interest in this later IR-UV DR study that the narrower optical bandwidths of these OPO-based IR pump and UV probe sources resulted in no fresh insight into IR-UV DR effects such as the CIQCB [278–280].

2.5.2.2 OPO Applications in Atmospheric Sensing

There is extensive literature on the foundation of laser-based atmospheric sensing [26, 281–291]. This field offers opportunities for OPOs in the IR region [26], where IR

lidar (light detection and ranging—an optical analogue of radar) usually embraces techniques that monitor an optically defined column of the atmosphere, as well as true range-resolved lidar. IR lidar relies on two key factors: the strength of IR light scattering from aerosols and particulates (relative to that from molecules), and the amenability of most small molecules to be monitored via their IR absorption spectra. Such factors are vital in the range-resolved form of IR DIAL (differential absorption lidar), which relies on elastic scattering from atmospheric aerosols (to act as a "distributed mirror") and on characteristic rovibrational absorption spectra as signatures of specific atmospheric molecules, such as H_2O, CH_4, ozone (O_3), and various pollutant species. The latter attribute also enables retro-reflected long-path IR laser absorption, which entails a trade-off between range resolution and sensitivity. There are additional opportunities for atmospheric sensing by OPO-based sources in the visible and UV regions, where the optical processes involved arise predominantly from electronic properties of molecules: Rayleigh and Raman scattering, electronic absorption, and fluorescence.

The high output power, optical coherence, and narrowband tunability of ns-pulsed OPOs are all advantageous for remote sensing of the atmosphere. Moreover, OPO pulse durations of 2–10 ns are amenable to range-resolution requirements of many lidar and DIAL applications. Narrowband ns-pulsed $LiNbO_3$ OPOs, with intracavity grating and étalon control, were realized before 1980 by Byer and coworkers [8–11] and successfully applied in a number of atmospheric remote-sensing demonstrations involving the following molecular species: CO (at 2.3 μm and a range of >100 m) [14], SO_2 (at 4.0 μm and 120-m range) [178, 179], CH_4 (at 1.66 μm and over a 2.7-km column) [179], and H_2O (around 1.75 μm, both for a 2-km atmospheric column [180], and range-resolved up to ~1 km [181]).

Following that early (pre-1982) progress on pulsed OPOs, there were relatively few OPO-based advances in IR lidar or DIAL during the next 15 years, after which OPOs appear to have regained acceptance as high-power pulsed tunable sources suitable for such applications. A TDL-seeded $LiNbO_3$ OPO was used by Milton et al. [221] to demonstrate range-resolved 3.4-μm IR DIAL measurements of atmospheric CH_4 at ranges up to 0.5 km.

Ehret, Fix, and coworkers [227, 228] have devised a significant TDL-seeded OPO system for airborne H_2O-vapor IR DIAL measurements; it comprises a BBO or KTP ring-cavity OPO pumped at 532 nm and TDL-seeded at signal wavelengths in the range of 920–950 nm with an average output power of 1.2 W and a spectral purity >99%. This system is designed to monitor the second-overtone 3–0 absorption band ($3\nu_{OH}$) of H_2O, which offers higher sensitivity than the third-overtone 4–0 band ($4\nu_{OH}$) region at ~725 nm accessed in earlier airborne dye-laser-based IR DIAL studies by the same group [292]. This form of OPO has now been incorporated in an airborne all-solid-state DIAL system and has enabled, for the first time, daytime measurements of two-dimensional H_2O-vapor cross-sections with high vertical (500–750 m) and horizontal (6–20 km) resolution in the tropopause region [293].

Multiwavelength or multiplex OPO operation (as already discussed in Section 2.4.2.4) is an essential feature of many DIAL instruments, so that (resonant) atmospheric signals of interest can be actively distinguished from the (nonresonant) background. For instance, the ns-pulsed OPO output of the above airborne H_2O-vapor DIAL instrument is able to be switched rapidly from narrowband, TDL-seeded,

on-resonance to broadband, unseeded, (predominantly) off-resonance [225, 226, 293, 294]. Injection-seeded OPOs are particularly amenable to multiwavelength or multiplex OPO operation, as is evident in our research at Macquarie University [140, 141] on multiline spectroscopic sensing (e.g., by dual-wavelength CARS diagnostics of N_2 in furnace air [141]). A novel spectroscopic tailoring concept (e.g., for DIAL), with a source of coherent, pulsed radiation simultaneously generating a set of discrete wavelengths, each selected (e.g., by injection-seeding a ns-pulsed OPO via an array of TDLs and a fiber-optic switch) to be on- or off-resonance with characteristic spectral features has also been proposed [26, 28, 29]. Such multiwavelength spectroscopic tailoring of OPO output is readily implemented by injection seeding in BPM media [26, 28, 29, 140, 141] or in QPM media [187, 229, 230, 295].

Injection-seeded ns-pulsed OPOs are useful for UV DIAL detection of ozone (O_3) in the troposphere [296–299]. Fix et al. [296] have devised such an OPO with intracavity SFG, generating output pulse energies up to 16 mJ in the 281–293-nm range, for DIAL studies of tropospheric O_3. More recently, Armstrong and Smith [297–299] have reported two laboratory prototype ns-pulsed UV sources for airborne or satellite-based DIAL remote sensing of O_3. These comprise OPOs pumped at 532 nm (from a frequency-doubled, Q-switched SLM Nd:YAG laser), generating a tunable signal output at ~803 nm. The OPO signal output is then mixed by SFG with additional 532-nm light *either* inside the OPO cavity *or* in a subsequent SFG stage, to generate 10-ns pulses at 320 nm. To optimize efficiency, three important characteristics are incorporated in the system design: a pump beam having a high-quality flat-topped spatial profile, an image-rotating nonplanar ring-cavity OPO capable of generating high-quality large-diameter flat-topped beams, and pulsed injection seeding of the OPO to achieve near-zero cavity buildup time to enhance the SFG efficiency. UV pulse energies approaching 300 mJ with competitive optical conversion efficiencies are projected [299].

Svanberg and coworkers have also developed a frequency-agile OPO system for wide-ranging (220 nm–4.3 μm) DIAL applications [300] and a versatile (deep-UV to mid-IR) mobile OPO/OPA lidar system for atmospheric and other environmental monitoring [301]. These employ fast switching by piezoelectric drivers to facilitate simultaneous multiwavelength DIAL measurements of several spectrally overlapping atmospheric species, with typical optical bandwidths of ~0.2 cm^{-1}.

A miniature near-IR laser system for high-resolution three-dimensional lidar has recently been reported by Zayhowski and Wilson [302]. This robustly packaged system incorporates a 1.064-μm passively Q-switched laser [303] with two amplifiers and a multipass KTA OPA [304], which is seeded by a DFB diode laser to generate output at 1.537-μm, which is eye-safe (the only spectroscopic aspect of this application). The system [302] is compact, rugged, and portable: qualities that are highly advantageous for airborne lidar-type systems.

2.5.2.3 OPO Applications in Industrial and Environmental Monitoring

Many of the principles that are relevant to remote sensing of the atmosphere (e.g., by methods such as long-path absorption, lidar, or DIAL) are also applicable to spectroscopic monitoring applications in other settings, such as those associated with industrial

process control (e.g., by detecting reactive plant streams), with inaccessible or hostile media (e.g., furnaces, flames, or other combustion media), with environmentally sensitive situations (e.g., natural or manufactured polluting emissions from industrial sites, human communities, or wilderness), with defence and security measures (e.g., screening for explosives or biological agents) with biomedical and life-science diagnostics (e.g., human breath analysis correlated with assorted physiological conditions).

A diverse range of laser-spectroscopic techniques is applicable in this context [247–250]. Tunable OPOs can be involved in many such techniques, as is indicated by Tables 2.4 and 2.5 and by the preceding discussion in Sections 2.5.1 and 2.5.2. Special issues of some journals [44–51] also help to indicate trends in OPO-based applications to industrial and environmental sensing. It is beyond the scope of this chapter to be comprehensive. We therefore merely highlight a few recent examples that are representative of OPO applications to spectroscopic sensing of gas-phase or airborne molecular species. Beyond that, the reader may find that Tables 2.4 and 2.5 can direct them to a wider range of useful applications.

For example, Table 2.4 reveals that OPO-spectroscopic sensing of ethane (C_2H_6) has been a proving ground for CW tunable OPOs, using detection by CRD [102] or PA [103, 251, 253–255]. C_2H_6 is of interest because it is produced by plants, animals, and humans via lipid peroxidation of cell membranes [305–307] and it indicates plant stress. Two of these CW OPO-based spectroscopic studies of C_2H_6, by CRD [102] and by PA [251] spectroscopies, employ single-frequency SLM CW PPLN OPOs that have sub-MHz optical bandwidths but no ready continuous tuning capability; the OPO idler output wavelength must therefore be "parked" (much like a line-tunable CO or CO_2 laser) at a particular position in the spectral profile that can be well chraracterized (e.g., by FTIR). In this way, sub-ppb detection sensitivities have been achieved for traces of C_2H_6 diluted in N_2 at 1 atm [102, 251]. In the same context, the Nd:YAG-laser-pumped CW fan-grating PPLN OPO developed by Bisson et al. [252] has been used to record high-quality mode-hop-scanned PA spectra of CH_4 [252], C_2H_6 [103], and C_2H_4 [103]; a 0.11-ppb detection limit is established for C_2H_6 diluted in N_2 at 1 atm [103]. The transportable, highly sensitive PA spectrometer reported by Müller et al. [103] is based on an advanced CW fan-grating PPLN OPO that is pump-resonant (for low threshold) and dual-cavity (for spectral agility). In three like papers, van Herpen et al. [253–255] report continuous tuning by intracavity étalon in a CW Nd:YAG-pumped SRO containing a PPLN fan-grating; as summarized in Table 2.4, this has been applied to PA spectroscopy of C_2H_6 diluted in N_2 at 1 atm with a projected detection limit as small as 0.01 ppb.

In a very recent spectroscopic application (also concerned with C_2H_6 sensing), Ngai et al. [256] have reported a diode-laser-pumped CW OPO based on periodically poled MgO:$LiNbO_3$ in a signal-resonant, étalon-tuned ring cavity pumped at 1.082 μm by a fiber-laser-amplified diode laser. The idler output of this CW OPO system has a power of up to 300 mW; it is continuously tunable without mode hops over 5.2 cm^{-1} and a spectral coverage of at least 16.5 cm^{-1} via pump-source tuning. It has been used for quartz-enhanced PA spectroscopy (QEPAS) [308] measurements at ~3.35 μm of a C_2H_6/N_2 mixture in laboratory air; a continuous spectral scan has been recorded over a 15.1-cm^{-1} range with a pressure-broadened linewidth of ~0.03 cm^{-1} (0.9 GHz) and is attributed to a multicomponent gas mixture comprising 2.2 ppmv of C_2H_6, 1.53 ppmv of CH_4, and 1.1% of H_2O in N_2 and O_2 at a total pressure of 0.2 atm [256].

There is much ongoing interest in using tunable OPOs and other optical parametric devices for spectroscopic sensing in the mid-IR region, particularly beyond the range that is accessible to convenient NLO media such as PPLN [39–41, 56, 66]. A number of mid-IR OPOs have been reported [40, 41, 76, 199, 246, 309], but their application to spectroscopy remains formative. For example, a broadly tunable $ZnGeP_2$ (ZGP) OPO, pumped at 2.8 μm by a 100-ns pulsed Er,Cr:YSGG laser and yielding an idler optical bandwidth of ~2 cm^{-1}, has been employed [309] for CRD-spectroscopic detection of common explosives (TNT, TATP, RDX, PETN, and Tetryl) at trace levels; a detection limit of 0.075 ppb is projected for TNT. The idler tuning range (6–10 μm) of this ZGP OPO provides access to the mid-IR "fingerprint" region, which is highly advantageous for many molecular sensing applications.

At this stage, significant narrowband spectroscopic sensing in the mid-IR by optical parametric devices appears to rely heavily on tunable DFG and OPG/OPA systems. It may be that more emphasis on genuine mid-IR OPOs will develop once OP GaAs and convenient long-wavelength (>2 μm) pump lasers become more widely available. Such trends are well illustrated by a sequence of papers by Bisson, Kulp, and coworkers as follows:

1999. CRD spectroscopy of CH_4 gas (e.g., 500 ppb in 1 atm of N_2) at ~3.3 μm using a 1-kHz pulsed mid-IR PPLN OPG/OPA system with optical bandwidth ≤0.08 cm^{-1} achieved via a Fabry–Perot étalon as a spectral filter between the OPG and OPA stages [200]

2000. A similar étalon-filtered mid-IR PPLN OPG/OPA source pumped by an SLM passively Q-switched Nd:YAG microlaser and applied to CRD spectroscopy of H_2O vapor (e.g., 30% relative humidity in room air) with an optical bandwidth of 0.05 cm^{-1} and a wide tuning range (e.g., a 350-cm^{-1} spectrum pieced together from 27 smaller continuous étalon scans) [201]

2002. A wide-ranging multiauthor, multi-institution survey of practical IR chemical sensing applications using QPM optical-parametric light sources, including a portable gas imager based on a fiber-pumped CW PPLN OPO, a 270-μs microlaser-pumped, TDL-seeded PPLN OPA for surveillance of natural gas pipeline leaks, the above-mentioned étalon-filtered CW PPLN OPG/OPA source applied to CRD-spectroscopic sensing of mixed hydrocarbon vapor, and an early report of the tuning behavior (in the wavelength range of 7.9–8.6 μm) of a CW OP GaAs DFG system (see also [74]) that is driven by two external-cavity diode lasers with ~0.2-cm^{-1} optical bandwidth [73]

2006. Application of the above-mentioned CW OP GaAs DFG system [73, 74] to CRD spectroscopy of N_2O gas (15 ppm in 1 atm of N_2, with traces of H_2O), in a continuous 25-cm^{-1} spectral scan with ~0.2-cm^{-1} optical bandwidth [75]

An OPO-based spectroscopic development at Macquarie University that is particularly innovative (but perhaps relatively unnoticed by colleagues elsewhere!) concerns our use of injection-seeded ns-pulsed BPM OPOs for dual-line CARS

spectroscopy [140], in which a passive-cavity OPO is simultaneously seeded by separate TDLs to generate two adjustable output wavelengths. As already explained in the final part of Section 2.4.2, we have shown that by setting these two TDL seeders to match Stokes wavelengths that are characteristic of low- and high-*J* rovibrational Raman peaks in the CARS spectrum, it is possible to devise a single-shot coherent-Raman thermometric instrument (e.g., for N_2 in furnace air [140]). This dual-line, injection-seeded approach to CARS spectroscopy complements conventional OPO CARS techniques, either continuously scanned [10, 135, 140, 142, 143] or multiplex [135, 136, 140, 310, 311], and is the precursor of proposed [26, 28, 29] multiwavelength OPO spectroscopic tailoring strategies that are promising for atmospheric, industrial, and environmental spectroscopic sensing.

Our preoccupation in this chapter with OPO-based spectroscopic sensing of gas-phase or airborne species should not disguise the fact that OPOs and other optical parametric devices have a wide range of spectroscopic and imaging applications in biology, medicine, and health sciences. Moreover, the substantial market opportunities for user-friendly OPO-type systems have not been overlooked by manufacturers of laser-based instruments.

To connect with this important field (and relate it to the above-mentioned multiwavelength OPO spectroscopic tailoring strategies), we cite a recent paper on OPO-based biosensing, in which Tiihonen et al. [312] report a tailored dual-wavelength source of coherent UV light for fluorescence spectroscopy of biomolecules. The state-of-the-art UV light source comprises a diode-pumped Nd:YAG laser passively Q-switched by an intracavity Cr:YAG saturable absorber to yield pulses of 2.3-ns FWHM duration at 100-Hz repetition rate and an average power of 130 mW. The astigmatic output beam of the diode-bar pump source is converted into an homogeneous beam profile by means of a "beam-twisting" mode converter to attain 50% conversion efficiency in a PPKTP frequency-doubler; the resulting 532-nm output comprises 1.8-ns, 0.65-mJ pulses at 100 Hz with excellent beam quality ($M^2 = 1.3$). This 532-nm pump source drives two separate signal-resonant PPKTP OPO cavities, each containing a Type-I (ooe) BBO SFG crystal. The resulting cascaded parametric UV-generation processes in the two PPKTP/BBO OPO/SFG systems generate 1-ns, 27-μJ output pulses with wavelengths of 293 nm and 343 nm and ~7% conversion efficiencies with respect to 532 nm. The former wavelength (293 nm) matches the LIF-excitation wavelength of the ubiquitous tryptophan amino-acid residue while the latter wavelength (343 nm) is chosen for LIF-excitation of NADH (the reduced form of nicotinamide adenine dinucleotide—a typical nucleotide that plays a key role in the oxidation of fuel biomolecules). The potential utility of this dual-wavelength UV source was demonstrated [312] by recording dispersed LIF spectra of nonpathogenic bacteria (e.g., *B. thuringiensis* at a concentration of 10 μg mL^{-1} in saline solution) and auxiliary background from NADH and other unidentified fluorescent biomolecules. Such an OPO-based dual-wavelength (or perhaps multiwavelength, for higher specificity) approach is proposed as a way to distinguish naturally occurring bacteria from other pathogens (e.g., biological warfare agents). A further significant OPO-based biomedical sensing and imaging application (CARS microscopy) will be considered in Section 2.5.3.

2.5.3 CARS Microscopy: A Biomedical Application of OPOs

2.5.3.1 Background to CARS Microscopy

Laser-based microscopy is already well established in biomedicine and the life sciences, yielding three-dimensional imaging with fine spatial resolution, high sensitivity, and discrete chemical or biomolecular selectivity. Well-established scanning confocal and multiphoton microscopies apply *either* to a restricted range of media containing natural endogenous fluorophores (e.g., certain amino acids, such as tryptophan [312]) *or* to substances that have been labeled with an exogenous fluorophore (which may be toxic, subject to photobleaching, and/or inconvenient to use). Another approach targets vibrational signature(s) of biomolecules by linear Raman spectroscopy, but this tends to be limited by weak cross-sections.

Coherent Raman spectroscopic sensing, notably CARS, has recently emerged as a promising approach to biomolecule-specific microscopic imaging and microspectroscopy. CARS microscopy [313–318] offers high sensitivity and collection efficiency, detection wavelengths that are blueshifted from excitation and fluorescent wavelengths, and amenability to three-dimensional imaging. The chemical specificity of CARS microscopy is derived from intrinsic molecular vibrational characteristics (revealed by Raman spectroscopy), rather than from an electronic fluorophore (which often must be attached as an exogenic label to biomolecules of interest); this avoids practical complications often associated with staining of biological media prior to fluorescence microscopy and simplifies *in vivo* examination of living cells and tissues. Moreover, as in multiphoton microscopy, the tight focusing used in CARS microscopy provides a fine sectioning capability for three-dimensional biomedical imaging and the NLO scattering mechanisms offer size-selectivity, including subwavelength spatial resolution. This facilitates observation of biochemical structures and processes at subcellular levels.

CARS microscopy can therefore address significant challenges in optical diagnostics and sensing, including characterization of tissues, cells, and biomolecules (e.g., imaging of lipids [313–320]) and wide-ranging applications (e.g., security screening of biological agents or explosives; microscopic imaging of photoresists and microelectronic circuits).

As explained in Section 2.5.1, CARS spectroscopy depends on the third-order NLO susceptibility $\chi^{(3)}$, by means of which two coherent light waves (ω_{pump} and ω_{Stokes}) combine to generate a coherent anti-Stokes wave ($\omega_{AS} = 2\omega_{pump} - \omega_{Stokes}$) when ($\omega_{pump} - \omega_{Stokes}$) matches a molecular Raman-active frequency Ω. CARS spectra can be recorded *either* by tuning ($\omega_{pump} - \omega_{Stokes}$) through Ω *or* in multiplex mode, where ω_{Stokes} is broadband with resonances at Ω in a continuum of output frequencies ω_{AS}. One of two popular CARS microscopy configurations (F-CARS) [313, 314] detects signal in the forward direction. The other (E-CARS) uses *epi*-detection, which outputs light at ω_{AS} counterpropagating back toward the source of the incident laser light at ω_P and ω_S. For example, mechanisms that allow *epi*-detection [313–316, 321] are vital in applications of CARS endoscopy [321].

2.5.3.2 Instrumentation for CARS Microscopy

Advanced laser scanning microscopes are established research instruments in numerous laboratories, where they enable biomedical diagnostics with a significantly extended microscopic imaging capability. However, the laser and detection systems required for high-performance CARS scanning microscopy are typically elaborate and expensive. Some aspects of CARS-microscopic instrumentation therefore need to be simplified, with associated cost reductions, if the technique is to be made accessible to a broader range of researchers and biomedical practitioners. For example, multiplex CARS microscopy can be performed relatively economically by using a single pulsed laser to generate broadband Stokes frequencies (ω_{Stokes}) in an NLO optical fiber, as well as serving as the narrowband pump source (ω_{pump}), and then dispersing the broadband output spectrum (ω_{AS}) [319, 322–327].

Experimental and theoretical studies [313–315, 322, 328] have shown that the optimum pulse duration for CARS microscopy of living biological samples is ~1–10 ps, using 0.5–500-nJ pulses. Shorter-duration pulses can cause NLO photodamage to *in vivo* targets [328], while light pulses longer than ~10 ns can thermally damage living tissue if the pulse energies (and hence peak powers) are high enough to generate detectable CARS signals. Such effects are aggravated by the high repetition rates that are regularly used to enhance CARS imaging efficiency. Moreover, Equation 2.23 [132] indicates that pulse durations shorter than ~2 ps FWHM exceed the FT limit required to match the FWHM spectral linewidth of ~10 cm^{-1} (~300 GHz) for typical Raman bands of molecules in aqueous solution or biological tissue. Likewise, a 10-fs pulse will have an FT-limited optical bandwidth of ~44 THz (~1500 cm^{-1}), which is poorly matched to the resonant portion of a typical CARS spectrum and many of its spectral components will contribute only to a nonresonant background that tends to mask features of interest in the CARS spectrum. Longer pulses (up to ~5 ns) can occasionally be used for CARS microscopy, as has been demonstrated in the case of large-area CARS microscopy with single nanosecond pulses from a 10 Hz laser [329, 330]. Such approaches to CARS microscopy [329–331] employ a wide-field microscope and dark-field condensing lens with an intensified CCD camera.

2.5.3.3 Challenges for CARS Microscopy

Ongoing challenges for research on CARS microspectroscopy and imaging include the following.

2.5.3.3.1 Optimization of CARS Epi-*Detection*

As mentioned, many key CARS techniques (e.g., CARS endoscopy [321]) rely on *epi*-detection (E-CARS), in which CARS ouput light (at ω_{AS}) counterpropagates back toward the source of the incident light (at ω_{pump} and ω_{Stokes}). Two mechanisms responsible for CARS *epi*-detection entail incomplete backward destructive interference, due to scattering *either* from small objects that are comparable in size to optical wavelengths (λ_{AS}, λ_{pump}, λ_{Stokes}—so that subwavelength structures can be resolved) *or* from interfaces between media with different $\chi^{(3)}$ values [313–316, 321]. A third *epi*-detection mechanism, only recently recognized [316, 321], involves multiple scattering of CARS light from thick samples (>100 μm) and is often the dominant source

of *epi*-scattering from turbid media such as human skin. Optimization of such *epi*-detection mechanisms is highly critical for applications such as CARS endoscopy, where light is delivered to and/or from the target by optical fiber [321, 332].

2.5.3.3.2 Suppression of Nonresonant CARS Background

A persistent problem in CARS microscopy is that spectroscopic information contained in the biomolecule-specific resonant susceptibility $\chi_R^{(3)}(\Omega)$ may be obscured by a nonresonant background (due to $\chi_{NR}^{(3)}$), since the CARS signal varies as $|\chi_R^{(3)}(\Omega) + \chi_{NR}^{(3)}|^2$ [313–318]. Some ways to eliminate (or at least reduce) this nonresonant background are elaborate: coherent control of exciting light pulses [333, 334]; ultrafast interferometric or optical-heterodyne (OH) approaches to CARS [323, 325, 326, 335, 336]; and various time-resolved and chirped-pulse CARS excitation schemes [337–342]. More straightforward approaches include: infrared excitation of CARS (reduced electronic contributions to $\chi_{NR}^{(3)}$) [313–318]; *epi*-detection of CARS (reduced solvent background) [313–318, 343, 344]; polarization-sensitive CARS detection [313–318, 345]; background subtraction in multiplex CARS spectra [322, 347]; FM CARS microscopy [348]; shot-noise-limited OH CARS detection [349].

The last of these background-suppression techniques [349] is particularly ingenious. It uses a frequency-doubled Nd:YAG laser (delivering ~15-ps pulses with a repetition rate of ~80 MHz) to synchronously pump a LiB_3O_5 (LBO) OPO, similar to a preceding design [350], in a cascaded phase-preserving chain that generates *not only* the CARS output wave of prime spectroscopic interest *but also* a more intense coherent local oscillator wave to enable OH detection. All wavelengths generated during the laser SHG and OPO processes have been used effectively to achieve shot-noise-limited OH detection of CARS signals. The CARS output (with frequency $\omega_{AS} = 2\,\omega_{pump} - \omega_{Stokes}$) is coherently excited at two frequencies: ω_{pump}, which is effectively AOM-shifted by ~20 kHz ($= |\omega_{pump} - \omega_{laser}|$) from the 1064-nm fundamental laser frequency ω_{laser}; and ω_I ($\equiv \omega_{Stokes}$) from the OPO idler output wave (e.g., at ~1578 nm for CARS spectroscopy of CH-stretch vibrations in toluene, for which $\Omega \approx 3060\ cm^{-1}$). The OPO, pumped at 532 nm (corresponding to $\omega_P = 2\,\omega_{laser}$), generates a signal output wave at ω_S ($= \omega_P - \omega_I = 2\,\omega_{laser} - \omega_{Stokes}$), which is phase-coherent with the CARS output at ω_{AS} and frequency-shifted from it by twice the AOM-shifted frequency ($= 2\,|\omega_{pump} - \omega_{laser}|$). The OPO signal beam therefore serves effectively as a local oscillator for OH detection and is combined with the CARS beam (e.g., both at ~803 nm) on a fast square-law photodetector. The AOM-induced beat frequency ($2\,|\omega_{pump} - \omega_{laser}|$) is chosen to fall in a window (at ~40 kHz) that avoids the 1/*f*-type noise of the electronic detection system, thereby enabling shot-noise-limited phase-sensitive detection below the point at which signal-to-noise ratio is appreciably affected by amplitude fluctuations [349]. This background-suppression technique results in improved sensitivity by at least 3 orders of magnitude, relative to direct CARS detection using a photodiode, and is expected to enable high-contrast CARS microscopy of biomolecular solutes at concentrations below the current mmol L^{-1} limit [349].

2.5.3.3.3 Trade-Offs between Duration, Power, etc., of Laser Pulses

There are complicated trade-offs in CARS microscopy between temporal resolution, spectral bandwidth, focal geometry (e.g., CARS phase-matching angles), pulse

repetition rate (including scanned imaging speed), peak power for optimal nonlinearity, damage thresholds (both *in vivo* and *in vitro*), spatial resolution, and optical coherence. The potential for optothermal or NLO photolytic damage is much more critical when the target is biological tissue (e.g., *in vivo*) [313–315, 322, 328], than in the case of inert materials. It is important to characterize such trade-offs carefully in developing new, compact, accessible CARS microspectroscopic instruments. There are also prospects for surface-enhanced CARS microscopy [346, 347], the emerging technique applicable to trace detection of biological and forensic materials, such as pathogens in drinking water, bacterial spores (e.g., anthrax), and explosives.

The challenges listed above are likely to be key issues in ongoing research on CARS microspectroscopy and imaging. State-of-the-art ultrafast tunable OPO systems, such as those outlined in Section 2.5.3.4, are expected to play a significant role in this regard.

2.5.3.4 OPO Systems for CARS Microscopy

Significant early research on high-performance scanning CARS microscopy, by Xie and coworkers at Harvard [313–315], was performed with ps-pulse trains from two separate tunable Ti:sapphire lasers to provide the necessary coherent-Raman pump and Stokes waves (at frequencies ω_{pump} and ω_{Stokes}, respectively). This approach is both expensive and technically complicated, in view of the need to ensure that the CARS-excitation pulse trains are coincident temporally as well as spatially within the focal region of the target. Technology to enable tight pulse-train synchronization (reducing the tolerance to ~20 fs, compared to the usual few ps) has been developed [351, 352]; this brings CARS signal fluctuations down to the shot-noise limit, which leads to enhanced vibrational CARS-microscopic images of living cells and polymer beads. However, subsequent research on CARS microscopy [314, 316, 349–353] has tended to favor one or more ps-pulsed tunable OPO systems, in which the temporal and spatial relationships between the pump, signal, and idler waves (at ω_P, ω_S, and ω_I) are automatically well-defined by the NLO processes in the OPO itself.

For instance, design features of the LBO OPO [350], mentioned above in the context of background-suppression by shot-noise-limited OH CARS detection [349], are as follows. The NLO crystal is a 30-mm-long Brewster-angled crystal of LBO (Type I, NCPM) in a signal-resonant SRO folded cavity with an intracavity Lyot filter to reduce the OPO signal bandwidth. NCPM operation ensures that all parts of the OPO cavity remain fixed during scanning and that no adjustment is required in setting up CARS measurements, apart from adjusting the synchronously pumped OPO cavity length to allow for variation in round-trip time. The OPO is pumped by an 80-MHz train of 12-ps pulses at 532 nm (with typical average power of 2 W and OPO threshold of ~0.55 W) via SHG from a passively modelocked Nd:YVO_4 laser generating ~5 W, 15-ps pulses at 1064 nm. The OPO signal output comprises a train of 6.4-ps pulses that can be tuned over the wavelength range 740–930 nm by varying the temperature of the LBO crystal between 105 °C and 145 °C. With an average 532-nm pump power of 1.2 W, the OPO signal output power exceeds 0.3 W over the full operating range, which is adequate for CARS spectroscopy and microscopy. The tunable signal beam (740–930 nm) of the OPO has been combined

with the 1064-nm Nd:YVO_4 laser fundamental to obtain high-resolution (~2 cm^{-1}) vibrational CARS spectra of molecules in the CH stretch region (2700–3100 cm^{-1}). The straightforward, convenient tunability of the OPO has been demonstrated by using laser scanning CARS microscopy to localize and identify different polymer microparticles of the same size and shape with lateral and axial resolutions less than 0.5 μm and 1 μm, respectively.

Xie and coworkers have developed a comparable broadly tunable ps-pulsed PPKTP OPO system for CARS microscopy [353]. It is pumped by an 80-MHz train of 6-ps pulses at 532 nm (with 5-W average power and an OPO threshold as low as ~40 mW for the 924/1254-nm combination of signal/idler wavelengths) from a commercially available modelocked Nd:YVO_4 laser. This PPKTP OPO system generates the two colors for CARS microscopy, with a continuously tunable frequency difference over a broad range of Raman shifts (100–3700 cm^{-1}) by varying the temperature of the single PPKTP crystal. Moreover, the near-IR output (900–1300 nm) allows for deep penetration into thick samples and reduced NLO photodamage. This compact single-laser OPO source of tunable ps pulses has been used for CARS-microscopic imaging *in vivo* cell and *ex vivo* tissue targets [353]. Its stable operation, broad tunability with a single NLO crystal, and improved penetration depth make it an optimal source for CARS imaging in chemical and biomedical research. In subsequent developments of CARS microscopy, the Xie research group has used the same commercially available form of modelocked Nd:YVO_4 laser together with one [316] or two [348] commercially available broadly tunable ps-pulsed LBO OPOs. The second OPO serves as a reference source for real-time subtraction of nonresonant CARS background by the FM CARS technique [348], which yields improved contrast in laser scanning vibrational microscopic imaging.

There are also instructive design and operating features in earlier reports of synchronously pumped ps-pulsed tunable OPOs based on LBO [354, 356] or PPLN [356, 357], all suitable for CARS microscopy, as follows:

- Temperature-tunable NCPM LBO OPO [354], synchronously pumped at 523.5 nm by the second harmonic of a modelocked Nd:YLF laser to generate a 140-MHz train of 1.8-ps pulses that are continuously tunable over the range 839–1392 nm with output power up to 88 mW
- Widely tunable laser/SHG/OPO/SHG system [355] based on two intracavity LBO crystals that combine input from a Ti:sapphire laser (fundamental, 770–910 nm; second harmonic, 385–455 nm) with 1.15–2.26-μm output from the NCPM OPO itself and its 585–771-nm OPO/SHG output, to yield almost-continuous tuning capability from 385 nm to 2.26 μm
- PPLN SRO [356], pumped at 1.047 μm and 360 mW by a 105-MHz train of 2.4-ps pulses from a CW modelocked Nd:YLF laser to generate signal and idler outputs with average powers of ~120 mW and ~90 mW and a tuning range of ~1.7–2.8 μm
- Tunable (1.45–1.56 μm) NCPM PPLN SRO [357] with adjustable pulse duration (1–16 ps) and output power up to ~600 mW, pumped at 1.064 μm by a passively modelocked Nd:YVO_4 laser (duration 6 ps or 16 ps; repetition rate 200 MHz; average power ~2.5 W)

Finally, it should be emphasized that ps-pulsed tunable OPOs are highly advantageous for CARS microscopy because their optical bandwidth enables virtually all of the light impinging on the target to be concentrated within the characteristic Raman linewidth of a single relevant feature in the vibrational spectrum of particular interest. Moreover, this effectively minimizes unwanted damage (particularly in the case of biological cells and tissue) and extraneous nonresonant background, in contrast to other forms of CARS microscopy that entail broader-band fs pulses and/or supercontinuum radiation. Indeed, it is questionable whether some physically elegant sub-ps multiplex CARS techniques can actually be applied nondestructively for real-life *in vivo* biomedical applications of CARS microscopy.

2.6 CONCLUDING REMARKS: NEW FRONTIERS FOR OPO SPECTROSCOPY

To round off this chapter, it is constructive to highlight just a few emerging frontiers that are likely to be "hot topics" in future OPO-related developments and associated spectroscopic applications.

2.6.1 Prospects for Orientation-Patterned GaAs

It is evident that the general availability of orientation-patterned gallium arsenide (OP GaAs) is eagerly awaited by many researchers with an interest in applications of mid-IR optical parametric devices. This subject has already been extensively considered (e.g., in the final paragraph of Section 2.2.3) [5, 6, 43, 66–79]. Significant applications of OP GaAs via various forms of NLO wavelength-conversion point the way to future important advances in OP GaAs mid-IR DFG-based spectroscopy [73–75], in mid-IR operation of ns-pulsed tunable OP GaAs OPOs [76], in wide-ranging mid-IR continua produced by an OP GaAs OPG [77], and in THz-wave generation in OP GaAs devices [78, 79, 358, 359].

2.6.2 Backward (Mirrorless) OPOs

One of the most poignant recent developments in OPO technology has been the practical realization by Canalias and Pasiškevičius [360] of a backward OPO, which had first been proposed by Harris [361] more than 40 years earlier—even longer than the period of approximately 30 years that separated the initial recognition of the now-ubiquitous QPM approach [57–59] from its practical implementation [43, 60–64].

The backward OPO relies on parametric interaction of counterpropagating optical waves, which automatically establishes distributed feedback and is thus able to realize novel sources of coherent, tunable radiation. Also known as a "mirrorless OPO," a backward OPO does not require alignment or any optical components other than the second-order NLO medium itself [360, 361]. The first experimental demonstration of such an OPO entails a QPM NLO photonic structure with sub-μm periodicity (compared to the tens-of-μm pitches that are used in typical QPM devices [43]). Backward OPOs were originally envisioned [361] as BPM devices that would operate in the mid-infrared (in view of the dispersion properties of available birefringent NLO materials). More recently, they have been extensively discussed as a theoretical

possibility [362, 363]. The enabling technology was the capability to write QPM gratings of very fine pitch on flux-grown PPKTP [364, 365], as is needed to achieve the phase-matching conditions in a backward OPO (with co-propagating signal and pump waves and a counterpropagating idler wave) [360] or in backward SHG (with counterpropagating fundamental and second harmonic waves) [365].

The recently reported backward (mirrorless) OPO [360] is based on a PPKTP QPM grating with $\Lambda = 0.8$ μm, pumped typically at ~0.82 μm by a focused 1-kHz train of 47-ps pulses from a Ti:sapphire regenerative amplifier; this yields signal and idler waves at ~1.14 μm and ~2.94 μm with pulse energies of ~16 μJ and ~6 μJ, respectively. The spectral profile of the OPO signal output is essentially a wavelength-shifted replica of the pump-laser spectrum, which has an FWHM optical bandwidth of ~300 GHz (~10 cm^{-1}); by contrast, the backward-propagating OPO idler output has an optical bandwidth, ~3 GHz (~0.1 cm^{-1}), that is two orders of magnitude narrower. This unique and useful spectral property results in generation of narrowband idler radiation from a free-running OPO, which requires no resonator mirrors or adjustable optics (such as intracavity grating, étalon, or injection seeder) [360, 366]. The signal and idler frequencies are also remarkably insensitive to temperature variations (with a tuning rate of ~0.9 GHz K^{-1}, i.e., ~0.03 cm^{-1} K^{-1}: ~50 times smaller than that of a conventional co-propagating PPKTP OPO) so that the narrowband idler frequency is temperature-stable and amenable to high-precision mid-IR temperature-tuning. It will be fascinating in the future to follow the development of applications for this ingenious form of tunable OPO, both in spectroscopy and elsewhere.

Incidentally, we note that the backward (mirrorless) OPO has been likened to the NLO equivalent of a distributed-feedback (DFB) laser, which also does not require conventional mirrors [366]. Several other DFB-based OPO wavelength-control strategies (the first two of which have already been discussed in Section 2.4.2) may also be noted in this context:

- A ns-pulsed tunable PPLN OPO [191], in which a permanent phase-conjugate grating is written in PPLN by UV light to provide DFB operation
- Our ns-pulsed self-adaptive tunable (SAT) OPO design [154], in which CW tunable seed radiation (e.g., at ~840 nm) writes a wavelength-selective Bragg grating in a photorefractive crystal (e.g., Rh:$BaTiO_3$) as a way to provide dynamic, adjustment-free DFB-type operation of a ns-pulsed narrowband SLM tunable PPKTP OPO
- Compact tunable ns-pulsed PPKTP OPO [367] incorporating a volume Bragg grating retro-reflector [368] and delivering signal output at ~760 nm with a tuning range of ~2.6 THz (~87 cm^{-1}) and an optical bandwidth of ~130 GHz (~4.3 cm^{-1})

2.6.3 Terahertz Waves from OPGs and OPOs

Terahertz (THz) waves (also known as the submillimeter waves, between the far-IR and microwave regions) offer distinctive opportunities for spectroscopic sensing [369–371] and comprise another frontier in which there is a key role for optical parametric devices [372, 373].

Designs for NLO sources of coherent narrowband THz radiation have been reviewed by Ito and coworkers [373], whose group has developed an impressive assortment of OPG- and OPO-based tunable THz-wave sources [373–383]. Incidentally, this section of the literature adopts a somewhat confusing convention in which the shorter-wavelength output wave is referred to as the "idler," contrary to the usual convention defined in the context of Equation 2.3; to avoid any such confusion, we refer to the two output waves as "IR wave" (i.e., signal, typically at ~1.07 μm) and "THz wave" (i.e., idler, typically at ~2 THz).

Such OPGs and OPOs employ NLO crystals of either $LiNbO_3$ or $MgO:LiNbO_3$ [373–383] with a noncollinear phase-matching geometry to ensure that the generated THz wave propagates at a large angle to the 1.064-μm pump and ~1.07-μm IR waves [374–377], thereby rapidly exiting the NLO crystal since the THz wave is strongly absorbed in this crystal [376]. Wide, continuous tuning is attained by varying the angle between the resonated IR wave and the pump wave. Injection seeding by a narrowband tunable source [373, 380–383] can reduce the optical bandwidth of the THz wave to <100 MHz (<0.003 cm^{-1}), as determined [382, 383] by recording low-pressure absorption spectra of H_2O vapor at ~1.92 THz (~64 cm^{-1}).

In many of these OPG and OPO designs [373, 378–383], a Si-prism array is used to enhance outcoupling of the THz wave [378]. A similar approach has been adopted by Dunn, Browne, and coworkers [384] in a compact, noncollinear phase-matched $MgO:LiNbO_3$ OPO system with a novel intersecting-cavity geometry, to locate the NLO medium within the high-circulating intracavity field of the pump-laser cavity. This allows the use of a lower-energy pump laser compared to previous work [373–383] and eliminates coupling optics between the pump laser and the OPO. The effective extracavity pump-laser energy required to reach threshold for OPO operation is thus reduced at least ~25-fold from >18 mJ/pulse to ~0.7 mJ/pulse [384]. The intersecting-cavity geometry therefore enables a compact Nd:YAG laser, excited at 808 nm and 20 W by 500-μs pulses from a quasi-CW diode laser, to be used. The observed downconversion efficiency is close to 50% when the OPO is operated at two times above threshold. Moreover, in contrast to conventional intracavity OPGs, the intersecting-cavity geometry incorporates a separate, independently rotatable IR-wave cavity, combining the advantages of wide spectral coverage via angle tuning, as well as rapid walk-off of the THz wave.

Brief mention has already been made of THz-wave generation by optical parametric devices based on OP GaAs [78, 79, 358, 359]. The most recent of these devices generates an average output power of 1 mW at 2.8 THz with an optical bandwidth of ~300 GHz (~10 cm^{-1}) and a ps-pulse repetition rate of 50 MHz, by DFG of the signal and idler waves of a near-degenerate, synchronously pumped doubly-resonant OPO [359]. Such THz-generating DFG processes effectively approach the limit of optical rectification—one of the most primitive of the second-order ($\chi^{(2)}$-based) NLO processes [58]. Backward-propagating difference-frequency THz generation has also been observed and proposed [385] as the precursor of THz generation via a backward OPO [359–361].

2.6.4 Photonic Crystals Meet OPOs

Finally, it is useful to mention the interplay between possible applications of optical parametric devices and photonic-crystal technology [386–388]. For instance,

a microscale OPO in a photonic crystal has recently been proposed [389]. There are much less speculative prospects for photonic crystal fibers (PCFs) and photonic bandgap fibers (PBFs) as long-path sample cells for long-path spectroscopic sensing of gases [390–392]. In particular, PBFs can serve as practical, robust light-beam guides for absorption spectroscopy over path lengths much greater than in conventional gas cells. As an example, Kornaszewski et al. [393] have explored this potential by sensing 5% CH_4 in N_2 in the hollow core of a PBF-based gas cell, using broadband idler pulses at 3.15–3.35 μm from a fs-pulsed PPLN OPO [394, 395] and FT-spectrometric detection with a resolution of ~3 cm^{-1}. While the FTIR spectra and detection sensitivities are not particularly impressive by conventional IR-spectroscopic standards, the approach is promising for trace-level gas sensing in remote or hazardous environments [393].

PCFs also provide the enabling technology for broad-spectrum optical frequency combs, which are important as optical frequency synthesizers for metrology and high-precision spectroscopy [395, 396]. Inaba et al. [397] have recently used a frequency-stabilized optical comb (generated by a modelocked Ti:sapphire laser and a PCF) to measure the optical frequency fluctuation of a doubly resonant CW OPO based on MgO:$LiNbO_3$. The free-running OPO operated stably with a fluctuation in its idler frequency at ~830 nm of ~10 MHz hr^{-1}; this was measured by means of an optical frequency comb that was phase-locked to an atomic clock. The OPO idler frequency was also phase-locked to the optical comb by PZT-control of the length of the pump-laser cavity with a low-speed loop bandwidth of 20 kHz and using an AOM to control the optical frequency of the OPO. This stabilized source of coherent IR light is considered to have promising prospects for high-performance IR spectroscopy [397].

2.6.5 Epilogue: A Selective View of OPOs and Spectroscopy

At the outset, it was envisioned that this chapter would simply update its predecessor [1], published in the first edition of this book. That earlier chapter was written at a time when ns-pulsed tunable OPOs and their spectroscopic applications had recently undergone a resurgence, after a period (~1975–1985) of relatively low activity, compared to developments in the 10 years following the initial realization of an OPO [155] and the diversity of outcomes in the post-1985 "boom" years when OPO-related resurgence has continued to proceed. A contemporary survey of the spectroscopic applications of tunable OPOs therefore proved to be a much more challenging task than it had been some 15 years ago, especially because we were determined that this chapter should retain an historical perspective alongside state-of-the-art developments. Moreover, whereas the previous chapter [1] had been confined to ns-pulsed OPOs, it is now appropriate also to cover the key roles that ultrafast-pulsed and CW OPOs have assumed, and to provide perspectives on $\chi^{(2)}$-based optical parametric devices in general (e.g., see Fig. 2.1): OPGs, OPAs, and DFGs, in addition to OPOs themselves.

It will perhaps disappoint some readers that this chapter is far from comprehensive, and that its scope allows no more than a superficial, biased sampling of the many things that have happened and are happening in the field of OPO-based

spectroscopy. Our personal research interests (e.g., on the use of linear or nonlinear atomic and molecular spectroscopy to verify the performance of injection-seeded ns-pulsed SLM tunable OPOs, as in most of Section 2.4 and much of Section 2.5) are unashamedly represented in the chosen topics. For instance, most of the examples cited concern rovibrational spectroscopy (either IR or Raman) and bypass much important OPO-based research in the visible and UV regions (e.g., LIF-based biosensing and biomolecular imaging). Nevertheless, an attempt has been made to deal, at least cursorily, with areas of the subject in which our expertise may not be well established. The chapter at first focuses on how tunable OPOs work (e.g., see Tables 2.1 and 2.2, and Figs. 2.2 through 2.5) and how spectroscopic measurements can be used to test their performance (e.g., see Tables 2.3 through 2.5 and Fig. 2.6), before moving on to selected examples where spectroscopy itself is the prime motivation. Nevertheless, optimizing spectroscopic performance of CW, ns-pulsed, or ultrafast-pulsed OPOs remains a pervasive theme throughout this chapter.

ACKNOWLEDGMENTS

The chapter has been significantly influenced by work of other researchers in this field, with whom we have worked, co-published, communicated, met at conferences, or merely enjoyed virtual contact with through the literature of OPOs and their spectroscopic applications. Such colleagues are too numerous to name explicitly, other than by citing some of their published work. We specifically acknowledge financial support from the Australian Research Council and from Macquarie University, including its former Centre for Lasers and Applications (which has now evolved into the recently established MQ Photonics Research Centre).

REFERENCES

1. Orr, B. J., M. J. Johnson, and J. G. Haub, Spectroscopic applications of pulsed tunable optical parametric oscillators, in *Tunable Laser Applications*, 1st edition, edited by F. J. Duarte, Marcel Dekker, New York, 1995, Chap. 2, pp. 11–82.
2. Stuke, M. (Ed.), *Dye Lasers: 25 Years*, Springer, Berlin, 1992.
3. Duarte, F. J. (Ed.), *High-Power Dye Lasers*, Springer, Berlin, 1992.
4. Segal, D. M., *J. Mod. Opt.* 40: 965–966 (1993); this is a book review of Ref. 3.
5. Sorokina, I. T., and K. L. Vodopyanov (Eds.), *Solid-State Mid-Infrared Sources*, Springer, Berlin, 2003.
6. Ebrahim-Zadeh, M., and I. T. Sorokina (Eds.), *Mid-Infrared Coherent Sources and Applications* (NATO Science for Peace and Security Series B: Physics and Biophysics), Springer, Berlin, 2007.
7. Harris, S. E., Tunable optical parametric oscillators, *Proc. IEEE* 57: 2096–2113 (1969).
8. Byer, R. L., Parametric oscillators, in *Laser Spectroscopy*, edited by R. G. Brewer and A. Mooradian, Plenum, New York, 1973, pp. 77–101.
9. Byer, R. L., Optical parametric oscillators, in *Quantum Electronics: A Treatise*, edited by H. Rabin and C. L. Tang, Academic, New York, 1975, Vol. I, Part B, pp. 578–702.
10. Byer, R. L., and R. L. Herbst, Parametric oscillation and mixing, in *Nonlinear Infrared Generation*, edited by Y.-R. Shen, Springer, Berlin, 1977, Chap. 3, pp. 81–137.
11. Brosnan, S. J., and R. L. Byer, Optical parametric oscillator threshold and linewidth studies, *IEEE J. Quantum Electron*. QE-15: 415–431 (1979).

12. Sackett, P. (US Air Force Cambridge Research Laboratory), cited in Ref. 9 as a private communication of R. L. Byer (1972).
13. Leone, S. R., and C. B. Moore, *V–V* energy transfer in HCl with tunable optical parametric oscillator excitation, *Chem. Phys. Lett.* 19: 340–344 (1973).
14. Henningsen, T., M. Garbuny, and R. L. Byer, Remote detection of CO by parametric tunable laser, *Appl. Phys. Lett.* 24: 242–244 (1974).
15. Michael, D. W., K. Kolenbrander, and J. M. Lisy, New cavity design for a $LiNbO_3$ optical parametric oscillator, *Rev. Sci. Instrum.* 57: 1210–1212 (1986).
16. Minton, T. K., S. A. Reid, H. L. Kim, and J. D. McDonald, A scanning, single-mode, $LiNbO_3$ optical parametric oscillator, *Opt. Commun.* 69: 289–293 (1989).
17. Bosenberg, W. R., W. S. Pelouch, and C. L. Tang, High-efficiency and narrow-linewidth operation of a two-crystal β-BaB_2O_4 optical parametric oscillator, *Appl. Phys. Lett.* 55: 1952–1954 (1989).
18. Bosenberg, W. R., and D. R. Guyer, Single-frequency optical parametric oscillator, *Appl. Phys. Lett.* 61: 387–389 (1992).
19. Bosenberg, W. R., and D. R. Guyer, Broadly tunable, single-frequency optical parametric frequency-conversion system, *J. Opt. Soc. Am. B* 10: 1716–1722 (1993).
20. Fix, A., T. Schröder, and R. Wallenstein, The optical parametric oscillators of beta-bariumborate and lithiumborate, and lithiumborate: new sources of powerful tunable laser radiation in the ultraviolet, visible and near infrared, *Laser Optoelektronik* 23(3): 106–110 (1991).
21. Tang, C. L., W. R. Bosenberg, T. Ukachi, R. J. Lane, and L. K. Cheng, Optical parametric oscillators, *Proc. IEEE* 80: 365–374 (1992).
22. Dmitriev, V. G., G. G. Gurzayan, and D. N. Nikogosyan, *Handbook of Nonlinear Optical Crystals*, Springer, New York, 3rd edition, 1999.
23. Nikogosyan, D. N., *Nonlinear Optical Crystals: A Complete Survey*, Springer, New York, 2005.
24. Smith, A. V., *SNLO Nonlinear Optics Code*, Windows-based free public domain software downloadable from http://www.as-photonics.com/?q=SNLO.
25. Koechner, W., *Solid-State Laser Engineering*, Springer, New York, 6th edition, 2006.
26. Orr, B. J., IR lidar applications in air monitoring, in *Encyclopedia of Analytical Chemistry: Applications, Theory and Instrumentation – Vol. 3, Applications of Instrumental Methods*, edited by R. A. Meyers, Wiley, Chichester, UK, 2000, pp. 2007–2032.
27. Baxter, G. W., M. A. Payne, B. D. W. Austin, C. A. Halloway, J. G. Haub, Y. He, A. P. Milce, J. W. Nibler, and B. J. Orr, Spectroscopic diagnostics of chemical processes: applications of optical parametric oscillators, *Appl. Phys. B* 71: 651–663 (2000).
28. He, Y., P. Wang, R. T. White, and B. J. Orr, Spectroscopic applications of optical parametric oscillators, *Optics and Photonics News* 13 (5): 56–60 and 76 (May 2002).
29. Orr, B. J., Optical parametric devices: overview, in *Encyclopedia of Modern Optics*, edited by R. D. Guenther, D. G. Steel, and L. Bayvel, Elsevier Physics, Oxford, UK, 2004, "Nonlinear optics – applications" section, pp. 43–51.
30. Tang, C. L., Optical parametric processes in nonlinear optics, *Int. J. Nonlinear Optical Physics* 3: 205–224 (1994).
31. Barnes, N. P., Optical parametric oscillators, in *Tunable Lasers Handbook*, edited by F. J. Duarte, Academic Press, San Diego, 1995, Chap. 7, pp. 293–348.
32. Sutherland, R. L., Optical parametric generation, amplification, and oscillation, in *Handbook of Nonlinear Optics – Optical Engineering Series, Vol. 52*, Marcel Dekker, New York, 1996, Chap. 3, pp. 111–206.
33. Piskarskas, A. P., Optical parametric generators: tunable, powerful and ultrafast, *Optics and Photonics News* 8 (7): 24–28 and 55 (1997).
34. Dixon, G. J., Periodically poled lithium niobate shines in the IR, *Laser Focus World* 33 (5): 105–111 (1997).

35. Tang, C. L., Tutorial on optical parametric processes and devices, *J. Nonlinear Optical Physics and Materials* 6: 535–547 (1997).
36. Byer, R. L., Quasi-phasematched nonlinear interactions and devices, *J. Nonlinear Optical Physics and Materials* 6: 549–592 (1997).
37. Dunn, M. H., and M. Ebrahimzadeh, Parametric generation of tunable light from continuous-wave to femtosecond pulses, *Science* 286: 1513–1517 (1999).
38. Ebrahimzadeh, M., and M. H. Dunn, Optical parametric oscillators, in *Handbook of Optics, Vol. IV, Fiber Optics and Nonlinear Optics*, edited by M. Bass, J. M. Enoch, E. W. Van Stryland, and W. L. Wolfe, McGraw-Hill, 2001, Chap. 22, pp. 22.1–22.73.
39. Vodopyanov, K. L., OPOs target the longwave infrared, *Laser Focus World*, 37: 225–232 (May 2002).
40. Vodopyanov, K. L., Pulsed mid-IR optical parametric oscillators, in Ref. 5, Chap. 4, pp. 141–178 (2003).
41. Ebrahimzadeh, M., Mid-infrared and continuous-wave optical parametric oscillators, in Ref. 5, Chap. 5, pp. 179–218 (2003).
42. Ebrahimzadeh, M., Parametric light generation, *Phil. Trans. Roy. Soc. London, Ser. A: Math., Phys. Eng. Sci*., 361: 2731–2750 (2003).
43. Hum, D. S., and M. M. Fejer, Quasi-phasematching, *Comptes Rendus Physique*, 8: 180–198 (2007).
44. Byer, R. L., and A. Piskarskas (Eds.), Optical parametric oscillation and amplification, Feature Issue of *J. Opt. Soc. Am. B* 10: 1656–1791 (1993).
45. Byer, R. L., and A. Piskarskas (Eds.), Optical parametric oscillation and amplification, Feature Issue of *J. Opt. Soc. Am. B* 10: 2148–2238 (1993).
46. Bosenberg, W. R., and R. C. Eckardt (Eds.), Optical parametric devices, Feature Issue of *J. Opt. Soc. Am. B* 12: 2084–2322 (1995).
47. Ebrahimzadeh, M., R. C. Eckardt, and M. H. Dunn (Eds.), Optical Parametric Devices and Processes, Feature Issue of *J. Opt. Soc. Am. B* 16: 1477–1602 (1999).
48. Schiller, S., and J. Mlynek (Eds.), Continuous-wave optical parametric oscillators, Special Issue of *Appl. Phys. B* 66: 661–764 (1998).
49. Tittel, F. K. (Ed.), Environmental trace gas detection using laser spectroscopy, Special Issue of *Appl. Phys. B* 67: 273–527 (1998).
50. Richter, D., A. Fried, and F. K. Tittel (Eds.), Trends in laser sources, spectroscopic techniques and their applications to trace-gas detection, Special Issue of *Appl. Phys. B* 75: 143–403 (2002).
51. Tittel, F. K., and A. A. Kosterev (Eds.), Optics: trends in laser sources, spectroscopic techniques and their applications to trace-gas detection, Special Issue of *Appl. Phys. B* 85: 171–477 (2006).
52. Shen, Y. R., *The Principles of Nonlinear Optics*, Wiley, New York, 1984 (reprinted in the Wiley Classics Series, 2003).
53. Yariv, A., *Quantum Electronics*, Wiley, New York, 3rd edition, 1989.
54. Butcher, P. N., and D. Cotter, *The Elements of Nonlinear Optics*, Cambridge University Press, Cambridge, UK, 1990.
55. Boyd, R. W., *Nonlinear Optics*, Academic Press, New York, 2nd edition, 2003.
56. Fischer, C., and M. W. Sigrist, Mid-IR difference-frequency generation, in Ref. 5, Chap. 3, pp. 97–141 (2003).
57. Armstrong, J. A., N. Bloembergen, J. Ducuing, and P. S. Pershan, Interaction between light waves in a nonlinear dielectric, *Phys. Rev.* 127: 1918–1939 (1962).
58. Franken, P. A., and J. F. Ward, Optical harmonics and nonlinear phenomena, *Rev. Mod. Phys.* 35: 23–39 (1963).
59. Miller, R. C., D. A. Kleinman, and A. Savage, Quantitative studies of optical harmonic generation in CdS, $BaTiO_3$, and KH_2PO_4 type crystals, *Phys. Rev. Lett.* 11: 146–149 (1963).

60. Fejer, M. M., G. A. Magel, D. H. Jundt, and R. L. Byer, Quasi-phase matched second harmonic generation: tuning and tolerances, *IEEE J. Quantum Electron*. 28: 2631–2654 (1992).
61. Yamada, M., N. Nada, M. Saitoh, and K. Watanabe, First-order quasi-phase matched $LiNbO_3$ waveguide periodically poled by applying an external yield for efficient blue second harmonic generation, *Appl. Phys. Lett*. 62: 435–436 (1993).
62. Burns, W. K., W. McElhanon, and L. Goldberg, Second harmonic generation in field poled, quasi-phase-matched, bulk $LiNbO_3$, *IEEE Photonics Technol. Lett*. 6: 252–254 (1994).
63. Myers, L. E., R. C. Eckardt, M M. Fejer, R. L. Byer, W. R. Bosenberg, and J. W. Pierce, Quasi-phase-matched optical parametric oscillators in bulk periodically poled $LiNbO_3$, *J. Opt. Soc. Am. B* 12: 2102–2110 (1995).
64. Houé, M., and P. D. Townsend, An introduction to methods of periodic poling for second harmonic generation, *J. Phys. D* 28: 1747–1763 (1995).
65. Miller, R. C., Optical second harmonic generation in piezoelectric crystals, *Appl. Phys. Lett*. 5: 17–19 (1964).
66. Schunemann, P. G., Improved NLO crystals for mid-IR laser applications, *Proc. SPIE*, 6455 (Nonlinear Frequency Generation and Conversion: Materials, Devices, and Applications VI): 64550R/1–64550R/7 (2007).
67. Skauli, T., K. L. Vodopyanov, T. J. Pinguet, A. Schober, O. Levi, L. A. Eyres, M. M. Fejer, J. S. Harris, B. Gerard, L. Becouarn, E. Lallier, and G. Arisholm, Measurement of nonlinear coefficient of orientation-patterned GaAs and demonstration of highly efficient second harmonic generation, *Opt. Lett*. 27: 628–630 (2002).
68. Skauli, T., P. S. Kuo, K. L. Vodopyanov, T. J. Pinguet, O. Levi, L. A. Eyres, J. S. Harris, M. M. Fejer, B. Gerard, L. Becouarn, and E. Lallier, Improved dispersion relations for GaAs and applications to nonlinear optics, *J. Appl. Phys*. 94: 6447–6455 (2003).
69. Ebert, C. B., L. A. Eyres, M. M. Fejer, and J. S. Harris, MBE growth of antiphase GaAs films using GaAs/Ge/GaAs heteroepitaxy, *J. Crystal Growth* 201–202: 187–193 (1999).
70. Eyres, L. A., P. J. Tourreau, T. J. Pinguet, C. B. Ebert, J. S. Harris, M. M. Fejer, L. Becouarn, B. Gerard, and E. Lallier, All-epitaxial fabrication of thick, orientation-patterned GaAs films for nonlinear optical frequency conversion, *Appl. Phys. Lett*. 79: 904–906 (2001).
71. Bliss, D. F., C. Lynch, D. Weyburne, K. O'Hearn, and J. S. Bailey, Epitaxial growth of thick GaAs on orientation-patterned wafers for nonlinear optical applications, *J. Crystal Growth* 287: 673–678 (2006).
72. Yu, X., L. Scaccabarozzi, A. C. Lin, M. M. Fejer, and J. S. Harris, Growth of GaAs with orientation-patterned structures for nonlinear optics, *J. Crystal Growth* 301–302: 163–167 (2007).
73. Kulp, T. J., S. E. Bisson, R. P. Bambha, T. A. Reichardt, U. B. Goers, K. W. Aniolek, D. A. V. Kliner, B. A. Richman, K. M. Armstrong, R. Sommers, R. Schmitt, P. E. Powers, O. Levi, T. Pinguet, M. Fejer, J. P. Koplow, L. Goldberg, and T. G. McRae, The application of quasi-phasematched parametric light sources to practical infrared chemical sensing systems, *Appl. Phys. B* 75: 317–327 (2002).
74. Levi, O., T. J. Pinguet, T. Skauli, L. A. Eyres, K. R. Parameswaran, J. S. Harris, M. M. Fejer, T. J. Kulp, S. E. Bisson, B. Gerard, E. Lallier, and L. Becouarn, Difference frequency generation of 8-μm radiation in orientation-patterned GaAs, *Opt. Lett*. 27: 2091–2093 (2002).
75. Bisson, S. E., T. J. Kulp, O. Levi, J. S. Harris, and M. M. Fejer, Long-wave IR chemical sensing based on difference frequency generation in orientation-patterned GaAs, *Appl. Phys. B* 85: 199–206 (2006).
76. Vodopyanov, K. L., O. Levi, P. S. Kuo, T. J. Pinguet, J. S. Harris, M. M. Fejer, J. S. Harris, B. Gerard, L. Becouarn, and E. Lallier, Optical parametric oscillation in quasi-phase-matched GaAs, *Opt. Lett*. 29: 1912–1914 (2004).

77. Kuo, P. S., K. L. Vodopyanov, M. M. Fejer, D. M. Simanovskii, X. Yu, J. S. Harris, D. Bliss, and D. Weyburne, Optical parametric generation of a mid-infrared continuum in orientation-patterned GaAs, *Opt. Lett.* 31: 71–73 (2006).
78. Imeshev, G., M. E. Fermann, K. L. Vodopyanov, M. M. Fejer, X. Yu, J. S. Harris, D. Bliss, and C. Lynch, High-power source of THz radiation based on orientation-patterned GaAs pumped by a fiber laser, *Opt. Express* 14: 4439–4444 (2006).
79. Vodopyanov, K. L., M. M. Fejer, X. Yu, J. S. Harris, Y.-S. Lee, W. C. Hurlbut, V. G. Kozlov, D. Bliss, and C. Lynch, Terahertz-wave generation in quasi-phase-matched GaAs, *Appl. Phys. Lett.* 89: 141119/1–141119/3 (2006).
80. Myers, L. E., R. C. Eckardt, M. M. Fejer, R. L. Byer, and W. R. Bosenberg, Multigrating quasi-phase-matched optical parametric oscillators in periodically poled $LiNbO_3$, *Opt. Lett.* 21: 591–593 (1996).
81. Eckardt, R. C., C. D. Nabors, W. J. Kozlovsky, and R. L. Byer, Optical parametric oscillator frequency tuning and control, *J. Opt. Soc. Am. B* 8: 646–667 (1991); see also an erratum in *J. Opt. Soc. Am. B* 12: 2322 (1995).
82. Henderson, A. J., M. J. Padgett, J. Zhang, W. Sibbett, and M. H. Dunn, Continuous frequency tuning of a cw optical parametric oscillator through tuning of its pump source, *Opt. Lett.* 20: 1029–1031 (1995).
83. Scheidt, M., B. Beier, R. Knappe, K.-J. Boller, and R. Wallenstein, Diode-laser-pumped continuous-wave KTP optical parametric oscillator, *J. Opt. Soc. Am. B* 12: 2087–2094 (1995).
84. Lindsay, I. D., G. A. Turnbull, M. H. Dunn, and M. Ebrahimzadeh, Doubly-resonant continuous-wave optical parametric oscillator pumped by a single-mode laser diode, *Opt. Lett.* 23: 1889–1891 (1998).
85. Schiller, S., K. Schneider, and J. Mlynek, Theory of an optical parametric oscillator with resonant pump and signal, *J. Opt. Soc. Am. B* 16: 1512–1524 (1999).
86. Yang, S. T., R. C. Eckardt, and R. L. Byer, Continuous-wave singly resonant optical parametric oscillator pumped by a single-frequency resonantly doubled Nd:YAG laser, *Opt. Lett.* 18: 971–973 (1993).
87. Schneider, K., P. Kramper, S. Schiller, and J. Mlynek, Toward an optical synthesizer: a single-frequency parametric oscillator using periodically poled $LiNbO_3$, *Opt. Lett.* 22: 1293–1295 (1997).
88. Schneider, K., and S. Schiller, Narrow-linewidth, pump-enhanced singly-resonant optical parametric oscillator pumped at 532 nm, *Appl. Phys. B* 65: 775–777 (1997).
89. Oshman, M. K., and S. E. Harris, Theory of optical parametric oscillation internal to the laser cavity, *IEEE J. Quantum Electron.* QE-4: 491–502 (1968).
90. Turnbull, G. A., M. H. Dunn, and M. Ebrahimzadeh, Continuous-wave, intracavity optical parametric oscillators: an analysis of power characteristics, *Appl. Phys. B* 66: 701–710 (1998).
91. Ebrahimzadeh, M., G. A. Turnbull, T. J. Edwards, D. J. M. Stothard, I. D. Lindsay, and M. H. Dunn, Intracavity continuous-wave singly resonant optical parametric oscillators, *J. Opt. Soc. Am. B* 16: 1499–1511 (1999).
92. Colville, F. G., M. H. Dunn, and M. Ebrahimzadeh, Continuous-wave, singly resonant intracavity parametric oscillator, *Opt. Lett.* 22: 75–77 (1997).
93. Turnbull, G. A., T. J. Edwards, M. H. Dunn, and M. Ebrahimzadeh, Continuous-wave singly resonant intracavity optical parametric oscillator based on periodically-poled $LiNbO_3$, *Electron. Lett.* 33: 1817–1818 (1997).
94. Stothard, D. J. M., M. Ebrahimzadeh, and M. H. Dunn, Low-pump-threshold, continuous-wave, singly resonant optical parametric oscillator, *Opt. Lett.* 23: 1895–1897 (1997).
95. Bosenberg, W. R., A. Drobshoff, J. I. Alexander, L. E. Myers, and R. L. Byer, Continuous-wave singly resonant optical parametric oscillator based on periodically poled $LiNbO_3$, *Opt. Lett.* 21: 713–715 (1996).

96. Bosenberg, W. R., A. Drobshoff, J. I. Alexander, L. E. Myers, and R. L. Byer, 93% pump depletion, 3.5-W continuous-wave, singly resonant optical parametric oscillator, *Opt. Lett.* 21: 1336–1338 (1996).
97. Powers, P. E., T. J. Kulp, and S. E. Bisson, Continuous tuning of a continuous-wave periodically poled lithium niobate optical parametric oscillator by use of a fan-out grating design, *Opt. Lett.* 23: 159–161 (1998).
98. Klein, M. E., D. H. Lee, J.-P. Meyn, K.-J. Boller, and R. Wallenstein, Singly resonant continuous-wave optical parametric oscillator pumped by a diode laser, *Opt. Lett.* 24: 1142–1144 (1999).
99. Gross. P., M. E. Klein, T. Walde, K.-J. Boller, M. Auerbach, P. Wessels, and C. Fallnich, Fiber-laser-pumped continuous-wave singly-resonant optical parametric oscillator, *Opt. Lett.* 27: 418–420 (2002).
100. Turnbull, G. A., D. McGloin, I. D. Lindsay, M. Ebrahimzadeh, and M. H. Dunn, Extended mode-hop-free tuning using a dual-cavity, pump-enhanced optical parametric oscillator, *Opt. Lett.* 25: 341–343 (2000).
101. Lindsay, I. D., C. Petridis, M. H. Dunn, and M. Ebrahimzadeh, Continuous-wave pump-enhanced singly-resonant optical parametric oscillator pumped by an external-cavity diode laser, *Appl. Phys. Lett.* 78: 871–873 (2000).
102. Popp, A., F. Müller, F. Kühnemann, S. Schiller, G. von Basum, H. Dahnke, P. Hering, and M. Mürtz, Ultra-sensitive mid-infrared cavity leak-out spectroscopy using a cw optical parametric oscillator, *Appl. Phys. B* 75: 751–754 (2002).
103. Müller, F., A. Popp, F. Kühnemann, and S. Schiller, Transportable, highly sensitive photoacoustic spectrometer based on a continuous-wave dual-cavity optical parametric oscillator, *Opt. Express* 11: 2820–2825 (2003).
104. Stothard, D. J. M., P.-Y. Fortin, A. Carleton, M. Ebrahimzadeh, and M. H. Dunn, Comparison of continuous-wave optical parametric oscillators based on periodically poled $LiNbO_3$ and periodically poled $RbTiOAsO_4$ pumped internal to a high-power Nd:YVO_4 laser. *J. Opt. Soc. Am. B* 20: 2102–2108 (2003).
105. Reid, D. T., G. T. Kennedy, A. Miller, W. Sibbett, and M. Ebrahimzadeh, Widely tunable near- to mid-infrared femtosecond and picosecond optical parametric oscillators using periodically poled $LiNbO_3$ and $RbTiOAsO_4$, *IEEE J. Sel. Top. Quantum Electron.* 4: 238–248 (1998).
106. Edelstein, D. C., E. S. Wachman, and C. L. Tang, Broadly tunable high repetition rate femtosecond optical parametric oscillator, *Appl. Phys. Lett.* 54: 1728–1730 (1989).
107. Pelouch, W. S., P. E. Powers, and C. L. Tang, Ti:sapphire-pumped, high-repetition rate femtosecond optical parametric oscillator, *Opt. Lett.* 17: 1070–1072 (1992).
108. Nebel, A., C. Fallnich, R. Beigang, and R. Wallenstein, Noncritically phase-matched continuous-wave mode-locked singly resonant optical parametric oscillator synchronously pumped by a Ti:sapphire laser, *J. Opt. Soc. Am. B* 10: 2195–2200 (1993).
109. Chung, J., and A. E. Siegman, Singly resonant continuous-wave mode-locked $KTiOPO_4$ optical parametric oscillator pumped by a Nd:YAG laser, *J. Opt. Soc. Am. B* 10: 2201–2210 (1993).
110. Grässer, C., D. Wang, R. Beigang, and R. Wallenstein, Singly resonant optical parametric oscillator of $KTiOPO_4$ synchronously pumped by the radiation from a continuous-wave mode-locked Nd:YLF laser, *J. Opt. Soc. Am. B* 10: 2218–2221 (1993).
111. Dudley, J. M., D. T. Reid, M. Ebrahimzadeh, and W. Sibbett, Characteristics of a non-critically phase-matched Ti:sapphire-pumped femtosecond optical parametric oscillator, *Opt. Commun.* 104: 419–430 (1994).
112. McCahon, S. W., S. A. Anson, D.-J. Jang, and T. F. Boggess, Generation of 3–4-μm femtosecond pulses from a synchronously pumped, critically phase-matched $KTiOPO_4$ optical parametric oscillator, *Opt. Lett.* 22: 2309–2311 (1995).

113. Fallnich, C., B. Ruffing, T. Herrmann, A. Nebel, R. Beigang, and R. Wallenstein, Experimental investigation and numerical simulation of the influence of resonator-length detuning on the output power, pulse duration and spectral width of a cw mode-locked picosecond optical parametric oscillator, *Appl. Phys. B* 60: 427–436 (1995).
114. Nebel, A., H. Frost, R. Beigang, and R. Wallenstein, Visible femtosecond pulses by second-harmonic generation of a cw mode-locked KTP optical parametric oscillator, *Appl. Phys. B* 60: 453–458 (1995).
115. French, S., M. Ebrahimzadeh, and A. Miller, High-power, high-repetition-rate picosecond optical parametric oscillator for the near- to mid-infrared, *Opt. Lett.* 21: 131–133 (1996).
116. Burr, K. C., C. L. Tang, M. A. Arbore, and M. M. Fejer, Broadly tunable mid-infrared femtosecond optical parametric oscillator using all-solid-state-pumped periodically poled lithium niobate, *Opt. Lett.* 22: 1458–1460 (1997).
117. Reid, D. T., Z. Penman, M. Ebrahimzadeh, W. Sibbett, H. Karlsson, and F. Laurell, Broadly tunable infrared femtosecond optical parametric oscillator based on periodically poled $RbTiOAsO_4$, *Opt. Lett.* 22: 1397–1399 (1997).
118. Kennedy, G. T., D. T. Reid, A. Miller, M. Ebrahimzadeh, H. Karlsson, G. Arvidsson, and F. Laurell, Broadly tunable mid-infrared picosecond optical parametric oscillator based on periodically poled $RbTiOAsO_4$, *Opt. Lett.* 23: 503–505 (1998).
119. Lefort, L., K. Peuch, G. W. Ross, Y. P. Svirko, and D. C. Hanna, Optical parametric oscillation out to 6.3μm in periodically poled lithium niobate under strong idler absorption, *Appl. Phys. Lett.* 73: 1610–1612 (1998).
120. Loza-Alvarez, P., C. T. A. Brown, D. T. Reid, W. Sibbett, and M. Missey, High repetition-rate ultrashort-pulse optical parametric oscillator continuously tunable from 2.8 to 6.8 μm, *Opt. Lett.* 24: 1523–1525 (1999).
121. Marzenell, S., R. Beigang, and R. Wallenstein, Synchronously pumped femtosecond optical parametric oscillator based on $AgGaSe_2$ tunable from 2 μm to 8 μm, *Appl. Phys. B* 69: 423–428 (1999).
122. Ebrahimzadeh, M., P. J. Phillips, and S. Das, Low-threshold, mid-infrared optical parametric oscillation in periodically poled $LiNbO_3$ synchronously pumped by a Ti:sapphire laser, *Appl. Phys. B* 72: 793–801 (2001).
123. Maus, M., E. Rousseau, M. Cotlet, G. Schweitzer, J. Hofkens, M. Van der Auweraer, F. C. De Schryver, and A. Krueger, New picosecond laser system for easy tunability over the whole ultraviolet/visible/near infrared wavelength range based on flexible harmonic generation and optical parametric oscillation, *Rev. Sci. Instrum.* 72: 36–40 (2001).
124. Sudmeyer, T., J. Aus der Au, R. Paschotta, U. Keller, P. G. R. Smith, G. W. Ross, and D. C. Hanna, Novel ultrafast parametric systems: high repetition rate single-pass OPG and fibre-feedback OPO, *J. Phys. D: Appl. Phys.* 34: 2433–2439 (2001).
125. Hoyt, C. W., M. Sheik-Bahae, and M. Ebrahimzadeh, High-power picosecond optical parametric oscillator based on periodically poled lithium niobate, *Opt. Lett.* 27: 1543–1545 (2002).
126. Tillman, K. A., D. T. Reid, D. Artigas, J. Hellstrom, V. Pasiškevičius, and F. Laurell, Low-threshold, high-repetition-frequency femtosecond optical parametric oscillator based on chirped-pulse frequency conversion, *J. Opt. Soc. Am. B* 20: 1309–1316 (2003).
127. Ebrahim-Zadeh, M., Efficient ultrafast frequency conversion sources for the visible and ultraviolet based on BiB_3O_6, *IEEE J. Sel. Top. Quantum Electron.* 13: 679–691 (2007).
128. Danielius, R., A. Piskarskas, A. Stabinis, G. P. Banfi, P. Di Trapani, and R. Righini, Traveling-wave parametric generation of widely tunable, highly coherent femtosecond light pulses, *J. Opt. Soc. Am. B* 10: 2222–2231 (1993); see also an erratum in *J. Opt. Soc. Am. B* 12: 2321 (1995).
129. Cerullo, G., and S. De Silvestri, Ultrafast optical parametric amplifiers, *Rev. Sci. Instrum.* 74: 1–18 (2003).

130. Dubietis, A., R. Butkus, and A. P. Piskarskas, Trends in chirped pulse optical parametric amplification, *IEEE J. Sel. Top. Quantum Electron*. 12: 163–172 (2006).
131. Tiihonen, M., V. Pasiškevičius, and F. Laurell, Broadly tunable picosecond narrowband pulses in a periodically-poled $KTiOPO_4$ parametric amplifier, *Opt. Express* 14: 8728–8736 (2006).
132. Siegman, A. E., *Lasers,* University Science, Mill Valley, CA, 1986, p. 334.
133. Haub, J. G., M. J. Johnson, B. J. Orr, and R. Wallenstein, A continuously tunable, injection-seeded β-barium borate optical parametric oscillator: spectroscopic applications, *Appl. Phys. Lett.* 58: 1718–1720 (1991).
134. Fix, A., T. Schröder, R. Wallenstein, J. G. Haub, M. J. Johnson, and B. J. Orr, A tunable β-barium borate optical parametric oscillator: operating characteristics with and without injection seeding, *J. Opt. Soc. Am. B* 10: 1744–1750 (1993).
135. Haub, J. G., M. J. Johnson, and B. J. Orr, Spectroscopic and nonlinear-optical applications of a tunable β-barium borate optical parametric oscillator, *J. Opt. Soc. Am. B* 10: 1765–1777 (1993).
136. Johnson, M. J., J. G. Haub, H.-D. Barth, and B. J. Orr, Rotationally resolved coherent anti-Stokes Raman spectroscopy by using a tunable optical parametric oscillator, *Opt. Lett*. 18: 441–443 (1993).
137. Johnson, M. J., J. G. Haub, and B. J. Orr, Continuously tunable, narrowband operation of an injection-seeded ring-cavity optical parametric oscillator: spectroscopic applications, *Opt. Lett.* 20: 1277–1279 (1995).
138. Haub, J. G., M. J. Johnson, A. J. Powell, and B. J. Orr, Bandwidth characteristics of a pulsed optical parametric oscillator: application to degenerate four-wave mixing spectroscopy, *Opt. Lett.* 20: 1637–1639 (1995).
139. Haub, J. G., R. M. Hentschel, M. J. Johnson, and B. J. Orr, Controlling the performance of a pulsed optical parametric oscillator: a survey of techniques and spectroscopic applications, *J. Opt. Soc. Am. B* 12: 2128–2141 (1995).
140. Baxter, G. W., M. J. Johnson, J. G. Haub, and B. J. Orr, OPO CARS: coherent anti-Stokes Raman spectroscopy using tunable optical parametric oscillators injection-seeded by external-cavity diode lasers, *Chem. Phys. Lett.* 251: 211–218 (1996).
141. Baxter, G. W., J. G. Haub, and B. J. Orr, Back conversion in a pulsed optical parametric oscillator: evidence from injection-seeded sidebands, *J. Opt. Soc. Am. B* 14: 2723–2730 (1997).
142. Baxter, G. W., H.-D. Barth, and B. J. Orr, Laser spectroscopy with a pulsed, narrowband infrared optical parametric oscillator system: a practical, modular approach, *Appl. Phys. B* 66: 653–657 (1998).
143. Baxter, G. W., Y. He, and B. J. Orr, A pulsed optical parametric oscillator, based on periodically poled lithium niobate (PPLN), for high-resolution spectroscopy, *Appl. Phys. B* 67: 753–756 (1998).
144. He, Y., G. W. Baxter, and B. J. Orr, Locking the cavity of a pulsed PPLN optical parametric oscillator to the wavelength of a cw injection-seeder by an 'intensity-dip' method, *Rev. Sci. Instrum.* 70: 3203–3213 (1999).
145. He, Y., and B. J. Orr, Tunable single-mode operation of a pulsed optical parametric oscillator pumped by a multi-mode laser, *Appl. Opt.* 40: 4836–4848 (2001).
146. He, Y., and B. J. Orr, Cavity ringdown spectroscopy: new approaches and outcomes, *J. Chinese Chem. Soc. (Taiwan)* 48: 591–601 (2001).
147. White, R. T., Y. He, B. J. Orr, M. Kono, and K. G. H. Baldwin, Pulsed injection-seeded optical parametric oscillator with low frequency chirp for high-resolution spectroscopy, *Opt. Lett.* 28: 1248–1250 (2003).
148. White, R. T., Y. He, B. J. Orr, M. Kono, and K. G. H. Baldwin, Control of frequency chirp in nanosecond-pulsed laser spectroscopy. 1. Optical-heterodyne chirp analysis techniques, *J. Opt. Soc. Am. B* 21: 1577–1585 (2004).

149. White, R. T., Y. He, B. J. Orr, M. Kono, and K. G. H. Baldwin, Control of frequency chirp in nanosecond-pulsed laser spectroscopy. 2. A long-pulse optical parametric oscillator for narrow optical bandwidth, *J. Opt. Soc. Am. B* 21: 1586–1594 (2004).
150. White, R. T., Y. He, B. J. Orr, M. Kono, and K. G. H. Baldwin, Transition from single-mode to multimode operation of an injection-seeded pulsed optical parametric oscillator, *Opt. Express* 12: 5655–5660 (2004).
151. Kono, M., K. G. H. Baldwin, Y. He, R. T. White, and B. J. Orr, Heterodyne-assisted pulsed spectroscopy with a nearly Fourier-transform limited, injection-seeded optical parametric oscillator, *Opt. Lett.* 30: 3413–3415 (2005).
152. Kono, M., K. G. H. Baldwin, Y. He, R. T. White, and B. J. Orr, CHAPS: a new precision laser-spectroscopic technique, *J. Opt. Soc. Am. B* 23: 1181–1189 (2006).
153. White, R. T., Y. He, B. J. Orr, M. Kono, and K. G. H. Baldwin, Control of frequency chirp in nanosecond-pulsed laser spectroscopy. 3. Spectrotemporal dynamics of an injection-seeded optical parametric oscillator, *J. Opt. Soc. Am. B* 24: 2601–2609 (2007).
154. He, Y., and B. J. Orr, Narrowband tuning of an injection-seeded pulsed optical parametric oscillator based on a self-adaptive, phase-conjugate cavity mirror, *Opt. Lett.* 29: 2169–2171 (2004).
155. Giordmaine, J. A., and R. C. Miller, Tunable coherent parametric oscillation in $LiNbO_3$ at optical frequencies, *Phys. Rev. Lett.* 14: 973–976 (1965).
156. Ebrahimzadeh, M., A. J. Henderson, and M. H. Dunn, An excimer-pumped β-BaB_2O_4 optical parametric oscillator tunable from 354 nm to 2.370 μm, *IEEE J. Quantum Electron.* 26: 1241–1252 (1990).
157. Myers, L. E., and W. R. Bosenberg, Periodically poled lithium niobate and quasi-phase-matched optical parametric oscillators, *IEEE J. Quantum Electron.* 33: 1663–1672 (1997).
158. Bader, U., J. Bartschke, I. Klimov, A. Borsutzky, and R. Wallenstein, Optical parametric oscillator of quasi-phase-matched $LiNbO_3$ pumped by a compact high repetition rate single-frequency passively Q-switched Nd:YAG laser, *Opt. Commun.* 147: 95–98 (1998).
159. Hellstrom, J., V. Pasiškevičius, F. Laurell, and H. Karlsson, Efficient nanosecond optical parametric oscillators based on periodically poled KTP emitting in the 1.8–2.5 μm spectral range, *Opt. Lett.* 24: 1233–1235 (1999).
160. Chen, Y.-H., Y.-Y. Lin, C.-H. Chen, Y.-C. Huang, Monolithic quasi-phase-matched nonlinear crystal for simultaneous laser *Q* switching and parametric oscillation in a Nd:YVO_4 laser, *Opt. Lett.* 30: 1045–1047 (2005).
161. Cho, K.-H., B. K. Rhee, Y. Sasaki, and H. Ito, Pulsed intracavity optical parametric oscillator with high average power based on periodically poled $LiNbO_3$, *J. Nonlinear Optical Physics and Materials* 14: 383–389 (2005).
162. Tsai, L. Y., Y. F. Chen, S.-T. Lin, Y.-Y. Lin, and Y.-C. Huang, Compact efficient passively *Q*-switched Nd:$GdVO_4$/PPLN/Cr^{4+}:YAG tunable intracavity optical parametric oscillator, *Opt. Express* 13: 9543–9547 (2005).
163. Zhang, X., B. Yao, Y. Wang, Y. Ju, and Y. Zhang, Middle-infrared intracavity periodically poled MgO:$LiNbO_3$ optical parametric oscillator, *Chinese Opt. Lett.* 5: 426–427 (2007).
164. Gorelik, P. V., F. N. C. Wong, D. Kolker, J.-J. Zondy, Cascaded optical parametric oscillation with a dual-grating periodically poled lithium niobate crystal, *Opt. Lett.* 31: 2039–2041 (2006).
165. Agnesi, A., E. Piccinini, G. C. Reali, and C. Solcia, Efficient all-solid-state tunable source based on a passively *Q*-switched high-power Nd:YAG laser, *Appl. Phys. B* 65: 303–305 (1997).

166. Karlsson, H., M. Olson, G. Arvidsson, F. Laurell, U. Bäder, A. Borsutzky, R. Wallenstein, S. Wickström, and M. Gustafsson, Nanosecond optical parametric oscillator based on large-aperture periodically poled $RbTiOAsO_4$, *Opt. Lett.* 24: 330–332 (1999).
167. Conroy, R. S., C. F. Rae, M. H. Dunn, B. D. Sinclair, and J. M. Ley, Compact, actively *Q*-switched optical parametric oscillator, *Opt. Lett.* 24: 1614–1616 (1999).
168. Baxter, G. W., P. Schlup, and I. T. McKinnie, Efficient, single frequency, high repetition rate, PPLN OPO pumped by a prelase *Q*-switched diode-pumped Nd:YAG laser, *Appl. Phys. B* 70: 301–304 (2000).
169. Elder, I. F., and J. A. C. Terry, Efficient conversion into the near- and mid-infrared using a PPLN OPO, *J. Optics A* 2: L19–L23 (2000).
170. Hansson, G., and D. D. Smith, Mid-infrared-wavelength generation in 2-μm pumped periodically poled lithium niobate, *Appl. Opt.* 37: 5743–5746 (1998).
171. Britton, P. E., D. Taverner, K. Puech, D. J. Richardson, P. G. R. Smith, G. W. Ross, and D. C. Hanna, Optical parametric oscillation in periodically poled lithium niobate driven by a diode-pumped *Q*-switched erbium fiber laser, *Opt. Lett.* 23: 582–584 (1998).
172. Britton, P. E., H. L. Offerhaus, D. J. Richardson, P. G. R. Smith, G. W. Ross, and D. C. Hanna, Parametric oscillator directly pumped by a 1.55-μm erbium-fiber laser, *Opt. Lett.* 24: 975–977 (1999).
173. Nakamura, K., T. Hatanaka, and H. Ito, High output energy quasi-phase-matched optical parametric oscillator using diffusion-bonded periodically poled and single domain LiNbO3, *Japanese J. Appl. Physics, Part 2: Letters* 40: L337–L339 (2001).
174. Zhang, B., J. Yao, H. Zhang, D. Xu, P. Wang, X. Li, and X. Ding, Angle-tuned signal-resonated optical parametric oscillator based on periodically poled lithium niobate, *Chinese Opt. Lett.* 1: 346–349 (2003).
175. Chiang, A.-C., T.-D. Wang, Y.-Y. Lin, C.-W. Lau, Y.-H. Chen, B.-C. Wong, Y.-C. Huang, J.-T. Shy, Y.-P. Lan, Y.-F. Chen, and P.-H. Tsao, Pulsed optical parametric generation, amplification, and oscillation in monolithic periodically poled lithium niobate crystals, *IEEE J. Quantum Electron.* 40: 791–799 (2004).
176. Balachninaite, O., R. Grigonis, V. Sirutkaitis, and R. C. Eckardt, A coherent spectrophotometer based on a periodically poled lithium niobate optical parametric oscillator, *Opt. Commun.* 248: 15–25 (2005).
177. Zhang, X.-B., B.-Q. Yao, Y.-L. Ju, Y.-Z. Wang, A 2.048-μm Tm,Ho:$GdVO_4$ laser pumped doubly resonant optical parametric oscillator based on periodically poled lithium $LiNbO_3$, *Chinese Phys. Lett.* 24: 1953–1954 (2007).
178. Baumgartner, R. A., and R. L. Byer, Remote SO_2 measurements at 4 μm with a continuously tunable source, *Opt. Lett.* 2: 163–165 (1978).
179. Baumgartner, R. A., and R. L. Byer, Continuously tunable ir lidar with applications to remote measurements of SO_2 and CH_4, *Appl. Opt.* 17: 3555–3561 (1978).
180. Endemann, M., and R. L. Byer, Remote single-ended measurements of atmospheric temperature and humidity at 1.77 μm using a continuously tunable source, *Opt. Lett.* 5: 452–454 (1978).
181. Brassington, D. J., Differential absorption lidar measurements of atmospheric water vapor using an optical parametric oscillator source, *Appl. Opt.* 21: 4411–4416 (1982).
182. Gloster, L. A. W., I. T. McKinnie, Z. X. Jiang, T. A. King, J. M. Boon-Engering, W. E. van der Veer, and W. Hogervorst, Narrow-band β-BaB_2O_4 optical parametric oscillator in a grazing-incidence configuration, *J. Opt. Soc. Am. B* 12: 2117–2121 (1995).
183. Boon-Engering, J. M., L. A. W. Gloster, W. E. van der Veer, I. T. McKinnie, T. A. King, and W. Hogervorst, Highly efficient single-longitudinal-mode β-BaB_2O_4 optical parametric oscillator with a new cavity design, *Opt. Lett.* 20: 2087–2089 (1995).

184. Huisken, F., M. Kaloudis, J. Marquez, Y. L. Chuzavkov, S. N. Orlov, Y. N. Polivanov, and V. V. Smirnov, Single-mode $KTiOPO_4$ optical parametric oscillator, *Opt. Lett.* 20: 2306–2308 (1995).
185. Schlup, P., S. D. Butterworth, and I. T. McKinnie, Efficient single-frequency pulsed periodically poled lithium niobate optical parametric oscillator, *Opt. Commun.* 154: 191–195 (1998).
186. Schlup, P., I. T. McKinnie, and S. D. Butterworth, Single-mode, singly resonant, pulsed periodically poled lithium niobate optical parametric oscillator, *Appl. Opt.* 38: 7398–7401 (1999).
187. Yang, S. T., and S. P. Velsko, Frequency-agile kilohertz repetition-rate optical parametric oscillator based on periodically poled lithium niobate, *Opt. Lett.* 24: 133–135 (1999).
188. Yu, C.-S., and A. H. Kung, Grazing-incidence periodically poled $LiNbO_3$ optical parametric oscillator, *J. Opt. Soc. Am. B* 16: 2233–2238 (1999).
189. Liang, G.-C., H.-H. Liu, A. H. Kung, A. Mohacsi, A. Miklos, and P. Hess, Photoacoustic trace detection of methane using compact solid-state lasers, *J. Phys. Chem. A* 104: 10179–10183 (2000).
190. Miklos, A., C.-H. Lim, W.-W. Hsiang, G.-C. Liang, A. H. Kung, A. Schmohl, and P. Hess, Photoacoustic measurement of methane concentrations with a compact pulsed optical parametric oscillator, *Appl. Opt.* 41: 2985–2993 (2002).
191. Chiang, A. C., Y. Y. Lin, T. D. Wang, Y. C. Huang, and J. T. Shy, Distributed-feedback optical parametric oscillation by use of a photorefractive grating in periodically poled lithium niobate, *Opt. Lett.* 27: 1815–1817 (2002).
192. Haidar, S., Y. Sasaki, E. Niwa, K. Masumoto, and H. Ito, Electro-optic tuning of a periodically poled $LiNbO_3$ optical parametric oscillator and mixing its output waves to generate mid-IR tunable from 9.4 to 10.5 μm, *Opt. Commun.* 229: 325–330 (2004).
193. Scherer, J. J., D. Voelkel, D. J. Rakestraw, J. B. Paul, C. P. Collier, R. J. Saykally, and A. O'Keefe, Infrared cavity ringdown laser absorption spectroscopy (IR-CRLAS), *Chem. Phys. Lett.* 245: 273–280 (1995).
194. Scherer, J. J., D. Voelkel, and D. J. Rakestraw, Infrared cavity ringdown laser absorption spectroscopy (IR-CRLAS) in low pressure flames, *Appl. Phys. B* 64: 699–705 (1997).
195. Busch, K. W., and M. A. Busch (Eds.), *Cavity-Ringdown Spectroscopy: An Ultratrace-Absorption Measurement Technique*, Vol. 720 of ACS Symposium Series, American Chemical Society, Washington, D.C., 1999.
196. Berden, G., R. Peeters, and G. Meijer, Cavity ring-down spectroscopy: experimental schemes and application, *Int. Rev. Phys. Chem.* 19: 565–607 (2000).
197. Richman, B. A., K. W. Aniolek, T. J. Kulp, and S. E. Bisson, Continuously tunable, single-longitudinal-mode, pulsed mid-infrared optical parametric oscillator based on periodically poled lithium niobate, *J. Opt. Soc. Am. B* 17: 1233–1239 (2000).
198. Raffy, J., T. Debuisschert, and J.-P. Pocholle, Widely tunable optical parametric oscillator with electrical wavelength control, *Opt. Lett.* 22: 1589–1591 (1997).
199. Ganikhanov, F., T. Caughey, and K. L. Vodopyanov, Narrow-linewidth middle-infrared $ZnGeP_2$ optical parametric oscillator, *J. Opt. Soc. Am. B* 18: 818–822 (2001).
200. Aniolek, K. W., P. E. Powers, T. J. Kulp, B. A. Richman, and S. E. Bisson, Cavity ringdown laser absorption spectroscopy with a 1 kHz mid-infrared periodically poled lithium niobate optical parametric generator/optical parametric amplifier, *Chem. Phys. Lett.* 302: 555–562 (1999).
201. Aniolek, K. W., R. L. Schmitt, T. J. Kulp, B. A. Richman, S. E. Bisson, and P. E. Powers, Microlaser-pumped periodically poled lithium niobate optical parametric generator-optical parametric amplifier, *Opt. Lett.* 25: 557–559 (2000).

202. Wu, S., V. A. Kapinus, and G. A. Blake, A nanosecond optical parametric generator/amplifier seeded by an external cavity diode laser, *Opt. Commun.* 159: 74–79 (1999).
203. Bjorkholm, J. E., and H. G. Danielmeyer, Frequency control of a pulsed optical parametric oscillator by radiation injection, *Appl. Phys. Lett.* 15: 171–173 (1969).
204. Kreuzer, L. B., Single mode oscillation of a pulsed singly resonant optical parametric oscillator, *Appl. Phys. Lett.* 15: 263–265 (1969).
205. Cassedy, E. S., and M. Jain, A theoretical study of injection tuning of optical parametric oscillators, *IEEE J. Quantum Electron.* QE-15: 1290–1301 (1979).
206. Fan, Y. X., R. C. Eckardt, R. L. Byer, J. Nolting, and R. Wallenstein, Visible BaB_2O_4 optical parametric oscillator pumped at 355 nm by a single-axial-mode pulsed source, *Appl. Phys. Lett.* 53: 2014–2016 (1988).
207. Hovde, D. C., J. H. Timmermans, G. Scoles, and K. K. Lehmann, High power injection seeded optical parametric oscillator, *Opt. Commun.* 86: 294–300 (1991).
208. Huisken, F., A. Kulcke, D. Voelkel, C. Laush, and J. M. Lisy, New infrared injection-seeded optical parametric oscillator with high energy and narrow bandwidth output, *Appl. Phys. Lett.* 62: 805–807 (1993).
209. Fix, A., R. Feldbausch, M. Inguscio, G. M. Tino, and R. Wallenstein, Injection-seeded single longitudinal mode optical parametric oscillator of beta-barium-borate, in *International Conference on Quantum Electronics Technical Digest Series*, *1992*, Optical Society of America, Washington, DC, 1992, Vol. 9, pp. 528–529.
210. Fix, A., R. Feldbausch, and R. Wallenstein, Tuning, output, and spectral characteristics of seeded and unseeded Nd:YAG laser-pumped optical parametric oscillators of beta-barium-borate, in *Conference on Lasers and Electro-Optics*, *1993*, Optical Society of America, Washington, DC, 1993, Vol. 11, pp. 244–246.
211. Milton, M. J. T., T. D. Gardiner, G. Chourdakis, and P. T. Woods, Injection seeding of an infrared optical parametric oscillator with a tunable diode laser, *Opt. Lett.* 19: 281–283 (1994).
212. Raymond, T. D., W. J. Alford, A. V. Smith, and M. S. Bowers, Frequency shifts in injection-seeded optical parametric oscillators with phase mismatch, *Opt. Lett.* 19: 1520–1522 (1994).
213. Smith, A. V., W. J. Alford, T. D. Raymond, and M. S. Bowers, Comparison of a numerical model with measured performance of a seeded, nanosecond KTP optical parametric oscillator, *J. Opt. Soc. Am. B* 12: 2253–2267 (1995).
214. Boon-Engering, J. M., W. E. van der Veer, J. W. Gerritsen, and W. Hogervorst, Bandwidth studies of an injection-seeded β-barium borate optical parametric oscillator, *Opt. Lett.* 20: 380–382 (1995).
215. Bourdon, P., M. Péalat, and V. I. Fabelinsky, Continuous-wave diode-laser injection-seeded β-barium borate optical parametric oscillator: a reliable source for spectroscopic studies, *Opt. Lett.* 20: 474–476 (1995).
216. Fröchtenicht, R., M. Kaloudis, M. Koch, and F. Huisken, Vibrational spectroscopy of small water complexes embedded in large liquid helium clusters, *J. Chem. Phys.* 105: 6128–6140 (1996).
217. Srinivasan, N., T. Kimura, H. Kiriyama, M. Yamanaka, Y. Izawa, S. Nakai, and C. Yamanaka, Bandwidth narrowing of an all-solid-state optical parametric oscillator amplifier system, *Jpn. J. Appl. Phys.* 35: 3457–3458 (1996).
218. Fix, A., and R. Wallenstein, Spectral properties of pulsed nanosecond optical parametric oscillators: experimental investigation and numerical analysis, *J. Opt. Soc. Am. B* 13: 2484–2497 (1996).
219. Plusquellic, D. F., O. Votava, and D. J. Nesbitt, Absolute frequency stabilization of an injection-seeded optical parametric oscillator, *Appl. Opt.* 35: 1464–1472 (1996).

220. Votava, O. J., R. Fair, D. F. Plusquellic, E. Riedle, and D. J. Nesbitt, High-resolution vibrational overtone studies of HOD and H_2O with single-mode, injection-seeded ring optical parametric oscillators, *J. Chem. Phys.* 107: 8854–8865 (1997).
221. Milton, M. J. T., T. D. Gardiner, F. Molero, and J. Galech, Injection-seeded optical parametric oscillator for range-resolved DIAL measurements of atmospheric methane, *Opt. Commun.* 142: 153–160 (1997).
222. Voelkel, D., Yu. L. Chuzavkov, J. Marquez, S. N. Orlov, Yu. N. Polivanov, V. V. Smirnov, and F. Huisken, Infrared degenerate four-wave mixing and resonance-enhanced stimulated Raman scattering in molecular gases and free jets, *Appl. Phys. B* 65: 93–99 (1997).
223. Borsutzky, A., Frequency control of pulsed optical parametric oscillators, *Quantum Semiclass. Opt.* 9: 191–207 (1997).
224. Bourdon, P., and M. Péalat, Coherent anti-Stokes Raman scattering spectroscopy using an optical parametric oscillator, *Quantum Semiclass. Opt.* 9: 269–278 (1997).
225. Ehret, G., A. Fix, V. Weiss, G. Poberaj, and T. Baumert, Diode-laser-seeded optical parametric oscillator for airborne water vapor DIAL application in the upper troposphere and lower stratosphere, *Appl. Phys. B* 67: 427–431 (1998).
226. Fix, A., V. Weiss, and G. Ehret, Injection-seeded optical parametric oscillator for airborne water vapour DIAL, *Pure Appl. Opt.* 7: 837–852 (1998).
227. Fix, A., R. Feldbausch, and R. Wallenstein, Tuning, output, and spectral characteristics of seeded and unseeded Nd:YAG laser-pumped optical parametric oscillators of beta-barium-borate, in *Conference on Lasers and Electro-Optics*, *1993*, Optical Society of America, Washington, DC, 1993, Vol. 11, pp. 244–246.
228. Abdullin, U. A., G. P. Dzhotyan, Yu. E. D'yakov, B. V. Zhdanov, V. I. Pryalkin, V. B. Sobolev, and A. I. Kholodnykh, Investigation of the spectral and energy characteristics of a pulsed optical parametric oscillator operating in the regime of external signal injection, *Sov. J. Quantum Electron.* 14: 538–543 (1984).
229. Smilgevičius, V., A. Stabinis, A. Piskarskas, V. Pasiškevičius, J. Hellström, S. Wang, F. Laurell, Noncollinear optical parametric oscillator with periodically poled KTP *Opt. Commun.* 173: 365–369 (2000).
230. Russell, S. M., P. E. Powers, M. J. Missey, and K. L. Schepler, Broadband mid-infrared generation with two-dimensional quasi-phase-matched structures, *IEEE J. Quantum Electron.* 37: 877–887 (2001).
231. Fischer, B., S. Sternklar, and S. Weiss, Photorefractive oscillators, *IEEE J. Quantum Electron.* 25: 550–569 (1989).
232. Partovi, A., J. Millerd, E. M. Garmire, M. Ziari, W. H. Steier, S. B. Trivedi, and M. B. Klein, Photorefractivity at 1.5 μm in CdTe:V, *Appl. Phys. Lett.* 57: 846–848 (1990).
233. Godard, A., G. Pauliat, G. Roosen, P. Graindorge, and P. Martin, Relaxation of the alignment tolerances of a 1.55-μm extended-cavity semiconductor laser by use of an intracavity photorefractive filter, *Opt. Lett.* 26: 1955–1957 (2001).
234. Fee, M. S., K. Danzmann, and S. Chu, Optical heterodyne measurement of pulsed lasers: Toward high-precision pulsed spectroscopy, *Phys. Rev. A* 45: 4911–4924 (1992).
235. Gangopadhyay, S., N. Melikechi, and E. E. Eyler, Optical phase perturbations in nanosecond pulsed amplification and second-harmonic generation, *J. Opt. Soc. Am. B* 11: 231–241 (1994).
236. Melikechi, N., S. Gangopadhyay, and E. E. Eyler, Phase dynamics in nanosecond pulsed dye laser amplification *J. Opt. Soc. Am. B* 11: 2402–2411 (1994).
237. Smith, A. V., R. J. Gehr, and M. S. Bowers, Numerical models of broad-bandwidth nanosecond optical parametric oscillators, *J. Opt. Soc. Am. B* 16: 609–619 (1999).
238. Arisholm, G., G. Rustad, and K. Stenersen, Importance of pump-beam group velocity for backconversion in optical parametric oscillators, *J. Opt. Soc. Am. B* 18: 1882–1890 (2001).

239. Anstett, G., A. Borsutzky, and R. Wallenstein, Investigation of the spatial beam quality of pulsed ns-OPOs, *Appl. Phys. B* 76: 541–545 (2003).
240. Anstett, G., M. Nitmann, and R. Wallenstein, Experimental investigation and numerical simulation of the spatio-temporal dynamics of the light pulses in nanosecond optical parametric oscillators, *Appl. Phys. B* 79: 305–313 (2004).
241. Anstett, G., and R. Wallenstein, Experimental investigation of the spectro-temporal dynamics of the light pulses of *Q*-switched Nd:YAG lasers and nanosecond optical parametric oscillators, *Appl. Phys. B* 79: 827–836 (2004).
242. Mahnke, P., and H. H. Klingenberg, Observation and analysis of mode competition in optic parametric oscillators, *Appl. Phys. B* 78: 171–177 (2004).
243. Smith, A. V., Bandwidth and group-velocity effects in nanosecond optical parametric amplifiers and oscillators, *J. Opt. Soc. Am. B* 22: 1953–1965 (2005).
244. Mahnke, P., H. H. Klingenberg, A. Fix, and M. Wirth, Dependency of injection seeding and spectral purity of a single resonant KTP optical parametric oscillator on the phase matching condition, *Appl. Phys. B* 89: 1–7 (2007).
245. Bergeson, S. D., K. G. H. Baldwin, T. B. Lucatorto, T. J. McIlrath, C. H. Cheng, and E. E. Eyler, Doppler-free two-photon spectroscopy in the vacuum ultraviolet: helium $1\ ^1S - 2\ ^1S$ transition, *J. Opt. Soc. Am. B* 17: 1599–1606 (2000).
246. Vodopyanov, K. L., J. P. Maffetone, I. Zwieback, and W. Ruderman, $AgGaS_2$ optical parametric oscillator continuously tunable from 3.9 to 11.3 μm, *Appl. Phys. Lett.* 75: 1204–1206 (1999).
247. Svanberg, S., *Atomic and Molecular Spectroscopy*, 4th edition, Springer, New York, 2004.
248. Demtröder, W., *Laser Spectroscopy*, Springer, New York, 3rd edition, 2003.
249. Sigrist, M. W. (Ed.), *Air Monitoring by Spectroscopic Techniques*, Wiley, New York, 1994.
250. Tittel, F. K., D. Richter, and A. Fried, Mid-infrared laser applications in spectroscopy, in Ref. 5, Chap. 11, pp. 445–510 (2003).
251. Kühnemann, F., K. Schneider, A. Hecker, A. A. E. Martis, W. Urban, S. Schiller, and J. Mlynek, Photoacoustic trace gas detection using a cw single-frequency parametric oscillator, *Appl. Phys. B* 66: 741–745 (1998).
252. Bisson, S. E., K. M. Armstrong, T. J. Kulp, and M. Hartings, Broadly tunable, mode-hop-tuned cw optical parametric oscillator based on periodically poled lithium niobate, *Appl. Opt.* 40: 6049–6055 (2001).
253. van Herpen, M., S. te Lintel Hekkert, S. E. Bisson, and F. J. M. Harren, Wide single-mode tuning of a 3.0–3.8-μm, 700-mW, continuous-wave Nd:YAG-pumped optical parametric oscillator based on periodically poled lithium niobate, *Opt. Lett.* 27: 640–642 (2002).
254. van Herpen, M. M. J. W., S. Li, S. E. Bisson, S. te Lintel Hekkert, and F. J. M. Harren, Tuning and stability of a continuous-wave mid-infrared high-power single resonant optical parametric oscillator, *Appl. Phys. B* 75: 329–333 (2002).
255. van Herpen, M. M. J. W., S. Li, S. E. Bisson, and F. J. M. Harren, Photoacoustic trace gas detection of ethane using a continuously tunable, continuous-wave optical parametric oscillator based on periodically poled lithium niobate, *Appl. Phys. Lett.* 81: 1157–1159 (2002).
256. Ngai, A. K. Y., S. T. Persijn, I. D. Lindsay, A. A. Kosterev, P. Gross, C. J. Lee, S. M. Cristescu, F. K. Tittel, K.-J. Boller, and F. J. M. Harren, Continuous wave optical parametric oscillator for quartz-enhanced photoacoustic trace gas sensing, *Appl. Phys. B* 89: 123–128 (2007).
257. Petelski, T., R. S. Conroy, K. Bencheikh, J. Mlynek, and S. Schiller, All-solid-state, tunable, single-frequency source of yellow light for high-resolution spectroscopy, *Opt. Lett.* 26: 1013–1015 (2001).

258. Kovalchuk, E. V., D. Dekorsy, A. I. Lvovsky, C. Braxmeier, J. Mlynek, A. Peters, and S. Schiller, High-resolution Doppler-free molecular spectroscopy with a continuous-wave optical parametric oscillator, *Opt. Lett.* 26: 1430–1432 (2001).
259. Kulatilaka, W. D., T. N. Anderson, T. L. Bougher, and R. P. Lucht, Development of injection-seeded, pulsed optical parametric generator/oscillator systems for high-resolution spectroscopy, *Appl. Phys. B* 80: 669–680 (2005).
260. Eckbreth, A. C., *Laser Diagnostics for Combustion Temperature and Species*, Abacus, Cambridge, MA, 1988.
261. Nibler, J. W., and G. A. Pubanz, Coherent Raman spectroscopy of gases, in *Advances in Non-Linear Spectroscopy*, edited by R. J. H. Clark and R. E. Hester, Wiley, New York, 1988, pp. 1–49.
262. Greenhalgh, D. A., Quantitative CARS spectroscopy, in *Advances in Non-Linear Spectroscopy*, edited by R. J. H. Clark and R. E. Hester, Wiley, New York, 1988, pp. 193–251.
263. Harvey, A. B. (Ed.), *Chemical Applications of Nonlinear Raman Spectroscopy*, Academic Press, New York, 1981.
264. Farrow, R. L., and D. J. Rakestraw, Detection of trace molecular species using degenerate four-wave mixing, *Science* 257: 1894–1900 (1992).
265. Vander Wal, R. L., B. E. Holmes, J. B. Jeffries, P. M. Danehy, R. L. Farrow, and D. J. Rakestraw, Detection of HF using infrared degenerate four-wave mixing, *Chem. Phys. Lett.* 191: 251–258 (1990).
266. Germann, G. J., A. McIlroy, T. Dreier, R. L. Farrow, and D. J. Rakestraw, Detection of polyatomic molecules using infrared degenerate four-wave mixing, *Ber. Bunsenges. Phys. Chem.* 97: 1630–1634 (1993).
267. Germann, G. J., R. L. Farrow, and D. J. Rakestraw, Infrared degenerate four-wave mixing spectroscopy of polyatomic molecules: CH_4 and C_2H_2, *J. Opt. Soc. Am. B* 12: 25–32 (1995).
268. Weiser, P. S., D. A. Wild, and E. J. Bieske, Infrared spectra of Cl^-–$(C_2H_2)n$ ($1 \leq n \leq 9$) anion clusters: spectroscopic evidence for solvent shell closure, *J. Chem. Phys.* 110: 9443–9449 (1999).
269. Wild, D. A., P. J. Milley, Z. M. Loh, P. S. Weiser, and E. J. Bieske, Infrared spectra of Br^-–$(C_2H_2)n$ complexes, *Chem. Phys. Lett.* 323: 49–54 (2000).
270. Wild, D. A., P. J. Milley, Z. M. Loh, P. P. Wolynec, P. S. Weiser, and E. J. Bieske, Structural and energetic properties of the Br^-–C_2H_2 anion complex from rotationally resolved mid-infrared spectra and *ab initio* calculations, *J. Chem. Phys.* 113: 1075–1089 (2000).
271. Weiser, P. S., D. A. Wild, and E. J. Bieske, Infrared spectra of I^-–$(C_2H_2)_n$ ($1 \leq n \leq 4$) anion complexes, *Chem. Phys. Lett.* 299: 303–308 (1999).
272. Bieske, E. J., Infrared investigations of negatively charged complexes and clusters, *Int. Rev. Phys. Chem.* 22: 129–151 (2003).
273. Fair, J. R., O. J. Votava, and D. J. Nesbitt, OH stretch overtone spectroscopy and transition dipole alignment of HOD, *J. Chem. Phys.* 108: 72–80 (1998).
274. Votava, O., D. F. Plusquellic, T. L. Myers, and D. J. Nesbitt, Bond-breaking in quantum state selected clusters: inelastic and nonadiabatic intracluster Ar–$H_2O \rightarrow$ Ar + H (^2S) + OH ($^2\Pi_{1/2,3/2}^{\pm}$; *N*), *J. Chem. Phys.* 112: 7449–7460 (2000).
275. Fitzpatrick, J. A. J., O. V. Chekhlov, J. M. F. Elks, C. M. Western, and S. H. Ashworth, An injection seeded narrow bandwidth pulsed optical parametric oscillator and its application to the investigation of hyperfine structure in the PF radical, *J. Chem. Phys.* 115: 6920–6930 (2001).
276. Chekhlov, O. V., J. A. J. Fitzpatrick, K. N. Rosser, C. M. Western, and S. H. Ashworth, An all solid-state narrow bandwidth optical parametric oscillator and its applications to the high resolution spectroscopy of free radicals, *J. Mod. Opt.* 49: 865–876 (2002).

277. Fitzpatrick, J. A. J., O. V. Chekhlov, C. M. Western, and S. H. Ashworth, Sub-Doppler spectroscopy of the PH radical: hyperfine structure in the A $^3\Pi$ state, *J. Chem. Phys.* 118: 4539–4545 (2003).
278. Orr, B. J., Spectroscopy and energetics of the acetylene molecule: dynamical complexity alongside structural simplicity, *Int. Rev. Phys. Chem.* 25: 655–718 (2006).
279. Payne, M. A., A. P. Milce, M. J. Frost, and B. J. Orr, Symmetry-breaking collisional energy transfer in the $4\nu_{CH}$ rovibrational manifold of acetylene: spectroscopic evidence of a quasi-continuum of background states, *Chem. Phys. Lett.* 324: 48–56 (2000).
280. Payne, M. A., A. P. Milce, M. J. Frost, and B. J. Orr, Rovibrational energy transfer in the $4\nu_{CH}$ manifold of acetylene viewed by IR-UV double resonance spectroscopy. 4. Collision-induced quasi-continuous background effects, *J. Phys. Chem. A* 110: 3307–3319 (2006).
281. Hinkley, E. D. (Ed.), *Laser Monitoring of the Atmosphere*, Springer, New York, 1976.
282. Grant, W. B., and R. T. Menzies, A Survey of Laser and Selected Optical Systems for Remote Measurement of Pollutant Gas Concentrations, *J. Air Pollut. Control Assoc.* 33: 187–194 (1983).
283. Killinger, D. K., and A. Mooradian (Eds.), *Optical and Laser Remote Sensing*, Springer, New York, 1983.
284. Killinger, D. K., and N. Menyuk, Laser Remote Sensing of the Atmosphere, *Science*, 235: 37–45 (1987).
285. Grant, W. B., Laser Remote Sensing Techniques, in *Laser Spectroscopy and Its Applications*, edited by L. J. Radziemski, R. W. Solarz, and J. A. Paisner, Marcel Dekker, New York, Chap. 8, 565–621 (1987).
286. Sigrist, M. W., Introduction to environmental sensing, in Ref. 249, Chap. 1, pp. 1–26 (1994).
287. Platt, U., Differential Optical Absorption Spectroscopy (DOAS), in Ref. 249, Chap. 2, pp. 27–84 (1994).
288. Svanberg, S., Differential Absorption LIDAR (DIAL), in Ref. 249, Chap. 3, pp. 85–161 (1994).
289. Grant, W. B., LIDAR for atmospheric and hydrospheric studies, in Ref. 1, Chap. 7, pp. 213–305 (1995).
290. Grant, W. B., E. V. Browell, R. T. Menzies, K. Sassen, and C.-Y. She (Eds.), *Selected Papers on Laser Applications in Remote Sensing*, SPIE Optical Engineering Press, Bellingham, WA, 1997, MS141.
291. Grant, W. B., *LIDAR Bibliography*, Optics Journal, Optical Society of America, Washington, DC, 2006, at http://www.opticsjournal.com/lidarbibliography.htm.
292. Ehret, G., C. Kiemle, W. Renger, and G. Simmet, Airborne remote sensing of tropospheric water vapor with a near-infrared differential absorption lidar system, *Appl. Opt.* 32: 4534–4551 (1993).
293. Poberaj, G., A. Fix, A. Assion, M. Wirth, C. Kiemle, and G. Ehret, Airborne all-solid-state DIAL for water vapor measurements in the tropopause region: system description and assessment of accuracy, *Appl. Phys. B* 75: 165–172 (2002).
294. Klingenberg, H. H., and P. Mahnke, Wavelength switching in the acceptance bandwidth of a dual injection seeded optical parametric oscillator, *Proc. SPIE* 5481 (Wavefront Transformation and Laser Beam Control): 108–114 (2004).
295. Henderson, S. W., T. J. Carrig, P. Gatt, D. D. Smith, and C. P. Hale, Tunable single-frequency near-IR lasers for DIAL applications, *Proc. SPIE* 4153 (Lidar Remote Sensing for Industry and Environment Monitoring): 443–454 (2001).
296. Fix, A., M. Wirth, A. Meister, G. Ehret, M. Pesch, and D. Weidauer, Tunable ultraviolet optical parametric oscillator for differential absorption lidar measurements of tropospheric ozone, *Appl. Phys. B* 75: 153–163 (2002).

297. Armstrong, D. J., and A.V. Smith, All solid-state high-efficiency source for satellite-based UV ozone DIAL, *Proc. SPIE* 5653 (Lidar Remote Sensing for Environmental Monitoring V): 1–15 (2005).
298. Armstrong, D. J., and A.V. Smith, Efficient all-solid-state UV lidar sources: from 100s of millijoules to 100s of microjoules, *Proc. SPIE* 5887 (Lidar Remote Sensing for Environmental Monitoring VI): 588703/1–588703/8 (2005).
299. Armstrong, D. J., and A.V. Smith, All solid-state high-efficiency tunable UV source for airborne or satellite-based ozone DIAL systems, *IEEE J. Sel. Top. Quantum Electron.* 13: 721–731 (2007).
300. Weibring, P., J. N. Smith, H. Edner, and S. Svanberg, Development and testing of a frequency-agile optical parametric oscillator for differential absorption lidar, *Rev. Sci. Instrum.* 74: 4478–4484 (2003).
301. Weibring, P., H. Edner, and S. Svanberg, Versatile mobile lidar system for environmental monitoring, *Appl. Opt.* 42: 3583–3594 (2003).
302. Zayhowski, J. J., and A. L. Wilson, Miniature eye-safe laser system for high-resolution three-dimensional lidar, *Appl. Opt.* 46: 5951–5956 (2007).
303. Zayhowski, J. J., Periodically poled lithium niobate optical parametric amplifiers pumped by high-power passively Q-switched microchip lasers, *Opt. Lett.* 22: 169–171 (1997).
304. Jeys, T. H., Multipass optical parametric amplifier, *Opt. Lett.* 21: 1229–1231 (1996).
305. Elstner, E. F., and J. R. Konze, Effects of point freezing on ethylene and ethane production by sugar beet leaf disks, *Nature* 263: 351–352 (1976).
306. Knutson, M. D., G. J. Handelman, and F. E. Viteri, Methods for measuring ethane and pentane in expired air from rats and humans, *Free Radical Biology & Medicine* 28: 514–519 (2000).
307. Kühnemann, F., Photoacoustic trace gas detection in plant biology, in *Laser in Environmental and Life Science*, edited by P. Hering, J. P. Lay, and S. Stry, Springer, Heidelberg-Berlin, 2003, Chap. 16.
308. Kosterev, A. A., F. K. Tittel, D. V. Serebryakov, A. L. Malinovsky, and I. V. Morozov, Applications of quartz tuning forks in spectroscopic gas sensing, *Rev. Sci. Instrum.* 76: 043105/1–043105/9 (2005).
309. Todd, M. W., R. A. Provencal, T. G. Owano, B. A. Paldus, A. Kachanov, K. L. Vodopyanov, M. Hunter, S. L. Coy, J. I. Steinfeld, and J. T. Arnold, Application of mid-infrared cavity-ringdown spectroscopy to trace explosives detection using a broadly tunable (6–8 μm) optical parametric oscillator, *Appl. Phys. B* 75: 367–376 (2002).
310. Brüggemann, D., J. Hertzberg, B. Wies, Y. Waschke, R. Noll, K.-F. Knoche, and G. Herziger, Test of an optical parametric oscillator (OPO) as a compact and fast tunable Stokes source in coherent anti-Stokes Raman spectroscopy (CARS), *Appl. Phys. B* 55: 378–380 (1992).
311. Hertzberg, J., D. Brüggemann, and B. Wies, Optical parametric oscillator (OPO) – compact and fast tunable Stokes source in CARS spectroscopy, in *Coherent Raman Spectroscopy: Applications and New Developments*, edited by E. M. Castellucci, R. Righini, and P. Foggi, World Scientific, Singapore, 1993, pp. 15–20.
312. Tiihonen, M., V. Pasiškevičius, and F. Laurell, Tailored UV-laser source for fluorescence spectroscopy of biomolecules, *Optics and Lasers in Engineering* 45: 444–449 (2007).
313. Cheng, J.-X., and X. S. Xie, Coherent anti-Stokes Raman scattering microscopy: instrumentation, theory, and applications, *J. Phys. Chem. B* 108: 827–840 (2004).
314. Potma, E. O., and X. S. Xie, CARS microscopy for biology and medicine, *Optics & Photonics News* 14 (11): 40–45 (November 2004).
315. Volkmer, A., Vibrational imaging and microspectroscopies based on coherent anti-Stokes Raman scattering microscopy, *J. Phys. D: Appl. Phys.* 38: R59–R81 (2005).

316. Evans, C. L., E. O. Potma, M. Puoris'haag, D. Côté, C. P. Lin, and X. S. Xie, Chemical imaging of tissue *in vivo* with video-rate coherent anti-Stokes Raman scattering microscopy, *Proc. Natl. Acad. Sci. (USA)* 102: 16807–16812 (2005).
317. Cheng, J.-X., Coherent anti-Stokes Raman scattering microscopy, *Appl. Spectrosc.* 61: 197A–208A (2007).
318. Müller, M., and A. Zumbusch, Coherent anti-Stokes Raman scattering microscopy, *ChemPhysChem* 8: 2156–2170 (2007).
319. Wurpel, G. W. H., H. A. Rinia, and M. Müller, Imaging orientational order and lipid density in multilamellar vesicles with multiplex CARS microscopy, *J. Microsc.* 218: 37–45 (2005).
320. Li, L., H. Wang, and J.-X. Cheng, Quantitative coherent anti-Stokes Raman scattering imaging of lipid distribution in co-existing domains, *Biophys. J.* 89: 3480–3490 (2005).
321. Légaré, F., C. L. Evans, F. Ganikhanov, and X. S. Xie, Towards CARS endoscopy, *Opt. Express* 14: 4427–4432 (2006).
322. Yakovlev, V. V., Advanced instrumentation for non-linear Raman microscopy, *J. Raman Spectrosc.* 34: 957–964 (2003).
323. Kee, T. W., and M. T. Cicerone, Simple approach to one-laser, broadband coherent anti-Stokes Raman scattering microscopy, *Opt. Lett.* 29: 2701–2703 (2004).
324. Petrov, G. I., and V. V. Yakovlev, Enhancing red-shifted white-light continuum generation in optical fibers for applications in nonlinear Raman microscopy, *Opt. Express* 13: 1299–1306 (2005).
325. Kee, T. W., H. Zhao, and M. T. Cicerone, One-laser interferometric broadband coherent anti-Stokes Raman scattering, *Opt. Express* 14: 3631–3640 (2006).
326. Greve, M., B. Bodermann. H. R. Telle, P. Baum, and E. Riedle, High-contrast chemical imaging with gated heterodyne coherent anti-Stokes Raman scattering microscopy, *Appl. Phys. B* 81: 875–879 (2005).
327. Andresen, E. R., C. K. Nielsen, J. Thøgersen, and S. R. Keiding, Fiber laser-based light source for coherent anti-Stokes Raman scattering microspectroscopy, *Opt. Express* 15: 4848–4856 (2007).
328. Fu, Y., H. Wang, R. Shi, and J.-X. Cheng, Characterization of photodamage in coherent anti-Stokes Raman scattering microscopy, *Opt. Express* 14: 3942–3951 (2006).
329. Heinrich, C., S. Bernet, and M. Ritsch-Marte, Wide-field coherent anti-Stokes Raman scattering microscopy, *Appl. Phys. Lett.* 84: 816–818 (2004).
330. Heinrich, C., C. Meusburger, S. Bernet, and M. Ritsch-Marte, CARS microscopy in a wide-field geometry with nanosecond pulses, *J. Raman Spectrosc.* 37: 675–679 (2006).
331. Toytman, I., K. Cohn, T. Smith, D. Simanovskii, and D. Palanker, Wide-field coherent anti-Stokes Raman scattering microscopy with non-phase-matching illumination, *Opt. Lett.* 32: 2701–2703 (2007).
332. Wang, H., T. B. Huff, and J.-X. Cheng, Coherent anti-Stokes Raman scattering imaging with photonic crystal fiber delivered laser source, *Opt. Lett.* 31: 1417–1419 (2006).
333. Dudovich, N., D. Oron, and Y. Silberberg, Single-pulse coherently controlled nonlinear Raman spectroscopy and microscopy, *Nature* 418: 512–514 (2002).
334. Oron, D., N. Dudovich, and Y. Silberberg, Femtosecond phase-and-polarization control for background-free coherent anti-Stokes Raman spectroscopy, *Phys. Rev. Lett.* 90: 213902/1–213902/4 (2003).
335. Oron, D., N. Dudovich, and Y. Silberberg, Single-pulse phase-contrast nonlinear Raman spectroscopy, *Phys. Rev. Lett.* 89: 273001/1–273001/4 (2002).
336. Potma, E. O., C. L. Evans, and X. S. Xie, Heterodyne coherent anti-Stokes Raman scattering (CARS) imaging, *Opt Lett.* 31: 241–243 (2006).
337. Volkmer, A., L. D. Book, and X. S.Xie, Time-resolved coherent anti-Stokes Raman scattering microscopy: Imaging based on Raman free induction decay, *Appl. Phys. Lett.* 80: 1505–1507 (2002).

338. Knutsen, K. P., J. C. Johnson, A. E. Miller, P. B. Petersen, and R. J. Saykally, High spectral resolution multiplex CARS spectroscopy using chirped pulses, *Chem. Phys. Lett.* 387: 436–441 (2004).
339. Lim, S.-H., A. G. Caster, and S. R. Leone, Single-pulse phase-control interferometric coherent anti-Stokes Raman scattering spectroscopy, *Phys. Rev. A* 72: 041803/1–041803/4 (2005).
340. Knutsen, K. P., B. M. Messer, R. M. Onorato, and R. J. Saykally, Chirped coherent anti-Stokes Raman scattering for high spectral resolution spectroscopy and chemically selective imaging, *J. Phys. Chem. B* 110: 5854–5864 (2006).
341. Lim, S.-H., A. G. Caster, O. Nicolet, and S. R. Leone, Chemical imaging by single pulse interferometric coherent anti-Stokes Raman scattering microscopy, *J. Phys. Chem. B* 110: 5196–5204 (2006).
342. Lim, S.-H., A. G. Caster, and S. R. Leone, Fourier transform spectral interferometric coherent anti-Stokes Raman scattering (FTSI-CARS) spectroscopy, *Opt. Lett.* 32: 1332–1334 (2007).
343. Cheng, J.-X., A. Volkmer, L. D. Book, and X. S. Xie, An epi-detected coherent anti-Stokes Raman scattering (E-CARS) microscope with high spectral resolution and high sensitivity, *J. Phys. Chem. B* 105: 1277–1280 (2001).
344. Volkmer, A., J.-X. Cheng, and X. S. Xie, Vibrational imaging with high sensitivity via epi-detected coherent anti-Stokes Raman scattering microscopy, *Phys. Rev. Lett.* 87: 023901/1–023901/4 (2001).
345. Cheng, J.-X., L. D. Book, and X. S. Xie, Polarization coherent anti-Stokes Raman scattering microscopy, *Opt. Lett.* 26: 1341–1343 (2001).
346. Hayazawa, N, T. Ichimura, M. Hashimoto, Y. Inouye, and S. Kawata, Amplification of coherent anti-Stokes Raman scattering by a metallic nanostructure for a high resolution vibration microscopy, *J. Appl. Phys.* 95: 2676–2681 (2004).
347. Koo, T.-W., S. Chan, and A. A. Berlin, Single-molecule detection of biomolecules by surface-enhanced coherent anti-Stokes Raman scattering, *Opt. Lett.* 30: 1024–1026 (2005).
348. Ganikhanov, F., C. L. Evans, B. G. Saar, and X. S. Xie, High-sensitivity vibrational imaging with frequency modulation coherent anti-Stokes Raman scattering (FM CARS) microscopy, *Opt. Lett.* 31: 1872–1874 (2006).
349. Jurna, M., J. P. Korterik, C. Otto, and H. L. Offerhaus, Shot noise limited heterodyne detection of CARS signals, *Opt. Express* 15: 15207–15213 (2007).
350. Jurna, M., J. P. Korterik, H. L. Offerhaus, and C. Otto, Noncritical phase-matched lithium triborate optical parametric oscillator for high resolution coherent anti-Stokes Raman scattering spectroscopy and microscopy, *Appl. Phys. Lett.* 89: 251116/1–251116/3 (2006).
351. Jones, D. J., E. O. Potma, J.-X. Cheng, B. Burfeindt, Y. Pang, Yang, J. Ye, and X. S. Xie, Synchronization of two passively mode-locked, picosecond lasers within 20 fs for coherent anti-Stokes Raman scattering microscopy, *Rev. Sci. Instrum.* 73: 2843–2848 (2002).
352. Potma, E. O., D. J. Jones, J.-X. Cheng, X. S. Xie, and J. Ye, High-sensitivity coherent anti-Stokes Raman scattering microscopy with two tightly synchronized picosecond lasers, *Opt. Lett.* 27: 1168–1170 (2002).
353. Ganikhanov, F., S. Carrasco, X. S. Xie, M. Katz, W. Seitz, and D. Kopf, Broadly tunable dual-wavelength light source for coherent anti-Stokes Raman scattering microscopy, *Opt Lett.* 31: 1292–1294 (2006).
354. Robertson, A., and A. I. Ferguson, Synchronously pumped all-solid-state lithium triborate optical parametric oscillator in a ring configuration, *Opt. Lett.* 19: 117–119 (1994).

355. French, S., M. Ebrahimzadeh, and A. Miller, High-power, high-repetition-rate picosecond optical parametric oscillator tunable in the visible, *Opt. Lett.* 21: 976–978 (1996).
356. Butterworth, S. D., V. Pruneri, and D. C. Hanna, Optical parametric oscillation in periodically poled lithium niobate based on continuous-wave synchronous pumping at 1.047 μm, *Opt. Lett.* 21: 1345–1347 (1996).
357. Agnesi, A., A. Lucca, G. Reali, and A. Tomaselli, All-solid-state high-repetition-rate optical source tunable in wavelength and in pulse duration, *J. Opt. Soc. Am. B* 18: 286–290 (2001).
358. Lee, Y.-S., W. C. Hurlbut, K. L. Vodopyanov, M. M. Fejer, and V. G. Kozlov, Generation of multi-cycle intracavity terahertz-wave generation in a synchronously pumped optical parametric oscillator using quasi-phase-matched GaAs, *Appl. Phys. Lett.* 89: 181104/1–181104/3 (2006).
359. Schaar, J. E., K. L. Vodopyanov, and M. M. Fejer, Intracavity terahertz-wave generation in a synchronously pumped optical parametric oscillator using quasi-phase-matched GaAs, *Opt. Lett.* 32: 1284–1286 (2007).
360. Canalias, C., and V. Pasiškevičius, Mirrorless optical parametric oscillator, *Nature Photonics* 1: 459–462 (2007).
361. Harris, S. E., Proposed backward wave oscillation in the infrared, *Appl. Phys. Lett.* 9: 114–116 (1966).
362. Ding, Y. J., and J. B. Khurgin, Backward optical parametric oscillators and amplifiers, *IEEE J. Quantum Electron.* 32: 1574–1582 (1996).
363. Su, H., S.-C. Ruan, and Y. Guo, Generation of mid-infrared wavelengths larger than 4.0 μm in a mirrorless counterpropagating configuration, *J. Opt. Soc. Am. B* 23: 1626–1629 (2006).
364. Canalias, C., V. Pasiškevičius, R. Clemens, and F. Laurell, Submicron periodically poled flux-grown $KTiOPO_4$, *Appl. Phys. Lett.* 82: 4233–4235 (2003).
365. Canalias, C., V. Pasiškevičius, M. Fokine, and F. Laurell, Backward quasi-phase-matched second-harmonic generation in submicrometer periodically poled flux-grown $KTiOPO_4$, *Appl. Phys. Lett.* 86: 181105/1–181105/3 (2003).
366. Khurgin, J. B., Optical parametric oscillator: mirrorless magic, *Nature Photonics* 1: 446–447 (2007).
367. Jacobsson, B., C. Canalias, V. Pasiškevičius, and F. Laurell, Narrowband and tunable ring optical parametric oscillator with a volume Bragg grating, *Opt. Lett.* 32: 3278–3280 (2007).
368. Hellström, J. E., B. Jacobsson, V. Pasiškevičius, and F. Laurell, Finite beams in reflective volume Bragg gratings: theory and experiments, *IEEE J. Quantum Electron.* 44: 81–89 (2008).
369. Fitzgerald, A. J., E. Berry, N. N. Zinovev, G. C. Walker, M. A. Smith, and J. M. Chamberlain, An introduction to medical imaging with coherent terahertz frequency radiation, *Phys. Med. Biol.* 47: R67–R84 (2002).
370. Mittleman, D. (Ed.), *Sensing with Terahertz Radiatio*n, Springer, Berlin, 2003.
371. Federici, J. F., B. Schulkin, F. Huang, D. Gary, R. Barat, F Oliveira, and D. Zimdars, THz imaging and sensing for security applications – explosives, weapons and drugs, *Semicond. Sci. Technol.* 20: S266–S280 (2005).
372. Ding, Y. J., and I. B. Zotova, Coherent and tunable terahertz oscillators, generators, and amplifiers, *Nonlinear Optical Physics and Materials* 11: 75–97 (2002).
373. Kawase, K., J.-I. Shikata, and H. Ito, Narrow-linewidth tunable terahertz-wave sources using nonlinear optics, in Ref. 5, Chap. 9, pp. 397–423 (2003).
374. Kawase, K., M. Sato, T. Taniuchi, and H. Ito, Coherent tunable THz-wave generation from $LiNbO_3$ with monolithic grating coupler, *Appl. Phys. Lett.* 68: 2483–2485 (1996).

375. Kawase, K., M. Sato, K. Nakamura, T. Taniuchi, and H. Ito, Unidirectional radiation of widely tunable THz wave using a prism coupler under noncollinear phase matching condition, *Appl. Phys. Lett.* 71: 753–755 (1997).
376. Shikata, J., K. Kawase, M. Sato, K. Nakamura, T. Taniuchi, and H. Ito, Enhancement of terahertz-wave output from $LiNbO_3$ optical parametric oscillators by cryogenic cooling, *Opt. Lett.* 24: 202–204 (1999).
377. Shikata, J.-I., K. Kawase, K.-I. Karino, T. Taniuchi, and H. Ito, Tunable terahertz-wave parametric oscillators using $LiNbO_3$ and MgO:$LiNbO_3$ crystals, *IEEE Trans. Microwave Theory Tech.* 48: 653–661 (2000).
378. Kawase, K., J. Shikata, H. Minamide, K. Imai, and H. Ito, Arrayed silicon prism coupler for a THz-wave parametric oscillator, *Appl. Opt.* 40: 1423–1426 (2001).
379. Kawase, K., K. Imai, K. Kawase, and H. Ito, A frequency-agile terahertz-wave parametric oscillator, *Opt. Express* 8: 699–704 (2001).
380. Imai, K., K. Kawase, J.-I. Shikata, H. Minamide, and H. Ito, Injection-seeded terahertz-wave parametric oscillator, *Appl. Phys. Lett.* 78: 1026–1028 (2001).
381. Kawase, K., J.-I. Shikata, K. Imai, and H. Ito, Transform-limited, narrow-linewidth, THz wave parametric generator, *Appl. Phys. Lett.* 78: 2819–2821 (2001).
382. Kawase, K., H. Minamide, K. Imai, J.-I. Shikata, and H. Ito, Injection-seeded terahertz-wave parametric generator with wide tunability, *Appl. Phys. Lett.* 80: 195–197 (2002).
383. Imai, K., K. Kawase, H. Minamide, and H. Ito, Achromatically injection-seeded terahertz-wave parametric generator, *Opt. Lett.* 27: 2173–2175 (2002).
384. Edwards, T. J., D. Walsh, M. B. Spurr, C. F. Rae, M. H. Dunn, and P. G. Browne, Compact source of continuously and widely-tunable terahertz radiation, *Opt. Express* 14: 1582–1589 (2006).
385. Ding, Y. J., From backward THz difference-frequency generation to parametric oscillation, *IEEE J. Sel. Top. Quantum Electron.* 12: 352–359 (2006).
386. Russell, P. S., Photonic crystal fibers, *Science* 299: 358–362 (2003).
387. Knight, J. C., Photonic crystal fiber, *Nature* 424: 847–851 (2003).
388. Markel, V. A., and T. F. George (Eds.), *Optics of Nanostructured Materials*, Wiley, New York, 2001.
389. Iliew, R., C. Etrich, U. Peschel, and F. Lederer, Microsized optical parametric oscillator in a photonic crystal, *IEEE J. Sel. Top. Quantum Electron.* 12: 377–382 (2006).
390. Konorov, S., A. Zheltikov, and M. Scalora, Photonic-crystal fiber as a multifunctional optical sensor and sample collector, *Opt. Express* 13: 3454–3459 (2005).
391. Benabid, F., F. Couny, J. C. Knight, T. A. Birks, and P. S. Russell, Compact, stable and efficient all-fibre gas cells using hollow-core photonic crystal fibres, *Nature* 434: 488–491 (2005).
392. Kornaszewski, L. W., N. Gayraud, J. M. Stone, W. N. MacPherson, A. K. George, J. C. Knight, D. P. Hand, and D. T. Reid, Mid-infrared methane detection in a photonic bandgap fiber using a broadband optical parametric oscillator, *Opt. Express* 15: 11219–11224 (2007).
393. Tillman, K. A., R. R. J. Maier, D. T. Reid, and E. D. McNaghten, Mid-infrared absorption spectroscopy across a 14.4 THz spectral range using a broadband femtosecond optical parametric oscillator, *Appl. Phys. Lett.* 85: 3366–3368 (2004).
394. Tillman, K. A., R. R. J. Maier, D. T. Reid, and E. D. McNaghten, Mid-infrared absorption spectroscopy of methane using a broadband femtosecond optical parametric oscillator based on aperiodically poled lithium niobate, *J. Opt. A: Pure Appl. Optics* 7: S408–S414 (2005).
395. Jones, D. J., S. A. Diddams, J. K. Ranka, A. Stentz, R. S. Windeler, J. L. Hall, and S. T. Cundiff, Carrier-envelope phase control of femtosecond mode-locked lasers and direct optical frequency synthesis, *Science* 288: 635–639 (2000).

396. Holzwarth, R., T. Udem, T. W. Hänsch, J. C. Knight, W. J. Wadsworth, and P. S. Russell, Optical frequency synthesizer for precision spectroscopy, *Phys. Rev. Lett.* 85: 2264–2267 (2000).
397. Inaba, H., T. Ikegami, H. Feng-Lei, A. Onae, Y. Koga, T. R. Schibli, K. Minoshima, H. Matsumoto, S. Yamadori, O. Tohyama, and S.-I. Yamaguchi, Phase locking of a continuous-wave optical parametric oscillator to an optical frequency comb for optical frequency synthesis, *IEEE J. Quantum Electron*. 40: 929–936 (2004).

3 Solid-State Dye Lasers

A. Costela, I. García-Moreno, and R. Sastre

CONTENTS

3.1 Introduction 97
3.2 Materials 100
3.2.1 Organic Polymers 100
3.2.2 Organic-Inorganic Hybrid Materials 110
3.2.3 Silicon-Modified Organic Matrices 114
3.2.4 Polymers with Nano- and Microparticles 116
3.3 Applications 117
References 118

3.1 INTRODUCTION

From the mid-1960s, dye lasers have been attractive sources of coherent tunable visible radiation because of their unique operational flexibility [1, 2]. Dye lasers can emit both pulsed and continuous-wave forms; can be pumped with a wide variety of excitation sources; and exhibit an inherent ability to yield high-pulse energies and high-average powers. Hundreds of dyes have been demonstrated to lase measurably, covering the range from the ultraviolet to the near infrared. The introduction of wavelength-selective elements in the laser cavity allows narrow-linewidth operation and tunability, and the large gain bandwidth of these molecules makes possible the generation of ultrashort pulses. The versatile nature of these lasers has resulted in their applicability to a wide range of different fields, from basic science, such as physics, chemistry, and spectroscopy, to medicine and industry.

Organic dyes are fluorescent molecules with large molecular weights, characterized by containing extended systems of conjugated double bonds. In a dye laser, these molecules are dissolved in an organic solvent or incorporated into a solid matrix. A simplified diagram of the rather complex energy-level structure of an organic dye is shown in Figure 3.1. When pumped with visible or ultraviolet light, higher vibrational levels of the first excited electronic singlet state S_1 of the dye molecules are populated. After fast radiationless relaxation, the excited dye molecules accumulate in the lowest vibrational level of S_1, which constitutes the upper level of the laser transition. Laser emission depopulates this level into higher-lying vibrational-rotational levels of the ground electronic state S_0. Finally, nonradiative processes remove molecules from the lower level of the laser transition. Competing with the

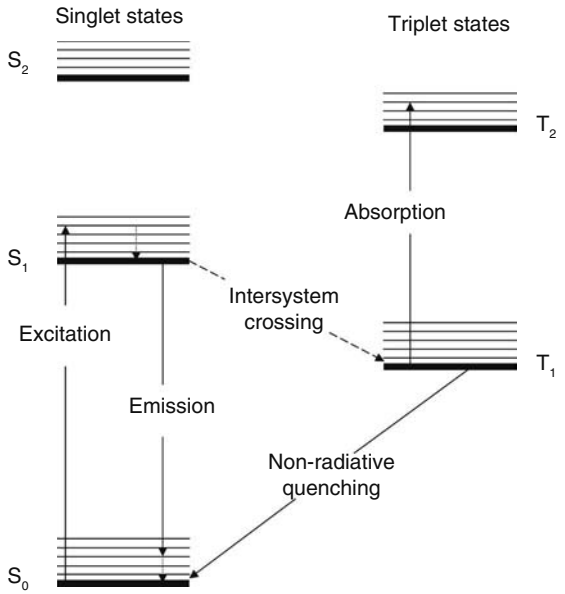

FIGURE 3.1 Schematic energy level diagram for a typical dye molecule.

radiative depopulation of S_1 are radiationless transitions into the lower triplet state T_1. This intersystem crossing process populates the lower metastable triplet state and could cause considerable losses if the triplet-triplet absorption bands overlap the lasing band, inhibiting or even halting the lasing process. The triplet losses can be reduced by adding small quantities of appropriate triplet quenchers. These losses are not very important under pulsed excitation with nanosecond pulses because the usual intersystem crossing rates are not fast enough to build up an appreciable triplet population in the nanosecond time domain.

The levels shown schematically in Figure 3.1 are spaced closely enough to form a continuum due to line-broadening mechanisms. Thus, the different fluorescent lines overlap, and absorption and fluorescence spectra consist of a broad continuum, as illustrated in Figure 3.2. Although dyes have been demonstrated to lase in the solid, liquid, or gas phase, it is in the liquid and solid phases that dyes have made a significant impact as laser media. From the early days of dye lasers, attempts were made to incorporate the dye molecules into solid hosts, and the first solid-state dye lasers were demonstrated by Soffer and McFarland in 1967 [3] and by Peterson and Snavely in 1968 [4] with pulsed laser and flashlamp pumping, respectively. Over the next decade, a variety of materials and pumping arrangements were tried for operation of dyes in the solid state, but the lasing efficiencies were low and the dye molecules experienced fast photodegradation, resulting in the laser emission fading rather quickly [5]. Thus, liquid solutions of dyes in organic solvents, where the active medium can be obtained with high optical quality and cooled by simply using a flow system, became the standard media for dye lasers. Nevertheless, this approach was never fully satisfactory because of the serious inconveniences evidenced by the liquid dye lasers, mainly the need to handle large volumes of messy and sometimes

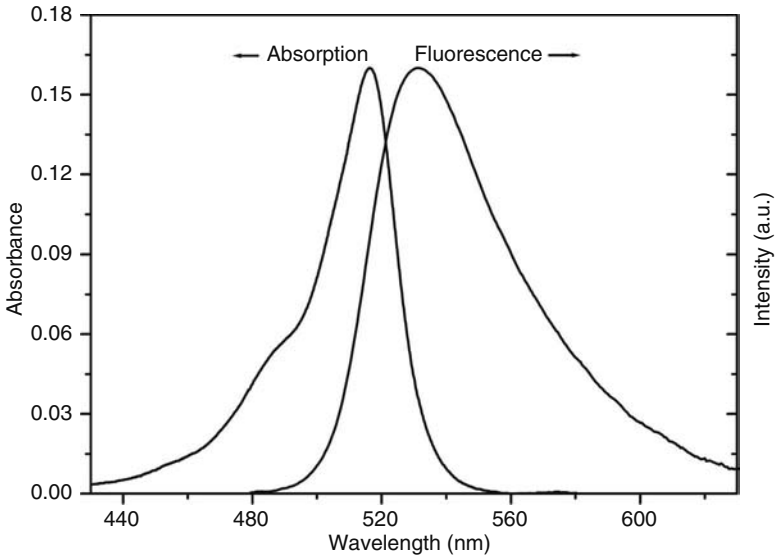

FIGURE 3.2 UV/VIS absorption and fluorescence spectra of the laser dye pyrromethene 567 in methanol solution.

toxic liquids. In addition, continuous circulation of the solution requires pumps and the design of complex and bulky cells, which, together with the large dye/solvent reservoirs, increase the size and cost of these dye laser systems and restrict their use outside the laboratory.

The problems posed by the liquid dye lasers stimulated further consideration of the solid-state dye laser approach, and in the early 1990s the development of improved host materials with higher laser damage resistance [5, 6] and the synthesis of new high-performance laser dyes [7–9], spurred a renaissance in the field of solid-state dye lasers. The 1990s witnessed a great deal of activity in the field and, as a result, significant advances were made toward the development of practical, tunable solid-state dye lasers [2, 10]. In recent years, approaches involving the use as host materials for the laser dyes of new polymeric formulations, organic-inorganic hybrid materials, polymeric media with dispersed silica nanoparticles, or silicon-modified organic matrices, are resulting in solid-state dye lasers that are fully competitive with their liquid counterparts. These promising results have been obtained with dyes emitting in the green to red spectral region. Much less work has been done with dyes emitting in the blue, and the obtained results in solid state are still far from the performance of the same dyes in liquid solution.

In this chapter we present an overview of the main recent developments of solid-state dye lasers (SSDL) and outline the state-of-the-art in the field. The focus will be in those developments that could lead to the practical implementation of SSDL in the short term. Thus, we concentrate mainly in results obtained with dyes with emission in the spectral region from the green to the red. SSDL narrow-linewidth oscillators are discussed in Chapter 4, and medical applications of dye lasers are described in Chapter 8.

3.2 MATERIALS

The basic requirements imposed on a solid matrix to be used as a host for lasing dye molecules are: high optical quality with low level of scattering, transparency at both pump and lasing wavelengths, high damage threshold to laser radiation, and good thermal and photochemical stabilities. A simple technology for doping the matrix material with different classes of organic dyes is also desirable. Thus, in the development of materials for tunable solid-state lasers problems to be addressed are: design and optimization of solid matrices with the required properties, selection or design of dyes with the desirable characteristics, and development of the appropriate fabrication technology.

Over the years a variety of materials have been tried as solid hosts for lasing dyes: from mixtures of solvents at low temperature, gelatine, or organic molecular crystals, to inorganic glasses, transparent polymers, and organic-inorganic hybrid materials [5, 10]. From work done over the last decade, it is becoming apparent that properly modified polymeric formulations and advanced hybrid materials are well-positioned candidates for developing efficient and stable solid-state dye lasers.

3.2.1 Organic Polymers

Polymers have been tried as a solid host for lasing dyes from the early days of solid-state dye lasers. These materials exhibit some features that make them very attractive in this application: good chemical compatibility with organic dyes; excellent optical homogeneity, important to avoid interference in the gain medium due to microscopic variation of the refractive index; adaptability to inexpensive fabrication techniques; and ease in modifying in a controlled way relevant characteristics, such as free volume, chemical composition, molecular weight, microstructure, or viscoelasticity. The main limitations of polymers as materials for SSDL are related to photodegradation processes, due to the low power-damage threshold of the matrix, as well as to thermal lensing effects due to the relatively high values of $\partial n/\partial T$ in these media [11].

A great part of the damage caused by laser radiation in the polymeric materials used in the early studies on SSDL, three decades ago, was due to the presence of absorbing centers in the material, such as molecular impurities and foreign absorbing inclusions. The first significant improvements in the laser-damage threshold of the organic polymers came from the generalized use of processes such as distillation, sonication, and microfiltration in the preparation of the materials. Optical uniformity of the polymer matrix, avoiding or minimizing the intrinsic anisotropy developed during polymerization, requires the strict control of the polymerization rate and the thermal conditions during the polymerization step.

There was soon enough evidence to establish that the resistance to laser damage depended on the viscoelastic properties of the matrix. This opened a new way to enhance the laser resistance of the material and led to two different approaches in the search for improved materials, which can be called external and internal plasticization. External plasticization of the polymer is achieved by adding different low-molecular-weight additives. It reduces the induced elastic limit of the polymer to below the brittle-fracture point, improving the laser resistance by several orders of magnitude [12]. The low-molecular-weight additives have certain mobility in the polymer matrix and can migrate and leach out over time, with unpredictable effects.

This problem can be overcome by using internal plasticization by copolymerization of the matrix basic compound with aliphatic acrylic comonomers [13].

By using the first approach, Maslyukov et al. [14] demonstrated, in 1995, lasing efficiencies in the range 40–60% with matrices of modified poly(methyl methacrylate) (MPMMA) doped with Rhodamine dyes and pumped longitudinally at 532 nm. The useful lifetime or normalized photostability of the samples (defined as the number of pump pulses that produce a 50% drop in the laser output) was 15,000 pulses at a pump repetition rate of 3.33 Hz. The internal plasticization approach was followed by Costela et al. who, also in 1995, demonstrated laser action with an efficiency of 21% using dye Rhodamine 6G (Rh6G) dissolved in a copolymer of 2-hydroxyethyl methacrylate (HEMA) and methyl methacrylate (MMA) under transversal pumping at 337 nm [13]. The useful lifetime of the samples was in this case 4500 pulses (20 GJ/mol in terms of total input energy per mole of dye molecule when the output energy is down to 50% of its initial value). Comparative studies on the laser performance of Rh6G incorporated either in copolymers of HEMA and MMA or in MPMMA were carried out by Giffin et al. in 1999 [15]. When longitudinally pumped, under identical experimental conditions, the MPMMA materials demonstrated higher efficiency, but the copolymer formulation exhibited superior normalized photostability (up to 240 GJ/mol).

When organic polymers are used as hosts for lasing dyes, the interesting possibility arises of covalently binding the chromophore to the main chain of the polymer. One important method of dye degradation when incorporated into polymeric matrices seems to be the thermal destruction of the dye due to poor thermal dissipation in the polymer host. When the dye is a part of the polymer chain, additional channels are open for the dissipation, along the polymer backbone, of the absorbed pump energy that is not converted into emission, with a corresponding increase in the laser photostability [16]. This effect is more important when a spacing group is introduced between the chromophore and the polymerizable double bonds incorporated into the dye molecule, so that the pendant group of the chromophore is far from the polymeric main chain, resulting in no direct interaction between the excited dye group and the macromolecule chains. Using this approach, Costela et al. demonstrated, in 1996, an increase of the useful lifetime to 12,000 pulses when the Rh6G chromophore was linked covalently to the polymeric chains [16].

At the beginning of the 1990s, the Rhodamine dyes, with emission in the yellow-red region of the spectrum, were known to give excellent laser results in liquid solution. Thus, they were an obvious first choice in any attempt to develop a dye laser in the solid state. The promising results obtained in solid state with Rhodamine dyes notwithstanding, a line of research aimed to obtain more efficient and stable laser dyes was vigorously pursued. As a result, a new class of laser dyes with reduced triplet-triplet absorption over the lasing spectral region was synthesized and characterized by Boyer and coworkers during the late 1980s and early 1990s [17]. These dyes are dipyrromethene.BF_2 (PM.BF_2) complexes (Fig. 3.3), with emission covering the spectral region from the green-yellow to the red, depending on the substituents on the chromophore. They are ionic and highly polar laser dyes, have high fluorescence quantum yields and low triplet extinction coefficients over the laser action spectral region, and exhibit good solubility in many solvents, including alcohol and MMA. These dyes have been demonstrated to lase with good performance both in liquid solution and incorporated into

solid hosts, and some of them outperform the most widely employed laser dye, Rh6G, considered in those days the benchmark in efficiency and photostability [10].

One disadvantage of the dipyrromethene dyes is the presence of amine aromatic groups in their structure (Fig. 3.3), which renders them vulnerable to photochemical reactions with oxygen and makes these dyes relatively unstable in air-saturated solutions [17]. In 1999, Ahmad and colleagues showed that this problem could be dealt with by incorporating quenchers of singlet oxygen in the liquid and solid solutions of the PM dyes [18]: When the singlet oxygen quencher 1,4-diazobicyclo [2,2,2] octane (DABCO) was present, the photostability of dye PM567 doubled, whereas the lasing efficiency remained about the same. In this way, laser conversion efficiencies in the range 60–70% were obtained for longitudinal pumping at 532 nm of PM567 dissolved in PMMA with DABCO as additive. The useful lifetime was 550,000 pulses, corresponding to a normalized photostability of 270 GJ/mol, at 2 Hz repetition rate. A substantial increase in the photostability of PM567, of up to 350 GJ/mol, was also achieved by the addition of coumarin C540A laser dye as coumarin reduces the effectiveness of *in situ* oxygen degradation of PM567 [19].

As pointed out, by the mid-1990s studies with Rhodamine dyes had demonstrated that, when the dyes were incorporated into polymer hosts, lasing efficiencies and photostability depended on the viscoelastic properties of the medium. In particular, studies carried out by our group showed that for each dye there is an optimum copolymer formulation that results in the best matrix/dye combination [10]. A next logical step was to extend our research to the new, high-performance dipyrromethene dyes and probe their lasing properties when incorporated into appropriate polymers. We began by using commercial PM dyes and, after characterizing their photophysical and lasing properties in a variety of solvents, proceeded to incorporate them into carefully chosen polymeric formulations, to gather information on the polymer parameters and structure composition, which optimized the laser operation. Next, we proceeded to synthesize new PM.BF_2 complexes and demonstrated that with appropriate chemical modifications in the pyrromethene chromophore new dyes could be obtained that outperformed the commercially available laser dyes.

In our studies, the solid samples were typically rods, 10 mm in diameter and 10 mm in length, with a cut along the axis of the cylinder defining a lateral flat surface. Pumping geometry was transversal, with the pump radiation (typically nanosecond pulses from a frequency-doubled Nd:YAG laser, 532 nm) being focused onto the lateral flat surface of the samples [19]. The dyes were incorporated into PMMA or into a variety

Dye	R
PM567	Et
PM597	*t*-Bu
PM580	*n*-Bu

FIGURE 3.3 Molecular structures of some commercial dipyrromethene.BF_2 complexes. Et: C_2H_5; Bu: $CH_3(CH_2)_3$.

of copolymers of MMA with different acrylic and methacrylic monomers (Fig. 3.4). MMA was chosen as the pivotal component in the formulations developed because the excellent optical transparency and relatively high-laser resistance of PMMA makes this material an obligatory reference in any strategy directed to improve laser performance in polymeric solid-state dye lasers.

In a first study, commercial dye PM567 was dissolved in homopolymer PMMA and copolymers of MMA with a number of linear and cross-linking acrylic and methacrylic monomers in different vol/vol proportions [20]. In this way, the polarity and rigidity of the final material was carefully controlled. It was found that an important parameter governing the lasing performance of the dye in polymeric materials is the polymer-free volume, which is controlled by the degree of cross-linking. As the degree of cross-linking in the material increases, the polymer-free volume decreases, which induces a significant reduction of the rotational and vibrational molecular freedom. As a result, nonradiative decay of excited dye molecules is prevented, leading to a significant increase of the emission quantum yield of the dye. For a certain concentration of the cross-linking monomer, the free volume available within the polymeric matrix will be completely occupied by the dye. Increasing the degree of cross-linking beyond this point will result in the dye molecules being partially excluded from the shrinking free volume, and formation of dimers and higher aggregates, with their deleterious effect on the laser operation, will be forced. Thus, for any given dye there will be an optimum degree of cross-linking that optimizes lasing performance. This effect is illustrated in Table 3.1, which lists relevant laser parameters for solid solutions of dye PM567 in homopolymer PMMA and copolymers of MMA with cross-linking monomers with three (TMPTMA, PETA) and four (PETRA) polymerizable double bonds in lateral chains attached to the same carbon atom (Fig. 3.4).

The complexity of the mechanisms involved in the laser action of dyes in solid matrix can be appreciated in the results obtained in matrices containing monomers TMPTMA and PETA. Both monomers are triple functionalized, so that when

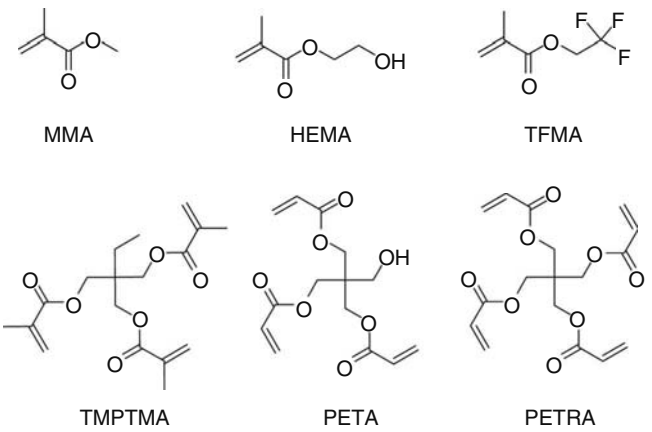

FIGURE 3.4 Molecular structures of some monomers used in solid-state dye lasers: methyl methacrylate (MMA), 2-hydroxyethyl methacrylate (HEMA), 2,2,2-trifluoroethyl methacrylate (TFMA), trimethylolpropane trimethacrylate (TMPTMA), pentaerythritol triacrylate (PETA), and pentaerythritol tetraacrylate (PETRA).

TABLE 3.1
Laser Parameters[a] for Dye PM567 Dissolved in Homopolymer PMMA and Cross-Linked Copolymers (COP)

Material	λ_{max} (nm)	$\Delta\lambda$ (nm)	Eff (%)	$I_{30,000}$ (%)[b]
PMMA	562	7	12	16
COP(MMA-TMPTMA 95:5)	564	5	19	20
COP(MMA-PETA 95:5)	568	5	21	12
COP(MMA-PETRA 95:5)	564	6	18	80

[a] λ_{max}: Peak of the laser emission; $\Delta\lambda$: FWHM of the laser emission; Eff: energy-conversion efficiency. Dye concentration: 1.5×10^{-3} M. Pump energy and repetition rate: 5.5 mJ and 10 Hz, respectively.

[b] Intensity of the laser output after n pump pulses in the same position of the sample referred to initial intensity I_0, I_n (%) = $(I_n/I_0) \times 100$.

copolymerized with MMA in the same vol/vol ratio they determine the same cross-linking degree. On the other hand, PETA is acrylic, which means an increased plasticity of the resulting polymer (that is, an increased mobility of the local segments between the cross-linking points of the resulting macromolecular net), and incorporating in its structure a hydroxyl group, which should result in a more polar polymer. As a result, the photostability of PM567 in the matrix containing PETA is lower than in the matrix containing TMPTMA.

Figure 3.5 illustrates the effect on the lasing photostability of the dye of modifying the relative proportions of monomers in a given copolymer. It should be noticed that the evolution of the laser output with the number of pump pulses shown in Figure 3.5 was

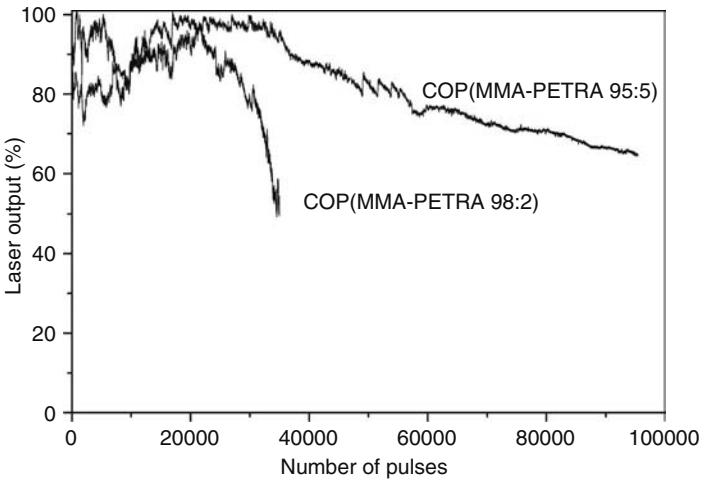

FIGURE 3.5 Normalized laser output as a function of the number of pump pulses for PM567 dissolved in copolymers of MMA and PETRA. Dye concentration: 1.5×10^{-3} M. Pumping at 532 nm with 5.5 mJ pulses at 5 Hz repetition rate. (From Costela, A., I. García-Moreno, and R. Sastre, Polymeric solid-state dye lasers: recent developments, *Phys. Chem. Chem. Phys.* 5: 4745–4763 (2003), reproduced by permission of the PCCP Owner Societies.)

obtained at a repetition rate of 5Hz, whereas the results in Table 3.1, which show faster degradation, were obtained at 10 Hz repetition rate. Thus, when the pump repetition rate increases so does the degradation rate. It seems that at a high repetition rate, the dissipation channels of the energy released to the medium as heat are not fast enough, and as a result the thermal degradation of the dye is enhanced. This interpretation was confirmed in studies on the effect of heat load on the stability of polymeric dye lasers, where the capability of each material to dissipate the heat generated in the sample as a consequence of pump energy excitation was characterized by photothermal deflection spectroscopy [21, 22]. These studies showed that the accumulation of heat into the material increases significantly for pumping repetition rates higher than 1 Hz.

Earlier studies to improve the lasing performance of the PM dyes had demonstrated that their photophysical and lasing properties depend on their molecular structure, and that adequate substituents in the molecular core can enhance laser action [23, 24]. Pursuing this approach, we studied the effect of introducing a number of substitutions at the 8 position of the PM567 molecule while maintaining the four methyl groups in the 1, 3, 5, and 7 positions and the ethyl groups in positions 2 and 6. In particular, we synthesized analogues of PM567 (Fig. 3.6) where the methyl group at position 8 was replaced by a methacryloyloxypolymethylene or an acetoxypolymethylene chain with *n* methylenes, resulting in monomeric dyes P*n*MA and their model compounds P*n*Ac, and analogues where the substituents at position 8 were *p*-(methacryloyloxypolymethylene)phenyl or *p*-(acetoxypolymethylene)phenyl groups with one or three methylene groups (dyes PAr*n*MA and PAr*n*Ac, respectively). The model dyes (P*n*Ac and PAr*n*Ac) were dissolved in different polymeric matrices, whereas the monomer dyes (P*n*MA and PAr*n*MA) were bonded covalently to the polymeric chains.

With dyes P*n*Ac and P*n*MA, lasing efficiencies of up to 40% were obtained, whereas the maximum efficiency obtained with dye PM567 in the same materials and under the same experimental conditions was 30% [25]. Table 3.2 collects some of the most relevant results obtained with these dyes incorporated into different polymeric formulations. The highest photostabilities were reached in cross-linked materials with the chromophores linked covalently to the polymer chains. In some of them, the laser output remained stable or dropped by less than 15% after 100,000 pump pulses in the same position of the sample at 10-Hz repetition rate. Figure 3.7 shows those materials

	R	n
PM567	-Me	-
PnAc	-$(CH_2)_n$OCOMe	1,3,5,10,15
PnMA	-$(CH_2)_n$OCOCMe=CH_2	1,3,5,10,15
P1ArnAc	$(CH_2)_n$OCOMe	1,3
P1ArnMA	$(CH_2)_n$OCOCMe=CH_2	1,3

FIGURE 3.6 Molecular structures of modified dipyrromethene.BF_2 complexes. Me: CH_3.

TABLE 3.2
Laser Parameters[a] for Model (P*n*Ac, PAr*n*Ac) and Monomeric (P*n*MA, PAr*n*MA) Dyes in COP and Terpolymers (TERP)

				Laser output[b]	
Material	λ_{max} **(nm)**	$\Delta\lambda$ **(nm)**	**Eff (%)**	$I_{60,000}$ **(%)**	$I_{100,000}$ **(%)**
P1Ac/COP(MMA-PETRA 95:5)	591	12	27	107	
COP(P3MA-MMA)	569	6	34	100	
TERP[P3MA-(MMA-HEMA 7:3)]	569	4	37	87	
TERP[P3MA-(MMA-TMPTMA 95:5)]	565	5	28	112	133
COP(P3MA-MMA)	568	5	36	75	
P5Ac/COP(MMA-HEMA 7:3)	565	6	39	83	
TERP[P5MA-(MMA-TFMA 7:3)]	565	9	38	80	70
TERP[P5MA-(MMA-PETA 95:5)]	562	5	23	87	
P10Ac/COP(MMA-TFMA 7:3)	561	8	40	50	
TERP[P10MA-(MMA-HEMA 7:3)]	566	5	27	80	
P10Ac/COP(MMA-PETRA 95:5)	563	10	34	87	
TERP[P10MA-(MMA-PETA 95:5)]	563	5	28	101	
COP(PAr1MA/MMA)	558	9	20		96
COP(PAr3MA/MMA)	555	9	16		96

[a] λ_{max}: Peak of the laser emission; $\Delta\lambda$: FWHM of the laser emission; Eff: energy-conversion efficiency. Dye concentration: 1.5×10^{-3} M.

[b] Intensity of the dye laser output after *n* pump pulses in the same position of the sample referred to initial intensity I_0, $I_n(\%) = (I_n/I_0) \times 100$. Pump energy and repetition rate: 5.5 mJ and 10 Hz, respectively.

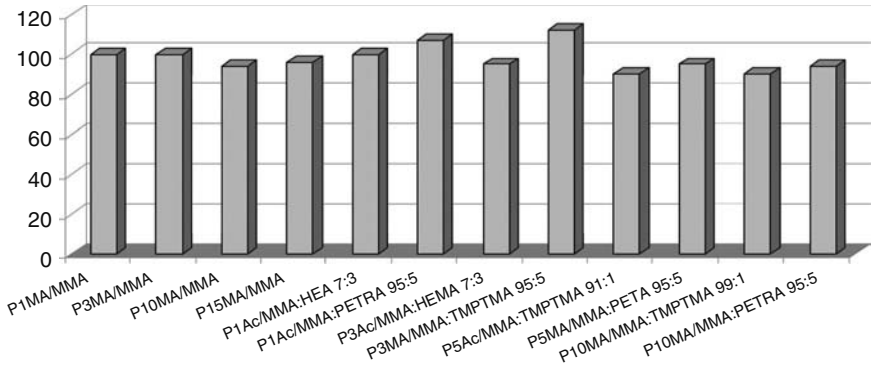

FIGURE 3.7 Percent intensity (referred to as initial intensity) of the laser output from a number of newly synthesized dipyrromethene.BF_2 dyes incorporated into linear and cross-linked copolymers of MMA, after 60,000 pump pulses at the same position of the sample. P*n*Ac/MMA-monomer: model dyes dissolved in copolymer; P*n*MA-MMA-monomer: monomer dyes linked covalently to polymeric chains, rendering terpolymers with the indicated MMA-monomer proportion. Pump energy and repetition rate: 5.5 mJ/pulse and 10 Hz, respectively.

where the laser output remained stable or decreased by less than 10% after 60,000 pump pulses. Figure 3.8 compares the evolution of the laser output with the number of pump pulses of a monomer dye linked covalently to the polymer matrix, the corresponding model dye dissolved in the same material and PM567 incorporated into homopolymer PMMA. The figure clearly shows an improvement in photostability in the covalently bonded material. We estimate for material TERP[P5MA-(MMA-PETRA 95:5)] in Figure 3.8 an accumulated absorbed pump energy per mole of dye molecule of 180 GJ/mol after 95,000 pump pulses at 10-Hz repetition rate, where the laser emission still remained at 88% of its initial value.

With dyes PAr*n*Ac and PAr*n*MA, the lasing efficiencies were lower, of the order of 20%, but the laser emission remained at the initial level after 100,000 pump pulses at 10 Hz repetition rate (Table 3.2).

Very recently, we have demonstrated that by using polymers with fluorine atoms incorporated into their structure, remarkable improvements are obtained in the lasing performance of dyes PM567 and PM597 [25]. The presence of fluorine atoms in the polymer matrix results in high thermal stability and enhanced chemical resistance compared to nonfluorinated analogues. We prepared fluorine-modified organic matrices where the total fluorine content was varied, adding to MMA different volumetric proportions of monomers with three (TFMA, Fig. 3.4), five (PFMA, as in Fig. 3.4 but with end group CF_2-CF_3), and seven (HFMA, as in Fig. 3.4 but with end group CF_2-CF_2-CF_3) fluorine atoms. Lasing efficiencies of up to 35% (PM567) and 42% (PM597) were obtained under transversal pumping. The highest photostability was recorded for PM597 dissolved in an MMA-HFMA 7:3 copolymer, with the laser output remaining at the initial level after 500,000 pump pulses in the same

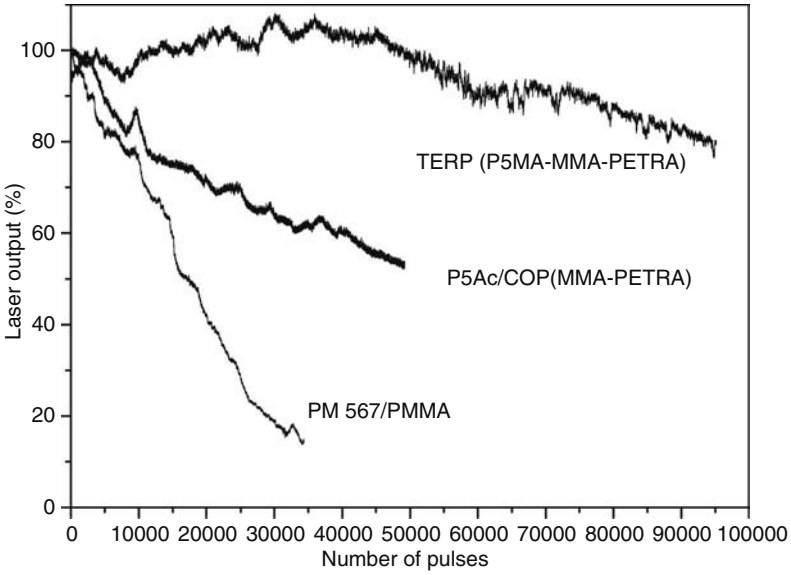

FIGURE 3.8 Evolution of the normalized laser output of monomer dye P5MA linked covalently to polymer matrix with composition MMA-PETRA 95:5, model dye P5Ac dissolved in the same matrix, and dye PM567 dissolved in PMMA.

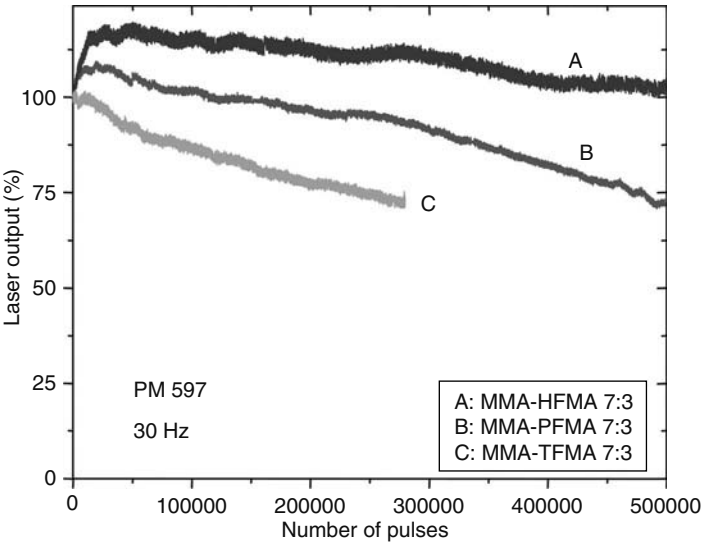

FIGURE 3.9 Evolution of the normalized laser output of PM597 in copolymers of MMA with fluorinated monomers at 30 Hz repetition rate. Dye concentration: 7×10^{-4} M. Pumping at 532 nm with 3.5 mJ pulses.

position of the sample at 30 Hz repetition rate, corresponding to an accumulated pump energy of 12,300 GJ/mol (Fig. 3.9).

Some potential important applications of solid-state dye lasers, such as photodynamic therapy or treatment of port-wine stains and other vascular anomalies, would require the laser energy to be applied in high-repetition rate pulses. Thus, we prepared solid laser samples in the form of coin-sized disks, 2 mm thick, consisting of dyes Rh6G or PM567 incorporated into polymeric matrices, and pumped them longitudinally with the green line of a copper-vapor laser at an average power of up to 800 mW and repetition rate of up to 1 kHz [26]. With PM567 dissolved in COP(MMA-PETA 95:5), 290 mW average power (37% lasing efficiency) at peak wavelength of 550 nm was obtained. The laser output decreased to 150 mW (52% of the initial power) after 30 min irradiation time at 1 kHz (1.8×10^6 shots) and to 32 mW (11% of the initial power) after 70 min operation (4.2×10^6 shots) (Fig. 3.10). Output power of up to 1 W at 6.2 kHz was obtained for short periods of time. When the pump repetition rate was increased to 10 kHz, by using as pump source a diode-pumped, Q-switched, frequency-doubled Nd:YLF laser (emission at 527 nm), the output power of Rh6G/COP(MMA-HEMA 1:1) decreased to half the initial value after about 6.6 min (or about 4.0 million shots). In the case of PM567/COP(MMA-PETRA 95:5), the output power decreased to half the initial value after about 7.8 min (Fig. 3.11) [27].

High repetition rate (16 kHz) laser emission, tunable in the wavelength range 605–635 nm, based on Rhodamine B dye incorporated into a copolymer of MMA and MAA (methacrylic acid) was demonstrated by Kytina et al. [28]. The disk-shaped polymer gain medium (94 mm diameter, thickness 20 mm) was rotated at

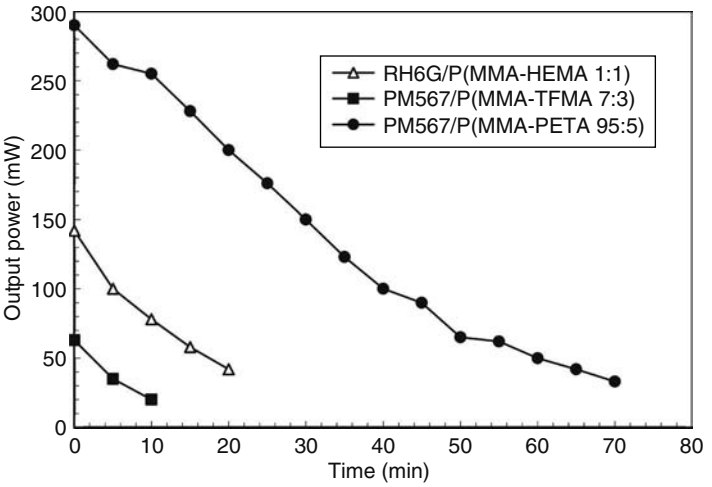

FIGURE 3.10 Evolution of the output power as a function of time of PM567 and Rh6G in different polymeric media when pumped with a copper-vapor laser at 1 kHz repetition rate. (Reprinted with permission from Costela, A., I. García-Moreno, R. Sastre, D. W. Coutts, and C. E. Webb, High-repetition-rate polymeric solid-state dye lasers pumped by a copper-vapor laser, *Appl. Phys. Lett.* 79: 452–454 (2001), Copyright 2001, American Institute of Physics.)

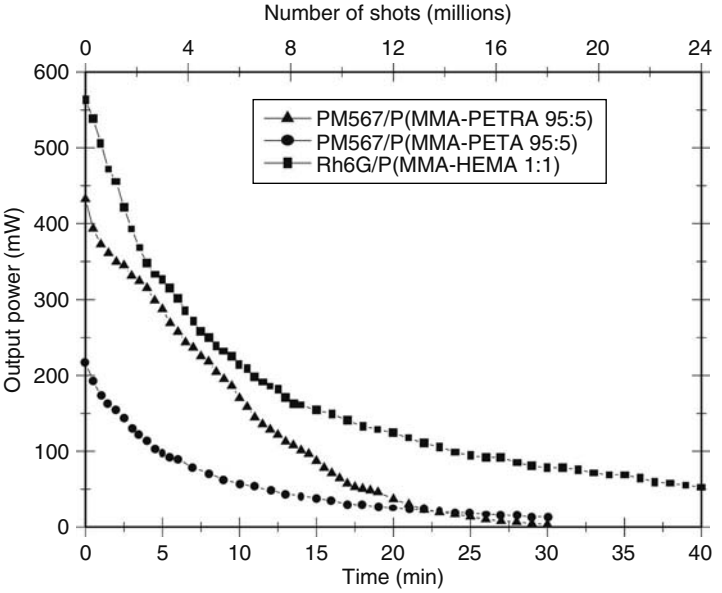

FIGURE 3.11 Evolution of the output power as a function of time of PM567 and Rh6G in different polymeric media when pumped with a Nd:YLF (second harmonic) laser at 10 kHz repetition rate. (Reprinted from Abedin, K. M., M. Álvarez, A. Costela, I. García-Moreno, O. García, R. Sastre, D. W. Coutts, and C. E. Webb, 10 kHz repetition rate solid-state dye laser pumped by diode-pumped solid-state laser, *Opt. Commun*. 218: 359–363 (2003), Copyright 2003, with permission from Elsevier.)

a frequency of 42 Hz and pumped transversely with radiation from a copper-vapor laser. Lasing efficiency of 15% (output power 1.5 W) was obtained. The laser output remained stable for 4 h, within 3% accuracy, in a cyclic operation mode with duty cycle 1/6 (1 min operation, 10 s pause). In permanently pumping mode (no pause in pumping with the copper-vapor laser), the maximum operation time (decrease of the output power of the dye laser to 70% of its initial value) was about 2 h for optimized transmission of the laser cavity output mirror.

The use of PMMA solid host incorporating pyrromethene dyes as laser amplifier has been reported [27, 28]. A 25 mm diameter, 7 mm thick sample of dye pyrromethene 650 (PM650) in PMMA rendered a single-pass gain of 500 at 616 nm [29]. Up to 62% amplifier efficiency was observed in disks (25 mm diameter, 3 mm thick) of PM567 dispersed in a modified PMMA matrix incorporating small amounts of PETRA and DABCO [30]. The photodegradation rate was found to be reduced substantially by an increase in the rate of stimulated emission, indicating an important role played by excited-state reactions in photodegradation.

Recently, a continuous-wave SSDL tunable from 565 to 615 nm has been reported [31]. The laser medium consisted of a thin film (thickness between 50 and 100 μm) of Rh6G dissolved in a photopolymer sandwiched between two DVD substrates. The resonator design was a folded cavity, derived from conventional liquid solvent dye laser geometry. The dye laser disk was rotated (50–100 Hz) and translated perpendicularly to the rotation axis (100–300 μm/s) by a combined motor-translation stage unit. Lasing threshold was 550 mW, slope efficiency 2%, and the emission was broadband. Using one disk, 30 min lasing operation was achieved before irreversible photodegradation.

3.2.2 Organic-Inorganic Hybrid Materials

Silicate-based inorganic-organic hybrid polymers are *a priori* good candidates for laser matrices since, due to their inorganic Si-O-Si backbone, they present improved thermal and mechanical properties compared with common organic polymers. These hybrid materials are prepared from organosilane precursors by sol-gel processing in combination with organic cross-linking of polymerizable monomers [32].

In one approach, the porous structure of a sol-gel inorganic matrix is filled with organic molecules by immersing the bulk in a solution containing laser dye, polymerizable monomer, and catalyst or photoinitiator. In a subsequent step, organic polymerization is started by ultraviolet irradiation or heating, and an interpenetrating polymer incorporating the laser dye is formed.

Hybrids can also be obtained from organically modified silicon alkoxides. In this method, both organic and inorganic networks are obtained in a two-step reaction. An initial inorganic network is formed by polycondensation of the silicon alkoxide. In a second step, organic polymerization is initiated, thermally or photochemically, via free radicals. The possibility of selecting different organic:inorganic ratios as well as the choice of the reaction conditions allow for materials with a wide range of properties to be obtained. The so-obtained materials are usually called ORMOCERS (organically modified ceramics) or ORMOSILS (organically modified silanes).

The first studies on laser emission from dyes incorporated into inorganic and inorganic-organic matrices prepared using sol-gel techniques were carried out in the late 1980s, and were demonstrated to be a promising approach. In 1995 Rahn and King [33] carried out a direct comparison study of laser performance of dyes Rh6G, PM567, Perylene Red, and Perylene Orange in organic, inorganic, and hybrid hosts. They found that the nonpolar perylene dyes had better performance in partially organic hosts, whereas the ionic Rhodamine and pyrromethene dyes performed best in the inorganic sol-gel glass host. The most promising combinations of dye and host for efficiency and photostability were found to be Perylene Orange in polycom glass and Rh6G in sol-gel glass. Nevertheless, lasing efficiencies and photostabilities were modest in all cases.

In 2002, Ahmad and colleagues demonstrated high efficiency and photostability for xanthene dyes in wet and dried sol-gel phases, but not for pyrromethene laser dyes [34]. In the next couple of years, lasing slope efficiencies of 79% and 60% were reported for dyes PM567 and PM597, respectively, incorporated via the sol-gel technique into ORMOSIL host matrices (PM567) [35] and hybrid xerogel matrices (PM597) [36]. These efficiencies were obtained under longitudinal pumping at 532 nm in optimized laser cavities. The useful lifetime for PM567 was 60,000 pulses, 50 GJ/mol in normalized photostability, at a pump repetition rate of 2 Hz and pump fluence of 0.1 J/cm^2, in samples of 4 mm thickness [35]. For PM597, the laser emission dropped to 50% of the initial value after 210,000 pump pulses, when pumped with 1.8 mJ pulses at 10 Hz repetition rate [36]. Under this same irradiation conditions, PM567 in xerogel matrix exhibited a slope efficiency of 80% and a useful lifetime of 180,000 pulses.

With dye Perylene Red incorporated into ORMOSIL matrices, slope efficiencies of up to 53% with normalized photostabilities of 24 GJ/mol were obtained with samples of 4 mm thickness at the pump fluence of 0.1 J/cm^2 and 2 Hz repetition rate [35]. Co-doping Perylene Red with an optimized coumarin dye concentration, the slope efficiency of Perylene Red in ORMOSIL matrix increases by a factor of 2, whereas the slope efficiency of PM567 was only marginally increased [37].

Under transversal pumping, slope efficiencies of 32% [38], 43%, and 20% [32] have been obtained for dyes PM567, PM597, and Rh6G, respectively, incorporated into ORMOSIL glass samples and placed in an optimized laser cavity consisting of a full reflector and a 50% broadband reflector as output coupler. Pumped by 1 mJ (20 mJ/cm^2) pulses, the useful lifetime of PM597 in ORMOSIL was 12,000 pulses, which increased to 22,000 pulses when the dye was incorporated into composite glass [38].

Beginning in 2002, our group carried out a detailed investigation on the laser performance of Rhodamine and pyrromethene dyes incorporated into organic-inorganic hybrid materials. For inorganic components we used tetraethoxysilane (TEOS) and tetramethoxysilane (TMOS) (Fig. 3.12) in different weight proportions. The organic part was composed of MMA or MMA-HEMA. The synthesis route of the hybrid materials was based on the *in situ* and simultaneous hydrolysis-condensation of the inorganic component during the free radical copolymerization of the organic monomers. The geometry of the samples was as previously described (10×10 mm rods with a lateral cut defining a flat surface), and pumping arrangement was transversal.

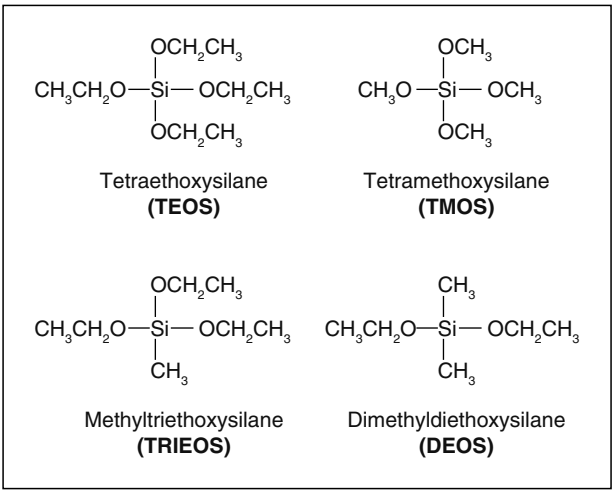

FIGURE 3.12 Molecular structure of inorganic alkoxides TEOS, TMOS, TRIEOS, and DEOS.

The lasing stability of TMOS-based hybrid matrices was significantly worse than in the materials based on TEOS, evidencing the influence of the size of the lateral substituent group of the alkoxide on the laser properties of the resulting material. When using Rh6G as gain medium, both the lasing efficiency and photostability first increase with the proportion of the inorganic component, peaking at compositions with 10–15% wt% proportions of TEOS. With pumping at 532 nm, laser efficiencies of up to 26% and laser emission with no sign of degradation, albeit with some oscillations, after 100,000 pump pulses in the same position of the sample at 10 Hz repetition rate were obtained [39]. Higher proportions of the alkoxide in the sample result in a drastic decrease in both efficiency and useful lifetime or stability of the laser emission. It is clear that the presence of the inorganic component in the matrix plays an important role in the photochemical degradation of the dye. The pump radiation leads to a fraction of the dye molecules being converted into active species (radicals, triplets) which, in turn, react with nearby dye molecules, impurities, oxygen, radicals, and groups from the polymer chains or any other active species present in the material. An increase in the proportion of the inorganic alkoxide in the material leads to an increase in the remanent acidity of the medium, which could boost these reactive processes. In addition, because the photochemical mechanism is at least bimolecular, the process can be highly dependent on the microstructure and flexibility of the polymeric chains in these materials. Thus, in order to optimize the photostability of the dye/hybrid system, a compromise must be reached between the enhancement of thermal dissipation in the material and the increase in the photochemical destruction of the dye by carefully controlling the inorganic-organic matrix composition.

When the pyrromethene dye PM567 was used as gain medium, the laser operation was optimized in matrices with 5% content of TEOS [40]. The lasing efficiency was 26% and, after an initial decrease, the laser output stabilizes and remains at 70% of its initial value after 60,000 pump pulses in the same position of the sample (Fig. 3.13).

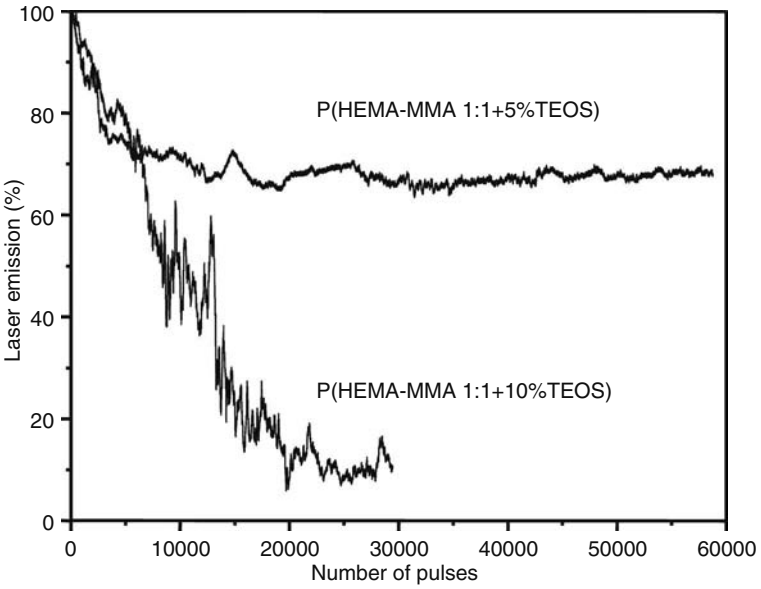

FIGURE 3.13 Normalized laser output as a function of the number of pump pulses for PM567 (1.5×10^{-3} M) in hybrid matrices. Pump energy and repetition rate: 5.5 mJ/pulse and 10 Hz, respectively. (Reprinted from Costela, A., I. García-Moreno, C. Gómez, O. García, and R. Sastre, Enhancement of laser properties of pyrromethene 567 dye incorporated into new organic-inorganic hybrid materials, *Chem. Phys. Lett.* 369: 656–661 (2003), Copyright 2003, with permission from Elsevier.)

The presence of the inorganic component in the hybrid matrices increases the rigidity and fragility of the resulting materials. A way to decrease the rigidity of the materials while maintaining, or even increasing, the proportion of the inorganic component could be decreasing the functionality of the inorganic compounds, selecting double and triple functionalized alkoxides instead of the usual tetrafunctionalized ones, TEOS and TMOS. Pursuing this idea, we prepared hybrid matrices where the inorganic compounds were trifunctional methyltriethoxysilane (TRIEOS) and difunctional dimethyldiethoxysilane (DEOS) (Fig. 3.12), and we performed a systematic study of the influence on the laser action of the composition and structure of these new hybrid matrices [41–43]. DEOS, with only two reactive positions, leads to linear chains of rapid growth inducing broad inorganic domains less miscible with the organic components, which is detrimental to the optical transparency of the samples. TRIEOS, on the other hand, results in a material with better structural and morphological uniformity, without phase separation at the nanometric scale. Laser operation with no decrease in the laser output after 100,000 pump pulses in the same position of the sample at 10 Hz repetition rate was obtained with Rh6G (in matrices with 20% TRIEOS), and PM597 (in matrices with 15% TRIEOS, Fig. 3.14).

Trying to further improve the photostability of the laser dyes when incorporated into solid hosts, we synthesized next new hybrid materials with improved

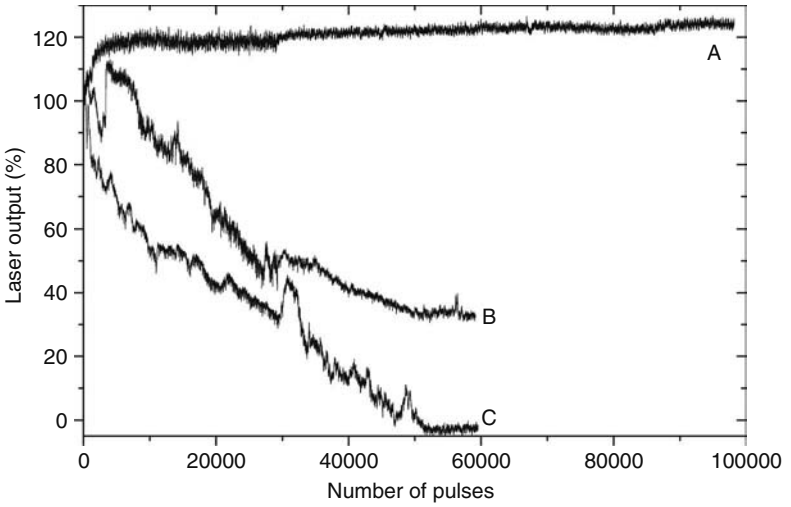

FIGURE 3.14 Normalized laser output as a function of the number of pump pulses for PM597 (6×10^{-4} M) in hybrid matrices of P(HEMA-MMA 1:1) with different wt% proportions of TRIEOS: (a) 15% and 10 Hz; (b) 15% and 30 Hz; and (c) 5% and 30 Hz. Pump energy: 5.5 mJ/pulse. Initial lasing efficiency: 23%. (Reprinted with permission from García-Moreno, I., A. Costela, A. Cuesta, O. García, D. del Agua, and R. Sastre, Synthesis, structure, and physical properties of hybrid nanocomposites for solid-state dye lasers, *J. Phys. Chem. B* 109: 21618–21626 (2005), Copyright 2005, American Chemical Society.)

thermooptical and mechanical properties based on silica aerogels. These are sponge-like glasses characterized by an extremely high porosity (80–99%) with well-accessible mesopores (20–100 nm) filled with air. The open pore structure of these materials forms an amorphous inorganic three-dimensional network of low density, which, under appropriate conditions, can be filled with adequate polymeric formulations incorporating a laser dye.

When using silica aerogels filled with fluorinated-modified polymers, lasing efficiencies of up to 37% were obtained with dye PM567 [44, 45]. Laser emission with a drop of only 10% after 10^6 pulses in the same position of the sample at 10 Hz repetition rate was demonstrated in nonfluorinated polymers, although this emission exhibited a rather irregular behavior with some strong fluctuations. In fluorinated samples, laser emission stable over 100,000 pump pulses was obtained with pumping at 10 Hz with pulses of 5.5 mJ (Fig. 3.15; compare with Fig. 3.13). Pumping with 3.5 mJ/pulse, the laser emission remained stable over 100,000 pulses at 30 Hz repetition rate.

3.2.3 Silicon-Modified Organic Matrices

In spite of the good results obtained with the hybrid materials, these compounds present their own problems such as: complex and lengthy synthesis process, fragility that makes mechanization and polishing of the final material difficult, and sometimes optical inhomogeneity caused by refractive index mismatch between organic

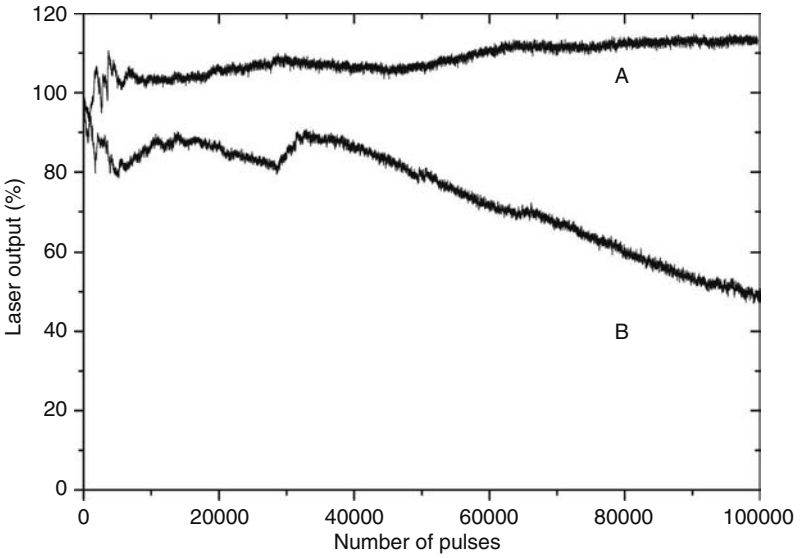

FIGURE 3.15 Normalized laser output as a function of the number of pump pulses for PM567 (1.5×10^{-3} M) incorporated into (a) silica aerogel filled with the copolymer COP(MMA:TFMA 7:3), and (b) organic matrix, without silica aerogel. Pump energy and repetition rate: 5.5 mJ/pulse and 10 Hz, respectively. (Reprinted from García, O., R. Sastre, D. del Agua, A. Costela, I. García-Moreno, and A. Roig, Efficient optical materials based on fluorinated-polymeric silica aerogels, *Chem. Phys. Lett.* 427: 375–378 (2006), Copyright 2006, with permission from Elsevier.)

and inorganic parts. A way to avoid these problems while maintaining the combined advantages of polymer and inorganic materials could be using organic compounds with silicon atoms directly incorporated into their structure. Thus, the matrix would remain organic, which means plasticity and a relatively more simple synthesis procedure, but with improved thermal properties due to the presence of the silicon atoms. Following this approach, we incorporated dyes PM567 and PM597 into copolymers of MMA or HEMA with 3-(trimethoxysilyl)propyl methacrylate (TMSPMA, Fig. 3.16) and into terpolymers of MMA, HEMA, and TMSPMA, and proceeded to study the photophysical, structural, and laser properties of these novel materials [46, 47].

Highly photostable laser operation was obtained with the silicon-modified organic matrices, with lasing efficiencies of up to 34% with PM567 and up to 42% with PM597 under transversal pumping at 532 nm in no optimized laser cavities. At 10 Hz repetition rate, formulations were found with no sign of degradation in the laser output after 100,000 pump pulses in the same position of the sample for both PM567 and PM597 dyes. This corresponds to an accumulated pump energy absorbed by the system per mole of dye molecules of 518 and 1295 GJ/mol for PM567 and PM597, respectively. When the pump repetition rate increased to 30 Hz, the dye PM567 exhibited a steady decrease in the laser output, which is rather drastic in the samples with the highest content of silicon (Fig. 3.17). Dye PM597 was

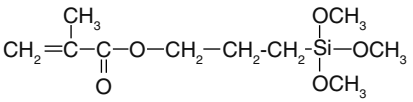

TMSPMA

FIGURE 3.16 Molecular structure of monomer 3-TMSPMA.

much more stable, and in all but one of the formulations the laser emission remained stable after 100,000 pump pulses at 30 Hz repetition rate (Fig. 3.17; compare with Fig. 3.14b and c), corresponding to an accumulated pump energy of 2472 GJ/mol. In two selected matrices, COP(MMA:TMSPMA 1:1) and COP(HEMA:TMSPMA 1:1), the laser emission of the dye PM597 remained stable after 700,000 pump pulses in the same position of the sample at 30 Hz repetition rate (Fig. 3.18), corresponding to an accumulated pump energy absorbed per mole of dye molecules of 17,300 GJ/mol.

3.2.4 Polymers with Nano- and Microparticles

Recently, Duarte and James [48, 49] demonstrated a class of dye-doped, organic-inorganic, solid-state gain media that exhibits lower $|\partial n/\partial T|$ values and improved optical homogeneity than previous composite gain media. The solid matrix consisted of silica nanoparticles uniformly dispersed in PMMA. Using Rh6G as laser dye and a longitudinal pumping scheme, laser conversion efficiencies of 63% were obtained. The laser beam exhibited near-TEM_{00} profile with a beam divergence of

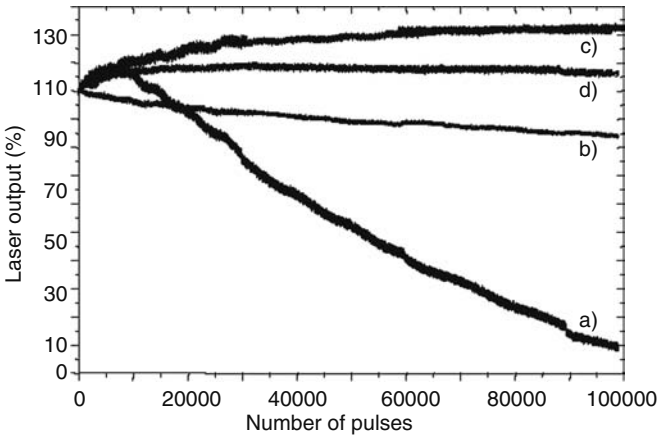

FIGURE 3.17 Normalized laser output as a function of the number of pump pulses for dye PM567 in (a) COP(MMA:TMSPMA 3:7) and (b) COP(HEMA:TMSPMA 7:3), and for dye PM597 in (c) COP(HEMA:TMSPMA 7:3) and (d) TERP(MMA:HEMA:TMSPMA 5:5:10). Dye concentration: 1.5×10^{-3} M (PM567) and 6×10^{-4} M (PM597). Pump energy and repetition rate: 3.5 mJ/pulse and 30 Hz, respectively. (Reprinted with permission from Costela, A., I. García-Moreno, D. del Agua, O. García, and R. Sastre, Highly photostable solid-state dye lasers based on silicon-modified organic matrices, *J. Appl. Phys.* 101 (2007), doi:10.1063/1.2359117, Copyright 2007, American Institute of Physics.)

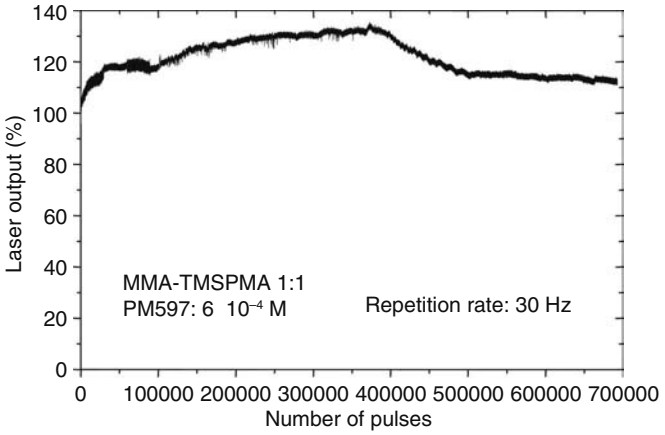

FIGURE 3.18 Normalized laser output as a function of the number of pump pulses in the same position of the sample for dye PM597 in silicon-modified organic matrix.

1.9 mrad (~1.3 times the diffraction limit). In Chapter 4, the use of these media in SSDL is discussed in detail.

The effect of incorporating dielectric-oxide microparticles into both solid host materials and liquid solutions has been investigated by Ahmad [50]. In particular, PMMA samples containing β-alumina microparticles with diameter less than 0.2 μm were prepared doped with PM567 and Rh6G. In these conditions, the photostability of the samples was greatly enhanced: Using samples 8 mm long doped with a PM567 dye concentration of 3.4×10^{-4} M and longitudinal pumping at 2 Hz repetition rate and pump fluence of 0.16 J/cm^2, the number of pulses for the conversion efficiency to fall to one-half of its initial value is seen to increase from 200,000 without microparticles to 400,000 for samples containing microparticles. Addition of both DABCO and microparticles results in an increase of the operational lifetime to 600,000 pulses, corresponding to a total absorbed pump energy of 365 GJ/mol. When the dye was Rh6G, the addition of microparticles to a solid PMMA sample resulted in the same proportion of enhancement to the photostability as for PM567.

3.3 APPLICATIONS

The unique operational flexibility of dye lasers has resulted in applications in many fields in science and technology. Their capability of providing coherent, tunable, narrow-linewidth radiation spanning the visible spectrum has made them an invaluable tool in high-resolution atomic and molecular spectroscopy. Isotope separation, remote sensing, and photochemistry are examples of applied fields where dye lasers have been successfully utilized. In the life sciences, dye lasers have found applications in biology, studying biomedical reaction kinetics of biological molecules, and in medicine, in cancer photodynamic therapy, dermatology, treatment of vascular lesions, and lithotripsy. The medical applications of dye lasers are considered in detail in Chapter 8.

We have already mentioned the problems posed by liquid dye lasers, which have restricted their use outside the laboratory. The SSDL are much more appropriate to be used in industrial and medical environments, but the photodegradation problems exhibited by these systems for many years were an insurmountable handicap for any practical use. As shown in this chapter, the technology of solid-state dye lasers has much improved over the last decade, and new dyes and hosts with performance comparable to that of liquid dye lasers are being developed. These improved SSDL systems, stable, cheap, and user-friendly, offer a promising alternative to liquid dye lasers as practical sources of coherent, tunable laser radiation.

REFERENCES

1. Duarte, F. J., and L. W. Hillman (Eds.), *Dye Laser Principles*, Academic, New York, 1990.
2. Duarte, F. J., and A. Costela, Dye lasers, in *Encyclopedia of Modern Optics*, edited by R. D. Guenther, D. G. Steel, and L. Bayvel, Elsevier, New York, 2004, pp. 400–414.
3. Soffer, B. H., and B. B. McFarland, Continuously tunable, narrow-band organic dye lasers, *Appl. Phys. Lett.* 10: 266–267 (1967).
4. Peterson, O. G., and B. B. Snavely, Stimulated emission from flashlamp-excited organic dyes in polymethyl methacrylate, *Appl. Phys. Lett.* 12: 238–240 (1968).
5. O'Connell, R. M., and T. T. Saito, Plastics for high-power laser applications: a review, *Opt. Eng.* 22: 393–399 (1983).
6. Zink, J. I., B. Dunn, R. B. Kaner, E. T. Knobbe, and J. McKiernan, Inorganic sol-gel glasses as matrices for nonlinear optical materials, in *Materials for Nonlinear Optics*, edited by S. R. Marder, J. E. Sohn, and G. D. Stucky, ACS Symposium Series, American Chemical Society, Washington, DC, 1991, pp. 541–552.
7. Pavlopoulos, T. G., M. Shah, and J. H. Boyer, Efficient laser action from 1,3,5,7,8-pentamethylpyrromethene-BF_2 complex and its disodium 2,6-disulfonate derivative, *Opt. Commun.* 70: 425–427 (1989).
8. Pavlopoulos, T. G., J. H. Boyer, M. Shah, K. Thangaraj, and M-L. Soong, Laser action from 2,6,8-position trisubstituted 1,3,5,7-tetramethylpyrromethene-BF_2 complexes: part 1, *Appl. Opt.* 29: 3585–3586 (1990).
9. Pavlopoulos, T. G., J. H. Boyer, K. Thangaraj, G. Sathyamoorthi, M. Shah, and M-L. Soong, Laser dye spectroscopy of some pyrromethene-BF_2 complexes, *Appl. Opt.* 31: 7089–7094 (1992).
10. Costela, A., I. García-Moreno, and R. Sastre, Materials for solid-state dye lasers, in *Handbook of Advanced Electronic and Photonic Materials and Devices*, edited by H. S. Nalwa, Academic, San Diego, CA, 2001, Vol. 7, Chap. 4.
11. Duarte, F. J., A. Costela, I. García-Moreno, and R. Sastre, Measurements of $\partial n/\partial T$ in solid-state dye laser gain media, *Appl. Opt.* 39: 6522–6523 (2000).
12. Dyumaev, K. M., A. A. Manenkov, A. P. Maslyukov, A. G. Matyushin, V. S. Nechitailo, and A. M. Prokhorov, Transparent polymers: a new class of optical materials for lasers, *Sov. J. Quantum Electron.* 13: 503–507 (1983).
13. Costela, A., F. Florido, I. García-Moreno, R. Duchowicz, F. Amat-Guerri, J. M. Figuera, and R. Sastre, Solid-state dye lasers based on copolymers of 2-hydroxyethyl methacrylate and methyl methacrylate doped with Rhodamine 6G, *Appl. Phys. B* 60: 383–389 (1995).
14. Maslyukov, A., S. Sokolov, M. Kaivola, K. Nyholm, and S. Popov, Solid-state dye laser with modified poly(methyl methacrylate)-doped active elements, *Appl. Opt.* 34: 1516–1518 (1995).

15. Giffin, S. M., W. J. Wadsworth, I. T. McKinnie, A. D. Woolhouse, G. J. Smith, and T. G. Haskell, Efficient, high photostability, high brightness, co-polymer solid state dye lasers, *J. Mod. Opt.* 46: 1941–1945 (1999).
16. A. Costela, I. García-Moreno, J. M. Figuera, F. Amat-Guerri, R. Mallavia, M. D. Santa-María, and R. Sastre, Solid-state dye lasers based on modified Rhodamine 6G dyes copolymerized with methacrylic monomers, *J. Appl. Phys.* 80: 3167–3173 (1996).
17. Pavlopoulos, T. G., Scaling of dye lasers with improved laser dyes, *Prog. Quantum Electron.* 26: 193–224 (2002).
18. Ahmad, M., M. D. Rahn, and T. A. King, Singlet oxygen and dye triplet-state quenching in solid-state dye lasers consisting of Pyrromethene 567-doped poly(methyl methacrylate), *Appl. Opt.* 38: 6337–6342 (1999).
19. Ahmad, M., T. A. King, D-K. Ko, B. H. Cha, and J. Lee, Highly photostable laser solution and solid-state media based on mixed pyrromethene and coumarin, *Opt. Laser Tecnol.* 34: 445–448 (2002).
20. Costela, A., I. García-Moreno, and R. Sastre, Polymeric solid-state dye lasers: recent developments, *Phys. Chem. Chem. Phys.* 5: 4745–4763 (2003).
21. R. Duchowicz, B. Scaffardi, A. Costela, I. García-Moreno, R. Sastre, and A. Acuña, Photothermal characterization and stability analysis of polymeric dye lasers, *Appl. Opt.* 39: 4959–4963 (2000).
22. Duchowicz, R., B. Scaffardi, A. Costela, I. García-Moreno, R. Sastre, and A. Acuña, Photothermal analysis of polymeric dye laser materials excited at different pump rates, *Appl. Opt.* 42: 1029–1035 (2003).
23. López Arbeloa, T., F. López Arbeloa, I. López Arbeloa, I. García-Moreno, A. Costela, R. Sastre, and F. Amat-Guerri, Correlations between photophysics and lasing properties of dipyrromethene-BF_2 dyes in solution, *Chem. Phys. Lett.* 299: 315–321 (1999).
24. Liang, F., H. Zeng, Z. Sun, Y. Yuan, Z. Yao, and Z. Xu, Eight-position substitution effects on laser action of the 1,3,5,7-tetramethyl-2,6-diethyl pyrromethene – BF_2 complexes, *J. Opt. Soc. Am. B* 18: 1841–1845 (2001).
25. García, O., R. Sastre, D. del Agua, A. Costela, I. García-Moreno, F. López Arbeloa, J. Bañuelos Prieto, and I. López Arbeloa, Laser and physical properties of BODIPY chromophores in new fluorinated polymeric materials, *J. Phys. Chem. C* 111: 1508–1516 (2007).
26. Costela, A., I. García-Moreno, R. Sastre, D. W. Coutts, and C. E. Webb, High-repetition-rate polymeric solid-state dye lasers pumped by a copper-vapor laser, *Appl. Phys. Lett.* 79: 452–454 (2001).
27. Abedin, K. M., M. Álvarez, A. Costela, I. García-Moreno, O. García, R. Sastre, D. W. Coutts, and C. E. Webb, 10 kHz repetition rate solid-state dye laser pumped by diode-pumped solid-state laser, *Opt. Commun.* 218: 359–363 (2003).
28. Kytina, I. G., V. G. Kytin, and K. Lips, High power polymer dye laser with improved stability, *Appl. Phys. Lett.* 84: 4902–4904 (2004).
29. Lam, S. Y., and M. J. Damzen, Characterisation of solid-state dyes and their use as tunable laser amplifiers, *App. Phys. B* 77: 577–584 (2003).
30. Ray, A. K., S. Kumar, N. V. Mayekar, S. Sinha, S. Kundu, S. Chattopadhyay, and K. Dasgupta, Role of the stimulated-emission rate in the photostability of solid-state dye lasers, *Appl. Opt.* 44: 7814–7822 (2005).
31. Bornemann, R., U. Lemmer, and E. Thiel, Continuous-wave solid-state dye laser, *Opt. Lett.* 31: 1669–1671 (2006).
32. Reisfeld, R., A. Weiss, T. Saraidarov, E. Yariv, and A. A. Ishchenko, Solid-state lasers based on inorganic-organic hybrid materials obtained by combined sol-gel polymer technology, *Polym. Adv. Technol.* 15: 291–301 (2004).
33. Rahn, M. D., and T. A. King, Comparison of laser performance of dye molecules in sol-gel, polycom, ormosil, and poly(methyl methacrylate) host media, *Appl. Opt.* 34: 8260–8271 (1995).

34. Ahmad, M., T. A. King, D-K. Ko, B. H. Cha, and J. Lee, Performance and photostability of xanthene and pyrromethene laser dyes in sol-gel phases, *J. Phys. D: Appl. Phys.* 35: 1473–1476 (2002).
35. Yang, Y., M. Wang, G. Qian, Z. Wang, and X. Fan, Laser properties and photostabilities of laser dyes doped in ORMOSILs, *Opt. Mater.* 24: 621–628 (2004).
36. Nhung, T. H., M. Canva, T. T. A. Dao, F. Chaput, A. Brun, N. D. Hung, Stable doped hybrid sol-gel materials for solid-state dye laser, *Appl. Opt.* 42: 2213–2218 (2003).
37. Yang, Y., J. Zou, H. Rong, G. D. Qian, Z. Y. Wang, M. Q. Wang, Influence of various coumarin dyes on the laser performance of laser dyes co-doped into ORMOSILs, *Appl. Phys. B* 86: 309–313 (2007).
38. Yariv, E., and R. Reisfeld, Lasing properties of pyrromethene dyes in sol-gel glasses, *Opt. Mater.* 13: 49–54 (1999).
39. Costela, A., I. García-Moreno, C. Gómez, O. García, L. Garrido, and R. Sastre, Highly efficient and stable doped hybrid organic-inorganic materials for solid-state dye lasers, *Chem. Phys. Lett.* 387: 496–501 (2004).
40. Costela, A., I. García-Moreno, C. Gómez, O. García, and R. Sastre, Enhancement of laser properties of pyrromethene 567 dye incorporated into new organic-inorganic hybrid materials, *Chem. Phys. Lett.* 369: 656–661 (2003).
41. Costela, A., I. García-Moreno, C. Gómez, O. García, and R. Sastre, Environment effects on the lasing photostability of Rhodamine 6G incorporated into organic-inorganic hybrid materials, *Appl. Phys. B* 78: 629–634 (2004).
42. Costela, A., I. García-Moreno, O. García, D. del Agua, and R. Sastre, Structural influence of the inorganic network in the laser performance of dye-doped hybrid materials, *Appl. Phys. B* 80: 749–755 (2005).
43. García-Moreno, I., A. Costela, A. Cuesta, O. García, D. del Agua, and R. Sastre, Synthesis, structure, and physical properties of hybrid nanocomposites for solid-state dye lasers, *J. Phys. Chem. B* 109: 21618–21626 (2005).
44. Costela, A., I. García-Moreno, C. Gómez, O. García, R. Sastre, A. Roig, and E. Molins, Polymer-filled nanoporous silica aerogels as hosts for highly stable solid-state dye lasers, *J. Phys. Chem B* 109: 4475–4480 (2005).
45. García, O., R. Sastre, D. del Agua, A. Costela, I. García-Moreno, and A. Roig, Efficient optical materials based on fluorinated-polymeric silica aerogels, *Chem. Phys. Lett.* 427: 375–378 (2006).
46. Costela, A., I. García-Moreno, D. del Agua, O. García, and R. Sastre, Highly photostable solid-state dye lasers based on silicon-modified organic matrices, *J. Appl. Phys.* 101: 073110 (2007).
47. Susdorf, T., del Agua, D., Tyagi, A., Penzkofer, A., García, O., Sastre, R., Costela, A., and García-Moreno, I., Photophysical characterization of pyrromethene 597 laser dye in silicon-containing organic matrices, *Appl. Phys. B* 86: 537–545 (2007).
48. Duarte, F. J., and R. O. James, Tunable solid-state lasers incorporating dye-dopes, polymer-nanoparticle gain media, *Opt. Lett.* 28: 2088–2090 (2003).
49. Duarte, F. J., and R. O. James, Spatial structure of dye-doped polymer nanoparticle gain media, *Appl. Opt.* 43: 4088–4090 (2004).
50. Ahmad, M., Enhanced photostability of photoluminescent dye-doped solutions and polymers with the addition of dielectric-oxide micro-particles, *Opt. Commun.* 271: 457–461 (2007).

4 Tunable Lasers Based on Dye-Doped Polymer Gain Media Incorporating Homogeneous Distributions of Functional Nanoparticles

F. J. Duarte and R. O. James

CONTENTS

4.1 Introduction 121
4.2 Tunable Laser Oscillator Review 123
4.3 Synthesis of DDPN Laser Gain Media 126
4.4 Experimental Results and Laser Emission 129
4.4.1 Tunable Laser Emission 129
4.5 Interferometric Interpretation 133
4.6 Invisibility of Nanoparticle Distributions in the Visible Electromagnetic Spectrum 136
4.7 Future Applications of DDPN Gain Media in Spectroscopy and Medicine 137
4.7.1 Laser Spectroscopy 138
4.7.2 Laser Medicine 138
References 139

4.1 INTRODUCTION

The first broadly tunable laser was the organic dye laser, discovered in 1966 by Sorokin and Lankard [1] and Schäfer et al. [2]. Dye-doped polymer gain media for tunable lasers were introduced shortly afterward by Soffer and McFarland [3] and Peterson

and Snavely [4]. However, due to initial difficulties with laser medium optical inhomogeneities and thermal problems these media were relegated to the archives, with the exception of some sporadic interest (see, for example, [5]), until the 1990s [6].

Using a highly homogeneous dye-doped polymer (DDP) medium named modified PMMA (MPMMA) Duarte [7] reported, for the first time, on single-transverse-mode beams and narrow-linewidth emission in 1994. The gain medium used by Duarte was developed by researchers in the former Soviet Union [8]. This research on narrow-linewidth solid-state dye lasers was an extension of an earlier effort involving silicate gain media [9]. These reports, in addition to further efforts in the United States and abroad (see, for example, [10, 11]), reenergized the interest in solid-state dye lasers worldwide. This interest and progress can be followed in various reviews [12–14] and in Chapter 3 on solid-state dye lasers by Costela et al. [15]. As of 2007 solid-state dye laser research activity has been reported in more than 30 laboratories around the world.

As mentioned, the early polymeric matrices presented difficulties in optical homogeneity and thermal dissipation. To solve the $\partial n/\partial T$ problem researchers introduced hybrid organic-inorganic matrices where the inorganic portion is silica based. Examples of such materials include the dye-doped organically modified silicate (ORMOSIL) [6], tetraethoxysilane [7, 9], and silica-polymer nanocomposites [16]. As reported by Duarte and Pope [16] these organic-inorganic matrices, due to minute refractive index differences, allowed internal interference, which resulted in laser beam inhomogeneities.

Thus, by 2003 the choice for laser researchers consisted of proven highly homogeneous DDP gain media, with poor $\partial n/\partial T$ characteristics, which limit pulse repetition frequencies, or organic-inorganic alternatives with improved thermal characteristics but with refractive index conditions resulting in internal interference or laser beam inhomogeneities. One alternative to neutralize the laser beam inhomogeneities was reported by Duarte and James [17]. This consisted of dispersing nearly uniform nanoparticle distributions in the dye-doped polymer matrices. The role of the nanoparticle distribution is to improve the $\partial n/\partial T$ factor while not introducing the conditions necessary for internal interference at the lasing wavelength. This was achieved by the near uniform distribution of the nanoparticles as will be explained in detail later. This new gain media was called dye-doped polymer nanoparticle (DDPN) gain medium.

This chapter first describes the tunable laser resonators and oscillators where this class of efficient dye-doped polymer gain media, including functional distributions of silica nanoparticles, is applicable, and then proceeds to present the laser and interference experiments used to characterize this gain media. A detailed material synthesis section follows and a discussion on nanoparticle distributions, invisible to laser wavelengths in the visible spectrum, is also included.

A brief literature survey indicates that DDPN gain media [17] have attracted the interest of researchers working on dye-doped organic-inorganic gain media [18–21], dye co-doped solid-state gain media [22, 23], nanocomposite materials for optical devices [24], dye-doped polymer films [25], photostability of solid-state organic gain media [26], polymeric networks [27], dye-doped polymer fibers [28], holographic media [29], and microcavity lasers [30, 31]. Albeit, so far, DDPN gain media have been demonstrated using Rhodamine 6G dye [17], other dyes such as pyrromethenes [32] are attractive candidates to dope this new tunable solid-state laser media.

4.2 TUNABLE LASER OSCILLATOR REVIEW

The narrow-linewidth tunable laser oscillators, or resonators, used to demonstrate the capabilities of solid-state dye lasers have been reviewed in [33, 34] and are explained in Chapter 5 as applied to semiconductor lasers. The architecture and performance of these oscillators are briefly outlined here.

The first multiple-prism grating narrow-linewidth solid-state dye laser oscillators were introduced by Duarte in 1994 [7]. These included the multiple-prism Littrow (MPL) grating oscillator and the hybrid multiple-prism near grazing incidence (HMPGI) grating oscillator. Experiments yielding improved performance of these oscillators [35] led eventually to an optimized HMPGI grating oscillator [36] and an optimized MPL grating oscillator [37]. These oscillators are depicted in Figures 4.1 and 4.2, respectively. In Table 4.1 the emission characteristics of these high-performance oscillators are tabulated. It should be noted that all of these experiments were performed in the nanosecond pulse time domain using Rhodamine 6G-doped MPMMA gain media. The most salient characteristics are single-transverse-mode beam characteristics and widely tunable single-longitudinal-mode emission in the 350 MHz $\leq \Delta\nu \leq$ 375 MHz range. In the wavelength domain, at $\lambda \approx 590$ nm, these linewidths correspond to the 0.00040 nm $\leq \Delta\lambda \leq$ 0.00043 nm range. The beam divergence for the optimized MPL grating oscillator was measured to be ~1.5 times the diffraction limit with similar characteristics observed for the HMPGI grating oscillator.

An additional oscillator architecture was introduced by Duarte et al. [38] in experiments aimed at demonstrating narrow-linewidth long-pulse lasing in solid-state dye laser oscillators. In these experiments the linewidths achieved were $\Delta\nu \approx 650$ MHz, pulsed as long as 105 ns. The architecture of this MPL grating oscillator is illustrated in Figure 4.3. An additional novelty in these experiments was the use of a Rhodamine 6G-doped HEMA:MMA matrix as the gain medium.

As apparent in the previous discussion, besides tunability, the two most important parameters in the description and characterization of narrow-linewidth tunable laser

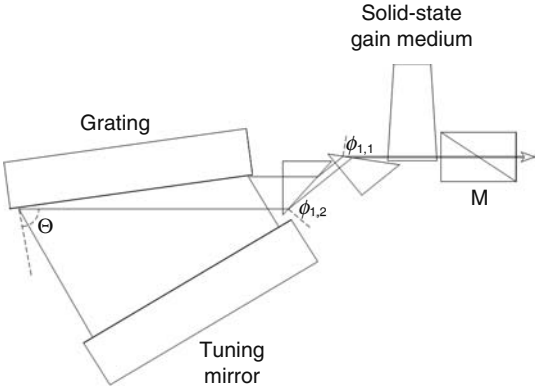

FIGURE 4.1 Solid-state HMPGI grating laser oscillator. (From Duarte, F. J., Multiple-prism near-grazing-incidence grating solid-state dye laser oscillator, *Opt. Laser Technol.* 29: 513–516 (1997).)

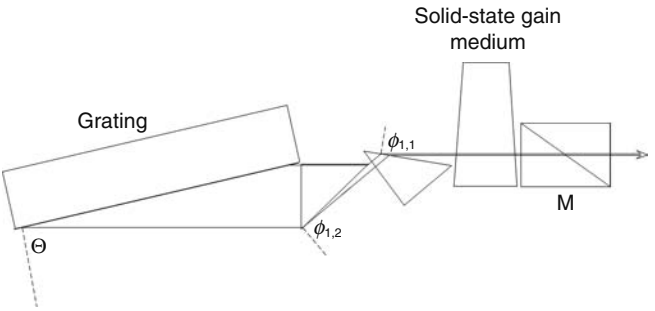

FIGURE 4.2 Optimized solid-state MPL grating laser oscillator. (From Duarte, F. J., Multiple-prism grating solid-state dye laser oscillator: optimized architecture, *Appl. Opt.* 38: 6347–6349 (1999).)

oscillators are beam divergence ($\Delta\theta$) and laser linewidth ($\Delta\lambda$). These two parameters are intimately related via the cavity linewidth equation [33, 34, 40]

$$\Delta\lambda \approx \Delta\theta_R (MR(\partial\Theta/\partial\lambda)_G \pm R(\partial\Phi/\partial\lambda)_P)^{-1} \tag{4.1}$$

where R is the number of intracavity return passes, M is the overall beam magnification provided by the multiple-prism beam expander, $(\partial\Theta/\partial\lambda)_G$ is the grating dispersion either in near grazing-incidence configuration, or Littrow configuration, and $(\partial\Phi/\partial\lambda)_P$ is the return-pass multiple-prism dispersion. All of these quantities are described in detail in the cited references and in Chapter 5. Since by design the multiple-prism dispersion can be reduced to $(\partial\Phi/\partial\lambda)_P \approx 0$ then Equation 4.1 can be expressed simply as

$$\Delta\lambda \approx \Delta\theta_R (MR(\partial\Theta/\partial\lambda)_G)^{-1} \tag{4.2}$$

where the beam divergence is given by [34, 40]

$$\Delta\theta_R \approx (\lambda/\pi w)(1 + (L/B_R)^2 + (LA_R/B_R)^2)^{-1} \tag{4.3}$$

TABLE 4.1
Performance of Narrow-Linewidth Solid-State Dye Laser Oscillators

Gain medium[a]	Oscillator architecture	$\Delta\theta$ (mrad)	$\Delta\nu$ (MHz)	Δt[b] (ns)	Tuning range (nm)	ASE[c]	Eff. (%)	Ref.
MPMMA	HMPGI	2.3	375	6	565–610	~10^{-7}	3–4[d]	36
MPMMA	MPL	2.2	350	3	550–603	~10^{-6}	~5[e]	37
HEMA: MMA	MPL	3.5	650	105	564–602	~10^{-4}	~2	38

[a] Belonging to the DDP class.
[b] At full width half-maximum (FWHM).
[c] Amplified spontaneous emission as defined in [39].
[d] Excitation performed with a coumarin 125 dye laser at $\lambda \approx 532$ nm.
[e] Excitation performed with a coumarin 125 dye laser at $\lambda \approx 525$ nm.

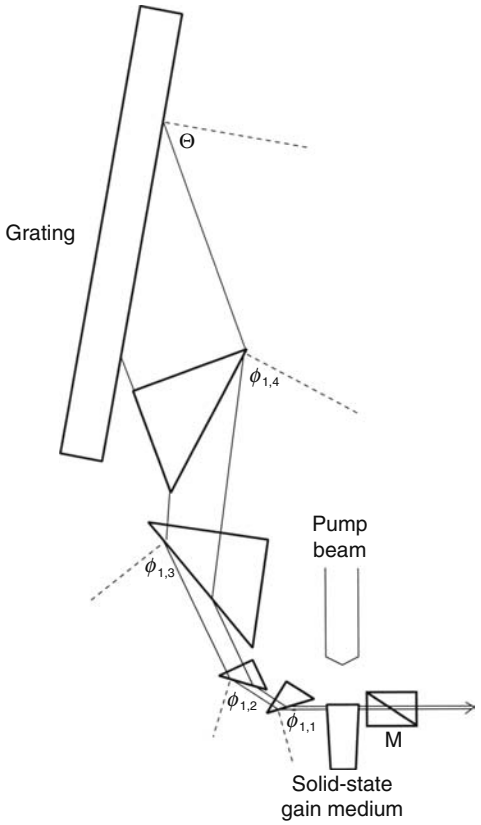

FIGURE 4.3 Long-pulse MPL grating laser oscillator. (From Duarte, F. J., T. S. Taylor, A. Costela, I. García-Moreno, and R. Sastre, Long-pulse narrow-linewidth dispersive solid-state dye laser oscillator, *Appl. Opt.* 37: 3987–3989 (1998).)

In this equation w is the beam waist, $L = (\pi w^2/\lambda)$ is known as the Rayleigh length, while A_R and B_R are the corresponding multiple-return-pass propagation matrix elements [34, 40]. The designer can engineer the cavity so that the term in parentheses becomes close to unity. This can be accomplished when using liquid gain media; however, in organic solid-state gain media, thermal lensing effects prevent reaching the diffraction limit value of the beam divergence. As mentioned, in an optimized dispersive oscillator design [37] the measured beam divergence is

$$\Delta\theta_R \approx (3/2)(\lambda/\pi w) \tag{4.4}$$

This is accomplished under experimental conditions, which result in $R \approx 3$ [40]. Also, it should be noted that either Equation 4.1 or 4.3 provides only an upper limit estimate of the linewidth so that the measured $\Delta\lambda$ is below the theoretical value [33, 34]. This discussion is very pertinent to the subject at hand since the main objective of introducing silica nanoparticles in the gain medium is to modify $\partial n/\partial T$ and thus reduce thermal lensing effects.

A useful observation, at this stage, is that the diffraction-limited expression of the beam divergence

$$\Delta\theta \approx (\lambda/\pi w) \tag{4.5}$$

can be derived [34] from the Heisenberg uncertainty principle [41]

$$\Delta p \Delta x \approx h \tag{4.6}$$

which can also be expressed as [34]

$$\Delta\lambda\Delta x \approx \lambda^2 \tag{4.7}$$

$$\Delta\nu\Delta x \approx c \tag{4.8}$$

and

$$\Delta\nu\Delta t \approx 1 \tag{4.9}$$

For the optimized MPL grating solid-state dye laser oscillator a laser linewidth of $\Delta\nu \approx 350$ MHz ($\Delta\lambda \approx 0.00041$ nm at $\lambda = 590$ nm) was measured at a pulse duration of $\Delta t \approx 3$ ns [37]. This means that the measured linewidth was close to the limit allowed by the uncertainty principle for that pulse duration. Also, the spectral power density delivered by this narrow-linewidth oscillator is $\rho \approx 95$ W/MHz at $\lambda \approx 590$ nm.

Besides the multiple-prism grating oscillators described here researchers have also successfully introduced solid-state distributed-feedback dye lasers [42–44]. Oki et al. [45, 46] have also investigated waveguide configurations. The dye-doped polymer matrices, including functional silica nanoparticle distributions, described here are applicable to all of the oscillator architectures mentioned in this section as well as simple broadband resonators.

Finally, it should also be mentioned that excitation methods of the dye-doped solid-state gain media should not be limited to traditional laser, or flashlamp, pumping. Recently a waveguide method of excitation, designed for an array of pulsed high-brightness light-emitting diodes (LED), was disclosed in the literature [47]. One particular waveguide was made of polished aluminum with an input aperture, for the diode array, having dimensions of 260 mm × 9 mm while the output aperture, designed for transverse excitation of the solid-state laser dye medium, has dimensions of 10 mm × 250 μm. The two apertures are separated by 270 mm. The wide dimension of the excitation aperture is parallel to the plane of incidence.

4.3 SYNTHESIS OF DDPN LASER GAIN MEDIA

The new gain media consists of dye-doped, high-purity polymethyl methacrylate (PMMA) including dispersed silica nanoparticles. One example of such DDPN laser gain media is a Rhodamine 6G-doped PMMA matrix containing 30% w/w silica in which the silica content is composed of ~12 nm SiO_2 particles. This particular DDPN gain medium shows conservation of TEM_{00} spatial beam characteristics approaching that observed in DDP gain media.

Synthesis and methods of fabrication of the DDPN gain media have been described in the recent literature [17, 48–51]; we provide a comprehensive review here. Note that several variations of gain media preparation are possible, but the approach taken here

to prepare homogeneous gain media was to obtain or prepare separate stable, moderately concentrated solutions, or dispersions, of (1) optical-grade PMMA polymers [51], (2) nanoparticulate silica organosols (see [17, 50, 51]), and (3) laser dyes in organic solvents or solvent mixtures. The process involves physically mixing colloidally stable SiO_2 nanoparticle dispersions (organosols) in methyl ethyl ketone (MEK) with solutions of optical-grade PMMA resins in solvents that are compatible with the silica sol over a wide range of concentrations. The laser dye is also added to the mixture as a dissolved component in a suitable, compatible solvent. We use the highest concentration of each separate component that is possible so that when the mixture of component solutions is made, the polymer/sol remains colloidally stable and the amount of solvent evaporation required to form the solid phase is minimized.

The materials used in DDPN gain media are all commercially available. The PMMA used was optical-grade resin manufactured for use in video laser disks (VLD) and/or video optical disks (VOD). Silica organosols are available in a range of organic solvents and particle sizes. In the work described here silica organosol in MEK was the principal component. For specific listings see [17, 48–51]. World Wide Web searches will also yield specific manufacturers.

The nanoparticle-polymer laser dye composite is formed from this dispersion mixture by slow solvent evaporation from a partially covered mold or container using a solvent-stripping method that provides a saturated vapor over the sample for a period

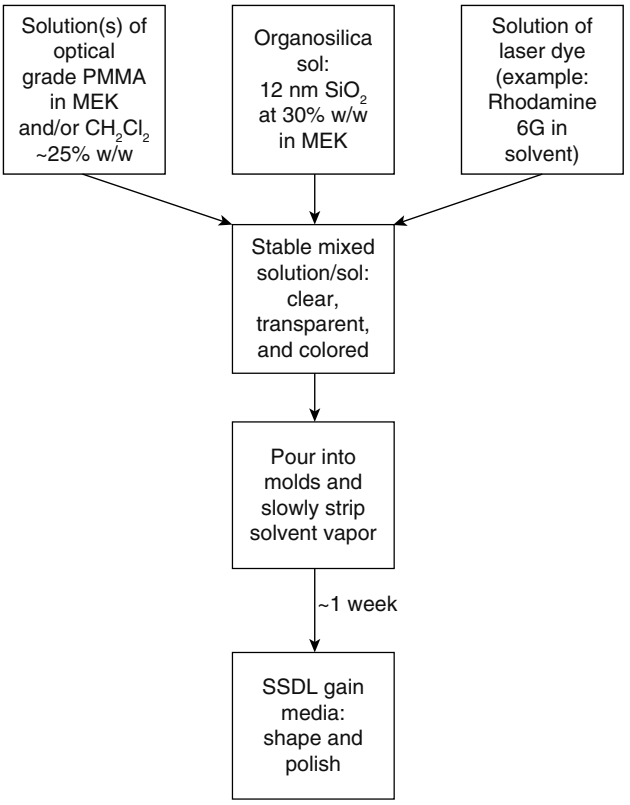
Solution(s) of optical grade PMMA in MEK and/or CH_2Cl_2 ~25% w/w
Organosilica sol: 12 nm SiO_2 at 30% w/w in MEK
Solution of laser dye (example: Rhodamine 6G in solvent)
Stable mixed solution/sol: clear, transparent, and colored
Pour into molds and slowly strip solvent vapor
~1 week
SSDL gain media: shape and polish

FIGURE 4.4 Synthesis-manufacturing process for DDPN gain media.

often exceeding 1 week. All proportions of the component solutions are figured on a spreadsheet to provide an aim concentration of silica and laser dye in the polymer matrix. The mechanics of the synthesis-manufacturing process is outlined in Figure 4.4.

An example preparation involves weighing and mixing the following:

1. 54.83 g of silica organosol, composed of 12 nm diameter particles, 30.5% w/w SiO_2 in MEK
2. 97.57 g of PMMA solution at 20.0% w/w solids in MEK
3. 65.05 g of PMMA solution at 30.0% w/w in methylene chloride
4. 37.17 g of 0.1% w/w solution of Rhodamine 6G in methylene chloride

This dispersion example is 21.92% solids, and the solids are composed of 29.98% SiO_2, 69.95% PMMA, and 0.069% Rhodamine 6G. The solvent blend is 41.55% $MeCl_2$ and 54.45% MEK. The mass balance of solids and solvents for components and final gain media is shown in Table 4.2.

After thorough mixing at room temperature the clear, colored sol samples are placed in covered containers, and the solvents are slowly stripped away to form a gel. Eventually this results in a colored, and transparent, solid rigid body. It is possible to vary the solvent mixture ratios and the SiO_2 particle content up to approximately 50% w/w to provide a range of nanoparticle-filled, laser dye-doped polymer gain media. Silica organosols are available with 9 nm and 5 nm particle diameter. Laser gain media have also been made with these smaller particles; however the 5 nm silica organosols haven proven more difficult to provide stable laser gain media. The magnitude of the thermooptic coefficient, $\partial n/\partial T$, of the PMMA-silica composite media decreases in a linear fashion with the concentration of silica. However, it is difficult to prepare samples with greater than 50% w/w silica. Consequently, the negative sign of $\partial n/\partial T$ for PMMA cannot be completely nullified by silica addition alone.

Gain media with trapezoidal cross-sections, at a plane parallel to the plane of propagation, are optically polished using slow polishing techniques. Since polymer properties are temperature dependent care should be exercised not to overheat the

TABLE 4.2
Mass Balances for Starting Components in Solid-State DDPN Gain Media[a]

Components dispersions	Mass (g)	Mass fraction	% w/w solids	Solids (g)	% w/w solids/sol	Volatiles	Solvents
Silica organosol (12 nm diam.)	54.83	0.305	30.5	16.723		38.11	MEK
PMMA	97.57	0.20	20	19.514		78.06	MEK
PMMA	65.02	0.30	30	19.506		45.51	$MeCl_2$
Rhodamine 6G	37.10	0.001	0.1	0.037		37.06	$MeCl_2$
Totals	254.52			55.780	21.92	198.74	

[a] SiO_2: 29.980%, PMMA: 69.953%, Rhodamine 6G: 0.067%.

[b] Solvent blend: $MeCl_2$: 41.55%, MEK: 58.45%.

sample during polishing. The Rhodamine 6G DDP medium, used as a comparison, is the same utilized in previous experiments [7, 35–37] and has been characterized in detail by Maslyukov et al. [8] and Popov [52].

4.4 EXPERIMENTAL RESULTS AND LASER EMISSION

In their 1995 paper Duarte and Pope [16] presented clear interferometric evidence that illustrated a comparison of the internal structure of DDP gain media to the internal structure of hybrid dye-doped organic-inorganic gain media. In their paper it was suggested that the high degree of internal homogeneity in the case of the DDP, such as dye-doped MPMMA, matrices resulted in the absence of internal interference, which manifested itself in the homogeneous emission and propagation of laser beams. In other words, laser emission using these matrices as a gain medium did not present evidence of laser beam breakup. At the time, the same was not the case for hybrid dye-doped organic-inorganic gain media where beam breakup was evident. The results of propagation of laser beams in dye-doped hybrid organic-inorganic matrices are shown in Figure 4.5 to illustrate the concepts just outlined.

The same experiment using a Rhodamine 6G-doped MPPMA gain matrix, as used in narrow-linewidth tunable laser oscillators, results in the preservation of the TEM_{00} beam profile as illustrated in Figure 4.6.

4.4.1 Tunable Laser Emission

The laser experiments were performed using a prismatic tunable coumarin 152 laser, as the excitation lasers, delivering approximately 2 mJ in the 520–552 nm region.

FIGURE 4.5 Distorted beam profile, following propagation through an inhomogeneous dye-doped organic-inorganic gain medium. Originally the beam, from a He–Ne laser emitting at $\lambda \approx 632.8$ nm, had a TEM_{00} profile. (From Duarte, F. J., and R. O. James, Tunable solid-state lasers incorporating dye-doped, polymer-nanoparticle gain media, *Opt. Lett.* 28: 2088–2090 (2003).)

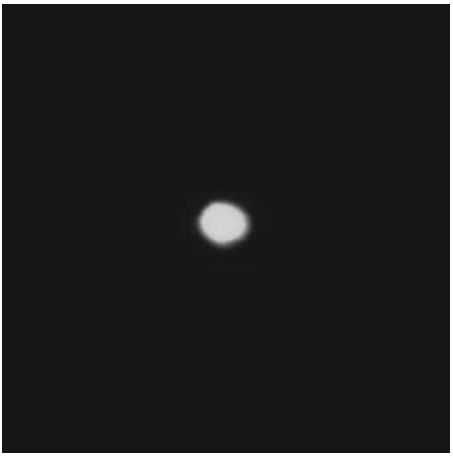

FIGURE 4.6 Preservation of laser beam profile, following propagation through a homogeneous dye-doped polymer gain medium. The preserved TEM_{00} beam profile is from a He–Ne laser emitting at $\lambda \approx 632.8$ nm. (From Duarte, F. J., and R. O. James, Tunable solid-state lasers incorporating dye-doped, polymer-nanoparticle gain media, *Opt. Lett.* 28: 2088–2090 (2003).)

This laser was pumped transversely by a nitrogen laser at 337 nm. The emission from the green tunable laser was used to excite longitudinally a simple mirror-grating resonator. This cavity is comprised by a 2400 lines/mm grating, deployed in Littrow configuration, and an output coupler mirror with a reflectivity of ~20%. The overall length of the cavity, illustrated in Figure 4.7, is about 75 mm, and it was configured to allow interchange of trapezoidal solid-state gain media without altering the alignment of the resonator. In fact, it was possible to easily switch from one medium to another without disturbing the alignment of the cavity. Effort was devoted to this feature to ensure a fair comparison among media. The trapezoidal configuration of the gain medium enables us to maintain a gain length of ~10 mm for all gain media utilized in these experiments. Lasing was also achieved, under direct nitrogen laser excitation, in a simple mirror-mirror cavity using a coumarin 500 DDPN at 30% w/w SiO_2 gain medium [17].

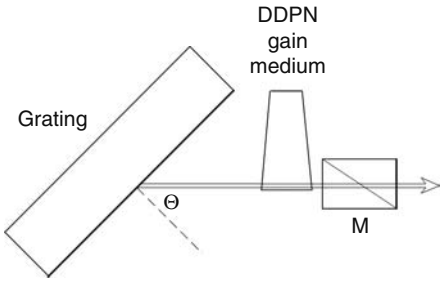

FIGURE 4.7 Mirror-grating cavity used in the DDPN gain media experiments.

Beam profiles were recorded using black-and-white silver halide film, and energetic and temporal measurements were performed using the usual instrumentation [17]. Given previous experience with single-transverse-mode single-longitudinal-mode tunable laser oscillators in the solid-state [7, 35–37], it was decided to characterize and compare the new DDPN gain media by measuring the beam emission profiles of the new lasers. This was done since single-transverse-mode emission is a crucial precondition to achieving narrow-linewidth emission [35]. In other words, it is not possible to achieve single-longitudinal-mode lasing in the presence of more than one single-transverse-mode beam. Further, one of our main hypotheses was that a more favorable $\partial n/\partial T$ for the gain medium would possibly yield improved beam divergences and open the door for higher pulse repetition frequencies (prf). A simple preliminary experiment is to observe the beam profile of a propagating TEM_{00} beam through the DDPN gain medium. The result of this observation is shown in Figure 4.8 where it is clear that, for a DDPN at 30% w/w SiO_2, the TEM_{00} beam profile of a He–Ne laser, at $\lambda = 593.93$ nm, is nicely preserved.

Besides the demonstration of lasing in these new DDPN gain media a primary objective of the measurements became the characterization of the laser emission beam. A typical profile of a laser beam from this new organic-inorganic media is shown in Figure 4.9.

This beam profile has the usual homogeneous characteristics associated with broadband liquid, or DDP, tunable dye lasers. Albeit a tenuous secondary ring structure is observed the profile can be fairly characterized as near TEM_{00}.

A summary of the laser emission results, for DDP and DDPN matrices, are presented in Table 4.3. In addition to the homogeneous beam profile the feature that immediately becomes of interest is the lower beam divergences observed in the emission from the DDPN lasers relative to the DDP laser. In fact, the beam divergence from the DDPN (30% w/w SiO_2) $\Delta\theta \approx 1.9$ (mrad) is found to be ~1.3 times the diffraction limit, which is slightly lower than the beam divergence reported

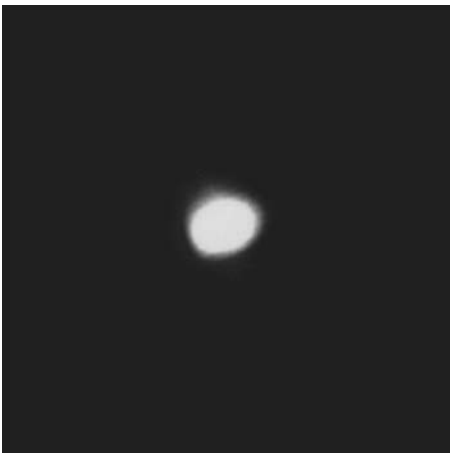

FIGURE 4.8 Conservation of TEM_{00} beam profile following propagation through a DDPN gain medium at 30% w/w SiO_2. The beam was generated by a He–Ne laser at $\lambda = 593.93$ nm.

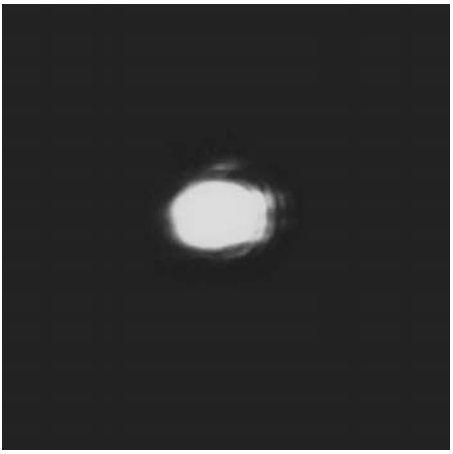

FIGURE 4.9 Laser beam profile generated with a mirror-grating resonator incorporating a Rhodamine 6G DPN gain medium. The beam is similar to those obtained with liquid media and is primarily distributed in a central mode while displaying some weak secondary ring structure. This beam was measured to have a divergence of $\Delta\theta \approx 1.9$ (mrad), which is ~1.3 times the diffraction limit. (From Duarte, F. J., and R. O. James, Tunable solid-state lasers incorporating dye-doped, polymer-nanoparticle gain media, *Opt. Lett.* 28: 2088–2090 (2003).)

for a single-transverse-mode single-longitudinal-mode narrow-linewidth DDP laser exhibiting ~1.5 times the diffraction limit [7].

It should be noted that the laser efficiencies observed in these experiments are in line with previously reported laser efficiencies for DDP lasers that are in the 40–64% range [7, 8].

The lower beam divergence observed with these DDPN lasers is a direct consequence of the improved $\partial n/\partial T$ values (see Table 4.4), which enable a faster dissipation of heat introduced by the pump laser and the thermal losses inherent to the excitation process [34, 53].

TABLE 4.3
Performance of Solid-State Lasers Incorporating DDP and DDPN Gain Matrices Using Rhodamine 6G Dye

Gain medium	C (mM)	λ_p (nm)	Tuning range (nm)	$\Delta\theta$ (mrad)	Eff. (%)[a]
DDP	0.50[b]	~525	563–610	2.3	49
DDPN 30% w/w SiO_2	0.31[b,c]	~525	567–603	1.9	63
DDPN 50% w/w SiO_2	0.31[b,c]	~550	575–600	1.6	9

Source: Adapted from Duarte, F. J., and R. O. James, *Opt. Lett.* 28, 2088–2090, 2003.

[a] Overall optical efficiency.

[b] Initial dye concentration.

[c] The dye concentration in the solid gain volume increases to ~1.9 mM.

TABLE 4.4
$\partial n/\partial T$ in DDP and PN Matrices

Matrix[a]	λ (nm)	$\partial n/\partial T$ ($\times 10^{-4}$)	Ref.
DDP	593.93	-1.4 ± 0.2	54[b]
PN 0% w/w SiO_2	632.82	−1.0317	17[c]
PN 30% w/w SiO_2	632.82	−0.8840	17[c]
PN 50% w/w SiO_2	632.82	−0.6484	17[c]

Source: Adapted from Duarte, F. J., and R. O. James, *Opt. Lett.* 28, 2088–2090, 2003.

[a] P stands for the PMMA polymer, N for nanoparticle.

[b] Refractive measurement at minimum deviation.

[c] The polymer was not dye-doped, and the measurement was performed in a thin-film configuration using a prism-coupling device.

One attractive characteristic of both DDP and DDPN gain media is their optical ruggedness. This means that following irradiation at energy densities above bleaching levels, at ~0.7 J/cm^2, the gain media tends to heal itself in a few days.

Note: Occasionally in the literature some confusion is expressed regarding the optical homogeneity of solid-state dye gain media. To summarize: This was a problem in early dye-doped organic-inorganic gain media as identified in [7, 16]. However, it was clearly established in [7] that DDP gain media, in the form of MPMMA, was perfectly homogeneous, thus enabling the generation of single-transverse-mode beams and narrow-linewidth emission. It was further established in [17] that DDPN gain media was also optically homogeneous, thus enabling the emission of single-transverse-mode beams.

4.5 INTERFEROMETRIC INTERPRETATION

Besides the improvement in thermal characteristics resulting in a decrease in the magnitude of $\partial n/\partial T$, which leads to lower observed laser beam divergences, the most remarkable effect observed in these DDPN matrices is the absence of beam inhomogeneities. As explained earlier this is observed both in the passive transmission of laser beams and in active laser emission.

In 1995 Duarte and Pope [16] suggested that the origin of beam inhomogeneities in organic-inorganic gain media was the presence of internal interference created by randomized diffraction grating structures formed by minute refractive index differentials. The same effect could be present in DDPN gain media. For instance, the measured refractive index for Rhodamine 6G-doped MPMMA is $n(\lambda) = 1.4953$, while the refractive index for fused silica is $n(\lambda) = 1.4582$, thus giving $\Delta n \approx 0.0371$. Both these measurements were performed at $\lambda = 593.93$ and T = 297 K [54].

To study the internal structure of the DDPN gain media it was decided to obtain electron microscope nanographs of the matrices. To this effect a JEOL electron microscope (JEM 100CX II), with a resolution of approximately 0.3 nm, was

used [50]. The gain media studied was Rhodamine 6G DDPN and coumarin 500 DDPN both at 30% w/w SiO_2. The nanographs from these gain media are shown in Figures 4.10 and 4.11.

In these nanographs it became clearly evident that there are areas of higher concentration of nanoparticles and areas that show a near total absence of nanoparticles. These are the areas that correspond to the dye-doped polymer. This morphology can be related to a nondeterministic volumetric transmission grating as previously suggested [16]. Looking at a cross-section of the two-dimensional planes observed in the nanographs, it is possible to estimate the average dimensions of slits and isles for DDPN matrices. These results are summarized in Table 4.5.

The effect of a diffractive morphology on the propagation of coherent emission, either deterministic or randomized, can be analyzed via three-dimensional, two-dimensional, or one-dimensional generalized *N*-slit interference equations [55, 56]. For a detailed description of the interferometric approach, the reader is referred to Chapter 12. In essence, the generalized one-dimensional interferometric equation is given by [55, 56]

$$|\langle x \mid s\rangle|^2 = \sum_{j=1}^{N} \Psi(r_j)^2 + 2\sum_{j=1}^{N} \Psi(r_j) \left(\sum_{m=j+1}^{N} \Psi(r_m) \cos(\Omega_m - \Omega_j) \right) \tag{4.10}$$

where the cosine term gives origin to the well-known diffraction equation [57, 58]

$$d_j(\sin\Theta_j \pm \sin\Phi_j) = m\lambda \tag{4.11}$$

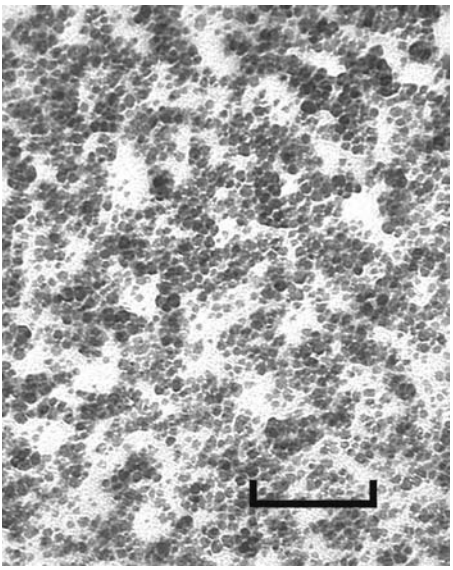

FIGURE 4.10 Nanograph of the Rhodamine 6G DDPN solid-state laser matrix. The indicated distance represents 200 nm. (From Duarte, F. J., and R. O. James, Spatial structure of dye-doped polymer nanoparticle laser media, *Appl. Opt.* 43: 4088–4090 (2004).)

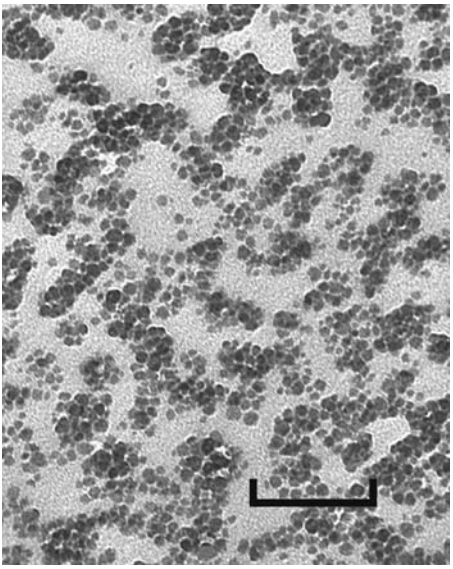

FIGURE 4.11 Nanograph of the coumarin 500 DDPN solid-state laser medium. The indicated distance represents 200 nm. (From Duarte, F. J., and R. O. James, Spatial structure of dye-doped polymer nanoparticle laser media, *Appl. Opt.* 43: 4088–4090 (2004).)

where λ is the wavelength, m is the diffraction order, d_j is the sum of the dimensions of the slits plus the islands, Θ_j is the angle of incidence, and Φ_j is the angle of diffraction.

Using the results from Table 4.4 it can be established that for the Rhodamine 6G DDPN matrix $d_j \approx 91$ nm, which, for $\lambda \approx 580$ nm, and $m = 1$ yields

$$(m\lambda)/d_j \approx 6.37 \tag{4.12}$$

For the coumarin 500 DDPN matrix $d_m \approx 99$ nm, $\lambda \approx 510$ nm, and $m = 1$ we have

$$(m\lambda)/d_j \approx 5.15 \tag{4.13}$$

TABLE 4.5
Dimensions of the Silicate Structure in the DDPN Matrices

Matrix	Slit dimensions (nm)	Island dimensions (nm)
Rhodamine 6G DDPN	49 ± 29	42 ± 31
Coumarin 500 DDPN	55 ± 32	57 ± 41

Source: From Duarte, F. J., and R. O. James, *Appl. Opt.* 43, 4088–4090, 2004.

Now, from Equation 4.2 the condition for diffraction is satisfied only with

$$(m\lambda)/d_j < 2 \tag{4.14}$$

which for the Rhodamine 6G DPN matrix, at $\lambda \approx 580$ nm, imposes $d_j > 290$ nm. For the coumarin 500 DPN matrix, $\lambda \approx 510$ nm, the imposition for diffraction becomes $d_j > 255$ nm.

Clearly the size of the nanoparticles coupled with their relative uniform distribution in the dye-doped polymer space do not meet the conditions for diffraction. Hence the absence of internal interference and the spatial homogeneity of the laser emission beam.

4.6 INVISIBILITY OF NANOPARTICLE DISTRIBUTIONS IN THE VISIBLE ELECTROMAGNETIC SPECTRUM

The subject of invisibility has evoked interest in the scientific literature for a long time [59–61]. In this particular section we are interested in invisibility qualities in the microscopic domain that may lead to new and useful optics materials and devices. Here *invisibility* is simply defined as the ability to avoid detection when illuminated in the visible portion of the electromagnetic spectrum. In particular, we are interested in transparency and in the ability to conserve the spatial characteristics of the electromagnetic field on transmission in an optical gain medium.

Two prominent tools to accomplish invisibility of a gain medium's internal structure are index of refraction matching and the use of extraordinarily small optical features. As mentioned, organic-inorganic gain matrices exhibiting a very slight mismatch of refractive indices can produce inhomogeneities in a propagating beam of coherent electromagnetic radiation in the visible spectrum. This is certainly true for a refractive index difference, of $\Delta n \approx 0.04$, between the dye-doped polymer and silica.

Given the existing mismatch in refractive indices, the improvement of $\partial n/\partial T$ characteristics, using silica, in a dye-doped solid-state organic-inorganic gain matrix requires a secondary approach. In our experience this secondary approach can be provided by silica nanoparticles provided they are uniformly distributed. In the previous section it was shown that albeit the nanoparticles do form clusters, these clusters are sufficiently small and assume a spatial distribution that is not favorable to the conditions necessary for internal diffraction. Hence, no diffraction means no distortion of the propagating electromagnetic field, thus no detection, and therefore *invisibility*. This was accomplished for distributions of SiO_2 nanoparticles in laser dye-doped polymer matrices as clearly shown in Figures 4.8 and 4.9 [17].

Albeit these experiments successfully demonstrated invisible distributions of nanoparticles, with a different refractive index to the host matrix, there is one further avenue to enhance the effect if necessary. This approach consists of augmenting the invisibility of the nanoparticles themselves. As explained by Duarte and James [51] and James et al. [62], using the teachings of Kerker [59–61], the conditions for invisibility can be improved if core-shell nanoparticles are used rather than traditional nanoparticles.

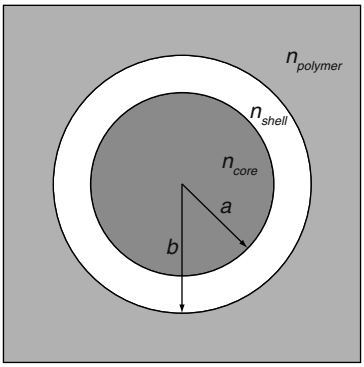

FIGURE 4.12 Simple diagram of a core-shell particle depicting the various parameters included in Equation 4.16.

For a composite core-shell nanoparticle it can be shown that for the condition [62]

$$n_{shell} < n_{polymer} < n_{core} \tag{4.15}$$

there is a particular ratio of shell core radius (a) to the coated composite radius (b) (see Fig. 4.11) at which the scattering produced by the coated nanoparticle will be a minimum so that the haze will be very low and hence transparency very high. This condition of particle invisibility is given at the ratio [59–62]

$$(b/a) = \left(\left(2f_2^2 + 1\right)\left(f_2^2 - f_1^2\right)/\left(f_2^2 - 1\right)\left(f_1^2 + 2f_2^2\right)\right)^{1/3} \tag{4.16}$$

where $f_1 = n_{core}/n_{polymer}$ and $f_2 = n_{shell}/n_{polymer}$. In [51, 62] an example is described using composite nanoparticles with a shell of silica and a core of ZnS dispersed in a polymer, like PMMA. This type of composite particle has a positive, higher value of $\partial n/\partial T$ than pure silica to offset the negative $\partial n/\partial T$ of the (PMMA) polymer matrix. This "core-shell" or "cloaked" particle in, say, PMMA provides an inorganic-organic hybrid with a lower magnitude $\partial n/\partial T$ than is possible with silica particles alone in PMMA. For detailed discussions of the electromagnetic theory applicable to core-shell particles dispersed in a polymeric matrix, readers are referred to additional papers published over the past two decades [63–65].

4.7 FUTURE APPLICATIONS OF DDPN GAIN MEDIA IN SPECTROSCOPY AND MEDICINE

Tunable dye lasers, in the liquid state, created a renaissance and golden age for a plethora of applications [66]. Prominent among these applications were laser spectroscopy [67] and laser medicine [68]. For an updated review of tunable dye laser applications in medicine please see Chapter 8 (Costela et al. [69]). Some of these applications have also become applications to solid-state dye lasers. Here we briefly

examine these two fields and suggest a number of areas where tunable solid-state dye lasers using DDPN gain media could be useful.

4.7.1 Laser Spectroscopy

Laser spectroscopy is a vast and diverse field. Among the numerous books and reviews on laser spectroscopy the following are particularly informative: Demtröder [70], Radziemski et al. [71], and Orr et al. [72]. In particular here we refer to pulse laser spectroscopy using narrow-linewidth tunable lasers. This class of solid-state tunable narrow-linewidth lasers is described in Section 4.2. The lasers yield tunable radiation in low-divergence single-transverse-mode beams, in the spatial domain, and single-longitudinal-mode emission, in the spectral domain. In particular, these solid-state lasers are capable of delivering linewidths in the 350 MHz $\leq \Delta\nu \leq$ 650 MHz range. Laser linewidths in this range are ideally suited for the excitation of single vibrational-rotational in small molecules, such as I_2, and of selective excitation in a wide range of atomic species [71, 73].

Albeit narrow-linewidth multiple-prism grating laser oscillators incorporating DDPN gain media have yet to be demonstrated, knowing what we already know about the spatial homogeneity of the emission with this media in the broadband domain, it is likely that the performance achieved with DDP media will be matched. The added advantage will be reduced beam divergence and the opportunity to operate at slightly higher pulse repetition frequencies. In summary: Narrow-linewidth tunable laser oscillators using solid-state DDP, or DDPN, gain media offer an attractive, optically rugged, and inexpensive alternative to perform laser spectroscopy to researchers involved in exploratory studies.

4.7.2 Laser Medicine

Dye lasers have an ample and rich history of applications in medicine. Relevant review and collective works include Goldman [68, 74] and Costela et al. [69]. Here we provide a very brief overview of the main applications of dye lasers to medicine and then mention more specific areas applicable to solid-state dye lasers that could also be applicable to solid-state dye lasers incorporating DDPN gain media.

Some of the more emblematic applications of tunable dye lasers in medicine include: photodynamic therapy (PDT) [68, 74], dermatology [68, 74], urology [75], and lithotripsy [75]. A dual tunable laser system for PDT, in which the excitation laser is also used as a diagnostic tool, was described by Duarte [76]. This concept is directly applicable to solid-state dye laser systems and other solid-state systems.

Solid-state pulsed dye lasers are often applicable where liquid dye lasers have been put to use. These applications include dermatology, lithotripsy, and urolithiasis. Further, solid-state dye lasers have already been applied in thrombolysis [77]. DDPN gain media offer improved thermal characteristics, good beam quality, and reduced beam divergence. Hence, it is reasonable to expect good performance in these medical applications using tunable lasers incorporating DDPN gain media.

As indicated previously the continuous tuning range demonstrated with narrow-linewidth solid-state dye lasers, powered by Rhodamine 6G-doped polymer gain media, is 565–610 nm [36]. The continuous tuning range demonstrated by

dye lasers, powered by Rhodamine 6G-doped polymer nanoparticle gain media, is 567–603 nm [17]. These tuning ranges overlap and overcover wavelength regions of interest for ophthalmology, dermatology, and biomedical diagnostics, for which fairly advanced all-solid-state media are being developed [78, 79]. The particular cited wavelength regions are 573 nm $\leq \lambda \leq$ 580 nm [78], and $\lambda \approx$ 588 nm [79], which are positioned near the maximum efficiency of the solid-state dye laser tuning ranges [17, 36].

For the above-mentioned medical applications, the wavelength coverage available, from dye-doped solid-state gain media, is optimum. The excellent performance of tunable narrow-linewidth laser oscillators, based on DDP gain media, has been amply documented [36–38]. Also, for applications needing relatively large pulse energies, at low prfs, these lasers are quite viable since they can be engineered to deliver tens to hundreds of mJ per pulse. The limitations in the area of average power can be partly minimized using DDPN gain media and other physical approaches that include rotation of the gain medium [80], which would have to be performed on a gain medium previously dimensioned using high-precision automated machinery, and using high-precision turning means in order to minimize measurable frequency jitter and microvariations in the beam profile.

REFERENCES

1. Sorokin, P. P., and J. R. Lankard, Stimulated emission observed from an organic dye, chloroaluminum phthalocyanine, *IBM J. Res. Dev.* 10: 162–163 (1966).
2. Schäfer, F. P., W. Schmidt, and J. Volze, Organic dye solution laser, *Appl. Phys. Lett.* 9: 306–309 (1966).
3. Soffer, B. H., and B. B. McFarland, Continuously tunable narrow-band organic dye lasers, *Appl. Phys. Lett.* 10: 266–267 (1967).
4. Peterson, O. G., and B. B. Snavely, Stimulated emission from flashlamp-excited organic dyes in polymethyl methacrylate, *Appl. Phys. Lett.* 12: 238–240 (1968).
5. Pacheco, D. P., H. R. Aldag, I. Itzkan, and P. S. Rostler, A solid-state flashlamp-pumped dye laser employing polymer hosts, in *Proceedings of the International Conference on Lasers '87*, edited by F. J. Duarte, STS, McLean, VA, 1988, pp. 330–337.
6. Dunn, B., J. D. Mackenzie, J. I. Zink, and O. M. Stafsudd, Solid-state tunable lasers based on dye-doped sol-gel materials, *Proc. SPIE* 1328: 174–182 (1990).
7. Duarte, F. J., Solid-state multiple-prism grating dye-laser oscillators, *Appl. Opt.* 33: 3857–3860 (1994).
8. Maslyukov, A., S. Solokov, M. Kaivola, K. Nyholm, and S. Popov, Solid-state dye laser with modified poly(methyl methacrylate)-doped active elements, *Appl. Opt.* 34: 1516–1518 (1995).
9. Duarte, F. J., J. J. Ehrlich, W. E. Davenport, T. S. Taylor, and J. C. McDonald, A new tunable dye laser oscillator: preliminary report, in *Proceedings of the International Conference on Lasers '92*, edited by C. P. Wang, STS, McLean, VA, 1993, pp. 293–296.
10. Hermes, R. E., T. H. Allik, S. Chandra, and J. A. Hutchinson, High-efficiency pyrromethene doped solid-state dye lasers, *Appl. Phys. Lett.* 63: 877–879 (1993).
11. Rahn, M. D., and T. A. King, Comparison of laser performance of dye molecules in sol-gel, polycom, ormosil, and poly(methyl methacrylate) host media, *Appl. Opt.* 34: 8260–8271(1995).
12. Costela, A., I. García-Moreno, and R. Sastre, in *Handbook of Advanced Electronic and Photonic Materials: Liquid Crystals, Display and Laser Materials*, edited by H. S. Nalwa, Academic, New York, 2001, pp. 161–208.

13. Costela, A., I. García-Moreno, and R. Sastre, Polymeric solid-state dye lasers: recent developments, *Phys Chem. Chem. Phys.* 5: 4745–4763 (2003).
14. Duarte, F. J., and A. Costela, Dye lasers, in *Encyclopedia of Modern Optics*, edited by B. D. Guenther, Elsevier, New York, 2004, pp. 400–414.
15. Costela, A., I. García-Moreno, and R. Sastre, Solid-state dye lasers, in *Tunable Laser Applications*, 2nd ed., edited by F. J. Duarte, Taylor and Francis, New York, 2008, Chap. 3.
16. Duarte, F. J., and E. J. A. Pope, Optical inhomogeneities in sol-gel derived ORMOSILs and nanocomposites, *Ceram. Transac.* 55: 267–273 (1995).
17. Duarte, F. J., and R. O. James, Tunable solid-state lasers incorporating dye-doped, polymer-nanoparticle gain media, *Opt. Lett.* 28: 2088–2090 (2003).
18. Costela, A., I. García-Moreno, D. del Agua, O. García, and R. Sastre, Silicon-containing organic matrices as host for highly photostable solid-state dye lasers, *Appl. Phys. Lett.* 85: 2160–2162 (2004).
19. Costela, A., I. García-Moreno, D. del Agua, O. García, and R. Sastre, Highly photostable solid-state dye lasers based on silicon-modified organic matrices, *J. Appl. Phys.* 101: 073110 (2007).
20. Costela, A., I. García-Moreno, D. del Agua, O. García, and R. Sastre, Solid-state dye lasers: new materials based on silicon, *Opt. J.* 1: 1–6 (2007).
21. Yang, Y., C. Ye, W. H. Ni, K. Y. Wong, M. Q. Wang, D. Lo, and G. D. Qian, Amplified spontaneous emission from infrared dye-doped zirconia-organically modified silicate thin film waveguides, *J. Sol-Gel Sci. Tech.* 44: 53–57 (2007).
22. Yang, Y., J. Zou, H. Rong, G. D. Qian, Z. Y. Wang, and M. Q. Wand, Influence of various coumarin dyes on the laser performance of laser dyes co-doped into ORMOSILs, *Appl. Phys. B* 86: 309–313 (2007).
23. Yang, Y., G. Lin, J. Zou, Z. Wang, M. Wang, and G. Qian, Enhanced laser performances based on energy transfer of multi-dyes co-doped solid media, *Opt. Commun.* 277: 138–142 (2007).
24. Sathiyamoorthy, K., C. Vijayan, and M. P. Kothiyal, Design of a low power optical limiter based on a new nanocomposite material incorporating silica-encapsulated phthalocyanine in nafion, *J. Phys. D: Appl. Phys.* 40: 6121–6128 (2007).
25. Nedumpara, R. J., K. Geetha, V. J. Dann, C. P. G. Vallabham, V. P. N. Nampoori, and P. Rhadakrishnan, Light amplification in dye-doped polymer films, *J. Opt. A: Pure Appl. Opt.* 9: 174–179 (2007).
26. Ray, A. K., S. Kumar, N. V. Mayekar, S. Sinha, S. Kundu, S. Chattopadhyay, and K. Dasgupta, Role of the stimulated-emission rate in the photostability of solid-state dye lasers, *Appl. Opt.* 44: 7814–7822 (2005).
27. Bañuelos Prieto, J., F. López Arbeloa, O. García, and I. López Arbeloa, Photophysics and lasing correlation of pyrromethene 567 dye in crosslinked polymeric networks, *J. Lumines.* 126: 833–837 (2007).
28. Maier, G. V., T. N. Kopilova, V. A. Svetlichnyi, V. M. Podgaetskii, S. M. Dolotov, O. V. Ponomareva, A. E. Monich, and E. A. Monich, Active polymer fibres doped with organic dyes: generation and amplification of coherent radiation, *Quantum Electron.* 37: 53–59 (2007).
29. Zhu, J., Y. Zhang, G. Dong, Y. Guo, and L. Guo, Single-layer dichromated gelatin material for Lippmann color holography, *Opt. Commun.* 241: 17–21 (2004).
30. Popov, S., S. Ricciardi, A. T. Friberg, and S. Sergeyev, Mode suppression in a microcavity solid-state dye laser, *J. Euro. Opt. Soc.* 2: 07023 (2007).
31. Ricciardi, S., S. Popov, A. Friberg, and S. Sergeyev, Thermally induced wavelength tenability of microcavity solid-state dye lasers, *Opt. Ex.* 15: 12971–12978 (2007).
32. López Arbeloa, F., J. Bañuelos, V. Martínez, T. Arbeloa, and T. López Arbeloa, Structural, photophysical and lasing properties of pyrromethene dyes, *Int. Rev. Phys. Chem.* 24: 339–371 (2005).

33. Duarte, F. J., Narrow-linewidth pulsed dye laser oscillators, in *Dye Laser Principles*, edited by F. J. Duarte and L. W. Hillman, Academic, New York, 1990, Chap. 4.
34. Duarte, F. J., *Tunable Laser Optics*, Elsevier Academic, New York, 2003.
35. Duarte, F. J., Solid-state dispersive dye laser oscillator: very compact cavity, *Opt. Commun.* 117: 480–484 (1995).
36. Duarte, F. J., Multiple-prism near-grazing-incidence grating solid-state dye laser oscillator, *Opt. Laser Technol.* 29: 513–516 (1997).
37. Duarte, F. J., Multiple-prism grating solid-state dye laser oscillator: optimized architecture, *Appl. Opt.* 38: 6347–6349 (1999).
38. Duarte, F. J., T. S. Taylor, A. Costela, I. García-Moreno, and R. Sastre, Long-pulse narrow-linewidth dispersive solid-state dye laser oscillator, *Appl. Opt.* 37: 3987–3989 (1998).
39. Duarte, F. J., Technology of pulsed dye lasers, in *Dye Laser Principles*, edited by F. J. Duarte and L. W. Hillman, Academic, New York, 1990, Chap. 5.
40. Duarte, F. J., Multiple-return-pass beam divergence and the linewidth equation, *Appl. Opt.* 40: 3038–3041 (2001).
41. Dirac, P. A. M., *The Principles of Quantum Mechanics*, 4th ed., Oxford, University, London, 1978.
42. Wadsworth, W. J., I. T. McKinnie, A. D. Woolhous, and T. G. Haskell, Efficient distributed feedback solid state dye laser with a dynamic grating, *Appl. Phys. B* 69: 163–165 (1999).
43. Zhu, X-L., S-K. Lam, and D. Lo, Distributed-feedback dye-doped solgel silicate lasers, *Appl. Opt.* 39: 3104–3107 (2000).
44. Oki, Y., S. Miyamoto, M. Tanaka, D. Zuo, and M. Maeda, Long lifetime and high repetition rate operation from distributed feedback plastic waveguided dye lasers, *Opt. Commun.* 214: 277–283 (2002).
45. Oki., Y., K. Aso, D. Zuo, N. J. Vasa, and M. Maeda, Wide-wavelength range operation of a distributed-feedback dye laser with a plastic waveguide, *Jpn. J. Appl. Phys.* 41: 6370–6374 (2002).
46. Oki, Y., M. Tanaka, Y. Ogawa, H. Watanabe, and M. Maeda, Development of quasi-end-fired waveguide plastic dye laser, *IEEE J. Quantum Electron.* 42: 389–396 (2006).
47. Duarte, F. J., Light emitting diode-pumped laser and method of excitation, US 2005/0083986A1 (2005).
48. Duarte, F. J., R. O. James, and L. A. Rowley, Dye-doped polymer nanoparticle gain medium for use in a laser, US 2004/0120373 A1 (2004).
49. Duarte, F. J., and R. O. James, Dye-doped polymer-nanoparticle gain media for tunable solid-state lasers, *Mat. Res. Soc. Symp. Proc.* 817: 201–206 (2004).
50. Duarte, F. J., and R. O. James, Spatial structure of dye-doped polymer nanoparticle laser media, *Appl. Opt.* 43: 4088–4090 (2004).
51. Duarte, F. J., and R. O. James, Dye-doped polymer nanoparticle gain medium, US Patent 6888862 B2 (2005).
52. Popov, S., Influence of pump repetition rate on dye photostability in a solid-state dye laser with a polymeric gain medium, *Pure Appl. Opt.* 7: 1379–1388 (1998).
53. Hillman, L. W., Laser dynamics, in *Dye Laser Principles*, edited by F. J. Duarte and L. W. Hillman, Academic, New York, 1990, Chap. 2.
54. Duarte, F. J., A. Costela, I. García-Moreno, and R. Sastre, Measurements of $\partial n/\partial T$ in solid-state dye-laser gain media, *Appl. Opt.* 39: 6522–6523 (2000).
55. Duarte, F. J., Dispersive dye lasers, in *High Power Dye Lasers*, edited by F. J. Duarte, Springer, Berlin, 1991, Chap. 2.
56. Duarte, F. J., On a generalized interference equation and interferometric measurements, *Opt. Commun.* 103: 8–14 (1993).
57. Duarte, F. J., *Tunable Laser Optics,* Elsevier Academic, New York, 2003, Chap. 2.

58. Duarte, F. J., Interference, diffraction, and refraction, via Dirac's notation, *Am. J. Phys.* 65: 637–640 (1997).
59. Kerker, M., *The Scattering of Light and Other Electromagnetic Radiation*, Academic, New York, 1969.
60. Kerker, M., Invisible bodies, *J. Opt. Soc. Am.* 65: 376–379 (1975).
61. Kerker, M., Elastic scattering, absorption, and surface-enhanced raman scattering by concentric spheres comprised of a metallic and a dielectric region, *Phys. Rev. B* 26: 4052–4063 (1982).
62. James, R. O., L. A. Rowley, D. F. Hurley, and J. Border, Core shell nanocomposite optical plastic article, US Patent 7091271 B2 (2006).
63. Duarte, F. J. (Ed.), *Proceedings of the International Conference on Lasers '87*, STS, McLean, VA, 1988.
64. Alu, A., and N. Engheta, Achieving transparency with plasmonic and metamaterials coatings, *Phys. Rev. E* 72: 016623 (2005).
65. Small, A., S. Hong, and D. Pine, Scattering properties of core-shell particles in plastic matrices, *J. Poly. Sci. B: Poly. Phys.* 43: 3534–3548 (2005).
66. Duarte, F. J., J. A. Paisner, and A. Penzkofer, Dye lasers: introduction by the feature editors, *Appl. Opt.* 31: 6977–6978 (1992).
67. Demtröder, W., *Laser Spectroscopy*, 3rd ed., Springer, Berlin, 2003.
68. Goldman, L., Dye lasers in medicine, in *Dye Laser Principles*, edited by F. J. Duarte and L. W. Hillman, Academic, New York, 1990, Chap. 10.
69. Costela, A., I. García-Moreno, and R. Sastre, Medical applications of dye lasers, in *Tunable Laser Applications*, 2nd ed., edited by F. J. Duarte, CRC, New York, 2008, Chap. 8.
70. Demtröder, W., *Laser Spectroscopy*, Springer, Berlin, 2003.
71. Radziemski, L. J., R. W. Solarz, and J. A. Paisner (Eds.), *Laser Spectroscopy and Its Applications*, Marcel Dekker, New York, 1987.
72. Orr, B. J., R. T. White, and Y. He, Spectroscopic applications of tunable optical parametric oscillators, in *Tunable Laser Applications*, 2nd ed., edited by F. J. Duarte, CRC, New York, 2008, Chap. 2.
73. Duarte, F. J., and D. R. Foster, Lasers, dye, in *The Optics Encyclopedia,* Volume 2, edited by T. G. Brown et al., Wiley-VCH, Weinheim, 2004, pp. 1065–1096.
74. Goldman, L. (Ed.), *Laser Non-Surgical Medicine*, Technomic, Lancaster, PA, 1991.
75. Floratos, D. L., and J. J. M. C. H. de la Rosette, Lasers in urology, *BJU Int.* 84: 204–211 (1999).
76. Duarte, F. J., Two-laser therapy and diagnosis device, EP 0284330 A1 (1988).
77. Aldag, H. R., Solid-state dye laser for medical applications, *Proc. SPIE* 2115: 184–189 (1994).
78. Sinha, S., C. Langrock, M. J. F. Digonnet, M. F. Fejer, and R. L. Byer, Efficient yellow-light generation by frequency doubling a narrow-linewidth 1150 nm ytterbium fiber oscillator, *Opt. Lett.* 31: 347–349 (2006).
79. Dekker, P., H. M. Pask, and J. A. Piper, All-solid-state 704 mW continuous-wave yellow source based on an intracavity, frequency doubled crystalline Raman laser, *Opt. Lett.* 32: 1114–1116 (2007).
80. Abedin, K. M., M. Alvarez, A. Costela, I. García-Moreno, O. García, R. Sastre, D. W. Coutts, and C. E. Webb, 10 kHz repetition rate solid-state dye laser pumped by diode-pumped solid-state laser, *Opt. Commun.* 218: 359–363 (2003).

5 Broadly Tunable External-Cavity Semiconductor Lasers

F. J. Duarte

CONTENTS

5.1 Introduction 143
5.2 Dispersive Oscillator Cavities 144
5.2.1 Optimized Dispersive Oscillator Cavities 147
5.3 Optical Theory 149
5.3.1 Interference and Diffraction 150
5.3.2 Intracavity Dispersion 150
5.3.3 Ray Transfer Matrices 155
5.3.4 Linewidth 157
5.3.5 Wavelength Tuning 158
5.3.6 Tuning Miniature MEMS-Driven Cavities 159
5.3.7 Tuning Using Bragg Gratings 163
5.4 Performance of Tunable External-Cavity Semiconductor Lasers 163
5.5 Performance of Ultrashort-Pulse External-Cavity Semiconductor Lasers 166
5.6 Applications 167
5.7 Conclusion 170
References 172

5.1 INTRODUCTION

Tunable semiconductor lasers have become widely used in a plethora of applications including communications, imaging, interferometry, medicine, metrology, remote sensing, and spectroscopy. Advantages of tunable semiconductor lasers include direct electrical excitation, compactness, low cost, and simplicity.

The approximate spectral coverage available from II–VI and III–V type tunable semiconductor lasers is outlined in Table 5.1. Lasers powered by II–VI semiconductors emit in the blue portion of the visible spectrum, while lasers powered by III–V semiconductors emit in the red and near-infrared parts of the spectrum. At present, the most widely used tunable external-cavity semiconductor (ECS) lasers belong to

TABLE 5.1
Approximate Wavelength Ranges Covered by Broadly Tunable Semiconductor Lasers

Semiconductor type	Spectral range
II–VI (GaN)	395 nm ≤ λ ≤ 410 nm
III–V (AlGaInP/GaAs)	660 nm ≤ λ ≤ 680 nm
III–V (GaAlAs)	815 nm ≤ λ ≤ 825 nm
III–V (InGaAsP/InP)	1255 nm ≤ λ ≤ 1335 nm
III–V (InGaAsP/InP)	1530 nm ≤ λ ≤ 1570 nm

the III–V classification and employ GaAlInP, GaAlAs, and InGaAsP semiconductors. Single-device continuous-wave (CW) power levels offered by these lasers, at room temperature, can range from a few milliwatts to hundreds of mW. CW powers in the multi-W regime are available from diode arrays. In general, these lasers are of the index-guided class with buried heterostructures.

Semiconductor lasers are intrinsically tunable, and the extent of their tunability depends approximately on the characteristics of the energy band gap, operating temperature, and current density. The basic physics and technological features are explained and discussed in several books and review articles [1–9].

This chapter focuses on semiconductor tunable lasers operating at room temperature. Further, the scope is limited to tunable semiconductor lasers utilizing external dispersive and/or frequency-selective optics. This approach is justified because external cavities are a very effective avenue to frequency tuning in semiconductor lasers. In addition, external cavities provide access to a variety of optical architectures and well-proven frequency-selective techniques previously developed for other tunable lasers, such as dye lasers, crystalline solid-state lasers, and gas lasers [10–13].

The discussion on frequency selectivity and tuning in this chapter is applicable in general to any emission wavelength, type of semiconductor, and physical dimensions of the active medium. Although most of the open literature information concerning tunable ECS lasers refers to III–V semiconductors, the event of II–VI type lasers [14–16] has also led to the introduction of ECS lasers, powered by II–VI gain media, which will be mentioned in Section 5.6.

5.2 DISPERSIVE OSCILLATOR CAVITIES

In general, tunable external-cavity semiconductor (ECS) lasers employ cavity configurations developed for earlier tunable lasers, such as the dye laser. A detailed survey and classification of dispersive cavity configurations for organic dye lasers, both in the liquid and solid state, is given in [10–13]. In this regard, it should be mentioned that cavity configurations developed for dye lasers have been specifically adopted to provide narrow-linewidth tunable emission in various other types of lasers including high-power gas lasers [12, 17] and semiconductor lasers [18].

Although, in principle, the concepts and configurations can be easily adopted from the domain of the dye laser for application to ECS lasers, there are some

intrinsic differences to consider. First, dye lasers are high-gain pulsed lasers and the boundary between the gain medium and the cavity can be easily made to yield low reflectivity with antireflection (AR) coating and windows at an angle relative to the plane of propagation. On the other hand, semiconductor and diode lasers of interest emit in the CW regime and the high-refractive indices available naturally yield relatively high reflectivity at the gain boundaries. Because extended wavelength tuning ranges, in ECS lasers, depend on the availability of facets with low reflectivities, antireflection coatings become very important. In this regard, antireflection coatings are particularly relevant to the semiconductor facet adjacent to the tuning optics.

Given the existence of facets with intrinsic higher reflectivity, the concepts of *open* and *closed* cavities assume more importance. This can be further emphasized by the need to protect the cavity from unwanted external optical feedback.

An open cavity is configured to couple the output beam via the reflection losses of one of its optical or dispersive components [12, 13]. In a closed cavity, the output beam exits the cavity through an output coupler mirror. The advantage of closed-cavity over open-cavity laser configurations was highlighted by Duarte and Piper [19, 20]. In those works, it was demonstrated that in the case of high-gain tunable laser oscillators, closed-cavity configurations yielded considerable reductions in optical noise emission, or amplified spontaneous emission (ASE), and prevented unwanted optical feedback with optical elements external to the cavity.

Here a survey is given of open and closed dispersive cavities. In the case of open cavities, it is assumed that one of the facets of the semiconductor is antireflection coated, whereas in the case of the closed-cavity configuration, both output facets must be antireflection coated.

Open cavities are illustrated in Figure 5.1 and include a simple mirror-grating cavity with intracavity étalon(s) where the output is coupled via an intracavity beamsplitter [21]. Additional open-cavity configurations include the single-prism grating cavity [22] and the pure grazing-incidence cavity [23] (Figs. 5.1b and c). In the case of the single-prism cavity, the output is coupled via the reflection losses of the prism, and in the case of the grazing-incidence cavity, the output emission exits the cavity via the reflection losses at the grating. This latter cavity can also be used in a closed configuration [24]. Grazing-incidence grating cavities are also known in the literature as Littman cavities.

Closed cavities are depicted in Figure 5.2. These include simple mirror-grating cavities where the output emission is coupled via the output mirror [25]. These cavities can also incorporate one or more étalons (Fig. 5.2b).

Additional closed-cavity configurations include the multiple-prism grating cavities [12, 13, 26] as illustrated in Figure 5.3. The multiple-prism Littrow (MPL) grating laser cavities utilize multiple-prism beam expanders in a variety of configurations [13] deployed to either augment or neutralize the intracavity multiple-prism dispersion (see Figs. 5.3a and b). The basic principle in these cavities is to expand the intracavity beam to totally illuminate the dispersion grating deployed in a Littrow configuration. An alternative design that yields higher dispersions but lower efficiencies is the hybrid multiple-prism near grazing-incidence (HMPGI) grating laser cavity depicted in Figure 5.4. However, HMPGI grating cavities can be more compact than MPL grating resonators and more efficient than pure

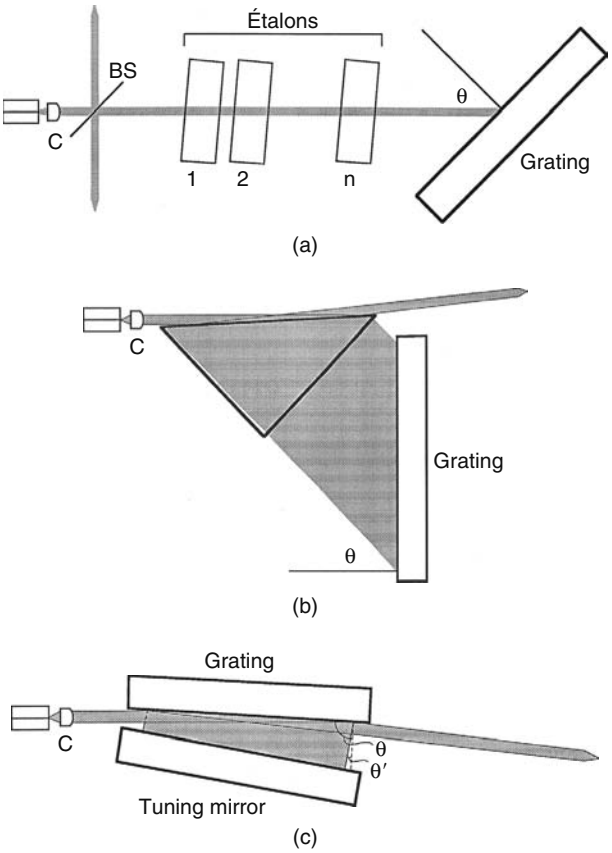

FIGURE 5.1 Open-cavity configurations: (a) mirror-grating cavity incorporating intracavity étalons; (b) single-prism grating cavity; and (c) grazing-incidence grating cavity.

grazing-incidence configurations used in a closed-cavity mode. Extensive discussions on the performance and design of these cavities are provided in [12, 13]. It should be noted that an alternative abbreviation for MPL grating cavities is MPLG cavities. Also, hybrid multiple-prism near grazing-incidence grating cavities can be abbreviated MPNGIG cavities. The early use of the word *hybrid* was meant to convey the dual use of prismatic beam expansion with gratings deployed in a near grazing-incidence configuration. Here we continue using MPL and HMPGI to maintain consistency with early literature on the subject. In general both configurations can be referred to as multiple-prism grating cavities.

Closed cavities in tunable semiconductor lasers were introduced early by Fleming and Mooradian [25] in a simple mirror-grating configuration. Also the emission characteristic advantages of these configurations have been clearly highlighted in cavities comprising generalized multiple-prism grating tuning configurations [18, 26–28] since the early 1990s. However, for a long time they were the exception rather than the rule. Slowly they have become more prevalent, and today they take center stage in tunable cavity configurations controlled by microelectromechanical systems (MEMS) [29].

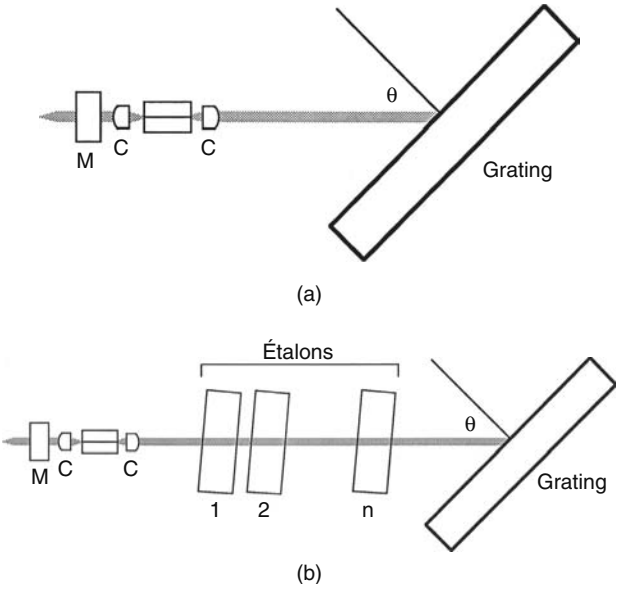

FIGURE 5.2 Closed-cavity configurations: (a) mirror-grating cavity and (b) mirror-grating cavity incorporating intracavity étalons. Note that the use of an independent output coupler mirror is still not common practice.

In the following discussion, tunable ECS lasers using dispersive optics for frequency selectivity are referred to as dispersive ECS lasers, or more appropriately as dispersive ECS laser oscillators.

5.2.1 Optimized Dispersive Oscillator Cavities

In addition to the open-cavity noise, and vulnerability to external coupling, designers of tunable semiconductor lasers have to deal with asymmetry of the emission beam, which is often not circular but ellipsoidal. These problems can be eliminated in an integrated approach to dispersive cavity configurations applicable to ESC lasers. Prior to further details the reader might wish to consult the literature of optimized solid-state organic tunable lasers where the basics are discussed [13, 30].

A variant of a closed cavity was introduced by Laurila et al. [31]. These authors coupled the output from a transmission grating deployed in Littrow configuration. An improvement on this approach can also solve the problem of beam asymmetry. This is because the cross-sectional area of the gain region, perpendicular to the plane of propagation, is often asymmetrical, with dimensions like 4 μm × 1 μm [32]. In this regard, deployment of the gain region to yield a vertically elongated ellipsoidal beam can be compensated by using prismatic, or multiple-prism, beam expansion parallel to the plane of propagation in order to yield a circular beam. Such cavity architecture was disclosed in [13].

A disadvantage with this concept, however, is that tuning performed by the angular rotation of the grating might lead to minor deviation of the output beam due to refraction induced at the substrate of the transmission diffraction grating. A better

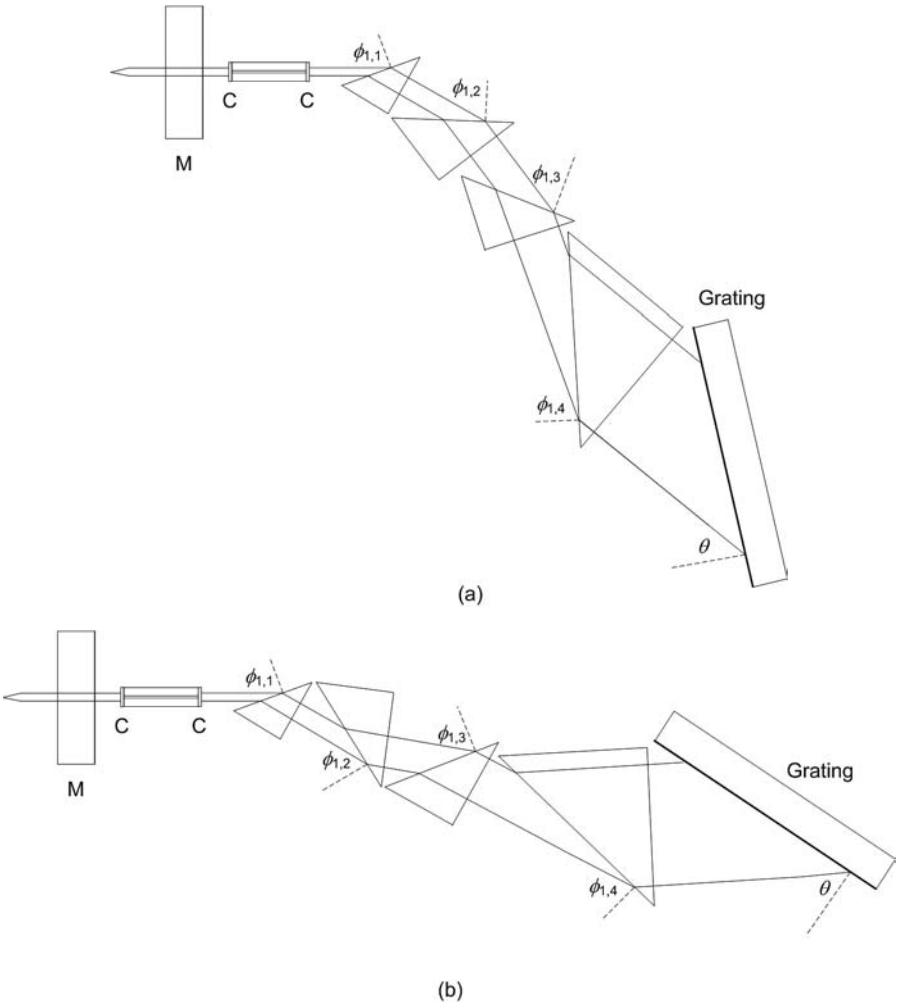

FIGURE 5.3 MPL grating oscillator configurations: (a) the multiple-prism expander can be deployed in a (+, +, +, −) configuration or (b) a (+, −, +, −) configuration. (These dispersive cavity configurations were introduced to ECS lasers in Duarte, F. J., Multiple-prism grating designs tune diode lasers, *Laser Focus World* 29 (2): 103–109 (1993).)

solution is to use beam expansion at both ends of the cavity—that is, beam expansion as previously disclosed to illuminate the tuning grating and reduced beam expansion at the output coupler end to correct for beam asymmetry. The architecture of such an oscillator is shown in Figure 5.5.

A reflection diffraction grating, in Littrow configuration, is illuminated with an expanded intracavity beam to induce narrow-linewidth oscillation. At the output end of the cavity, moderate beam expansion is used to produce a near circular beam profile. Although more elaborate, this double multiple-prism architecture eliminates the possible beam deviations induced by substrate refraction, while coupling the beam via a transmission grating. It should also be noted that in this configuration the

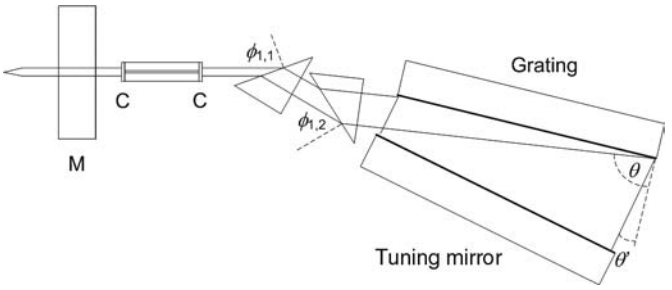

FIGURE 5.4 HMPGI grating laser oscillator. (This dispersive cavity configuration was introduced to ECS lasers in Duarte, F. J., Multiple-prism grating designs tune diode lasers, *Laser Focus World* 29 (2): 103–109 (1993).)

beam expansion illuminating the grating can be as large as necessary to illuminate the whole useful diffractive length of the grating. This circular-beam concept also applies to hybrid multiple-prism near grazing-incidence (HMPGI) grating configurations. Collimators, adjacent to the gain media, are identified by the letter C, while the output coupler mirrors are labeled M.

5.3 OPTICAL THEORY

In this section, theoretical elements applicable to the characterization of intracavity beam propagation are summarized. Topics considered are interference and/or diffraction, intracavity dispersion, and beam propagation matrices.

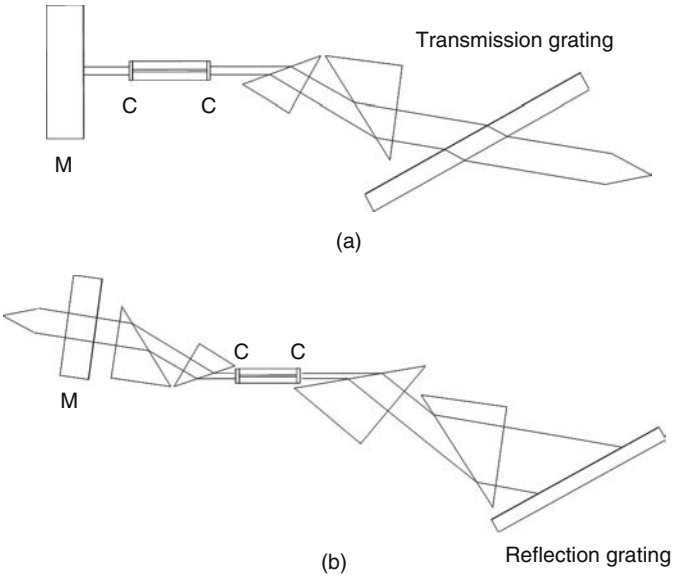

FIGURE 5.5 Circular-beam close-cavity MPL grating laser oscillators: (a) Moderate beam expansion corrects the asymmetry of the vertically elongated beam and enhances the dispersion of the cavity via the expanded illumination of a transmission diffraction grating; (b) beam expansion at both ends of the cavity.

5.3.1 Interference and Diffraction

Application of the Dirac method [33] to describe the interaction of electromagnetic radiation and a generalized grating led to the probability equation [11, 34]

$$\left|<x \mid s>\right|^2 = \sum_{j=1}^{N}\Psi(r_j)^2 + 2\sum_{j=1}^{N}\Psi(r_j)\left(\sum_{m=j+1}^{N}\Psi(r_m)\cos(\Omega_m - \Omega_j)\right) \tag{5.1}$$

In this generalized, one-dimensional, interferometric equation $<x \mid s>$ represents the probability amplitude for propagation from a source (s) to a screen (x) via a grating (j) comprised of N slits. The wave functions $\Psi(r_j)$ and $\Psi(r_m)$ are "ordinary wave functions of classical optics" as described by Dirac [33], and $\cos(\Omega_m - \Omega_j)$ is the interference term. The interference term, in conjunction with the geometry of the N-slit interferometer, give origin to the diffraction grating equation [34, 35]

$$m\lambda = d(\sin\theta \pm \sin\theta') \tag{5.2}$$

where λ is the wavelength, m is the order of diffraction, d is the number of slits (or grooves) per meter, θ is the angle of incidence, and θ' is the angle of diffraction. For further detail, see Chapter 12.

Equation 5.1 can be used to describe diffraction by a single wide slit, or aperture, by representing the aperture by a large number of small slits [34, 35]. Hence, the transverse-mode structure characteristic of given physical dimensions of a gain region can also be established.

As the cross-sectional areas (transverse to the optical axis) of the gain regions in semiconductor lasers are very small, the corresponding Fresnel numbers are also small. An example where these calculations can be useful concerns relatively wide cross-sectional areas. For instance, Voumard [36] discusses the use of GaAlAs lasers in an external cavity at $\lambda \approx 874$ nm. The dimensions of the gain region are given as 285 μm long and 20 μm wide [36]. Hence, the Fresnel number along the 20-μm width becomes $N \approx 0.4$, and the beam profile along this dimension can be calculated using Equation 5.1. At this stage, it should be emphasized that for a true external cavity, where the facets of the diode are antireflection coated, the beam profile will be determined by the emission wavelength, the dimensions of the aperture, and the *overall length* of the cavity.

5.3.2 Intracavity Dispersion

Dispersive cavities incorporate prisms, gratings, and/or combinations of these optical elements. Indeed, multiple-prism grating assemblies are widely used in narrow-linewidth tunable dye, gas, and solid-state lasers [10, 13]. Here, the basic dispersion formulas of gratings, multiple prisms, and multiple-prism grating assemblies are given.

Starting from Equation 5.2 the dispersion of a grating mirror combination (see Fig. 5.4) can be shown [23, 24, 37] to be given by

$$\left(\frac{\partial\theta}{\partial\lambda}\right)_G = \frac{2(\sin\theta \pm \sin\theta')}{\lambda\cos\theta} \tag{5.3}$$

or in its equivalent form

$$\left(\frac{\partial\theta}{\partial\lambda}\right)_G = \frac{2m}{d\cos\theta} \tag{5.4}$$

where m is the diffraction order and d is the groove spacing. For a grating in a Littrow configuration (Fig. 5.3), the dispersion is given by [38]

$$\left(\frac{\partial\theta}{\partial\lambda}\right)_G = \frac{2\tan\theta}{\lambda} \tag{5.5}$$

Note that in the Littrow configuration, the angle of incidence θ equals the angle of diffraction θ'.

For a multiple-prism grating assembly, the double-pass dispersion is given by [10, 11]

$$\left(\frac{\partial\theta}{\partial\lambda}\right) = M\left(\frac{\partial\theta}{\partial\lambda}\right)_G + \left(\frac{\partial\Phi}{\partial\lambda}\right)_P \tag{5.6}$$

where the generalized multiple-prism dispersion for a prismatic assembly composed of r prisms (see Fig. 5.6) is given, for a single-pass, by [10, 11, 13, 39]

$$\left(\frac{\partial\phi_{2,m}}{\partial\lambda}\right) = \mathcal{H}_{2,m}\left(\frac{\partial\phi_{2,m}}{\partial n_n}\right) + (k_{1,m}k_{2,m})^{-1}\left(\mathcal{H}_{1,m}\left(\frac{\partial\phi_{1,m}}{\partial n_m}\right) \pm \frac{\partial\phi_{2,m-1}}{\partial\lambda}\right) \tag{5.7}$$

whose double-pass version, in a more explicit notation, becomes [10, 40]

$$\begin{aligned}\left(\frac{\partial\Phi}{\partial\lambda}\right)_P = {} & 2M\sum_{m=1}^{r}(\pm1)\mathcal{H}_{1,m}\left(\prod_{j=m}^{r}k_{1,j}\prod_{j=m}^{r}k_{2,j}\right)^{-1}\left(\frac{\partial n_m}{\partial\lambda}\right) \\ & + 2\sum_{m=1}^{r}(\pm1)\mathcal{H}_{2,m}\left(\prod_{j=1}^{m}k_{1,j}\prod_{j=1}^{m}k_{2,j}\right)\left(\frac{\partial n_m}{\partial\lambda}\right)\end{aligned} \tag{5.8}$$

where

$$\mathcal{H}_{1,m} = (\tan\phi_{1,m})/n_m \tag{5.9}$$

$$\mathcal{H}_{2,m} = (\tan\phi_{2,m})/n_m \tag{5.10}$$

and

$$M = \prod_{j=1}^{r}k_{1,j}\prod_{j=1}^{r}k_{2,j} \tag{5.11}$$

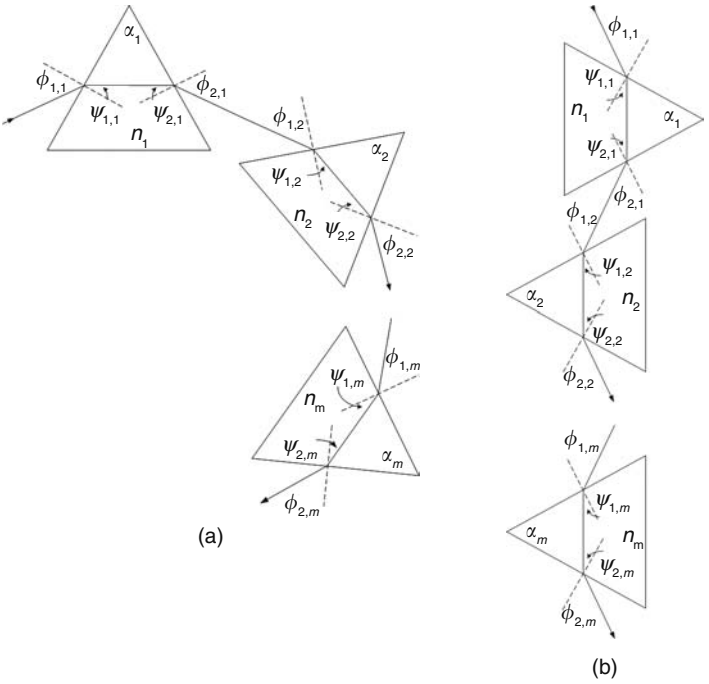

FIGURE 5.6 Generalized multiple-prism array deployed in (a) an additive configuration and (b) a compensating configuration.

is the total beam expansion. Also

$$k_{1,j} = \frac{\cos\psi_{1,j}}{\cos\phi_{1,j}} \tag{5.12}$$

$$k_{2,j} = \frac{\cos\phi_{2,j}}{\cos\psi_{2,j}} \tag{5.13}$$

where $\phi_{1,j}$ and $\phi_{2,j}$ are the incidence and exit angles, respectively, at each individual prism. The angles of incidence and refraction are related by the law of refraction also known as Snell's law

$$\sin\phi_{1,j} = n(\lambda)\sin\psi_{1,j} \tag{5.14}$$

As a matter of generality the reader should be aware that both the diffraction grating equation (Equation 5.2), Snell's law, and the reflection law can be derived, in sequence, from the generalized interference equation (Equation 5.1) [13, 35].

The single-pass dispersion provided by the multiple-prism beam expander can be obtained by multiplying $(\partial\Phi/\partial\lambda)_P$ by $1/(2M)$ (this is given in Chapter 12).

For the case of a multiple-prism expander composed of right-angled prisms (see Fig. 5.3) designed for orthogonal beam exit, that is, $\phi_{2,m} = \phi_{2,m} = 0$, Equation 5.8 reduces to

$$\left(\frac{\partial \Phi}{\partial \lambda}\right)_P = 2M \sum_{m=1}^{r} (\pm 1)\mathcal{H}_{1,m}\left(\prod_{j=m}^{r} k_{1,j}\right)^{-1}\left(\frac{\partial n_m}{\partial \lambda}\right) \tag{5.15}$$

where the beam-expansion factor now assumes the simpler form

$$M = \prod_{j=1}^{r} k_{1,j} \tag{5.16}$$

Further, if the angle of incidence at each prism is the Brewster's angle and all prisms are made of the same material, then Equation 5.15 can be succinctly expressed as [10]

$$\left(\frac{\partial \Phi}{\partial \lambda}\right)_P = 2\sum_{m=1}^{r} (\pm 1) n^{m-1}\frac{\partial n}{\partial \lambda} \tag{5.17}$$

and the beam-expansion coefficient becomes

$$M = n^r \tag{5.18}$$

In Equations 5.8, 5.15, and 5.17, the (±1) factor designates whether the prism is being deployed in a positive (+) or compensating (–) configuration. Explicit examples of closed-form analytical design of dispersionless, that is, $(\partial\Phi/\partial\lambda)_P = 0$, multiple-prism beam expanders are given in [11] and [40].

Dispersionless multiple-prism beam expanders are useful to relinquish control of the tuning characteristics of the oscillator to the grating exclusively. Further, as discussed by Duarte [10], the design of a multiple-prism beam expander with $(\partial\Phi/\partial\lambda)_P = 0$ reduces intracavity beam deviations due to thermal changes because [10]

$$\frac{\partial \phi_{2,r}}{\partial T} = \left(\frac{\partial \phi_{2,r}}{\partial \lambda}\right)\left(\frac{\partial n}{\partial \lambda}\right)^{-1}\left(\frac{\partial n}{\partial T}\right) \tag{5.19}$$

where

$$\frac{\partial \phi_{2,r}}{\partial \lambda} = (2M)^{-1}\left(\frac{\partial \Phi}{\partial \lambda}\right)_P \tag{5.20}$$

This can be quite important in the design and construction of stabilized dispersive oscillators.

For pulse-compression calculations in lasers incorporating multiple-prism compressors, the single-pass dispersion is given by [39, 41, 42]

$$\left(\frac{\partial \phi_{2,m}}{\partial n_m}\right) = \mathcal{H}_{2,m} + (k_{1,m}k_{2,m})^{-1}\left(\mathcal{H}_{1,m} \pm \frac{\partial \phi_{2,m-1}}{\partial n_m}\right) \tag{5.21}$$

and the second derivative can be written as [41, 42]

$$\left(\frac{\partial^2\phi_{2,m}}{\partial n_m^2}\right) = \mathcal{H}_{2,m}n_m\left(\frac{\partial\phi_{2,m}}{\partial n_m}\right)^2 + (k_{2,m})^{-1}\left(\frac{\partial\psi_{1,m}}{\partial n_m} + \frac{\partial\psi_{2,m}}{\partial n_m}\right)$$
$$+ (k_{2,m})^{-1}\mathcal{H}_{1,m}n_m\tan\psi_{1,m}\frac{\partial\phi_{1,m}}{\partial n_m} \pm (k_{1,m}k_{2,m})^{-1}\frac{\partial^2\phi_{2,m-1}}{\partial n_m^2} \quad (5.22)$$
$$+ \left(\mathcal{H}_{1,m} \pm \frac{\partial\phi_{2,m-1}}{\partial n_m}\right)\left((k_{1,m}k_{2,m})^{-1}\tan\psi_{1,m}\frac{\partial\psi_{1,m}}{\partial n_m}\right.$$
$$\left. - (k_{2,m})^{-1}n_m\tan\psi_{1,m}\frac{\partial\phi_{1,m}}{\partial n_m} - (k_{1,m})^{-1}\mathcal{H}_{2,m}\frac{\partial\psi_{2,m}}{\partial n_m}\right)$$

For the case of a multiple-prism compressor designed for collinear beam transmission and composed by two balanced compensating pairs [43], the derivatives reduced to [41, 42]

$$\frac{\partial\phi_{2,1}}{\partial n} = \frac{\partial\phi_{2,3}}{\partial n} = 2 \quad (5.23)$$

$$\frac{\partial\phi_{2,2}}{\partial n} = \frac{\partial\phi_{2,4}}{\partial n} = 0 \quad (5.24)$$

$$\frac{\partial^2\phi_{2,1}}{\partial n^2} = \frac{\partial^2\phi_{2,3}}{\partial n^2} = 4n - \frac{2}{n^3} \quad (5.25)$$

$$\frac{\partial^2\phi_{2,2}}{\partial n^2} = \frac{\partial^2\phi_{2,4}}{\partial n^2} = 0 \quad (5.26)$$

for minimum deviation and incidence of the Brewster angle. Certainly, for incidence at angles other than the Brewster angle, Equations 5.21 and 5.22 must be used. Duarte [42] has calculated the $\partial\phi_{2,m}/\partial n$ and $\partial^2\phi_{2,m}/\partial n^2$ values for incidence at angles other than the Brewster angle.

The $\partial\phi_{2,m}/\partial n$ and $\partial^2\phi_{2,m}/\partial n^2$ values are used in calculating the second derivative of the optical path length ($d^2P/d\lambda^2$) through the prisms. In turn, $d^2P/d\lambda^2$ is used to determine the value of the group velocity dispersion (GVD) constant [43].

Recent progress in prismatic, and multiple-prism, pulse compression includes the detailed experimental measurements of Osvay et al. [44, 45], where the effect of beam deviations was studied. These researchers studied, using an 18 fs Ti:sapphire laser, the effect of slight beam deviations on a double-prism pulse compressor [44]. They obtained excellent agreement from theoretical predictions, using Equations 5.21 and 5.22, and measurements. These studies were extended to include the effect

of noncompensated angular dispersion on the temporal lengthening of femtosecond pulses [45]. A more recent study of pulse compression with prism pairs was reported by Arissian and Diels [46]. An excellent review on the subject of prismatic pulse compression is given by Diels and Rudolph [47]. Equations 5.21 and 5.22 are also given, using a more succinct notation, in [13] and Chapter 13.

The transmission efficiency of an intracavity multiple-prism can be estimated using expressions for the cumulative reflection losses at the incidence face of the *m*th prism [11],

$$L_{1,m} = L_{2,m-1} + (1 - L_{2,m-1})R_{1,m} \tag{5.27}$$

and the cumulative reflection losses at the exit face,

$$L_{2,m} = L_{1,m} + (1 - L_{1,m})R_{2,m} \tag{5.28}$$

Here, $R_{1,m}$ and $R_{2,m}$ are the individual losses occurring at the *m*th prism and are given by the well-known Fresnel equations [13, 37] for *s*- and *p*-polarization. At this stage, it should be mentioned that the oscillators incorporating multiple-prism grating assemblies emit radiation that is strongly polarized parallel to the plane of incidence (or propagation) [10, 13]. The issue of polarization in multiple-prism grating oscillators is discussed in [10].

5.3.3 Ray Transfer Matrices

Ray transfer matrices of interest include the well-known *ABCD* matrices and more complete 3×3 and 4×4 matrix systems. For an introduction to ray transfer matrix systems, the reader should consult [11, 48–51]. Ray transfer matrices of interest to ECS lasers include those incorporating parameters to describe intracavity space, lenses, grating, mirrors, and prisms. In this regard, ray transfer matrices describing the overall optical system can be derived and used in describing the profile of the intracavity beam [52] via

$$w(x) = w_0\left[A^2 + \left(\frac{B}{L_R}\right)^2\right]^{1/2} \tag{5.29}$$

where w_0 is the beam waist at the output facet of the gain region and

$$L_R = (\pi w^2)/\lambda \tag{5.30}$$

is the Rayleigh length.

The *ABCD* ray transfer matrix for a length of space *L* with a refractive index *n* is given by [49]

$$\begin{pmatrix} A & B \\ C & D \end{pmatrix} = \begin{pmatrix} 1 & L/n \\ 0 & 1 \end{pmatrix} \tag{5.31}$$

For a lens, the ray transfer matrix is given by

$$\begin{pmatrix} A & B \\ C & D \end{pmatrix} = \begin{pmatrix} 1 & 0 \\ C & 1 \end{pmatrix} \tag{5.32}$$

where $C = -1/f$ for a convex lens and $C = 1/|f|$ for a concave lens. Here f is the focal length of the lens. For a flat grating, the corresponding matrix is given by [53]

$$\begin{pmatrix} A & B \\ C & D \end{pmatrix} = \begin{pmatrix} \cos\theta'/\cos\theta & 0 \\ 0 & \cos\theta/\cos\theta' \end{pmatrix} \tag{5.33}$$

where θ and θ' are the corresponding angles of incidence and diffraction, respectively. For a grating deployed in the Littrow configuration, the A and D components, in Equation 5.33, become unity; that is, $A = D = 1$ and $C = B = 0$, which also applies for a mirror used at normal incidence [11].

For a generalized multiple-prism beam expander array, the ray transfer matrix is [11, 54]

$$\begin{pmatrix} A & B \\ C & D \end{pmatrix} = \begin{pmatrix} M & B \\ 0 & 1/M \end{pmatrix} \tag{5.34}$$

where M is defined by Equation 5.11 and the B term is given in Chapter 12. For an étalon, the ray transfer matrix can be written as [11]

$$\begin{pmatrix} A & B \\ C & D \end{pmatrix} = \begin{pmatrix} 1 & (l_e/n)(\cos\phi_e/\cos\psi_e)^2 \\ 0 & 1 \end{pmatrix} \tag{5.35}$$

where l_e is the thickness of the étalon. Here, ϕ_e is the angle of incidence and ψ_e is the corresponding angle of refraction. At normal incidence, Equation 5.35 takes the form of Equation 5.31.

A more elaborate system of matrices is the 4×4 matrices that can take the form of [51]

$$\begin{pmatrix} A & B & D & E \\ C & D & 0 & F \\ G & H & 1 & I \\ 0 & 0 & 0 & 1 \end{pmatrix} \tag{5.36}$$

In these matrices, the four upper-left components are the usual *ABCD* terms. Other components are related to quantities representing well-known optical phenomena. This has been particularly well established for the F term of the 4×4 matrix system describing a generalized multiple-prism array where the single-pass dispersion can be written as [54]

$$\frac{1}{2M}\left(\frac{\partial\Phi}{\partial\lambda}\right)_P = F\frac{\partial\nu}{\partial\lambda} \tag{5.37}$$

For further discussions on matrices applicable to pulse compression and intracavity dispersion the reader should consult [51, 54, 55].

The usefulness of the matrix approach, via terms such as A and B, becomes self-evident when determining the beam profile, using Equation 5.29, and the beam divergence through equations such as [11]

$$\Delta\theta = \frac{w}{L_R}\left[1+\left(\frac{L_R}{B}\right)^2+\left(\frac{L_R A}{B}\right)^2\right]^{1/2} \tag{5.38}$$

5.3.4 Linewidth

The double-pass dispersive linewidth of a multiple-prism grating oscillator is given by [56]

$$\Delta\lambda_D = \Delta\theta\left[M\left(\frac{\partial\theta}{\partial\lambda}\right)_G+\left(\frac{\partial\Phi}{\partial\lambda}\right)_P\right]^{-1} \tag{5.39}$$

where $\Delta\theta$ is the beam divergence, $(\partial\theta/\partial\lambda)_G$ is the grating dispersion either in Littrow or near grazing-incidence configuration, and

$$M\left(\frac{\partial\theta}{\partial\lambda}\right)_G \gg \left|\left(\frac{\partial\Phi}{\partial\lambda}\right)_P\right| \tag{5.40}$$

for specific dispersionless multiple-prism beam expanders $(\partial\Phi/\partial\lambda)_P \approx 0$. Dispersion values for various multiple-prism configurations are given in [11].

In high-gain pulsed lasers, such as laser-pumped dispersive dye laser oscillators, Equation 5.39 provides an upper limit for the observed linewidth [10]. For long-pulse dispersive dye laser oscillators the measured linewidth can be significantly narrower than the estimate provided by Equation 5.39 [10, 57]. For instance, for a laser yielding pulses $\Delta t \approx 200$ ns in duration, the estimated double-pass dispersive linewidth is $\Delta\nu \approx 2.16$ GHz, whereas the measured linewidth is $\Delta\nu \leq 360$ MHz [58]. This measured laser linewidth corresponds to double-longitudinal-mode oscillation, that is, $\Delta\nu \leq c/2L_c$, where L_c is the length of the cavity. Further, if oscillation is restricted to a single longitudinal mode by reducing the cavity length, for example, the measured $\Delta\nu$ can be even narrower. In this regard, Equation 5.39 can be used to estimate the dispersion necessary to restrict oscillation to a single longitudinal mode. Further insight into the multiple-pass linewidth narrowing mechanism is given in [56, 59].

Since ECS lasers are used mainly in the CW regime, the measured linewidth will be always much narrower than the calculated dispersive linewidth. In this regard, the main objective is to design a dispersive cavity that would be characterized by $\Delta\nu_D \leq c/2L_c$. The linewidth of a single longitudinal mode in an ECS laser can be characterized using the expression given by Harrison and Mooradian [60]. In this equation,

the modified Schawlow–Townes linewidth is multiplied by a factor having the length of the external cavity at the denominator. The equation is [60]

$$\Delta\nu = \Delta\nu_m \left(\frac{n_g L}{n_g L + L_c} \right)^2 \left(\frac{g_c}{g} \right)^2 \tag{5.41}$$

Here, $\Delta\nu_m$ is the modified Schawlow–Townes linewidth, n_g is the ratio of c to the group velocity, and L is the length of the semiconductor active region. The g factors are related to the gains at threshold with (g_c) and without (g) the external cavity [60]. The basic message from Equation 5.41 is that single-longitudinal-mode linewidths can be reduced substantially by the use of external cavities with lengths in the 10 cm range.

Gavrilovic et al. [61], using external dispersive cavities, have noted that at higher-power levels the emission changes from single-longitudinal-mode oscillation to multimode oscillation. Under these conditions, the linewidth of the emission is limited to the dispersive linewidth at 4 GHz [61]. Duarte [27] has estimated the double-pass dispersive linewidths for both MPL and HMPGI oscillators to be $\Delta\nu_D \approx 2.37$ GHz and $\Delta\nu_D \approx 1.2$ GHz, respectively. These calculations were made for an index-guided diode laser emitting at 670 nm. In both cases, the cavity lengths are about 10 cm, yielding a free spectral range of $FRS \approx 1.5$ GHz [27].

5.3.5 Wavelength Tuning

Semiconductor lasers are inherently tunable devices whose tuning characteristics depend on the energy gap of the semiconductor. Additional parameters affecting emission wavelength are current density and temperature. Cassidy et al. [62] provides a good survey of temperature-dependent wavelength tuning in semiconductor lasers emitting in a single longitudinal mode. The widest tuning ranges quoted are 1485–1527 nm in a InGaAsP laser for $\Delta T = 120$ °C, and 752–781 nm in a GaAlAs laser for $\Delta T = 135$ °C [62].

Here, optical means of wavelength tuning are considered, and the temperature is assumed to remain constant to maintain the optical path length of the semiconductor fixed. Using grating tuning, one of the largest wavelength tuning ranges reported has been 80 nm in InGaAsP/InP by Zorabedian [26].

Tuning in a grating is straightforward and follows the diffraction grating equation

$$m\lambda = d(\sin\theta \pm \sin\theta') \tag{5.42}$$

For a grating in Littrow configuration, this reduces to

$$m\lambda = 2d\sin\theta \tag{5.43}$$

Thus, the simple angular rotation of the grating relative to the optical axis of the cavity yields a change in the resonant wavelength. Note that for multiple-prism

grating cavities incorporating multiple-prism expanders in the compensating mode, the wavelength characteristics of the cavity depend on the grating exclusively.

In the case of a prismatic cavity with prisms deployed in an additive configuration (see Fig. 5.6), the exit angle of the mth prism as a function of wavelength is given by [10]

$$\phi_{2,m} = \arcsin\left\{ n(\lambda)\sin\left[\alpha_m - \arcsin\left(\frac{\sin\phi_{1,m}}{n(\lambda)} \right) \right] \right\} \tag{5.44}$$

where α_m is the apex angle of the mth prism, and the incidence angle of this prism ($\phi_{1,m}$) is related geometrically to the exit angles of the previous prism ($\phi_{2,m-1}$).

For an étalon the tuning properties can be characterized by the simple equation [37]

$$m_e\lambda = 2n(\lambda)d_e\cos\psi_e \tag{5.45}$$

where m_e is an integer, d_e is the distance between the reflective surfaces, and ψ_e is related to the angle of incidence by $\sin\phi_e = n(\lambda)\sin\psi_e$. The dispersion of an étalon is given by [10]

$$\left(\frac{\partial\phi_e}{\partial\lambda} \right) = \left(\frac{\sin\psi_e}{\cos\phi_e} \right)\frac{\partial n}{\partial\lambda} + n\left(\frac{\cos\psi_e}{\cos\phi_e} \right)\frac{\partial\psi_e}{\partial\lambda} \tag{5.46}$$

where

$$\left(\frac{\partial\psi_e}{\partial\lambda} \right) = \frac{1}{\tan\psi_e}\left(\frac{1}{n}\frac{\partial n}{\partial\lambda} - \frac{1}{\lambda} \right) \tag{5.47}$$

Wavelength tuning by rotation of the grating, or by rotating a mirror at the end of a prismatic array, or by rotating an étalon does not guarantee smooth wavelength tuning over an extensive wavelength range. This is due to the change in the optical cavity length as λ is varied.

In order to achieve synchronous wavelength tuning, a number of schemes have been implemented [63–65]. Synchronous wavelength tuning in semiconductor lasers is described by Favre et al. [66] who reports a 15-nm tuning range at 1260 nm, and by Trutna and Stokes [67] who achieved a 17-nm tuning range at 1310 nm. Synchronous tuning in MEMS-driven cavities is described in the next section.

5.3.6 Tuning Miniature MEMS-Driven Cavities

Miniature semiconductor laser cavities tuned by microelectromechanical systems (MEMS) are of intense interest for various applications, including telecommunications. Here, three wavelength tuning approaches compatible with MEMS techniques are described, although the techniques are applicable in general. These are the basic

grating tuning technique, synchronous tuning technique, and the longitudinal tuning technique based on changing the cavity length of the resonator.

From Heisenberg's uncertainty principle [33]

$$\Delta x \Delta p \approx h \tag{5.48}$$

it follows that [13]

$$\Delta\lambda \approx \lambda^2/\Delta x \tag{5.49}$$

which can also be expressed as

$$\delta\lambda \approx \lambda^2/\Delta x \tag{5.50}$$

where $\delta\lambda$ can be related to the separation, in the wavelength domain, between two longitudinal modes, and Δx can be related to twice the cavity optical length ($\Delta x = 2L$) of the resonator, or oscillator, generating the emission. This version of Heisenberg's uncertainty principle indicates that whenever wavelength changes, that is, whenever the oscillator is tuned, the free spectral range (*FSR*) or spacing between modes ($\delta\lambda$), also changes. This phenomenon can lead to abrupt jumps, in the wavelength domain, as a cavity is tuned, and is known in the literature as *mode hopping*. The solution to this phenomenon is given by Equation 5.50, which indicates that in order to maintain $\delta\lambda$ fixed, as λ changes, Δx must vary accordingly. In order to be consistent with the terminology of the literature it is useful to also write Equation 5.50 as the familiar identity

$$FSR \approx \lambda^2/2L \tag{5.51}$$

In order to maintain $\delta\lambda$, or the *FSR*, constant we need to define a central value for this quantity $(\delta\lambda)_c$ which is then maintained as constant, as determined from the initial central wavelength λ_i of the scan so that

$$(\delta\lambda)_c \approx \lambda_i^2/\Delta x \tag{5.52}$$

Then using

$$m\lambda = d(\sin\theta \pm \sin\theta') \tag{5.53}$$

the cavity optical length should be maintained according to

$$\Delta x \approx (\delta\lambda)_c^{-1}(d/m)^2(\sin\theta \pm \sin\theta')^2 \tag{5.54}$$

as the wavelength is scanned. This equation is applicable to a grazing-incidence grating cavity being tuned by rotating its tuning mirror around its central axis, thus

changing θ', which is perpendicular to the plane of incidence. For a cavity using a grating in Littrow configuration this expression reduces to

$$\Delta x \approx 4(\delta\lambda)_c^{-1}(d/m)^2 \sin^2\theta \tag{5.55}$$

This time the tuning is performed by changing θ by rotating the grating about its central axis, which is centered at the optical axis of the cavity and is perpendicular to the plane of incidence. Thus maintaining Δx according to Equations 5.54 or 5.55 ensures the condition of a constant free spectral range or $(\delta\lambda)_c$. It should be noted that these equations also apply to multiple-prism grating cavities since, for either a Littrow or grazing-incidence configuration, the dispersive contribution of the multiple-prism expander in

$$\Delta\lambda_D = \Delta\theta\left[M\left(\frac{\partial\theta}{\partial\lambda}\right)_G + \left(\frac{\partial\Phi}{\partial\lambda}\right)_P\right]^{-1} \tag{5.56}$$

can be nearly eliminated, by design, so that

$$\left(\frac{\partial\Phi}{\partial\lambda}\right)_P \approx 0 \tag{5.57}$$

In all these $(\delta\lambda)_c$ approaches it is necessary to precision change Δx as either θ or θ' is changed. This requires careful control, and calibration, of the angular and longitudinal parameters mentioned.

An approach that simultaneously changes Δx as θ' is varied was introduced by Liu and Littman [63] for grazing-incidence grating cavities in dye lasers. This type of tuning is geometrically accomplished by establishing a common rotational point, also referred to as the pivot point, defined by the intersection of the projections from the diffraction grating surface, the tuning mirror surface, and the reflective surface of the output coupler. In this setup L_f is the distance from the center of the diffraction grating surface to the reflective surface of the output coupler while L_p is the distance from the center of the diffraction grating to the rotational point. Thus, in this approach the overall cavity length is made a function of θ' and is given by [63]

$$L = (L_f + L_p \sin\theta') \tag{5.58}$$

This type of synchronous tuning was first demonstrated in a miniature grazing-incidence grating cavity, driven by MEMS, by Berger et al. [68].

An additional type of fine-tuning applicable to MEMS-driven miniature laser cavities is one of the most basic types of tuning and consists simply in changing the cavity length as outlined in Figure 5.7. In this regard, this approach exploits the very fact that the free spectral range of the cavity is a function of Δx.

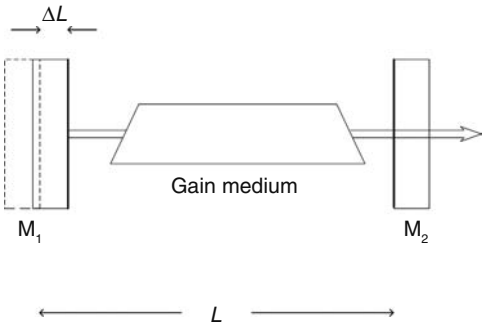

FIGURE 5.7 Wavelength tuning using the displacement of one of the mirrors of the resonator thus effectively changing the length of the cavity L.

Going back to

$$\delta\lambda \approx \lambda^2/\Delta x \tag{5.59}$$

one can write for an initial wavelength λ_1

$$\delta\lambda_1 \approx \lambda_1^2/2L \tag{5.60}$$

and for a subsequent wavelength λ_2

$$\delta\lambda_2 \approx \lambda_2^2/(2(L \pm \Delta L)) \tag{5.61}$$

In addition, it is useful to define the number of longitudinal modes in each case as

$$N_1 = \Delta\lambda_1/\delta\lambda_1 \tag{5.62}$$

$$N_2 = \Delta\lambda_2/\delta\lambda_2 \tag{5.63}$$

where $\Delta\lambda_1$ and $\Delta\lambda_2$ are the corresponding laser linewidths. Now, if the laser line width during this ΔL change is maintained so that $\Delta\lambda_1 \approx \Delta\lambda_2$, then taking the ratio of Equations 5.60 and 5.61 leads to [13]

$$\lambda_2 \approx \lambda_1(N_1/N_2)^{1/2}(1 \pm (\Delta L/L))^{1/2} \tag{5.64}$$

Further, for $N_1 \approx N_2$, or single-longitudinal-mode oscillation, this equation reduces to [13]

$$\lambda_2 \approx \lambda_1(1 \pm (\Delta L/L))^{1/2} \tag{5.65}$$

Uenishi et al. [69] report on experiments using the $\Delta L/L$ method to perform wavelength tuning in a MEMS-driven semiconductor laser cavity. In their experiment

Uenishi et al. [69] observed wavelength tuning in the absence of mode-hopping as long as the change in wavelength did not exceed $\lambda_1 - \lambda_2 \approx 1$ nm. Using their graphical data for the scan initiated at $\lambda_1 \approx 1547$ nm, it is established that $\Delta L \approx 0.4$ μm, and using $L \approx 305$ mm, Equation 5.65 yields $\lambda_2 \approx 1548$ nm, which approximately agrees with the authors' observations [69]. In this regard it should be mentioned that Equation 5.65 was implicitly derived with the assumption of a wavelength scan obeying the condition $\delta\lambda_1 \approx \delta\lambda_2$.

5.3.7 Tuning Using Bragg Gratings

One further method of wavelength tuning, applicable to ECS lasers, which recently has gained renewed interest involves the use of Bragg gratings [70]. A Bragg grating can be visualized as a wavelength-selective mirror satisfying the Bragg condition

$$\lambda = 2n\Lambda \tag{5.66}$$

where n is the refractive index, and Λ is the grating period. The linewidth selectivity can be estimated using Equation 5.49, with $\Delta x = 2nd$, for propagation in a bulk material of refractive index n

$$\Delta\lambda \approx \lambda^2/2nd \tag{5.67}$$

where d is the thickness of the grating. The grating period can also be defined as $\Lambda = d/N$ where N is the number of planes in the grating. Thus, in terms of explicit grating parameters the wavelength can be expressed as

$$\lambda \approx 2nd/N \tag{5.68}$$

and the linewidth as

$$\Delta\lambda \approx 2nd/N^2 \tag{5.69}$$

For assessment and comparison purposes it is useful to restate this identity in frequency units

$$\Delta\nu \approx c/2nd \tag{5.70}$$

Further aspects of Bragg grating tuning are discussed in Chapter 6 as applied to fiber lasers.

5.4 PERFORMANCE OF TUNABLE EXTERNAL-CAVITY SEMICONDUCTOR LASERS

A common feature in most tunable ECS lasers considered here is the use of antireflection (AR) coatings in the internal facet of the semiconductor leading to the

intracavity frequency-selective optics. As discussed previously, this is an important requirement to achieve oscillation with characteristics that are totally dependent on the intracavity frequency-selective optics. In this regard, excessive amounts of reflectivity at the facet adjacent to the frequency-selective optics can lead to uncontrolled emission, or noise, and lack of control of the frequency characteristics by the tuning optics. This problem is analogous to the competition between narrow-linewidth emission and ASE observed in dispersive dye laser oscillators [10, 11]. Evidence of background superluminescence in narrow-linewidth tunable ECS lasers is provided by Gavrilovic et al. [61]. These authors utilized a semiconductor with an internal facet adjacent to the dispersive optics AR coated to 2%. The design adopted by these authors was a grazing-incidence grating cavity in an open configuration [61].

One traditional feature in tunable laser oscillators is the use of an independent output coupler mirror (see [10, 11] for example). In the realm of the ECS laser, very few designs have implemented that feature [25, 27]. Although the use of an independent output coupler mirror can add to cost, complexity, and physical dimensions, it can provide a further degree of alignment control and the means to collimate the output beam intracavity [27] (see Figs. 5.4 and 5.5). The reflectivity of the output coupler mirror can vary from 40–95% [25, 61]. So far, however, most authors utilizing closed-cavity configurations have opted for the use of high-reflectivity coatings at the external, or output, facet of the semiconductor.

The performance of ECS laser oscillators using dispersive intracavity optic elements is listed in Table 5.2. The reported linewidths vary from 10 kHz to 32 MHz and the output powers from 1 mW to 70 mW. It should be noted that the tuning range reported by Favre et al. [66] corresponds to synchronous wavelength tuning.

The performance of ECS lasers using alternative frequency selective methods such as Bragg gratings, liquid crystals, and acousto-optic filters is given in Table 5.3. Again, AR coatings are used at the internal facet of the semiconductor adjacent to the frequency-selective optics. One method that appears particularly promising is the use of external volumetric Bragg gratings. This method has been demonstrated in ECS lasers [77, 78], optically pumped solid-state lasers [79], and fiber lasers [80]. In the case of the ECS lasers the Bragg grating configuration has been successful in providing frequency selectivity to diode laser arrays [77, 78]. In one particular experiment a total CW power of 13.5 W is reported at a laser linewidth of 7 GHz [78].

Another important area of activity in tunable semiconductor lasers is frequency stabilization [84–89]. A subtle distinction here is that many of these lasers can be classified, according to Weiman and Hollberg [90], as *pseudo*-ECS-lasers. As discussed previously, in true ECS lasers the semiconductor facet adjacent to the frequency-selective optics is AR coated. Under these conditions, oscillation is achieved with the feedback from the frequency-selective optics. In the case of pseudo-ECS-lasers, oscillation can proceed in the absence of external optics although lasing can also be established in a regime where the dispersive optics provides the frequency information of the emission [90].

A widely applied method of frequency stabilization is the use of external reference cavities such as confocal Fabry–Pérot resonators [84–87]. In this regard,

TABLE 5.2
Performance of External-Cavity Semiconductor Lasers

Laser semiconductor	Cavity	$\Delta\nu$	Tuning range	Power	AR coating[a]	Ref.
InGaAsP/InP	Littrow grating	10 kHz	55 nm @ 1500 nm		3–4%	73
InGaAsP/InP	Littrow grating[b]	31 kHz	1285–1320 nm	≥1 mW		74
	Littrow grating	20 kHz	15 nm @ 1260 nm		<0.01% (SiO)	66
InGaAsP/InP	MPL grating[b]	100 kHz	1255–1335 nm		<0.01% (SiO)	26
GaAlAs	Littrow grating[b,c]	<1.5 MHz	815–825 nm	5 mW	<0.2% (SiO)	25
GaAlAs	Littrow grating[b]	~200 kHz	32 nm @ 850 nm	1 mW	<0.5%	75
GaAlAs	Double étalon[b]	32 MHz	10 nm @ 875 nm		Yes	36
GaAlAs	Etalon[b]	4 kHz			<0.4% ($SiO–Si_2O_3$)	60
GaAlAs	GI grating[d]	10 kHz	~20 nm @ 780 nm		>2%	76
	GI grating[d]	≤15 MHz	~30 nm @ 820 nm	30 mW	2% (Al_2O_3)	61
InGaAsP/InP	GI grating[d,e]	2 MHz	42 nm @ 1550 nm	70 mW		68
Index guided	Littrow grating plus étalon[d]		20 nm @ ~670 nm	6 mW	~1% (SiO)	21
	Mirror[e]		20 nm @ 1540 nm			69
	Mirror[e]	12.7 GHz	16 nm @ 1536 nm	~17 nW		71
InGaAsP/InP	Littrow grating[e]	~1.3 GHz	30 nm @ 1525 nm	~1 mW	0.19%	72

[a] AR coating of the internal facet adjacent to the frequency-selective optics.
[b] Closed-cavity configuration.
[c] Employs an independent output coupler mirror.
[d] Open-cavity configuration.
[e] Tuned using MEMS.

Laurent et al. [84] report on a 50–60 dB frequency noise reduction and linewidths of less than 4 kHz [84]. Hollberg [91] provides an excellent review of various methods of frequency stabilization applicable to tunable lasers. The techniques discussed in [91] include cavity side locking, modulation locking, radio-frequency-optical heterodyne locking, and postlaser stabilization. The three locking techniques use external reference cavities.

TABLE 5.3
Performance of External-Cavity Semiconductor Lasers Using Alternative Tuning Methods

Laser semiconductor	Tuning method	$\Delta\nu$	Tuning range	AR coating[a]	Ref.
	Bragg grating	7 GHz	750–758 nm	0.5 %	78
GaInAsP	Fiber grating		45 nm @ 1500 nm	~1% (Pb–SiO_2)	81
GaInAsP/InP	Liquid crystal filter[b]	~350 MHz	6 nm @ 1500 nm	0.02%	82
GaAs	Acousto-optic filter[b]		35 nm @ 850 nm	1.5%	83

[a] AR coating of the internal facet next to the frequency-selective optics.
[b] Closed-cavity configuration.

5.5 PERFORMANCE OF ULTRASHORT-PULSE EXTERNAL-CAVITY SEMICONDUCTOR LASERS

External-cavity semiconductor lasers have been demonstrated to oscillate using passive [92], active [93, 94], and hybrid [95] modelocking techniques. The saturable absorber demonstrated in the passively modelocked ECS laser is a multiple-quantum well (MQW) section adjacent to the gain MQW region [92]. Delfyett et al. [95] also uses an MQW region as a saturable absorber. In this latter case, however, the saturable absorber is removed from its substrate and placed in contact with the end mirror of the cavity [95]. In addition to MQW semiconductors, saturable absorbers can also result from damaged semiconductor materials that develop saturable absorbing regions [93].

The hybrid modelocked ECS laser of Delfyett et al. [95] employs a four-prism sequence configured for collinear transmission in a compensating mode [43]. To this prism sequence the first and second derivative values given in Equations 5.23 through 5.26 apply directly.

An alternative pulse compression multiple-prism array is that used by Pang et al. [94] and shown in Figure 5.8. This is a six-prism array where the first three prisms are deployed in an additive configuration, with the second group of three prisms also deployed in a positive configuration. However, the two groups of prisms are deployed in a compensating configuration relative to each other. By adjusting the prism separation, these authors were able to continuously vary the GVD from positive to negative [94]. In Figure 5.9 the pulse shape is shown as a function of intracavity prism separation [94]. It should be emphasized that for this more general class of prismatic configuration, the special case considered by Equations 5.23 through 5.26 does not apply. Instead, the generalized equations given by [39, 41, 42], namely, Equations 5.21 and 5.22, are used. The generality of this approach was elegantly demonstrated in the experiments by Osvay et al. [44, 45].

Another interesting cavity design is that of Salvatore et al. [92]. These authors use a 5% AR coating on the facet of the gain section of their four-quantum well laser.

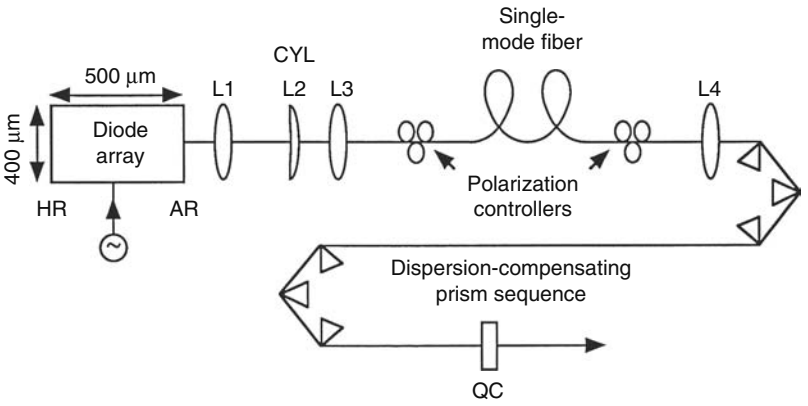

FIGURE 5.8 Ultrashort-pulse ECS laser using a six-prism array to control the value of the GVD. (From Pang, L. Y., J. G. Fujimoto, and E. S. Kintzer, Ultrashort-pulse generation from high-power diode arrays by using intracavity optical nonlinearities, *Opt. Lett.* 17: 1599–1601 (1992).)

This AR facet leads to a Littrow-mounted grating that is used for tuning. The second section is the MQW saturable absorber whose output facet leads to a double-grating pulse compressor. This facet is coated for 90% reflectivity. A schematic of the cavity is shown in Figure 5.10.

The performance of the short-pulse ECS lasers outlined in this section is listed in Table 5.4. At this stage it is clear that this is a field that offers ample opportunities for further development in the areas of spectral coverage and in attaining shorter emission pulses.

5.6 APPLICATIONS

External-cavity semiconductor lasers have been shown to yield narrow-linewidth tunable emission in a variety of configurations (see Table 5.2). Since the publication of the first edition of this book [28], these lasers have become widely applied and what is more important they have made significant contributions in areas such as laser cooling and Bose–Einstein condensation [97]. ECS lasers have also become workhorses in the optical communications industry that requires narrow-linewidth tunable radiation in their C-band (~1530–1565 nm) and L-band (~1570–1610 nm) [68, 98]. Additional applications that have benefited directly from the availability of tunable ECS lasers include imaging, interferometry, remote sensing, and spectroscopy. Applications to imaging and interferometry are described in Chapter 12.

Given wavelength agility, direct electrical excitation, light weight, and compactness, an application that is quite suitable for ECS lasers is that of remote sensing and light detection and ranging (lidar) [99]. An informative, and widely referenced, discussion on the various categories of lidar applications is given by Grant [100]. Grant's discussion also details the various laser systems applied to perform the measurements in each lidar category. His extensive bibliography is current until 1995

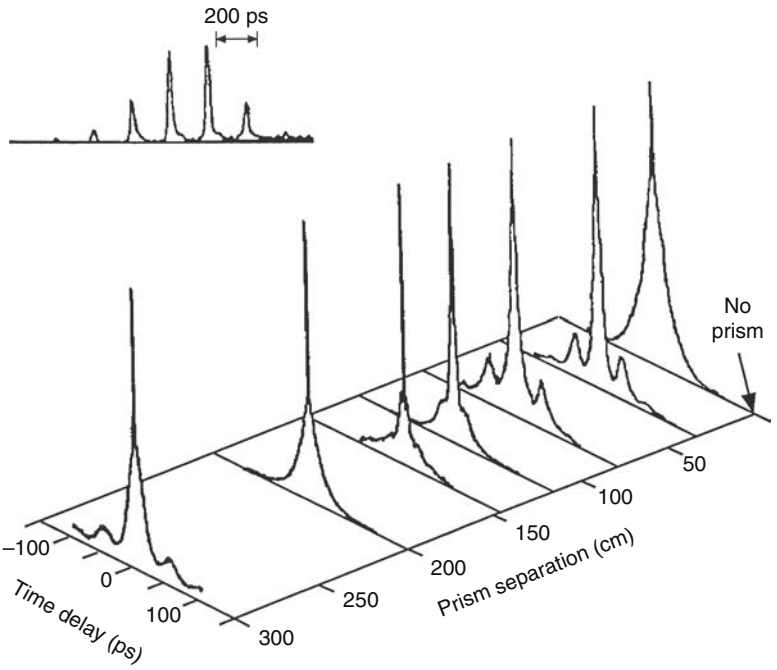

FIGURE 5.9 Dependence of pulse shape as a function of intracavity prism separation in the six-prism ECS laser. The inset shows a modelocked pulse train. (From Pang, L. Y., J. G. Fujimoto, and E. S. Kintzer, Ultrashort-pulse generation from high-power diode arrays by using intracavity optical nonlinearities, *Opt. Lett.* 17: 1599–1601 (1992).)

[100]. A description on the application of ECS lasers to lidar can be obtained from Diekmann [99] (and references therein). This author employed an electronically tuned diode laser in conjunction with a fiber Mach–Zehnder interferometer and a Michelson interferometer to perform distance measurements [99]. In addition to

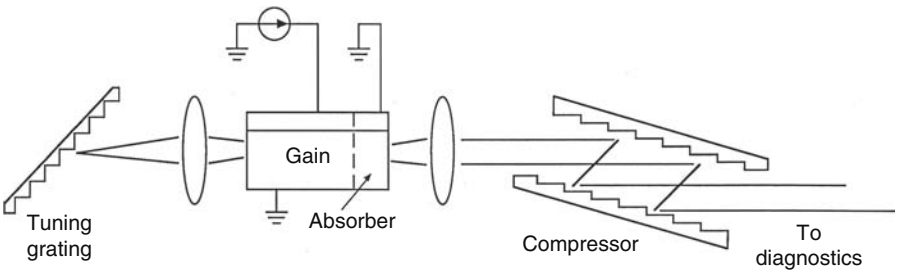

FIGURE 5.10 Grating tuned passively modelocked MQW laser using grating-pair compressor. (From Salvatore, R. A., T. Schrans, and A. Yariv, Wavelength tunable source of subpicosecond pulses from CW passively mode-locked two-section multiple-quantum-well laser, *IEEE Photo. Tech. Lett.* 5: 756–758 (1993).)

TABLE 5.4
Performance of Ultrashort-Pulse External-Cavity Semiconductor Lasers

Laser semiconductor	Cavity	Modelocking technique	Δt	Tuning range or emission λ	AR coating[a]	Ref.
InGaAsP	Étalon[b]	Active	580 fs	1300 nm	<1%	93
InGaAsP	Littrow grating[c]	Internal SA[d]	2.5 ps	40 nm @ 1300 nm	No	96
AlGaAs	Four prisms[c]	Hybrid, MQW SA[d]	200 fs	~838 nm		95
AlGaAs	Six prisms[b]	Active, uses intracavity SA[d]	650 fs	805 nm	Yes	94
MQW	Littrow grating and grating pair compressor[c]	Passive	260 fs	16 nm @ 846 nm	<5%	92

[a] AR coating of the internal facet next to the frequency-selective optics.
[b] Closed-cavity configuration.
[c] Open-cavity configuration.
[d] Saturable absorber.

the advantages already mentioned, ECS lasers also offer to lidar applications the alternative of fairly narrow emission linewidths and attractive tuning ranges.

A particular application that has made significant use of tunable semiconductor lasers is spectroscopy [90, 101]. Wieman and Hollberg [90] provide an excellent listing of the different areas of spectroscopy employing semiconductor lasers. These areas include optical pumping, fast frequency modulation, high-resolution spectroscopy, high-sensitivity spectroscopy, and trapping and cooling of atoms [90]. Here it should be noted that high-resolution and high-sensitivity spectroscopy are applications that benefit from the availability of frequency-stabilized diode lasers. Also, stabilized narrow-linewidth ($\Delta\nu < 1$ MHz) semiconductor lasers are very useful in the trapping and cooling of atoms [90]. As mentioned, tunable ECS lasers have been central to laser cooling and Bose–Einstein condensation experiments [90, 97]. For an interesting description of the use of tunable semiconductor lasers in the cooling of atoms, the reader should refer to Weidemuller et al. [102]. This experiment uses two excitation lasers, a repumping laser, a probing laser, and a counterpropagating cooling laser. This latter laser is a Littrow grating tuned semiconductor laser with $\Delta\nu \leq 1$ MHz and a 6-GHz continuous tuning range at ~670 nm [102]. All five lasers are semiconductor lasers.

One application mentioned in detail in Chapter 11 is that of laser isotope separation (LIS) in Li atoms using a tunable ECS laser emitting at the visible red end of the spectrum [103]. In these experiments ^{7}Li was separated from ^{6}Li using sequential laser excitation. This required smooth wavelength tuning of the ECS laser in the 670.77–670.81 nm region capable of resolving the hyperfine spectrum of lithium

involving the ^{6}Li D_1, ^{6}Li D_2, ^{7}Li D_1, ^{7}Li D_2 lines [103]. Note that for spectroscopy and laser cooling applications in addition to narrow linewidth oscillation ($\Delta\nu \leq 1$ MHz [102], for example), the availability of continuous and smooth wavelength tuning, without mode hopping, is important. A comparison of ECS lasers, based on Littrow grating and a grazing-incidence grating configuration, for applications to Raman spectroscopy has been provided by Cooney et al. [104].

Spectroscopy applications of blue GaN ECS lasers emitting in the 373–472 nm portion of the spectrum have been reported by Scheibner et al. [105] and Olejnicek et al. [106]. These authors used open-cavity Littrow grating configurations to study the $^2S_{1/2}$–$^2P_{1/2}$ and $^2S_{1/2}$–$^2P_{3/2}$ transitions of Al in hollow cathode and magnetron discharges, respectively.

Finally, tunable ECS lasers, at shorter wavelengths, might be suitable for cancer diagnostics using molecules such as HpD that absorb in the blue and fluoresce in the red [107, 108]. In this regard, the availability of higher average-power oscillator-amplifier systems [32], emitting at the red end of the spectrum, opens the possibility of compact and reliable systems for laser photodynamic therapy (PDT). A diode-laser-based system, analogous to that described by Duarte [109] for tunable dye lasers, could provide both diagnosis and PDT for suitable cancers. For a description of PDT using tunable lasers the reader is referred to Goldman [107]. One medical area that has already benefited from tunable diode lasers is that of gas monitoring in human sinuses [110]. For that spectroscopic-medical application researchers have employed distributed feedback diode lasers emitting near 760 nm and 935 nm at power levels ~4 mW. An additional area that might benefit from ECS lasers delivering well-controlled circular beams, at suitable power levels, is retinal treatment. Traditional laser wavelength used in photocoagulation of the retina include the 647.09 nm transition of Kr^+ and the 694.3 nm transition of Al_2O_3:Cr^{3}. Both these wavelengths belong to a region of the red spectrum that is accessible using ECS lasers powered by III–V semiconductors.

A brief summary of applications, including communications, isotope separation, laser cooling, and spectroscopy, that utilize ECS lasers in Littrow grating and grazing-incidence grating configurations is given in Table 5.5.

5.7 CONCLUSION

In this chapter, the architecture, optical elements, and performance characteristics of tunable ECS lasers have been outlined. Particular attention was given to dispersive optical oscillator configurations relevant to the design of tunable ECS lasers. The oscillator configuration and the elements of optical theory considered apply, in general, to any class of semiconductor material irrespective of physical dimensions and/or emission wavelength region.

The difference between open- and closed-cavity configurations has been highlighted and the importance of AR coatings at the semiconductor facet adjacent to the frequency-selective optics has been discussed.

In general, it is found that dispersive ECS laser oscillators offer very narrow linewidth emission and excellent wavelength tuning ranges. Further, it should be

TABLE 5.5
Brief Survey of ECS Laser Applications

Laser semiconductor	Cavity	Tuning range	Application	Ref.
GaN	Littrow grating[a]	394.40–396.15 nm[b]	Spectroscopy of Al in hollow-cathode discharges ($^2S_{1/2}$ –$^2P_{1/2}$ and $^2S_{1/2}$ –$^2P_{3/2}$ transitions)	105
GaN	Littrow grating,[a] $\Delta\nu \approx 1$ MHz	394.40–396.15 nm[b,c]	Absorption spectroscopy of Al in a magnetron discharge	106
AlGaAs	Littrow grating	~5 GHz @ 780 nm	Measurement of the hyperfine structure of the $^5S_2$ state of ^{17}O	111
Index guided	Littrow grating plus étalon[d]	20 nm[e] @ 670 nm	Fluorescence spectrum of ^{6}Li ($2S_{1/2}$–$2P_{1/2}$ transition)	21
	Littrow grating, $\Delta\nu \leq 100$ kHz	6 GHz @ 670.8 nm	Cooling of Li atoms ($2\ ^2S_{1/2}$–$2\ ^2P_{3/2}$ transition)	102
	Littrow grating[f]	18 GHz @ 670 nm	Absorption spectrum of ^{7}Li (D_1 and D_2 transitions)	112
	GI grating,[a] $\Delta\nu \approx 100$ kHz	25 nm @ 672 nm	Laser isotope separation in Li	103
InGaAsP/InP	GI[g] grating $\Delta\nu \approx 2$ MHz	42 nm @ 1550 nm	Optical communications	68

[a] Commercial ECS laser.
[b] The overall tuning range of these lasers is approximately 373 nm $\leq \lambda \leq$ 472 nm including several gaps.
[c] Quoted tuning range includes several gaps.
[d] AR coating of the semiconductor facet adjacent to the frequency-selective optics. Laser output is coupled via an intracavity beam-splitter.
[e] This is a coarse tuning range. A 1.2-GHz range is quoted for continuous fine-tuning.
[f] The semiconductor facet adjacent to the grating is not AR coated.
[g] Tuned using MEMS.

indicated that, as disclosed in the literature, dispersive optical oscillators utilizing closed-cavity configurations offer enhanced reduction of background emission noise and greater protection against unwanted external optical feedback.

By the time of publication of the first edition of *Tunable Laser Applications* (1995) dispersive ECS laser oscillators had been demonstrated to cover spectral regions in the red and near-infrared using III–V semiconductors to power the various dispersive laser oscillator architectures described here. Since then, the development of commercially available II–VI laser semiconductors has extended the reach of tunable ECS lasers into the blue region of the spectrum, thus enhancing the utilitarian aspect of these lasers.

The stable, narrow-linewidth emission characteristics of dispersive ECS laser oscillators make them attractive for many spectroscopic applications. One disadvantage, however, is the relatively low peak power available. Hence, the use of these optical oscillators in hybrid tunable laser systems where amplification is provided by a complementary class of laser remains an attractive alternative. For instance, the use of dispersive ECS laser oscillators in conjunction with existing tunable solid-state laser technology should open doors for further applications in need of high peak powers. In this regard, recent advances in solid-state dye lasers [113, 114] suggest the realization of low-cost hybrid systems incorporating dispersive ECS laser oscillators and solid-state dye laser media at the amplification stages. Indeed, as blue dispersive ECS lasers become more widely available the injection of high-power lasers in that region of the spectrum is only a matter of time. In addition to dye lasers, a possible gas laser amplifier in the blue region is the Ca^{+} laser, emitting at 373.7 nm.

On a more futuristic note: The recent demonstration of spatial coherence, characterized in the form of nearly diffraction limited beams, and emission linewidths comparable to broadband dye laser emission, from electrically excited dye-doped organic semiconductors [115–117] could lead to a new generation of compact tunable sources emitting throughout the visible spectrum.

In the area of applications, the use of ECS lasers is a field poised for significant growth. This growth should be reinforced as ECS lasers become easily available and as the versatility of ECS lasers is augmented. Here, opportunities exist in the extension of wavelength ranges, achievement of shorted pulses in the femtosecond regime, the engineering of narrow-linewidth multiwavelength devices (see, for example [118, 119]), and most certainly in the increase of output power levels.

REFERENCES

1. Yariv, A., *Quantum Electronics*, Wiley, New York, 1975.
2. Yariv, A., *Optical Electronics,* Holt, Rinehart and Winston, New York, 1985.
3. Murata, S., and I. Mito, Frequency-tunable semiconductor lasers, *Opt. Quantum Electron.* 22: 1–15 (1990).
4. Ohtsu, M., *Highly Coherent Semiconductor Lasers,* Artech House, Boston, 1992.
5. Zory, P. S. (Ed.), *Quantum Well Lasers,* Academic, New York, 1993.
6. Coleman, J. J., Semiconductor lasers, in *Electro-Optics Handbook,* edited by R. Waynant and M. Ediger, McGraw-Hill, New York, 1994, Chap. 6.
7. Chow, W. W., and S. W. Koch, *Semiconductor Laser Fundamentals*, Springer, Berlin, 1999.
8. Kapon, E., *Semiconductor Lasers II*, Academic, New York, 1999.
9. Ye, C., *Tunable External Cavity Diode Lasers*, World Scientific, Singapore, 2004.
10. Duarte, F. J., Narrow linewidth pulsed dye laser oscillators, in *Dye Laser Principles,* edited by F. J. Duarte and L. W. Hillman, Academic, New York, 1990, Chap. 4.
11. Duarte, F. J., Dispersive dye lasers, in *High Power Dye Lasers,* edited by F. J. Duarte, Springer-Verlag, Berlin, 1991, Chap. 2.
12. Duarte, F. J., *Tunable Lasers Handbook*, Academic, New York, 1995.
13. Duarte, F. J., *Tunable Laser Optics*, Elsevier-Academic, New York, 2003.
14. Zmudzinski, C. A., Y. Guan, and P. S. Zory, Room temperature photopumped ZnSe lasers, *IEEE Photo. Tech. Lett.* 2: 685–687 (1991).
15. Jeon, H., M. Hagerott, J. Ding, A. V. Nurmikko, D. C. Grillo, W. Xie, M. Kobayashi, and R. L. Gunshor, Pulsed room-temperature operation of a blue-green ZnSe quantum-well diode laser, *Opt. Lett.* 18: 125–127 (1993).

16. Nakamura, S., and G. Fasol, *The Blue Laser Diode*, Springer, Berlin, 1998.
17. Duarte, F. J., Multiple-prism Littrow and grazing-incidence pulsed CO_2 lasers, *Appl. Opt.* 24: 1244–1245 (1985).
18. Zorabedian, P., Tunable external cavity semiconductor lasers, in *Tunable Lasers Handbook*, edited by F. J. Duarte, Academic, New York, 1995, Chap. 8.
19. Duarte, F. J., and J. A. Piper, A double-prism beam expander for pulsed dye lasers, *Opt. Commun.* 35: 100–104 (1980).
20. Duarte, F. J., and J. A. Piper, Prism preexpanded grazing-incidence grating cavity for pulsed dye lasers, *Appl. Opt.* 20: 2113–2116 (1981).
21. Boshier, M. G., D. Berkeland, E. A. Hinds, and V. Sandoghdar, External-cavity frequency-stabilization of visible and infrared semiconductor lasers for high resolution spectroscopy, *Opt. Commun.* 85: 355–359 (1991).
22. Hanna, D. C., P. A. Karkkainen, and R. Wyatt, A simple beam expander for frequency narrowing of dye lasers, *Opt. Quantum Electron.* 7: 115–119 (1975).
23. Shoshan, I., N. N. Danon, and U. P. Oppenheim, Narrowband operation of a pulsed dye laser without intracavity beam expansion, *J. Appl. Phys.* 48: 4495–4497 (1977).
24. Littman, M. G., and H. J. Metcalf, Spectrally narrow pulsed dye laser without beam expander, *Appl. Opt.* 17: 2224–2227 (1978).
25. Fleming, M. W., and A. Mooradian, Spectral characteristics of external-cavity controlled semiconductor lasers, *IEEE J. Quantum Electron.* QE-17: 44–59 (1981).
26. Zorabedian, P., Characteristics of a grating-external-cavity semiconductor laser containing intracavity prism beam expanders, *J. Lightwave Technol.* 10: 330–335 (1992).
27. Duarte, F. J., Multiple-prism grating designs tune diode lasers, *Laser Focus World* 29(2): 103–109 (1993).
28. Duarte, F. J., Dispersive external cavity semiconductor lasers, in *Tunable Laser Applications*, 1st ed., edited by F. J. Duarte, Marcel Dekker, New York, 1995, Chap. 3.
29. Liu, A. Q., and X. M. Zhang, A review of MEMS external-cavity tunable lasers, *J. Micromec. Microeng.* 17: R1–R13 (2007).
30. Duarte, F. J., Multiple-prism grating solid-state dye laser oscillator: optimized architecture, *Appl. Opt.* 38: 6347–6349 (1999).
31. Laurila, T., T. Joutsenoja, R. Hernberg, and M. Kuittinen, Tunable external-cavity laser at 650 nm based on a transmission diffraction grating, *Appl. Opt.* 27: 5632–5637 (2000).
32. Fox, R. W., L. Hollberg, and A. S. Zibrov, Semiconductor diode lasers, in *Atomic, Molecular, and Optical Physics: Electromagnetic Radiation*, edited by F. B. Dunning and R. G. Hulet, Academic, New York, 1999, Chap. 4.
33. Dirac, P. A. M., *The Principles of Quantum Mechanics,* 4th ed., Oxford University, London, 1978.
34. Duarte, F. J., On a generalized interference equation and interferometric measurements, *Opt. Commun.* 103: 8–14 (1993).
35. Duarte, F. J., Interference, diffraction, and refraction, via Dirac's notation, *Am. J. Phys.* 65: 637–640 (1997).
36. Voumard, C., External-cavity-controlled 32-MHz narrow-band CW GaAlAs-diode lasers, *Opt. Lett.* 1: 61–63 (1977).
37. Born, M., and E. Wolf, *Principles of Optics,* 7th ed., Cambridge, New York, 1999.
38. Hänsch, T. W., Repetitively pulsed tunable dye laser for high resolution spectroscopy, *Appl. Opt.* 11: 895–898 (1972).
39. Duarte, F. J., and J. A. Piper, Dispersion theory of multiple-prism beam expanders for pulsed dye lasers, *Opt. Commun.* 43: 303–307 (1982).
40. Duarte, F. J., Transmission efficiency in achromatic nonorthogonal multiple-prism laser beam expanders, *Opt. Commun.* 71: 1–5 (1989).
41. Duarte, F. J., Generalized multiple-prism dispersion theory for pulse compression in ultrafast dye lasers, *Opt. Quantum Electron.* 19: 223–229 (1987).

42. Duarte, F. J., Prismatic pulse compression: Beam deviations and geometrical perturbations, *Opt. Quantum Electron.* 22: 467–471 (1990).
43. Fork, R. L., O. E. Martínez, and J. P. Gordon, Negative dispersion using pairs of prisms, *Opt. Lett.* 9: 150–152 (1984).
44. Osvay, K., A. P. Kovács, Z. Heiner, G. Kurdi, J. Klebniczki, and M. Csatári, Angular dispersion and temporal change of femtosecond pulses from misaligned pulse compressors, *IEEE J. Selec. Topics Quantum Electron.* 10: 213–220 (2004).
45. Osvay, K., A. P. Kovács, G. Kurdi, Z. Heiner, M. Divall, J. Klebniczki, and I. E. Ferincz, Measurements of non-compensated angular dispersion and the subsequent temporal lengthening of femtosecond pulses in a CPA laser, *Opt. Commun.* 248: 201–209 (2005).
46. Arissian, L., and J. C. Diels, Carrier to envelope and dispersion control in a cavity with prism pairs, *Phys. Rev. A.*, 75: 013814 (2007).
47. Diels, J. C., and W. Rudolph, *Ultrashort Laser Pulse Phenomena*, 2nd ed., Academic, New York, 2006.
48. Brouwer, W., *Matrix Methods in Optical Instrument Design,* W. A. Benjamin, New York, 1964.
49. Siegman, A. E., *Lasers,* University Science Books, Mill Valley, CA, 1986.
50. Wollnik, H., *Optics of Charged Particles,* Academic, New York, 1987.
51. Kostenbauder, A. G., Ray-pulse matrices: A rational treatment for dispersive optical systems, *IEEE J. Quantum Electron.* 26: 1148–1157 (1990).
52. Turunen, J., Astigmatism in laser beam optical systems, *Appl. Opt.* 25: 2905–2911 (1986).
53. Siegman, A. E., *ABCD*-matrix elements for a curved diffraction grating, *J. Opt. Soc. Am. A* 2: 1793 (1985).
54. Duarte, F. J., Multiple-prism dispersion and 4×4 ray transfer matrices, *Opt. Quantum Electron.* 24: 49–53 (1992).
55. Martinez, O. E., Matrix formalism for pulse compressors, *IEEE J. Quantum Electron.* 24: 2530–2536 (1988).
56. Duarte, F. J., and J. A. Piper, Multi-pass dispersion theory of prismatic pulsed dye lasers, *Optica Acta* 31: 331–335 (1984).
57. Schäfer, F. P., Principles of dye laser operation, in *Dye Lasers,* edited by F. P. Schäfer, Springer-Verlag, Berlin, 1990, Chap. 1.
58. Duarte, F. J., J. J. Ehrlich, W. E. Davenport, and T. S. Taylor, Flashlamp pumped narrow-linewidth dispersive dye laser oscillators: Very low amplified spontaneous emission levels and reduction of linewidth instabilities, *Appl. Opt.* 29: 3176–3179 (1990).
59. Duarte, F. J., Multiple-return-pass beam divergence and the linewidth equation, *Appl. Opt.* 40: 3038–3041 (2001).
60. Harrison, J., and A. Mooradian, Linewidth and offset frequency locking of external cavity GaAlAs lasers, *IEEE J. Quantum Electron.* QE-25: 1152–1155 (1989).
61. Gavrilovic, P., A. V. Chelnokov, M. S. O'Neill, and D. M. Beyea, Narrow-linewidth operation of broad-stripe single quantum well laser diodes in a grazing incidence external cavity, *Appl. Phys. Lett.* 60: 2977–2979 (1992).
62. Cassidy, D. T., D. M. Bruce, and B. F. Ventrudo, Short-external-cavity module for enhanced single-mode tuning of InGaAsP and AlGaAs semiconductor diode lasers, *Rev. Sci. Instrum.* 62: 2385–2388 (1991).
63. Liu, K., and M. G. Littman, Novel geometry for single-mode scanning of tunable lasers, *Opt. Lett.* 6: 117–118 (1981).
64. Littman, M. G., Single-mode pulsed tunable dye laser, *Appl. Opt.* 23: 4465–4468 (1984).
65. McNicholl, P., and H. J. Metcalf, Synchronous cavity mode and feedback wavelength scanning in dye laser oscillators with gratings, *Appl. Opt.* 24: 2757–2761 (1985).

66. Favre, F., D. LeGuen, J. C. Simon, and B. Landousies, External-cavity semiconductor laser with 15 nm continued tuning range, *Electron. Lett.* 22: 795–796 (1986).
67. Trutna, W. R., and L. F. Stokes, Continuously tuned external cavity semiconductor laser, *J. Lightwave Technol.* 11: 1279–1286 (1993).
68. Berger, J. D., and D. Anthon, Tunable MEMS devices for optical networks, *Opt. Photon. News* 14 (3): 43–49 (2003).
69. Uenishi, Y., K. Honna, and S. Nagaoka, Tunable laser diode using a nickel micromachined external mirror, *Electron. Lett.* 32: 1207–1208 (1996).
70. Kogelnik, H., and C. V. Shank, Coupled-wave theory of distributed feedback lasers, *J. Appl. Phys.* 43: 2327–2335 (1972).
71. Liu, A. Q., X. M. Zhang, V. M. Murukeshan, and Y. Lam, A novel integrated micromachined tunable laser using polysilicon 3-D mirror, *IEEE Photon. Tech. Lett.* 13: 427–429 (2001).
72. Zhang, X. M., A. Q. Liu, C. Lu, and D. Y. Tang, Continuous wavelength tuning in micromachined Littrow external-cavity lasers, *IEEE J. Quantum Electron.* 41: 187–197 (2005).
73. Wyatt, R., and W. J. Devlin, 10 kHz linewidth 1.5 μm InGaAsP external cavity laser with 55 nm tuning range, *Electron. Lett.* 19: 110–112 (1983).
74. Shan, X., A. S. Siddiqui, D. Simeonidou, and M. Ferreira, Rebroadening of spectral linewidth with shorter wavelength detuning away from the gain curve peak in external cavity semiconductor laser sources, in *Conference on Lasers and Electro-Optics, 1991,* Optical Society of America, Washington, DC, 1991, pp. 258–259.
75. DeLabachelerie, M., and P. Cerez, An 850 nm semiconductor laser tunable over a 30 nm range, *Opt. Commun.* 55: 174–178 (1985).
76. Harvey, K. C., and C. J. Myatt, External-cavity diode laser using a grazing-incidence diffraction grating, *Opt. Lett.* 16: 910–912 (1991).
77. Volodin, B. L., S. V. Dolgy, E. D. Melnik, E. Downs, J. Shaw, and S. V. Bans, Wavelength stabilization and spectrum narrowing of high-power multimode laser diodes and arrays by use of volume Bragg gratings, *Opt. Lett.* 29: 1891–1893 (2004).
78. Meng, L. S., B. Nizamov, P. Nadasami, J. K. Brasseur, T. Henshaw, and D. K. Newmann, High-power 7-GHz bandwidth external-cavity diode laser array and its use in optically pumping singlet delta oxygen, *Opt. Ex.* 14: 10469–10474 (2006).
79. Chung, T-Y, A. Rapaport, V. Smirnov, L. B. Glebov, M. C. Richardson, and M. Bass, Solid-state laser spectral narrowing using a volumetric photothermal refractive Bragg grating cavity mirror, *Opt. Lett.* 31: 329–331 (2006).
80. Jelder, P., and F. Laurell, Efficient narrow-linewidth volume-Bragg grating-locked Nd: fiber laser, *Opt. Ex.* 15: 11336–11340 (2007).
81. Whalen, M. S., K. L. Hall, D. M. Tennant, U. Koren, and G. Raybon, Tunable fibre-extended-cavity laser, *Electron. Lett.* 23: 313–314 (1987).
82. Wacogne, B., J. P. Goedgebuer, A. P. Onokhov, and M. Tomilin, Wavelength tuning of a semiconductor laser using nematic liquid crystals, *IEEE J. Quantum Electron.* 29: 1015–1017 (1993).
83. Coquin, G. A., and K. W. Cheung, Electronically tunable external-cavity semiconductor laser, *Electron. Lett.* 24: 599–600 (1988).
84. Laurent, P., A. Clairon, and C. Breant, Frequency noise analysis of optically self-locked diode lasers, *IEEE J. Quantum Electron.* 25: 1131–1142 (1989).
85. Hemmerich, A., D. H. McIntyre, D. Schropp, D. Meschede, and T. W. Hänsch, Optically stabilized narrow linewidth semiconductor laser for high resolution spectroscopy, *Opt. Commun.* 75: 118–122 (1990).
86. Fox, R. W., A. S. Zibrov, H. G. Robinson, L. Hollberg, N. Mackie, and R. Ellingsen, Diode lasers stabilization, in *Proceedings of the International Conference on Lasers '91,* edited by F. J. Duarte and D. G. Harris, STS, McLean, VA, 1992, pp. 601–607.

87. Celikov, A., F. Riehle, V. L. Velichansky, and J. Helmcke, Diode laser spectroscopy in a Ca atomic beam, *Opt. Commun.* 107: 54–60 (1994).
88. Maki, J. J., N. S. Campbell, C. M. Grande, R. P. Knorpp, and D. H. McIntyre, Stabilized diode-laser system with grating feedback and frequency-offset locking, *Opt. Commun.* 102: 251–256 (1993).
89. Lee, S., and L. W. Hillman, Frequency stabilization of diode lasers, in *Proceedings of the International Conference on Lasers '91,* edited by F. J. Duarte and D. G. Harris, STS, McLean, VA, 1992, pp. 608–612.
90. Weiman, C. E., and L. Hollberg, Using diode lasers for atomic physics, *Rev. Sci. Instrum.* 62: 1–20 (1991).
91. Hollberg, L., CW dye lasers, in *Dye Laser Principles,* edited by F. J. Duarte and L. W. Hillman, Academic, New York, 1990, Chap. 5.
92. Salvatore, R. A., T. Schrans, and A. Yariv, Wavelength tunable source of subpicosecond pulses from CW passively mode-locked two-section multiple-quantum-well laser, *IEEE Photo. Tech. Lett.* 5: 756–758 (1993).
93. Corzine, S. W., J. E. Bowers, G. Przybylek, U. Koren, B. I. Miller, and C. E. Soccolich, Actively mode-locked GaInAsP laser with subpicosecond output, *Appl. Phys. Lett.* 52: 348–350 (1988).
94. Pang, L. Y., J. G. Fujimoto, and E. S. Kintzer, Ultrashort-pulse generation from high-power diode arrays by using intracavity optical nonlinearities, *Opt. Lett.* 17: 1599–1601 (1992).
95. Delfyett, P. J., L. Florez, N. Stoffel, T. Gmitter, N. Andreadakis, G. Alphonse, and W. Ceislik, 200 fs optical pulse generation and intracavity pulse evolution in a hybrid mode-locked semiconductor diode-laser/amplifier system, *Opt. Lett.* 17: 670–672 (1992).
96. Bouchoule, S., N. Stelmakh, M. Cavelier, and J. M. Lourtioz, Highly attenuating external cavity for picosecond-tunable pulse generation from gain/Q-switched laser diodes, *IEEE J. Quantum Electron.* 29: 1693–1700 (1993).
97. Myatt, C. J., N. R. Newbury, R. W. Ghrist, S. Loutzenhizer, and C. E. Wieman, Multiply loaded magneto-optical trap, *Opt. Lett.* 21: 290–292 (1996).
98. Berger, J. D., Y. Zhang, J. D. Grade, H. Lee, S. Hrinya, H. Jerman, A. Fennema, A. Tselikov, and D. Anthon, External cavity diode lasers tuned with silicon MEMS, *IEEE LEOS Newslett.* 15 (5): 9–10 (2001).
99. Dieckmann, A., FMCW-LIDAR with tunable twin-guide laser diode, *Electron. Lett.* 30: 308–309 (1994).
100. Grant, W. B., Lidar for atmospheric and hydrospheric studies, in *Tunable Laser Applications*, 1st ed., edited by F. J. Duarte, Marcel Dekker, New York, 1995, Chap. 7.
101. Camparo, J. C., The diode laser in atomic physics, *Contemp. Phys.* 26: 443–477 (1985).
102. Weidemuller, M., C. Gabbanini, J. Hare, M. Gross, and S. Harcoche, A beam of laser cooled lithium Rydberg atoms for precision microwave spectroscopy, *Opt. Commun.* 101: 342–346 (1993).
103. Olivares, I. E., A. E. Duarte, E. A. Saravia, and F. J. Duarte, Lithium isotope separation with tunable diode lasers, *Appl. Opt.* 41: 2973–2977 (2002).
104. Cooney, T. F., H. T. Skinner, and S. M. Angel, Evaluation of external-cavity diode lasers for Raman spectroscopy, *Appl. Spectrosc.* 49: 1846–1851 (1995).
105. Scheibner, H., St. Franke, S. Solyman, J. F. Behnke, C. Wilke, and A. Dinklage, Laser absorption spectroscopy with a blue diode laser in an aluminum hollow cathode discharge, *Rev. Sci. Instrum.* 73: 378–382 (2002).
106. Olejnicek, J., H. T. Do, Z. Hubicka, R. Hippier, and L. Jastrabik, Blue diode laser absorption spectroscopy of pulse magnetron discharge, *Jpn. J. Appl. Phys.* 45: 8090–8094 (2006).

107. Goldman, L., Dye lasers in medicine, in *Dye Laser Principles,* edited by F. J. Duarte and L. W. Hillman, Academic, New York, 1990, Chap. 10.
108. Dougherthy, T. J., Tumor detection and treatment: hematoporphyrin derivative and photofrin II, in *Laser Non-Surgical Medicine*, edited by L. Goldman, Technomic, Lancaster, PA, 1991.
109. Duarte, F. J., Two-laser therapy and diagnosis device, EP 0284330 A1 (1988).
110. Persson, L., M. Andersson, M. Cassel-Engquist, K. Svanberg, and S. Svanberg, Gas monitoring in human sinuses using tunable laser diode spectroscopy, *J. Biomed. Opt.* 12: 054001 (2007).
111. Tino, G. M., L. Hollberg, A. Sasso, M. Inguscio, and M. Barsanti, Hyperfine structure of the metastable $^5S_2$ state of ^{17}O using a AlGaAs diode laser at 777 nm, *Phys. Rev. Lett.* 64: 2999–3002 (1990).
112. Atutov, S. N., E. Mariotti, M. Meucci, P. Bicchi, C. Marinelli, and L. Moi, A 670 nm external-cavity single mode diode laser continuously tunable over 18 GHz range, *Opt. Commun.* 107: 83–87 (1994).
113. Duarte, F. J., Multiple-prism grating solid-state dye laser oscillators: optimized architecture, *Appl. Opt.* 38: 6347–6349 (1999).
114. Duarte, F. J., and R. O. James, Tunable solid-state lasers incorporating dye-doped polymer-nanoparticle gain media, *Opt. Lett.* 28: 3088–3090 (2003).
115. Duarte, F. J., L. S. Liao, K. M. Vaeth, Coherence characteristics of electrically excited tandem organic light-emitting diodes, *Opt. Lett.* 30: 3072–3074 (2005).
116. Duarte, F. J., Coherent electrically excited organic semiconductors: visibility of interferograms and emission linewidth, *Opt. Lett.* 32: 412–414 (2007).
117. Duarte, F. J., Coherent electrically excited organic semiconductors: coherent or laser emission? *Appl. Phys. B* 90: 101–108 (2008).
118. Papen, G. C., G. M. Murphy, D. J. Brady, A. T. Howe, J. M. Dallesasse, R. Y. Dejule, and D. J. Holmgren, Multiple-wavelength operation of a laser-diode array coupled to an external cavity, *Opt. Lett.* 18: 1441–1443 (1993).
119. Lotem, H., Z. Pan, and M. Dagenais, Tunable dual-wavelength continuous-wave diode laser operated at 830 nm, *Appl. Opt.* 32: 5270–5273 (1993).

6 Tunable Fiber Lasers

T. M. Shay and F. J. Duarte

CONTENTS

6.1 Introduction 179
6.2 Core and Cladding Pumped Fiber Lasers 180
6.3 Tunable Fiber Laser Configurations 182
6.3.1 Multiple-Prism Grating Configuration 187
6.4 Demonstrated Tunable Fiber Laser Performance 190
6.5 Summary 193
References 194

6.1 INTRODUCTION

Fiber lasers have become ubiquitous with the emergence of the telecommunications industry. Fiber lasers have been demonstrated to span the wavelengths from just below 400 nm to nearly 3 μm. Among fiber lasers the most widely used rare-earth-doped silica fibers are doped with Er^{+3}, Nd^{+3}, Yb^{+3}, and Tm^{+3}. These systems have the advantage of pump bands that are compatible with highly efficient diode lasers as well as quantum efficiencies that range from 0.63 to 0.95 depending upon the rare-earth ion being excited and the pump and emission wavelengths. All-fiber-based systems provide tunable performance with a minimal sensitivity to environmental disturbances as well as high reliability due to the fact that the all-fiber laser cavity cannot be misaligned and diffraction-limited beams are generally ensured by the use of single-mode optical fibers. As a result of these advantages fiber lasers are being employed in a steadily increasing number of applications that previously employed conventional solid-state lasers. Finally, the availability of very efficient and very high-power fiber amplifiers offers a simple means of scaling the output power of tunable fiber laser systems.

The three most widely tunable fiber laser media, Er^{+3}, Yb^{+3}, and Tm^{+3}, will be discussed. The tunable Yb-doped fiber lasers (YDFL) and the tunable Tm-doped fiber lasers (TDFL) are not as well explored a technology as the tunable Er-doped fiber lasers (EDFL) used for telecommunications applications. In the remaining sections some of the tuning techniques that have been employed in tunable YDFL, EDFL, and TDFL will be discussed.

6.2 CORE AND CLADDING PUMPED FIBER LASERS

Conceptually, the simplest fiber laser configuration is to efficiently launch a high-brightness laser into the single-mode core with reflectors on both ends. This configuration can lead to very short cavities and hence can provide a laser with fewer cavity modes than are achievable in equivalent lasers with longer cavities. Core-pumped lasers have the disadvantage that the pump must be high brightness for efficient coupling into the single-mode core of the fiber. In order for an optical fiber to be single-mode, the product of the mode-field-diameter and the numerical aperture must be

$$2 \cdot a_{laser} \cdot NA \leq \frac{\lambda}{\pi} \cdot 2.405 \tag{6.1}$$

where a_{laser} represents the fiber core radius and NA represents the numerical aperture of the fiber. In a typical $\lambda \approx 1$ μm single-mode fiber laser, the core diameter is 10 μm, and the NA is 0.08. The numerical aperture for an optical fiber is defined as

$$NA = n \cdot sin\,(\theta) \tag{6.2}$$

where n represents the index of refraction for the optical fiber and θ represents the fiber acceptance angle. The conservation of brightness requires that the product of the numerical aperture and the beam radius at any two points in the beam path be conserved

$$NA_1 \cdot r_1 = NA_2 \cdot r_2 \tag{6.3}$$

where $NA_{1,2}$ and $r_{1,2}$ represent the numerical apertures and radii at two points in the beam path.

The practical impact of Equation 6.3 for a fiber laser is that it requires that the product of the pump lasers' NA and spot radius be conserved. Therefore, the only sources that can efficiently pump a core-pumped single-mode fiber laser are very nearly diffraction-limited laser diodes that are only available at relatively low continuous wave (CW) powers. To achieve high efficiency and high power in fiber lasers it is necessary to pump the gain medium with low-brightness, very high CW power diode lasers. A dual-cladding fiber [1] can be used to efficiently convert the high CW power low-brightness light into a high-power diffraction-limited output beam from a single-mode optical fiber. The dual-cladding fiber geometry is illustrated in Figure 6.1.

In a dual-clad fiber design, a single-mode rare-earth-doped core is embedded within a multimode pump waveguide. The pump light from a low-brightness fiber laser can be efficiently coupled into the multimode pump waveguide, and the pump light is absorbed only in the single-mode core since the pump waveguide is undoped silica with insignificant optical losses. The practical advantage of this configuration is that the dual-clad fiber laser acts as an efficient brightness converter, taking the high output power from diode lasers that have between 50–75% electrical efficiency and converting that low-brightness light into the diffraction-limited output beam from the single-mode fiber core. In YDFL the optical diode pump radiation has been converted

- Large diameter pump waveguide
  - inner cladding surrounded by low-index outer cladding
  - efficient low brightness diode can pump single-mode core
- Single-mode-doped core embedded within the pump waveguide

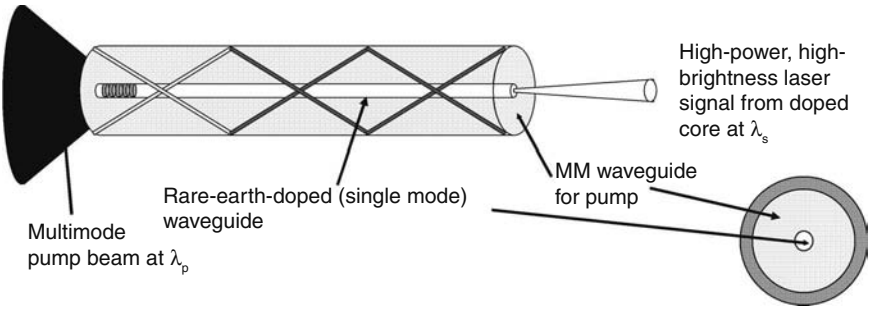
High-power, high-brightness laser signal from doped core at λ_s
MM waveguide for pump
Rare-earth-doped (single mode) waveguide
Multimode pump beam at λ_p

FIGURE 6.1 Dual-clad gain fiber configuration.

to the single-mode fiber laser output beam with an optical-to-optical conversion efficiency of 85% or more. The dual-clad fiber laser geometry was a key catalyst [2] in the development of high-power, high-efficiency, diffraction-limited lasers.

The increase in brightness available from dual-clad fiber lasers relative to the pump light can be estimated from the following equation

$$B_{ratio} = \frac{P_{Laser}}{\pi\left(NA_{Laser} \cdot a_{Laser}\right)^2} \frac{1}{\frac{P_{pump}}{\pi\left(NA_{pump} \cdot a_{pump}\right)^2}} = \eta_{optical} \frac{\left(NA_{pump} \cdot a_{pump}\right)^2}{\left(NA_{Laser} \cdot a_{Laser}\right)^2} \quad (6.4)$$

where P_{Laser} and P_{pump} represent the fiber laser and pump powers, respectively. NA_{Laser} and NA_{pump} represent the single-mode laser core and pump cladding numerical apertures, respectively. a_{Laser} and a_{pump} represent the laser and pump deliver fiber radii, respectively. $\eta_{optical}$ represents the optical conversion efficiency of pump power into single-mode fiber laser power. For example, a typical single-mode fiber laser operating at $\lambda \approx 1.064$ μm has a 5 μm core radius and a numerical aperture of 0.08. A pump cladding for this single-mode core can have a pump cladding diameter of between 125 and 400 μm with a numerical aperture of 0.44. Assuming a typical value for $\eta_{optical}$ of 80% and a pump cladding diameter of 400 μm with a single-mode core at $\lambda \approx 1.064$ μm the brightness enhancement can be calculated from Equation 6.4 as

$$B_{ratio} = \eta_{optical} \frac{\left(NA_{pump} \cdot a_{pump}\right)^2}{\left(NA_{Laser} \cdot a_{Laser}\right)^2} \cong 38{,}000 \quad (6.5)$$

The application of dual-clad fibers [2] has been a key enabling technology that has allowed the development of efficient high-power fiber lasers.

Er-, Yb-, and Tm-doped silica fiber lasers all have very wide absorption and emission bands. For example, Yb has absorption from 910 nm peaking at 977 nm and tailing off rapidly beyond 1060 nm, while the emission is relatively low for wavelengths below 970 nm, peaks at 977 nm like the absorption, and remains relatively high for wavelengths as long as 1100 nm. In Yb-doped fiber lasers tunable laser action has been demonstrated from 1020 nm to 1100 nm [3]. Er absorbs between 920 nm and 1480 nm with an absorption peak at 975 nm, and the emission wavelength for Er extends from 1480 nm to 1600 nm with most systems designed to operate at wavelengths in the 1520–1560 nm range. Finally, Tm has absorption bands between 780 nm and 1880 nm and has emission wavelengths between 1800 nm and 2500 nm. These rare-earths are popular laser media for tunable fiber lasers in part because of the wide tuning ranges and also because the absorption bands are compatible with highly efficient diode laser systems.

6.3 TUNABLE FIBER LASER CONFIGURATIONS

Fiber laser systems have been tuned using both ring and linear cavity geometries. In addition the frequency selective elements encompass external-cavity gratings [4–8], fiber Bragg gratings [9–18], fiber loop mirrors [19], multiple coupled ring cavities [19], fiber Fabry–Perot cavities [19, 20], acousto-optic tunable filters [21, 22], and several other tuning methods have also been employed. In many of the tunable fiber lasers, several frequency selective elements are used in a single tunable laser. As is typical of many widely tunable lasers the highest power tunable laser oscillators usually have fairly broad spectral widths. While the narrowest spectral width, or narrowest linewidth, oscillators produce lower output powers, there are a great many tunable fiber laser configurations. In this chapter a number of the most common and interesting configurations from the literature will be discussed.

The external grating tuned cavities typically are operated in the Littrow or the grazing-incidence grating configurations. Those two configurations are illustrated in Figures 6.2 and 6.3, respectively. For both configurations the laser consists of an optical pump beam, an output coupler, a doped fiber gain medium, an optional cladding mode stripper, a collimating lens, and a diffraction grating. The pump beam is generally launched through the output coupler for the laser cavity. The output coupler can be a bulk mirror or a fiber Bragg grating or in the case of a high-power laser simply the ~4% reflection from a flat cleaved silica fiber end. The gain medium is a rare-earth-doped fiber. The cladding mode strippers shown in Figures 6.2 and 6.3 are sometimes used in high-power cladding pumped fiber lasers to prevent the unabsorbed pump power from damaging the tuning elements. The laser light exits the fiber core and is collimated by a lens, and then the light is directed to the tuning element. A fiber laser tuned directly by a diffraction grating in Littrow configuration is shown in Figure 6.2, while Figure 6.3 illustrates a fiber laser tuned by the diffraction grating-mirror combination of the GI grating configuration.

The wavelength tuning of a diffraction grating is determined by the diffraction grating equation [23]

$$m\lambda = d(\sin\theta \pm \sin\theta') \tag{6.6}$$

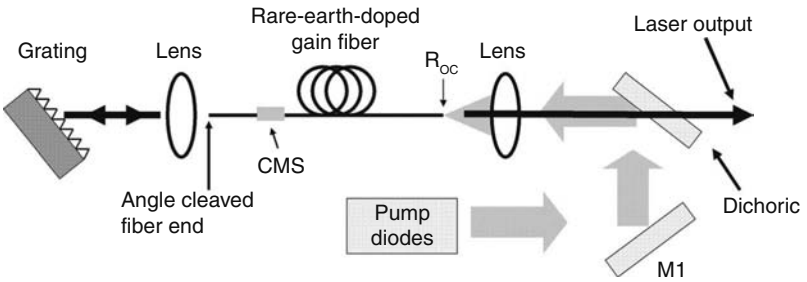

FIGURE 6.2 Littrow diffraction grating tuned rare-earth-doped fiber laser. CMS represents a cladding mode stripper, and R_{OC} represents the output coupler mirror.

where m represents the diffraction order, λ represents the wavelength, d represents the groove spacing, while θ and θ' represent the angles of incidence and diffraction on the grating, respectively. Equation 6.6 is used to calculate the oscillation wavelength for both the GI grating and Littrow grating laser cavities (see Chapter 5 for further details).

The spectral resolution of a diffraction grating depends upon the number of grooves illuminated by collimated light incident upon the grating. The well-known resolution of the diffraction grating is

$$R = \frac{\lambda}{\Delta\lambda} = m \cdot N \tag{6.7}$$

where $\Delta\lambda$ represents the spectral width of the diffraction grating and N represents the number of grooves illuminated on the grating surface. Substituting for m from Equation 6.6 into Equation 6.7 and solving for the spectral width, or linewidth $\Delta\lambda$, we obtain

$$\Delta\lambda = \lambda^2/(N d(\sin\theta \pm \sin\theta')) \tag{6.8}$$

where N times d represents the product of the groove spacing and the number of grooves.

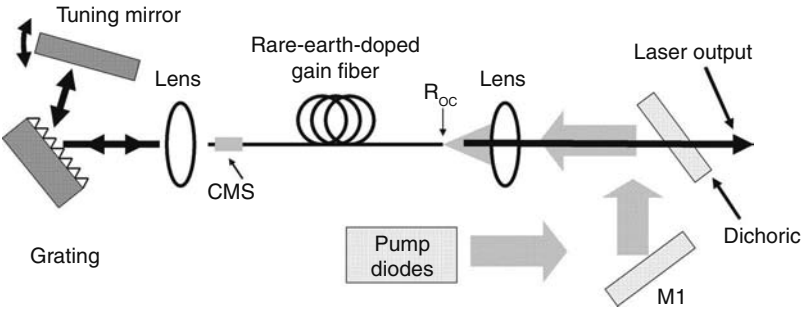

FIGURE 6.3 Grazing-incidence (GI) diffraction grating rare-earth-doped fiber laser. This type of cavity is also known in the literature as Littman–Metcalf or Littman cavity. CMS represents a cladding mode stripper, and R_{OC} represents an output coupler.

For the Littrow grating tuned laser cavity the angles of incidence and refraction are the same, so that $\theta = \theta'$, therefore the lasing wavelength is

$$\lambda = (2d/m)\sin\theta \tag{6.9}$$

and

$$\Delta\lambda = \lambda^2/(2Nd(\sin\theta)) \tag{6.10}$$

These linewidth equations implicitly assume illumination of the whole grating length (Nd) by a nearly collimated beam with a Gaussian profile. For the GI grating tuned laser cavity the incident angle, θ is typically ~88° to 89°. Therefore, the lasing wavelength of a GI grating tuned laser cavity is to a very good approximation

$$\lambda \cong (2d/m)(1+\sin\theta') \tag{6.11}$$

In fiber lasers the GI grating configuration has produced narrower spectral widths than the Littrow configuration [4]. The disadvantage of bulk grating tuned fiber lasers is that both the pump and signal light are free-space coupled in and out of the fiber laser. These free-space coupled fiber lasers are less robust than the all-fiber tunable lasers. For a general discussion of the efficiency and linewidth performances of both Littrow and GI grating cavities the reader should refer to [23].

An all-fiber tunable oscillator is much less sensitive to environmental and mechanical disturbances than a free-space coupled tunable fiber oscillator. The development of fiber Bragg grating tuning elements has allowed the production of all-fiber tunable lasers. The reflection of a fiber Bragg grating is the result of a periodic small permanent index variation along a short length of fiber. The periodic index variation is induced by irradiation of the fiber with an ultraviolet laser. The fiber Bragg grating reflection wavelength, λ_B, is

$$\lambda_B = 2 \cdot n \cdot \Lambda \tag{6.12}$$

where n represents the average index of the grating and Λ represents the grating period. The spectral selectivity associated with a Bragg grating can be expressed as (see Chapter 5)

$$\Delta\lambda_B \approx \lambda^2/2nd \tag{6.13}$$

where d is the thickness of the Bragg grating. Commercial fiber Bragg gratings are frequency selective in reflection, and gratings with reflection spectral widths as low as $\Delta\lambda_B \approx 0.1$ nm are readily available. The fiber Bragg grating reflection wavelength depends upon the grating period Λ. Therefore any physical effect that results in a change in the grating period will tune the grating wavelength. Physical processes that change the fiber Bragg grating period include applying stress, strain, or thermal expansion or contraction applied to tune the fiber Bragg grating. Therefore, the fiber Bragg grating reflection wavelengths can be tuned thermally [9, 10], by stretching [9, 11, 12], or by compressing [13–15] the fiber Bragg gratings. Compressing the fiber

Bragg grating is most easily induced by bending the fiber. The maximum tuning range for a fiber Bragg grating of 45 nm was demonstrated in an Yb^{+3}-doped fiber laser tuned by bending the grating [15]. The wavelength shift in the Bragg wavelength, $\delta\lambda_B$, as a function of strain and temperature is given by [24]

$$\delta\lambda_B = 2n\Lambda\{(1-(n^2/2)[p_{12}-\nu_p(p_{11}+p_{12})])\varepsilon + (\alpha+n^{-1}(dn/dT))\Delta T\} \quad (6.14)$$

where the p_{ij} represents the Pockels coefficients of the stress-optic tensor, ν_p represents Poisson's ratio, α represents the coefficient of thermal expansion of the fiber material, and ΔT represents the temperature change. In a typical silica fiber the temperature effects account for 95% of the observed wavelength shift [9]. However, temperature tuning is slow and therefore most fiber Bragg grating tuned lasers are tuned by strain.

A fiber Bragg grating compression configuration is shown in Figure 6.4. The fiber Bragg grating is glued to a beam and then the beam is bent to compress the fiber. Under those conditions the strain in the fiber is given by [15]

$$\varepsilon = -0.5 \cdot \frac{d}{R} \quad (6.15)$$

where d represents the thickness of the beam and R represents the radius of curvature of the beam. Note that care must be taken to keep the strain below the fiber's breaking point [16] of approximately 0.07.

The common basic linear and basic ring cavity configurations for all-fiber rare-earth-doped fiber lasers are shown in Figures 6.5 and 6.6.

The basic tunable linear all-fiber cavity consists of a tunable fiber Bragg grating (TFBG) that selects lasing wavelength, a diode pump source, a pump coupler, a rare-earth-doped gain fiber, an optional cladding mode stripper, and an output coupler. For a core-pumped single-mode fiber laser the pump is coupled in by a wavelength division multiplexor that couples the pump light into the doped laser core. The wavelength division multiplexor is designed to be transparent to the fibers' lasing

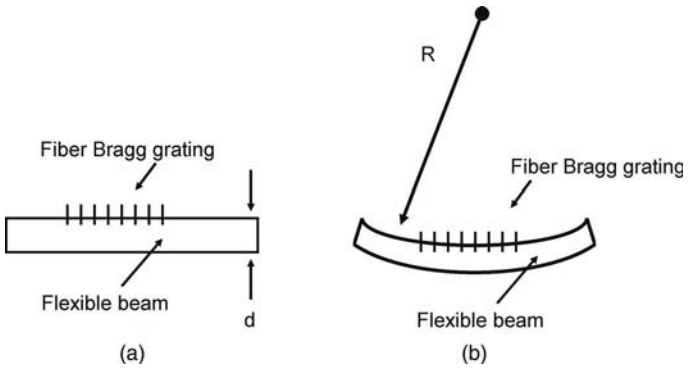

FIGURE 6.4 (a) Flexible beam of thickness d with fiber Bragg grating glued to the beam. (b) Flexible beam bent at radius of curvature R with compressed fiber Bragg grating.

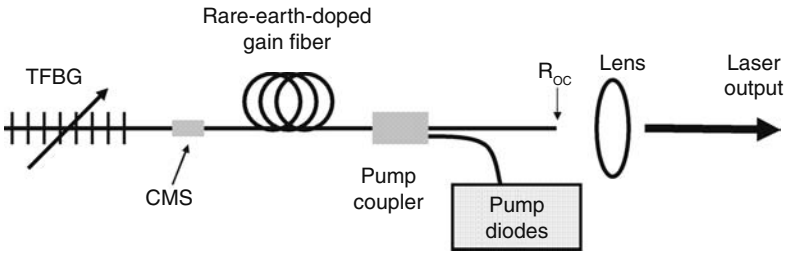

FIGURE 6.5 Generic linear cavity all-fiber tunable rare-earth-doped fiber laser. CMS represents a cladding mode stripper, and R_{OC} represents the output coupler mirror.

wavelength. In the case of cladding pumped fiber lasers either a tapered fiber bundle or side couplers are used to launch the pump light into the pump cladding. The single-mode region of the gain fiber is doped with the rare-earth ions that absorb the pump light to create the population inversion. The cladding pumped configurations are preferred for fiber lasers with output powers exceeding a few watts. In high-power cladding pumped lasers a cladding mode stripper is used to prevent the unabsorbed pump power from damaging the pumps or other power-sensitive laser components. A cladding mode stripper consists of a short section of fiber where the low-index outer cladding that trapped the pump light has been removed and is replaced by a high-index coating that allows any unabsorbed pump light to escape from the pump cladding. The output coupler for these systems can be either a partially transmitting fiber Bragg grating or simply a flat cleaved fiber end.

A generic tunable all-fiber ring cavity is illustrated in Figure 6.6. The ring cavity has a few more elements compared to the linear cavity; however, it generally produces a significantly narrower laser linewidth. The ring cavity consists of a tunable fiber Bragg grating (TFBG) that selects lasing wavelength, a diode pump source, a pump coupler, a rare-earth-doped gain fiber, an optical isolator, an optical circulator, an output coupler, and an optional cladding mode stripper. As was the case for the

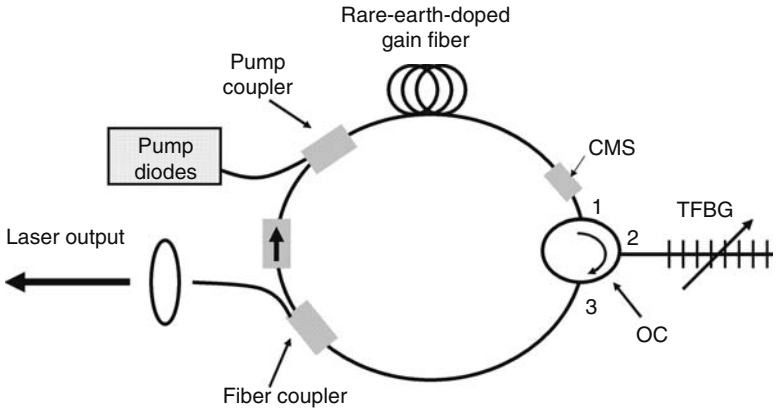

FIGURE 6.6 Generic unidirectional ring cavity all-fiber tunable rare-earth-doped fiber laser. CMS represents a cladding mode stripper, OC represents a three-port optical circulator, and the output coupler is a fiber power splitter.

linear fiber cavity, the pump coupler consists either of a wavelength division multiplexor that couples the pump light into the doped core or core pumped fibers. For cladding pumped fibers, a tapered fiber bundle or side couplers are used to launch the pump light into the pump cladding. The single-mode region of the gain fiber is doped with the rare-earth ions that absorb the pump light to create the population inversion. The optical isolator ensures that the laser light only travels in one direction. Unidirectional oscillation of the ring laser ensures that hole-burning effects will be avoided and that the ring laser cavity oscillates with fewer modes than the comparable linear cavity laser. Because tunable fiber Bragg gratings are frequency selective only in reflection, the three-port optical circulator allows light from port 1 to be directed to the TFBG at port 2. Here, the narrow bandwidth reflection from the TFBG spliced to port 2 provides frequency selection. The light reflected from the TFBG is then returned to port 3 of the optical circulator thus providing frequency selection in each trip around the ring laser cavity. The output coupler for these systems is generally an evanescent coupled fiber power splitter that outcouples some fraction of the power in the laser cavity. In general, the output power from fiber ring cavities is polarized by a polarizing element in the laser cavity. Common polarizing elements include a polarization-sensitive optical circular or polarization-sensitive optical isolators.

Those elements in conjunction with polarization-maintaining coupled fibers, or manual polarization control paddles, will provide stable polarized output from the ring laser. While polarization control paddles and nonpolarization-maintaining fibers can be used, this system often requires frequent adjustments and therefore a much more robust system is obtained if polarization-maintaining gain fibers are used. As with the linear cavity case, the cladding pumped system is preferred for fiber lasers with output powers exceeding a few watts. In the case of high-power cladding pumped lasers a cladding mode stripper is used to prevent the unabsorbed pump power from damaging the pumps, tunable fiber Bragg grating, or other optical components in the laser.

6.3.1 Multiple-Prism Grating Configuration

Now we revisit the linewidth issue from a slightly different perspective. The cavity linewidth equation is given by [23]

$$\Delta\lambda \approx \Delta\theta\,(\partial\Theta/\partial\lambda)^{-1} \tag{6.16}$$

where $\Delta\theta$ is the beam divergence of the beam, at the gain region, with a beam waist of w, and $(\partial\Theta/\partial\lambda)$ is the overall cavity dispersion. For a single-transverse-mode beam, with a Gaussian profile, experiencing a beam expansion M from the exit of the gain medium, to the entrance of the grating, the linewidth is given by

$$\Delta\lambda \approx \Delta\theta\,(M\,(\partial\Theta/\partial\lambda)_G)^{-1} \tag{6.17}$$

where $(\partial\Theta/\partial\lambda)_G$ is the grating dispersion either in grazing-incidence, near-grazing incidence, or Littrow configuration. Assuming a nearly diffraction limited beam [23]

$$\Delta\theta = \lambda/\pi w \tag{6.18}$$

profile and a GI or near GI grating configuration the linewidth equation takes the form of

$$\Delta\lambda \approx (\lambda^2/\pi Mw)(\cos\theta/(\sin\theta \pm \sin\theta')) \tag{6.19}$$

Again, this equation assumes that the whole diffractive length of the grating is being illuminated by a Gaussian beam of modified, or expanded, width $2Mw$. The linewidth expression for Littrow configuration follows by setting the angle of incidence equal to the angle of diffraction, that is $\theta = \theta'$.

Multiple-prism grating configurations, with the grating deployed either in Littrow or near grazing-incidence configuration, have been applied and demonstrated with a variety of gain media [23]. Beyond traditional high-gain, homogeneously broadened, broadly tunable lasers media, these configurations have also been applied to gas lasers [25–27] and semiconductor lasers [28, 29]. In the case of gas lasers, single-longitudinal-mode oscillation has been reported, for cavity lengths of approximately 107 cm, with a laser linewidth of $\Delta\nu \approx 140$ MHz [26]. This result is particularly relevant to contemporary fiber lasers where optimized multiple-prism grating configurations should yield tunable single-longitudinal-mode lasing.

For example, let us consider a hypothetical Yb-doped fiber laser oscillator with a core fiber diameter of $2w = 30$ μm and an overall cavity length of 1 m. These types of lasers have been demonstrated to lase in the 1531 nm $\leq \lambda \leq$ 1568 nm range [30] so we shall consider a central wavelength $\lambda = 1550$ nm. Following the approach outlined in [23] a five-prism achromatic expander is selected to illuminate a 1200 lines/mm grating deployed in its first diffraction order. For this, a grating with a length of 100 mm is selected (see Fig. 6.7). The parameters imposed by the core of the fiber and the dimensions of the grating dictate that the multiple-prism beam expander should provide an overall magnification factor of $M \approx 990$. The multiple-prism dispersion equation, for orthogonal beam exit, is given by [23] (also, see Chapters 5 and 13)

$$\nabla_\lambda \phi_{2,r} = \sum_{m=1}^{r} (\pm 1)\mathcal{H}_{1,m}\left(\prod_{j=m}^{r} k_{1,j}\right)^{-1} \nabla_\lambda n_m \tag{6.20}$$

Setting $\nabla_\lambda \phi_{2,m} \approx 0$ then, for four right-angle prisms, with identical angular dimensions, deployed at the same angle of incidence, and designed for orthogonal beam exit, plus a fifth compensating prism we arrive at

$$(k_{1,1} + k_{1,1}k_{1,2} + k_{1,1}k_{1,2}k_{1,3} + k_{1,1}k_{1,2}k_{1,3}k_{1,4})n\tan\psi_{1,1} = (k_{1,1}k_{1,2}k_{1,3}k_{1,4})\tan\phi_{1,5} \tag{6.21}$$

For fused silica at 1550 nm ($n \approx 1.44402$) selecting the beam expansion of the first four prisms as

$$k_{1,1} = k_{1,2} = k_{1,3} = k_{1,4} = 5 \tag{6.22}$$

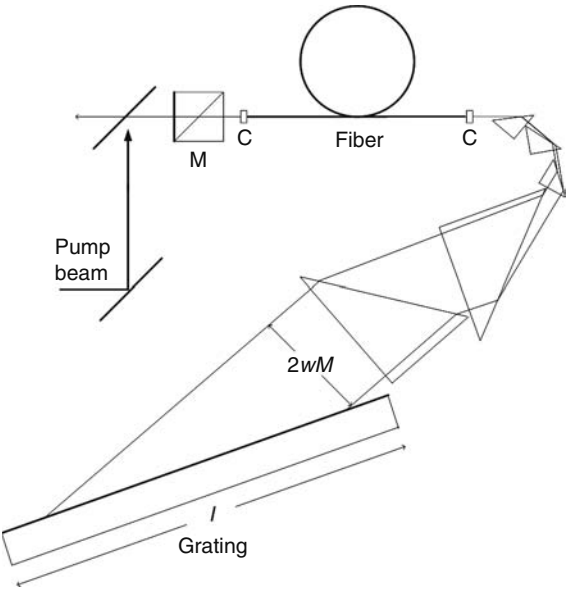

FIGURE 6.7 Multiple-prism Littrow (MPL) grating configuration for narrow-linewidth tunable fiber lasers. This simplified diagram is not drawn to scale. The length of the grating is $l = 100$ mm and the width of the one-dimensional expanded beam illuminating the grating is calculated to be $2wM \approx 29.61$ mm. The letter C indicates the position of collimators and the M at the output stands for mirror. This output-coupler mirror is a Glan–Thompson polarizer with its reflective coating at the exit surface (see text).

yields

$$\phi_{1,1} = \phi_{1,2} = \phi_{1,3} = \phi_{1,4} \approx 81.65^{\circ} \tag{6.23}$$

and

$$\psi_{1,1} = \psi_{1,2} = \psi_{1,3} = \psi_{1,4} \approx 43.25^{\circ} \tag{6.24}$$

Then using Equation 6.21 the parameters for the fifth prism, deployed in a compensating mode, become $\phi_{1,5} \approx 59.46^{\circ}$, $\psi_{1.5} \approx 36.62^{\circ}$, and $k_{1,5} \approx 1.58$, so that

$$k_{1,1}k_{1,2}k_{1,3}k_{1,4}k_{1,5} \approx 987 \tag{6.25}$$

Thus, assuming a single-transverse mode, with nearly diffraction limited divergence, and using $M \approx 987$, in [23]

$$\Delta\lambda \approx \Delta\theta(M(\partial\Theta/\partial\lambda)_G)^{-1} \tag{6.26}$$

the estimated double-pass, or single return-pass, linewidth becomes $\Delta\lambda \approx 0.01$ nm or $\Delta\nu \approx 1.27$ GHz at $\lambda = 1550$ nm. It should be noted that double-pass dispersive linewidth estimates are known to be an upper limit of the observed laser linewidth [23, 31, 32]. This means that for long pulse, or CW operation, the emission might

well approach a single-longitudinal mode for a cavity length of approximately 1 m where the longitudinal mode spacing is ~150 MHz. In the present configuration only ~81 mm of the grating are illuminated at 1550 nm leaving ample diffractive space at the grating for tuning to longer wavelengths. It should be noted that the use of high-density diffraction gratings with diffractive lengths of up to 140 mm is a known, and proven, feature in long-pulse narrow-linewidth tunable laser oscillators [33]. In practice, the beam expansion needed should be somewhat smaller given that the emerging beam diameter from the collimators will be greater than the $2w$ generated at the exit of the gain medium.

Although this design might appear somewhat unusual it should be remembered that the multiple-prism beam expansion can be accomplished in a fairly compact manner requiring little extra cavity space. Also the cavity configuration remains *closed* (see Chapter 5), thus reducing the amount of ASE in the output. Compared to grazing-incidence grating designs, deployment in a Littrow configuration is known to offer higher efficiencies. Again, the efficiency of grazing-incidence grating configurations can be improved using prism preexpansion [23, 26, 32].

As hinted at previously this should be considered the first step, in an iterative process, to design an optimized multiple-prism configuration capable of yielding single-longitudinal-mode oscillation at reasonable efficiencies. An alternative design using only a four-prism expander with $k_{1,1}k_{1,2}k_{1,3} \approx 8$ and an overall beam expansion of $M \approx 773$ yields a double-pass linewidth estimate of $\Delta\lambda \approx 0.013$ nm or $\Delta\nu \approx 1.63$ GHz at $\lambda = 1550$ nm. This would also require the use of 1200 lines/mm grating; however, its length only needs to be ~70 mm.

As far as polarization is concerned, the multiple-prism grating assembly induces a strong polarization parallel to the plane of incidence [23, 32–34], which is further reinforced by the Glan–Thompson output coupler mirror [23, 35]. In this polarizer output-coupler the inner surface is antireflection coated while the exit surface is typically coated at ~20% depending on the gain conditions. This added polarization feature also reduces the amount of ASE in the output emission [23].

In general the aim in this multiple-prism grating approach to linewidth narrowing is to illuminate the whole available diffractive length of the grating with a single-transverse mode of near-Gaussian profile. The larger the number of grooves that are thus illuminated, the narrower the dispersive linewidth [23].

6.4 DEMONSTRATED TUNABLE FIBER LASER PERFORMANCE

A selected summary of a few specific demonstrations of fiber laser performance are listed in Tables 6.1 and 6.2. The tables list for the most part some recently reported results. Table 6.1 lists tunable fiber laser results reported in the literature for Er-doped fiber lasers. The tunable Er-doped fiber lasers have received the most attention due to their importance in fiber telecommunications. All of the techniques described in this chapter and other techniques have been employed to tune Er-doped fiber lasers. In the case of Yb- and Tm-doped tunable fiber lasers only bulk diffraction grating tuning and fiber Bragg gratings have been used for wavelength tuning.

Table 6.1 lists a high-power and a narrow-linewidth result for most of the tuning techniques. For example the first entry is the high-power bulk diffraction grating tuned system reported by Nilsson et al. [6]. In their experiments a Littrow configuration was

TABLE 6.1
Characteristics of Er-Doped Tunable Fiber Lasers

Tuning technique	Tuning range (nm)	Linewidth	Power (W)	η_{slope} (%)	Ref.
Diffraction grating	1533–1600	0.25 nm	6.7	38	6
Fiber Bragg grating	1532–1567	0.15 nm	43	32	8
	1510–1580	100 MHz	5×10^{-4}	NR	17
Multiple ring cavities	1481–1513	0.02 nm	1×10^{-3}	NR	19
Acousto-optic tunable filter	1540–1578	9 GHz	0.1	NR	22
	1533–1581	1.3 kHz	1.2×10^{-4}	NR	21

used for frequency selectivity. They demonstrated a very wide tuning range of 67 nm and moderate power with a linewidth of 0.25 nm at a slope efficiency of 38%.

A fiber Bragg grating tuned Er-doped fiber laser providing a 35 nm of tuning, with 43 W of output power, at a linewidth of 0.15 nm, and a slope efficiency of 32%, was reported by Jeong et al. [8]. In rare-earth-doped fiber lasers the oscillation shifts to longer wavelengths as the fiber length is increased. It is well known that in an Er-Yb co-doped glass the Yb^{+3} ions excited by 975 nm photons will transfer their energy to the upper laser level of the Er^{+3}. To ensure that the tunable oscillator remained in the 1550 nm spectral region, the 3.5-m-long large-mode area gain fiber was co-doped with Yb. The diameter of the large-mode area fiber was 30 μm. The large-mode area fiber is a multimode fiber where coiling has been used to increase the losses in the higher-order modes and hence nearly single-mode output can be maintained in a multimode fiber [36]. This laser was a free-space pumped linear cavity where a dichroic mirror was used at the output of the laser to separate the pump light delivered to the dual-cladding laser and the single-mode tunable laser light. The unabsorbed pump light is prevented from reaching the tunable fiber Bragg grating by a 1-m-long section of single-mode fiber that was taper-spliced to the large-mode Er–Yb doped gain fiber. To prevent broadband reflections from contributing optical feedback the end of the TFBG was angle cleaved. The TFBG was tuned by compression.

A fiber ring laser with a 100 MHz linewidth that tuned over 70 nm, with an output power of 0.5 mW, was reported by Chen et al. [17]. The linewidth was narrowed by a tunable fiber Bragg filter, a fiber Fabry–Perot filter and a saturable absorption section of Er-doped fiber was located at a port of an optical circulator.

TABLE 6.2
Characteristics of Tunable Yb- and Tm-Doped Fiber Lasers

Tuning technique	Tuning range (nm)	Linewidth	Power (W)	η_{slope} (%)	Ref.
Diffraction grating (Yb^{+3})	1027–1100	0.3 nm	2.8	16	3
Diffraction grating (Tm^{+3})	1859–2061	<0.5 nm	17.4	65	7
	2275–2415	210 MHz	0.006	19	4
Fiber Bragg grating (Yb^{+3})	1048–1093	0.15 nm	6	60	15
	1040–1100	0.1 nm	0.8	52	18

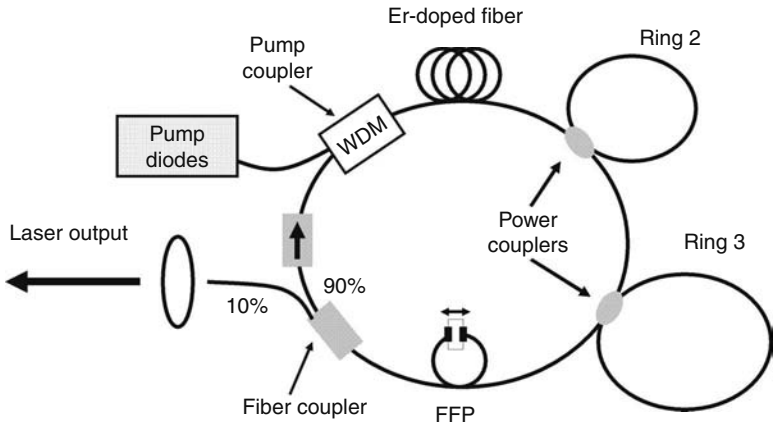

FIGURE 6.8 A multiring cavity all-fiber tunable Er-doped fiber laser. FFP represents a fiber Fabry–Perot filter, the pump coupler is a wavelength division multiplexor (WDM), two passive ring cavities coupled to the laser cavity, and the output coupler is a 90/10 fiber power splitter.

A multiple ring cavity fiber laser that was tunable over 32 nm with a linewidth of 0.02 nm, at an output power of 1 mW, was reported by Yeh et al. [19]. The multiple ring cavity is an all-fiber configuration that is a variation of the ring cavity illustrated in Figure 6.8, where a tunable fiber Fabry–Perot cavity and a main fiber ring with two subrings form coupled cavities with the main ring. In this design the only wavelengths that can oscillate are the wavelengths that resonate, simultaneously, in all three ring cavities and the fiber Fabry–Perot cavity. Unidirectional oscillation is guaranteed by optical isolators, and the output coupling is accomplished by an evanescent outcoupler as described earlier.

The final two entries in Table 6.1 are the acousto-optically tuned lasers. The acousto-optically tuned lasers both have very narrow linewidths. Tuning over 38 nm was reported with a linewidth of 9 GHz at an output power of 100 mW [22]. This acousto-optically tuned all-fiber laser is another all-fiber configuration that is a variation of the ring configuration of Figure 6.6, where an inline acousto-optic tunable filter replaces the tunable fiber Bragg grating and optical circulator combination shown in Figure 6.6. One significant advantage of the acousto-optic-tuned fiber laser is that the laser wavelength can be shifted on timescales of a few milliseconds [22].

The final laser configuration listed in Table 6.1 is an all-fiber ring laser variation with an inline acousto-optic tunable filter again replacing the tunable fiber Bragg grating and optical circulator configuration and adding an unpumped Er-doped fiber segment as a saturable absorber at port 2 of an optical circulator. This design was tunable over 48 nm at an output power ~100 μW but with a linewidth of 1.3 kHz. This implies that this system operated in a single longitudinal mode.

As shown in Table 6.1, Er-doped fiber lasers have demonstrated tuning ranges of up to 70 nm, up to 43 W of tuned laser power, and linewidths as low as 1.3 kHz. However, at the present time each of those impressive results was obtained using a different laser cavity design. Perhaps in the future a single system will be available that can simultaneously provide all of these characteristics.

Table 6.2 lists some of the recent tunable laser performance reported for Yb- and Tm-doped fiber laser systems. There has been much less research on tunable Yb- and Tm-doped fiber lasers compared to Er-doped tunable fiber lasers.

The bulk diffraction grating systems are listed first in Table 6.2. A bulk diffraction grating tuned Yb-doped fiber laser with a tuning range of 73 nm, at an output power of 2.8 W, with a 0.3 nm linewidth and a slope efficiency of 16% was reported in [3]. This design is a variation of the linear cavity configuration shown in Figure 6.2 where the light exiting the tuning end of the fiber is reflected off a dichroic mirror that reflects the signal light and transmits the pump light to protect the diffraction grating from damage by the unabsorbed pump light. The signal light is turned 90 degrees by the dichroic mirror so that it is incident upon the Littrow grating and then the frequency selected light is sent back into the linear laser cavity.

The last rows of Table 6.2 list the all-fiber Yb-doped fiber laser systems. Tuning over 45 nm with a linewidth of 0.15 nm, at an output power of 6 W, with a 60% slope efficiency, were reported in [15]. This all-fiber linear cavity design uses the configuration of Figure 6.5 with a tunable fiber Bragg grating. The fiber Bragg grating is tuned in compression by gluing the fiber Bragg grating to a flexible beam and bending the beam as shown in Figure 6.4. The authors report that compressing the fiber Bragg grating increases the grating reflection coefficient and in their case results in increased output power. The next laser is in an all-fiber ring cavity configuration (see Fig. 6.6) with a tunable filter in the ring. This system reported 60 nm of tuning with a 0.1 nm linewidth, at an output power of 0.8 W, and a sloped efficiency of 52% [18].

Finally, the Tm-doped tunable fiber lasers selected are both bulk grating tuned devices. The highest power results listed are 17.4 W, with a tuning range of 202 nm, at a 0.5 nm linewidth and a slope efficiency of 65% [7]. This cladding pumped design is a variation of the linear cavity configuration shown in Figure 6.2 where the light exiting the tuning end of the fiber is reflected off a dichroic mirror that reflects the signal light and transmits the pump light to protect the diffraction grating from damage by the unabsorbed pump light. The signal light is turned 90 degrees by the dichroic mirror so that it is incident upon the Littrow grating and then the frequency selected light is sent back into the linear laser cavity. These authors also report tuning a core-pumped Tm-doped fiber laser from 1723 nm to 1973 nm. The final Tm-doped tunable fiber laser design is a GI grating design. This bulk grating tuned laser was tunable over 140 nm, at an output power of 6 mW, with a slope efficiency of 19%, and a linewidth of 210 MHz [4].

Table 6.2 indicates that Tm-doped tunable fiber lasers can have tuning ranges of 202 nm, powers of 17 W, and linewidths as low as 210 MHz. However, similar to the Er-doped tunable fiber laser systems all of the above accomplishments cannot be demonstrated in a single device. Finally, the research on tunable Yb-doped fiber has also shown wide tuning ranges and significant powers.

6.5 SUMMARY

There are a large number of tunable fiber oscillator laser configurations. A few of the most common and some interesting tunable fiber laser systems have been discussed in this chapter. All-fiber tunable lasers with linewidths in the kHz range have been demonstrated [21]. All-fiber tunable lasers with tuning ranges of 70 nm have also

been reported [17]. Bulk diffraction grating tuned fiber lasers have been demonstrated with a tuning range of 202 nm [7]. Linewidths as low as 210 MHz have also been demonstrated in a GI grating fiber laser cavity [4]. Many of the tunable fiber lasers have demonstrated slope efficiencies of more than 30%. There is a great deal of activity in the development of tunable fiber laser systems and further improvements are to be expected in the near future.

While this chapter has only discussed tunable laser oscillators, it is important to note that all-fiber kHz linewidth fiber amplifiers with power levels of 177 W have been reported. A properly designed fiber amplifier seeded by a tunable source is a straightforward method for producing a high-power narrow-linewidth tunable fiber source. There is currently a great deal of effort devoted to developing narrow-linewidth fiber amplifiers. Recently, a narrow-linewidth Yb-doped fiber amplifier [37] has amplified a 1 mW source up to 500 W. It is possible to design a high-power narrow-linewidth tunable optical source by using a narrow-linewidth tunable low-power oscillator as a seed for a chain of high-power fiber amplifiers. As previously shown, in other types of high-power tunable lasers [23], when this master oscillator power amplifier approach is used, tunable high power and narrow linewidth are completely compatible.

REFERENCES

1. Maurer, R., Optical waveguide light source, US Patent 3808549 (1974).
2. Zenteno, L., High power double-clad fiber lasers, *IEEE J. Lightwave Tech.* 11: 1435–1446 (1993).
3. Nilsson, J., W. A. Clarkson, R. Selvasa, J. K. Sahu, P. W. Turner, S.-U. Alam, and A. B. Grudinin, High power wavelength-tunable cladding-pumped rare-earth-doped silica fiber lasers, *Opt. Fiber Tech.* 10: 5–30 (2004).
4. McAleavey, F. J., J. O'Gorman, J. F. Donegan, B. D. MacCraith, J. Hegarty, and G. Maze, Narrow linewidth, tunable Tm^{+3}-doped fluoride fiber laser for optical-based hydrocarbon gas sensing, *IEEE J. Selec. Top. Quantum Electron.* 3: 1103–1111 (1997).
5. Soh, D. B. S., S. Yoo, J. Nilsson, J. K. Sahu, K. Oh, S. Baek, Y. Jeong, C. Codemard, P. Dupriez, J. Kim, and V. Philippov, Neodymium-doped cladding pumped aluminosilicate fiber laser tunable in the 0.9-μm wavelength range, *IEEE J. Quantum Electron.* 40: 1275–1282 (2004).
6. Nilsson, J., S. Alam, J. A. Alvarez-Chavez, P. W. Turner, W. A. Clarkson, and A. B. Grudinin, High-power and tunable operation of Erbium-Ytterbium co-doped cladding-pumped fiber lasers, *IEEE J. of Quantum Electron.* 39: 987–993 (2003).
7. Shen, D. Y., J. K. Sahu, and W. A. Clarkson, High-power widely tunable Tm:fibre lasers pumped by an Er, Yb co-doped fibre laser at 1.6-μm, *Opt. Ex.* 14: 6084–6090 (2006).
8. Jeong, Y., C. Alegria, J. K. Sahu, L. Fu, M. Ibsen, C. Codemard, M. R. Mokhtar, and J. Nilsson, A 43-W C-band tunable narrow-linewidth Erbium-Ytterbium codoped large-core fiber laser, *IEEE Photon. Tech. Lett.* 16: 756–758 (2004).
9. Liaw, S-K., W. Y. Jang, C-J. Wang, and K. L. Hung, Pump efficiency improvement of a C-band tunable fiber laser using an optical circular and tunable fiber gratings, *Appl. Opt.* 46: 2280–2285 (2007).
10. Liaw, S-K., K.-L. Hung, Y.-T. Lin, C.-C. Chinag, and C.-S. Shin, C-Band tunable lasers using tunable fiber Bragg gratings, *Opt. Laser Technol.* 39: 1214–1217 (2007).
11. Hernandez-Cordero, J., J. B. Escalante-Garcia, and F. Nunez-Orozco, Programmable control system for wavelength tuning and stabilization of optical fiber lasers, *Opt. Engr.* 44: 044201 (2005).

12. Zhang, S-M., F.-Y. Lu, and J. Wiang, High-power narrow linewidth tunable cladding pumped Er:Yb co-doped fiber laser, *Micowave Opt. Tech. Lett.* 48: 1736–1739 (2006).
13. Goh, C. S., S. Y. Set, and K. Kikuchi, Widely tunable optical filters based on fiber Bragg gratings, *IEEE Photon. Tech. Lett.* 14: 1306–1308 (2002).
14. Fu, L. B., M. Ibsen, D. J. Richardson, J. Nilsson, D. N. Payne, and A. B. Grudinin, Compact high-power tunable three-level operation of double cladding pumped Nd-doped fiber laser, *IEEE Photon. Tech. Lett.* 17: 306–308 (2005).
15. Akulov, V. A., D. M. Afanasiev, S. A. Babin, D. V. Churkin, S. I. Kablukov, M. A. Rybakov, and A. A. Vlasov, Frequency tuning and doubling in Yb-doped fiber lasers, *Laser Physics* 17: 124–129 (2007).
16. Mokhtar, M. R., C. S. Goh, S. A. Butler, S. Y. Set, K. Kikuchi, D. J. Richardson, and M. Ibsen, Fiber Bragg grating compression-tuned over 110-nm, *Electron. Lett.* 39: 509–511 (2003).
17. Chen, H., F. Babin, M. Leblanc, and G. W. Schinn, Widely tunable single-frequency Erbium-doped fiber lasers, *IEEE Photon. Tech. Lett.* 15: 185–187 (2003).
18. Hideur, A., T. Chartier, and C. Ozkul, All-fiber tunable ytterbium-doped double-clad fiber ring laser, *Opt. Lett.* 26: 1054–1056 (2001).
19. Yeh, C-H., T-T. Huang, H-C. Chien, C-H. Ko, and S. Chi, Tunable S-band erbium-doped triple-ring laser with single-longitudinal-mode operation, *Opt. Ex.* 15: 382–386 (2007).
20. Zheng, L., J. Vaillancourt, C. Armiento, and X. Lu, Thermo-optically tunable fiber ring laser without any mechanical moving parts, *Opt. Engr.* 45: 070503 (2005).
21. Kang, M. S., M. S. Lee, J. C. Yong, and B. Y. Kim, Characterization of wavelength-tunable single-frequency fiber laser employing acoustooptic tunable filter, *IEEE J. Lightwave Tech.* 24: 1812–1823 (2006).
22. Yun, S. H., D. J. Richardson, D. O. Culverhouse, and B. Y. Kim, Wavelength-swept fiber laser with frequency shifted feedback and resonantly swept intra-cavity acoustooptic tunable filter, *IEEE J. Select. Top. Quantum Electron.* 3: 1087–1096 (1997).
23. Duarte, F. J., *Tunable Laser Optics*, Elsevier-Academic, New York, 2003.
24. Kersey, A. D., M. A. Davis, H. J. Patrick, M. LeBlanc, K. P. Koo, C. G. Akins, M. A. Putnam, and E. J. Friebele, Fiber grating sensors, *J. Lightwave Tech.* 15: 1442–1463 (1997).
25. Duarte, F. J., Variable linewidth high-power TEA CO_2 laser, *Appl. Opt.* 24: 34–37 (1985).
26. Duarte, F. J., Multiple-prism Littrow and grazing-incidence pulsed CO_2 lasers, *Appl. Opt.* 24: 1244–1245 (1985).
27. Sze, R. C., and D. G. Harris, Tunable excimer lasers, in *Tunable Lasers Handbook*, edited by F. J. Duarte, Academic, New York, 1995, Chap. 3.
28. Duarte, F. J., Dispersive external-cavity semiconductor lasers, in *Tunable Laser Applications*, 1st ed., edited by F. J. Duarte, Marcel Dekker, New York, 1995, Chap. 3.
29. Zorabedian, P., Tunable external-cavity semiconductor lasers, in *Tunable Lasers Handbook*, edited by F. J. Duarte, Academic, New York, 1995, Chap. 8.
30. Shen, D. Y., J. K., Sahu, and W. A. Clarkson, Highly efficient Er, Yb-doped fiber laser with 188 W free running and >100 W tunable output power, *Opt. Ex.* 13: 4916–4921 (2005).
31. Schäfer, F. P. (Ed.), *Dye Lasers*, Springer-Verlag, Berlin, 1990.
32. Duarte, F. J., Narrow linewidth pulsed dye laser oscillators, in *Dye Laser Principles,* edited by F. J. Duarte and L. W. Hillman, Academic, New York, 1990, Chap. 4.
33. Duarte, F. J., W. E. Davenport, J. J. Ehrlich, and T. S. Taylor, Ruggedized narrow-linewidth dispersive dye laser oscillator, *Opt. Commun.* 84: 310–316 (1991).
34. Duarte, F. J., and J. A. Piper, Narrow-linewidth, high-prf copper laser-pumped dye-laser oscillators, *Appl. Opt.* 23: 1391–1394 (1984).

35. Duarte, F. J., Solid-state multiple-prism grating dye-laser oscillators, *Appl. Opt.* 33: 3857–3860 (1994).
36. Koplow, P., L. Golberg, R. P. Moeller, and D. A. V. Kliner, Single-mode operation of a coiled multimode fiber amplifier, *Opt. Lett.* 25: 442–444 (2000).
37. Jeong, Y., J. Nilsson, J. K. Sahu, D. N. Payne, R. Horley, L. M. B. Hickey, and P. W. Turner, Power scaling of single-frequency Ytterbium-doped fiber master-oscillator power-amplifier sources up to 500-W, *IEEE J. Select. Top. Quantum Electron.* 13: 546–551 (2007).

7 Fiber Laser Overview and Medical Applications

S. Popov

CONTENTS

7.1 Introduction 197
7.2 Lasers in Medicine and Life Sciences 198
7.2.1 Optical versus Thermal Response 200
7.3 Principles, Types, and Performance of Fiber Lasers 202
7.3.1 Host Fibers: Silica-, Phosphate-, and Fluoride-Based Glasses 203
7.3.2 Gain Media 203
7.3.3 Lasing Wavelengths 205
7.3.4 Pumping and Laser Efficiency 207
7.3.5 Advantages and Challenges 208
7.4 Gain Materials and Operational Mode Relation to Particular Applications 209
7.4.1 Erbium Lasers 209
7.4.2 Ytterbium Lasers 213
7.4.3 Thulium Lasers 214
7.4.4 Holmium Lasers 215
7.4.5 Co-Doped and ZBLAN Fiber Lasers 216
7.4.6 Supercontinuum Fiber Lasers 217
7.4.7 Making and Marking Tools and Instruments for the Medical Industry 220
Acknowledgments 221
References 221

7.1 INTRODUCTION

Fiber lasers began their remarkable history in the early 1960s when the first working laser of its kind was demonstrated and, very soon after, optical fibers with reasonably small attenuation were developed [1, 2]. Initially, optical fibers were mainly thought to find applications for signal transmission in optical telecom networks. It took about two decades before fully functional fiber-based optical amplifiers, and fiber lasers, appeared on the scene of research and industrial applications. Optical fibers with different dopants, mainly rare-earth metal ions, have opened virtually unlimited opportunities as unique

gain materials operating in the near- and mid-infrared bands of the optical spectrum. Currently, fibers of complicated chemical structure with gain properties in the far infrared, over 3 μm and farther, are being actively explored [3–6].

The earliest implementations of fibers in active optical components were realized in fiber lasers and fiber optical amplifiers (FOA) almost simultaneously [7, 8]. Originally targeted to enhance the performance of fiber-optic networks for telecommunications, erbium-doped fiber amplifiers (EDFA) have stimulated the development of a large class of fiber lasers with an outstanding performance record. Such lasers have quickly found their own place in various research and industrial areas. Rapidly progressing technology in the development of lasing materials and sophisticated design of optical fibers have firmly positioned fiber lasers as indispensable leaders in such fields as the automotive and processing industry, machinery, metrology, telecom, the biosciences, and medicine.

Medicine and the biosciences are important fields for implementing fiber lasers. Interest has been significantly driven by the fortunate matching of a wide variety of wavelengths generated by fiber lasers to several absorption spectral bands of organic compounds and water- (or hydroxyl-) based molecule groups, found in a wide variety of organic tissues and living cells. Various operational regimes—CW, Q-switched, or modelocked—along with wavelength tunability, have opened additional opportunities for fiber lasers in this field. During the infancy period of fiber lasers, before versatile gain materials with rich sets of transition spectra were developed, their medical applications were primarily in laser micromachining and marking of instruments and tools used in surgery, dentistry, and ophthalmology.

A fair amount of information and discussion about recent achievements, technical performance, and ubiquitous applications of fiber lasers is continually generated in the literature, from scientific journals to commercial booklets and manuals. In this survey, we present key areas of fiber lasers used in medicine-related branches. This chapter focuses on practical applications of fiber lasers and their specific advantages provided by radiation with tunable wavelengths for medical tasks, whereas most physical aspects and design details related to the laser tunability itself are discussed in Chapter 6. It is worth mentioning that fiber lasers have not been the first actors in laser history to demonstrate impressive tunability. In this context, dye lasers might be considered direct competitors of fiber lasers due to broadband wavelength tunability accompanied with high-intensity radiation, especially in Q-switched or modelocked operation regimes. Chapter 8 provides an excellent basis to make a comparative analysis for trade-offs in both types of lasers.

Since fiber lasers are part of a larger laser group, it is reasonable to start with a short overview of common laser usage in medicine, both in clinical and research areas. It is also instructive to recollect the main physical principles of the interaction of laser radiation with organic tissues, as well as the basics of the gain properties and operation principles of fiber lasers.

7.2 LASERS IN MEDICINE AND LIFE SCIENCES

Even before early lasers had left research laboratories for industrial applications, medicine was considered an important “consumer” of laser technologies, first as manufacturing tools for medical instruments, then as working instruments themselves. Practically all types of lasers have found their specific niches in important

branches of medicine: research, monitoring, imaging, probing, therapy, surgery, and others. Referring to more specific applications, lasers are used literally everywhere. In biomedical investigation: fluorescent spectroscopy, microscopy, and flow cytometry. In surgery: "bloodless" operations in cardiology, on abdominal and thoracic organs, and skull and brain microsurgery. In cosmetics and aesthetic medicine: smoothing wrinkles, resurfacing the skin, and bleaching tattoos. In therapy: the treatment of cancer, spider veins, and vascular dysfunction. In diagnostics: endoscopic investigations and optical coherence tomography (OCT). This list can be extended further by going deeper into subclassifications and interdisciplinary topics.

Depending on the particular requirements, numerous types of lasers can provide different wavelengths, energy levels, and operation modes. As a short overview, Table 7.1 provides some examples of the most typical and commercially available systems, as well as their particular uses.

Fiber lasers should be considered successors of trends in medical applications rather than "pioneers" discovering untouched fields. However, due to their inherent flexibility of physical principles and design, as well as outstanding performance, fiber lasers have enormous potential to bring new opportunities to medicine.

TABLE 7.1
Main Laser Types and Fields of Applications in Medicine

Laser type and operation mode	Wavelength (μm)	Application
Carbon dioxide (CW, pulsed)	10.6	Surgery: general and eye; dental therapy
Argon (CW)	0.488, 0.514	Sealing blood vessels in retina, eye microsurgery, plastic surgery, photodynamic therapy
Nd:YAG (CW, Q-switched)	1.06	General surgery, dentistry: therapy and surgery
Nd:YAG (Q-switched)	0.532 (double frequency)	Surgery, ophthalmology, dermatology, cosmetic, photodynamic therapy
Ruby (Q-switched)	0.694	Plastic surgery, dermatology, photodynamic therapy
Er:YAG (Q-switched)	2.94	Skin resurfacing (superficial ablation), dental therapy and surgery
Ho:YAG (CW, pulsed)	2.12	Ablation, incision, tissue hemostatic vaporization, cancer tumor treatment
Diode lasers (CW, pulsed)	0.63, 0.82, 0.83, 0.98, 1.45	Photodynamic therapy, endovenous treatment, aesthetic medicine, vascular lesions
Alexandrite lasers (CW, Q-switched)	0.755	Pigmented lesions, tattoo bleaching, vascular lesions, skin treatment, hair removal
Dye lasers (CW, Q-switched, tunable)	0.570–0.650	Treatment of malignant tissues, photodynamic therapy, cosmetics, vascular lesions, hair removal

Before specifying particular applications of fiber lasers in medicine, it is instructive to briefly depict some of the main fields in which lasers are commonly used for health care, monitoring, and research regardless of which particular type of laser is considered. Such a classification is commonly arranged according to how organic tissues react to laser radiation.

7.2.1 Optical versus Thermal Response

Using the terminology adopted among medical professionals, the reaction of organic tissues to laser radiation is typically described as an optical or thermal response (Fig. 7.1 [9, 10]). In the optical response, the light energy absorbed does not damage or destroy the tissues. Most effects are achieved either (1) by selective resonance absorption of specific laser wavelengths by fluorophores or photosensitizers with sequentially photoinduced changes of the tissues, or (2) by exposure with short light pulses of high peak intensity leading to material ablation. Thermal response is normally produced by CW or long-pulse laser radiation, when larger power delivered to organs is converted into heat and destroys the surrounding tissue. How tissues react to laser radiation in particular depends on the chosen wavelength, mode of operation, pulse duration, and energy, as well as the laser spot size.

Optical response is fundamental to various therapeutic and cosmetic treatments using physical and chemical photoinduced processes, either directly or as side effects. The former are based on direct absorption of light by organic compounds and cells naturally constituting the tissues, with subsequent conversion of the energy, through nonradiative transitions, into chemical changes or tissue ablation. A second type of the photoinduced effect exploits the light absorption by specialized photoacceptors (photosensitizers), or separate molecules that are not natural parts of the tissues but are artificially injected into the patient's body to be treated. The molecules transfer the energy to other agents, like rhodopsin, phytochrome, or chlorophyll, which

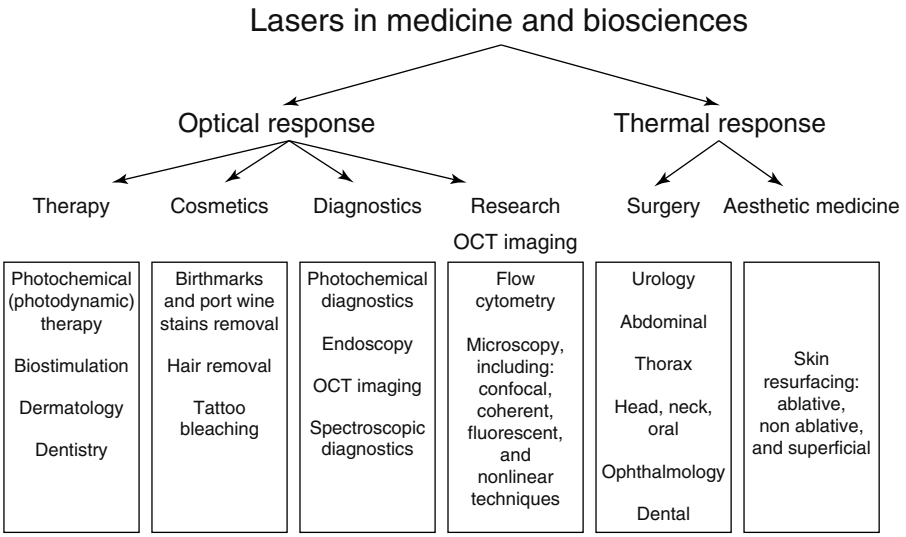

FIGURE 7.1 General applications of lasers in medicine and life sciences.

participate in the activation of chemical reactions in the tissue and its surroundings [10]. For example, these reactions are essential for photodynamic therapy (PDT) of tumors or for treating skin diseases in dermatology (Fig. 7.1). The photosensitizers alone are harmless and have no effect on either healthy or abnormal tissues until they are illuminated with the light of necessary wavelength. Typically, treatment and therapy based on the optical response do not require high-power laser radiation.

An example of PDT without using external agents is the removal of port wine stains, or reddish birthmarks typically found on the neck or face. Port wine stains, which consist of thousands of blood vessels, are exposed to green laser light and are literally burned away. The surrounding skin remains unharmed and unheated since it does not absorb the green light as efficiently as the red formations. A similar procedure is used to remove tattoos when the colors are bleached with appropriately chosen laser light. For this type of PDT, laser wavelength is a crucial parameter because the procedure efficiency strongly depends on how accurately the wavelength matches the resonance absorption of the treated tissue. Thus, the ability to tune the laser wavelength, as first demonstrated in dye lasers (Table 7.1), is essentially a favorable feature for this application [11].

An example of the optical response without resonance absorption of laser radiation is the scattering or attenuation of light during its propagation inside a tissue. Physical and chemical properties of the surrounding area remain unchanged during this process, which is extensively used for investigation purposes. One of the most well-known uses of such scattering is OCT, introduced in the early 1990s [12, 13]. This noninvasive imaging technique is primarily conducted by the low-coherence Michelson interferometer. It requires broadband light sources, such as supercontinuum or short-pulse lasers, and provides resolution of the order of micrometers with possible penetration to a depth of millimeters inside the tissue to be investigated. These days OCT is rapidly developing as a versatile investigation method demanded in practically all life-science branches [14, 15].

Compared to nondestructive optical effects, the thermal response of the laser-tissue interaction involves damage of treated organic matter: cutting, fragmentation, vaporization, or coagulation. Such destructive changes are caused by intensive heating of the tissues by high-power radiation, delivered by either CW or pulsed lasers.

Traditionally the most well-known and popular medical application for lasers using the light-tissue thermal response is surgery. It can include both open and endoscopic implementations. In the latter case, laser energy is delivered by a fiber to the treated organ without dissecting the patient's body, for example, through large blood vessels in cardiovascular operations, or urethral channels. Focused to a microscopic dot of high-energy density, the laser beam works as the tiniest of cutting and cauterizing instruments [10, 16, 17].

Resonance absorption of laser radiation by water contained in organic tissues is a main cause of the thermal laser-tissue response. Such absorption is used to produce different results depending on the mode and power of the laser applied. Operating in the pulse mode, either Q-switched or CW-modulated, the laser heats water very rapidly to several hundred degrees Celsius. The overheated water is expanded explosively and, depending on the hardness of the tissue, either breaks it into fragments (for example, tiny stones) or vaporizes it into medium-hard substances. The energy absorption in water takes place regardless of the composition, hardness, or color of the matter, and allows for a highly efficient procedure, roughly the same for both hard

and soft tissues. With such immediate impact, heating is restricted to the area in the close vicinity while the surrounding area remains almost unaffected. Such thermal ablation is useful in many surgical treatments. Varying the power and pulse duration of the laser, it is possible to achieve different impacts on various organs and tissues. Use of high-energy in short pulses increases the effect in lithotripsy (stone fragmentation), while operation with longer pulses enhances coagulation. This is another irrefutable advantage of the laser "scalpels," an excellent alternative to traditional methods. In such cases, typical pulse repetition rates can vary between 10 and 20 Hz.

Laser surgery is also a well-established technique used in dentistry. Exactly tuning the radiation wavelength, one can selectively adjust absorption of the laser pulses by different parts of the teeth, either enamel or dentin. This can significantly relieve the patient's painful and irritating feelings during the drilling and burning typical of the work necessary to repair tooth cavities. Lasers also make dental procedures more accurate.

Another branch, ophthalmology, is probably the most "natural" area for noninvasive treatments applying medical lasers. Propagating through the transparent cornea and crystal, laser light can be directly used for restoring detached retinas, removing blood vessels, treating glaucoma, or reshaping the cornea.

It is not an exaggeration to say that the combination of laser and fiber-optic technology has revolutionized noninvasive surgery. For example, cutting prostate or superficial bladder cancer tumors, lithotripsy, and vessel treatment with lasers are hugely beneficial. An optical fiber inserted into a blood vessel through a needle-size opening can deliver laser light to practically any part of the blood system and enable noninvasive angioplasty, that is, the removal of fatty plaques from arteries, to prevent heart attacks or strokes caused by clogged blood vessels. This approach can also be used to perform endovenous laser treatment to cure spider and varicose veins. A comprehensive review of the laser methods used for health care is given in [9, 10].

More examples of the laser applications, not included in Figure 7.1, will be discussed in the sections considering particular types of fiber lasers. In comparison to other fields that use fiber lasers, medical and bioscience do not demand very high-power instruments, say, of the kW range that is typical for machinery or the automotive industry. Depending on which of the two main effects of laser radiation on the organic tissues is required—optical or thermal—fiber lasers with average power between hundreds of mW and tens of Watts are needed.

Although it will be briefly discussed later, we did omit in Figure 7.1 one more application marginally related to medicine: the implementation of lasers for making and marking medical instruments, components, and devices. This involves the interaction of radiation with inorganic materials (metals, plastics, ceramics) rather than treatment of biological tissues. For such tasks, fiber-based systems, delivering necessary power at the corresponding wavelengths, are becoming widely used.

To elucidate the reasons for its leading role, as well as to comprehend the advantages and potential of fiber lasers in medicine, we should review the basic features of these lasers.

7.3 PRINCIPLES, TYPES, AND PERFORMANCE OF FIBER LASERS

Optical fibers can be used in fiber lasers either as the gain medium, combined with the cavity functionality, or as a passive part of the laser cavity solely to realize

conditions for forming cavity modes. In the latter case, another active component, such as a semiconductor gain material, should be included for amplification and lasing. Here we consider exclusively "classical" fiber lasers, that is, those using the optical fibers as key components for the gain, building up the modes, and lasing.

7.3.1 Host Fibers: Silica-, Phosphate-, and Fluoride-Based Glasses

Amplification in optical fibers is realized by embedding dopants in the form of ions of rare-earth metals into host fibers. These dopants provide specific energy transitions available for the laser generation. Main host materials used in contemporary optical fibers are silica-, silica-fluoride-, or phosphate-based glasses. Traditional silica-based fibers are employed in lasers based on direct transition, 3- (4-) level schemes. For most rare-earth ions, easily allowed lasing transitions are allocated in near- and mid-IR bands. Until recently, this property precluded developing fiber lasers in the visible range, although there exist numerous medical applications demanding lasers with these wavelengths (Table 7.1).

Advances in the development of two novel types of fibers, namely phosphate- and fluoride-based glasses, have dramatically pushed progress with high-power and efficient fiber lasers. Phosphate fibers provide higher internal gain in comparison with silica-based fibers and allow more efficient and high-power fiber lasers with very short active fibers [18, 19]. Another family member is the ZBLAN fiber, or fluoride-based fiber incorporating additives of heavy metals like zirconium or lead, and a more complicated composition of barium, lanthanum, aluminum, and sodium. The acronym ZBLAN stands for its components. ZBLAN fibers demonstrate important advantages: they exhibit high transparency in the mid-IR range whereas silica-based fibers start to absorb around 2 μm; and rare-earth dopants in ZBLAN fibers reduce the quenching caused by multiphonon transitions, thus increasing the lifetime of metastable states. Therefore, ZBLAN fibers have encouraged the development of a novel class of fiber lasers exploiting upconversion, or excited state transitions (EST), and radiating in the visible range [20, 21]. Although the fluoride-based fibers are not free from problems, such as fragility and soaking ambient moisture (first of all water), rapid development of glass materials demonstrate considerable progress with ZBLAN fiber lasers [22, 23].

Active optical fibers utilizing different host glasses and various active rare-earth dopants allow covering near-IR, mid-IR, and visible parts of the spectrum. More details, energy level structures, and corresponding wavelengths for different fiber lasers will be discussed along with particular applications in further sections.

7.3.2 Gain Media

To build a complete fiber laser, the gain fiber should be equipped with two reflectors playing the roles of back mirror and output coupler/mirror. They can be either traditional external mirrors using free space optics components to couple the light in and out of fibers, or deposited directly on the fiber facets; or components embedded inside fibers, for example, fiber Bragg gratings (FBG) [24]. An intermediate variant for the back mirror is a semiconductor saturable absorbing mirror (SESAM) (Fig. 7.2), which is an external semiconductor device fiber-coupled to the gain fiber [25].

Some applications, like nonthermal ablation in dentistry, sophisticated microsurgery in the human brain, or refractive eye surgery, combined with an endoscopic

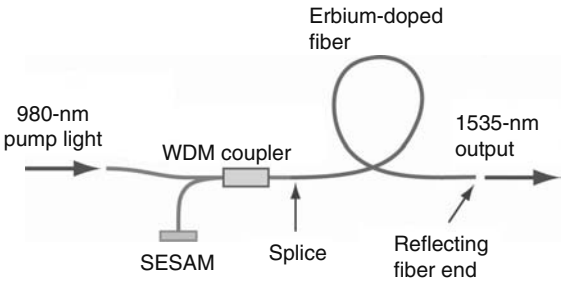

FIGURE 7.2 Classical design of fiber laser using SESAM as a back mirror. Depending on the particular parameters of the SESAM, the laser can operate in Q-switched or modelocked regime. (Courtesy of Dr. R. Paschotta, RP Photonics Consulting GmbH, Switzerland.)

approach, require fiber lasers generating ultrashort pulses, in the picosecond (ps) or femtosecond (fs) range [26, 27]. To achieve this goal, a fiber loop mirror and a strongly nonlinear fiber in the gain section can be used (Fig. 7.3). Strong fiber nonlinearity is commonly used to manipulate the fiber dispersion properties over large wavelength bandwidth, which is in demand to create ultrashort optical pulses [28]. Recent progress with photonics crystal fibers (PCF), or fibers having a crystal-looking structure in their cross-section (Fig. 7.4), has opened novel opportunities for creating extremely broadband and ultrafast fiber lasers [29]. In certain cases, possessing a very sophisticated design (Fig. 7.5), such fibers can provide conditions for zero-dispersion and single-mode operation over a very wide wavelength range, creating high gain, and maintaining high-power density inside the core [30, 31]. These are important issues for the practical realization of fiber lasers in medicine.

As it does not affect essential operational or performance parameters, in this survey we do not specify laser cavity details or output coupling design of fiber lasers. For a discussion on cavities for tunable fiber lasers, please refer to Chapter 6. To focus on medical applications, we discuss the gain material, operating mode (CW or pulsed), wavelength, and energy characteristics, such as average power or pulse energy. All these parameters are relevant to specific applications of interest for fiber lasers in medicine.

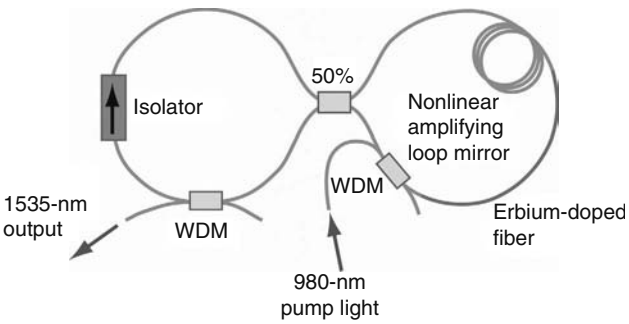

FIGURE 7.3 Modelocked fiber laser with loop-mirror cavity design with nonlinear fiber to obtain fs-pulse generation. (Courtesy of Dr. R. Paschotta, RP Photonics Consulting GmbH, Switzerland.)

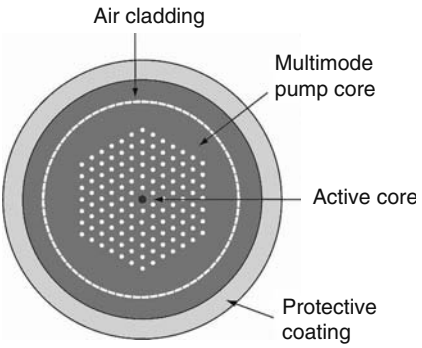

FIGURE 7.4 Schematic overview of most typical PCF cross-sections. (Courtesy of Dr. R. Paschotta, RP Photonics Consulting GmbH, Switzerland.)

7.3.3 Lasing Wavelengths

An essential parameter for medical applications is wavelength, which defines how efficiently the laser radiation is transmitted, scattered, or absorbed by the tissue. For example, 2–3 μm wavelengths are suitable for accurate cutting, removing, or coagulation of soft tissues due to strong absorption of this radiation by water present in the majority of biological objects [32, 33]. On the other hand, radiation within the wavelength band of 650–1200 nm can penetrate up to several millimeters into tissue, which is advantageous for imaging and diagnostic procedures [34]. Various fiber lasers are capable of generating a rather large set of wavelengths utilizing various physical phenomena.

The main and most developed approach is doping the fibers with different rare-earth ions, such as erbium (Er^{3+}), praseodymium (Pr^{3+}), thulium (Tm^{3+}), neodymium (Nd^{3+}), holmium (Ho^{3+}), or ytterbium (Yb^{3+}). Direct energy transitions characteristic of these elements cover almost the whole near- and mid-IR range of the spectrum. A

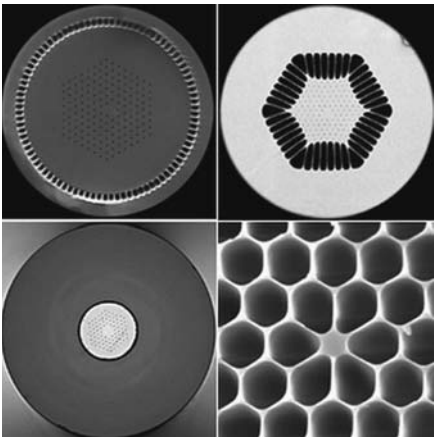

FIGURE 7.5 Examples of crystal fibers designed for double-cladding pumping schemes and supercontinuum fiber laser sources. (Courtesy of Dr. K. P. Hansen, Crystal Fibre A/S, Denmark.)

complementary method to build fiber lasers operating in the visible spectrum is the use of upconversion transitions. With this technique, also known as the excited-state absorption, several ladder-like energy levels of rare-earth ion are excited sequentially to reach the highest lasing level. Compared to classical laser schemes, the lasing wavelength is shorter than the pumping one in this case.

Figure 7.6 displays one of the typical transition structures for the thulium fiber laser radiating in the blue range [35]. However, such a scheme requires rather high pump intensity and intermediate levels with long lifetimes. Standard silica-based fibers are not capable of providing such features. The problem can be resolved with ZBLAN fibers using fluoride-based materials mentioned earlier. With increased lifetimes of the intermediate levels, it is easier to start upconversion lasing. Recently demonstrated upconversion fiber lasers covering the visible spectrum from blue to red, using erbium, praseodymium, and thulium ions have been reported [36–39]. Lasers in the visible spectrum are in high demand for numerous therapies and noninvasive treatments for dermatology, aesthetic medicine, cosmetic surgery, and cancer photodynamic therapy (Table 7.1).

Another effect enabling more lasing frequencies from fiber lasers is stimulated Raman scattering (SRS) producing the Raman gain inside the fiber [40–42]. This strongly nonlinear phenomenon reveals itself under high-intensity pumping, typically provided by another laser, semiconductor, or fiber. The remarkable feature of the Raman gain is its manifestation in practically all fibers and its frequency dependence on the pump wavelength only rather than on a particular fiber material. The lasing wavelength is typically shifted at 80–100 nm apart from the pumping source. With several pairs of FBG nested into each other, one can shift the Raman gain in several steps, thus realizing a cascaded Raman laser with the wavelength transfer up to hundreds of nanometers [43]. The efficiency and strength of the Raman gain can be manipulated by appropriate chemical composition of the fiber compounds and suitable design of the fiber core [44].

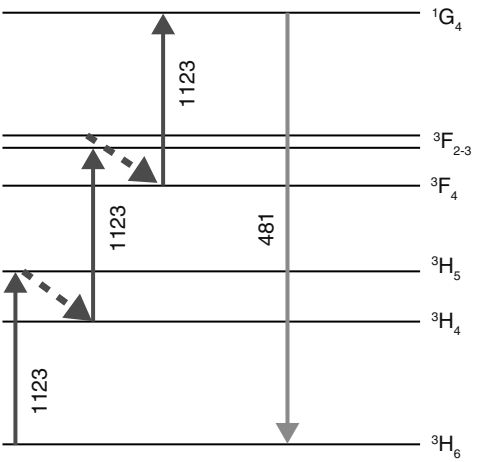

FIGURE 7.6 Energy levels of thulium (Tm^{3+}) ions, showing how multiphoton excitation with 1123 nm wavelength results in blue fluorescence through upconversion (dotted arrows denote relaxation transitions).

7.3.4 Pumping and Laser Efficiency

In addition to the generous choice of available wavelengths and tunability, fiber lasers offer attractive conversion efficiencies. More pumping energy converted into useful radiation than to heating the gain media makes it possible to abandon bulky cooling systems. This leads to smaller sizes, simpler constructions, and lower costs of reliable turnkey devices. With optimized pumping sources and carefully engineered active fiber cores, pump-lasing optical efficiencies of about 20–30% are routinely reported for fibers with almost all rare-ion dopants [6, 18, 23]. For some elements with a "lucky" energy structure, like Yb^{3+} dopants, being considered later, optical conversion efficiency of 80%, and up to 30% wall-plug efficiencies have been reported [45, 46].

In addition to high conversion efficiencies, excellent heat dissipation of fiber lasers is facilitated by a large surface to volume ratio of the active medium. Gradual pump absorption and smooth distribution of the amplification within the fiber provide high beam quality of the guided mode, which is defined by the core design rather than pumping or generated power. This is a significant advantage for high-power devices. Near perfect withstanding against power dissipation and heating, as well as against thermal optical problems, makes fiber lasers good candidates for power scaling. Being coupled with negligible losses into amplifying fibers and strictly confined within the core, the pumping wave interacts efficiently with the lasing radiation. This results in low-pump threshold and high gain, which can be an order of magnitude larger than that in crystalline solid-state lasers. Really high-power fiber lasers operating in CW mode (kW-class and more) have been routinely reported and commercially available during recent years [47–49].

However, lasers requiring high pump intensity may suffer from nonlinear effects, which can worsen conditions and cause beam quality distortion. Fortunately, there are some techniques and solutions to overcome the nonlinear phenomena induced by high power [28]. On the other hand, nonlinear effects such as Raman or Brillouin stimulated scattering can, under proper control, provide additional opportunities for the wavelength conversion as was exemplified earlier [43, 50].

An important factor contributing to the growth in popularity, and applicability, of fiber lasers is pumping solutions. Rapid progress in the development of high-power laser diodes continually leads to gradual displacement of other pump sources, such as flashlamps and traditional lasers. Until recently, a high-quality beam could be generated by a single-mode fiber laser where the pumping beam also propagates in the same core. This used to restrict the output power of the laser to only tens of mW. Using multimode fibers to enhance pumping and lasing power would immediately destroy the beam quality. An efficient alternative to increase the fiber laser power, yet maintain high quality of the beam, is the implementation of double-clad pumping. This breakthrough technology utilizes crystal fibers with inner cladding placed between the main core (which, in turn, has a complicated structure, e.g., PCF) and outer cladding, and separated by air holes from each other (Fig. 7.7).

The double-clad pumping technique considerably releases the requirements for the quality of pump sources. Due to high numerical aperture (NA) of the PCF, a low-quality beam from a high-power diode laser can be easily launched into the fiber and can propagate while being trapped inside inner cladding. The simple circular symmetry shown in Figure 7.7 does not ensure the best possible coupling between the pumping and lasing modes because the light partially propagates as skewed "beams"

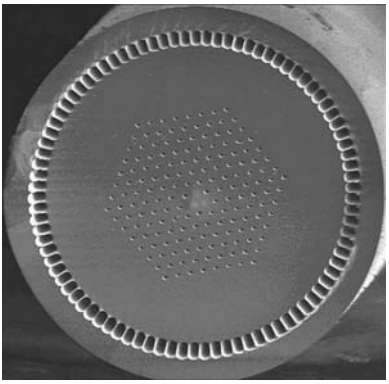

FIGURE 7.7 Double-clad PCF providing high NA acceptance of the pumping beam. (Courtesy of Dr. K. P. Hansen, Crystal Fibre A/S, Denmark.)

outside the central core. Avoiding circular symmetry in the PCF mitigates the problem of poor pump/lasing mode overlap. The most commonly used alternatives for the double-clad design (shown in Fig. 7.8) can admit low-quality high-power pumping and provide efficient absorption by the active area [51, 52].

Employing symmetry-broken double-clad pumping in crystal fibers produces several advantages in one step. First, due to much better pump-lasing overlap and enlarged core area (50–60 μm in comparison with traditional 12 μm in standard single-mode fibers), high-power lasing can be obtained in a shorter fiber. This significantly reduces the risk of nonlinear phenomena, such as self-phase modulation, SBS, or undesired SRS. On the other hand, inherent physical properties of the PCF restrict the lasing to a single-mode field across the whole large-mode area (LMA) for broad wavelength bands. Single-mode CW operation of almost diffraction-limited quality (factor $M^2 < 1.05$) was demonstrated with 100–500 W fiber lasers [47, 53, 54]. Finally, owing to the LMA, implementing multidiode pumping is a natural solution to combine single-mode operation, capability for power scaling, and excellent conditions for heat dissipation described above. Fiber lasers with power-independent beam quality and delivering output power levels in the kW range, both in CW and pulse mode, have been increasingly reported [55–57].

7.3.5 Advantages and Challenges

Summarizing the basic facts about fiber lasers, one can argue they might gradually replace other types of lasers employed in biomedical branches. As discussed in the

FIGURE 7.8 Different shapes of the double-clad fibers to improve pump-lasing modes overlapping. (Courtesy of Dr. R. Paschotta, RP Photonics Consulting GmbH, Switzerland.)

beginning of this chapter, laser radiation with practically all wavelengths in visible and infrared is in strong demand for medical applications. One of the main obstacles precluding successful "switching" of traditional procedures and methods in medicine to relevant laser technologies is the cost of equipment.

Considerably lower costs for fiber lasers are mainly based on higher lasing efficiency and excellent heat dissipation performance, which allow abandoning cooling systems and shrinking many advanced systems into A4 footprint sizes. Rather cheap and simple maintenance is also a considerable contribution to increasing fiber laser competitiveness.

There is no significant price variation for fiber lasers depending on the wavelength, operation mode, and power (except a minor scaling factor for the pump diode costs) since they exploit the same physical principles and similar material technologies.

Depending on the particular biomedical application, fiber lasers can operate in all required regimes—CW, pulsed, Q-switched, or modelocked—producing the necessary power. Additional advantages of fiber lasers are wavelength tunability and power-independent high-quality beams deliverable directly to an application area without coupling losses.

Although only certain types of fiber lasers have been established in the medical market thus far, numerous promising results for biomedicine and medical applications are continually being demonstrated in research labs and preliminary clinical trials.

7.4 GAIN MATERIALS AND OPERATIONAL MODE RELATION TO PARTICULAR APPLICATIONS

In the previous sections, we outlined general laser uses in medicine and bioscience, and reviewed some of the basics of fiber lasers. Here we are going to depict application examples customary for particular types of fiber lasers. Since the application diversity exceeds the assortment of lasers, it is more instructive to link a certain laser type to relevant applications rather than vice versa. It is also more convenient to discuss fiber lasers in reference to the dopant ions responsible for amplification in the active fibers, because other features, such as wavelength, power, and CW/pulsed operation mode, cannot be attributed uniquely to any laser in particular.

Although almost all rare-earth metal ions have been tested and investigated for possible lasing with direct, upconversion, or Raman-shifted transitions, only a limited number have been demonstrated as practical active media in fiber lasers [58]. Thus, our discussion will concern only those rare-earth ions that are used in fiber lasers outside the research labs, namely: erbium, ytterbium, thulium, holmium, neodymium, and praseodymium (Table 7.2). As host materials, both silica- and fluoride-based fibers are used where they can demonstrate proper advantages.

7.4.1 Erbium Lasers

Erbium-doped lasers can be considered veterans and founders of the family of fiber lasers. A manifold energy level structure with easily allowed transitions made them a popular object for research and applications. The set of most often used transitions, shown in Figure 7.9, offers numerous opportunities to build erbium fiber lasers [58].

TABLE 7.2
Rare-Earth Metal Ions Commonly Used in Fiber Lasers and Laser Applications in Medicine

Laser, host fiber, and operational mode	Wavelengths (μm)	Applications
Er^{3+}, silica, ZBLAN, CW, pulsed	0.55, 1.5–1.6, 2.7, 3	Optical coherence tomography; cosmetic surgery and therapy; soft-tissue surgery
Yb^{3+}, silica, ZBLAN, CW, pulsed	0.98–1.1, 0.512–0.532 (SHG)	Optical coherence tomography; dermatology; PDT; soft- and hard-tissue surgery; dentistry, gynecology
Tm^{3+}, silica, ZBLAN, CW, pulsed	0.48, 0.8, 1.45–1.53, 1.7–2.1	Surgery: thorax, otolaryngology, urology, ophthalmology, cardiology, neurosurgery; lithotripsy
Nd^{3+}, silica, CW, pulsed	0.9–0.95, 1.03–1.1, 1.32–1.35	Dentistry; hard-tissue surgery; orthopedic surgery
Ho^{3+}, silica, ZBLAN, CW, pulsed	2.1, 2.8–2.9	Gastroenterology with endoscopic or direct access; surgery on blood-rich tissues; lithotripsy
Pr^{3+}, silica, ZBLAN, CW, pulsed	0.49, 0.52, 0.6, 0.635, 1.3	Cosmetic surgery and therapy; cancer therapy; photodynamic therapy

Soon after pioneering the demonstration of broadband amplification and lasing, in the near-IR range around 1500–1600 nm [59–61], erbium-doped fiber lasers became widely applied in the fields of medicine and biology. Their use in OCT is well documented [62, 63]. After promising performances were proved with erbium lasers, other fiber lasers have manifested their potential to replace complicated and

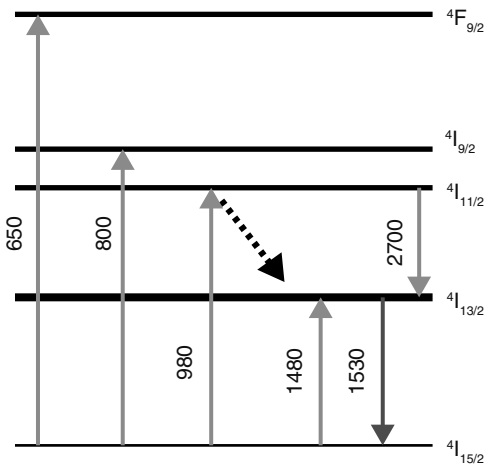

FIGURE 7.9 Energy levels of erbium (Er^{3+}) ions and main transitions (in units of nm) in silica-based fibers used to get amplification and lasing.

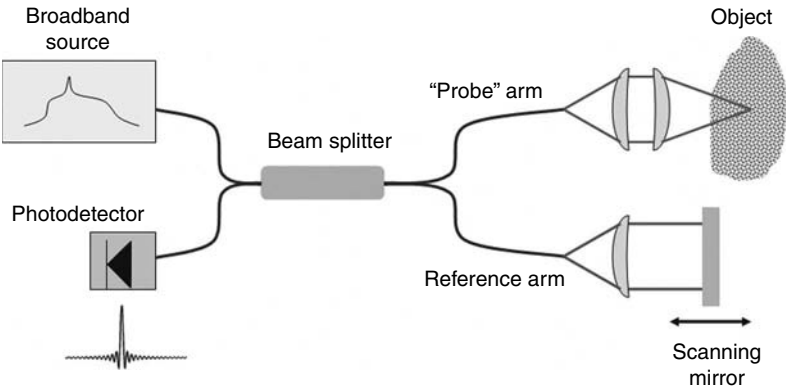

FIGURE 7.10 The simplified fiber scheme for OCT.

expensive fs-pulsed lasers commonly used in OCT systems [64, 65]. Briefly, the OCT method is based on the use of a Michelson interferometer with a broadband light source. Unlike the classical Michelson interferometer, where the light propagates in free space between a beam splitter and mirrors, a fiber-based four-port optical coupler (typically of 50/50 splitting ratio) plays the role of beam splitter, where two output optical fibers form the two-arm interferometric system to deliver the optical signal both to the object under investigation and to the reference mirror (Fig. 7.10).

The broadband spectrum of the source results in low coherence of radiation and considerably limits the area of high visibility of the interference pattern. Thus, high visibility (or high intensity peak on an interferogram, see Chapter 12) is achieved when full optical paths of the light in the "probe" and reference arms are equal within high accuracy. If light in the probe arm is scattered by some material, position of the scanning mirror in the reference arm defines a corresponding tiny area inside the tissue, which scatters most of the light contributing to the interfering signal. Displacing the mirror and processing the scattered signal, one can restore the information about the tissue properties depending on the depth. Choosing the appropriate broadband light source and suitable central wavelength within the IR range, the tissue structure, to a depth of several millimeters can be imaged due to good penetration of this radiation into biological objects. The short coherence length due to the broadband spectrum results in smaller tissue volume, contributing to the main interferometric response and higher spatial resolution. Since the probe light is scattered by all regions in the tissue where it propagates and produces noise background scattering, a high-brightness source is required to provide a strong response signal. Classical light sources, like high-intensity tungsten or xenon lamps, cannot compete with fiber lasers or optical amplifiers generating broadband amplified spontaneous emission (ASE). The results reported with Er-doped fiber lasers have stimulated development of other broadband fiber-based light sources for OCT applications, including supercontinuum lasers and low-noise ASE amplifiers [66–68].

Cosmetic therapy and surgery is one more field that is being conquered by erbium-doped fiber lasers, mainly with its radiation wavelength around 1550 nm. A challenging application of these lasers is treating wrinkles and skin photoaging due to UV

exposure, which is unavoidable in everyday life. The final effect of photoaging might be very unpleasant since sunlight causes thinning of the epidermis and can lead to the growth of skin lesions, such as actinic keratoses and cell carcinomas [69].

Treating wrinkles, or photoaging, is a procedure of skin resurfacing that can be performed in both ablative and nonablative forms. Traditionally practiced ablative treatments exploit high-power lasers and can be a rather painful procedure with a long recovery time. It removes the overlaying epidermal skin surface with the subsequent growth of renewed tissue. With nonablative skin resurfacing, the fiber laser with subablative energy pulses generates heat within dermal connective tissue without necessarily removing the overlying skin surface. Such a method offers higher efficiency, more convenient handling, and lower risks for side effects as compared to the use of traditional lasers in this area. A commercially available 1550 nm system has demonstrated very promising results in nonablative treatment of atrophic facial acne with 8–16 J/cm^2 pulse energy in modulation mode [70, 71].

An intermediate variant of the laser therapy efficiently treating wrinkles and photoaging is fractional resurfacing. Here again, an erbium-fiber laser is the main working instrument, albeit the operating mode is a bit different. High-intensity short pulses, up to 40 J/cm^2 drill small pinpoint areas of the skin. The light penetrates to the right depth, ~1.3 mm instead of 300–800 μm attained with nonablative curing, and as it heals, the tissue tightens. This procedure has exhibited quick recovery after the treatment [72].

Potentials of erbium-fiber lasers for cosmetology and aesthetic medical applications are practically unlimited. This fact has been apparently recognized by leading players in the market of fiber lasers. Today, they offer a big family of lasers oriented to this branch of medicine: models with wavelengths of 1065, 1075, 1090, and 1550 nm operating in CW and modulated-pulsed modes and delivering between 10 and 100 W average power [73].

Rapid progress in the development of fibers co-doped with different rare-earth ions and using efficient double-clad diode pumping schemes has opened for the erbium lasers a gate to other branches of surgery, such as cardiology, dentistry, and ophthalmology. Using ZBLAN fluoride-based fibers doped with Er^{3+}-Yb^{3+} or Er^{3+}-Pr^{3+} combinations made it possible to realize high-power lasers operating at the wavelengths of 2.7 and 3 μm with output power up to 1 W and more [74, 75]. For example, using high-intensity diode pumping with 980 nm and Pr^{3+} as a co-dopant allows for increasing depopulation of the lower level and obtaining efficient lasing at the 2.7 μm transition, which is rather weak in standard silica-based fibers. Operation at 3 μm can be achieved using absorption from excited states (or upconversion) and relaxation through upper states (transition schemes similar to those shown in Fig. 7.6) [76]. More discussion of ZBLAN upconversion fiber lasers is given in a further section.

The growing popularity, and active penetration, of the medical market by erbium fiber lasers, operating at 2.7 and 3 μm, is easily explained by their advantages over alternative counterparts such as the Er^{3+}:YAG solid-state lasers operating at 2.94 μm. Being cheaper, more efficient, more compact, and easier to operate, the use of erbium fiber lasers is continually expanding in areas such as dentistry, dermatology, angioplasty, and ophthalmology [77].

7.4.2 Ytterbium Lasers

As far as popularity in biomedical applications goes, erbium lasers are closely followed by ytterbium fiber lasers. Possessing a rather simple energy level structure (Fig. 7.11), Yb^{3+}-ion transitions offer potentially high pumping efficiency due to small quantum defect, i.e., energy (or frequency) difference between the pumping and lasing photons. The ytterbium laser, operating around 1 μm, offers small nonradiative losses, low heating, and provides conversion efficiencies approaching 80% and approximately 25% wall-plug efficiency.

As a result, high-power CW ytterbium fiber lasers continue to advance in the market due to lower cost, compact design, and simpler maintenance [53, 78]. Numerous sublevels exhibit the broadband fluorescence spectrum, which allows tunability of the Yb^{3+}-fiber lasers within the 100 nm window [79]. Utilizing high lasing efficiency and broadband tunability, ytterbium-pulsed lasers with high peak power operating in Q-switched and mode-locking regimes have been rapidly advancing [80–82]. With radiation around the wavelength of 1030–1080 nm, Q-switched ytterbium fiber lasers are becoming an attractive alternative to Nd:YAG lasers, which traditionally occupied a large sector of the medical applications industry employing the 1064 nm wavelength. Pulsed Yb-lasers delivering more than 80 W of peak power with μs-pulses are applicable to diverse areas such as gynecology, abdominal surgery, cardiovascular surgery, and dental curing [83]. The Yb-fiber laser tunability opens additional possibilities. Tunable subnanosecond pulsed Yb-lasers utilizing second harmonic generation to achieve lasing in the visible range have found use in bioscience investigations: DNA sequencing, flow cytometry, and laser microscopy [84, 85]. In addition, attaining green emission (515–532 nm) with frequency doubling is very advantageous for applications in dermatology and PDT. The generous tunability of ytterbium lasers is also favorable for high-resolution OCT techniques [86].

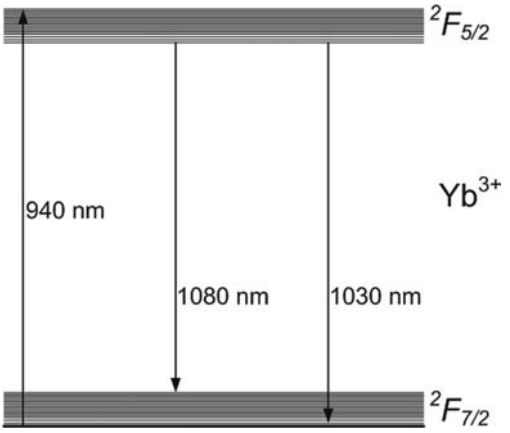

FIGURE 7.11 Two-level transition structure for Yb^{3+} ions.

7.4.3 Thulium Lasers

Among other fibers containing rare-earth ion dopants, thulium-doped materials occupy a special place due to the specific and efficient properties usable in fiber lasers. What makes thulium lasers attractive for many applications is the manifold and sophisticated structure of Tm^{3+} transitions available for lasing (Figure 7.12) [87, 88]. Operating typically around the 2 μm wavelength with silica-based fibers and going further to the 3–4 μm range in co-doped (with other rare-earth ions) or ZBLAN fibers, Tm^{3+}-fiber lasers fill an important mid-infrared gap, which enables minimally invasive surgery in various branches: otolaryngology, urology, ophthalmology, and cardiology [32]. Along with lasing in the mid-infrared, several almost equidistantly allocated transition levels (shown in a more complete transition scheme in Fig. 7.6) offer the opportunity to realize fiber lasers generating several wavelengths in the visible range using multiple ESA, or upconversion, mechanisms [37]. This unique feature is realized in ZBLAN fibers, thus bringing thulium fiber lasers to the field of dermatology, cosmetic, and cancer treatment.

The growing selection of laser designs with a versatile choice of power and operation modes are continually demonstrated. One of the first widely tunable thulium lasers (1.9–2.1 μm) delivering about 5 W in the CW regime was reported by Jackson and King as long as 10 years ago [89]. This wavelength range has great practical importance for abdominal, thoracic, and neurological surgery where soft tissues are treated. Practical advantages of the 2 μm thulium fiber lasers over traditionally used CO_2 lasers were demonstrated in comparative clinical research by Verdaasdonk et al. [90]. In these trials, the CW thulium lasers have proved high efficiency, for superficial tissue ablation, with minimal coagulation depth both in air and in water, which makes such lasers very useful for the treatment of tissues containing a lot of water, such as the lungs or liver.

The wide tunability of thulium fiber lasers around 2 μm makes them very attractive for other important branches in surgery, including such critical issues in health

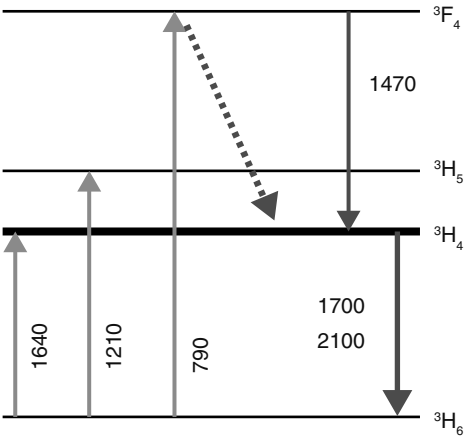

FIGURE 7.12 Selected set of energy levels of thulium (Tm^{3+}) in silica-fiber with pumping, absorption, and lasing transitions.

care like lithotripsy (kidney fragmentation) and the treatment of benign hyperplasia of the prostate [91]. The laser tunability in the range of strong water absorption allows adjusting the laser radiation on or off the absorption peak, thus carefully manipulating the degree of interaction with specific tissues.

A high-power, 110 W thulium laser radiating at the wavelength of 1.91 μm in CW mode was highly efficient in testing for vaporization and coagulation of the urinary tissue (prostate) [91, 92]. Providing a small coagulation zone, about 500–2000 μm, and rapid tissue vaporization at the rate of 0.83 ± 0.11 g/min, such lasers have proved their potential for practically bloodless surgery of the soft tissues. Successful urinary stone fragmentation was reported with a high-power thulium laser using a slightly different wavelength at 1.94 μm. Operating in CW mode with a modulation of 10 Hz repetition rate, the 100 W laser was capable of breaking both hard and soft urinary stones with a mass of 800 mg into 2 mg pieces with rates of about 400 and 25 mg/min, respectively [93].

However, to be qualified for full-scale clinical use, high-power thulium fiber lasers operating in short-pulse modes have to be developed to provide sufficiently rapid vaporization of tumor tissues and more precise incision of the urethral/bladder-neck structures [94]. When the necessary performance is achieved such lasers might replace traditional crystalline solid-state lasers for this application.

7.4.4 Holmium Lasers

Holmium fiber lasers exhibit an interesting example in technology development. As considered in the previous section, thulium fiber lasers have rapidly attracted much interest as a replacement for Ho:YAG crystal lasers widely used in soft-tissue surgery. After tunable Tm^{3+}-fiber lasers achieved a mature level and became available on the market as research and industrial instruments, they turned out to be a suitable pumping source for holmium fiber lasers [95]. Being rather expensive instruments and gradually yielding to more efficient thulium lasers, Ho:YAG lasers still keep their position as a working tool in some specific fields of surgery, such as in the laparoscopic sector or in treating benign prostatic hyperplasia, or noncancerous enlargement of the prostate gland [96]. Holmium-based lasers continue to be used in surgical applications because their radiation wavelength slightly over 2.1 μm falls at the very edge of the thulium-fiber laser bandwidth where they cannot achieve high power. In the given example, a high-power device, about 80–100 W, operating in modulated mode with the pulse energy of 2–3 J and repetition rate of 25–40 Hz combines the thermal ablation of the soft tissues and coagulation of the operated area. This results in less blood loss during treatment.

Energy levels of Ho^{3+}-doped fibers offer additional opportunities for lasing (Fig. 7.13). Along with typical generation around 2.1 μm and reaching record 83 W with 42% slope efficiency (in Tm^{3+}-co-doped version), holmium fiber lasers emitting at 3 μm have been demonstrated [95, 97]. Operation in this mid-infrared part of the spectrum and the possibility to move farther over the 3 μm boundary makes holmium fiber lasers almost a unique tool. This mid-infrared lasing can be obtained in combination with other rare-earth dopants and/or in ZBLAN-based fibers using upconversion transitions to affect the lifetime of lower levels. More details are given in the next section devoted to co-doped fiber lasers.

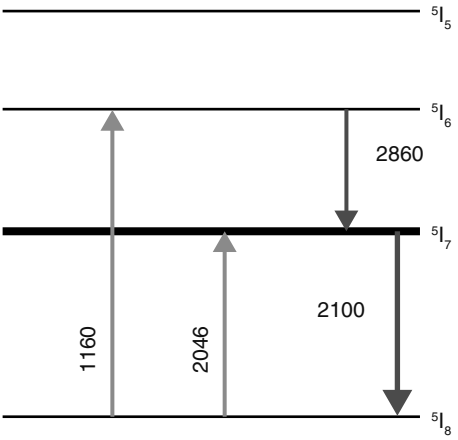

FIGURE 7.13 Simplified energy levels of holmium (Ho^{3+}) in silica fiber.

Confirming their promising results in research projects and clinical tests, holmium fiber lasers are rapidly acquiring the status of reliable and cost-effective commercial systems designed for use in delicate fields of surgery such as urology, orthopedics, lithotripsy, or gastroenterology with endoscopic or direct access.

7.4.5 Co-Doped and ZBLAN Fiber Lasers

The main effect of ZBLAN host glasses in fiber-optic technology is the impact on the lifetime of dopants impregnated into fibers. Complicated interactions between the host material and doping ions of rare-earth metals typically used in fiber lasers (Er^{3+}, Pr^{3+}, Tm^{3+}, and Ho^{3+}) influence the kinetics of excitation and phonon relaxation of the active levels. The induced changes allow "turning on" lasing transitions, which otherwise are low-efficiency, or almost prohibited, while using traditional silica-based host glasses [98]. The versatile set of ZBLAN laser wavelengths is typically found at the mid-IR range. This makes these fiber lasers attractive tools for surgery due to strong absorption of the radiation by organic tissues around the 3 μm wavelength range. Utilizing the thermal response in radiation/tissue interactions and operating mainly in the CW regime, ZBLAN lasers are efficient instruments for endoscopic abdominal, thoracic, and brain surgery. Numerous examples and clinical data about the use of ZBLAN lasers in surgery are given in [6, 32].

Although the ZBLAN lasers were introduced about two decades ago, they possessed a number of drawbacks, which precluded their practical use in medicine. At the beginning of the fiber laser era, when Er-ion doping was the most developed and popular approach, first ZBLAN lasers were also actively tried with Er^{3+} ions [99]. Among the most challenging tasks were attempts to improve the resistance of fluoride-based glasses against water absorption and to increase the lasing efficiency [100, 101]. A significant obstacle to bring the lasers into medical applications was also the modest output power due to the relatively long lifetime of the Er^{3+} ions at the lower

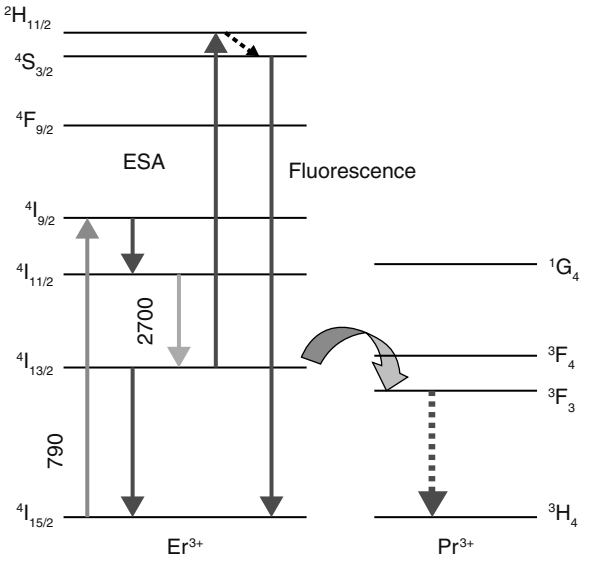

FIGURE 7.14 Energy levels of co-doped Er^{3+}:Pr^{3+}:ZBLAN glass fiber.

lasing level. Recently, a 10-W Er-ZBLAN laser with a heavily doped double-clad structure was demonstrated to have a promising performance, which might solve the problems mentioned [102]. In this particular solution, energy-transfer upconversion was used to diminish the lifetime of the lower lever thus increasing the lasing efficiency dramatically.

In contemporary fiber-optic technology, co-doping the fiber host with several different rare-earth ions simultaneously has become a popular technique. Along with the advances in developing high-power semiconductor diode lasers for pumping, implementing other dopants has broadened the range of the operating wavelengths of ZBLAN fiber lasers. Co-doped Er^{3+}:Pr^{3+} (with low-intensity double-clad diode pumping) and Ho^{3+}:Pr^{3+} (pumped with a Nd:YAG laser) ZBLAN lasers were capable of delivering over 1 W power in CW mode at 2.78 and 2.87 μm wavelengths, respectively [32, 103]. In this design, a rather sophisticated excitation scheme was used to overcome the bottleneck related to the long lifetime of the Er^{3+} low level (Fig. 7.14).

For the CW operation mode aimed to thermal ablation of soft and hard water-rich tissues, ZBLAN lasers do not need to provide extremely high powers: 1–10 W class lasers proved their efficiency for diverse surgery applications [6, 32, 104].

7.4.6 Supercontinuum Fiber Lasers

The stream of breakthrough achievements related to fiber lasers and the intensive research in biomedicine, biophysics, and other sectors of the life sciences would not be complete without highlighting sophisticated monitoring and imaging techniques. We have already mentioned optical coherent tomography. Fluorescent imaging (including flow cytometry and confocal fluorescence microscopy) and 2D/3D

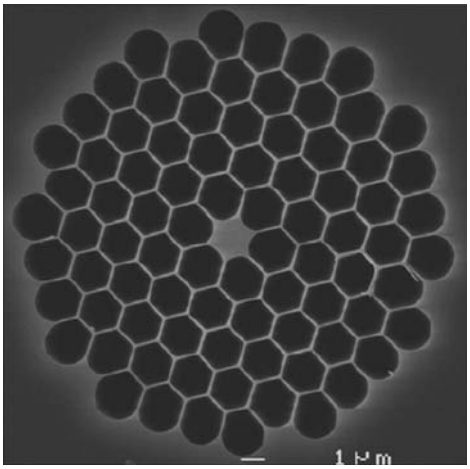

FIGURE 7.15 Multimode fiber with zero-dispersion at the visible wavelength. (Courtesy of K. P. Hansen, Crystal Fibre A/S, Denmark.)

live-cell imaging are just selective examples that extensively use advanced spectroscopic and microscopic instrumentations (see Chapter 9 for a discussion on laser microscopy). To attain the best efficiency, these methods require broadband light sources with high brightness that is extremely difficult to obtain with classical thermal (black-body) radiation sources such as tungsten-based lamps. Supercontinuum (SC) fiber lasers turned out to be excellent tools for solving this problem.

The first fiber supercontinuum sources were reported at around 2000. They were capable of covering the spectral band from 400 nm to almost 2 µm and used high-nonlinear optical fibers as active media, such as photonic crystal fibers (PCF) or tapered fibers [66, 105, 106]. To obtain such a broadband spectrum, a short light pulse (in the fs to ns range) from a Q-switched or modelocked laser, for example a Ti:sapphire or ytterbium-fiber, is launched into PCF with carefully engineered core structure providing close to zero dispersion in the visible range (Fig. 7.15) [107, 108]. This allows generating more than 1000 nm spectral band of extremely bright light (Fig. 7.16). Although the first systems could offer rather modest total radiation power, supercontinuum fiber lasers have rapidly turned into a mature technology, and reliably deliver several watts of high-quality laser beam ($M^2 < 1.1$) with commercially available systems [109].

Immediately after the first demonstrations, the supercontinuum fiber lasers were in high demand for OCT imaging to replace relatively narrowband sources (30–40 nm), radiating within the 1.3–1.5 µm range, which were mainly amplified spontaneous emission (ASE) from fiber-optic amplifiers or superluminescent light-emitting diodes (SLED). Although these wavelengths are attractive for the investigation of biological species due to good penetration into the tissues, they limit longitudinal resolution, which is inversely proportional to the spectral width of the light source. Using SC radiation with wide bandwidth leads to tremendous improvement of the resolution. In 2001, Hartl et al. reported 2.5 µm longitudinal resolution with a 370 nm

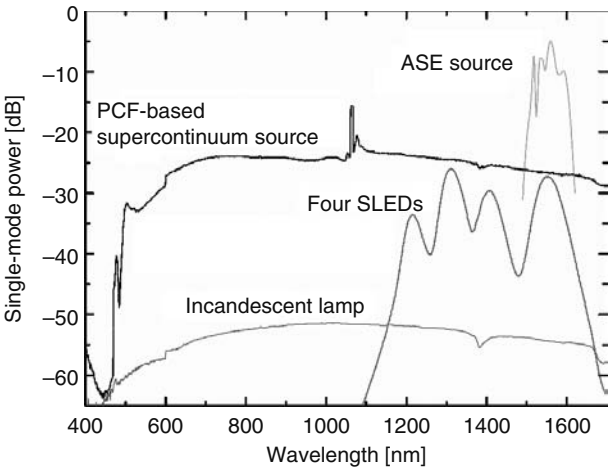

FIGURE 7.16 Comparison of supercontinuum spectra generated by different sources. The spectrum obtained with photonic crystal fiber is shown in black. (Courtesy of Dr. K. P. Hansen, Crystal Fibre A/S, Denmark.)

wide SC source centered around 1300 nm, which was built using a 100-fs Ti:sapphire modelocked laser and a nonlinear photonic crystal fiber [110].

Another approach to achieve ultrahigh resolution using SC sources is to implement dual wavelength combination. Results of the OCT with the resolution around 1.8 μm were demonstrated with the sources emitting at 840 and 1230 nm with a 200 nm bandwidth at each wavelength [111]. Using both wavelengths simultaneously has also improved the image quality with reduced speckle pattern.

Fluorescent imaging is one more domain in biology-related applications that insistently requires the use of bright white sources. Flow cytometry relies on the laser excitation of fluorophores, which have versatile spectral structure and demand broadband illumination for detailed analysis. Before SC lasers were introduced, sources with discrete numbers of wavelengths were used, thus leaving a rather large spectrum gap uncovered. Many types of fluorophores were unusable due to this limitation [112].

Confocal fluorescent microscopy is another imaging technique valuable in the biosciences and which definitely gains from the use of SC fiber lasers. A high-power supercontinuum fiber laser covering a 450–700 nm spectral range and equipped with acousto-optical tunable filters was recently used to realize a scanning microscope providing 3D live-cell image [113]. This laser is also a commercially available system incorporating low-power modelocked Yb-fiber master laser and high-power fiber amplifier with nonlinear PCF [109].

In spite of its rather short history, SC laser sources have drastically progressed during the last 5 years. At the moment, instruments routinely generating up to 6 W within tremendous range of 460–2500 nm are off-the-shelf turnkey devices. Figure 7.17 displays one of the models revealing its supercontinuum spectrum by means of a diffractive grating.

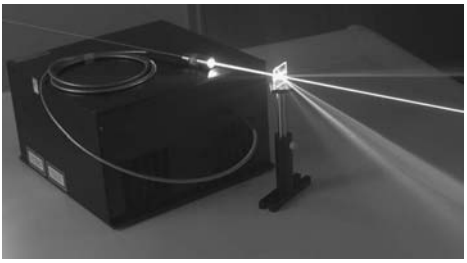

FIGURE 7.17 Air-cooled compact system SC450 generating supercontinuum radiation within 450–2000 nm bandwidth. (Courtesy of Prof. A. Grudinin, Fianium Ltd., UK.)

7.4.7 Making and Marking Tools and Instruments for the Medical Industry

To complete the survey of fiber laser applications in life sciences and medicine, it is worth mentioning one more domain implicitly related to medicine. This is the industry of making, postprocessing, and marking medical instruments and tools. Regulations in many countries on the market of medical instruments impose strict requirements for the quality and identification of most surgical tools and implants.

Numerous tools used in contemporary medicine, especially in branches like neurosurgery or ophthalmology, are often manufactured with microscaled accuracy from extremely hard materials or alloys containing cobalt, chrome, nitinol, and tantalum. To provide the highest quality for such instruments, in a cost-effective way, no ordinary mechanical machinery equipment can compete with high-power-pulsed fiber lasers built with ytterbium-doped fibers. Outperforming laser properties such as high-pulse power up to 40 kW, excellent beam profile (often $M < 1.05$ for TEM_{00} mode), and small beam size, satisfy production quality specifications [57]. Very small cutting width, and a small heat-affected zone, can be achieved by carefully choosing the suitable laser tool and its operational mode.

On the other hand, laser processing such components as burs, narrow and parallel kerfs, scalpels, tweezers, and others, can drastically improve the working properties of the instruments without thermally induced stresses or distortions, which are hardly avoidable with mechanical processing. Making "active" tools for surgery or implants is not the only branch gaining from the use of fiber lasers as processing instruments. Nonintrusive devices for cardiovascular and neurological applications, such as catheters, medical stems, implants, and biodegradable components can be efficiently and easily manufactured by the use of fiber lasers [114]. Laser technology also provides diverse opportunities for reliably joining various materials, like polymers, metals, and glasses, together [115].

Strictly speaking, all the applications mentioned here have been already served by the laser machinery exploiting lasers other than fiber. Employing technical and cost advantages discussed in the chapter, such as higher power and efficiency, smaller sizes, easier operation and maintenance routines, the fiber lasers are gradually expanding their influence over the biomedical application sector.

ACKNOWLEDGMENTS

The author is greatly thankful to Dr. F. J. Duarte for supportive discussions, criticisms, and enthusiastic guidance during the preparation of this chapter. For providing factual materials and fruitful comments, the following colleagues are acknowledged: Prof. A. Grudinin (Fianium Ltd., UK), Dr. R. Paschotta (RP Photonics Consulting GmbH, Switzerland), and Dr. K. P. Hansen (Crystal Fibre A/S, Denmark).

REFERENCES

1. Koester, C. J., E. Snitzer, Amplification in a fiber laser, *Appl. Opt.* 3: 1182–1186 (1964).
2. Snitzer, E., Proposed fiber cavities for optical masers, *J. Appl. Phys.* 32: 36–39 (1961).
3. Moizan, V., V. Nazabal, J. Troles, P. Houizot, J-L. Adam, F. Smektala, J-L. Doualan, R. Moncorge, G. Canat, and J-P. Cariou, Mid-infrared fiber laser application: Er^{3+}-doped chalcogenide glasses, *Proc. SPIE* 6469: 64690E (2007).
4. Coleman, D., S. Jackson, P. Golding, T. King, H. Se, B. Yong, and H. Jong, Heavy metal oxide and chalcogenide glasses as new hosts for Er^{3+} and Er^{3+}/Pr^{3+} mid-IR fiber lasers, *OSA Proceedings, Trends in Optics and Photonics: Advanced Solid State Lasers* 34: 434–439 (2000).
5. Carrig, T., G. Wagner, W. Alford, and A. Zakel, Chromium-doped chalcogenide lasers, *Proc. SPIE* 5460: 74–82 (2004).
6. Tafoya, J., J. Pierce, R. Jain, and B. Wong, Efficient and compact high-power mid-IR (~3 μm) lasers for surgical applications, *Proc. SPIE* 5312: 218–222 (2004).
7. Mears, R., L. Reekie, S. Poole, and D. Payne, Neodymium-doped silica single-mode fibre lasers, *Electron. Lett.* 21: 738–740 (1985).
8. Mears, R., L. Reekie, I. Jauncey, and D. Payne, Low-noise erbium-doped fibre amplifier operating at 1.54 μm, *Electron. Lett.* 23: 1026–1028 (1987).
9. Welch, A. J., and M. J. C. van Gemert (Eds.), *Optical-thermal Response of Laser-Irradiated Tissue*, Springer, 1995.
10. Waynant, R. W. (Ed.), *Lasers in Medicine*, CRC Press, 2002.
11. Goldman, L., Dye lasers in medicine, in *Dye Laser Principles*, F. J. Duarte and L. W. Hillman (Eds.), Academic, New York, 1990, Chap. 10.
12. Huang, D., E. Swanson, C. Lin, J. Schuman, W. Stinson, W. Chang, M. Hee, T. Flotte, K. Gregory, C. Puliafito, and J. Fujimoto, Optical coherence tomography, *Science* 254: 1178–1781 (1991).
13. Swanson, E., J. Izatt, M. Hee, D. Huang, C. Lin, J. Schuman, C. Puliafito, and J. Fujimoto, In vivo retinal imaging by optical coherence tomography, *Opt. Lett.* 18: 1864–1866 (1993).
14. Brezinski, M. E. *Optical Coherence Tomography Principles and Applications*, Academic Press, 2006.
15. Tearney, G., B. Bouma, S. Boppart, B. Golubovic, E. Swanson, and J. Fujimoto, Rapid acquisition of in vivo biological images by use of optical coherence tomography, *Opt. Lett.* 21: 1408–1410 (1996).
16. Chen, W., P. Xue, T. Yun, and D. Chen, Medical application of ultrafast laser, *Proc. SPIE* 3934: 87–92 (2000).
17. Palumbo, G., and R. Pratesi (Eds.), *Lasers and Current Optical Techniques in Biology*, European Society for Photobiology, Royal Society of Chemistry, 2004.
18. Wu, R., J. Myers, and M. Myers, New generation high power rare-earth-doped phosphate glass fiber and fiber laser, *Proc. SPIE* 4267: 56–60 (2001).

19. Dianov, E., M. Grekov, I. Bufetov, S. Vasiliev, O. Medvedkov, V. Plotnichenko, V. Koltashev, A. Belov, M. Bubnov, S. Semjonov, and A. Prokhorov, CW high power 1.24 μm and 1.48 μm Raman lasers based on low loss phosphosilicate fibre, *Electron. Lett.* 33: 1542–1544 (1997).
20. Smart, R., D. Hanna, A. Tropper, S. Davey, S. Carter, and D. Szebesta, CW room temperature upconversion lasing at blue, green and red wavelengths in infrared-pumped Pr^{3+}-doped fluoride fibre, *Electron. Lett.* 27: 1307–1309 (1991).
21. Whitley, T., C. Millar, R. Wyatt, M. Brierley, and D. Szebesta, Upconversion pumped green lasing in erbium doped fluorozirconate fibre, *Electron. Lett.* 27: 1785–1786 (1991).
22. Poulain, M., Fluoride glass fibers: applications and prospects, *Proc. SPIE* 3416: 2–12 (1998).
23. Xiushan, Z., and R. Jain, Numerical analysis and experimental results of high-power Er/Pr:ZBLAN 2.7 μm fiber lasers with different pumping designs, *Appl. Opt.* 45: 7118–7125 (2006).
24. Kashyap, R., *Fiber Bragg Gratings*, Academic Press, 1999.
25. Gomes, L., L. Orsila, T. Jouhti, and O. Okhotnikov, Picosecond SESAM-based ytterbium mode-locked fiber lasers, *IEEE J. Quantum Electron.* 10: 129–136 (2004).
26. Perry, M., B. Stuart, P. Banks, D. Feit, V. Yanovsky, and A. Rubenchik, Ultrashort-pulse laser machining of dielectric materials, *J. Appl. Phys.* 85: 6803–6810 (1999).
27. Juhasz, T., F. Loesel, R. Kurtz, C. Horvath, J. Bille, and G. Mourou, Corneal refractive surgery with femtosecond lasers, *IEEE J. Quantum Electron.* 5: 902–910 (1999).
28. Dausinger, F., F. Lichtner, and H. Lubatschowski (Eds.), *Femtosecond Technology for Technical and Medical Applications* (Topics in Applied Physics, v 96), Springer, 2004.
29. Andersen, T., O. Schmidt, C. Bruchmann, J. Limpert, C. Aguergaray, E. Cormier, A. Tünnermann, High repetition rate tunable femtosecond pulses and broadband amplification from fiber laser pumped parametric amplifier, *Opt. Ex.* 14: 4765–4773 (2006).
30. De Matos, C. J. S., R. Kennedy, S. Popov, and J. Taylor, 20-kW peak power all-fiber 1.57-μm source based on compression in air-core photonic bandgap fiber, its frequency doubling, and broadband generation from 430 to 1450 nm, *Opt. Lett.* 30: 436–438 (2005).
31. Hansen, K., J. Broeng, A. Petersson, M. Nielsen, P. Skovgaard, C. Jakobsen, and H. Simonsen, High-power photonic crystal fibers, *Proc. SPIE* 6102: 61020B (2006).
32. Pierce, M., S. Jackson, P. Golding, B. Dickinson, M. Dickinson, T. King, and P. Sloan, Development and application of fiber lasers for medical applications, *Proc. SPIE* 4253: 144–154 (2001).
33. Steiner, R., New laser technology and future applications, *Med. Laser Appl.* 21: 131–140 (2005).
34. Tearney, G., B. Bouma, S. Boppart, B. Golubovic, E. Swanson, and J. Fujimoto, Rapid acquisition of in vivo biological images by use of optical coherence tomography, *Opt. Lett.* 21: 1408–1410 (1996).
35. Paschotta, R., N. Moore, W. Clarkson, A. Tropper, D. Hanna, and G. Maze, 230 mW of blue light from a thulium-doped upconversion fiber laser, *IEEE J. Quantum Electron.* 3: 1100–1102 (1997).
36. Gaebler, V., and H. Eichler, Monolithic blue upconversion fiber laser, *Proc. SPIE* 4629: 94–98 (2002).
37. Qin, G., S. Huang, Y. Feng, A. Shirakawa, M. Musha, and K.-I. Ueda, Power scaling of Tm^{3+} doped ZBLAN blue upconversion fiber lasers: Modeling and experiments, *Appl. Phys. B* 82: 65–70 (2006).
38. Tohmon, G., H. Sato, J. Ohya, T. Uno, Thulium:ZBLAN blue fiber laser pumped by two wavelengths, *Appl. Opt.* 36: 3381–3386 (1997).

39. Ping, X., and T. Gosnell, Room-temperature upconversion fiber laser tunable in the red, orange, green, and blue spectral regions, *Opt. Lett.* 20: 1014–1016 (1995).
40. Chernikov, S., N. Platonov, D. Gapontsev, D. Chang, M. Guy, and R. Taylor, Raman fibre laser operating at 1.24 μm, *Electron. Lett.* 34: 680–681 (1998).
41. Dianov, E., Advances in Raman fibers, *J. Lightwave Technol.* 20: 1457–1462 (2002).
42. Dianov, E., and A. Prokhorov, Medium-power CW Raman fiber lasers, *IEEE J. Quantum Electron.* 6: 1022–1028 (2000).
43. Rini, M., I. Cristiani, V. Degiorgio, A. Kurkov, and V. Paramonov, Experimental and numerical optimization of a fiber Raman laser, *Opt. Commun.* 203: 139–144 (2002).
44. Xiong, Z., N. Moore, Z. Li, G. Lim, D. Liu, and D. Huang, Experimental optimization of high power Raman fiber lasers at 1495 nm using phosphosilicate fibers, *Opt. Commun.* 239: 137–145 (2004).
45. Goldberg, L., J. Koplow, and D. A. V. Kliner, Highly efficient 4-W Yb-doped fiber amplifier pumped by a broad-stripe laser diode, *Opt. Lett.* 24: 673–675 (1999).
46. Dominic, V., S. MacCormack, R. Waarts, S. Sanders, S. Bicknese, R. Dohle, E. Wolak, P. Yeh, and E. Zucker, 110 W fibre laser, *Electron. Lett.* 35: 1158–1160 (1999).
47. Limpert, J., A. Liem, H. Zellmer, A. Tunnermann, 500 W continuous-wave fibre laser with excellent beam quality, *Electron. Lett.* 39: 645–647 (2003).
48. Dorsch, F., V. Bluemel, M. Schroeder, D. Lorenzen, P. Hennig, and D. Wolff, Fiber coupled diode laser systems up to 2 kW output power, *Proc. SPIE* 3945: 42–44 (2000).
49. Hecht, J., High-power fiber lasers: pumping up the power, *Laser Focus World* 41 (8): 66–70 (2005).
50. De Matos, C. J. S., J. Taylor, and K. Hansen, All-fibre Brillouin laser based on holey fibre yielding comb-like spectra, *Opt. Commun.* 238: 185–189 (2004).
51. Bedo, S., W. Luthy, and H. Weber, The effective absorption coefficient in double-clad fibres, *Opt. Commun.* 99: 331–335 (1993).
52. Anping, L., and K. Ueda, The absorption characteristics of circular, offset, and rectangular double-clad fibers, *Opt. Commun.* 132: 511–518 (1996).
53. Gapontsev, V., N. Platonov, O. Shkurihin, and I. Zaitsev, 400 W low-noise single-mode CW ytterbium fiber laser with an integrated fiber delivery, in *Proc. Conference on Lasers and Electro-Optics (CLEO'2003)* (Cat. #CH37419-TBR): 3 (2003).
54. Carter, A., K. Tankala, B. Samson, D. Machewirth, V. Khitrov, and U. Manyam, Continued advancements in the design of double clad fibers for use in high output power fiber lasers and amplifiers, *Proc. SPIE* 5662: 470–475 (2004).
55. Limpert, J., F. Roser, S. Klingebiel, T. Schreiber, C. Wirth, T. Peschel, R. Eberhardt, and A. Tünnermann, The rising power of fiber lasers and amplifiers, *IEEE J. Quantum Electron.* 13: 537–545 (2007).
56. Tünnermann, A., S. Hofer, A. Liem, J. Limpert, M. Reich, F. Roser, T. Schreiber, H. Zellmer, T. Peschel, and V. Guyenot, Power scaling of high-power fiber lasers and amplifiers, *Las. Phys.* 15: 107–117 (2005).
57. Babushkin, A., N. Platonov, V. Gapontsev, Multi-kilowatt peak power pulsed fiber laser with precise computer controlled pulse duration for materials processing, *Proc. SPIE* 5709: 98–102 (2005).
58. Digonnet, M. J. F. (Ed.), *Rare-Earth-Doped Fiber Lasers and Amplifiers*, 2nd edition, CRC Press, 2001.
59. Reekie, L., R. Mears, S. Poole, and D. Payne, Tunable single-mode fiber lasers, *J. Lightwave Technol.* LT-4: 1985 (1985).
60. Laming, D., M. Farries, P. Morkel, L. Reekie, D. Payne, P. Scrivener, F. Fontana, and A. Righetti, Efficient pump wavelengths of erbium-doped fibre optical amplifier, *Electron. Lett.* 25: 12–14 (1989).
61. Barnes, W., P. Morkel, L. Reekie, and D. Payne, High-quantum-efficiency Er^{3+} fiber lasers pumped at 980 nm, *Opt. Lett.* 14: 1002–1004 (1989).

62. Bouma, B., L. Nelson, G. Tearney, D. Jones, M. Brezinski, and J. Fujimoto, Optical coherence tomographic imaging of human tissue at 1.55 μm and 1.81 μm using Er and Tm-doped fiber sources, *J. Biomed. Opt.* 3: 76–79 (1998).
63. Fercher, A., W. Drexler, and C. Hitzenberger, Ocular partial coherence tomography, *Proc. SPIE* 2732: 229–241 (1996).
64. Hee, M., J. Izatt, E. Swanson, and J. Fujimoto, Femtosecond transillumination tomography in thick tissues, *Opt. Lett.* 18: 1107–1109 (1993).
65. Povazay, B., B. Hofer, B. Hermann, A. Unterhuber, J. Morgan, C. Glittenberg, S. Binder, and W. Drexler, Minimum distance mapping using three-dimensional optical coherence tomography for glaucoma diagnosis, *J. Biomed. Opt.* 12: 1–8 (2007).
66. Wadsworth, W., A. Ortigosa-Blanch, J. Knight, T. Birks, T.-P Man, and P. Russell, Supercontinuum generation in photonic crystal fibers and optical fiber tapers: A novel light source, *J. Opt. Soc. Am. B* 19: 2148–2155 (2002).
67. Rulkov, A., A. Ferin, J. Travers, S. Popov, and J. Taylor, Broadband, low intensity noise CW source for OCT at 1800 nm, *Opt. Commun.* 281: 154–156 (2008).
68. Rusu, M., A. Grudinin, and O. Okhotnikov, Slicing the supercontinuum radiation generated in photonic crystal fiber using an all-fiber chirped-pulse amplification system, *Opt. Ex.* 13: 6390–6400 (2005).
69. Oppel, T., and H. Korting, Actinic keratosis: the key event in the evolution from photoaged skin to squamous cell carcinoma, *J. Pharmacol. Physiol. Res.: Skin Pharmacol. Physiol.* 17: 67–76 (2004).
70. Wanner, M., E. Tanzi, and T. Alster, Fractional photothermolysis: treatment of facial and nonfacial cutaneous photodamage with a 1550-nm erbium-doped fiber laser, *Dermatolog. Surg.* 33: 23–28 (2007).
71. Kincade, K., Biophotonics: fiber lasers find opportunities in medical applications, *Laser Focus World* 41 (9): 76–80 (2005).
72. Lawrence, S., Rejuvenation of the aging face using Fraxel laser treatment, *Aesthetic Surg. J.* 25: 307–309 (2005).
73. Norman, S., and M. Zervas, Fiber lasers prove attractive for industrial applications, *Laser Focus World* 43 (8): 93–98 (2007).
74. Srinivasan, B., J. Tafoya, and R. Jain, High-power "Watt-level" CW operation of diode-pumped 2.7 μm fiber lasers using efficient cross-relaxation and energy transfer mechanisms, *Opt. Ex.* 4: 490–495 (1999).
75. Pollnau, M., Ch. Ghisler, M. Bunea, W. Luthy, and H. Weber, Erbium 3-μm fiber laser in the power range for surgery, *Proc. SPIE* 2629: 234–244 (1996).
76. Pollnau, M., Route toward a diode-pumped 1-W erbium 3-μm fiber laser, *IEEE J. Quantum Electron.* 33: 1982–1990 (1997).
77. Serafetinides, A., and D. Papadopoulos, Lasers and new trends in laser-tissue interaction, *Proc. SPIE* 5449: 212–221 (2004).
78. Even, P., and D. Pureur, High power double clad fiber lasers: a review, *Proc. SPIE* 4638: 1–12 (2002).
79. Okhotnikov, O., L. Gomes, N. Xiang, T. Jouhti, and A. Grudinin, Mode-locked ytterbium fiber laser tunable in the 980-1070-nm spectral range, *Opt. Lett.* 28: 1522–1524 (2003).
80. Nickel, D., A. Liem, J. Limpert, H. Zellmer, U. Griebner, S. Unger, G. Korn, and A. Tünnermann, Fiber based high repetition rate, high energy laser source applying chirped pulse amplification, *Opt. Commun.* 190: 309–315 (2001).
81. Limpert, J., S. Hofer, A. Liem, H. Zellmer, A. Tunnermann, S. Knoke, and H. Voelckel, 100-W average-power, high-energy nanosecond fiber amplifier, *Appl. Phys. B* B75: 477–479 (2002).
82. Limpert, J., A. Liem, T. Gabler, H. Zellmer, A. Tünnermann, S. Unger, S. Jetschke, and H-R. Muller, High-average-power picosecond Yb-doped fiber amplifier, *Opt. Lett.* 26: 1849–1851 (2001).

83. Engelbrecht, M., D. Wandt, D. Kracht, Microsecond-pulsed ytterbium fiber laser system with a broad tuning range and a small spectral linewidth, *Proc. SPIE* 6453: 645321 (2007).
84. Laroche, M., P. Leproux, V. Couderc, C. Lesvigne, H. Gilles, and S. Girard, Compact sub-nanosecond wideband laser source for biological applications, *Appl. Phys. B* 86: 601–604 (2007).
85. Kang, J., K. Chang-Seok, J. Khurgin, Fiber laser SHG yields broad bandwidth at high power, *Laser Focus World* 2: 55–58 (2002).
86. Hyungsik, L., J. Yi, W. Yimin, H. Yu-Chih, C. Zhongping, and F. Wise, Ultrahigh-resolution optical coherence tomography with a fiber laser source at 1 μm, *Opt. Lett.* 30: 1171–1173 (2005).
87. Agger, S., J. Povlsen, and P. Varming, Single-frequency thulium-doped distributed-feedback fiber laser, *Opt. Lett.* 29: 1503–1505 (2004).
88. Jackson, S., and T. King, Theoretical modeling of Tm-doped silica fiber lasers, *J. Lightwave Technol.* 17: 948–956 (1999).
89. Jackson, S., T. King, High-power diode-cladding-pumped Tm-doped silica fiber laser, *Opt. Lett.* 23: 1462–1464 (1998).
90. Verdaasdonk, R., A. Rem, S. van Thoor, T. de Boorder, J. Klaessens, and H-O.Teichmann, Comparison of the CO_2, cw thulium and diode laser in a thermal imaging model for the optimization of various clinical applications, *Proc. SPIE* 6084: 126–136 (2006).
91. Fried, N., and K. Murray, High-power thulium fiber laser ablation of the canine prostate, *Proc. SPIE* 5686: 176–182 (2005).
92. Fried, N., High-power laser vaporization of the canine prostate using a 110 W Thulium fiber laser at 1.91 μm, *Las. Surg. Med.* 36: 52–56 (2005).
93. Fried, N., Thulium fiber laser lithotripsy: An in vitro analysis of stone fragmentation using a modulated 110-watt Thulium fiber laser at 1.94 μm, *Las. Surg. Med.* 37: 53–58 (2005).
94. Fried, N., and K. Murray, High-power thulium fiber laser ablation of urinary tissues at 1.94 μm, *J. Endourology* 19: 25–31 (2005).
95. Jackson, S., Midinfrared holmium fiber laser, *IEEE J. Quantum Electron.* 42: 187–191 (2006).
96. Kuo, R., S. Kim, J. Lingeman, R. Paterson, S. Watkins, G. Simmons, and R. Steele, Holmium laser enucleation of prostate (HoLEP): the Methodist Hospital experience with greater than 75 gram enucleations, *J. Urology* 170: 149–152 (2003).
97. Jackson, S., A. Sabella, A. Hemming, S. Bennetts, and D. Lancaster, High-power 83 W holmium-doped silica fiber laser operating with high beam quality, *Opt. Lett.* 32: 241–243 (2007).
98. Allain, J. Y., M. Monerie, and H. Poignant, Tunable CW lasing around 0.82, 1.48, 1.88 and 2.35 μm in thulium-doped fluorozirconate fibre, *Electron. Lett.* 25: 1660–1662 (1989).
99. Auzel, F., D. Meichenin, and H. Poignant, Laser cross-section and quantum yield of Er^{3+} at 2.7 μm in a ZrF_4-based fluoride glass, *Electron. Lett.* 24: 909–910 (1988).
100. Robinson, M., and G. L. Tangonan, Light scattering in fluoride glass, *Mat. Res. Bull.* 23: 943–951 (1988).
101. Esterowitz, L., R. Allen, G. Kintz, I. Aggarwal, and R. J. Ginther, Laser emission in Tm^{3+} and Er^{3+}-doped fluorozirconate glass at 2.25, 1.88, and 2.70 μm, in *Proc. Conference on Lasers and Electro-Optics (CLEO'1988)* 7: 318–320 (1988).
102. Zhu, X., and R. Jain, 10-W-level diode-pumped compact 2.78 μm ZBLAN fiber laser, *Opt. Lett.* 32: 26–28 (2007).
103. Qamar, F., T. King, S. Jackson, and Y. Tsang, Holmium, praseodymium-doped fluoride fiber laser operating near 2.87 μm and pumped with a Nd:YAG laser, *J. Lightwave Technol.* 23: 4315–4320 (2005).

104. Sumiyoshi, T., H. Sekita, T. Arai, S. Sato, M. Ishihara, and M. Kikuchi, High-power continuous-wave 3- and 2-μm cascade Ho^{3+}:ZBLAN fiber laser and its medical applications, *IEEE J. Quantum Electron*. 5: 936–943 (1999).
105. Husakou, A., and J. Herrmann, Supercontinuum generation of higher-order solitons by fission in photonic crystal fibers, *Phys. Rev. Lett.* 87: 203901 (2001).
106. Hundertmark, H., D. Kracht, D. Wandt, C. Fallnich, V. V. Kumar, A. George, J. Knight, and P. Russell, Supercontinuum generation with 200 pJ laser pulses in an extruded SF6 fiber at 1560 nms, *Opt. Ex.* 11: 3196–3201 (2003).
107. Hansen, K., Dispersion flattened hybrid-core nonlinear photonic crystal fiber, *Opt. Ex.* 11: 1503–1509 (2003).
108. Andersen, T., K. Hilligsoe, C. Nielsen, J. Thogersen, K. Hansen, S. Keiding, and J. Larsen, Continuous-wave wavelength conversion in a photonic crystal fiber with two zero-dispersion wavelengths, *Opt. Ex.* 12: 4113–4122 (2004).
109. Clowes, J., Next generation light sources for imaging, *Imaging and Microscopy* 9: 55–57 (2007).
110. Hartl, I., X. Li, C. Chudoba, R. Hganta, T. Ko, J. Fujimoto, J. Ranka, and R. Windeler, Ultrahigh-resolution optical coherence tomography using continuum generation in an air-silica microstructure optical fiber, *Opt. Lett.* 26: 608–610 (2001).
111. Spoler, F., S. Kray, P. Grychtol, B. Hermes, J. Bornemann, M. Forst, and H. Kurz, Simultaneous dual-band ultra-high resolution optical coherence tomography, *Opt. Ex.* 15: 10832–10841 (2007).
112. Kapoor, V., F. Subach, V. Kozlov, A. Grudinin, V. Verkhusha, and W. Telford, New lasers for flow cytometry: filling the gaps, *Nature Methods* 4: 678–679 (2007).
113. Frank, J., A. Elder, J. Swartling, A. R. Venkitaraman, A. Jeyasekharan, C. Kaminski, A white light confocal microscope for spectrally resolved multidimensional imaging, *J. Microscopy* 227: 203–215 (2007).
114. Kleine, K., B. Whitney, and K. Watkins, Use of fiber lasers for micro cutting applications in the medical device industry, *Proc. on 21st International Congress on Applications of Lasers and Electro-Optics (ICALEO 2002)* 2: 923–932 (2002).
115. Mian, A., G. Newaz, L. Vendra, N. Rahman, D. Georgiev, G. Auner, R. Witte, and H. Herfurth, Laser bonded microjoints between titanium and polyimide for applications in medical implants, *J. Materials Science: Materials in Medicine* 16: 229–237 (2005).

8 Medical Applications of Dye Lasers

A. Costela, I. García-Moreno, and R. Sastre

CONTENTS

8.1 Introduction 227
8.2 Laser Treatment of Vascular Lesions 228
8.2.1 Laser Treatment of Port-Wine Stains 229
8.2.2 Laser Treatment of Hemangiomas 230
8.3 Laser Treatment of Scars and Keloids 231
8.4 Laser Treatment of Tattoos 232
8.5 Lithotripsy 234
8.6 Laser Angioplasty 234
8.7 Dye Lasers for Photodynamic Therapy 235
8.8 Laser Safety in Medicine 238
References 239

8.1 INTRODUCTION

Laser systems have been applied in medicine since they first became available, and today they are continuing to figure prominently in diagnostic and therapeutic procedures.

Dye lasers as medical instruments have potential advantages over other lasers. They are unique sources of tunable coherent radiation, from the near ultraviolet to the near infrared, through hundreds of laser dye molecular species. The tuning range of pulsed narrow-bandwidth emission achievable with a single dye can be up to 50 nm. Significantly broader tuning ranges (up to 100 nm) can be obtained with some dyes under pulsed broadband and continuous-wave (CW) operation.

In addition to tunability, an intrinsic feature of dye lasers is their inherent ability to yield high-pulse energies and high powers in the visible spectrum. Furthermore, dye lasers can be operated in a wide range of temporal regimes: from femtosecond pulses to CW operation, with optical simplicity and potential reliability. This great versatility has favored their use in medicine, although interest in these applications has been hindered by the complexity and inherent risks that the use of dyes in the liquid phase entails (e.g., large volumes of toxic and flammable solvents and potentially carcinogenic organic dyes, complexity of the system, and need for highly

specialized manpower). Areas of development for improving applications of the dye laser in medicine are decreasing weight and volume of the systems to increase compactness and increasing dye lifetime, beam quality, spatial and temporal coherence, and brightness. To this aim it is important to develop more efficient, longer lived dyes spanning the near-UV to near-IR spectrum, as well as potentially low-cost, simple sources of dye laser radiation exploiting proven solid-state technology.

Some of the most important clinical applications of dye lasers are presented below. Our aim is not so much to carry out an exhaustive review as to give a general overview of the field. Further aspects of dye laser medical applications are discussed in Chapter 4, while medical applications of fiber lasers are discussed in Chapter 7.

Note: Due to editorial policy, to avoid the use of commercial nomenclature, the discussion in some sections has been constrained.

8.2 LASER TREATMENT OF VASCULAR LESIONS

There are a number of congenital vascular anomalies consisting of lesions that vary according to signs, symptoms, and clinical behavior. Vascular malformations are lesions present at birth that grow commensurately and fail to regress. Thus, it is advantageous to treat these malformations at an early age to avoid complications and progression of lesions.

Most vascular abnormalities can be successfully treated with lasers, and there has been a great deal of careful research on diagnosis and indications for laser treatment over the last decades. This is a rapidly evolving field, and new and improved laser systems are appearing on a regular basis. It is important to use a laser with the appropriate specifications for a given application.

In the early 1980s, Anderson and Parrish [1] presented a theory of selective photothermolysis, which predicted that selective destruction of blood vessels is possible by matching the wavelength of light absorbed by hemoglobin into the vessels. Defining thermal relaxation time as the time required for the target tissue to lose 50% of its heat, they proposed using a pulsed laser with the appropriate wavelength and with a temporal pulse length shorter than the calculated thermal relaxation time for blood vessels [2]. This led to the development of flashlamp-pumped pulsed dye lasers (FPDL) especially designed for treatment of cutaneous vascular lesions.

The FPDL, with its intrinsic capability of being wavelength-tunable, replaced the blue-green argon ion laser, which had the inconvenience of emitting at just two fixed wavelengths, 488 and 514 nm, which were too short and caused a coagulation effect of the epidermis and dermis. The first FPDL systems used in the treatment of vascular lesions were tuned to yellow, at 577 nm, a wavelength in the region of the third absorption spectral peak of oxyhemoglobin. The pulse duration was in the range 300–500 ms, calculated to match the thermal relaxation time of cutaneous blood vessels. With these laser parameters the prognoses was better, and clearance of malformations with normalization in texture and color of treated skin was observed.

After a few years of practice, in the early 1990s the emission wavelength of the FPDL systems was adjusted to 585 nm, as this somewhat longer wavelength allowed for deeper penetration in the vascular injury. The depth of light penetration in a given tissue is a critical limiting factor, and function of the wavelength. For irradiation at 585 nm, the penetration depth for 50% of the energy is 0.8 mm [2, 3]. As the facial

skin's dermal depth varies from 0.6 mm in children to about 0.9 mm in adults [4], the FPDL with emission at 585 nm provides adequate penetration for cutaneous vascular lesions.

Changing from 577 to 585 nm releases more intravascular hemoglobin, because of the larger blood vessels and concentration of oxyhemoglobin found in the deep vascular plexus of the dermis, and intravascular thrombus formation without epidermal and dermal damage was produced [3]. This resulted in the destruction of abnormally ecstatic blood vessels and replacement by normal-appearing new vessels with little or no dermal scarring after 1 month of treatment [5]. Because of this selective vascular injury, the area can be repeatedly treated with minimal risk of complications until desired degree of lightening has been achieved.

An important limitation of the described FPDL is its inability to penetrate to the level of the deep vessels. Thus, the treatment was not successful for vessels lying beyond the 1.5-mm penetration depth of the 585-nm laser beam, and lesions at this depth were not completely cleared. Improvements have been sought by developing FPDL systems tuned to 595 nm to increase the penetration depth, and with pulse durations in the range from 200 μs to 2 ms, as an exposure time of 1 ms or less is recommended to confine the heat to the vessel, decreasing the risk of heat diffusion, which can cause scarring. The beam is focused to a spot of 5 to 12 mm. Long-term results with the 595 nm wavelength have not yet been reported, because treatment with this method began just at the turn of the century [6].

8.2.1 Laser Treatment of Port-Wine Stains

Port-wine stains (PWS) were one of the first vascular malformations to be treated with laser radiation. They are congenital malformations consisting of superficial and deep dilated capillaries in the skin. The swollen blood vessels cause a reddish-purplish discoloration of the skin. Although PWS can appear in any part of the body, they occur more often in the face and persist throughout life.

Initially, treatments of PWS were carried out with fixed-wavelength lasers such as pulsed CO_2 and Nd:YAG lasers, with emission in the infrared, the yellow emission of the high-repetition-rate copper-vapor laser (578 nm), the second harmonic of Nd:YAG laser at 532 nm (usually misnamed KTP laser in the medical literature because the second harmonic of the Nd:YAG laser was obtained by using a nonlinear KTP crystal after the Nd:YAG unit), and the continuous-wave argon ion laser. In all cases, results were not fully satisfactory, with relatively high incidences of scarring and permanent depigmentation [2]. The introduction of the tunable FPDL overcame these difficulties, and now this laser has become the standard choice in the treatment of these vascular lesions [2, 7–12].

Optical fibers conduct light from the laser head to the malformed area, and convex lenses focus the laser beam directly onto the skin to a spot of at most 1-cm diameter, to reach energy fluences in the range 4–10 J/cm^2, depending on the age of the patient and the region irradiated. Children, with smaller overall lesions and more superficial vessels with smaller diameters, require lower energy fluence than adults. Sensitive areas, such as eyelids and hands, require as well reduced energy fluence. Pulse durations are in the range 100–500 μs and the repetition rate is kept at 1 or 2 Hz. Typically, a spot overlap of 20% is used.

Treatments are started at the lowest energy fluence that shows a high degree of lightening, and are repeated at 6-week intervals until complete clearing is obtained. The high pulse peak power of the FPDL disrupts the vessels and produces photocoagulation, resulting in progressive lightening of the lesion as treatment is repeated. The degree of response depends greatly on the color of the PWS lesion and its anatomical location. Red lesions require more treatments than light pink ones to achieve the same degree of lightening. Lesions in centrofacial regions involving the medial portion of the cheek, upper lip, and nose in both adults and children show a lesser degree of lightening than lesions on other locations of the face (periorbital, forehead, temple, lateral aspect of the cheek), which respond quickly [2, 13, 14]. Furthermore, lesions on the hand and arm respond less well than lesions on the face, neck, and torso.

Laser treatment of PWS can be undertaken safely in infancy [15]. In patients younger than 4 years of age fewer treatments are required to obtain the same degree of response as in older patients [2, 7, 9, 12]. The structural characteristics of the dermis change with age and a correlation between age, progression, and increase in the vascular area and mean vessel area has been found [16]. In addition, skin thickness increases linearly with age up to 20 years, so that laser treatment early in life penetrates deeper in the PWS lesion [4].

The laser pulses can produce a mild to moderate degree of discomfort. Adult and teenage patients can often be treated without anaesthesia, although this is dependent upon the size and anatomic location of the lesion itself. A significant reduction of pain as well as skin protection during laser treatment can be achieved using a cooling chamber containing a cooling fluid, such as a 40% water-glycol solution at –18 °C. Combining cooling with the use of FPDL systems tuned to the longer wavelength of 595 nm, fluences up to 9.5 mJ/cm^2 were found to be safe and effective in treating infants less than 6 months of age without needing general anaesthesia [15].

After successful treatment, no textural changes or damage to the surrounding dermis is seen in treated skin. The use of the FPDL results in a very low number of incidences of scarring or pigmentary loss. In addition, early treatment prevents the evolution that makes the lesion dark purple, raised, and nodular in many adults [15]. Thus, it is hoped that hypertrophy of affected areas, which is a common complication of extensive PWS, and permanent deformity associated with the lesions can be mitigated.

8.2.2 Laser Treatment of Hemangiomas

Hemangiomas are common benign vascular tumors caused by an overgrowth of endothelial cells—the cells that line blood vessels. These malformations are present at birth in ca. 3% of newborns and about 10% by the end of the first year of life [17, 18], and are more common in girls. Although over 80% of hemangiomas occur on the head and neck area, they can appear anywhere on the body. In most patients, a single lesion is present. However, in approximately 15–20% of infants, the lesions are multiple [19]. In the latter cases in some instances, even other organs such as the lung or liver can be affected. Nearly all childhood hemangiomas eventually involute and disappear without treatment. However, some hemangiomas can be disfiguring and psychologically distressing, so early medical intervention is sometimes necessary.

Although treatments such as electrosurgery, cryosurgery, surgical excision, sclerotherapy, embolization, and drug therapy have been tried, they have some adverse effects and are not advised for patients with cutaneous hemangiomas. On the contrary, the FPDL, with its optimal combination of color and pulse duration, has proven to be an effective and safe tool in the treatment of these lesions in children, minimizing significantly any adverse cutaneous effects, preventing enlargement, and promoting involution of cutaneous hemangiomas [2, 20–26]. The laser conditions are the same used for treatment of port-wine stains, although recent reports [26] indicate that in the treatment of early childhood hemangiomas, use of long-pulse FPDL with emission tuned to 595 nm shortens the average time period of maximum hemangioma proliferation with less adverse effects. The pulse duration was in the range 10–20 ms, and cryogen spray cooling was used to protect the epidermis. Therapy should be initiated as soon as possible, as studies have shown that the thicker the lesion the less effective is the FPDL treatment [21, 23–25, 27].

In spite of early intervention, FPDL treatment of hemangiomas cannot prevent proliferation of the deep component, and in the case of subcutaneous or mixed hemangiomas the deep component can continue to proliferate after the cutaneous component has been eliminated. In these cases, prior treatment with infrared Nd: YAG laser radiation, which penetrates deeper than visible radiation, has proved to be advantageous. Once the underlying subcutaneous vessels have been treated with infrared radiation, the superficial component may respond to treatment with the pulsed dye laser much better.

8.3 LASER TREATMENT OF SCARS AND KELOIDS

A keloid is a type of scar that results in an overgrowth of tissue at the site of a healed skin injury. After the skin is injured, the healing process usually leaves a flat scar. Sometimes the scar is hypertrophic, or thickened, but confined to the margin of the wound, and subsides by itself (although in a process that can take more than a year). A keloid, by contrast, is a tough heaped-up scar that rises abruptly over the rest of the skin. It may start some time after the injury and extend beyond the wound site. This tendency to migrate into surrounding areas that weren't injured distinguishes keloids from hypertrophic scars. Keloids typically appear following surgery or injury, but they can also appear spontaneously or as a result of some slight inflammation. They develop most often on the chest, back, shoulders, and earlobes, and rarely on the face (with the exception of the jawline). Although keloids are benign and noncontagious, they not only represent a cosmetic problem but usually are accompanied by severe itchiness, sharp pains, and changes in texture. In severe cases, the movement of skin can be affected.

Despite increasing knowledge of wound healing and collagen metabolism, so far no universally accepted and completely satisfying method in the treatment of hypertrophic scars and keloids has been established. Although numerous methods have been tried [28, 29], the response of keloids is often unsatisfactory and they often reoccur after therapy. Some of these methods are excisional surgery and cryotherapy, adjunctive intralesional corticosteroid application, pressure therapy, and covering with silicon gel sheets. Radiation therapy following surgical removal has also been used, although it was abandoned due to possible long-term carcinogenicity.

As an alternative to traditional therapies, different laser systems and techniques have been used as treatment of hypertrophic scars and keloids for several years, with distinct success [30–35]. In order to choose the best type of laser or technique with specific effects, a previous assessment of the clinical appearance of these lesions, with their individual color, shape, size, or vascularization is necessary. During the last few years, systematic and well-controlled studies have demonstrated that the flashlamp-pumped pulsed dye laser at 585 nm (hemoglobin absorption band), inducing the selective photothermolysis with irreversible destruction of microvessels, can be used to treat hypertrophic scars and keloids with very good and promising results [36–41]. This laser treatment reduces scar microcirculation and leads to a reduction of erythema with lightening of scars and keloids. Significant improvement in scar texture, bulk, and pliability were obtained, and symptoms like pain and pruritus diminished significantly.

A typical laser therapy for these lesions uses pulses from the FPDL with fluences of 6–8 J/cm^2, although fluences as high as 18 J/cm^2 have been used in some cases, with pulse duration of 300 μs and spot size of 5 mm, and with spatial overlap between pulses of 10–20% [36–42]. To reduce pain and thermal side effects at the epidermis, continuous cooling of the skin surface is used. With these laser parameters improvement is significant after just one or two laser sessions. Observed side effects of laser treatment are: a purpuric tissue response developing immediately after laser irradiation, which disappears within 10–15 days; small bubbles or crusts in the treated area; and, rarely, hyperpigmentation or infection. The recurrence rate of the lesion after full laser treatment is very low.

In general, the best results are obtained with erythematous hypertrophic scars, especially hypertrophic burn scars, keloids with small elevations, and newer lesions. The results are less satisfactory in the treatment of prominent and fibrotic keloids, proliferate keloids, and dermal contractures within the scars or lesions older than 2 years [40, 41, 43]. In these cases, it is advisable to use a primary transcutaneous or interstitial Nd:YAG laser treatment, although data with longer observation time are necessary.

8.4 LASER TREATMENT OF TATTOOS

The practice of tattooing is an old one, and evidence of tattoos has been found in ancient Egyptian mummies. Tattooing is accomplished by injecting colored pigment into small deep holes made in the skin, resulting in marks or designs that are relatively permanent. Although over the last decade tattoos have experienced increased popularity all over the world, there are still negative associations with tattoos, and improved self-image or social stigmatization lead people to turn to physicians to remove tattoos.

Many different methods for tattoo removal have been explored over the centuries. Older techniques involve destruction or removal of the outer skin layers either by mechanical (dermabrasion, salabrasion, excision), chemical, or thermal (direct heat, cautery, infrared coagulator) means. Transepidermal elimination of pigment occurs through denuded skin [44–47] and via an exudative phase that allows tattoo pigment to migrate to the wound surface to be absorbed into the dressing. In all these methods, some scarring or color variations are likely to remain and inflammation appears. The inflammatory response may promote macrophase activity with increased phagocytosis, enabling additional pigment loss during the healing phase. Tattoos that have been on the skin for a considerable length of time may be more difficult to remove.

Lasers have been demonstrated to be effective in tattoo removal [48–53]. The above-mentioned principle of selective photothermolysis, established by Anderson and Parrish [48], revolutionized the treatment of tattoos. They proposed that the heat generated by the incident laser radiation would be confined to the target if the wavelength was well absorbed by the tattoo inks and the pulse-width was equal to or shorter than the thermal relaxation time of the target. To specifically target tattoos, laser wavelength and pulse duration must be appropriately chosen.

One of the earliest studies [54] examined the effects of a tunable dye laser at three wavelengths (505, 577, and 680 nm) using a 1 μs pulse to remove black, blue, red, and white tattoo pigment. It was shown that the threshold dose to induce the same histological changes was much less than that required for the argon laser, and that each wavelength reacted only with complementary colors of tattoo pigment. However, despite the short 1 μs pulse, widespread tissue necrosis was observed and tattoo lightening occurred only as a result of significant dermal necrosis and resultant fibrosis. These studies suggested that shorter nanosecond pulses would interact best with the micron-sized granules of pigment because they approximate the thermal relaxation time of pigments.

To target tattoo ink, the best laser wavelength could be that which achieves selective absorption for each ink color while minimizing absorption by the primary endogenous chromophores, hemoglobin, and melanin. Reflectance spectrum data for tattoo ink colors may assist in selecting the best available wavelength. Black pigment is absorptive at all wavelengths (having minimal reflectance), and competition from melanin absorption in the epidermis decreases gradually as wavelength increases. Absorption for blue and green is greatest for wavelengths of 600–800 nm, whereas red absorbs best below 575 nm, tan below 560 nm, flesh-colored pigment below 535 nm, and yellow below 520 nm [55].

The flashlamp-pumped pulsed dye laser (510 nm, pulsewidth of 300 ± 100 nsec) is well absorbed by red pigment and the pulsewidth is short enough to fragment ink granules. Successful clearing without scarring usually occurred in three to seven treatments performed at 1-month intervals using 3–3.75 J/cm^2 [56]. Purple, orange, and yellow pigments required an average of five treatments for complete ink removal. During treatment, no hypopigmentation, textural changes, or scarring was noted. Histologically, fragmentation of red pigment particles is observed followed by macrophage engulfment. In addition, because of the epidermal absorption of this laser, transepidermal ink loss occurs.

Direct comparison studies of the various available wavelengths are difficult as treatment parameters including pulsewidth, spot size, and fluences are hard to standardize and results are often inconclusive [57, 58]. Recently, it has been reported that for some laser energy levels, tattoo removal becomes more efficient as the laser pulse length is shortened [59].

It is in this application where the solid-state dye lasers (SSDL) considered in Chapter 3 are probably going to find immediate application. As described in Chapter 3, it is precisely in the yellow-red region of the spectrum where efficient and stable SSDL lasers have already been developed, exhibiting performances comparable to those of the liquid dye lasers emitting in the same region. Thus, the technology is mature for cheap and compact SSDL lasers appearing in the market in the near future.

8.5 LITHOTRIPSY

Lithotripsy is a medical procedure that uses shock waves to break up stones that form in the kidney, bladder, ureters, or gallbladder. There are several forms of lithotripsy. The most common is extracorporal shock wave lithotripsy; however, for atypical stone types and restricted access, laser lithotripsy acts as a complementary technique.

In the usual extracorporal shock wave lithotripsy (ESWL) technique, an externally applied, focused, high-intensity acoustic pulse passes through the body to the area on the stones. The succesive shock wave pressure pulses break the stones into tiny pieces that then can pass easily through the ureters or the cystic duct.

When a laser is used, a train of laser pulses is guided by a fiber to the application site and ignites plasma at the surface of the stone. The breakdown of the plasma creates a shock wave, which detaches some fragments. After many repetitions, the stone will be fragmented into smaller pieces, which then can pass spontaneously.

Laser lithotripsy using pulsed-dye lasers is especially indicated for choledochal stones inaccessible to simple extraction techniques and for fragment urinary tract calculi. It is also the technique of choice for removal of pancreatic stones, since it significantly reduces mechanical trauma to the pancreas.

The laser parameters appropriate for lithotripsy differ in a wide range, depending on fiber diameter, lasing wavelength, location, and composition of stones, which define their absorption bands. Typical operational parameters of flashlamp-pumped dye lasers used in lithotripsy treatment are: emission wavelength of 504 nm and 595 nm, depending on stone composition; pulse energy ranging from 50–120 mJ/pulse; pulse duration from 1–42.5 μs; and repetition rate of 1–10 Hz. The procedure requires endoscopic control of laser effects and a system for stone recognition. Since the laser light is green, there is minimal tissue absorption and almost negligible tissue damage. Because the energy effects take place on structures with crystalline makeup, soft tissue is basically unaffected. Thus, even if the laser fiber fires repeatedly against the urethral wall, very little tissue damage takes place.

8.6 LASER ANGIOPLASTY

Arteries can become narrowed or blocked by deposits called plaque. Plaque is made up of fat and cholesterol that builds up on the inside of the artery walls. This condition is called atherosclerosis. Angioplasty is a medical procedure to open arteries that are obstructed by atherosclerotic plaque. It involves different forms of minimally invasive vascular interventions, which can be exemplified by balloon angioplasty, a procedure in which a balloon is used to open a blockage in an artery narrowed by atherosclerosis.

Laser angioplasty is a promising alternative method to open arteries obstructed by atherosclerotic plaque, with potential advantages over surgery, balloon angioplasty, and other forms of vascular interventions. Laser radiation can be introduced into arteries via small optical fibers, thus avoiding major surgery. The radiation can remove plaque rather than displacing it, thus potentially reducing the high rate of restenosis (gradual re-narrowing of the artery during several months following the procedure) that occurs with balloon angioplasty. Laser radiation with the appropriate wavelength is preferentially absorbed by plaque, thereby adding an element of specificity and safety that does not exist with mechanical devices.

Early laser angioplasty systems suffered from some complications, such as hematoma formation, perforation, dissection, thrombosis, and vascular spasm, of which the most significant was perforation of the underlying normal artery wall [60–62]. This damage resulted from the laser-tissue interaction or from the laser-delivery system.

Much progress has been made to avoid damage produced by interaction of laser radiation with tissue. Calcified plaque, which could not be removed with low to moderate intensity lasers, is now known to be readily plasma-ablated with high-intensity radiation [63]. Selective ablation of plaque is achieved at wavelengths where plaque absorption is much greater than normal artery absorption [64–67]. If plaque absorption is not strong enough, the efficacy of treatment can be improved by enhancing plaque absorption with exogenous chromophores [68, 69].

Laser delivery problems have been more difficult to resolve [70]. The bare, quartz optical fibers that were used initially had sharp edges, which perforated arteries even when the laser was not on. To avoid these problems and improve the performance of fibers to transmit the laser energy, different devices have been developed and fibers with tapered ball-tipped ends have been used [71, 72]. In a typical procedure, small, flexible fibers deliver light from a flashlamp-excited dye laser at the wavelength of 480 nm in the form of pulses of 8 μs duration, up to 1 J of energy, and 10 Hz repetition rate, allowing for recanalization of 2–3 mm diameter channels [72]. There are no losses along the fiber from extra optical interfaces, and the "stiff" region at the fiber tip is short. The fluence of the 480 nm radiation is selected to ablate calcified plaque with laser-induced plasma and to selectively ablate yellow plaque, minimizing mechanical injury and avoiding perforating normal arteries. A fluence of 85 J/ cm^2, which is enough to recanalize arteries, is higher than the ablation threshold for plaque (56 J/cm^2) but well below the fluence required to ablate normal artery and perforate (226 J/cm^2). Following the process by means of time-delayed flash photography, it was observed that a high-pressure vapor bubble formed with each ablative pulse, producing an expanding effect similar to balloon angioplasty. Thus, the laser procedure results in an interaction of optical, thermal, and mechanical mechanisms that involves not only ablation of plaque but also stretching open the artery. In this way, the laser treatment does not need to be complemented by balloon angioplasty, as was the case with early laser systems used in this application.

8.7 DYE LASERS FOR PHOTODYNAMIC THERAPY

Photodynamic therapy is a noninvasive or minimally invasive procedure that utilizes photosensitizer drugs, which once administered to a patient may be selectively retained by diseased tissues while normal tissues remain unaltered. These photosensitizer drugs, retained in the diseased tissues, can be activated under intense visible light irradiation in order to achieve the selective photochemical destruction of the diseased cells and neovasculature [73]. Generally, the photosensitizer drug is activated by light of the appropriate wavelength and then generates the cytotoxic photodynamic reaction conventionally mediated by singlet oxygen [74].

Although healing properties of light have been appreciated since many thousands of years ago, the more recent use of photodynamic therapy (PDT) in oncology

dates to the early 1970s when the group led by Dr. Dougherty began research on the mechanism and clinical uses of some hematoporphyrin derivatives [75], in spite of the 100-year-old concept of cell death induced by the photochemical interaction of light and chemicals. An historical review of this therapy and its evolution, predominantly focused on the treatment of oncologic diseases, can be found in [76, 77].

Now, PDT is considered both a curative and palliative procedure—a treatment of precancerous and cancerous lesions and superficial tumors, using light. The list of medical fields in which PDT has managed to find a place as an accepted option for treatment of specific diseases includes: dermatology, ophthalmology, gynecology, gastroenterology, and so on [78]. The increasing interest and importance of PDT are based on the serious inconveniences for the patient's health that often accompanies traditional chemotherapy and radiotherapy. It is well known that the toxicity of these well-established therapies limits their therapeutic use, while PDT not only shows a distinct degree of tumor specificity but also can be repeatedly applied without significantly damaging patients' health.

The three basic elements involved in the PDT process are photosensitizer, light, and oxygen. The photosensitizer absorbs energy in the form of light of appropriate wavelength, converts it to excitation electronic energy, and transmits or transfers it to oxygen molecules present in the medium, thereby forming highly aggressive forms of oxygen singlet as well as other reactive oxygen-based species, such as ozone, superoxide radicals, hydroxyl, and peroxide radicals.

The basis of the development and application in PDT of the first photosensitizers were the numerous studies directed to establish the role of porphyrin and hematoporphyrin derivatives as fluorescent probes in the detection and photodiagnosis of tumors, as described in [79]. In 1978, after the successful treatment of tumors in animals using porphyrin-based PDT, Dougherty reported on the first of a large series of patients successfully treated with PDT after other conventional therapies had failed [80]. Since then, major efforts have been invested in the development of new photosensitizers able to absorb light at longer wavelengths to get better tissue penetration, greater photochemical efficiency, improved selective tumor tissues localization, and minor toxicity and skin photosensitivity. Although many photosensitizers have been described, up to now only a few have received the approval for PDT [77–79]. Specifically named photosensitizers include the hematoporphyrin derivatives HpD and DHE [81].

Aminonevulinic acid HCl, which is commercially available, has been approved for the treatment of actinic keratosis on the face and scalp. This photosensitizer is activated at 630 nm and has found a commercial success as a topical cream [82].

Other photosensitizers have been developed and tested on patients with excellent clinical results, but as of yet no FDA approval has been obtained for them. Future research will undoubtedly be directed toward the development of improved photosensitizers with increased tumor selectivity and fewer side effects, reduced systemic toxicity, and shorter duration of the photosensitivity. For the purposes of this chapter, we will focus next on the oncologic applications of dye lasers for PDT.

Although the first light sources used in PDT were conventional lamps and filters, now the most common light sources used in this application are lasers, because they emit monochromatic light of known wavelength that can be chosen according to the absorption wavelengths of the photosensitizer used and the required depth of tissue

necrosis. Also, the laser light can be conducted by an optical fiber for localized treatments, which allows adaptation of the irradiation to the target area or lesion. Microlenses and diffuser fibers can be used to optimize irradiation at the target. Both CW and pulsed dye lasers are used.

One of the systems most widely utilized, which sometimes has been considered to be the standard source for PDT, is the argon/dye laser (lasing dye Rhodamine 640 pumped with argon ion laser) capable of delivering from 1 W to 7 W of 630 nm CW radiation, depending on the model. An advantage presented by these argon/dye lasers is the possibility to change the emitted wavelength to match the optimum absorption wavelength of the photosensitizer by simply adjusting internal filters of the laser system, thus providing the capability to be used with different photosensitizers. In this way, these lasers can easily generate 630 nm and 635 nm, used with appropriate photosensitizers, and 652 nm for use with m-tetra(hydroxyphenyl) porphyrins. Initially, high-power argon/dye lasers were employed in the PDT clinical trials on malignant tumors. These lasers were commercially available, of large size, mounted as a fixed unit on an optical bench, and able to emit argon ion pump powers of 15–20 W, enough to generate up to 7 W from the dye unit at the required wavelength. This high power allowed the specialist to split the main beam into multiple beams, enabling, by means of coupling to different optical fibers, the irradiation of multiple areas. These large argon/dye lasers became the tool of choice for early PDT studies. Together with the use of multiple optical fibers the systems provided enough flexibility to adjust the prescribed dosimetry. Later, smaller and easier to manage argon/dye lasers designed for clinical use in PDT became commercially available to produce the appropriate wavelength and power for each treatment.

One of the more significant advances in tunable laser technology for PDT was the so-called KTP/dye laser. This is a modular system consisting of a Nd:YAG laser emitting radiation at 1064 nm with a KTP (potassium-titanyl-phosphate) doubling crystal to generate the second harmonic of the fundamental beam at 532 nm, which pumped the dye unit. A company based in California manufactured lasers of this kind for PDT applications working at a repetition rate of ~25 kHz and incorporating a specially designed dye laser head via an optical fiber connection. Different models offered at least two alternatives, in the few Watt range, at a wavelength of 630 nm. These systems provided pulsed light instead of the CW output of the argon/dye laser, which led initially to some controversy regarding the possible different effects in the laser-tissue interaction between pulsed and CW radiation [83]. Nevertheless, in the commercially available pulsed laser, the high-pulse repetition rate (~25 kHz) and low peak power produced results not markedly different from CW irradiation, with equivalent photobiological effects. On the other hand, side effects such as nonlinear absorption or photosensitizer saturation were negligible. These more advanced systems exhibit some advantages over other lasers employed in PDT: portability (although somewhat limited by weight, size, and water-cooling requisites), tunability, and ease of use and handling.

The availability of a wide number of commercial laser dyes with emission covering the visible spectrum, from the blue to the infrared region [84], allows choosing the appropriate dye emission wavelength to overlap with the photosensitizer absorption band. As described in Chapter 3, adequate modifications in the structure of commercial dyes have allowed increasing significantly their efficiency

and photostability, both in liquid and solid state. When incorporated into solid matrices, careful choice of matrix composition (linear or cross-linked copolymers; incorporation of fluorine and/or silicon atoms in the matrix structure; hybrid materials or aerogels) allows further improvements of laser performance, resulting in solid-state dye lasers competitive with their liquid counterparts. Although most of these improvements have been obtained with dyes emitting in the yellow-orange region, no difficulties are anticipated to extend these results to dyes with emission in the red region, appropriate for use in PDT applications. In this way, low-cost, simple sources of dye laser radiation could be obtained, which will greatly facilitate the use of dye lasers in PDT and will provide much desired flexibility for selecting between different emission wavelengths.

On the other hand, current research is also focused on improving and obtaining new photosensitizers, as well as directed on developing more efficient light delivery systems, and obtaining an increased understanding of the optical properties of tissues and the photophysical and photochemical behavior and effects of the interaction between drug and light. Once all these challenges have been overcome PDT will fully show its potential as a major treatment for minimally invasive cancer therapy.

8.8 LASER SAFETY IN MEDICINE

The increased variety of lasers with emission at different wavelengths makes safe laser use a complex issue that needs to be carefully assessed [85]. The laser surgeon and hospital staff must be concerned with the protection of both the patient and the operating room staff. Safety hazards that should be especially considered when using lasers in medical applications are: eye protection, plumes of vaporized tissue, and potential fire hazards.

The one hazard that is truly unique to the laser and that requires special attention is the laser beam itself. Unlike other light sources, the laser beam is collimated and propagates over long distances; hence, the area of potential hazard is not limited to the immediate surgical site. Laser beams are reflected to some extent from any surface contacted, and reflected light can still cause serious injuries if it reaches the eye, because of the eye focusing capability. In fact, an examination of laser accident records indicates that the source of accidental ocular exposure is most frequently a reflected beam. Thus, special care should be taken to avoid potentially hazardous reflections, and wearing appropriate eye protection is mandatory. Patient safety is assured by limiting needless exposure to laser radiation of tissues adjacent to those treated (by choice of wavelength and to a large extent by surgical technique), using noncombustible materials adjacent to the beam, and by protecting the patient's eyes. It has proven to be of advantage to occlude the eyes completely with compresses and adhesive strips instead of glasses. The staff and the surgeon, however, should wear goggles or glasses, which must be chosen in accordance with the relevant wavelengths as well as to the type and intensity of irradiation.

Skin damage from laser radiation is not as great a concern as eye damage because the skin is less vulnerable to injury. Nevertheless, uncontrolled movements of the laser by the surgeon, reflected laser light, or inattentiveness of the staff may lead to burns in the skin during laser therapy. The severity of the injury depends upon the

length of exposure and the penetration depth of the laser radiation. As the irradiation of unanaesthetized skin is, in general, quickly noticed because of pain, the affected area is quickly removed from the laser beam, so that serious injuries are prevented.

The potential hazard from breathing airborne contaminants produced during the vaporization of tissues is probably the issue that has caused more concern in surgical laser safety. Although photocoagulation does not produce a smoke plume, any laser cutting of tissues will produce gases and airborne particulates that must be evaluated as a potential respirable hazard. A number of careful studies of both the chemical toxicity of pyrolysis products and the potential viability of infectious particulates have shown real cause for concern unless very good exhaust ventilation and respiratory protection are employed [86–89].

In addition to the optical radiation hazards introduced by lasers, several more familiar safety and health hazards are associated with their use. Primary among these hazards is the potential for electrical shock. Many lasers require a high-voltage power supply. Charged condensers can be dangerous even if the laser is disconnected from the electrical supply. Users of this equipment must be familiar with safe procedures and electrical safety controls. Pulsed lasers may additionally interfere electromagnetically with other electronic medical equipment.

As discussed in Chapter 3, liquid dye lasers use toxic compounds as a lasing medium that, in the case of an accident, can leak out of the laser and cause health injuries. Moreover, such substances must be disposed of according to the manufacturers' guidelines. The solid-state dye lasers (SSDL) considered in Chapters 3 and 4 avoid the problems of toxicity and provide a low-cost gain medium; they are also compact and easy to operate and maintain. Thus, they are much more appropriate to be used in a medical environment than the usual liquid dye lasers. The technology of the SSDL lasers is maturing fast, and it is expected that their appearance in the market as competitive products in the near future will rise.

We cannot end without insisting on the fact that medical lasers represent complex systems whose effective service depends on different factors such as wavelength, pulse duration, fluences, and so on. To be able to use this service purposefully and safely, it is necessary not only to have theoretical knowledge of optical physics, but also appropriate training. Thus, participation in specific courses of training programs is strongly recommended. Accidents can only be prevented by a well-trained staff and an administrative policy that encourages a sustained effort toward safe laser use.

REFERENCES

1. Anderson, R. R., and J. A. Parrish, The optics of human skin, *J. Invest. Dermatol.* 77: 9–13 (1981).
2. Geronemus, R. G., Pulsed dye laser treatment of vascular lesions in children, *J. Dermatol. Surg. Oncol.* 19: 303–310 (1993).
3. Nakagawa, H., O. T. Tan, and J. A. Parrish, Ultrastructural changes in human skin after exposure to a pulsed laser, *J. Invest. Dermatol.* 84: 396–400 (1985).
4. Tan, O. T., B. Statham, R. Marks, and P. A. Payne, Skin thickness measurements by pulsed ultrasound: its reproducibility, validation and variability, *Br. J. Dermatol.* 106: 657–667 (1982).

5. Tan, O. T., J. M. Carney, and R. Matgolis, Histological response of port-wine stains treated by argon, carbon dioxide, and tunable dye laser: a preliminary report, *Art. Dermatol.* 122: 1016–1022 (1986).
6. Baniandrés, O., P. Boixeda, P. Belmar, and A. Pérez, Treatment of lupus erythematosus with pulsed dye laser, *Laser Surg. Med.* 32: 327–330 (2003).
7. Ashinoff, R., and R. G. Geronemus, Flashlamp-pumped pulsed dye laser for port-wine stains in infancy: earlier versus later treatment, *J. Am. Dermatol.* 24: 467–472 (1991).
8. Goldman, M. P., R. E. Fitzpatrick, and J. Ruiz-Esparza, Treatment of port-wine stains (capillary malformation) with the flashlamp-pumped pulsed dye laser, *J. Pediatr.* 122: 71–77 (1993).
9. Holy, A., and R. G. Geronemus, Treatment of periorbital port-wine stains with the flashlamp-pumped pulsed dye laser, *Arch. Ophthalmol.* 110: 793–797 (1992).
10. Poetke, M., C. Philipp, A. Groβewineklmann, P. Urban, and H. P. Berlien, Die behandlung von naevi flammei bei Sáuglingen und kleinkindern mit dem blitzlampengepumpten farbstofflaser, *Monatsschr. Kinderheilkd* 32: 405–415 (2001).
11. Reyes, B. A., and R. G. Geronemus, Treatment of port-wine stains during childhood with the flashlamp-pumped pulsed dye laser, *J. Am. Dermatol.* 23: 1142–1148 (1990).
12. Tan, O. T., K. Sherwood, and B. A. Gilchrest, Treatment of children with port-wine stains using the flashlamp-pumped pulsed dye laser, *New. Engl. J. Med.* 320: 416–421 (1989).
13. Renfro, L., and R. G. Geronemus, Anatomical differences of port-wine stains in response to treatment with the pulsed dye laser, *Arch. Dermatol.* 129: 182–188 (1993).
14. Tallman, B., O. T. Tan, J. G. Morelli, B. S. Piepenbrink, T. J. Stafford, T. Shawn, and W. L. Weston, Location of port-wine stains and the likelihood of ophthalmic and/or central nervous system complications, *Pediatrics* 87: 323–327 (1991).
15. Chapas, A. M., K. Eickhorst, and R. G. Geronemus, Efficacy of early treatment of facial port wine stains in newborns: a review of 49 cases, *Laser Surg. Med.* 39: 563–568 (2007).
16. Noe, J. M., S. H. Barsky, D. E. Geer, and S. Rosen, Port-wine stains and the response to argon laser therapy: successful treatment and the predictive role of color, age and biopsy, *Plat. Reconstr. Surg.* 65: 130–136 (1980).
17. Jacobs, A. H., and R. G. Walton, The incidence of birth-marks in the neonate, *Pediatrics* 58: 218–222 (1976).
18. Urban, P., and B. Algermissen, Stadieneinteilung kindlicher hämangiome nach FKDS-kriterien, *Ultraschall Med.* 20: 36–40 (1999).
19. Requena, L., and O. P. Sangueza, Cutaneous vascular proliferations. Part II. Hyperplasias and benign neoplasms, *J. Am. Acad. Dermatol.* 37: 887–919 (1997).
20. Garden, J. M., A. D. Bakus, and A. S. Paller, Treatment of cutaneous haemangiomas by the flashlamp-pumped pulsed dye laser: prospective analysis, *J. Pediat.* 120: 555–560 (1992).
21. Hohenleutner, U., and M. Landthaler, Die behandlung der säuglingshämangiome, *Kinderarzt* 28: 989–1000 (1997).
22. Landthaler, M., U. Hohenleutner, A. B. D. Talal Ahnmed, and A. El Raheem, Therapie vaskulärer fehlbildungen, *Medwelt.* 46: 357–359 (1995).
23. Poetke, M., O. Bültmann, C. Phillipp, and H. P. Berlien, Hämangiome und vaskuläre malformationen im säuglings- und kindesalter, *Vasomed.* 184: 40–47 (1998).
24. Poetke, M., C. Philipp, and H. P. Berlien, Flashlamp-pumped pulsed dye laser for haemangiomas in infancy, *Arch. Dermatol.* 136: 628–632 (2000).
25. Sherwood, K. A., and O. T. Tan, Treatment of a capillary haemangioma with the flashlamp-pumped dye laser, *J. Am. Acad. Dermatol.* 22: 136–137 (1990).
26. Kono, T., H. Sakurai, W. F. Groff, H. H. Chan, M. Takeuchi, T. Yamaki, K. Soejima, and M. Nozaki, Comparison study of a traditional pulsed dye laser versus a long-pulsed dye laser in the treatment of early childhood hemangiomas, *Laser Surg. Med.* 38: 112–115 (2005).

27. Billson, V. R., and G. I. Gilliam, An unusual case of Sturge-Weber syndrome, *Pathology* 16: 462–465 (1984).
28. Berman, B., and H. B. Bieley, Keloids, *J. Am. Acad. Dermatol.* 33: 117–123 (1995).
29. Lawrence, W. T., In search of the optimal treatment of keloids: report of series and a review of the literature, *Ann. Plast. Surg.* 27: 164–178 (1991).
30. Henderson, D. L., T. A. Cromwell, and L. G. Mes, Argon and carbon dioxide laser treatment of hypertrophic and keloid scars, *Laser Surg. Med.* 3: 271–277 (1984).
31. Henning, J. P. H., Y. Roskam, and M. J. C. Van Gemert, Treatment of keloids and hypertropic scars with an argon laser, *Laser Surg. Med.* 6: 72–75 (1986).
32. Kantor, M. R., D. G. Wheeland, and P. L. Bailin, Treatment of earlobe keloids with carbon dioxide laser excision: report of 16 cases, *J. Dermatol. Surg. Oncol.* 11: 1063–1067 (1985).
33. Apfelberg, D. B., M. R. Maser, and D. N. White, Failure of carbon dioxide excision of keloids, *Laser Surg. Med.* 9: 382–388 (1989).
34. Apfelberg, D. B., T. Smith, and H. Lash, Preliminary report on use of the neodymium-YAG laser in plastic surgery, *Laser Surg. Med.* 7: 189–198 (1987).
35. Sherman, R., and H. Rosenfeld, Experience with Nd:YAG laser in the treatment of keloid scars, *Ann. Plast. Surg.* 21: 231–235 (1988).
36. Alster, T. S., Improvement of erythematous and hypertrophic scars by the 585-nm flashlamp-pumped pulsed dye laser, *Ann. Plast. Surg.* 32: 186–190 (1994).
37. Alster, T. S., and C. M. Williams, Treatment of keolid sternotomy scars with 585 nm flashlamp-pumped pulsed dye laser, *Lancet* 345: 1198–1200 (1995).
38. Dierickx, C., M. P. Goldmann, and R. E. Fitzpatrick, Laser treatment of erythematous/hypertrophic and pigmental scars in 26 patients, *Plast. Reconstr. Surg.* 95: 84–89 (1995).
39. Alster, T. S., and C. Handrick, Laser treatment of hypertrophic scars keloids and striae, *Semin. Cutan. Med. Surg.* 19: 287–292 (2000).
40. Scharschmidt, D., B. Algermissen, C. Philipp, and H. P. Berlien, Prinzipien der laserbehandlung von narben and keloiden, *Journal DGPW* 16: 7–9 (1998).
41. Paquet, P., J. F. Hermanns, and G. E. Pierard, Effect of the 585 nm flashlamp-pumped pulsed dye laser for the treatment of keloids, *Dermatol. Surg.* 27: 171–174 (2001).
42. Kuo, Y-R., W-S. Wu, and F-S. Wang, Flashlamp pulsed-dye laser suppressed TGF-β1 expression and proliferation in cultured keloid fibroplasts is mediated by MAPK pathway, *Laser Surg. Med.* 39: 358–364 (2007).
43. McCraw, J. B., J. A. McCraw, and N. Bettencourt, Prevention of unfavourable scars using early pulse dye lasers treatments: a preliminary report, *Ann. Plst. Surg.* 42: 7–14, (1999).
44. Boo-Chai, K., The decorative tattoo-its removal by dermabrasion, *Plast. Reconstr. Surg.* 32: 559–563 (1963).
45. Clabaugh, W., Removal of tattoos by superficial dermabrasion, *Arch. Dermatol.* 98: 515–521 (1968).
46. Clabaugh, W., Tattoo removal by superficial dermabrasion, *Plast. Reconstr. Surg.* 55: 401–405 (1957).
47. Bunke, H. J., and H. Conway, Surgery of decorative and traumatic tattoos, *Plast. Reconstr. Surg.* 20: 67–77 (1957).
48. Anderson, R. R., and J. A. Parrish, Selective photothermolysis: precise microsurgery by selective absorption of pulsed radiation, *Science* 220: 524–527 (1983).
49. Kilmer, S. L., and R. R. Anderson, Clinical use of the Q-switched ruby and the Q-switched Nd:YAG (1064 nm and 532 nm) lasers for treatment of tattoos, *J. Dermatol. Surg. Oncol.* 19: 330–338 (1993).
50. Sheehan-Dare, R. A., and J. A. Cotterill, Lasers in dermatology, *Br. J. Dermatol.* 129: 1–8 (1993).

51. Zelickson, B. D., D. A. Mehregan, A. A., Zarrin, G. Coles, P. Hartwing, S. Olson, and J. Leaf-Davis, Clinical, histologic, and ultrastructural evaluation of tattoos treated with three laser systems, *Laser Surg. Med*. 15: 364–372 (1994).
52. Stafford, T. J., R. Lizek, and T. T. Oon, Role of the Alexandrite laser for removal tattoos, *Laser Surg. Med*. 17: 32–38 (1995).
53. Kilmer, S. A., Laser treatment of tattoos, *Lasers in Dermatol*. 15: 409–417 (1997).
54. Diette, K. M., R. R. Bronstein, and J. A. Parrish, Histologic comparison of argon a tunable dye lasers in the treatment of tattoos, *J. Invest. Dermatol*. 85: 368–373 (1985).
55. Baumler, W., E. T. Eibler, U. Hohenleutner, B. Sens, J. Sauer, and M. Landthaler, Q-switch laser and tattoo pigments: first results of chemical and photophysical analysis of 41 compounds, *Lasers Surg. Med*. 26: 13–21 (2000).
56. Grekin, R. C., R. M. Shelton, and J. K. Geisse, 510-nm pigmented lesion dye laser: its characteristics and clinical uses, *J. Dermatol. Surg. Oncol*. 19: 380–387 (1993).
57. Prinz, B. M., S. R. Vavricka, P. Graf, G. Burg, and R. Dummer, Efficacy of laser treatment of tattoos using lasers emitting wavelengths of 532nm, 755 nm, and 1064 nm *B. J. Derm*. 150: 245–251 (2004).
58. Bernstein, E. F., Laser treatment of tattoos, *Clin. Dermatol*. 24: 43–55 (2006).
59. Ross, E. V., G. S. Nasaeef, C. P. Lin, M. W. Kelly, N. Michaud, T. Flotte, J. Raythen, and R. R. Anderson, Comparison of responses of tattoos to picosecond and nanosecond Q-switched Nd:YAG lasers, *Arch. Dermatol*. 134: 167–171 (1998).
60. Lee, G., R. M. Ikeda, J. H. Theis, M. C. Chan, D. Stobbe, C. Ogata, A. Kumagai, and D. T. Mason, Acute and chronic complications of laser angioplasty: vascular wall damage and formation of aneurysms in the atherosclerotic rabbit, *Am. J. Cardiol*. 53: 290–293 (1984).
61. Abela, G. S., J. M. Seeger, E. Barbieri, D. Franzini, A. Fenech, C. J. Pepine, and C. R. Conti, Laser angioplasty with angioscopic guidance in humans, *J. Am. Coll. Cardiol*. 8: 184–192 (1986).
62. Borst, C., Percutaneous recanalization of arteries: Status and prospects of laser angioplasty with modified fibre tips, *Laser. Med. Sci*. 2: 137–151 (1983).
63. Prince, M. R., G. M. LaMuraglia, P. Teng, T. F. Deutsch, and R. R. Anderson, Selective ablation of calcified arterial plaque with laser-induced plasmas, *IEEE J. Quantum. Electron*. QE-23: 1783–1786 (1987).
64. Prince, M. R., T. F. Deutsch, M. M. Mathews-Roth, R. Margolis, J. A. Parrish, and A. R. Oseroff, Preferential absorption in artheromas in vitro: implications for laser angioplasty, *J. Clinic. Investig.* 78: 295–302 (1986).
65. Prince, M. R., T. F. Deutsch, A. H. Shapiro, R. J. Margolis, A. R. Oseroff, J. T. Fallon, J. A. Parrish, and R. R. Anderson, Selective laser ablation of atheromas using a flashlamp-excited dye lasers, *Proc. Nat. Acad. Sci. USA* 83: 7064–7068 (1986).
66. Murray, A., R. F. M. Wood, D. C. Mitchell, D. H. Edwards, M. Grasty, and R. Basu, Peripheral laser angioplasty with pulsed dye laser and ball-tipped optical fibres, *Lancet* 23: 1471–1474 (1989).
67. Geschwind, H. J., J. L. Dubois-Rande, E. Shafton, G. Boussigac, and M. Wexman, Percutaneous pulsed laser assisted balloon angioplasty guided by spectroscopy, *Amer. Heart. J*. 117: 1147–1152 (1989).
68. Singleton, D. L., G. Paraskevopoulos, R. S. Taylor, and L. A. J. Higginson, Excimer laser angioplasty: tissue ablation, arterial response, and fiber optic delivery, *IEEE J. Quantum. Electron*. QE-23: 1772–1782 (1987).
69. Prince, M. R., G. M. LaMuraglia, and E. F. MacNichol, Increased preferential absorption in atherosclerotic plaque with oral beta carotene: Implications for laser endarterectomy, *Circulation* 78: 338–344 (1988).
70. Isner, J. M., and R. H. Clarke, Laser angioplasty: unraveling the gordian knot, *J. Am. Coll. Cardiol*. 7: 705–708 (1986).

71. Gregory, K. W., and R. R. Anderson, Liquid core light guide for laser angioplasty, *IEEE J. Quantum Electron*. QE-26: 2289–2296 (1990).
72. Prince, M. R., G. M. LaMraglia, C. E. Seidlitz, A. Prahl, C. A. Athanasoulis, and R. Birngruber, Ball-tipped fibers for laser angioplasty with the pulsed dye laser, *IEEE J. Quantum Electron*. QE-26: 2297–2304 (1990).
73. Allison, R., T. S. Mang, G. Hewson, W. Snider, and D. Dougherty, Photodynamic therapy for chest wall progression from breast carcinoma is an underutilized treatment modality, *Cancer* 91: 1–8 (2001).
74. Dougherty, T. J., Photodynamic therapy, *Photochem. Photobiol*. 58: 895–900 (1993).
75. Dougherty, T. J., J. E. Kaufman, and A. Goldfarb, Photoradiation therapy for the treatment of malignant tumours, *Cancer Res*. 38: 2628–2635 (1978).
76. Mang, T. S., Lasers and light sources for PDT: past, present and future, *Photodiagnosis and Photodynamic Therapy* 1: 43–48 (2004).
77. Allison, R., H. C. Mota, and C. H. Sibata, Clinical PD/PDT in North America: an historical review, *Photodiagnosis and Photodynamic Therapy* 1: 263–277 (2004).
78. Berlien, H. P., and G. J. Müller, *Applied Laser Medicine*, Springer-Verlag, Berlin, 2003.
79. Ackroyd, R., C. Kelty, N. Brown, and M. Reed, The history of photodetection and photodynamic therapy, *Photochem. Photobiol*. 74: 656–669 (2001).
80. Dougherty, T. J., J. E. Kaufman, A. Goldfarb, K. R. Weishaupt, D. Boyle, and A. Mittleman, Photoradiation therapy for the treatment of malignant tumors, *Cancer Res.* 36: 2628–2635 (1978).
81. Goldman, L., Dye lasers in medicine, in *Dye Laser Principles*, edited by F. J. Duarte and L. W. Hillman, Academic, New York, 1990, Chap. 10.
82. Christiansen, K., P. Bjerring, and A. Troilius, 5-ALA for photodynamic photorejuvenation-optimization of treatment regime on normal-skin fluorescence measurements, *Laser Surg. Med*. 39: 302–310 (2007).
83. Wilson, B. C., Photodynamic therapy: light delivery and dosage for second generation photosensitizers, in *Photosensitizing Compounds: Their Chemistry, Biology and Clinical Use*, John Wiley & Sons, Chichester, 1989, pp. 60–73.
84. Brackmann, U., *Lambdachrome Laser Dyes*, Lambda Physics GmbH, Göttingen, 1994.
85. Sliney, D. H., and S. L. Rokel, *Medical Lasers and Their Safe Use*, Springer, Berlin, Heidelberg, New York, 1992.
86. Baggish, M. S., B. J. Poiesz, D. Joret, P. Williamson, and A. Refai, Presence of human immunodeficiency virus DNA in laser smoke, *Laser Surg. Med*. 11: 197–203 (1991).
87. Baggish, M. S., and J. Elbakry, The effect of laser smoke on the lungs of rats, *Am. J. Obstet. Gynecol*. 156: 1260–1265 (1987).
88. Miller, G. W., J. Geraci, and D. A. Schumrich, Smoke evacuation for laser surgery, *Otolaryngol. Head Neck Surg*. 92: 582–586 (1983).
89. Kokasa, J. M., and J. Eugene, Chemical composition of laser tissue interaction smoke plume, *J. Laser Appl*. 1: 59–63 (1989).

9 Biological Microscopy with Ultrashort Laser Pulses

J. L. Thomas and W. Rudolph

CONTENTS

9.1 Introduction 246
9.2 Fundamentals 246
9.2.1 Nonlinear Microscopy 247
9.2.2 Signal Increase and Resolution Enhancement 251
9.2.2.1 Plasmon Excitation 251
9.2.2.2 Coherent Quantum Control in Microscopy 252
9.2.2.3 Saturation Microscopies 253
9.2.3 Microscopy with Time and Coherence Gating 254
9.3 Laser Sources 256
9.3.1 Femtosecond Oscillators (Kerr-Lens Modelocked Lasers) 256
9.3.2 Femtosecond Fiber Laser 257
9.3.3 Q-Switching 258
9.3.4 Cavity Dumping 258
9.3.5 Long Cavities 258
9.3.6 External Storage Cavities 258
9.3.7 Pulse Amplification 259
9.4 Examples of Nonlinear Microscopic Imaging and Applications Using Short Laser Pulses 259
9.4.1 Multiphoton Fluorescence Microscopy 259
9.4.1.1 General 259
9.4.1.2 Advantages and Applications 260
9.4.1.3 Challenges and Cautions 262
9.4.1.4 Resolution in Multiphoton Fluorescence Microscopy 263
9.4.2 Harmonic Microscopies 264
9.4.2.1 General 264
9.4.2.2 Geometric Properties of Harmonic Sources and Emissions 265
9.4.2.3 Advantages and Applications of SHG 267
9.4.2.4 Third Harmonic Generation 269

9.4.3 Four-Wave Mixing Microscopies 270
9.4.3.1 General 270
9.4.3.2 Advantages and Applications 270
9.4.3.3 Challenges and Solutions 271
9.4.3.4 Short-Pulse Lasers and CARS 274
9.4.3.5 SPF 275
9.5 Summary 276
Acknowledgments 276
References 276

9.1 INTRODUCTION

Since the invention of the laser, the generation of ever-shorter laser pulses has always opened up fascinating new application fields outside of physics and engineering. Light is what we need to see, and therefore it is no surprise that these light bullets have been explored for their use as illumination sources for microscopy. Today, pulses as short as a few femtoseconds (fs) can readily be obtained directly from lasers operating in the near-infrared spectral region. There are two features these pulses have that are particularly attractive for imaging, in particular for microscopy: (1) the high peak power at relatively low energy and mean power and (2) the short geometrical and/or coherence length. The shortness of the wave packet allows for imaging modalities with detector gating that have found applications in range gating and in imaging through scattering layers. Because of the high peak powers, fs pulses can readily excite nonlinear optical processes as opposed to the linear light-matter interaction known from ordinary light sources. The associated nonlinear signals can be used to create images showing sample properties that remain hidden in ordinary microscopy.

In this chapter we will first review the fundamentals of microscopic imaging with short (femtosecond) laser pulses. We will continue with a description of typical laser sources and their parameters used for illumination. Finally, we will describe examples of some nonlinear microscopies that have found interest in particular in the biosciences.

9.2 FUNDAMENTALS

Microscopy with ultrashort (femtosecond) light pulses in most cases refers to scanning microscopy [1] (see Fig. 9.1a). The laser is focused onto the sample and then subsequently raster-scanned across a certain horizontal plane. Alternatively, the sample is scanned while the laser focus is stationary. In classical linear scanning microscopy with continuous wave, low-power laser illumination the image signal is proportional to the incident laser power.

$$P_{im} \propto P_{in} \tag{9.1}$$

The image signal, which is collected at each sample location and displayed on a computer, can be the power or polarization change of the transmitted light, the reflected (backscattered) light, or an excited fluorescence to name a few examples.

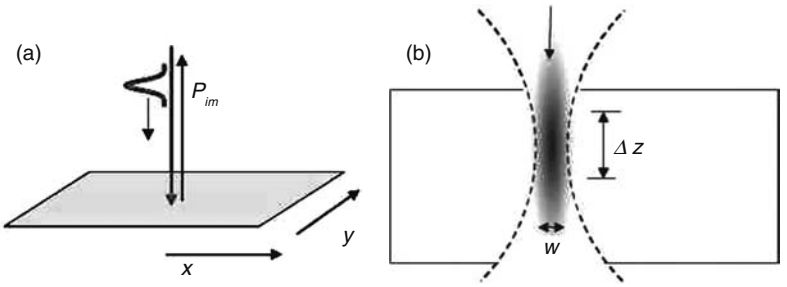

FIGURE 9.1 (a) Schematic diagram of scanning microscopy with short-pulse illumination producing an imaging signal P_{im} while either the focused laser beam or the sample is raster-scanned. (b) A laser beam focused into a sample. The lateral intensity distribution is characterized by a width w and the longitudinal distribution by a length Δz.

As mentioned, the two features of ultrashort pulses that make them attractive for microscopy are (1) high intensity at low pulse energy and (2) short geometrical length (coherence length). We will first discuss nonlinear imaging utilizing the high intensities and then describe imaging with time gating utilizing the short coherence and geometrical length of femtosecond pulses.

9.2.1 Nonlinear Microscopy

With ultrashort (femtosecond) laser pulse illumination, peak intensities in the focus area can easily exceed GW/cm^2 at low input energy and average power [2]. At such intensities nonlinear optical signals can be generated whose power P_{im} is proportional to the incident intensity I_{in} raised to a certain power of n

$$P_{im} = q_i \int I_{in}^n(t)dt \tag{9.2}$$

Here n characterizes the order of the nonlinear optical process, and the integral encompasses the integration time of the detector, the latter being unable to resolve fs transients. Here and in equations that follow coefficients q_i are constants of proportionality that we will not specify for simplicity.

With $n > 1$, the image signal is produced predominantly in the focus of the beam where the intensity is large (see Fig. 9.1b). This feature makes possible optical sectioning—that is, imaging at certain sample depths without a confocal pinhole. This 3D imaging capability is one of the unique and powerful features of nonlinear microscopy.

A great number of nonlinear optical processes have been explored for microscopy. The most successful are two-photon fluorescence (TPF) [3], second and third harmonic generation (SHG and THG) [4, 5], and coherent anti-Stokes Raman scattering (CARS) [6]. It should be noted that n is not necessarily equal to the order of the nonlinearity involved, but rather characterizes the dependence of the image signal on the incident intensity (cf. Equation 9.2). For example, two-photon fluorescence is initiated by a two-photon absorption, which is a nonlinear process of third

order, while the image signal $P_{TPF} \propto I_{in}^2$. This is the same dependence as for SHG microscopy, which is based on a nonlinear optical process of second order. The difference is that the TPF signal is not coherent to the input field; the fluorescence is emitted into a 4π solid angle and does not carry any phase information of the input field. In contrast the SH is a coherent image signal that propagates in a spatial mode defined by the input field and also carries the phase information of the input. While these differences have an effect on the actual resolution of the nonlinear microscope [7], we will not distinguish between coherent and incoherent imaging modes in this chapter, but will describe the imaging properties only in terms of the exponent n.

In general, the response of the material to ultrashort pulse illumination can be monitored with spatial resolution and the response parameters can be used as image signals. Examples are lifetime imaging and pump-probe imaging (see, for example, references [8, 9]). In pump-probe imaging a pump pulse excites the sample and a (time-delayed) probe pulse probes a certain sample property, for example, the transmission or the induced birefringence [10]. Images taken for different delay times can be combined to an image that represents the spatial distribution of a certain relaxation or sample response parameter.

Biological microscopy is often plagued by low contrast. In classical microscopy this means that the sample exhibits only small spatial variations in the transmission, reflection, or optical birefringence. For this reason biological objects are often stained with marker dyes that accumulate differently in different parts of the sample, for example, the cell [11]. Fluorescence or absorption images can then show the desired structures with higher contrast. In nonlinear microscopy the time-averaged image signal

$$S_n(x,y) = q_2 \left|\chi^{(n)}(x,y)\right|^2 \int \left[E_{in}^n(t)\right]^2 dt = q_3(n) \left|\chi^{(n)}(x,y)\right|^2 E_0^{2n} \tau_p f T \qquad (9.3)$$

is proportional to the absolute value squared of a nonlinear susceptibility of certain order n, $|\chi^{(n)}(x,y)|^2$. Nonlinear microscopy is particularly attractive in situations where the $\chi^{(n)}$ image shows contrast while "classical" microscopic images do not. In Equation 9.3 the integral represents the detector response, which is much slower than the pulse duration τ_p and (in many cases) the repetition rate f of the illumination source. The time T is the pixel dwell time and E_0^2 is proportional to the peak intensity of the pulse.

In ordinary laser scanning microscopy the resolution is given by the size of the focus spot of the laser beam on the sample [1]. In a nonlinear microscope the spot size that is responsible for the signal generation decreases with the parameter n. This is immediately evident if we consider the intensity of a Gaussian beam in the focal plane $I(r) = \exp(-2r^2/w^2)$, where w characterizes the spot size, and raise this intensity distribution to a power of n to obtain the image signal. The resulting Gaussian represents a spot size $\omega/\sqrt{n}$. The depth (z) resolution improves as $\Delta z \propto 1/n$, which for Gaussian beams is easily recognized from the dependence of the Rayleigh range on the spot size. The potential increase in transverse resolution is another reason for the success of nonlinear microscopy. Resolution limits derived for CW lasers cannot always be used for short pulse illumination [12–14]. The reason is chromatic aberration, which requires that the focusing optics be carefully designed. Achromatic designs are key to distribute the excitation pulse spectrum spatially uniformly on the sample for optimum resolution and signal strength.

For biological applications image acquisition speed is often an issue. For the imaging of dynamical processes, such as neuronal transmission, fast acquisition rates are desired. With the fast detectors and data acquisition systems that are available today the ultimate limit is set by the signal to noise ratio and consequently the quantum shot noise limit. For this reason one wishes to maximize the nonlinear optical image signal that can be obtained from each pixel. Equation 9.3 provides the basis for a simple discussion that will exemplify specific issues related to nonlinear microscopy and the preferred parameters of the short pulse laser illumination sources. Clearly, upper limits for the dwell time T are set by the desired or required image acquisition rate and the total number of pixels per image. Since $|\chi^{(n)}(x,y)|^2$ is a sample property and beyond our control (this is the image to be taken) the task is to maximize the product

$$Q_n = E_0^{2n} \tau_p f \tag{9.4}$$

by choosing an optimum combination of pulse duration, pulse peak intensity, and laser repetition rate. Apart from the limitations set by available laser sources, which we will neglect for now, practical limits are given by the damage mechanisms and thresholds of the samples to be studied.

If we assume that there exists a critical damage fluence $F_c = \beta \tau_p^{\kappa}$ (energy $W_c \sim E_0^2 \tau_p$ per area A, $0 < \kappa < 1$) that must not be exceeded and that the area of the laser spot is determined by the desired resolution:

$$Q_n = \frac{\beta^n}{\tau_p^{n-1-n\kappa}} f, \tag{9.5}$$

assuming square pulses in the temporal domain. Illumination lasers with large repetition rates and shortest possible pulse durations are favored. The existence of such a critical fluence is typical for the interaction of subpicosecond near-IR pulses with transparent (dielectric) materials [15], including biological samples [16]. The reason for the τ_p^{κ} law is that the energy deposition is associated with multiphoton ionization.

There are other situations in which there is a critical average power $P_c = I_c A$, for example, as a result of sample heating owing to linear absorption. In this case

$$Q_n = \frac{P_c^n}{\tau_p^{n-1} f^{n-1}}, \tag{9.6}$$

and consequently short pulse lasers with low repetition rates should be used.

The third case is where the pulse peak intensity has a critical value, I_c, that must not be exceeded.

$$Q_n = I_c^n \tau_p f \tag{9.7}$$

Longer pulses and higher repetition rates are favored here. It should be mentioned that the above cases are limiting scenarios, and compromises have to be sought for real samples. For example, increasing the pulse duration and repetition rate as

suggested by Equation 9.7 can increase the mean illumination power to the point where this becomes the limiting parameter.

In all these cases, for given pulse energy, shorter pulses will produce larger signals, assuming that the nonlinear optical process has a large enough bandwidth, which is mostly, but not always, true. (For example, coherent anti-Stokes Raman spectroscopy, CARS, probes very narrow-bandwidth vibrational resonances.) Today laser pulses as short as 5 fs can be produced directly in laser oscillators that have a bandwidth (full width at half maximum) exceeding 200 nm at a center wavelength of 800 nm [17]. However, the pulse duration in the above equations refers to the pulse at the position of the sample, that is, after the pulse has propagated through several optical components, including the focusing objective. These optical elements needed to steer and focus the beam while minimizing aberrations that affect the pulse shape through group velocity dispersion (GVD). The use of reflective optics with low net dispersion whenever possible is recommended. For high-resolution imaging high-NA refractive objectives are required, which often introduce the equivalent of several cm of glass path into the beam.

Assuming a Gaussian transform-limited pulse at the output of the laser of duration τ_{p0}, the pulse duration at the location of the sample [2]

$$\tau_p = \tau_{p0}\sqrt{1+\left(\frac{4\ln 2}{\tau_{p0}^2}\right)^2\left(\sum_i \Phi_i^{''}\right)^2} \tag{9.8}$$

Here $\Phi_i'' = d^2\Phi_i/d\omega^2$ is the second derivative of the phase response of element i in the path of the pulse. For a slab of glass of refractive index n and length L

$$\Phi^{''} = \frac{\lambda^3}{2\pi c^2}\frac{d^2 n}{d\lambda^2}L \tag{9.9}$$

Figure 9.2a shows the pulse duration at the sample as a function of the input pulse duration if the overall GVD is lumped into a slab of BK7 glass of certain length L. Figure 9.2b displays the relative strength of the image signal for a nonlinear process with $n = 2$, for example SHG assuming a constant pulse fluence. For a given glass path (cumulative dispersion of the optical components), shorter pulses from the laser do not necessarily produce larger signals.

To utilize the potential provided by ultrashort pulse lasers, the dispersion of the optical setup can be precompensated. To this end the pulse is sent first through an optical element whose GVD has the same magnitude but the opposite sign of the dispersion produced by the steering optics and the microscope. Such a compensator can be built from prisms and gratings.

For very short pulses, higher-order dispersion of the optical components becomes critical and needs to be compensated. Liquid crystal arrays acting on the pulse spectrum [18] or the interaction of the pulse with a suitably shaped acoustic waveform in a crystal [19] can provide control over several dispersion orders. Figure 9.2 also shows that for pulses larger than about 100 fs, dispersion effects play a minor role and not much is gained by dispersion compensation.

For many applications these pulse durations are sufficient, and several commercial laser-microscope systems operate in this regime, which simplifies the design

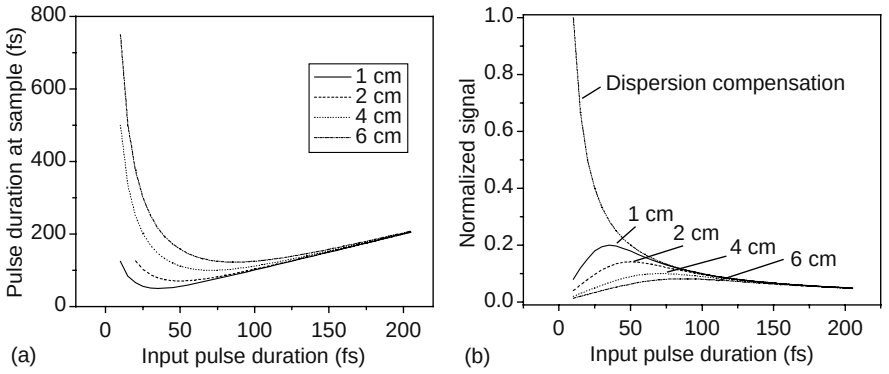

FIGURE 9.2 (a) Pulse duration at the sample location as a function of the pulse duration out of the laser for different lengths of BK7 glass paths. (b) Normalized image signal for $n = 2$ as a function of the pulse duration produced by the laser for different BK7 glass paths. The case of perfect dispersion compensation is shown for comparison.

and operation. Sometimes it is convenient to deliver the pulse from the laser to the microscope through an optical fiber whose length is of the order of meters. On the one hand this provides ease of operation and alignment, while on the other hand dispersion compensation is absolutely necessary even for pulses longer than 100 fs.

9.2.2 Signal Increase and Resolution Enhancement

9.2.2.1 Plasmon Excitation

To increase signals and to confine the signal generation to volumes that are smaller than the far-field diffraction limit of the optical system, structures have been invented that use surface-plasmon-polaron effects [20]. Large field enhancements are possible that can aid in the generation of nonlinear optical signals. The structures can be metal beads of nm size and planar metal structures on dielectric substrates.

To discuss some of the basic effects let us look at a metal (Au) film deposited to the hypotenuse of a prism (see Fig. 9.3a). The prism geometry is one (of several) possibility to couple light into the film at the angle of the surface plasmon resonance at which a distinct dip in the reflection curve is visible. In this geometry the field enhancement at the film-air interface can be explained by the standing electromagnetic wave in the metal film and the evanescent wave probing the adjacent material (air in the absence of a sample). This feature has been used in many different modifications for sensor applications. For nonlinear microscopy the field enhancement and localization is attractive as a means to increase the nonlinear optical signal and/or the resolution [21]. Note that the excitation is confined longitudinally to less than a wavelength owing to the interaction of the sample with an evanescent field.

Excitation of the plasmon is possible if the projection of the wave vector of the incident field along the film is matched to the wave vector of the plasmon [20]. In this sense the plasmon excitation acts as a k-space and frequency filter at the same time. This seems detrimental to the necessity to tightly focus a laser beam (large k-vector spectrum) with a broad frequency spectrum (short pulse), defeating the goal of producing a short light pulse at the sample location. Figure 9.3b shows the theoretically

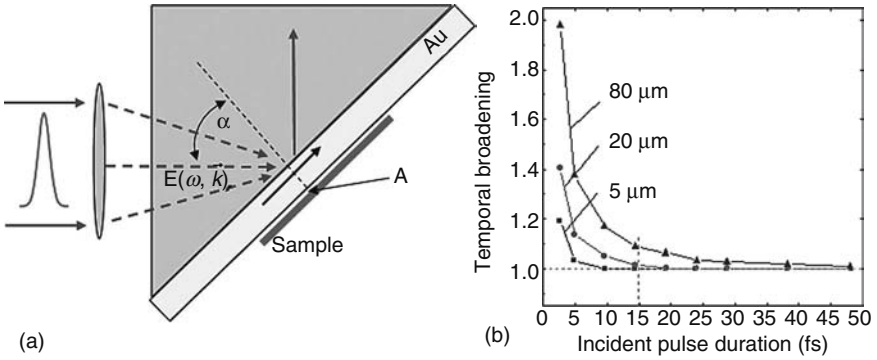

FIGURE 9.3 (a) Excitation geometry of surface plasmons at the interfaces of an Au film and air. (b) Duration of the excitation relative to the incident pulse duration as a function of the incident pulse duration for different spot sizes at sample location A. (Courtesy of Lin, X., University of New Mexico.)

expected duration of the evanescent field as a function of the duration of the input pulse and the focusing parameters. Field enhancement and excitation localization are possible at the same time, which can increase nonlinear signal generation mediated by plasmons [22, 23].

9.2.2.2 Coherent Quantum Control in Microscopy

Coherent quantum control involves the manipulation of a quantum state by adjusting the relative phase of interfering quantum pathways that can contribute to the excitation of this state [24]. Using fs laser excitation, the control parameter can be the spectral phase of the pulse. In microscopy, the goal is usually to maximize the population of a certain state, which is responsible for the image signal, while avoiding the excitation of undesired states. It is particularly straightforward to look at the situation of a two-photon nonlinear process like two-photon absorption [25], which, for example, is the excitation process in a two-photon fluorescence microscope. Roughly speaking, the overlap of the second-order field spectrum of the incident pulse $|E_2(\omega)|^2$ with the two-photon absorption spectrum $\sigma^{(2)}(\omega)$ determines the excitation strength. The second-order field spectrum can be written in terms of the spectral amplitude $A(\omega)$ and phase $\Phi(\omega)$ of the incident pulse [26]:

$$|E_2(\omega)|^2 \propto \left| \int d\omega' A(\omega')A(\omega-\omega')\exp\left[i\Phi(\omega')+i\Phi(\omega-\omega')\right] \right|^2 \tag{9.10}$$

By shaping the spectral phase, one can control which frequency components will interfere constructively (maximum signal) and destructively (no signal). As a result, the second-order spectrum can be tailored, for example, to the two-photon absorption spectrum of the fluorophore to be excited, minimizing fluorescence from and photobleaching of other molecules. More complex nonlinear processes can also benefit from coherent quantum control. CARS, using single fs pulses, was demonstrated in a scanning microscope [27]. The spectral phase of the laser pulse can be shaped using the techniques of complex spectral filtering mentioned previously.

9.2.2.3 Saturation Microscopies

It is now generally recognized that resolution in fluorescence microscopy can exceed the far-field diffraction limit that the Abbé diffraction limit applies only to linear processes, and that the fluorescent molecule itself provides a nonlinearity in its excitation and emission processes. Two examples will be discussed: stimulated emission depletion microscopy; and structured illumination saturation microscopy [28]. We will introduce the concept here for its importance and potential even though it does not require short pulse illumination.

Consider first the excitation of fluorescent molecules of number density N_t that we will describe as two-level systems interacting with the incident laser of intensity *I(r)*. The upper state population density N_1 is given by the rate equation

$$\frac{d}{dt}N_1(r,t) = \frac{\sigma}{h\nu}I(r,t)(N_t - 2N_1) - \frac{N_1}{\tau_F}, \tag{9.11}$$

where σ is the absorption cross-section, v is the frequency, h is Planck's constant, and τ_F is the fluorescent lifetime. Using CW illumination the fluorescence signal is proportional to the steady-state population density in the upper state

$$N_1(r) = \frac{N_t}{2}\left[1 + \frac{h\nu}{2\sigma\tau_F I(r)}\right]^{-1} \tag{9.12}$$

The fraction of excited-state molecules saturates at one-half, owing to the balance of stimulated emission and absorption. Let us use a simple one-dimensional model where r represents the Cartesian coordinate x in the (transverse) plane of the sample to illustrate the ramifications of saturation for possible resolution enhancements.

A sinusoidal illumination pattern ($I \propto \sin kx$) will produce a concentration of excited-state fluorophores that will not be sinusoidal. As shown in Figure 9.4a, increasing intensity results in progressively narrower bands of unexcited fluorophores. By means of "structured illumination" (i.e., by shifting the illumination pattern in small increments), one can subtractively construct a superresolution image. More sophisticated image reconstruction approaches use Fourier processing to effectively extend the optical transfer function to high spatial frequencies.

One disadvantage of structured saturation microscopy is that the localization of a fluorophore is determined largely by which illumination pattern does *not* excite it—the troughs of the excitation pattern are narrow. Each illumination pattern strongly excites most fluorophores, and as a consequence photobleaching can be prohibitive. These disadvantages can be overcome by using stimulated fluorescence to reduce the excited-state populations [29]. This is possible because real fluorophores are not two-level systems and excited-state populations can actually create a population inversion.

In practice, stimulated emission depletion microscopy (STED) has been performed using a diffraction-limited Gaussian pump beam, followed by a concentric Gaussian–Laguerre "doughnut" mode-stimulated emission beam. This second beam "trims" the distribution of excited-state fluorophores; the remaining distribution may be many-fold smaller in spatial extent than the original Gaussian pump (Fig. 9.4b).

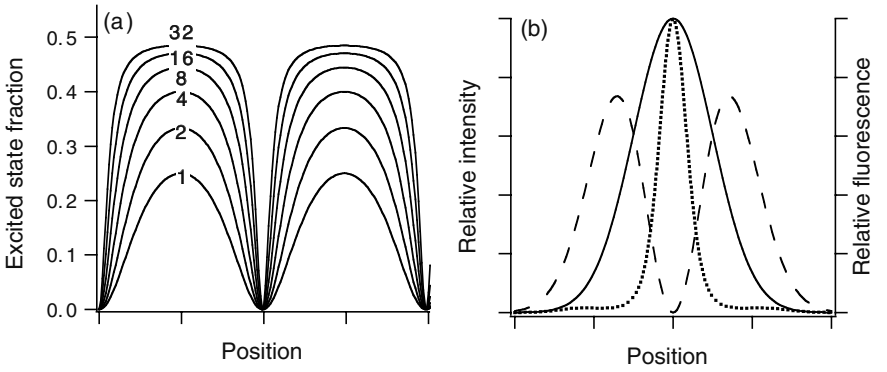

FIGURE 9.4 (a) Distribution of fluorescence emission for increasing intensities of spatially sinusoidal illumination, $I(x) = I_0 \sin(kx)$. Numbers on curves represent the quantity $2\sigma\tau_F I_0/h\nu$. (b) A Gaussian illumination profile (black line) will give a fluorescence distribution that is equally broad, in the absence of saturation. If a Laguerre–Gaussian mode is used for stimulated emission (dashed line), the distribution of spontaneous fluorescence may be narrowed (dotted line).

Although the fluorescent molecules are excited at a high rate, photobleaching is largely suppressed by the fact that most of these molecules are driven back to the ground state before they can convert to the triplet state by intersystem crossing [30].

As mentioned previously, neither saturation microscopy nor STED microscopy require ultrashort pulses. In both, the relevant parameter is the product of the photon flux (in the sense of number per unit area per unit time) and the cross-section (for absorption or stimulated emission). This product must be large compared with the spontaneous emission rate, $1/\tau_F$, in order to saturate the transition. In fact, there is no *a priori* requirement for pulsed lasers in either method, and STED microscopy has been demonstrated with CW beams [31]. However, the use of pulsed lasers reduces the required average powers to achieve a given resolution, in proportion to the ratio of the fluorescence lifetime to the pulse repetition period.

9.2.3 Microscopy with Time and Coherence Gating

The short geometrical and coherence length of fs pulses makes it possible to combine (microscopic) imaging with gating the detector on fs timescales corresponding to propagation length differences of microns. This is particularly attractive for imaging through transparent layers that scatter light (see Fig. 9.5a). If the scattering coefficient is μ and the thickness of the top layer is d, the power of the pulse that reaches the focus and returns to the sample surface unscattered (ballistic pulse) is $P_{im} = P_0 \exp(-2\mu d)$ assuming a perfect reflector in the focus (best-case scenario). $P_{sc} = P_0 - P_{im}$ is the scattered light, which does not carry any image information. Techniques are desired that allow one to separate the ballistic from the scattered light reaching the detector.

Classical confocal microscopy [32] provides a spatial gate by imaging the focal spot in the sample onto a pinhole in front of the detector. Out-of-focus light and scattered light are attenuated relative to the in-focus ballistic light (see Fig. 9.5b). Owing

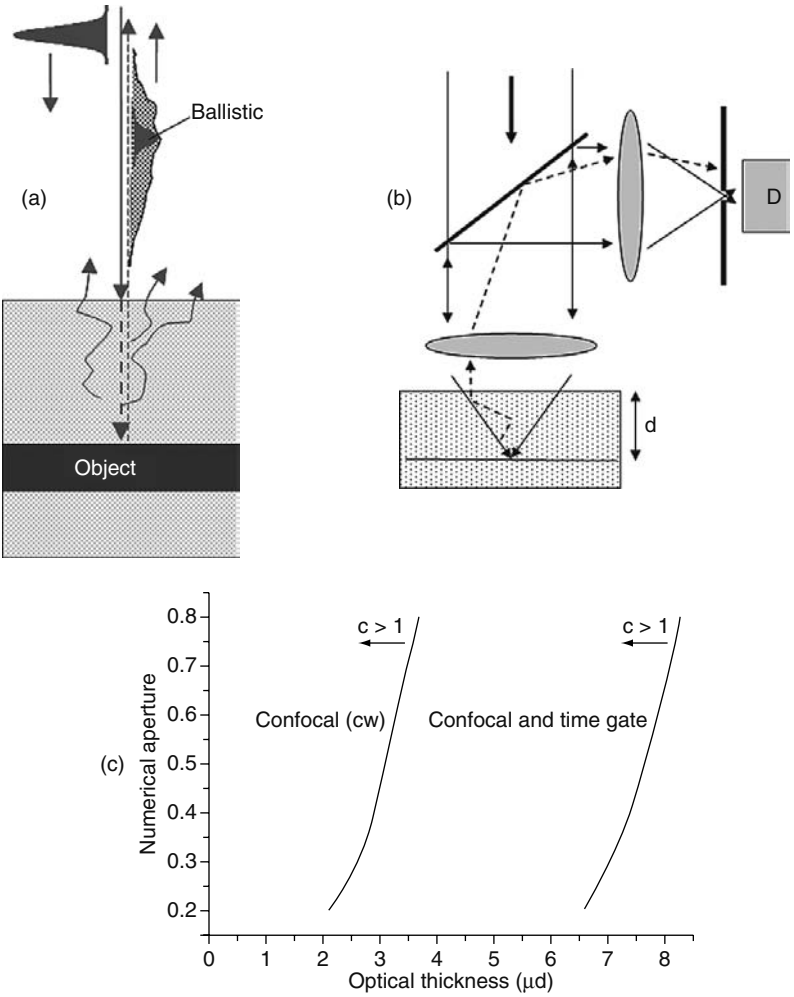

FIGURE 9.5 (a) Imaging through scattering layers with short-pulse illumination. (b) Schematic diagram of confocal gating. (c) Parameter space (numerical aperture versus thickness of the scattering layer μd) in which imaging is possible (contrast $C > 1$) with confocal microscopy with and without fs time gating of the detection. (Reprinted from Magnor, M., P. Dorn, and W. Rudolph, Simulation of confocal microscopy through scattering media with and without time gating, *J. Opt. Soc. Am. B* 18: 1695–1700 (2001). Copyright 2001, Optical Society of America, with permission.)

to the random path of scattered photons, the suppression of the scatter is not perfect and at certain μd the scattering signal will dominate and the image information (contrast) is lost.

Larger scattering densities are possible if, in addition to the confocal gate, a temporal gate is employed. As suggested in Figure 9.5a the ballistic pulse will arrive at the detector at a certain time, while (most of) the scattered light will reach the detector outside this window and can thus be suppressed by gating. Compared

with confocal imaging without the time gate, larger scattering densities are possible for image acquisitions. Figure 9.5c compares the results of a Monte-Carlo simulation of confocal microscopy through scattering layers with and without time gate [33].

For optimum contrast the gate time should be on the order of the pulse duration calling for all-optical techniques. Nonlinear optical processes have been explored; see, for example, reference [9]. However, the most successful technique relies on optical coherence gating, which is a linear technique based on an interferometer. The interference signal is the correlation of a reference (the gate) pulse and light from the sample. Known as optical coherence tomography [34], this technique has found attractive applications in microscopy and imaging in general and in many biological and medical areas [35].

9.3 LASER SOURCES

In the early days of microscopy with ultrashort laser pulses the required lasers were complex, expensive, and often needed someone with a PhD to operate them. Consequently, research and applications of this type of microscopy were confined to the laboratories of physicists and engineers. Over the past two decades things have changed dramatically. The laser sources are still expensive, but reliability and ease of use make their operation possible in the traditional microscopy laboratories of the biological and medical sciences. Here the laser of choice in most cases is a femtosecond pulse oscillator that operates with repetition rates on the order of 100 MHz. These lasers typically operate in the near-infrared spectral region. Optical parametric oscillators pumped by fs pulse lasers can provide tunable pulse excitation throughout the near-IR and (using frequency doubling) visible spectral region. If larger energy per pulse is required, pulses from the oscillator can be amplified in a separate pulse amplifier at the cost of repetition rate. Roughly speaking, the product of pulse energy and repetition rate does not change much. Through various techniques such as Q-switching, cavity-dumping, and the use of very long cavities, the energy levels from the oscillator can be increased, again at the expense of repetition rate.

Table 9.1 includes typical pulse parameters for different pulsed femtosecond sources.

9.3.1 Femtosecond Oscillators (Kerr-Lens Modelocked Lasers)

Since its invention in the early 1990s [36], the Kerr-lens modelocked fs (Ti:sapphire) laser has become the workhorse of fs laser sources in laser research laboratories and also the laser most often sold as an illumination source for nonlinear microscopy. As is the case with most modelocked lasers [2], a combination of linear and nonlinear optical processes provides a time window in which the cavity round-trip gain exceeds the round-trip loss and in which an ultrashort light pulse will eventually develop. In a Kerr-lens modelocked laser (KML), the laser crystal does not only act as a gain medium but also as a nonlinear lens through the Kerr effect, that is, through the dependence of the refractive index on the laser intensity. This lens in combination with an aperture represents an intensity-dependent loss element whose transmission favors short pulses over long-pulse or CW operation (Fig. 9.6). The

TABLE 9.1
Laser Sources Used as Illumination Sources for Nonlinear Microscopy and Their Typical Parameters

Pulse source	Spectral range	Pulse duration	Mean power/ pulse energy	Repetition rate
Ti:sapphire oscillator	750 nm–1000 nm	4 fs–200 fs	<1 W	100 MHz
Cr:LiSAF oscillator (diode-pumped)	~850 nm	>12 fs	<100 mW	100 MHz
Cr:Fosterite oscillator	1200 nm–1500 nm	>14 fs	100 mW	100 MHz
Cavity-dumped Ti:sapphire oscillator	800 nm	>15 fs	100 nJ	100s kHz to MHz
Fiber oscillator	1550 nm	>40 fs	2 nJ	100 MHz
Long-cavity Ti:sapphire oscillator	800 nm	30 fs	200 nJ	Few MHz
Optical parametric oscillator	1 μm–1.8 μm	>50 fs	<100 mW	100 MHz
Fs amplifier (Ti:sapphire)	800 nm	>20 fs	<100 mJ	10 Hz–500 kHz
Storage cavity	800 nm	few ps	150 nJ	250 kHz

aperture can be a hard aperture, for example an iris or an edge, placed at a suitable location in the cavity, or can come in the form of a soft aperture. A soft aperture can be realized by the overlap of the pumped volume and the laser mode volume in the gain medium. At proper cavity alignment, the laser mode produces optimum overlap leading to maximum gain if there is a lens at the location of the gain medium.

The laser pulses develop from the initial noise fluctuations produced by spontaneous emission and the oscillator reaches a steady state after a few thousand round-trips after turn-on of the pump laser. The steady-state pulse duration is determined from a delicate balance of broadening mechanisms (cavity GVD and spectral filters owing to the finite gain profile) and pulse-shortening processes (intensity-dependent loss element) during each round-trip. KMLs are pumped by CW lasers. Frequency-doubled Nd:vanadate lasers are often used as pump sources for Ti:sapphire oscillators. Attractive diode laser pumping is possible for Cr:LiSAF fs lasers, for example [37].

9.3.2 Femtosecond Fiber Laser

Fiber lasers (FLs) have the advantage of compactness and very user-friendly operation, which makes them particularly attractive for microscopy laboratories outside the optics and photonics community. Together with diode lasers they certainly represent the illumination sources of the future in scanning nonlinear microscopy. Currently the pulse duration, the average power, and the tunability from a fiber oscillator cannot compete with the Ti:sapphire laser. The latter is therefore still used by most microscopists. There are several possibilities to introduce an intensity-dependent loss element in a fiber laser. Examples are (1) nonlinear polarization

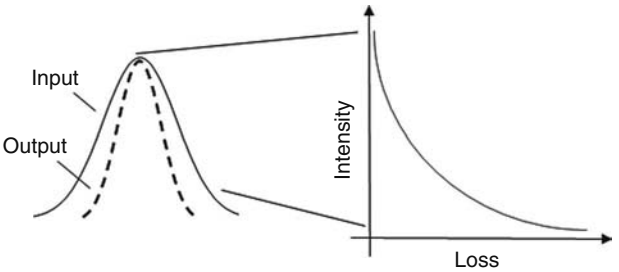

FIGURE 9.6 The essential part of a fs oscillator is an element or process that represents loss that decreases with intensity. The result of the interaction with such an element is pulse shortening.

rotation, (2) nonlinear loop mirrors, and (3) semiconductor saturable absorbers (see, for example, [38]).

There are a variety of techniques available to increase the pulse energy, which all come at the expense of repetition rate.

9.3.3 Q-Switching

In traditional Q-switching the active medium is pumped while the laser is prevented from lasing by a switchable element. The stored energy is released in a giant pulse when the cavity Q is switched to allow for lasing. For fs pulse output modelocking is also required and one can utilize the tendency of solid-state lasers to show self-Q-switching and relaxation oscillations [39].

9.3.4 Cavity Dumping

The fs pulse is allowed to build up in a laser cavity that has no traditional outcoupling mirrors. Once the pulse has reached a certain energy level, an element in the cavity is switched to couple the pulse out (cavity dumping), for example, an acousto-optic modulator [40, 41]. Roughly speaking, the gain in pulse energy is the ratio of the cavity round-trip frequency to the frequency of the cavity dumper.

9.3.5 Long Cavities

Another way to increase the energy per pulse is to use longer cavities. That way the pump energy can be accumulated in the active medium over a longer period of time, resulting in larger laser pulse energies. Careful cavity designs including dispersion control are necessary to avoid the evolution of multiple pulses per round trip [42].

9.3.6 External Storage Cavities

The idea is to couple frequency-stabilized pulses from an oscillator into a high-finesse Fabry–Perot cavity (FPC). If the length of this cavity is an integer multiple of the length of the oscillator cavity and its dispersion is carefully chosen, the pulses are in resonance with the FPC. As a result the FPC intracavity pulse can reach a peak

power that is much larger than the power coupled out of the oscillator. At this point a switchable element in the FPC couples the pulse out [43]. Roughly, the gain in peak power is the ratio of the FPC cavity lifetime (with the switch off) and the period of the pulse train from the oscillator. Cavity dispersion is a serious problem for broadband fs pulses, and the best results so far have been achieved with few ps input pulses.

9.3.7 Pulse Amplification

The most straightforward way to increase pulse energy is through amplification (see, for example, [2]). This usually requires an additional gain medium and pump laser. The two most common approaches are (1) multiple-pass amplifiers and (2) regenerative amplifiers. The repetition rate of the pump laser determines the repetition rate of the amplifier. In (1) the pulse passes through the gain medium multiple times while the pump deposits energy. In (2) the pulse is coupled into a cavity that contains the gain medium. When the gain is depleted the amplified pulse is coupled out. To avoid undesired nonlinear effects as a result of the large intensities of amplified pulses, the pulse is broadened (and chirped) before amplification. At the output of these amplifiers is therefore a compression stage. This concept, known as chirped pulse amplification (CPA) [44], can produce pulse powers in the PW range. Instead of a traditional gain process through stimulated emission, a $\chi^{(2)}$ nonlinear process known as parametric amplification can also be used [45].

9.4 EXAMPLES OF NONLINEAR MICROSCOPIC IMAGING AND APPLICATIONS USING SHORT LASER PULSES

In the remainder of this chapter, three specific nonlinear imaging modalities and application examples will be discussed, along with their strengths and weaknesses.

9.4.1 Multiphoton Fluorescence Microscopy

9.4.1.1 General

The theoretical possibility of two-photon absorption was first noted by Maria Göppert-Mayer in 1931 [46], and experimentally applied to biological microscopy nearly 60 years later [3]. From an intuitive point of view, two-photon absorption is allowed by virtue of the Heisenberg uncertainty principle. Although there is no real excited state at the energy of a single photon, a virtual excited state may be reached provided its lifetime Δt does not violate $\Delta E \Delta t \geq \hbar$, where ΔE is the photon energy. The fact that this virtual lifetime is on the order of an optical cycle accounts for the very high instantaneous intensities required for significant multiphoton excitation.

From quantum mechanical selection rules, the absorption of a single photon must result in a change in parity of the electronic wave function, while a two-photon absorption must not. Fortunately, organic fluorophores are complex molecules with a manifold of excited vibronic levels. Thus, two-photon excitation is essentially always possible, though the specific vibronic levels involved differ from those in one-photon excitation. As a consequence, two-photon absorption spectra are different from

(generally broader and blueshifted compared with) their one-photon counterparts. The two-photon absorption rate by a single molecule can be expressed as

$$r = \sigma_{2p}\Phi^2 \tag{9.13}$$

where the photon flux density Φ is in photons/cm^2·s (intensity $I = h\nu\Phi$) and the two-photon cross-section σ_{2p} is in cm^4·s. By convention, 10^{-50} cm^4·s is called a Göppert-Mayer or GM.

The quantity most important to microscopists is the two-photon action cross-section, which has been defined as the product of the absorption cross-section and the quantum yield for two-photon excited fluorescence. Two-photon action cross-sections can be measured by a careful estimate of the incident intensity and the rate of two-photon fluorescence emission; they have been measured for a large number of popular fluorophores [47]. Most common fluorophores have measured action cross-sections of tens or hundreds of GM.

Action cross-sections differ greatly from absorption cross-sections, even for fluorophores with high quantum yields under single-photon excitation. This can be clearly seen in the phenomenon of fluorophore saturation. Owing to the nanosecond fluorescence lifetime, each fluorophore can emit at most one fluorescent photon per laser pulse. If the action cross-section is taken as the absorption cross-section, saturation should occur when $r\tau \approx 1$ (where τ is the pulse duration). For example, for a cross-section of 200 GM (measured for tetramethyl Rhodamine, TMR), saturation should not occur with mean illumination powers below ~50 mW (for a diffraction-limited beam at high NA; 100 fs pulses at 100 MHz). In fact, saturation of two-photon excited fluorescence emission from TMR was found to occur at about 0.1 mW [48]. This nearly two order of magnitude difference likely results, at least in part, from excited-state absorption to give long-lived, nonfluorescent molecular states.

In general, it is important to recognize different interpretations of the word *saturation* in multiphoton microscopy. Fluorescence saturation, as discussed above, refers to a maximum in the mean rate of fluorescence emission with increasing illumination intensity; this is the parameter that is most relevant for microscopy. Using an illumination intensity that saturates the fluorescence emission leads to a broadening of the excitation profile and a loss in resolution. Absorption saturation, as discussed in regard to two-photon absorption measurements on solutions of fluorophores (using, for example, the z-scan technique [49]), may refer to the inability of the solution to absorb the incident light once a saturating intensity is reached. This depends on the concentration of the fluorophore. By carefully measuring two-photon absorption under nonsaturating illumination, it can be shown that two-photon *absorption* cross-sections are often much larger than the action cross-sections. In addition, nonfluorescent proteins (or nonfluorescent amino acids in genetically encoded fluorescent protein, GFP) do contribute a background to the two-photon absorption cross-section [50].

9.4.1.2 Advantages and Applications

The widespread and rapid growth of two-photon fluorescence microscopy after its initial biological application was driven both by the availability of commercial, turnkey

laser systems that could reliably provide ~100 fs pulses in a useful wavelength range (700–900 nm) and by several important advantages of multiphoton excitation in specific applications.

The first advantage is that multiphoton excitation using near-IR lasers provides unsurpassed optical sectioning capabilities in thick tissues [51]. This is in part a consequence of the greater penetration depth of near-IR radiation, compared with visible light. More important, however, optical sectioning in multiphoton microscopy is inherent, in that the signal is produced almost exclusively at the laser focus. To obtain optical sectioning in linear microscopy, a confocal pinhole is required to largely exclude photons emitted from fluorophores above or below the focal plane. Since no confocal pinhole is required in multiphoton excitation, scattering of the emitted fluorescent photons does not decrease the image quality. Figure 9.7 shows two-photon excited

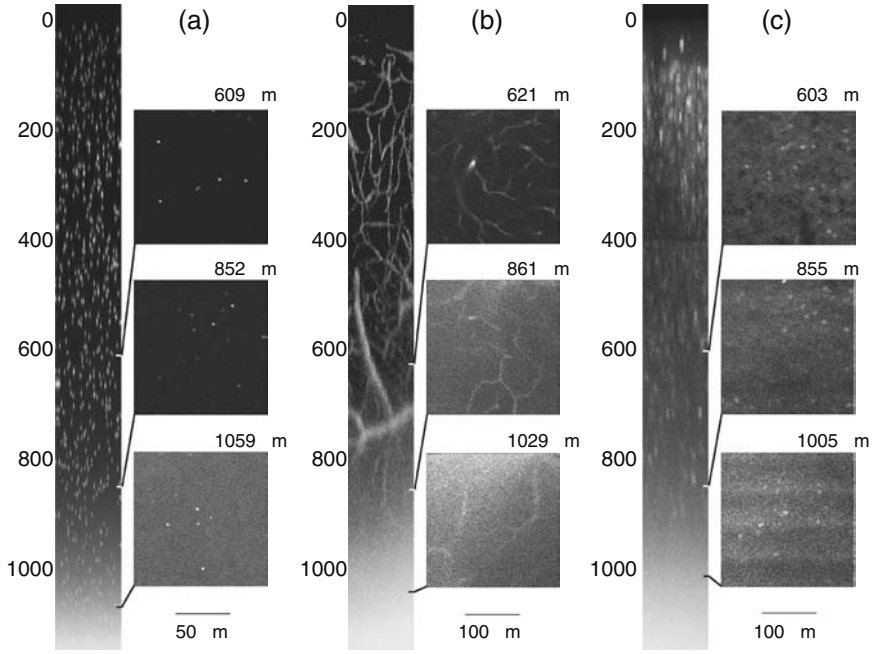

FIGURE 9.7 Deep tissue imaging using two-photon fluorescence and pulses from a Ti:sapphire regenerative amplifier. Shown are xz sections and xy scans at the indicated depths. (a) A tissue phantom consisting of fluorescent beads in an agarose gel; (b) and (c) images of the brain of a living mouse. (b) Fluorescein-dextran stained blood vessels; (c) neurons expressing green fluorescent protein (GFP). The photon mean-free path for the excitation at 925 nm is about 95 μm; it is shorter for the fluorescence emission. To compensate for increasing scattering of the excitation light, the laser power must be increased exponentially with increasing depth. Eventually, the illumination becomes so intense that two-photon fluorescence is generated from the surface of the sample, even though the beam is quite large there. This determines the ultimate depth limit in two-photon imaging. (Reprinted from Theer, P., M. Hasan, and W. Denk, Two-photon imaging to a depth of 1000 microns in living brains by use of a Ti:Al2O3 regenerative amplifier, *Opt. Lett.* 28: 1022–1024 (2003). Copyright 2003, with permission from the Optical Society of America.)

fluorescence in optical sectioning to a depth of nearly 1 mm, using a Ti:sapphire laser with a regenerative amplifier to increase pulse power [52]. To reduce damage from linear effects, such as sample heating, the pulse repetition rate was kept low. At greater depths in the sample, greater power must be used, in order to make up for losses caused by scattering of the illuminating beam. Since scattered IR light produces little two-photon absorption, the resolution is still fairly good to great depths. However, a depth limit is reached when the required imaging power is so high that two-photon excitation at the sample surface exceeds that at the waist itself: At this depth, a uniformly bright image is produced. Using a confocal pinhole can provide no gain in depth resolution or penetration, since the overwhelming majority of the fluorescence photons are scattered at least once on leaving the tissue. A confocal pinhole would simply eliminate essentially all of the detected signal.

Optical sectioning with one-photon fluorescence confocal microscopy presents an additional problem: Because out-of-focus planes do absorb the excitation light, photobleaching occurs throughout the entire sample during the imaging process. (Photobleaching is any excited-state reaction that results in the irreversible loss of fluorescence.) In single-photon confocal microscopy, although the beam is less intense above and below the focal plane, points in these planes are illuminated for a larger fraction of time, simply because the beam is much larger there. Out-of-focus fluorophores are subject to very nearly the same average illumination intensity as in-focus ones; thus, they are excited nearly as frequently and photobleach nearly as quickly. In multiphoton excitation, no absorption occurs and thus no photobleaching occurs, except in the plane being imaged.

In fact, it is not merely out-of-focus photobleaching that can be problematic in one-photon confocal microscopy. Unlike the near-IR wavelengths used for two-photon excitation, the green-blue visible light used in one-photon excitation can often be absorbed by intrinsic chromophores or fluorophores. This causes autofluorescence of the sample, but in addition the oxidative excited-state reactions of these intrinsic chromophores can be lethal to cells. In single-photon confocal imaging, these deleterious reactions occur throughout the entire tissue; with two-photon excitation, they are confined to the focal plane [53].

A second, lesser advantage of multiphoton excitation is that, because multiphoton absorption spectra are typically broader than single-photon counterparts, multiple fluorophores can often be excited with the same illumination.

Because multiphoton absorption is confined to the focal region, multiphoton excitation is generally useful in any application that benefits from three-dimensional control of molecular photochemistry. Such applications include (1) 3D photobleaching/recovery measurements to study molecular diffusion, (2) fluorescence correlation spectroscopy to study molecular association and dynamics, and (3) uncaging of metabolites or second messengers by a photoinitiated cleavage of a protecting group. In applications (1) and (2), the absence of out-of-plane photobleaching improves experimental reproducibility when measuring diffusion in finite compartments, such as cells.

9.4.1.3 Challenges and Cautions

From studies of multiphoton photobleaching and saturation, it appears that *multiphoton illumination increases the rate of excited-state reactions.* In a molecule that

has a two-photon resonance, photobleaching rates vary not quadratically with laser intensity, but typically as a cubic power [54, 55]. This cubic dependence likely results from the absorption of an IR photon by a two-photon excited state of a fluorophore. Since single-photon photobleaching is essentially linear with intensity, the two photobleaching processes proceed through different pathways—in essence, short pulse IR illumination often brings new molecular excited states into play. The existence of such states can also be inferred from the fact that fluorescence emission saturates at a very low rate (compared with the fluorescence lifetime or pulse repetition rate), and at a rate considerably lower than that reached with one-photon excitation. For example, under two-photon illumination, the maximum emission rate from a molecule of tetramethyl Rhodamine was one-quarter of that obtained with single-photon excitation. (Both rates were considerably lower than the reciprocal of the fluorescence lifetime, owing to population of the long-lived triplet state [48].)

In one study, at photon emission rates of about 1500 photons/s, photobleaching by two-photon excitation was twice as rapid as that caused by one-photon excitation [56]. These rates of emission, and the powers used (490 μW mean power, or a peak intensity of about 50 GW/cm^2) were relatively low—with increased illumination intensities the problem would only be exacerbated, owing to the cubic power dependence of photobleaching. Because of problems with photobleaching, and resolution considerations (see below), it has been suggested that, for thin samples or single-molecule studies, multiphoton excitation is generally *to be avoided* [57].

9.4.1.4 Resolution in Multiphoton Fluorescence Microscopy

When comparing resolution between single-photon and multiphoton excitation, one should properly consider the same fluorophore in both, using a longer wavelength illumination for multiphoton excitation. For calculations, it is typically assumed that the multiphoton excitation wavelength λ_m is m times the single-photon excitation wavelength, $m\lambda_s$ (i.e., the slight blueshift in multiphoton excitation spectra is ignored). The diffraction-limited laser beam waist scales with the wavelength, while the spatial extent of the excitation for an n-photon process narrows with approximately $1/\sqrt{n}$. As a consequence, the lateral resolution for thin specimens in two-photon (nonconfocal) microscopy is expected to be about $\sqrt{2}$ poorer than for one-photon excitation of the same fluorophore. Using a confocal pinhole (in the paraxial approximation) should improve both resolutions by a factor of $\sqrt{2}$. Of course, only with a confocal pinhole does one-photon excitation give axial resolution or transverse resolution of thick specimens. Two-photon excitation is typically used without a pinhole, both to avoid alignment difficulties and to increase the collection of scattered signal—fluorescent photons emitted from the focal region, but scattered before leaving the specimen. Without a confocal pinhole, the theoretical lateral resolution of a two-photon microscope is thus about a factor of two poorer than a one-photon confocal microscope with pinhole. More exact resolution calculations, taking into account high numerical apertures, give results similar to these simple estimations; they also show that axial resolution is also a factor of two poorer in two-photon nonconfocal imaging than in one-photon confocal imaging [58]. Of course, in highly scattering tissue, image quality is more important than theoretical (or even actual) resolution limits, and it is for such samples that multiphoton excitation is most beneficial.

The focal volume of a focused laser, used in two-photon excitation, has been calculated. The squared intensity near the beam waist can be reasonably well fit by a 3D Gaussian; useful expressions for the $1/e^2$ radii are:

$$w_{x,y} \cong \begin{cases} 0.320\lambda \cdot \mathrm{NA}^{-1} & \mathrm{NA} < 0.7 \\ 0.325\lambda \cdot \mathrm{NA}^{-0.91} & \mathrm{NA} > 0.7 \end{cases}$$
$$w_z = 0.532\lambda \left[n - \sqrt{n^2 - \mathrm{NA}^2} \right]^{-1/2} \tag{9.14}$$

where n is the medium index of refraction, NA is the numerical aperture, and λ is the illuminating wavelength [59]. These expressions were obtained by fits to exact but unwieldy calculations of the field distribution [60, 61], and assume no fluorophore saturation. Fluorophore saturation increases the effective focal volume; under moderate conditions (e.g., 20 mW illumination), the focal volume can increase three-fold, giving a significant decrease in effective optical resolution. Nor do the formulas given here take into account the spherical aberration that is inevitable when imaging deep into samples. This aberration (which varies with depth into the sample) can be compensated using deformable mirrors.

In summary, multiphoton and linear microscopy have similar theoretical resolution limits, though two-photon fluorescence microscopy without a confocal pinhole is about a factor of two poorer than single-photon confocal in both lateral and axial resolution. In practice, multiphoton excitation excels where scattering diminishes effective resolution or image quality, but can perform very poorly if fluorophore saturation occurs, broadening the excitation profile.

9.4.2 Harmonic Microscopies

9.4.2.1 General

Classically, harmonic generation in materials is caused by the anharmonicity of the material potential interacting with incident radiation. When subject to a harmonic driving force (the incident radiation), the classical motion of the oscillator will then contain overtones of the fundamental driving frequency—motions, and thus accelerations, at the harmonics of the fundamental. As a consequence, if we identify the oscillator with an optical dipole made up of an electron oscillating in a molecular potential, the electron will reradiate at these harmonic frequencies. A direct (and correct) conclusion from this picture is that a molecule with a symmetric electronic potential can generate only odd harmonics (third, fifth, etc.) of the incident radiation. From either a classical or a quantum mechanical analysis, it can be shown that light at a frequency that is resonant with the electronic oscillator will more efficiently generate harmonics than light at nonresonant frequencies; a full quantum mechanical analysis shows that an electronic resonance at the output (harmonic) frequency also gives enhanced harmonic production [62]. In harmonic microscopy, these resonances are primarily responsible for generating image contrast.

In a material, the total harmonic radiation produced is obtained from the coherent sum of the individual radiating (or scattering) atoms or molecules. For macroscopic

materials illuminated by a plane wave, the coherent sum of harmonic radiators produces a forward-propagating plane wave. However, owing to dispersion, the index of refraction for the harmonic cannot be the same as that for the fundamental frequency. As the fundamental propagates through the material, the locally generated harmonic will eventually be out of phase with harmonics generated earlier. As these waves add coherently, the intensity in the harmonic will begin to decrease with increasing material thickness. Assuming collinear geometry, a back-of-the envelope estimate of the phase-matching length can be obtained by considering the difference between the k vector for the *jth* harmonic and j times the fundamental k vector:

$$\Delta k = jk_1 - k_j \tag{9.15}$$

called the wave vector mismatch. Phase cancellation of the harmonic will then occur after a distance L on the order of $L \approx \pi/\Delta k$. (With phase mismatch, energy moves from the harmonic back into the fundamental.) Note that Δk is quite small compared to the inverse wavelength of light, so that phase coherence is usually maintained over many wavelengths of the incident light, typically tens or hundreds of microns.

In microscopy applications, phase matching *per se* is not a concern, since the incident illumination is focused so as to generate harmonics only from a probe region that is much smaller than the phase-matching length. The coherent addition of signals is still important, however, and gives rise to several unique features of harmonic imaging. These include:

- Importance of sample geometry and interfaces
- Directionality of emission
- Quadratic dependence on scatterer density

9.4.2.2 Geometric Properties of Harmonic Sources and Emissions

As mentioned above, second harmonic generation (SHG) can only arise from an asymmetric electronic potential. Most organic resonant molecules do have such asymmetry. However, the fact that harmonic signals add coherently demands that, within the illuminated region, the molecules contributing SHG signals are themselves nonrandomly oriented; otherwise, oppositely oriented molecules will contribute SHG signals that are entirely out of phase and thus cancel. This effect has been used to study the biomembrane permeation of resonant SH scatterers [63], as shown in Figure 9.8. Addition of a resonant, membrane-binding chromophore results in a rapid increase in SH signal, as the chromophore binds to the membrane with a preferred orientation. SHG then slowly decreases as permeation leads to equilibration of the chromophore between the inner and outer surfaces of the membrane. (In this experiment, the size of the membranes was carefully chosen to prevent cancellation from opposing hemispheres.)

Note that, in principle, SH signals from small numbers of randomly oriented molecules should not perfectly cancel. The electric field sum from the SH scatterers, represented as phasors, will undergo a random walk, giving an SH field amplitude that increases with $\sqrt{N}$ and thus a mean SH intensity increasing with N.

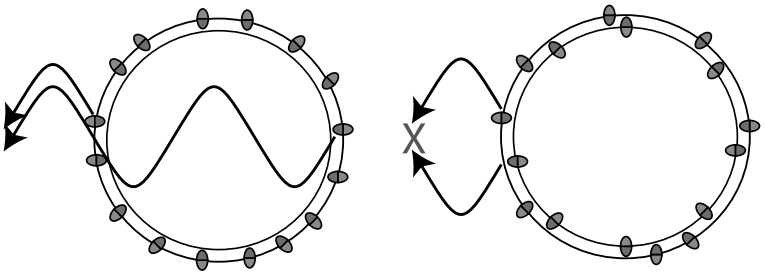

FIGURE 9.8 Second harmonic generation *is* possible in centrosymmetric systems, such as liposomes. Chromophores adsorbed on the outer surface (leaflet) have a preferred orientation, so that SHG from opposite surfaces will be out of phase. However, if the diameter of the liposome is a half-integral number of wavelengths, SHG can add coherently, giving a strong signal (left). If the chromophore is able to permeate through the membrane, SHG vanishes (right).

The importance of sample geometry can be clearly seen in SHG microscopy images of giant liposomes (artificial cell membranes) [64] (Fig. 9.9). These membranes are two-dimensional fluids, and thus, resonant molecules that are adsorbed or embedded in the membrane can have no preferred in-plane orientation. As a consequence, SHG microscopy with a polarized excitation can generate strong signals only when the membrane surface is perpendicular to the exciting polarization, that is, when the driving electric field is oriented along the direction of asymmetry.

Unlike SHG, third harmonic generation (THG) is possible in material lacking an asymmetry in the potential. Nonetheless, THG microscopy can also reveal interfaces. Again, this effect is based on coherence. In the absence of an interface, the axially scattered THG *induced by a Gaussian beam near its waist* vanishes, owing to the Gouy phase shift: The Gaussian beam wavelength is increased slightly at the beam waist, resulting in a half-wave phase difference between points before and after the beam waist, compared with a plane wave. Near an interface, the symmetry is broken, and TH signals from before and after the beam waist need not cancel.

9.4.2.2.1 Directionality of Emission

Harmonic emission from a point source is simple dipole radiation, with fields propagating in all directions except in the direction of dipole axis (which need not be oriented parallel to the incident E field). The coherent sum from many emitters will in general exhibit a different radiation pattern. If the emitters are well ordered on the length scale of the illuminated volume, then the harmonic emission will be predominantly in the forward direction, and will lie within the cone of illumination. (Nonetheless, there is some emission backwards, and backscattering SHG microscopy has been done [65].)

For both SHG and THG, the Gouy phase shift suppresses emission directly along the incident beam. For surface SHG, two emission lobes are predicted, deviating from the incident beam in the direction of the surface normal; for volume THG, the emission is predominantly in a cone [64].

If emitters are not orientationally ordered, then, as discussed above, the emission intensity increases *linearly* with the number of scatterers, and the very weak SH radiation may be scattered into large angles [66]. This has been called incoherent

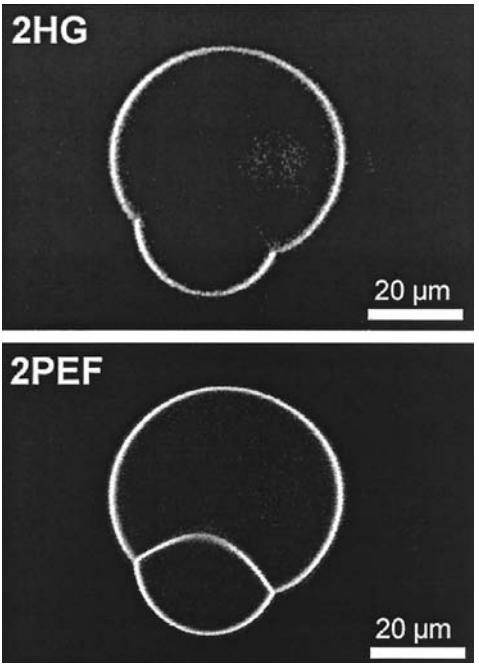

FIGURE 9.9 Second harmonic generation (top) and two-photon excited fluorescence (bottom) from two adherent liposomes labeled in their outer leaflets with the dye di-6-ASPBS. The laser polarization is horizontal in the images, giving a stronger SHG on the right and left and weaker SHG on the top and bottom of the imaged liposomes. Where the liposomes are in contact, SHG vanishes because of the symmetrical distribution of dyes. (Reprinted from Moreaux, L., O. Sandre, S. Charpak, M. Blanchard-Desce, and J. Mertz, Coherent scattering in multiharmonic microscopy, *Biophys. J.* 80: 1568–1574 (2001). Copyright 2001, Biophysical Society, with permission.)

SH. Assuming oriented scatterers in the case of SHG, the intensity of scattered light depends quadratically on the number of contributing scatterers. This allows for the production of fairly strong SHG signals from polar biological assemblies, which are typically fibrils.

9.4.2.3 Advantages and Applications of SHG

Harmonic microscopy has been proven to be of great utility in several important applications:

- Intrinsic signals
- Membrane potential sensing
- Membrane imaging

9.4.2.3.1 Intrinsic Signals

SHG was first demonstrated on biological samples of rat tail tendon, a collection of collagen fibrils [66]. It has subsequently been found that strong SH signals can be

obtained from several different ordered biomolecular structures, including myosin fibrils and microtubules (formed by the polar self-association of the protein tubulin). These biological structures combine resonant enhancement of SHG, as shown by the wavelength dependence [67, 68], with a noncentrosymmetric geometry that provides for the coherent addition of SH signals from many monomeric protein units.

Intrinsic signals, as opposed to signals from attached dye molecules, may offer two important advantages: reduced photodamage, since the coherent SHG does not require absorption of light; and direct access to molecular properties such as orientation and ordering, through the polarization dependence of the SHG. SHG from microtubules, for example, is directly related to the fact that these filamentous protein aggregates are polar, with distinct plus and minus ends [68]. As expected, SHG from biological filaments is maximized when the incident laser polarization lies along the fiber axial direction [65].

9.4.2.3.2 Membrane Potential Sensing

It has been found that fluorescent dyes originally designed for fluorescence sensing of membrane potential (i.e., transmembrane electric field) show a large second harmonic response as well, often much larger than the fluorescence responsivity, with changes of up to 40% per 100 mV. These dye molecules are typically push-pull compounds, meaning that they are comprised of electron donor and acceptor end groups connected by a conjugated electron path. *A priori,* it is possible that either a field-induced change in the ordering of the dye in the membrane, or a change in the electro-optic hyperpolarizability, could be the cause of the SHG response. Careful study of the dye response in giant liposomes has shown no evidence for a change in dye order parameter in different applied fields, and the dye response could be well modeled by the change in the nonlinear susceptibilities $\chi^{(2)}(-2\omega; \omega, \omega)$ and $\chi^{(3)}(-2\omega; \omega, \omega, 0)$ expected in a two-state system [69]. In other words, the SHG *response* to the membrane potential (produced by a static electric field E_{mem}) is caused by the third-order nonlinear susceptibility $\chi^{(3)}(-2\omega; \omega, \omega, 0)$. The total SH field and signal are then given by

$$\begin{aligned} E_{2\omega} &\propto \chi^{(2)} E_{\omega} E_{\omega} + \chi^{(3)} E_{\omega} E_{\omega} E_{mem} \\ I_{2\omega} &\propto \left| E_{2\omega}^{2} \right| \propto \left\{ \left| \chi^{(2)} \right|^{2} + 2\chi^{(2)} \chi^{(3)} E_{mem} + O\left(\left| \chi^{(3)} \right|^{2} E_{mem}^{2} \right) \right\} E_{\omega}^{4} \end{aligned} \tag{9.16}$$

Because $\chi^{(3)}|E_{mem}|$ is much smaller than $\chi^{(2)}$, the third term is negligible and the SH signal is seen to vary linearly with the electric field across the membrane. Because this response does not involve dye reorientation, it is essentially instantaneous and can be used to image ~10 ms membrane depolarization that occurs in nerve transmission [55, 70]. Although there are linear optical techniques that can also detect these action potentials, SHG microscopy should allow for higher resolution deeper into nerve tissue. SHG has also permitted imaging the membrane potential in micron-sized dendritic spines, structured neuronal protrusions that are thought to be the locus of neuronal communication [71].

9.4.2.3.3 Membrane Imaging

As previously noted, biological membranes are a natural target for second harmonic imaging when chromophores (or harmonophores) are asymmetrically distributed

between the two membrane leaflets. An obvious application is in measuring the permeation or flip-flop rates of membrane-associated chromophores, since the equilibration of the chromophore across the membrane abolishes the SH signal. This has been achieved in artificial lipid vesicles (liposomes), in both nonimaging (bulk) [63] and imaging modalities [72]; applications to living cells have not yet been described. (In bulk measurements, the liposome diameter must be a significant fraction of the optical wavelength to avoid phase cancellation of second harmonic signals from opposite sides [73]. Moreover, the SH signals from multiple liposomes add incoherently.)

Cell membranes also possess an inherent compositional asymmetry between inner and outer leaflets. In principle, either this compositional asymmetry, or the effect of membrane potential on the ordering of water [74], should give rise to detectable SH signals in membranes without chromophores. Without resonant enhancement, however, SH signals are extremely weak, and probeless SH imaging of cell membranes or cell membrane potential has not yet been reported.

Finally, because second harmonic signals depend on the alignment of chromophores, the intensity of SH depends implicitly on molecular organization at length scales that are much smaller than the optical wavelength. In principle, then, SH imaging can give information about membrane structure on subdiffraction-limited length scales. For example, SH from sea urchin eggs stained with di-8-ANEPPS decreases on fertilization. This result was interpreted as indicating an increase in membrane protrusions or invaginations that cause disordering of the membrane-bound probe molecule. From capacitance measurements, the membrane area is known to double on fertilization, consistent with this explanation [75].

9.4.2.4 Third Harmonic Generation

At very high laser intensities, >300 GW/cm^2, third harmonic generation (THG) microscopy becomes feasible [76, 77]. Although the Gouy phase shift makes imaging of interfaces possible, many subcellular structures are small compared with the Rayleigh range and thus phase cancellation of third harmonic signals is not a difficulty. In this case, it is simply the difference in $\chi^{(3)}$ of the different biological materials that generates contrast. Physiological concentrations of amino acids, sugars, and their polymers do not give third harmonic $\chi^{(3)}$s (with 1180 nm excitation) that differ significantly from water. These biological materials generate contrast in THG only when they are aggregated into dense structures. On the other hand, lipids have a $\chi^{(3)}$ nearly twice that of water, so THG is a sensitive technique to image lipid-inclusion bodies (droplets) in hepatocytes or other lipid-storing cells [78, 79].

The optical power used for THG microscopy is too low to cause dielectric breakdown and plasma formation in water (typically 6000 GW/cm^2 for 100 fs pulses at 800 nm [80]). Nonetheless, short pulses can give rise to some ionization through multiphoton absorption by intrinsic chromophores such as NAD(P)H, tryptophan residues, porphyrins, flavins, melanin, or DNA, and can result in the formation of reactive oxygen species, or ROS. Cell damage at intensities <1 GW/cm^2 has been observed in cessation of cell division, changes from normal cell morphology/size, or cell death through apoptosis-like (genetically programmed) mechanisms [81]; 400 GW/cm^2 has been found to break DNA and permeabilize membranes [82, 83]. These damage studies were done using ~800 nm wavelength, while THG is usually

measured using an optical parametric oscillator with an output wavelength near 1200 nm; cellular damage thresholds are likely to be higher for the longer wavelength. Nonetheless, cell damage is a reasonable concern at power levels that give appreciable third harmonic generation.

9.4.3 Four-Wave Mixing Microscopies

9.4.3.1 General

Four-wave mixing is usually considered a coherent nonlinear optical interaction that produces a signal at sums and differences of three input frequencies. Four-wave mixing is a third-order, $\chi^{(3)}$ process. As with harmonic generation, the strength of four-wave mixing signals is increased when photon energies, or combinations of photon energies, are close to (i.e., resonant with) energy eigenstates of the molecule (system) of interest. As with all multiphoton processes, four-wave mixing microscopies are inherently optical sectioning techniques, since only at the laser focus can significant nonlinear interactions occur.

9.4.3.2 Advantages and Applications

Most of the emphasis in four-wave mixing microscopy has been placed on CARS, which probes molecular vibrational eigenstates through resonance with the difference frequency between two incident photons (laser fields) (Fig. 9.10). Vibrational energy levels provide rather unique molecular fingerprints, and thus CARS offers the possibility to image chemical composition without exogenous labeling. In principle, vibrational levels can be probed with infrared absorption, or with Raman microscopy depending on whether they are infrared or Raman active. However, in microscopy applications, absorption measurements present the problem of trying to measure a small change in a large signal. Moreover, at the mid-IR wavelengths resonant with molecular vibrations, spatial resolution is poor. Spontaneous Raman scattering using a visible laser line can have good spatial resolution, but the process has a small cross-section, and is thus easily swamped by the ubiquitous autofluorescence in biological

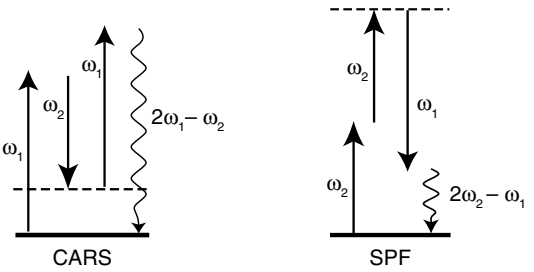

FIGURE 9.10 Energy level diagrams illustrating how certain terms in the perturbation expansion for $\chi^{(3)}$ are enhanced by resonance with molecular energy eigenstates. Left: CARS refers to enhancement by a vibrational level that is resonant with the difference between two applied frequencies. Right: SPF refers to enhancement by a two-photon absorption resonance, which (at optical and near-IR frequencies) is necessarily an electronic resonance.

samples. CARS signals are typically five orders of magnitude stronger than spontaneous Raman scattering signals for biologically tolerable power levels [84].

Recently, there has been increasing interest in probing *electronic* resonances by four-wave mixing. A wide variety of biological molecules have signature electronic absorption spectra, including DNA and certain amino acids (in the near UV), and hemoglobin, chlorophyll, melanin, carotenoids, flavins, cytochromes, and ferredoxins in the visible. Rather than trying to match the *difference* frequency of two deep-UV lasers to these electronic resonances, a two-photon absorption resonance is used, combined with a probe pulse that gives coherent stimulated parametric emission from the (virtual) excited state (Fig. 9.10). This process has been termed stimulated parametric fluorescence (SPF).

9.4.3.3 Challenges and Solutions

In any sample, both CARS and SPF processes occur. To be more precise, these processes are really just different terms in the time-dependent perturbation expansion for the field-molecule interaction that gives $\chi^{(3)}$. These different terms are resonantly enhanced when molecular energy eigenstates match different combinations of input photon energies. Each term in $\chi^{(3)}$ has a resonant denominator containing terms of the form

$$\omega_{nm} - \omega_{pqr} - i\gamma_{nm} \tag{9.17}$$

where $\hbar\omega_{nm}$ is the energy difference between molecular eigenstates, ω_{pqr} is a sum or difference involving one-, two-, or three-photon frequencies, and γ_{nm} is a damping term describing the width of the resonance. Energy eigenstates will resonantly enhance the $\chi^{(3)}$ signal if $|\omega_{pqr} - \omega_{nm}|$ is not much larger than γ_{nm}. Most electronic resonances are broad (consider typical UV/VIS spectra, for example), and thus these make substantial contributions to $\chi^{(3)}$ across a broad range of the input wavelengths. Moreover, electronic excited states consist of many vibronic sublevels; the combined effect of these is to introduce a large background contribution to $\chi^{(3)}$ that is nonresonant (i.e., real). This is problematic: In a CARS experiment, for example, a desired vibrational signature may be swamped by the nonresonant electronic background from water. In an SPF experiment, the background is even more problematic, as the targeted electronic resonance itself is likely to be broad.

For CARS, the targeted vibrational resonances are typically sharp, so the ratio of signal to nonresonant background is improved by using narrowband picosecond optical pulses. To detect weak signals, however, additional techniques are needed to suppress the nonresonant background. Techniques developed include:

- Polarization-sensitive detection
- Optical heterodyne detection
- Temporal methods
- Wave vector mismatch techniques

9.4.3.3.1 Polarization-Sensitive Detection

If two lasers of different frequency are used for CARS or SPF, nonresonant signals can be suppressed by polarized detection [85, 86]. Consider a CARS experiment with

the pump beam (the beam from which two photons are absorbed) polarized along the $\hat{x}$ direction, and the Stokes beam (into which one photon is emitted) polarized at an angle ϕ with respect to $\hat{x}$. The third-order polarization at the CARS frequency in a nonresonant material along $\hat{x}$ and $\hat{y}$ is then given by

$$\begin{aligned} P_x &= 3\chi_{1111}^{(3)nr} E_p^2 E_s^* \cos\phi \\ P_y &= 3\chi_{2112}^{(3)nr} E_p^2 E_s^* \sin\phi \end{aligned} \tag{9.18}$$

Although $\chi^{(3)}$ is a rank 4 tensor (reflecting the polarizations of each input photon and the output material polarization), for an isotropic, nonresonant material there is only *one* independent tensor element, from which all others may be derived. In particular,

$$\chi_{1111}^{(3)} = \chi_{1122}^{(3)} + \chi_{1212}^{(3)} + \chi_{1221}^{(3)}, \tag{9.19}$$

for any isotropic material, and

$$\chi_{1122}^{(3)nr} = \chi_{1212}^{(3)nr} = \chi_{1221}^{(3)nr} \tag{9.20}$$

for a nonresonant material, since *far from resonance* permutation of the indices can have no effect (Kleinman symmetry). Thus

$$\chi_{1111}^{(3)nr} = 3\chi_{1221}^{(3)nr} = 3\chi_{2112}^{(3)nr} \tag{9.21}$$

and

$$\frac{P_y}{P_x} = \tan\alpha = \tfrac{1}{3}\tan\phi \tag{9.22}$$

where ϕ is the angle of the material polarization, and consequently the polarization of the CARS emission. For resonant molecules and materials, the Kleinman symmetry does not hold, and the CARS emission will have a different polarization direction. Thus, by using a linear polarizer in front of the detector, the nonresonant background can be suppressed. Of course, in most cases, polarization suppression also results in a significant reduction in resonant signal as well.

9.4.3.3.2 Optical Heterodyne Detection

Background suppression can also be accomplished by interferometrically mixing CARS signals with a coherent, nonresonant CARS reference, called a local oscillator [87]. The local oscillator (electric field E_{LO}) can be produced by using part of the excitation field to produce a CARS signal in a sample cell containing a nonresonant material, such as deuterated DMSO (for near-IR input fields). The CARS field is

$$E_C \propto E_p^2 E_s^* \left(\chi^{(3)nr} + \chi^{(3)r}\right), \tag{9.23}$$

where $\chi^{(3)nr,r}$ are the nonresonant and resonant contributions to the third-order nonlinear susceptibility, respectively. If this is mixed with a local oscillator field with an added phase Φ, the total signal will be

$$S \propto \left|E_{LO}\right|^2 + \left|E_C\right|^2 + 2E_{LO}E_p^2E_s^*\left[\left(\chi^{(3)nr} + \mathrm{Re}\,\chi^{(3)r}\right)\cos\Phi + \mathrm{Im}\,\chi^{(3)r}\sin\Phi\right] \quad (9.24)$$

The first two (homodyne) terms can be suppressed by applying a small sinusoidal modulation in Φ (using a phase modulator) and lock-in detection. If $\cos\Phi \approx 0$, only the imaginary part of $\chi^{(3)}$ will be imaged. Nonresonant signals have negligible imaginary contributions to $\chi^{(3)}$ ($\gamma_{nm} \ll |\omega_{nm} - \omega_{pqr}|$) so background-free imaging of resonances is possible. Moreover, the signal size increases in proportion to the strength of the local oscillator field and is linear in scatterer density (since the resonant $\chi^{(3)}$ is proportional to density of resonant scatterers).

In polarized detection, internal optical heterodyne detection can be used to separate real and imaginary parts of $\chi^{(3)}$. Since the nonresonant $\chi^{(3)}$ contribution to the signal is polarized along α, rotating the analyzer to admit a small part of the nonresonant signal effectively mixes the resonant signal with a local oscillator (i.e., the nonresonant signal).

9.4.3.3.3 Temporal Methods

CARS signals arise from vibrational resonances, which typically have dephasing times that are a picosecond or even longer. Using two short-pulse (~100 fs) lasers, it is possible to coherently excite these vibrations at the difference frequency; a third short pulse can then be applied at a later time to generate the anti-Stokes Raman signal [88, 89]. Importantly, the nonresonant (or electronically resonant) contributions to $\chi^{(3)}$ will decay or dephase on a femtosecond timescale. Like polarization methods, there is some loss of signal with time-delay background suppression. However, polarization techniques can be used for SPF as well as CARS, whereas time delay is typically useless for detecting the rapidly dephasing electronic resonances.

9.4.3.3.4 Wave Vector Mismatch Techniques

Wave vector mismatch is not a technique for background suppression *per se*; rather, it is a method for reducing the effective sample volume from which signals can coherently add. In practice, this can reduce background when examining small objects. As with harmonic microscopy, coherent addition of signals from dispersed scattering centers requires proper phasing. The length over which this can occur is determined by the wave vector mismatch. For collinear beams, the mismatch is caused by the dispersion in the index of refraction and is small (compared with the photon k-vectors). Thus, the coherence length is generally much larger than the focal volume of a focused beam, and in this geometry it plays essentially no role in imaging. (Note also that, unlike third harmonic imaging, the Gouy phase shift does not play a significant role in CARS and SPF imaging, owing to the participation of both pump and conjugate Stokes beams [90].)

Consider, however, either detection in the backwards direction (epi-detection) or using anticollinear excitation in either a CARS or an SPF experiment [91]. In these geometries, the wave vector mismatch (i.e., the wave vector difference $2\vec{k}_p - \vec{k}_s - \vec{k}_{sig}$)

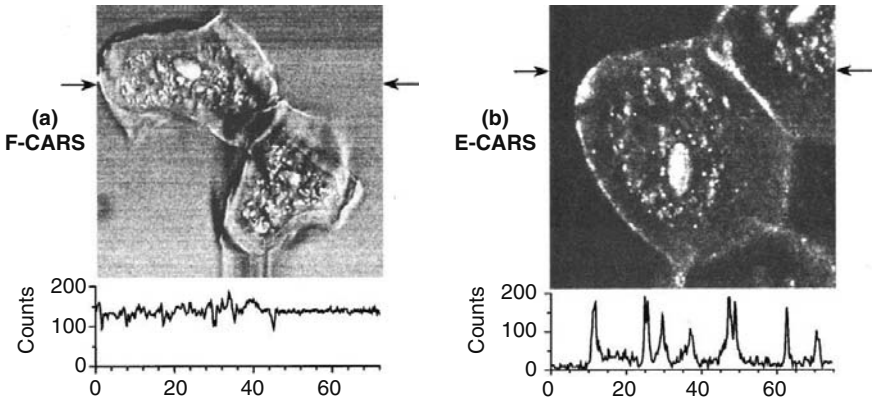

FIGURE 9.11 A comparison of collinear CARS (F-CARS) and epi-CARS microscopy on unstained epithelial cells, with $\omega_p - \omega_s$ tuned to the fingerprint region for biomolecules (~1570 cm^{-1}). F-CARS images are dominated by the water background, as seen from the intensity profile, while E-CARS images are largely background-free. Neither technique is selective for resonant effects, and both can generate contrast from differences in $\chi^{(3)nr}$. (Reprinted from Cheng, J.-X., A. Volkmer, and X. Xie, Theoretical and experimental characterization of coherent anti-Stokes Raman scattering microscopy, *J. Opt. Soc. Am. B* 19: 1363–1375 (2002). Copyright 2002, Optical Society of America, with permission.)

is about twice the photon k-vector, and so the effective depth from which coherent signals can add is much smaller than a wavelength. Weak, nonresonant signals, when integrated over this small coherence volume, give little total signal; resonant signals, particularly from biological structures (such as lipid granules) that fill the coherence volume are then clearly imaged (Fig. 9.11).

9.4.3.4 Short-Pulse Lasers and CARS

CARS with transform-limited femtosecond excitation give poor spectral resolution, since vibrational resonances have a narrower linewidth than the pulses used to probe them. Moreover, the nonresonant background problem is exacerbated by excitation with spectral components that are not in resonance. While it is always possible to simply filter the femtosecond pulses with a narrowband filter (creating narrowband picosecond pulses), this discards most of the pulse energy. One solution to this difficulty is to chirp the femtosecond pulses, stretching them into picoseconds but with a better defined wavelength at each time during the pulse. This can be done with one [92] or both of the CARS pulses [93]; with two pulses, the frequency difference can be maintained at the target vibrational frequency throughout the pulse duration, greatly improving both the spectral selectivity and the optical energy efficiency (at constant pulse energy).

Another attractive approach is to use a single short pulse (~20 fs) to provide *both* spectral components needed for CARS. With sufficient power, this can be done by filtering to obtain the two desired wavelengths [94]. A very exciting approach is to use the entire pulse, but to use phase shaping to ensure that only when the difference

between two wavelength components match the vibrational resonance are the two spectral components in phase. This is generally called coherent control [27]. Such single-laser approaches to four-wave mixing microscopy may soon make these techniques as widespread as two-photon fluorescence microscopy.

9.4.3.5 SPF

Stimulated parametric fluorescence, while not so well explored as CARS, is gaining in interest as a possible contrast mechanism for microscopy. As noted above, SPF suffers from high background, as does CARS. If SPF is to be simply used as a contrast mechanism, this need not be prohibitive: Digital image processing techniques can be used to enhance small image differences. Note that, without background suppression, resonant signals are often out of phase with the nonresonant background, giving a negative contrast image [95]. Moreover, SPF detected at visible wavelengths can suffer from nonresonant CARS backgrounds.

One approach is to detect IR-SPF produced by the (two-photon) absorption of longer wavelength (1050 nm) photons from an OPO and parametric emission stimulated by a shorter wavelength pulse (790 nm) from a Ti:sapphire laser. This signal is at 1550 nm, in the infrared. To resonantly enhance this emission, a vibrational energy level would have to be below the ground state—thus, vibrational resonances can contribute only very weakly to the background. Nonetheless, there remains a strong nonresonant electronic contribution, even in materials that do not have significant two-photon absorption at 1050 nm. Just as with CARS, polarization selection can be used to strongly suppress the nonresonant contribution (Fig. 9.12).

SPF and IR-SPF have only recently gained attention as imaging modalities, and their potential has not yet been established. Nonetheless, many biological materials do provide strong electronic resonances, and thus SPF may become an important biological imaging tool.

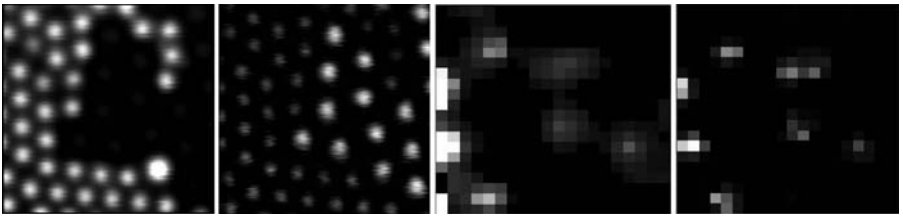

FIGURE 9.12 Two-photon excited fluorescence and SPF images. Far left: a two-photon fluorescence image of Rhodamine-dyed 3 micron and blank 4 micron polymer beads, in an approximately hexagonal packing. Center left: a nonresonant SPF image of the same field. The smaller dyed beads appear dimmer in the SPF image both because of their size (signal $\propto r^2$ in this geometry) and the phase shift between the resonant (dye) and nonresonant contributions. Center right: a two-photon fluorescence image of a smaller (different) field of view, containing both dyed and undyed beads. Only the dyed beads are visible by fluorescence. Far right: a *resonant* SPF image of the same field. Again, for resonant SPF, only the dyed beads are visible. (Courtesy of X. Liu, J. Thomas, W. Rudolph, *Ultrafast Optics 2007,* Santa Fe, NM.)

9.5 SUMMARY

Short-pulse lasers have played a critical role in the development of nonlinear microscopies for biological imaging, by providing peak field intensities that are high enough to drive $\chi^{(2)}$ and $\chi^{(3)}$ processes at modest average power levels. These nonlinear microscopies have already had an enormous impact in the biosciences, by allowing for otherwise unachievable 3D imaging in deep tissue, spatial control of chemical reactions, imaging that reveals structural and orientational information on molecular length scales, and vibrational imaging for chemical specificity. New contrast mechanisms based on nonlinear molecular susceptibilities will soon contribute their part to our arsenal of imaging tools. Ultrashort pulses, <100 fs, are likely to find increasing application, even in techniques requiring narrow bandwidth, thanks to coherent control techniques that manipulate the phase, amplitude, and frequency behavior of such pulses to drive desired nonlinear optical processes.

In parallel to these developments, ultrashort laser pulse sources are becoming more user-friendly and compact. This will help push these new nonlinear imaging techniques out of physics and engineering research and development laboratories into the biosciences. Through high-harmonic generation fs pulses can be converted to coherent x-ray bursts of attosecond durations. These novel light sources already begin to show promise for imaging modes with attractive contrast features and extremely high resolution.

ACKNOWLEDGMENTS

The authors wish to thank Xuejun Liu and Mark Mero for helpful discussions. Support from the Air Force Office of Scientific Research (W911NF-05-1-0464) is gratefully acknowledged.

REFERENCES

1. Wilson, T., and C. J. R. Sheppard, *Theory and Practice of Scanning Optical Microscopy*, Academic, London, 1984.
2. Diels, J.-C., and W. Rudolph, *Ultrashort Laser Pulse Phenomena*, 2nd ed., Academic, New York, 2006.
3. Denk, W., J. H. Strickler, and W. W. Webb, Two-photon laser scanning fluorescence microscopy, *Science* 248: 73–76 (1990).
4. Gannaway, J. N., and C. J. R. Sheppard, Second harmonic imaging in the scanning optical microscope, *Opt. Quant. Electr.* 10: 435–439 (1978).
5. Barad, Y., H. Eisenberg, M. Horowitz, and Y. Silberberg, Nonlinear scanning laser microscopy by third harmonic generation, *Appl. Phys. Lett.* 70: 922–924 (1997).
6. Zumbusch, A., G. R. Holtom, and X. S. Xie, Three-dimensional vibrational imaging by coherent anti-Stokes Raman scattering, *Phys. Rev. Lett.* 82: 4142 (1999).
7. Deitche, J., M. Kempe, and W. Rudolph, Resolution in nonlinear scanning microscopy, *J. Microscopy* 174: 69–73 (1994).
8. Lakowicz, J. R., *Principles of Fluorescence Spectroscopy*, Plenum, New York, 1999.
9. Rudolph, W., and M. Kempe, Topical review: trends in biomedical imaging, *J. Mod. Optics* 44: 1617–1642 (1997).
10. Potma, E., W. P. De Boeji, and D. Wiersma, Femtosecond dynamics of intracellular water probed with nonlinear optical Kerr effect microspectroscopy, *Biophys. J.* 80: 3019–3024 (2001).

11. Pawley, J. P. (Ed.), *Handbook of Biological Confocal Microscopy*, Plenum Press, New York, 1995.
12. Kempe, M., and W. Rudolph, Linear microscopy through thick layers based on linear correlation, *Opt. Lett.* 19: 1919–1921 (1994).
13. Kempe, M., and W. Rudolph, Femtosecond pulses in the focal region of lenses, *Phys. Rev. A* 48: 4721–4729 (1993).
14. Gu, M., *Advanced Optical Imaging Theory*, Springer, New York, 1999.
15. Mero, M., J. Zeller, and W. Rudolph, Ultrafast processes in highly excited wide-gap dielectric thin films, in *Femtosecond Laser Spectroscopy*, 1st ed., edited by P. Hannaford, Springer, New York, 2005, Chap. 11.
16. Loesel, F., M. Niemz, J. Bille, and T. Juhasz, Laser-induced optical breakdown on hard and soft tissues and its dependence on the pulse duration: experiment and model, *IEEE J Quant Electr* 32: 1717–1722 (1996).
17. Ell, R., U. Morgner, F. Kaertner, J. Fujimoto, E. Ippen, V. Scheuer, G. Angelow, T. Tschudi, M. Lederer, A. Boiko, and B. Luther-Davis, Generation of 5-fs pulses and octave-spanning spectra directly from a Ti:sapphire laser, *Opt. Lett.* 26: 373–375 (2001).
18. Weiner, A. M., Femtosecond pulse shaping using spatial light modulation, *Rev. Sci. Instrum.* 71: 1929 (2000).
19. Verluise, F., V. Laude, Z. Cheng, C. Spielmann, and P. Tournois, Amplitude and phase control of ultrashort pulses by use of an acousto-optic programmable dispersive filter: pulse compression and shaping, *Opt. Lett.* 25: 575–577 (2000).
20. Raether, H., *Surface Plasmons on Smooth and Rough Surfaces*, Springer, New York, 1988.
21. Kawata, S. (Ed.), *Near-Field Optics and Surface Plasmon Polaritons: Topics in Applied Physics*, Springer, Berlin, 2001.
22. Kano, H., and S. Kawata, Two-photon-excited fluorescence enhanced by a surface plasmon, *Opt. Lett.* 21: 1848–1850 (1996).
23. Yelin, D., D. Oron, S. Thiberge, E. Moses, and Y. Silberberg, Multiphoton plasmon-resonance microscopy, *Opt. Ex.* 11: 1385–1391 (2003).
24. Judson, R. S., and H. Rabitz, Teaching lasers to control molecules, *Phys. Rev. Lett.* 68: 1500–1503 (1992).
25. Meshulach, D., and Y. Silberberg, Coherent quantum control of two-photon transitions by a fs laser pulse, *Nature* 396: 239–242 (1998).
26. Walowicz, K., I. Pastirk, V. Lozovoy, and M. Dantus, Multiphoton intrapulse interference: control of multiphoton processes in condensed phases, *J. Phys. Chem.* 106: 9369–9373 (2002).
27. Dudovich, N., D. Oron, and Y. Silberberg, Single-pulse coherently controlled nonlinear Raman spectroscopy and microscopy, *Nature* 418: 512–515 (2002).
28. Gustafsson, M. G. L., Nonlinear structured-illumination microscopy: wide-field fluorescence imaging with theoretically unlimited resolution, *Proc. Natl. Acad. Sci. USA* 102: 13081–13086 (2005).
29. Hell, S. W., and J. Wichmann, Breaking the diffraction resolution limit by stimulated emission: stimulated-emission-depletion fluorescence microscopy, *Opt. Lett.* 19: 780–782 (1994).
30. Donnert, G., J. Keller, R. Medda, M. Andrei, S. Rizzoli, R. Luhrmann, R. Jahn, C. Eggeling, and S. W. Hell, Macromolecular-scale resolution in biological fluorescence microscopy, *Proc. Natl. Acad. Sci. USA* 103: 11440–11445 (2006).
31. Willig, K., B. Harke, R. Medda and S. W. Hell, STED microscopy with continuous wave beams, *Nature Meth.* 4: 915–918 (2007).
32. Wilson, T. (Ed.), *Confocal Microscopy*, Academic Press, London, 1990.
33. Magnor, M., P. Dorn, and W. Rudolph, Simulation of confocal microscopy through scattering media with and without time gating, *J. Opt. Soc. Am. B* 18: 1695–1700 (2001).

34. Huang, D., E. Swanson, C. P. Lin, J. S. Schuman, W. Stinson, W. Chang, H. R. Hee, T. Flotte, K. Gregory, C. Puliafito and J. Fujimoto, Optical coherence tomography, *Science* 254: 1178–1181 (1991).
35. Bouma, B., and G. Terarney (Ed.), *Handbook of Optical Coherence Tomography*, Marcel Dekker, New York, 2001.
36. Spence, D., P. Kean, and W. Sibbett, 60-fs pulse generation from a self-modelocked Ti: sapphire laser, *Opt. Lett.* 16: 42–44 (1991).
37. Kopf, D., K. Weingarten, G. Zhang, M. Moser, M. Emanuel, R. Beach, J. Skidmore, and U. Keller, High-average power diode pumped femtosecond Cr:LiSAF lasers, *Appl. Phys. B* 65: 235–243 (1997).
38. Ferman, M., A. Galvanauskas, G. Sucha, and D. Harter, Fiber lasers for ultrafast optics, *Appl. Phys. B* 65: 259–275 (1997).
39. Jasapara, J., V. Kalashnikov, D. Krimer, G. Poloyko, W. Rudolph, and M. Lenzner, Automodulations in Kerr-lens modelocked Ti:sapphire lasers, *J. Opt. Soc. Am. B* 17: 319–326 (2000).
40. Ramaswamy, M., M. Ulman, J. Paye, and J. Fujimoto, Cavity dumped fs Kerr-lens mode-locked Ti:sapphire laser, *Opt. Lett.* 18: 1822–1824 (1993).
41. Pshenichnikov, M., W. De Boeji, and D. Wiersma, Generation of 13 fs, 5 mW pulses from a cavity dumped Ti:sapphire laser, *Opt. Lett.* 19: 572–574 (1994).
42. Cho, S. H., F. X. Kartner, U. Morgner, E. Ippen, J. Fujimoto, J. Cunningham, and W. Knox, Generation of 90-nJ pulses with a 4-MHz repetition-rate Kerr-lens mode-locked Ti:Al2O3 laser operating with net positive and negative intracavity dispersion, *Opt. Lett.* 26: 560–562 (2001).
43. Jones, R. J., and J. Ye, Femtosecond pulse amplification by coherent addition in a passive optical cavity, *Opt. Lett.* 27: 1848–1850 (2002).
44. Strickland, D., and G. Mourou, Compression of amplified chirped optical pulses, *Opt. Commun.* 56: 219–221 (1985).
45. Dubietis, A., G. Jonusauskas, and A. Pskarskas, Powerful fs pulse generation by chirped and stretched pulse parametric amplification in BBO crystals, *Opt. Commun.* 88: 437–440 (1992).
46. Göppert-Mayer, M., Uber elementarakte mit zwei quantensprüngen, *Ann. Phys.* 9: 273–294 (1931).
47. Xu, C., Cross-sections of fluorescence molecules in multiphoton microscopy, in *Confocal and Two-Photon Microscopy: Foundations, Applications, and Advances,* edited by A. Diaspro, Wiley-Liss, New York, 2001, pp. 75–99.
48. Schwille, P., U. Haupts, S. Maiti, and W. Webb, Molecular dynamics in living cells observed by fluorescence correlation spectroscopy with one- and two-photon excitation, *Biophys. J.* 77: 2251–2265 (1999).
49. Sheik-Bahae, M., A. Said, T.-H. Wei, D. Hagan, and E. Van Stryland, Sensitive measurement of optical nonlinearities using a single beam, *IEEE J. Quantum Electron.* 24: 760–769 (1990).
50. Kirkpatrick, S., R. Naik, and M. Stone, Nonlinear saturation and determination of the two-photon absorption cross section of green fluorescent protein, *J. Phys. Chem.* 105: 2867–2873 (2001).
51. Centonze, V. E., and J. G. White, Multiphoton excitation provides optical sections from deeper within scattering specimens than confocal imaging, *Biophys. J.* 75: 2015–224 (1998).
52. Theer, P., M. Hasan, and W. Denk, Two-photon imaging to a depth of 1000 microns in living brains by use of a Ti:Al2O3 regenerative amplifier, *Opt. Lett.* 28: 1022–1024 (2003).
53. Helmchen, F., and W. Denk, Deep tissue two-photon microscopy, *Nature Meth.* 2: 932–940 (2005).

54. Patterson, G. H., and D. W. Piston, Photobleaching in two-photon excitation microscopy, *Biophys, J* 78: 2159–2162 (2000).
55. Sacconi, L., D. A. Dombeck, and W. Webb, Overcoming photodamage in second-harmonic generation microscopy: real-time optical recording of neuronal action potentials, *Proc. Natl. Acad. Sci. USA* 103: 3124–3129 (2006).
56. Sánchez, E., L. Novotny, G. R. Holtom, and X. S. Xie, Room-temperature fluorescence imaging and spectroscopy of single molecules by two-photon excitation, *J. Phys. Chem. A* 101: 7019–7023 (1997).
57. Diaspro, A., G. Chirico, and M. Collini, Two-photon fluorescence excitation and related techniques in biological microscopy, *Quart. Rev. Biophys.* 38: 97–166 (2005).
58. Gu, M., and C. J. R. Sheppard, Comparison of three-dimensional imaging properties between two-photon and single-photon fluorescence microscopy, *J. Microscopy* 177: 128–137 (1995).
59. Zipfel, W., R. Williams, and W. Webb, Nonlinear magic: multiphoton microscopy in the biosciences, *Nature Biotech.* 21: 1369–1377 (2003).
60. Richards, B., and E. Wolf, Electromagnetic diffraction in optical systems. 2. Structure of the field in an aplanatic system., *Proc. Royal. Soc. Lon. Ser. A* 253: 358–379 (1959).
61. Sheppard, C. J. R., and H. Matthews, Imaging in high-aperture optical systems, *J. Opt. Soc. Am. A* 4: 1354–1360 (1987).
62. Boyd, R. W., *Nonlinear Optics*, Academic Press, Boston, 1992.
63. Srivastava, A., and K. Eisenthal, Kinetics of molecular transport across a liposome bilayer, *Chem. Phys. Lett.* 292: 345–351 (1998).
64. Moreaux, L., O. Sandre, S. Charpak, M. Blanchard-Desce, and J. Mertz, Coherent scattering in multiharmonic microscopy, *Biophys. J.* 80: 1568–1574 (2001).
65. Theodossiou, T., C. Thrasivoulou, C. Ekwobi, and D. Becker, Second harmonic generation confocal microscopy of collagen type I from rat tendon cryosections, *Biophys. J.* 91: 4665–4677 (2006).
66. Freund, I., and M. Deutsch, Second-harmonic microscopy of biological tissue, *Opt. Lett.* 11: 94–96 (1986).
67. Zoumi, A., A. Yeh, and B. Tromberg, Imaging cells and extracellular matrix in vivo by using second-harmonic generation and two-photon excited fluorescence, *Proc. Natl. Acad. Sci. USA* 99: 11014–11019 (2002).
68. Dombeck, D. A., K. Kasischke, H. Vishwasrao, M. Ingelsson, B. Hyman, and W. Webb, Uniform polarity microtubule assemblies imaged in native brain tissue by second-harmonic generation microscopy, *Proc. Natl. Acad. Sci. USA* 100: 7081–7086 (2003).
69. Moreaux, L., T. Pons, V. Dambrin, M. Blanchard-Desce, and J. Mertz, Electro-optic response of second-harmonic generation membrane potential sensors, *Opt. Lett.* 28: 625–627 (2003).
70. Dombeck, D. A., M. Blanchard-Desce, and W. W. Webb, Optical recording of action potentials with second-harmonic generation microscopy, *J. Neurosci.* 24: 999–1003 (2004).
71. Nuriya, M., J. Jiang, B. Nemet, K. Eisnethal, and R. Yuste, Imaging membrane potential in dendritic spines, *Proc. Natl. Acad. Sci. USA* 103: 786–790 (2006).
72. Pons, T., L. Moreaux, and J. Mertz, Photoinduced flip-flop of amphiphilic molecules in lipid bilayer membranes, *Phys. Rev. Lett.* 89: 288104-1-4 (2002).
73. Wang, H., E. C. Y. Yan, E. Borguet, and K. Eisenthal, Second harmonic generation from the surface of centrosymmetric particles in bulk solution, *Chem. Phys. Lett.* 259: 15–20 (1996).
74. Ong, S., X. Zhao, K. B. Eisenthal, Polarization of water molecules at a charged interface: second harmonic studies of the silica/water interface, *Chem. Phys. Lett.* 191: 327–335 (1992).

75. Millard, A. C., M. Terasaki, and L. Loew, Second harmonic imaging of exocytosis at fertilization, *Biophys. J.* 88: L46–L48 (2005).
76. Squier, J., M. Müller, G. Brakenhoff, and K. Wilson, Third harmonic generation microscopy, *Opt. Ex.* 3: 315–324 (1998).
77. Yelin, D., and Y. Silberberg, Laser scanning third-harmonic-generation microscopy in biology, *Opt. Ex.* 5: 169–175 (1999).
78. Débarre, D., and E. Beaurepair, Quantitative characterization of biological liquids for third-harmonic generation microscopy, *Biophys. J.* 92: 603–612 (2007).
79. Débarre, D., W. Supatto, A.-M. Pena, A. Fabre, T. Tordjmann, L. Combettes, M.-C. Schanne-Klein, and E. Beaurepair, Imaging lipid bodies in cells and tissues using third-harmonic generation microscopy, *Nature Meth.* 3: 47–53 (2006).
80. Vogel, A., J. Noack, G. Hüttman, and G. Paltauf, Mechanisms of femtosecond laser nanosurgery of cells and tissues, *Appl. Phys. B* 81: 1015–1047 (2005).
81. König, K., Laser tweezers and multiphoton microscopes in the life sciences, *Histochem. Cell Biol.* 114: 79–92 (2000).
82. Tirlapur, U., K. König, C. Peuckert, R. Krieg, and K.-J. Halbhuber, Femtosecond near-infrared laser pulses elicit generation of reactive oxygen species in mammalian cells leading to apoptosis-like death, *Exp. Cell Res.* 263: 88–97 (2001).
83. Tirlapur, U., and K. König, Targeted transfection by femtosecond laser, *Nature* 418: 290–291 (2002).
84. Volkmer, A., Vibrational imaging and microspectroscopies based on coherent anti-Stokes Raman scattering microscopy, *J. Phys. D: Appl. Phys.* 38: R59–R81 (2005).
85. Oudar, J.-L., R. W. Smith, and Y.-R. Shen, Polarization-sensitive coherent anti-Stokes Raman spectroscopy, *Appl. Phys. Lett.* 34: 758–760 (1979).
86. Cheng, J. X., L. D. Book, and X. S. Xie, Polarization coherent anti-Stokes Raman scattering microscopy, *Opt. Lett.* 26: 1341–1343 (2001).
87. Potma, E., C. Evans, and X. S. Xie, Heterodyne coherent anti-Stokes Raman scattering (CARS) imaging, *Opt. Lett.* 31: 241–243 (2006).
88. Laubereau, A., and W. Kaiser, Vibrational dynamics of liquids and solids investigated by picosecond light pulses, *Rev. Mod. Phys.* 50: 607–665 (1978).
89. Volkmer, A., L. D. Book, and X. S. Xie, Time-resolved coherent anti-Stokes Raman scattering microscopy: imaging base on Raman free induction decay, *Appl. Phys. Lett.* 80: 1505–1507 (2002).
90. Cheng, J.-X., A. Volkmer, and X. Xie, Theoretical and experimental characterization of coherent anti-Stokes Raman scattering microscopy, *J. Opt. Soc. Am. B* 19: 1363–1375 (2002).
91. Volkmer, A., J.-X. Cheng, and X. S. Xie, Vibrational imaging with high sensitivity via epidetected coherent anti-Stokes Raman scattering microscopy, *Phys. Rev. Lett.* 87: 023901-4 (2001).
92. Knutsen, K., J. Johnson, A. Miller, P. Petersen, and R. Saykelly, High spectral resolution multiplex CARS spectroscopy using chirped pulses, *Chem. Phys. Lett.* 387: 436–441 (2004).
93. Hellerer, T., A. Enejder, and A. Zumbusch, Spectral focusing: high spectral resolution spectroscopy with broad-bandwidth laser pulses, *Appl. Phys. Lett.* 85: 25–27 (2004).
94. Porter, R., F. Shan, and T. Guo, Coherent anti-Stokes Raman scattering microscopy with spectrally tailored ultrafast pulses, *Rev. Sci. Instrum.* 76: 043198-5 (2005).
95. Isobe, K., S. Kataoka, W. Watanabe, T. Higashi, S. Kawakami, S. Matsunaga, K. Fukui, and K. Itoh, Stimulated parametric fluorescence microspectrometry, *Opt. Ex.* 14: 786–793 (2006).

10 Pulsed, Tunable, Monochromatic X-Rays: Medical and Nonmedical Applications

F. E. Carroll

CONTENTS

10.1 Introduction 281
10.2 The Medical Free-Electron Laser Program 283
10.2.1 How Do Monochromatic X-Rays Differ from Other X-Rays Currently Available? 284
10.2.2 Generation 2 284
10.2.3 Desirable Design Characteristics for a Practical Compact Device 286
10.2.4 Generation 3 288
10.3 Applications 289
10.3.1 Therapeutic Applications 289
10.3.2 What About the Children? 297
10.3.3 Diagnostic Applications 298
10.3.3.1 Tunable, Monochromatic Mammography in 3D without Breast Compression 298
10.3.3.2 K-Edge Imaging 301
10.3.3.3 Phase Contrast Imaging 302
10.3.3.4 Time-of-Flight Imaging 304
10.3.3.5 Protein Crystallography 304
10.3.4 Military and Industrial Applications 305
10.4 The Future 306
References 306

10.1 INTRODUCTION

X-rays have been used to diagnose and treat human illnesses for over 100 years. During that time, little has changed when it comes to the production of those x- rays

or of their application to patients. High voltages applied across an evacuated tube and the acceleration of electrons with the purpose of crashing them into a metal anode material still yields a spectrum of broadband radiation with its many drawbacks. Disadvantages include high radiation doses, chaotic scattering, and flux limitations engendered by heat produced within the x-ray tube itself. Low-energy x-rays produced in this way contribute significantly to the radiation dose delivered to an individual, since they are too soft to penetrate large body parts. High-energy photons (beyond those within a narrow optimal diagnostic range) create annoying scatter, reducing clarity in diagnostic images.

Filtering standard x-ray tubes to narrow the spectrum emanating from the tube is not very useful nor is there any way to convert the beam into an "infinitely" tunable source. Tricks such as using multiple detectors each peaked in performance characteristics to different x-ray energies and then doing weighted calculations to "in effect" see quasimonochromatic effects in the image offer no reduction in radiation dose to the patient and in fact frequently increase their dose.

Physicians in the imaging and therapeutic specialties of medicine have long awaited the development of a *practical*, compact, powerful, inexpensive, robust, safe, and easily tunable source of reasonably monochromatic x-rays in a geometry and range of energies that would address previously unmet needs of their clinical colleagues (the "dream beam"). These needs include high-contrast low-dose *diagnostic* examinations, increased lethality for therapeutic radiation beams, molecular imaging, and molecular therapy on a meaningful scale.

Uses of these x-ray beams are as diverse as the performance of a new kind of radiation therapy for cancers called Auger cascade radiotherapy, and utilization for low-dose 3D mammography without the use of breast compression. Additionally, k-edge imaging, phase contrast imaging, time-of-flight imaging, and many military/industrial uses are now possible using these devices.

The search for a method to produce narrow bandwidth, tunable x-ray beams found a seemingly reasonable solution in the form of synchrotron development. However, while these machines have been used quite elegantly to research and define the uses of this type of radiation, they are extremely large, expensive, daunting pieces of hardware that are not exactly user-friendly, nor are they found in every town in the country.

Stemming from the author's frustrations in the reading of mammograms and other diagnostic x-ray studies, a concept arose in the early 1970s that laid the framework for the development of a machine that could produce monochromatic beams. The evolution from that concept to reality required the joining of opportunity and major advancements in multiple fields of endeavor, not the least of which involved the Strategic Defense Initiative Organization (SDIO) and the free-electron laser (FEL).

10.2 THE MEDICAL FREE-ELECTRON LASER PROGRAM

SDIO and Vanderbilt University partnered in 1987 to place a free-electron laser into a building designed solely to bring together a multidisciplinary group of scientists and physicians for the purpose of exploring new uses of tunable lasers in the medical and materials sciences. This opened the way for experiments aimed at the production of pulsed, tunable, monochromatic x-rays using the phenomenon of inverse Compton

scattering. This process used the FEL as a source of both a high-energy electron beam and a very powerful (IR) laser beam.

In this process, a near-relativistic electron beam was accelerated to energies between 12 and 50 MeV and then focused down to a 100 micrometer focal spot in an area designated the interaction zone (IZ). After the IZ, the electron beam was then reconditioned and projected into the FEL wiggler where it produced the tunable, megawatt infrared beam for which it is so famous. The IR beam from the FEL was then returned to the IZ and counterpropagated against another packet of electrons in the electron beam in a 180-degree geometry (head-to-head collision).

Here, the laser was focused to the same-sized focal spot. In that collision, the IR photons were Doppler shifted by the inverse Compton process to x-ray energies. Hence, an IR photon went in and an x-ray photon came out. X-rays were generated in a somewhat slowly diverging conebeam along the axis and in the direction traveled by the electron beam, exiting the machine through a beryllium window for use in various applications. Since the accelerator could be tuned, the x-rays emanating from the machine were tunable. Since all of the electrons were not at exactly the same energy level, some reduction in monochromaticity of the x-rays was seen but since the laser light was nearly monochromatic, the x-rays on the whole were nearly monochromatic. The x-ray photons from that proof-of-principal experiment had energies that were tunable from 12–17.9 keV in fluxes of 10^8 photons per second [1, 2].

While these experiments late in 1998 were successful in producing pulsed, tunable, monochromatic x-rays, the process of using an FEL was not particularly *practical* for a number of reasons. These included: (1) the need for an 8-ft-thick shielding concrete vault to protect the users from intense background radiation, (2) a rather low flux per pulse, necessitating long exposure times during imaging, (3) the high cost and large size of the FEL and its beamline, (4) poor performance of the FEL when other parameters were optimized to increase x-ray output, and (5) the

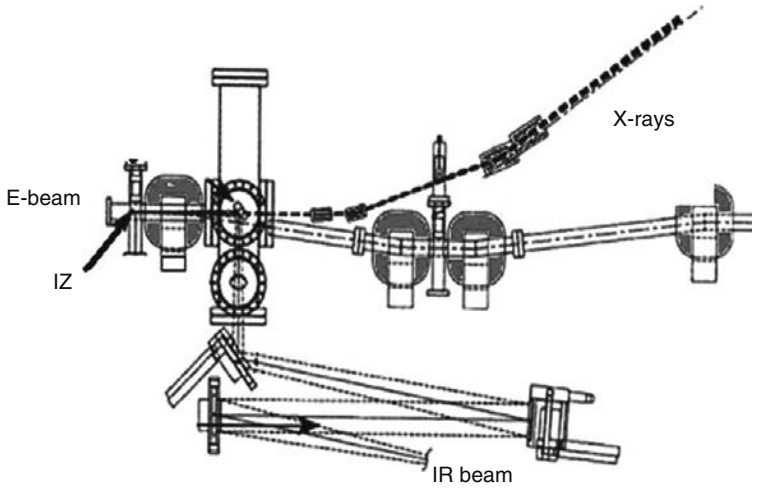

FIGURE 10.1 On the FEL, the electron beam entered from the left and the IR beam entered the beamline from the bottom. The interaction zone (IZ) was at the arrowhead on the left. X-rays exited from the beamline (top right).

necessity for turning the x-rays approximately 40 degrees around a corner to bring them into a shirtsleeves environment where they could easily be used.

10.2.1 How Do Monochromatic X-Rays Differ from Other X-Rays Currently Available?

While this explanation may seem simplistic, the assumption here is that some individuals reading this chapter may not be particularly familiar with the physics of x-ray production.

One can think of an x-ray tube rather like a white lightbulb. The light from a lightbulb looks white, but in actuality it contains all different colors mixed together (red, orange, yellow, green, blue, etc.). When these colors all hit the eye at the same time, the brain perceives this as white light.

A standard x-ray tube is similar, in that it puts out all different "colors" of x-rays at the same time. X-ray detectors for the most part cannot discriminate the different energies/colors. Many of the x-rays are wasted inside the patient because they are too soft to go through the patient. A large number are also not very useful because they scatter around before hitting the detector, acting kind of like the glare from brightly lit scenes.

Monochromatic x-ray machines only make those x-rays that are needed for the job at hand. If one wants to do a mammogram, one can make much softer x-rays (only one color) than one would use to go through a patient's chest or large bones (an entirely separate color). So the x-rays are more like a laser beam than like a lightbulb. The softest x-rays are not there, so the radiation dose to the individual goes way down. The hardest x-rays are also not there, making it easier to see.

In the medical x-ray field a monochromatic beam is expected to exhibit a bandwidth of 10%, or less, of the emission energy.

10.2.2 Generation 2

To overcome the limitations experienced with the FEL described above, a new device was designed and built by a team at Vanderbilt University (VU) with funds from the

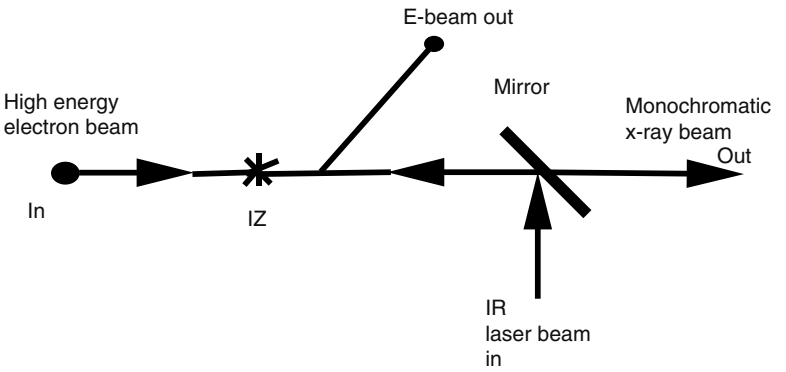

FIGURE 10.2 The head-on collision was accomplished in the Generation 2 device as shown schematically above.

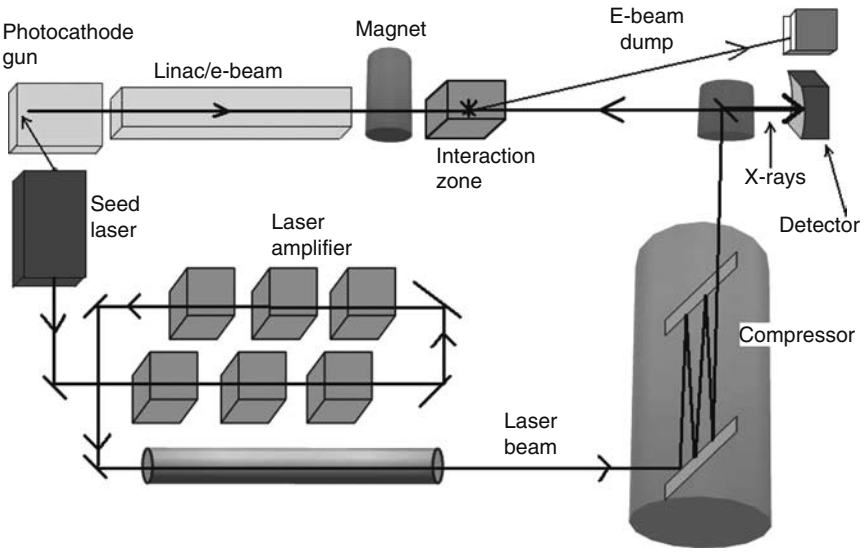

FIGURE 10.3 This machine (Generation 2) currently operates at the W. M. Keck Free-electron Laser Center at Vanderbilt University. It has been operational since April 2001.

Office of Naval Research and VU. The new machine used a linear accelerator running in the single-pulse mode and a tabletop terawatt laser.

To better understand this device, we need to remember that standard linacs run in such a way that electrons are produced in macropulses at 20–60 Hz. Each of these macropulses typically contains 17,156 micropulses each lasting about 3 ps spaced about 350 ps apart. This adds up to about 1 million high-energy electron pulses exiting the machine into the electron beam dump per second. This creates high-energy gamma and neutron radiation in the linac vault, hence the need for the shielding concrete.

A portion of the light produced by the seed laser in this new machine is used to generate electrons from a copper photocathode in the electron gun of the accelerator, while the remainder of the light from the seed is amplified, compressed, and focused into the IZ to create the x-rays via inverse Compton scattering.

Single pulse mode, as used in the Vanderbilt University Generation 2 machine, means only one electron pulse is propagated through the accelerator when the terawatt laser "fires" at full power. This reduces beam dump requirements significantly and lowers the ambient radiation environment to the point that a shielding vault is no longer needed. The machine can, therefore, be housed in an area occupied by unbadged personnel. The electron and laser beams in this machine are counter-propagated in a head-to-head geometry that is exactly the same as that used in the free-electron laser device.

Construction began on this unit in 1999, culminating with successful operation of the machine in April 2001 [3, 4].

This new prototype unit produced tunable x-rays between 10 and 55 keV in 8–10 ps "shots" with fluxes of 10^{10} photons per shot, in a shirtsleeves environment. The machine produced an x-ray pulse only once every 5 minutes, dictated by the need

for cooling the Nd:glass rods within the terawatt laser. It has been used over the last 6 years for applications research and to test machine modifications that will allow it to evolve into a much more practical commercial device.

While this prototype unit was only approximately one-quarter the size of the free-electron laser beamline, it too suffered from several shortcomings, including relatively large size and weight, high cost, and slow repetition rate. Once more, practicality would need to override just the successful production of tunable, monochromatic x-rays, if this device was to see the light of day in a clinical setting.

10.2.3 Desirable Design Characteristics for a Practical Compact Device

It does little good for new technologies and machine designs to be built in a vacuum by engineers without the input of clinicians, as has occasionally happened in the past, so determining the patient's and physician's needs first would be prudent if the machine design is to be optimal when fielded. Since the eventual goal for the monochromatic machines is to deliver tunable beams on demand to patients in the clinical setting, they must be designed to seamlessly interdigitate into the applications to which they will be put.

To begin with, they must be easy to use by those not holding PhD degrees. Most diagnostic and therapeutic procedures are actually performed on a patient by radiological technologists, who do not hold advanced degrees, and in many cases have received training that consists of two years of specialized instruction after high school. The fewer bells and whistles that such a machine has, the more likely it will be accepted by the users. The machines must be self-tuning, self-monitoring, and manufactured with extremely robust components that will hold up in the hospital or clinic setting, where blood, vomitus, and other nasty bodily fluids have a tendency to make more than an occasional appearance.

Why is a high repetition rate so desirable in a clinical system? The reasons for this are numerous, including: (1) the need for ease in machine setup and maintenance of optimization of the various beam parameters while the device is running, (2) reduction in the length of therapy sessions for cancer patients, and (3) prevention of motion artifacts for multiple exposure diagnostic studies.

When setting up the counterpropagating beams for optimal x-ray flux output, one needs to compare the output x-ray flux while minor corrections are made to each of the two input beams (e-beam and laser beam). Because the machine produces picosecond packets of electrons and photons that are focused to very tiny focal spots, pointing stability is extremely important, as is timing of the arrival of both beams to the interaction zone. Z-position optimization (i.e., along the longitudinal axis of the electron beam), of course, is both a timing and a focusing issue. Since the laser beam is traveling at the speed of light and the e-beam is traveling near the speed of light and they both "originate" from the same starting point but take separate paths to the IZ, getting them there at precisely the same time is clearly a very important issue. Since the beam packets are exceedingly short (only 5–8 ps long), overlap for optimal x-ray generation is also very tricky.

The Rayleigh ranges of both beams should be perfectly overlapped for optimal x-ray generation and for proper x-ray beam pointing at the beamline exit window.

If the electrons are diverging after they have left the interaction zone or if they are converging toward the IZ, and the laser light is at its tightest focus in one of those suboptimal regions, any x-rays produced will point in the direction of the convergence or divergence of the electrons, since it is the direction of the electrons that is the determining factor as to where the x-rays will "point." Needless to say, the flux of x-rays will drop significantly when the beams overlap with one another in those "unfocused" areas outside of their Rayleigh ranges on either side of the IZ. So, as the machine is set up and continuously running, optimization of beam positioning in X-, Y- and Z-positions is extremely important and must be constantly monitored for shot-to-shot stability in x-ray flux and position.

High-energy "hard" x-ray production is a must for the beams to be used effectively in our patient population. Since patients exhibit great variety in body habitus, size, infirmities, and phobias, a one-size x-ray beam rarely fits all. Patients, as we have all noticed, get thicker every year. Obese patients have become a problem for users of all diagnostic and therapeutic machines. We must have the ability to deliver the beam deep within even the largest patient, particularly if one is attempting to deliver therapeutic x-rays to a tumor near the center of the patient, while at the same time keeping the radiation dose to the skin and superficial structures to a minimum. These hard x-rays must extend to at least 100 keV (n.b. not KVP, which refers to kilovolts potential applied across the terminals of an x-ray tube), if they are to be useful with the most interesting and most commonly used drugs that adhere to DNA (e.g., platinum whose k-edge is at 78.4 keV—more on this later).

Sessions designed to deliver rather large doses of monochromatic x-rays to patients with cancer require very large numbers of pulses to be delivered over a time frame that will not exhaust the patient. However, we also must keep open a window of safety toward shutting the beam off if one of the input beams, the output beam, or the patient's tumor should wander off of the intended axis for optimal beam dosage when treating cancer. Constant monitoring and the ability to shut down between pulses are crucial for patient safety. Delivery of beams to very small and clearly defined areas deep within the body requires immobilization of the patient. Patients will not tolerate this for long periods of time, so therapy sessions need to be relatively short and reproducible, which is another reason for a high repetition rate design.

While ps pulses would obviously eliminate motion artifacts from images made with such monochromatic beams, CT types of acquisitions with many views from different angles require the absence of movement between shots. If a machine is only capable of firing once every 5 or 6 minutes, it is highly unlikely that a patient could hold still for a CT data acquisition session necessitating anywhere from 60 to 360 views or more. However, if images could be made 10 times per second, even the longest acquisitions would be only a few seconds long. This is easily accomplished with imaging of the breast, the brain, or the extremities. It also lends itself to "gating" (synchronization to the cardiac and/or respiratory cycle), if one wishes to image thoracic or abdominal structures, with only minimal increases in the length of the study.

Space, power, and water are all commodities that command a premium in medical facilities. Modular designs that can be installed in standard hospital x-ray rooms, in prefabricated buildings, or in portable tractor trailers, lend maximum versatility

TABLE 10.1
Machine Specifications: Generation 3 Tunable, Monochromatic X-Ray Source

E-beam	Linac running in "single pulse" mode
	Up to 75 MeV
	Up to 2 nanocoulombs/pulse
	Emittance ≈ 0.7 π mm-mrad
	Copper photocathode
	Electron beam-normalized brightness: 5×10^{11} A/m^2
Laser	Tabletop terawatt
	$\lambda = 532$ nm
	1.5 J/pulse
	10 Hz pulse repetition rate
X-ray beam	10^9 photons/5 ps shot
	(10^{10}/s)
	Tunable from 10 to 100 keV
	0.1–10% bandwidth
	Cone beam geometry
	(X-ray beam – brilliance – 3×10^{34}/m^2/steradian/s)

For conversion from photon energy in eV to wavelength units, see Chapter 15.

and lower costs to clinical facilities. So machines that do not require a shielding concrete vault and that have small power requirements, low cooling water needs, and diminished HVAC consumption, will become the darlings of the hospital administrators who are required to address the fixed and variable costs attached to this kind of "exotic" technology.

The smaller the footprint, the cheaper the bottom-line costs and the more clearly defined the benefits to the patients, then the more likely the success of compact, tunable, monochromatic sources, and the more likely it is that third-party payers will reimburse hospitals, physicians, and patients for procedures performed with these devices.

10.2.4 Generation 3

While applications research continues on the Vanderbilt prototype, the march to commercialization of a practical device would require further modifications to that machine (such as those previously discussed). These changes are embodied in a third-generation device now under construction [5, 6]. The machine specifications for this device are listed in Table 10.1.

Newer, high-power, high-repetition-rate, terawatt laser systems with much smaller footprints, higher reliability, and lower overall costs are now available. The compact design of these newer systems shrinks the tunable, monochromatic x-ray machines even further, such that they now fit in a space smaller than one-half of a tractor trailer, making them both modular and portable.

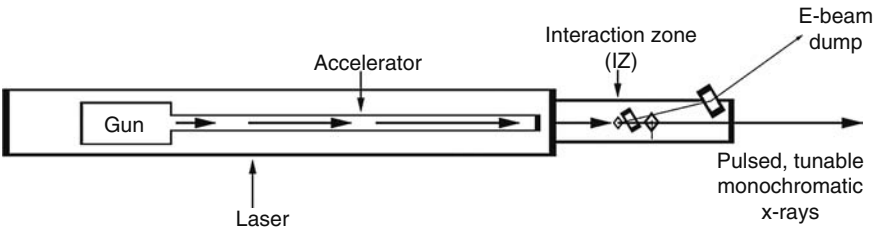

FIGURE 10.4 In this embodiment, the laser sits atop the accelerator and the beamline is markedly shorter than that on the earlier devices.

X-rays produced by the newest generation machine span the hard x-ray range of 10–100 keV in 5–8 ps bursts at 10 Hz. Each short burst of x-rays produces 10^9 photons or 10^{10} photons/s. These emanate from a 20–50 μ spot size into a somewhat forwardly directed conebeam geometry most useful in the human setting. The bandwidth of the x-rays is from 0.1–10%, selectable by the user.

Because the x-rays are produced by a forward-scattering process, the resultant x-ray beam diverges at a slow rate (narrow divergence angle, which is typically a few milliradians). Hence, instead of a beam that radiates into a rapidly expanding spherical wavefront, such as with standard x-ray tubes, these beams remain well collimated over long distances. To give an example, the monochromatic beam emanating from a 20 μm spot at the machine's IZ when the machine is operating at 30 keV, will have diverged to cover a spot that is 0.25 cm in diameter at 0.30 meters from the source to 1.2 cm at 1.52 meters, and to 2.4 cm at 3.04 meters. It will have a bandwidth of about 10%. (At 50 keV, the beam covers 0.175 cm at 0.30 meters, 0.925 cm at 1.52 meters, and 1.875 cm at 3.04 meters). So, there is no need to refocus the beam to conform to a target within the body, as this can be accomplished by moving a patient closer to or farther away from the source of the x-ray beam (the IZ).

10.3 APPLICATIONS

This technology is what we describe as an *enabling technology*. It allows us to do things that could not previously be done with current technologies, either in diagnostic imaging or in the delivery of therapeutic radiation [7]. First of all, let us consider uses in the treatment of patients.

10.3.1 Therapeutic Applications

In order to kill a cancerous cell in a tumor, one needs to take away its ability to reproduce itself. It is that simple.

That said, many different methods have been devised in an attempt to kill tumor cells while hopefully sparing normal tissues around the tumor.

Chemicals (chemotherapy, or chemo), heat, cold, and radiation have all been enlisted in some form or another to kill these cells. Currently, the treatment of many cancers relies upon: (1) surgery to remove the bulk of the tumor, (2) a wide variety of chemotherapeutic drugs to kill cells left behind that might be dividing rapidly,

(3) radiation therapy to kill cells where surgery may not be an option, or in some cases, (4) a combination of all three.

Of all patients with cancer, 50% get radiation therapy. Of those, 90% get external beam radiation treatment. Standard external beam radiotherapy, as now practiced, entails the delivery of *lethal doses of radiation* to a tumor and its surrounding areas. With such therapy, x-rays or sometimes nuclear particles (electrons, neutrons, or protons) are directed into the patient's body in an attempt to kill the errant cells. The vast majority of the time that such therapy is performed, it is basically like shooting a shotgun at the cell. One hopes that one of the pellets will hit some absolutely vital structure in a cell to kill it. One may or may not damage a critical intracellular structure or component, but just as likely might damage a part of the cell that can repair itself quite easily. This I call random radiolysis.

The random radiolytic process must take into account the fact that cells go through phases in their growth whereby they alternate between bouts of resting and replicating. Cells are more resistant to standard radiotherapy in the resting state and so one must fractionate (break up the delivery of radiation into sessions spread out over several days or weeks) in an effort to kill cells not destroyed during the original therapy session. Current radiotherapy also depends heavily on blood supply and oxygenation to the tumor. If the tumor is oxygen-starved, it is actually *more resistant* to formation of singlet oxygen during irradiation. Singlet oxygen is one of the substances that we rely upon rather extensively, that is so very damaging to intracellular elements. Many cells that have undergone sublethal damage contain mechanisms that will allow them to repair themselves rather quickly, with a half-life for cell repair being in the neighborhood of 1–3 hours. One wishes therefore to deliver another punch to the cell while it is on its knees before it can repair itself, because regrowth of tumor cells or repopulation will only cause one to lose ground toward defeating the tumor.

Most important of all, however, is the fact that the information that the cell uses to replicate itself (and therefore make the tumor grow) resides within the intranuclear DNA. If one wishes to inflict maximal damage to a cell, one merely needs to disrupt the flow of information from along the double helical chain of DNA. An example of this is an exciting new type of cancer treatment called Auger (pronounced very much like "O.J.") cascade radiotherapy (ACR). This type of therapy allows us to target DNA in a very specific way (see Fig. 10.5).

Auger cascade radiotherapy is a mouthful of a name, but what it boils down to is that if one combines certain drugs, a beam of monochromatic x-rays, and some of the techniques of radiotherapy, one can revolutionize the treatment of many cancers, delivering only a small fraction of the radiation dose that patients now must receive. This reduces the damaging effects to normal tissues and more specifically delivers the magic bullet to the molecular target within the cell where it does the most good. This is extremely exciting to radiotherapists who have looked at and understand this method.

To understand the process more fully, one must first examine the k-edge effect. It is well known that electrons swarm around atomic nuclei in predictable orbits and suborbital shells that have binding energies that are characteristic for each of the atoms in the periodic chart. Monochromatic x-rays can be tuned selectively to those binding energies quite nicely. Simplistically, one tunes the x-rays to the binding

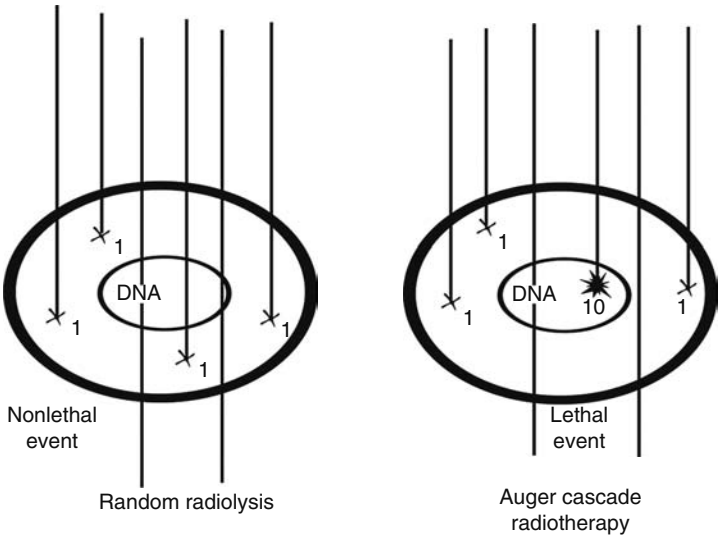

FIGURE 10.5 Schematic difference between random events versus specifically targeting the DNA. Numbers indicate the relative effectiveness of a given x-ray photon toward inflicting damage to a cellular component.

energy of the k-shell electron of an atom of interest, for instance the binding energy for iodine is 33.2 keV, for gadolinium it is 50.2 keV, and for platinum it is 78.4 keV. When the monochromatic x-ray hits the atom of one's choosing, the k-shell electron can be ejected from its orbit, extinguishing the x-ray photon.

When the k-shell electron is displaced from the inner orbit, outer orbital electrons cascade inwardly to fill the void shell by shell, each giving up energy in the form of more photons, which are converted to many energetic electrons. This cascade (the Auger cascade) delivers all of its energy in close proximity to the cascading atom (i.e., within nanometers of the atomic locus).

This phenomenon can be used to great advantage in the treatment of malignant tumors. The monochromatic x-rays that we use have the added benefit of being stopped by the target atoms in the drug and so they don't go on to damage the deeper organs, arteries, or nerves farther into the patient's body.

Hydrogen, oxygen, carbon, and nitrogen make up most of the body, whether in normal cells or tumor cells. Of course, one doesn't want to target those atoms since there is no way of discriminating whether or not they reside in cancer cells. Additionally, the binding energies of their k-shell electrons are extremely low, so that photons that could conceivably target them are too soft to penetrate to any significant depth anyway.

How then does one best target the DNA within the cell nucleus? In order to do this one needs to position a target atom within or onto the surface of the DNA itself. Of the atoms that can most easily be incorporated into the DNA, iodine, gadolinium [8], and platinum are the three most attractive elements attached to drugs for this purpose.

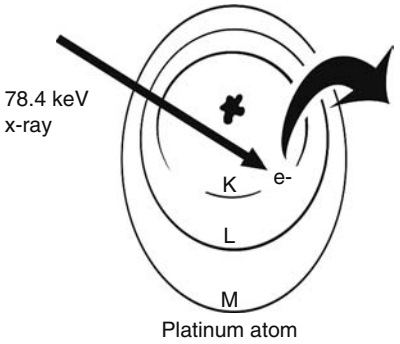

FIGURE 10.6 A photon tuned to the k-shell binding energy of the platinum atom will displace the electron from that orbit, while extinguishing the photon itself.

Fortunately for us, there are many FDA-approved chemotherapy drugs that are known to adhere to or incorporate themselves into the DNA.

Among the most commonly used chemotherapy drugs for many of the most common and most deadly cancers that we are faced with today are platinum-containing compounds (e.g., cis-platinum, carboplatin, and oxaliplatin). When administered to a cancer patient, platinum drugs have a tendency to form bonds of a sort called adducts at the cytosine-guanine (CG) base-pair units within the DNA in rapidly replicating cells (i.e., cancer cells). Once adherent to the DNA, the drug remains in place for long periods of time, even years. The platinum atoms in the drug make an ideal target for a beam of x-rays having an energy close to and even slightly above the k-edge of platinum. Beams of radiation at energies much higher (in the hundreds

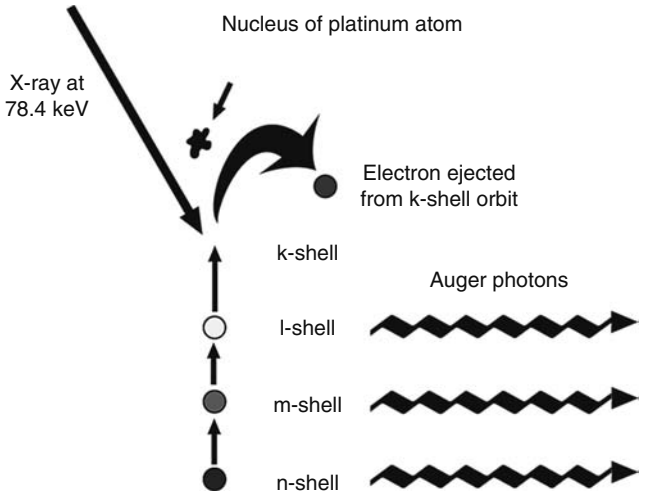

FIGURE 10.7 When the k-shell electron is displaced there is a cascade of outer shell electrons to replace the inner shell electrons, the Auger cascade. The energy released is deposited within nanometers of the target atom.

of keV or MeV range) will have very little effect toward creating the Auger cascade sought after. As an example, at 935 keV only 0.1% of radiation will be absorbed toward creating the cascade. This type of targeting is similar in some respects to photon activation therapy wherein light photons from lasers "activate" or split the compounds that have previously accumulated in cancer cells. Many of those drugs are porphyrin derivatives. They are now used, not uncommonly, for the treatment of airway and esophageal cancers. Molecular targeting for deeper structures, however, requires x-rays, not light, to reach the dark recesses many tens of centimeters within the body.

Auger cascade radiotherapy is particularly effective in head and neck tumors, brain tumors, and skin cancers that have invaded the head. However, we are not restricted to use just in the brain, head, or neck. Since the distribution of malignant tumors in the body approximates 12% in the brain, 9% in other parts of the head and neck, 7% in colon, 14% in the lung, 19% in breast, and 19% in the prostate, we have a very target rich environment in which to work for our patients. Platinum-containing chemotherapy agents are now used in almost all of these areas.

Since DNA is predominantly what is damaged during the course of ACR, one doesn't have to use anywhere near as much radiation as is now given to patients to kill a tumor. This significantly reduces or eliminates the undesirable radiation side effects known collectively as radiation sickness. The complications that make up radiation sickness consist of bleeding, nerve damage, skin "burns," and damage to surrounding organs, all of which increase in frequency and severity with increasing levels of radiation delivered.

An additional salubrious effect of Auger cascade radiation therapy is the fact that these atomic cascades have a very low toxicity when the cascade occurs outside of the cell nucleus (as in the extranuclear cytoplasm of the cell, outside of the cells themselves in the extravascular interstitial spaces, on the surface of cells during transport through the bloodstream or on the cell membrane where they usually adhere when antibodies are coupled with radionuclides to target specific cell types).

One must also take into account the possibility that a cell might not take up any of the target compound into its DNA. In that regard, it has been shown that some cells that do not contain target atoms (and are interspersed among others that do contain the tagged DNA) may die when neighboring "support" (so to speak, in the form of nutrients, communications, and other related structures) is lost changing the milieu so significantly that the cells can't continue to function adequately. This represents one type of bystander effect, killing the cell even though it didn't contain the target platinum atom.

While others have tried processes similar to ACR using "radiosensitizers" and high-energy standard external beam therapy, the mismatch of the atoms of interest, the great discrepancy between the k-edge of the atoms (keV) and the beams being used (MeV), and the high radiation doses still needed to influence damage outside of the confines of the DNA, have shown little additional effect toward improving patient outcome. In the past, it has also made sense to some to interfere with the ongoing oxygenation within the *normal* cells around a tumor by adding radioprotective compounds to those surrounding cells. More commonly though, there are some drugs, such as a few gadolinium-containing compounds, that have been designed

to enter tumor cells and to seriously affect the oxidation-reduction pathways that all cells rely upon for normal metabolism and to interrupt reparative mechanisms within cells that are attempting to repair themselves after damage caused by random radiolysis [9]. The fact that many of the radiosensitizers do not target the nuclear DNA means that their effects are wasted to some extent, causing modifications in the mechanics of the cell's everyday processing of metabolites.

Fortunately for all of us, tunable, monochromatic x-rays can now selectively target cellular DNA through Auger cascade radiotherapy. The effectiveness of ACR using monochromatic radiation is *3 to 5 times greater than what one achieves with standard radiotherapy!*

An additional benefit to the Auger cascade radiotherapy process is that it does not need to be as conformal to the tumor, and can indeed better treat the tumor and any adjacent infiltrating cells that contain the target atom, if it is not tightly focused on the tumor. An enormous amount of effort is now expended in the planning and delivery of radiotherapy by attempting to ensure that the beams from a standard radiotherapy machine conform precisely to the edges of the tumor. Additionally, it is important with standard beams to constantly modulate the intensity of the beam depending upon the thickness of the tumor in any given projection because a lethal dose delivered to tumor cells is also being delivered to any normal cells in the treatment area.

A monochromatic beam that is being used to take advantage of the Auger effect is being delivered in a dose that is far below one that is lethal to normal cells. So, one would want to encompass any cells that had infiltrated away from the primary tumor via microscopic fingers that extend into the adjacent normal-looking regions around a tumor, that wouldn't normally be included in standard radiotherapy beam planning. These little fingers or metastases would likely contain the high Z monochromatic beam target as they are an active region of the tumor's growth. In fact, the high Z atoms contained within the tumor act like a double-edged sword. While they have a tendency to self-shield the area behind the tumor, reducing dose to deeper organs, they can be too effective in stopping the beam such that the deepest portion of the tumor may get too little of the monochromatic x-rays for adequate treatment.

An example of the dose distributed to an irregular tumor with a bump on one side of it, and to a satellite lesion nearby, as well as to the surrounding tissues, is highly specific for the monochromatic beam and rather ugly for an IMRT-treated tumor. Figure 10.8 is the output of a GEANT code Monte-Carlo simulation of such a scenario. In this image it can be seen that a lethal dose (100% on the scale shown) is delivered to a tumor that has an iodine-containing drug in concentrations expected to be obtainable within a lesion, by a single rotating 50 keV monochromatic beam. The bump and the satellite lesion both receive the lethal dose, but the normal tissues between the tumor and "metastasis" receive a dose that is far below lethality, sparing those tissues—very important if this were a tumor situated within the brain.

Figure 10.9 is a comparison output for the same scenario, but instead a moving 7 MeV beam is used. This is the type of beam now delivered by a standard radiotherapy device. Here, one certainly would kill the tumor and the metastatic satellite lesion, but look at all of the surrounding normal tissue that has received a lethal dose as well.

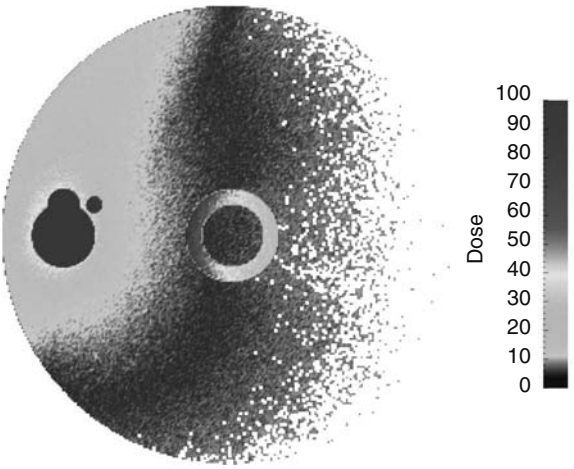

FIGURE 10.8 **(See color insert following page 288.)** Percentage of lethal dose delivered to a tumor using a single rotating 50 keV monochromatic beam. The tumor is laced with an iodine-containing DNA drug. Radiation dose needed for lethality is 3 to 5 times less than that needed in standard radiotherapy. The irregular tumor and the adjacent metastasis receive a lethal dose, yet the normal intervening tissues receive far less of a radiation dose. The monochromatic x-rays target the tumor, not the normal tissues. (Courtesy of Marcus H. Mendenhall, Ph.D. W.M. Keck Foundation Free-Electron Laser Facility, Vanderbilt University.)

A monochromatic beam of 78.4–90 keV (this range is necessary depending on the depth of the tumor within the body due to scattering effects) will couple extremely well to the platinum k-edge creating not only one cascade of radiation, but as many cascades as one would like. This is possible because the platinum atom reconstitutes itself back into a stable atom within femtoseconds of the original cascade, making it available for additional cascades. This latter fact makes this type of internal atomic radiation release superior to that realized using drugs containing radionuclides, which disintegrate only once and not uncommonly accumulate in other organs.

Dose distribution within the tissues is very important here. If one uses a radioisotope of iodine I-125, for example, to create an Auger cascade, the radiation dose distribution can be thought of like the spherical layers or shells within an onion. One cascade creates the highest dose within the smallest innermost sphere of the onion at an equivalent dose of 1.6 MGy or a 22,000 times higher dose to that same volume than what would be delivered with conventional external beam irradiation with 70 Gy delivered over several weeks [10]!

Alternatively, by infusing IUdR (iodinated deoxyuridine) into a patient one can replace between 10% and 20% of the thymidine in the DNA of rapidly dividing cells. Unfortunately, IUdR incorporates only during the S phase of the cell cycle so that it must be given to the patient over long periods of time to ensure incorporation into most tumor cells. By then tuning to an energy (45–50 keV) somewhat above the k-edge of iodine (33.2 keV), one can interact with the k-shell electron. The enhancement obtained via the Auger cascade process is called the DER (Dose Enhancement Ratio) [11–14].

Since monochromatic beams with higher keV are available via inverse Compton scattering, more energy can be released within a tissue per quantum delivered,

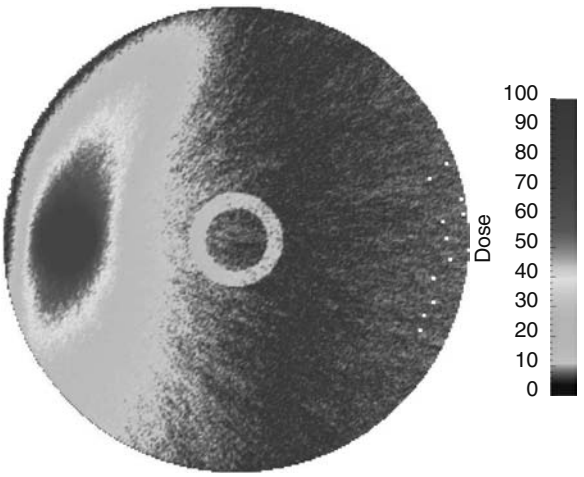

FIGURE 10.9 (See color insert following page 288.) Distribution of the dosage of radiation to the tumor and satellite lesion with a 7 MeV rotating beam. The tumor contains the same iodine concentration as in the prior figure, and requires a dose of 60 Gy to kill the tumor.

so that fewer than 78.4 keV photons need be directed at a platinum atom to deliver more energy to the tumor than would be delivered by 33.2 keV photons delivered to a similarly placed iodine atom. This makes platinum-containing drugs more attractive, as does their tendencies to incorporate at all phases of the cell cycle, since they do not replace base pairs in the DNA, but only attach to certain base-pair sites on existing DNA strands. Platinum chemotherapy drugs do not, however, accumulate in as large amounts in cancerous cells as iodinated drugs like IUdR, but the mere size of the platinum atom that is adherent to the DNA also has the very nice secondary effect that it acts to retard or totally prohibit the docking and function of *reparative* enzymes or compounds onto the DNA.

When alpha, beta, and gamma emitters are used for therapy, it must be remembered that they spread their energies along tracks over much wider areas than in ACR. These particle emitters deliver their ionizing energy over linear tracks measured in microns, millimeters, or even meters. The linear energy transfer along the particle's track is more diffuse and winds up being closer in efficiency to the random radiolysis obtained with external beam delivery as discussed previously. Many adjacent cells other than the ones in which the radionuclides were deposited are damaged or killed by this linear distribution along the particle's track. This too is a form of bystander effect. It represents good news if the bystanders are cancer cells, but bad news if they happen to be normal cells [15].

A clear example of the effectiveness of the ACR approach to treating brain tumors is documented in a very nice paper wherein the authors established very radioresistant tumors in the brains of rats. They then irradiated some at a synchrotron facility with a monochromatic beam at 78.8 keV, gave some rats cis-platinum alone (since it is a DNA avid drug), and treated others with both the cis-platinum and the monochromatic x-ray beam. There was very little improvement in survival in the

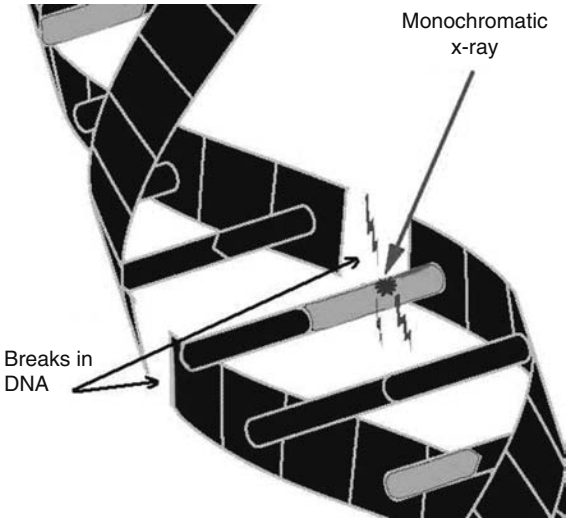

FIGURE 10.10 Since the radiation in an Auger cascade is delivered within nanometers of the location of the target atom, it tends to break both DNA strands.

rats receiving the x-rays or the drug alone, but in those receiving both together there was an improvement in median survival of over *seven* times, with some of the animals exhibiting *apparent cures* from the tumors [16]. Scientists at many other facilities have confirmed the utility and effectiveness of this approach, and even the feasibility of targeting the l-shell instead of the k-shell [17].

10.3.2 What About the Children?

Needless to say, use of x-rays on children carries with it a more onerous burden. Children are more radiation sensitive than adults, and even small doses are to be avoided if possible [18]. However, monochromatic x-rays that are tunable to just the imaging task at hand, or to treating a tumor by the Auger cascade method, can significantly cut the radiation burden to "little people." This latter issue is particularly problematic in *the youngest* children who are even more sensitive to x-rays. They now suffer many radiation-induced cancers after having successfully survived treatment of their original brain tumors. In addition, these children are shown to suffer from difficulties with organization, memory, and language. If that weren't enough, they also exhibit problems with attention deficit hyperactivity disorder and show cognitive impairment with difficulties interacting socially, along with anger and underachievement in school [19–23].

Since the monochromatic ACR delivers so much less radiation throughout the normal tissue, it does not come anywhere near a lethal dose to those normal tissues that become included in the path of the beam, and induction of new cancers caused by the therapy to the original tumor is less likely to occur.

The fact that pulsed, tunable, monochromatic beams are so fast also makes them very useful in these little "wiggly" persons, so that images needn't be repeated

because of motion. Retakes currently contribute somewhat to the overall radiation burden to the pediatric population. The fact that there is less scatter from the x-rays means that images can be made without "grids" that are currently used by some to clean up scattered radiation reaching the film. Use of grids can require as much as 30 times as much radiation in some imaging geometries. By eliminating motion retakes and grids, far less radiation need be given to children to start with. Think of the value of reducing the overall radiation burden to a child who might require radiotherapy, if one is able to use the Auger techniques.

One of the difficulties with the delivery of radiation *to both adults and children* is the distribution of an unwanted dose to tissues outside of the primary beam due to scattering or to the methods used to produce the beam from the machine in the first place. Even if this scatter is delivered over the volume of an adult, it is still a significant total body burden, adding up to 3% of the dose that has been delivered "just to the tumor." Since children are smaller physically, the scattered dose is delivered over a proportionately larger portion of their body and so carries with it even more of a burden to vital organs such as bone marrow. This applies to both IMRT and to proton beam therapy [24]. Again, even if beams such as proton beams are capable of more clearly defining at which depth the protons deliver their energy, one must still use what is considered a lethal dose of radiation to effect a "cure." Even the slightest misalignment of such a beam delivers that lethality to normal (nontumor) cells.

Another method now finding an expanded use is image guided radiotherapy (IGRT). The tumor is imaged using a CT scanner that is attached to the same table and linac machine that will deliver the therapy. Positioning of the patient can then be checked for relevance to the therapy plan to be used in delivery of each dose, since the patient will not have moved off the table between imaging the tumor's location and the delivery of the therapeutic dose of radiation. While the dose will indeed be more accurately delivered, think of the radiation burden to the patient of having a CT scan every day that a radiation dose fraction is to be delivered. The risk is not inconsequential here.

Other forms of radiotherapy require different imaging systems from those that can deliver the therapy. Most treatment planning today is done using CT imaging performed on a CT that is physically in another facility, removed from the linac vault, so that the patient's tumor is not easily "perfectly registered," and assumed to be in the same location on both machines. Continuous imaging of a heavy-metal-containing tumor with the small residual percentage of the beam passing through the patient is feasible with keV beams. The detectors are peaked for radiation of this energy and can occupy a position directly opposite the beam while the treatment beam is on, offering a free CT with real-time observation of the tumor without any additional radiation burden.

10.3.3 Diagnostic Applications

10.3.3.1 Tunable, Monochromatic Mammography in 3D without Breast Compression

The current best practice for the performance of screening and diagnostic mammography entails the use of specialized x-ray tubes (with molybdenum anodes) that

deliver rather high radiation doses to the woman during the examination. In addition, the woman's breast must be extensively compressed during the study. This is necessitated by a desire to even out the overall x-ray exposure needed for both thick and thin portions of the breast and to spread out the internal structures of the breast in an attempt to avoid mistakes attributed to misinterpreting overlapping structures as tumor masses. Compression of the breast is uncomfortable at the least and downright painful to the majority of women. The diagnostic accuracy of mammograms is not as good as physicians and patients would hope, with many cancers being missed or misinterpreted as benign tumors. Many examinations yield somewhat ambiguous results leading to performance of biopsies to determine the character of something seen on the mammogram. The vast majority of these biopsies are proven to yield benign tissues. Women's activist groups have rightfully pressured the federal government to establish some sort of stringent quality control over mammography. This has, in turn, resulted in three federal agencies that oversee and mandate the manner in which mammography will be performed. While this is a good thing for mammography, it leaves little room for the rapid development of some new technologies meant to improve examination of the breast, and leaves us locked into a standard of care that has been frozen in time and proven to be suboptimal at best.

Fortunately, monochromatic x-rays are ideally suited to bring out the inherent and sometimes rather small contrast differences in soft tissues, particularly in places like the breast.

In 1987, Johns and Yaffe showed that cancerous breast tissues exhibit a higher effective Z than normal breast tissues when their linear attenuation characteristics were studied using monochromatic x-rays from a synchrotron spanning energies from 20 to 100 keV [25].

In 1993, our group took similar specimens to Brookhaven National Laboratories to study such tissues from 14 to 18 keV obtaining a similar result. The linear attenuation is increased by about 11% in cancers relative to normal tissues [26].

These data and that of others confirm that monochromatic x-rays are ideal for improving contrast resolution in the breast. So, soft tissue abnormalities can show up much better with monochromatic x-rays than when one uses standard mammography. This promises to make x-ray examinations of the breast a much more accurate exam, and certainly a much more reproducible exam from year-to-year (which is important for catching changes), while, at the same time, being much easier on the woman herself. Figure 10.11 shows comparison images of a breast phantom containing materials that mimic breast cancers *in situ*. The image on the right side of Figure 10.11 has been made using the current "standard" polychromatic techniques. The image on the left is an image made using a monochromatic x-ray beam from the Vanderbilt University Generation 2 machine. The arrows in the left image point to "lesions" that mimic breast tumors. These are extremely difficult or impossible to discern in the polychromatic image. The monochromatic image on the left was made using a radiation dose that was 60 times less than the dose utilized to make the polychromatic image on the right.

Since the monochromatic x-ray beam created via inverse Compton scattering exhibits a conebeam geometry, it is possible to use approximately 60 plain film images using digital detectors and conebeam back projection algorithms to calculate

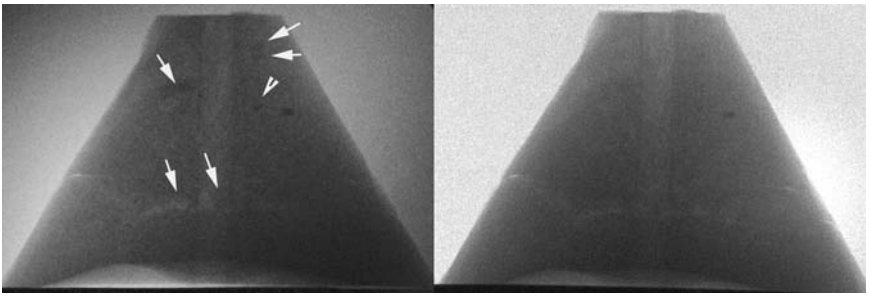

FIGURE 10.11 Side-by-side comparison of monochromatic (on the left) and polychromatic images of a breast phantom showing simulated cancerous lesions (dark spots at arrows) seen to greatest advantage on the monochromatic image.

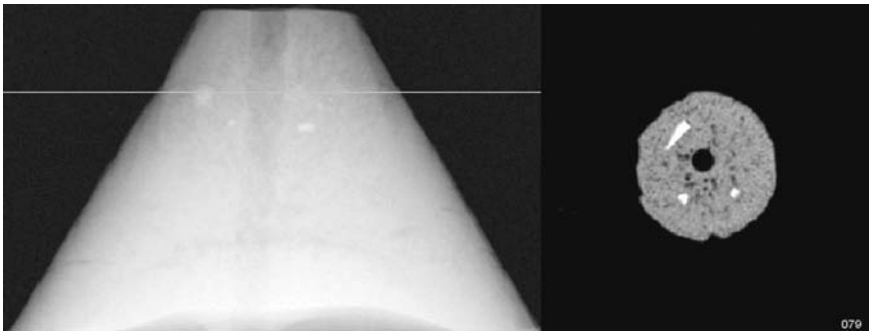

FIGURE 10.12 Sixty views, each performed with three degrees of rotation from the last (one of which is seen on the left above) were used to reconstruct a CT (3D) image of a breast phantom. Only one slice of that CT data set is shown on the right in the combined image above.

a full CT study. Our group has been successful in developing techniques that result in a 1000-slice computerized tomography (3D) examination of the breast using 60 shots at different angles around the breast *without using breast compression*. We have shown that the radiation dose for the full 60 views can still be 5 times less than what a woman would receive with a two-view mammogram, as presently performed.

Spatial and contrast resolution is enhanced using the monochromatic x-rays, particularly with the small (20 micron) focal spot [27]. A special mammography table that allows data acquisition to be comfortable for the woman while encompassing the entire breast, axilla, and chest wall is currently under design in collaboration with biomedical engineering personnel at Vanderbilt University. Additionally, 60 views might not be necessary and experiments have been done to determine what degree of spatial resolution and contrast resolution is sacrificed using fewer views. Subsets of the full 60-view study have been reconstructed using 30, 20, and even 10 views, with remarkable retention of diagnostic information, which, if used clinically, could lower the dose even further.

Once an abnormality is found on a mammogram, a needle biopsy is usually necessary to determine whether it is malignant or benign. However, when x-rays pass through a body part, they are known to scatter at small angles, with these various scattering angles being characteristic for different tissue types, each of which has it own unique chemical composition. Use of techniques that collect these scattered photons and characterize them and/or reconstruct CT data from them will allow the analysis of those abnormalities seen on monochromatic mammograms. The hope here is that one may be able to do noninvasive "biopsies" using only the small angle scattering data collected as the x-rays exit the breast.

10.3.3.2 K-Edge Imaging

In many diagnostic x-ray exams performed in radiology departments of hospitals and clinics, iodine is used (injected intravenously) like a dye to look at the kidneys, vessels, brain, heart, and so forth. It can be very toxic to all of those organs and can be deadly to many patients. Even a very small test dose to check the patient for allergies can kill. Still, if we can decrease the amount of dye that we give to a patient, we can make studies less harmful and much safer for all patients.

Currently, one must attain about a 1:16 dilution of x-ray dye in blood to perform acceptable first-pass angiography using digital equipment. Since we can tune monochromatic x-rays to relatively narrow bandwidth through a wide range of energies, we can specifically target the k-edge of many atomic species (Sr, Y, In, Ag, Cd, I, Ba, Gd, Au, Pt, etc.). By tuning to the binding energy of the k-shell electron we can image very dilute concentrations of these elements (1:256 dilution in plain films using iodine, 1:2048 with monochromatic CTs, and 1:100,000 in certain imaging geometries). It is also possible to substitute elements such as gadolinium (used in off-the-shelf MRI contrast agents) in place of iodinated contrasts now used in angiography or other vascular studies, or to use currently available drugs (or to design drugs) using elements not normally thought of as x-ray contrast agents.

While gadolinium-containing contrasts are already used occasionally as a replacement contrast material for angiograms in individuals who are allergic to iodinated contrast, the density of gadolinium is such that more material must be used to obtain the same radiographic density on the detector, thereby pushing the dose of the gadolinium agent needed much higher toward its own toxic limit.

Tumors are known to have very abnormal vasculature and it has been observed that these vessels are also "leaky." Injection of intravascular contrast agents makes tumors and other abnormalities easier to see, due to leakage of these agents from the vascular spaces into the extravascular interstitial spaces between cells. This phenomenon can be taken advantage of by infusing iodinated x-ray dye into a patient, then x-raying an area, such as the breast, first at an energy below the k-edge of the iodine (using a molybdenum tube), and then again above that k-edge (using a tungsten tube), and then subtracting one image from the other. Since these tubes put out spectra that are peaked above and below the k-edge, the data will be different in the two images. The subtracted image will bring out the k-edge effects caused by the presence of iodine and its selective interaction and markedly increased absorption at 33.2 keV. The area containing the leaked iodine becomes very obvious [28]. This same phenomenon can be used in a different way, however, with only one element

infused, that being a gadolinium-containing agent, which will also leak out of abnormal vessels, followed by imaging only at an energy level just above the gadolinium k-edge. For this to work most effectively, one needs a monochromatic beam. Breast tissues become more transparent the higher the x-ray energy used. At 50.2 keV and above the breast becomes much less "visible" to the beam and the detector, making it much easier to spot the leaked gadolinium without the need for two images or for the use of subtraction techniques.

New drugs that stick to certain tissues, tumors, or organs can and are being developed to take advantage of k-edge effects as well. This opens the door to doing coronary arteriography (a cardiac cath) merely by giving a small injection of dye into an arm vein rather than having to snake a catheter through the main veins and arteries of the heart itself to check on the status of those structures [29].

Drugs have also been designed to accumulate in certain tissues. By tuning the monochromatic x-rays to the k-edge of the metal or other atom engineered into the drug, one may reveal where the drug is then located, improving the ability to diagnose diseases of all sorts. Consider the improvements in early detection of coronary artery disease if one could administer a drug containing a heavy metal that was designed to accumulate in soft plaque (the substance that collects beneath the lining of heart vessels that causes heart attacks).

COX-2, on the other hand, is a protein that is produced in large quantities in many tumors (lung, colon, stomach, and breast) and in inflamed areas of the body. Oral anti-inflammatory agents exist that target COX-2. Imagine, if you would, that a patient could consume a pill containing one of these anti-inflammatory agents that was labeled with iodine, gadolinium, or platinum. It would then circulate and accumulate in the abnormal areas containing the COX-2 protein and show up quite nicely to a monochromatic beam tuned to the appropriate k-edge. This is truly molecular imaging at its best.

10.3.3.3 Phase Contrast Imaging

An entirely new field of x-ray imaging has emerged, using monochromatic x-rays. The images obtained contain new information and are quite striking. They may have applicability in mammography and the imaging of small parts and small animals. This is called phase contrast imaging [30–38].

Since the discovery of x-rays, imaging has relied on absorption information. If I were to pass an x-ray beam through your hand, the dense bones in your hand would absorb or block the x-rays from getting through. The shadow cast by the bones shows up on the film placed behind the hand as white areas. So an x-ray is like a shadowgram. Figure 10.13 is a high-resolution absorption image of a mimosa blossom and twig made at 10 keV at a synchrotron facility by Dr. Giorgio Margaritondo's group at Trieste, Italy.

Phase information picked up by x-rays traversing an imaged part contains far more information than that received via the absorption technique. Every x-ray that goes through your hand or a mimosa blossom and reaches the film carries with it 100 to 1000 times more information about the tissues or materials that it passed through than what one retrieves via the absorption method of imaging. This information relates to how dense the tissues are, where certain edges of different tissues lie, and

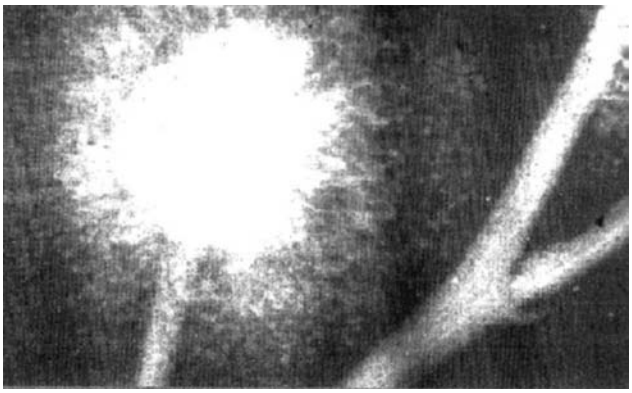

FIGURE 10.13 Standard x-ray absorption image of a mimosa blossom and twig using 10 keV monochromatic x-rays from a synchrotron. (Courtesy of Giorgio Margaritondo.)

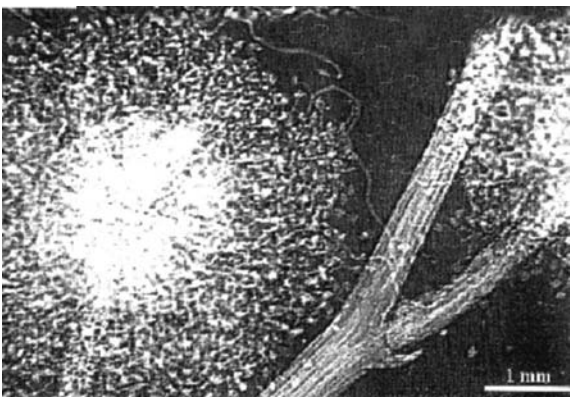

FIGURE 10.14 Phase contrast image of the same mimosa blossom and twig demonstrating the marked improvement in visibility of structural detail. (Courtesy of Giorgio Margaritondo.)

how much the tissues bend/refract the x-rays. If one can bring out those differences, one gets a phase contrast image of sorts. Figure 10.14 is a phase contrast image of the same mimosa blossom. The amount of detail revealed using this technique is striking.

The small effective focal spot used in the inverse Compton process is frequently in the sub-100-micron range, lending some lateral coherence to the beam. While many have published examples of work done at synchrotrons and articles on the usefulness of this type of imaging, none of the techniques to extract the phase information have been very practical. There are several techniques for obtaining phase contrast information with such a beam. These include: (1) x-ray interferometry [39], which requires intricate silicon interferometers that are small and difficult to make and are too fragile for everyday use in humans; (2) Laue crystal analysis [40], which

requires exceedingly difficult and expensive alignment of crystals and line scanning to build up an image; and (3) large object to detector distances [41], which entails merely moving back far enough to allow the diffracted/refracted beams to separate from the nonrefracted portion of the beam. These large separations of imaged part and detector create enormous magnification in the completed image, such that a bee's head is as large as a man's.

There are, however, very useful techniques that can be brought into play, which entail the use of distances much smaller/closer to both the source and the detector. These techniques are quite amenable to phase contrast work, and are moving forward at Vanderbilt University in an attempt to shorten the imaging distances to only a few feet, eliminating analyzing crystals and allowing one to acquire the image in one shot over an area of the body [42, 43].

10.3.3.4 Time-of-Flight Imaging

The x-rays produced by the monochromatic machines described herein emerge in bursts that last only 5–8 trillionths of a second. Because the beam is pulsed so quickly it has uses for unique types of imaging and for many military and industrial applications.

When x-rays traverse an object, some of them scatter about. Other x-rays don't hit anything and come through unscathed, so to speak. These latter photons are usually called ballistic photons. They exit an imaged part in a few picoseconds. Scattered x-ray photons describe a somewhat longer and circuitous path causing them to exit in nanoseconds. A detector observing the object, which goes "brain-dead" in about 100 ps after the beginning of an imaging acquisition, can be used to great advantage in time-of-flight (TOF) studies. The detector will ignore the nanosecond scattered photons. To date, the TOF detectors available to us are only good for softer beams (around 10 keV), so they are not yet practical for use in humans. They can be used though for physical processes that need to be studied in the picosecond timeframe. Using them in this way, we can improve the clarity with which we can detect things in the object imaged by 6 to 9 times, so it is worthwhile [44].

The pulsed structure of the x-ray beam can also be used to great effect for backscatter imaging and pulse ranging experiments or applications.

10.3.3.5 Protein Crystallography

Proteins are made up of many small building blocks, amino acids, strung together in a very complex way. It is the unique structure and folding of this string of beads back on itself that make protein work the way it does in our bodies. For scientists in the United States to completely determine the three-dimensional structure of a protein or a drug (for example, to be able to utilize the information for more rational drug development), they must grow the protein in their lab at very high purity, try to get it to crystallize into a little bead, then get dedicated time on an x-ray beamline at one of the six multibillion-dollar synchrotron facilities in the United States, go to that facility, study the crystal, decode the dots, so to speak, and then figure out the three-dimensional structure of the beast. Unfortunately, scientists don't really know if they have a nearly perfect crystal until they get it into the monochromatic beam

at the synchrotron. Currently, this all entails from 6 to 9 months of hard work, travel away from home, and trying to get a smoking canister containing specimens packed in dry ice through airport security (no mean feat in this day and age).

Standard copper anode x-ray sources delivering relatively bright x-ray outputs at 8.6 keV (the copper k-alpha line) can be used in the local laboratory setting to determine some of the information about a crystal, but one cannot glean the phase information needed for total reconstruction of the architecture of that crystal without the use of a narrow wavelength bright x-ray source (at 12.6 keV, the selenium k-edge) obtainable at synchrotrons. Does that kind of beam sound familiar?

Inverse Compton scattering is an ideal source of monochromatic x-rays for the performance of protein crystallography [45]. These sources cannot only put out the narrow bandwidth desired, but also can deliver beams of near-monochromatic x-rays that are more broadband to perform a wider range of crystallographic procedures, namely, standard crystallography, Laue crystallography (which uses several different wavelengths of x-rays at one time), and multiple anomalous dispersion (MAD) to obtain the phase information described above. This versatility is not even available at some synchrotrons. While a tabletop synchrotron source will require a longer time to obtain the diffraction pattern needed than at a regular synchrotron, an $8 million beamline is not needed, removing significant cost and allowing this type of x-ray beam to be readily available to universities and pharmaceutical firms on a 24/7 basis.

Should one desire to do crystallography using the beam from an inverse Compton device, such as that described here, one need only refocus the beam onto the protein crystal using a multilayered focusing optic such as those now available from commercial sources.

A tabletop monochromatic machine can do the same protein analysis at the scientist's home lab, so that it is immediately known whether the crystal is good, therefore speeding up the research process.

10.3.4 Military and Industrial Applications

There are many more applications for this type of x-ray device. Testing military and industrial hardware is among these.

The insides of turbines (jet engines, machines for generating electricity, etc.) are exposed to incredibly hostile environments. When one wants to get better efficiency out of these machines, it might be advantageous to run them at higher temperatures and pressures. Unfortunately, when pushed like this, they may fail catastrophically. This is not good, if the turbine failing is attached to the wing of the airplane in flight! To test new designs, manufacturers may ramp up the engine to test how far they can go before failure (testing to destruction). After the engine fails they frequently pick up the pieces and try to figure out what went wrong. However, if they could see inside the engine while it was running at full power and full temperature, they could get a better handle on what design changes need to be made to make it work harder and safer.

Since the energy levels of monochromatic x-ray machines can be pushed up very easily and since the beam is so fast, the insides of a turbine would look like they are standing still if imaged by one of these devices. One of our scientists likes to give an example of how fast our beam really is. He states with flair, "If a satellite were to

pass through a room at orbital velocity (the speed at which it orbits the earth—namely 17,500 miles per hour), and we were to take an x-ray of it with our beam while it was passing through, it would have moved only 1/100th the width of a human hair while we were taking its picture." So pulsed, tunable, monochromatic x-rays can be used to do nondestructive testing on items such as turbines or rocket engines without having to test them to destruction.

Studying explosive events would be easy for the beam as well. Munitions could be studied as they blow up, armor-piercing shells could be stopped at each layer as they penetrate various types of armor, and even small models of nuclear detonations could be studied to help in the stewardship of the nation's nuclear arsenal, so that weapons don't need to be set off in the atmosphere or underground.

Another obvious use for this type of radiation beam is the examination of composite materials to look for internal defects. This is particularly important when studying materials such as carbon-carbon composites that are now being used in the construction of new airplanes. In this regard, phase contrast imaging holds the most clearly defined advantage toward revealing abnormalities in low-Z materials that are not easily imaged by any other means in such high resolution [46–48].

10.4 THE FUTURE

While there have been various proposed modifications to electron accelerators, such as superconducting linacs and cyclotrons, and so on, to create x-rays with near-monochromaticity, only practical, relatively inexpensive, and compact machines will find usefulness at the point of applying the resultant beams to everyday problems that are just begging for more elegant solutions.

The ideas presented here are designed to decrease medical costs, reduce morbidity and mortality for patients, improve quality of life, and open up the new fields of molecular imaging and therapy where one's medical care can be tailored to each individual. Without powerful, tunable lasers, the realm of pulsed, tunable monochromatic x-rays would not have developed within our lifetimes. As accelerator and laser technology progresses, we anticipate that these monochromatic x-ray units will become even smaller, more portable, and eventually evolve into "all light" driven devices (as in laser wakefield accelerators) [49, 50].

Multidisciplinary planning, design, and execution will remain an absolute necessity for the success of this field. It behooves us all to find interested individuals with the knowledge surrounding these complex technologies and to establish the types of collaboration needed to move this field forward with all due speed. After all, we all come to a point in life where excellent medical care becomes most important to us and to our families. We can't let these types of opportunities go unexplored.

REFERENCES

1. Carroll, F. E., J. W. Waters, R. R. Price, C. A. Brau, C. F. Roos, N. H. Tolk, D. R. Pickens, and W. H. Stephens, Near-monochromatic x-ray beams produced by the Free Electron Laser and Compton backscatter, *Invest. Radiol*. 25: 465–471 (1990).
2. Carroll, F. E., J. W. Waters, R. H. Traeger, M. H. Mendenhall, W. W. Clark, and C. A. Brau, Production of tunable, monochromatic x-rays by the Vanderbilt Free-Electron Laser, *Proceedings SPIE. Free Electron Laser Challenges II*. 3614: 139–146 (1999).

3. Carroll, F. E., Tunable monochromatic x rays: a new paradigm in medicine, *AJR* 179: 583–590 (2002).
4. Carroll, F. E., M. H. Mendenhall, R. H. Traeger, C. A. Brau, and J. W. Waters, Pulsed tunable monochromatic X-ray beams from a compact source: new opportunities, *AJR* 181: 1197–1202 (2003).
5. Carroll, F. E., R. H. Traeger, M. H. Mendenhall, J. W. Waters, G. Edwards, and C. A. Brau, System and method for producing pulsed monochromatic X-rays, US Patent 6332017 (2001).
6. Carroll, F. E., R. H. Traeger, M. H. Mendenhall, J. W. Waters, G. Edwards, and C. A. Brau, System and method for producing pulsed monochromatic X-rays, US Patent 6687333 (2004).
7. Carroll, F. E., Tunable, monochromatic X-rays: an enabling technology for molecular/cellular imaging and therapy, *J. Cell Biochem.* 90: 502–508 (2003).
8. Goorley, T., R. Zamenhof, and H. Nikjoo, Calculated DNA damage from gadolinium auger electrons and relation to dose distributions in a head phantom, *Int. J. Radiat. Biol.* 80: 933–940 (2004).
9. Miller, R. A., K. Woodburn, Q. Fan, M. F. Renschler, J. L. Sessler, and J. A. Koutcher, In vivo animal studies with gadolinium (III) texaphyrin as a radiation enhancer, *Int. J. Rad. Oncol. Bio. Phys.* 45: 981–989 (1999).
10. Buchegger, F., F. Perillo-Adamer, Y. M. Dupertuis, and A. B. Delaloye, Auger radiation targeted into DNA: a therapy perspective, *EJNM* 33: 1352–1363 (2006).
11. Karnas, S. J., Y. Edward, R. C. McGarry, and J. J. Battista, Optimal photon energies for IUdR k-edge radiosensitization with filtered X-ray and radioisotope sources, *Phys. Med. Biol.* 44: 2537–2549 (1999).
12. Karnas, S. J., V. V. Moiseenko, E. Yu, P. Truong, and J. J. Battista, Monte Carlo simulations and measurement of DNA damage from x-ray-triggered Auger cascades in iododeoxyuridine (IUdR), *Rad. Environ. Biophys.* 40: 199–206 (2001).
13. Pignol, J. P., E. Rakovitch, D. Beachey, and C. L. Sech, Clinical significance of atomic inner shell ionization (ISI) and Auger cascade for radiosensitization using IUdR, BUdR, platinum salts, or gadolinium porphyrins compounds, *Int. J. Radiat. Oncol. Biol. Phys.* 55: 1082–1091 (2003).
14. Young, L. A., I. J. Kalet, J. S. Rasey, and J. A. Nelson, 125I brachytherapy k-edge dose enhancement with AgTPPS4, *Med. Phys.* 25: 709–718 (1998).
15. Mackonis, E. C., N. Suchowerska, M. Zhang, M. Ebert, D. McKenzie, and M. Jackson, Cellular response to modulated radiation fields, *Phys. Med. Biol.* 52: 5469–5482 (2007).
16. Biston, M. C., A. Joubert, J. F. Adam, H. Elleaume, S. Bohic, A. M. Charvet, F. Estève, N. Foray, and J. Balosso1, Cure of fisher fats bearing Radioresistant F98 Glioma treated with *cis*-Platinum and irradiated with monochromatic synchrotron x-rays, *Cancer Res.* 64: 2317–2323 (2004).
17. Laster, B., private communication.
18. Brody, A. S., D. P. Frush, W. Huda, and R. L. Brent, Radiation risk to children from computed tomography, *Pediatrics* 120: 677–682 (2007).
19. Middleton, J. A., Brain injury in children and adolescents, *Adv. Psy. Treat.* 7: 257–265 (2001).
20. Chuba, P. J., P. Aronin, K. Bhambhani, M. Eichenhorn, L. Zamarano, P. Cianci, M. Muhlbauer, A. T. Porter, and J. Fontanesi, Hyperbaric oxygen therapy for radiation-induced brain injury in children, *Cancer* 80: 2005–2012 (1997).
21. Oi, S., T. Kokunai, A. Ijichi, S. Matsumoto, and A. J. Raimondi, Radiation-induced brain damage in children. Histological analysis of sequential tissue changes in 34 autopsy cases, *Neurol. Med. Childr.* 30: 36–42 (1990).
22. Armstrong, C. L., K. Gyato, A. W. Awadalla, R. Lustig, and Z. A. Tochner, A critical review of the clinical effects of therapeutic irradiation damage to the brain: the roots of controversy, *Neuropsy. Rev.* 14: 65–86 (2004).

23. Qui, D., D. L. Kwong, G. C. Chan, L. H. Leung, and P. L. Khong, Diffusion tensor magnetic resonance imaging finding of discrepant fractional anisotropy between the frontal and parietal lobes after whole-brain irradiation in childhood medulloblastoma survivors: reflection of regional white matter radiosensitivity? *Int. J. Rad. Oncol. Biol. Phys.* 69: 846–851 (2007).
24. Hall, E. J., Intensity-modulated radiation therapy, protons, and the risk of second cancers, *Int. J. Rad. Oncol. Biol. Phys.* 65: 1–7 (2006).
25. Johns, P. C., and M. J. Yaffe, X-ray characterization of normal and neoplastic breast tissues, *Phys. Med. Biol.* 32: 675–695 (1987).
26. Carroll, F. E., J. W. Waters, W. W. Andrews, R. R. Price, D. R. Pickens, R. Willcott, P. Tompkins, C. Roos, D. Page, G. Reed, A. Ueda, R. Bain, P. Wang, and M. Bassinger, Attenuation of monochromatic x-rays by normal and abnormal breast tissues. *Invest. Rad.* 29: 266–272 (1994).
27. Boone, J. M., Glandular breast dose for monoenergetic and high energy x-ray beams: monte carlo assessment, *Radiology* 213: 23–37 (1999).
28. Lewin, J. M., P. K. Isaacs, V. Vance, and F. J. Larke, Dual energy contrast enhanced digital subtraction mammography: feasibility, *Radiology* 229: 261–268 (2003).
29. Sarnelli, A., A. Taibi, P. Baldelli, M. Gambaccini, and A. Bravin, Quantitative analysis of the effect of energy separation in k-edge digital subtraction imaging, *Phys. Med. Biol.* 552: 3015–3026 (2007).
30. Arfeli, F., and V. Bonvicine, Mammography with synchrotron radiation phase detection techniques, *Radiology* 215: 286–293 (2000).
31. Dilmanian, F. A., Computed tomography with monochromatic x-rays, *Am. J. Physiol. Im.* 7: 175–193 (1992).
32. Kirby, B. J., J. R. Davis, J. A. Grant, and M. J. Morgan, Monochromatic microtomographic imaging of osteoporotic bone, *Phys. Med. Biol.* 7: 1375–1385 (1997).
33. Dilmanian, F. A., X. Y. Wu, E. C. Parsons, B. Ren, J. Kress, T. M. Button, L. D. Chapman, J. A. Coderre, F. Giron, D. Greenberg, D. J. Krus, Z. Liang, S. Marcovici, M. J. Petersen, C. T. Roque, M. Shleifer, D. N. Slatkin, W. C. Thomlinson, K. Yamamoto, and Z. Zhong, Single- and dual-energy CT with monochromatic synchrotron x-rays, *Phys. Med. Biol.* 42: 371–387 (1997).
34. Kleuker, U., P. Suortti, W. Weyrich, and P. Spanne, Feasibility study of x-ray diffraction computed tomography for medical imaging, *Phys. Med. Biol.* 43: 2911–2923 (1998).
35. Burattini, E., M. Gambaccini, P. L. Indovina, M. Pocek, and G. Simonetti, Synchrotron radiation: a new source in x-ray mammography, *Rad. Med. (Torino)* 84: 181–188 (1992).
36. Johnston, E., D. Washburn, E. Pisano, C. Burns, W. C. Thomlinson, L. D. Chapman, F. Arfelli, N. F. Gmur, Z. Zhong, and D. Sayers, Mammographic phantom studies with synchrotron radiation, *Radiology* 200: 659–663 (1996).
37. Lewis, R., Medical applications of synchrotron radiation x-rays, *Phys. Med. Biol.* 42: 1213–1243 (1997).
38. Arfelli, F., et al., Digital mammography with synchrotron radiation, *Rev. Sci. Instrum.* 66: 1325–1328 (1995).
39. Takeda, T., A. Momose, Y. Itai, J. Wu, and K. Hirano, Phase-contrast imaging with synchrotron x-rays for detecting cancer lesions. Preliminary investigation, *Acad. Rad.* 2: 799–803 (1995).
40. Chapman, D., W. Thomlinson, R. E. Johnston, D. Washburn, E. Pisano, N. F. Gmur, Z. Zhong, R. Menk, F. Arfelli, and D. Sayers, Diffraction enhanced x-ray imaging, *Phys. Med. Biol.* 42: 2015–2025 (1997).
41. Hwu, Y., W. L. Tsai, H. M. Chang, H. I. Yeh, P. C. Hsu, Y. C. Yang, Y. T. Su, H. L. Tsai, G. M. Chow, P. C. Ho, S. C. Li, H. O. Moser, P. Yang, S. K. Seol, C. C Kim, J. H. Je, E. Stefanekova, A. Groso, and G. Margaritondo, Imaging cells and tissues with refractive index, *Rad. Biophys. J.* 87: 4180–4187 (2004).

42. Donnelly, E. F., R. R. Price, and D. R. Pickens, Dual focal-spot imaging for phase extraction in phase-contrast radiography, *Med. Phys*. 30: 2292–2294 (2003).
43. Donnelly, E. F., R. R. Price, K. G. Lewis, and D. R. Pickens, Polychromatic phase-contrast computed tomography, *Med. Phys*. 34: 3165–3168 (2007).
44. Gordon, C. L., Y. Yin, B. E. Lemoff, P. M. Bell, and C. P. N. Barty, Time-gated imaging with an ultrashort pulse, laser-produced plasma x-ray source, *Opt. Letts*. 20: 1056–1058 (1995).
45. Harteman, F. V., H. A. Baldis, A. K. Kerman, A. Le Foll, N. C. Luhmann, and B. Rupp, Three-dimensional theory of emittance in Compton scattering and x-ray protein crystallography, *Phys Rev. E*. 64: 016501 (2001).
46. Martin-Herrero, J., and Ch. Germain, Microstructure reconstruction of fibrous C/C composites from x-ray microtomography, *Carbon* 45: 1242–1253 (2007).
47. Pawar, P. M., and R. Ganguli, On the effect of progressive damage on composite helicopter rotor system behavior, *Comp. Struct*. 78: 410–423 (2007).
48. Hentschel, M. P., A. Lange, and J. Schors, NDE of microstructured materials by X-ray diffraction and refraction topography, *Proc. Euro. Conf. Non Destruct. Testing*, Th. 1.2.4, 1–8 (2006).
49. Luttihof, M. J. H., A. G. Khachatryan, F. A. van Goor, and K. J. Boller, The effect of vacuum-plasma transition and injection angle on electron-bunch injection into a laser wakefield, *Phys. Plasmas* 14: 83101 (2007).
50. Leemans, W. P., B. Nagler, A. J. Gonsalves, C. S. Toth, K. Nakamura, C. G. R. Geddes, E. Esarey, C. B. Schroeder, and S. M. Hooker, GeV electron beams form a centimeter-scale accelerator, *Nature Phys*. 2: 696–699 (2006).

11 Lithium Spectroscopy Using Tunable Diode Lasers

I. E. Olivares

CONTENTS

11.1 Introduction 311
11.2 Description of Saturated Absorption Spectroscopy 312
11.3 Multilevel Atoms 314
11.4 Semiquantitative Ideas at Two-Level Atoms 314
11.5 Detailed Saturated Absorption Calculations Using Matrix Elements 315
11.6 The Saturated Absorption Spectrometer 319
11.7 Spectroscopic Calculations 320
11.8 Using a Diode Laser for Resonance Ionization Spectroscopy 321
11.8.1 Energy Level Diagram 322
11.8.2 Estimate of the Laser-Produced Ions at the End of a Laser Pulse 323
11.8.3 Resonance Ionization Spectrometer 326
11.8.4 Resonance Ionization Spectra 328
11.8.5 Discussion and Conclusion 329
11.9 Lithium Isotope Separation Using Tunable Diode Lasers 330
11.9.1 Experimental Details 331
11.9.2 Laser System 331
11.9.3 Isotope Separation Apparatus 332
11.9.3.1 Calibration of the Magnetic Sector 332
11.9.4 Experimental Overview 333
11.9.5 Lithium Laser Isotope Separation 334
11.9.6 Discussion and Conclusion 336
11.10 Application of Lithium Isotopes 336
Acknowledgments 336
References 337

11.1 INTRODUCTION

Dispersive external-cavity semiconductor lasers have been widely used over the last few decades in laser spectroscopy [1–3]. They have been employed in environmental

physics, basic fundamental physics with slow atoms, and in Bose–Einstein condensation [4], electromagnetic induced transparency [5], saturated absorption spectroscopy [6–9], basic research on atomic clocks [10], plasma spectroscopy [11], fiber-optic communications, resonance ionization spectroscopy [12], and isotope separation [13]. They have been used to detect the effect of the electric field in the breakdown of discharges and to measure densities and concentrations of impurities in research plasmas [14]. The use of diode lasers for spectroscopic applications is developed in detail in [1–3, 15–17].

This chapter presents the use of this class of lasers in neutral gas experiments, describing the physics of the interaction between the laser and metal vapors. We also show how to use a diode laser combined with a Nd:YAG laser to ionize selectively previously excited species. A resonant ionization spectroscopy experiment in a heat pipe oven serves as a starting point to demonstrate the possibility of selectively ionizing lithium isotopes employing a diode laser in a two-step ionization scheme. Furthermore, in an isotope separation experiment the previously selected isotope ions can be separated physically with a mass spectrometer consisting of an acceleration stage and an ion extraction stage. Ion-focusing optics and a permanent magnet were used for simplicity. The experiment has a high sensitivity and selectivity and allowed for the resolution of all lithium lines. This was the first time these lasers were used for this purpose. Tunable lasers that are useful for this type of application include CW dye lasers [18] and narrow-linewidth copper-vapor-laser (CVL)-pumped dye lasers [19–24]. This is relevant in the nuclear power industry [25].

11.2 DESCRIPTION OF SATURATED ABSORPTION SPECTROSCOPY

Saturated absorption spectroscopy is a simple technique to measure the narrow-line atomic spectral feature limited only by the natural linewidth, which is typically 6 MHz or less [6–9]. A strong laser beam called a pump beam is sent through a cell that contains a vapor, as shown in Figure 11.1.

A small part of the pump laser beam is used as a probe beam and is sent in the opposite direction and detected by a simple photodiode. To obtain the full spectral feature, the laser should be scanned in frequency. In the case of a two-level system the spectral feature with and without a pump beam looks like Figure 11.2.

The upper feature is the detected intensity when the pump laser is blocked (Fig. 11.2a). It shows the Doppler-broadened spectral line, which is much broader than the natural linewidth. In the case of weak absorption the feature is a simple

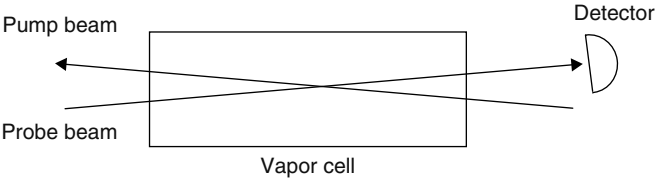

FIGURE 11.1 Basic setup for saturation absorption spectroscopy.

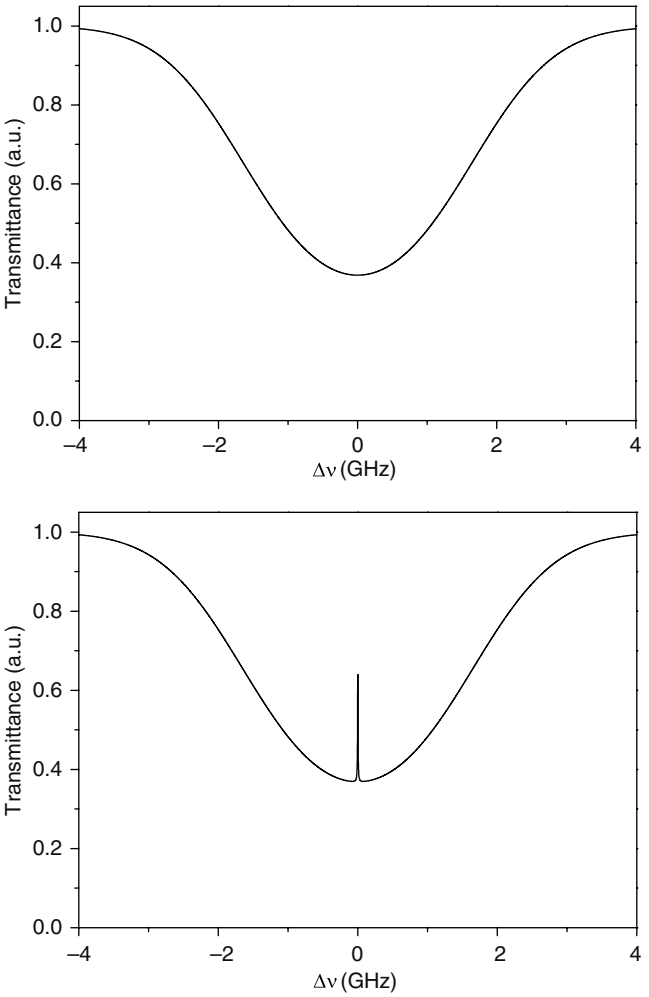

FIGURE 11.2 Absorption (a) with and (b) without pump laser, Lamb dip.

Gaussian profile. The atoms in the vapor move with different velocities following the Boltzmann velocity distribution. Defining longitudinal velocity as the velocity component of the atoms along the probe beam, we observe that some atoms move with longitudinal velocity opposite from the probe beam propagation, and other atoms move with longitudinal velocity in the same direction as the probe beam propagation. The lower feature (Fig. 11.2b) is the detected intensity of the probe beam with a pump laser. It shows a spike just at the frequency v_0 for atomic resonance. When the laser is tuned at $v_0 - \Delta v$, it will be absorbed only by the atoms moving toward the probe laser with longitudinal velocity $\upsilon \approx c\Delta v/v_0$. Other atoms with different longitudinal velocities will not be absorbed by this beam because they are not in resonance with the probe beam, so they don't contribute to the absorption. The pump laser coming from the opposite direction will be absorbed only by the atoms with opposite velocity

and the signal of the probe beam will not be affected. The only case where this does not apply is for atoms with $\upsilon = 0$. In this case the pump laser will bring atoms from the ground state to the excited state, and, if the pump laser is strong enough, the probe laser will find the excited state populated and the absorption of the probe laser will decrease. This is due to stimulated emission. In the case the pump beam is infinity, the population will be inverted and the atoms are saturated. In this case no photon can be absorbed. The Doppler-free saturated absorption spectroscopy allows for removing the Doppler feature due to the saturation of the atoms at rest.

11.3 MULTILEVEL ATOMS

If the atoms have two excited states (1 and 2) whose separation is smaller than the Doppler linewidth, and a single ground state, the spectra will show two spikes at each atomic resonance frequency ν_1 and ν_2 and one spike just half between these resonance frequencies, for instance, at the frequency $\nu_c = (\nu_1 + \nu_2)/2$. The extra spike is called the crossover resonance. It appears because the laser beam with frequency ν_c will be in resonance with the group of atoms with longitudinal velocity $\upsilon \approx c(\nu_1 - \nu_c)/\nu_0$ moving toward one of the beams, and the opposite beam will be in resonance with the group of atoms with the same velocity but moving in the opposite direction. In this case, when the pump beam is strong enough, the single ground state will be depleted and the probe beam will not be absorbed. The spike at the crossover will show a decrease in the absorption.

If the atoms have two ground states (1 and 2) whose separation is smaller than the Doppler linewidth, and a single excited state, the crossover will be inverted compared to the previous case. The reason for this is optical pumping [26]. The pump laser will excite the atoms from one ground state, but these atoms will decay due to spontaneous emission to the other ground state. The probe laser will find a full ground state, and its absorption will increase.

11.4 SEMIQUANTITATIVE IDEAS AT TWO-LEVEL ATOMS

The basic ideas obtained from this two-level system can be used for understanding multilevel atoms. In the case of a two-level atom it is possible to obtain a crude calculation of the Doppler-free spectra by considering the transmission of the probe laser beam through the cell $e^{-\tau(\nu)}$, where $\tau(\nu)$ is the optical depth of the vapor.

The contribution to $\tau(\nu)$ from one velocity group of atoms is given by

$$d\tau(\nu,\upsilon) \sim (P_1 - P_2)F(\nu,\upsilon)dn(\upsilon) \tag{11.1}$$

where P_1 is the relative population of the ground state, P_2 is the relative population of the excited state,

$$dn = \exp(-m\upsilon^2/k_B T)d\upsilon \tag{11.2}$$

is the Boltzmann distribution (for υ along the beam axis), and representing the group of atoms with velocities between υ and $\upsilon + d\upsilon$

$$F(\nu,\upsilon) = \frac{\Gamma/2\,\pi}{(\nu - \nu_0 + \nu_0\upsilon/c)^2 + \Gamma^2/4} \tag{11.3}$$

is the normalized Lorentzian absorption profile of an atom with natural linewidth Γ, including the Doppler shift, which can be explained by a forced dipole oscillator model. In summary, the differential contribution to the optical depth for laser frequency ν and atomic velocity υ is

$$d\tau(\nu,\upsilon) = \tau_0(P_1 - P_2)F(\nu,\upsilon)\exp(-m\upsilon^2/k_BT)d\upsilon \tag{11.4}$$

τ_0 is the optical depth at the center of resonance line $\nu = \nu_0$ when the pump laser is blocked. The integral is over all velocity groups. The population rate equations are

$$P_1 + P_2 = 1 \tag{11.5}$$

and

$$\dot{P}_1 = \Gamma P_2 - B_{12} I\,(P_1 - P_2) \tag{11.6}$$

where the first term is from spontaneous emission, with Γ = 5.8 MHz for the case of lithium, and the second term is from the absorption and stimulated emission, with B_{12} proportional to $F(\nu, -\upsilon)$ and the intensity I of the laser beam. The minus sign for velocity is because the pump beam acts on atoms with opposite velocity. In the steady state $\dot{P}_1 = \dot{P}_2 = 0$, and defining $\delta_- = \nu - \nu_0 - \nu_0\upsilon/c$, which is the pump beam detuning from resonance, we have

$$P_2(\nu,\upsilon) = \frac{s/2}{1 + s + 4\delta_-^2/\Gamma^2} \tag{11.7}$$

with $s = I/I_{sat}$ the saturation parameter and $I_{sat} = 2\pi^2 hc\Gamma/3\lambda^3$.

Equation 11.4 can be plotted for different saturation parameters and different optical depths showing the Lamb dip. For three or more levels a detailed calculation is necessary.

11.5 DETAILED SATURATED ABSORPTION CALCULATIONS USING MATRIX ELEMENTS

The rate equations for populations at different levels are given by [8, 27–28]

$$\dot{\rho}_{ii} = \sum_{f=1}^{12} W_{if}(\rho_{ff} - \rho_{ii}) + (\gamma_T + \gamma_{VC})(\rho_{ii}^0 - \rho_{ii}) + \sum_{f=1}^{12} a_{fi}\rho_{ff}$$

$$\dot{\rho}_{ff} = \sum_{i=1}^{6} W_{if}(\rho_{ii} - \rho_{ff}) + (\gamma_T + \gamma_{VC})(\rho_{ff}^0 - \rho_{ff}) - \gamma\rho_{ff} \tag{11.8}$$

where $W_{if} = \dfrac{1/2\,|\Omega_{if}|\Gamma}{(\delta_{if} - \mathrm{k}v)^2 + \Gamma^2}$ is the transition rate,

$$|\Omega_{if}|^2 = \frac{8\pi I K_e}{c\hbar^2}\left|\langle i|D_0|f\rangle\right|^2 \text{ is the Rabi frequency}$$

for linear polarized light, $K_e = 8.99 \times 10^9$ Vm/C, I is the intensity of the laser radiation, $\Gamma = \gamma/2 + \Gamma_T + \Gamma_L + \Gamma_{VC}$ is the homogeneous broadening, $\delta_{if} = \omega - \omega_{if}$ is the laser detuning from resonance, $\omega_{if} = 2\pi(v_1 - v_f)$ is the resonance angular frequency of the line, $\gamma/2$ is the natural linewidth, Γ_c is the broadening that is due to collisions, Γ_L is the laser linewidth, and Γ_T is the transit-time broadening. The apparent pumping by transit among different states is caused by the exit or entrance of atoms in the excitation region. This effect occurs because outside the excitation region the atoms are distributed uniformly among their ground states, and inside the region the distribution of levels is controlled by the laser. The transit-time relaxation rate is given by $\gamma_T = \upsilon/d$, where υ is the mean velocity of the atoms and d is the diameter of the laser beam. The velocity changing collisions (VCC) act similarly to transit-time broadening. VCCs caused by buffer-gas perturbers remove atoms from a velocity group out of resonance and bring atoms from other velocity groups into resonance. When optical pumping or buffer-gas pressure is low, and collisional relaxation and spontaneous emission are fast enough with respect to velocity of the atoms, the population of the atoms outside the resonant velocity group can be approximated by $\rho_{ff}^0 \approx 0$ and $\rho_{ii}^0 \approx 1$, where n is the number of ground states. In the D_2 line of ^{6}Li there are 18 states grouped into three excited and two ground Zeeman multiplets (see Fig. 11.3). In the case of the D_2 line of ^{6}Li we have $i = 1$ to 6 and $f = 7$ to 18.

In the case of lithium, 18 states are distributed in five Zeeman multiplets. As the collisional relaxation is relatively strong, the population of each state can be considered approximately equal to the other states of the same multiplet. With this approximation it is possible to consider each multiplet as a single state. For example, the rate equations for the first two states (Fig. 11.3) are given by

$$\begin{aligned}
\dot{\rho}_{11} &= W_{17}(\rho_{77} - \rho_{11}) + W_{1,10}(\rho_{10,10} - \rho_{11}) \\
&\quad + 3\gamma(8/81\rho_{77} + 16/81\rho_{88} + 5/27\rho_{99} + 10/81\rho_{10,10} + 5/81\rho_{11,11}) \\
&\quad + (\gamma_T + \gamma_{VC})(1/6 - \rho_{11}) \\
\dot{\rho}_{22} &= W_{28}(\rho_{88} - \rho_{22}) + W_{2,11}(\rho_{11,11} - \rho_{22}) \\
&\quad + 3\gamma(16/81\rho_{77} + 8/81\rho_{88} + 5/81\rho_{10,10} + 10/81\rho_{11,11} + 5/27\rho_{12,12}) \\
&\quad + (\gamma_T + \gamma_{VC})(1/6 - \rho_{22})
\end{aligned} \tag{11.9}$$

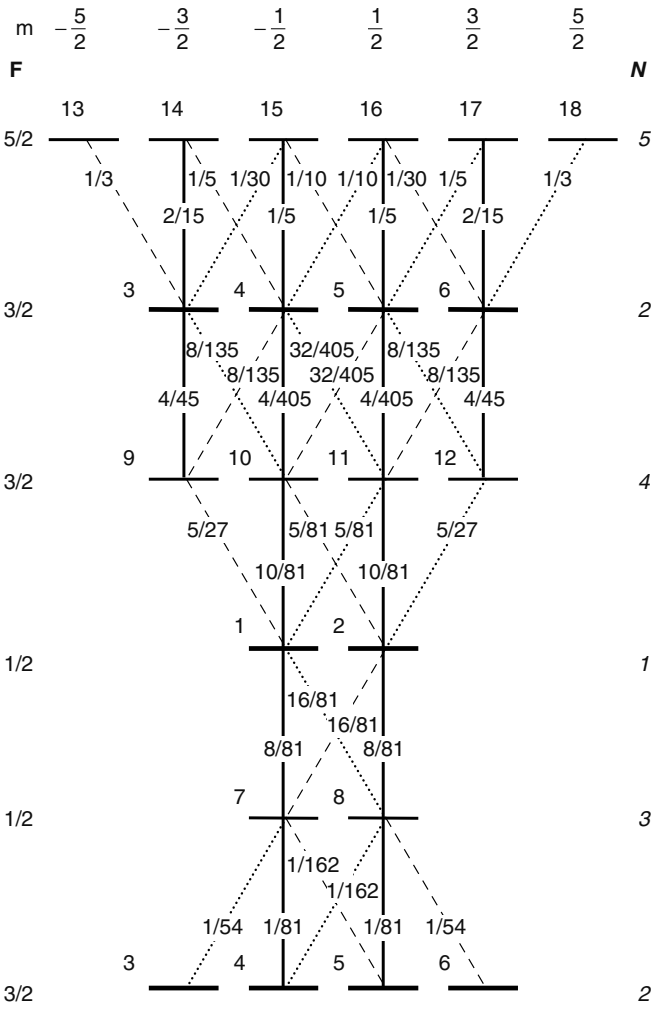

FIGURE 11.3 Values of $N_{ifq} = |\langle i|D_q|f\rangle|^2/\|D\|^2$ for each transition of Li. N labels the five Zeeman multiplets discussed in the text (note that $N = 2$ is shown twice). Thicker horizontal lines, ground states ($J = 1/2$); thinner horizontal lines, excited states ($J = 3/2$); dotted lines, transitions with $q = -1$; vertical lines, transitions with $q = 0$; dashed lines, transitions with $q = 1$.

With the approximation indicated above and the multiplet numbering of Figure 11.3, the rate equation for the first multiplet is

$$\begin{aligned}\dot{\rho}_{11} = {} & W_{13}(\rho_{33} - \rho_{11}) + W_{14}(1/2\,\rho_{44} - \rho_{11}) + \gamma(8/9\rho_{33} + 5/9\rho_{44}) \\ & + (\gamma_T + \gamma_{VC})(1/3 - \rho_{11})\end{aligned} \tag{11.10}$$

where W_{13} is the average of W_{17} and W_{28} and $\rho_{77} = \rho_{88} = 1/2\rho_{33}$ as the multiplet 3 has two states. Analogously, it is possible to obtain equations for all five multiplets.

$$\dot{\rho}_{11} = W_{13}(\rho_{33} - \rho_{11}) + W_{14}(1/2\rho_{44} - \rho_{11}) + \gamma(8/9\rho_{33} + 5/9\rho_{44}) + (\gamma_T + \gamma_{VC})(1/3 - \rho_{11})$$

$$\dot{\rho}_{22} = W_{25}(2/3\rho_{55} - \rho_{22}) + W_{24}(\rho_{44} - \rho_{22}) + W_{23}(\rho_{33} - 1/2\rho_{22}) + \gamma(1/9\rho_{33} + 4/9\rho_{44} + \rho_{55}) + (\gamma_T + \gamma_{VC})(2/3 - \rho_{22})$$

$$\dot{\rho}_{33} = W_{13}(\rho_{11} - \rho_{33}) + W_{23}(1/2\rho_{22} - \rho_{33}) - \gamma\rho_{33} - (\gamma_T + \gamma_{VC})\rho_{33} \tag{11.11}$$

$$\dot{\rho}_{44} = W_{24}(\rho_{22} - \rho_{44}) + W_{14}(\rho_{11} - 1/2\rho_{44}) - \gamma\rho_{44} - (\gamma_T + \gamma_{VC})\rho_{44}$$

$$1 = \rho_{11} + \rho_{22} + \rho_{33} + \rho_{44} + \rho_{55}$$

The absorption of the laser light in a vapor with density n and length dx is

$$dI(\nu) = h\nu_{if} n \left\langle \sum_{if} W_{if}(\rho_{ff} - \rho_{ii}) \right\rangle dx = h\nu_{if} n\gamma' \left\langle \rho_e \right\rangle dx \tag{11.12}$$

where the angle brackets indicate the average over the normalized velocity distribution for a vapor at temperature T, given by

$$F(\upsilon) = \left(\frac{m}{2\pi k_B T} \right)^{1/2} \exp\left(-\frac{m\upsilon^2}{2k_B} T \right) \tag{11.13}$$

for a vapor at temperature T, and $W_{if} = W_{if}(I_d, \upsilon)$ is the transition rate given only by the diagnostic beam with intensity I_d.

Extending the absorption equations to the Doppler-free saturation spectroscopy amplitude modulation case, we have

$$dI_d^0 - dI_d = h\nu_{if} n \left\langle \sum_{if} W_{if}^+ (\rho_{ff}^+ - \rho_{ii}^+) \right\rangle dx - h\nu_{if} n \left\langle \sum_{if} W_{if}^+ (\rho_{ff}^- - \rho_{ii}^-) \right\rangle dx \tag{11.14}$$

The populations depends on $W^+ = W(I_d, \upsilon)$, which is the transition rate given by the diagnostic beam with intensity I_d, and $W^- = W(I_p, -\upsilon)$, which is the transition rate given by the pump beam with intensity I_p propagating in the opposite direction. $\rho_{ii}^+ = \rho_{ii}(W^+)$, $\rho_{ii}^- = \rho_{ii}(W^+ + W^-)$, $dI^0{}_d$ is the absorption during the dark periods of the modulation cycle ($I_p = 0$), and dI_d is the absorption during the illumination period.

When optical pumping is slow compared with the collisional transition rate, it is possible to make the two-state approximation

$$\dot{P}_1 = W_{12}\left(\frac{g_1}{g_2} P_2 - P_1 \right) - \gamma' P_2 \tag{11.15}$$

where $P_1 = \rho_{11} + \rho_{22}$ is the population of the ground states, P_2 is the population of the excited states, $\rho_{11} = P_1/3$, $\rho_{22} = 2P_1/3$, $\rho_{33} = P_2/6$, and $\rho_{55} = P_2/2$. The transition rate W_{12} is the sum of the transition rates W_{ij} divided by the number of ground states and g_1 and g_2 are the degeneracies of each level.

Considering Equation 11.12 at low laser intensity we have

$$dI = -\sigma In \, \mathrm{d}x \tag{11.16}$$

where

$$\sigma = \frac{h\nu\gamma'}{I}\langle P_2 \rangle \tag{11.17}$$

is the absorption cross-section. As the homogeneous broadening is small compared to the Doppler width, and isolating P_2 in the steady state in Equation 11.15 and inserting it into Equation 11.17, we obtain the absorption coefficient

$$k_\nu = \sigma n = \frac{g_2}{g_1}\frac{n}{\tau}\frac{\lambda^2\sqrt{\ln 2}}{4\pi^{3/2}}\frac{1}{\Delta\nu_D}\frac{1}{\sqrt{1+S_0}} \times \exp\left[-\frac{4\ln 2}{\Delta\nu_D^2}(\nu-\nu_0)^2\right] \tag{11.18}$$

where

$$\Delta\nu_D = \left(\frac{8k_B T \ln 2}{m\lambda^2}\right)^{1/2} \tag{11.19}$$

is the Doppler width that can be used to estimate the temperature and

$$S_0 = \frac{1}{2}\left(1+\frac{g_2}{g_1}\right)\frac{1}{\gamma'\Gamma}\frac{\lambda^3 I}{2\pi ch\tau}\frac{g_2}{g_1} \tag{11.20}$$

is the saturation parameter. The intensity of the transmitted light is given by $I_\nu = I_0 \exp(-k_\nu x)$ where k_ν is the absorption coefficient and x is the length of the Li vapor path. The density of the different isotopes can be obtained integrating k_ν over each line

$$\int k_\nu d\nu = \frac{\lambda_0^2}{8\pi}\frac{g_2}{g_1}\frac{n}{\tau} \tag{11.21}$$

11.6 THE SATURATED ABSORPTION SPECTROMETER

The setup of a typical saturated absorption experiment is depicted in Figure 11.4.

The Li vapor is produced in a heat pipe cell (Comstock, Model HP-802) that permits the heating of Li to 700 °C. The cell should be purged initially and be held

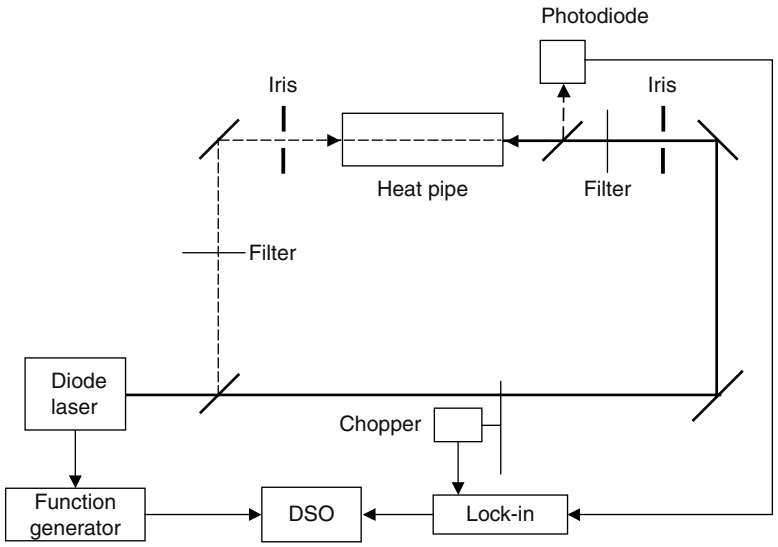

FIGURE 11.4 Doppler-free experimental setup: DSO, digital storage oscilloscope.

at a pressure of 2–3 bar Ar, which is used as a buffer gas to avoid deposition of Li onto the windows. The cell contains a stainless-steel grid that collects Li condensed at the cold regions. The main advantage of the heat pipe cell is an isothermal vapor with constant density and clean windows for absorption measurements.

A narrowband tunable diode laser was used for excitation (NewFocus, Model 6200). It has a central wavelength of 671 nm, tunable over 12 nm with a power of 6 mW.

The experiments presented here used 95% enriched Li. The laser was divided in two parts using a glass plate. The low-intensity beam was used as a probe beam and steered through the cell to a second glass plate and a photodiode. The pump beam was steered in the opposite direction. The modulation amplitude technique used a lock-in amplifier and an optical chopper.

11.7 SPECTROSCOPIC CALCULATIONS

Typical Doppler-limited absorption spectra are shown in Figures 11.5a and b. The circles represent the experimental points, and the curves are theoretical fits from Equation 11.18 and Beer's law $I_\nu = I_0 \exp(-k_\nu x)$.

A typical Doppler-free spectrum for the ^{6}LiD_2 line at low Ar pressure is shown in Figure 11.6a. The crossover signal in this figure is well resolved and just halfway between the two hyperfine Lamb dips. The right and left peak lines correspond to the transition $2s(F = 1/2)$–$2p$ and $2s(F = 3/2)$–$2p$ hyperfine lines, respectively separated by 228 MHz. In this case the pump beam is tuned to one transition, increasing in the common upper level that decays to the other lower level, thereby increasing the absorption.

The competition between optical pumping and collisional relaxation determined the size of the crossover dip. In the case of low pressure, optical pumping dominates and we have a negative crossover signal (Fig. 11.6a). In the case of high Ar pressure, the collision process that produces relaxation from the lower filled state to the other

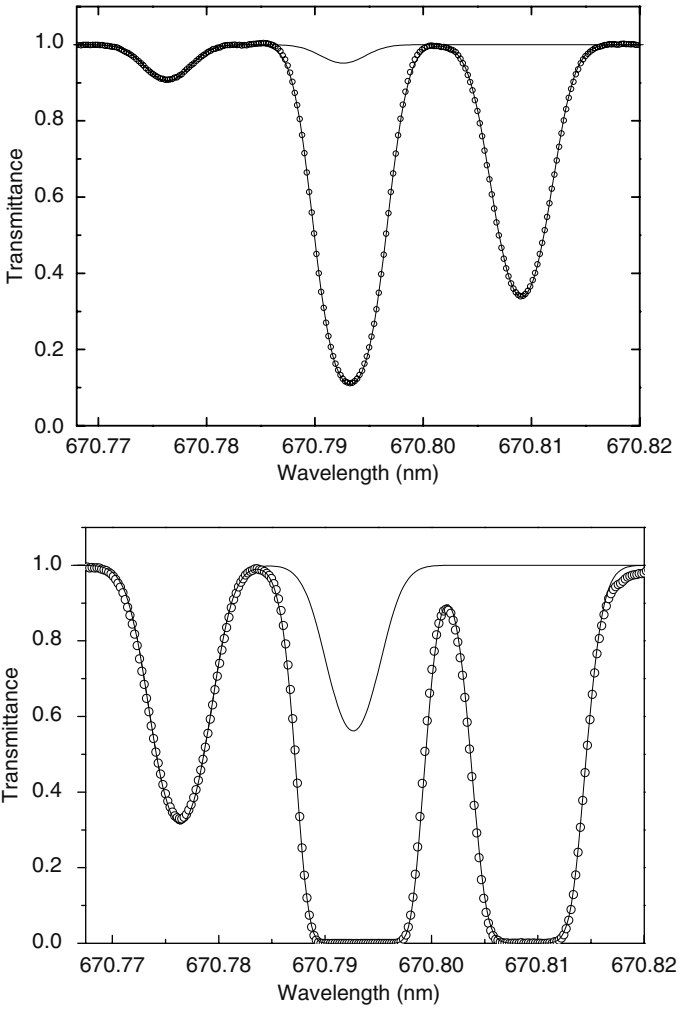

FIGURE 11.5 (a) Doppler-limited ^{7}Li only and for the sum of ^{6}Li and ^{7}Li. $n(^7\text{Li}) = 1.9 \times 10^{-9}$ cm^{-3}, $n(^6\text{Li}) = 4.6 \times 10^{10}$ cm^{-3}, $T = 480$°C, ^{7}Li(4.1%). (b) Optically thick Doppler-limited Li lines. Experimental and least squares fits for ^{7}Li only and for the sum of ^{6}Li and ^{7}Li. $n(^7\text{Li}) = 2.5 \times 10^{10}$ cm^{-3}, $n(^6\text{Li}) = 4.6 \times 10^{11}$ cm^{-3}, T = 549 °C.

lower level (the opposite velocity group) causes an increase in transmission, reducing the crossover signal. This result is shown in Figure 11.6b. These experimental spectra (Figs. 11.6a and b) show excellent resolution of the hyperfine spectra and are fairly well fitted with our density matrix model.

11.8 USING A DIODE LASER FOR RESONANCE IONIZATION SPECTROSCOPY

A tunable diode laser and a fourth harmonic generation (FHG) Nd:YAG laser emitting at $\lambda = 266$ nm were employed to resolve the photoionization spectra at $^2P\ 2s$–$2p$ for the ionization process in lithium isotopes. A well-collimated lithium beam and

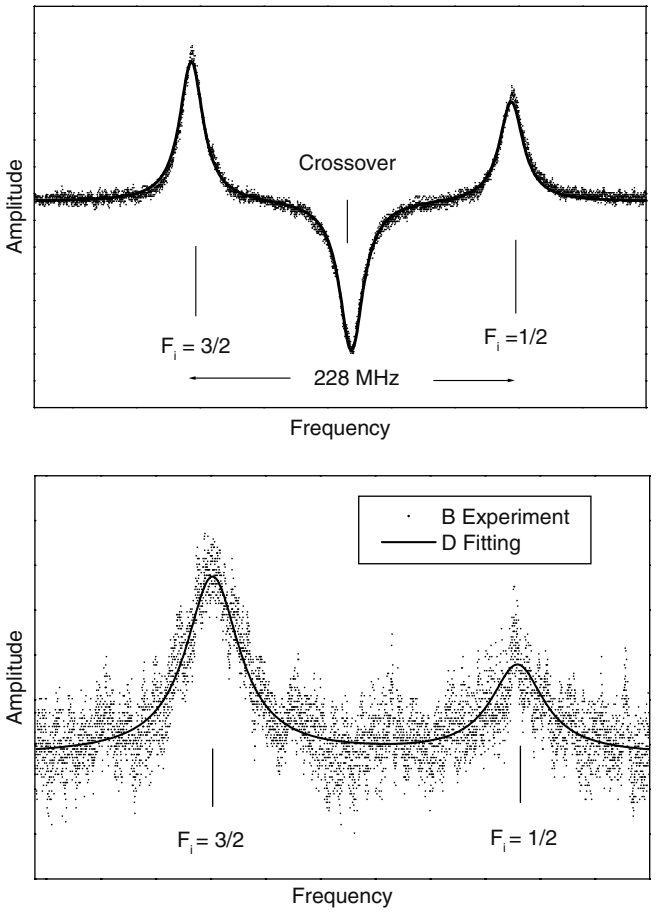

FIGURE 11.6 (a) Doppler-free spectrum at low Ar pressure: $P_{Ar} = 0.0018$ Torr, $I_P = 21$ W/m^2, $n(\text{Li}) = 5 \times 10^9$ cm^{-3}, $T = 375$ °C. Result of the fitting: $\Gamma = 5.9 \times 10^7$ s^{-1}, $\gamma_{VC} = 4.5 \times 10^6$ s^{-1}. (b) Doppler-free spectrum at high Ar pressure: $P_{Ar} = 4.46$ Torr, $I_P = 79$ W/m^2, $n(\text{Li}) = 5 \times 10^9$ cm^{-3}, $T = 375$ °C. Result of the fitting: $\Gamma = 1.5 \times 10^8$ s^{-1}, $\gamma_{vc} = 2.5 \times 10^7$ s^{-1}.

a narrow-linewidth laser for selective excitation of ^{6}Li and ^{7}Li lines were used. The diminishment of the photocurrent due to relaxation mechanisms is explained using the saturation absorption curve for the diode laser excitation.

11.8.1 Energy Level Diagram

As both lithium isotopes have fine structure at the $2p$ level, lithium atoms in the ground state ($S_{1/2}$) can be excited selectively to any of the doublet states $^2P_{1/2}$ and $^2P_{3/2}$ (which are separated by 0.0151 nm) using a narrow-linewidth laser and a well-collimated atomic beam. The energy level diagram for lithium isotopes illustrating the UV and red radiation is shown in Figure 11.7.

The wavelengths of the transitions $2s$–$2p$ have been assigned as corresponding to 670.7764 nm for the ^{7}Li D_2 line and 670.7915 nm for the ^{7}Li D_1 line. The

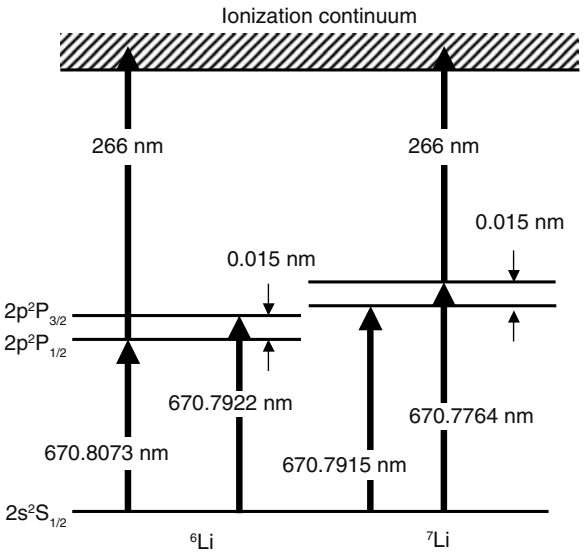

FIGURE 11.7 Energy level diagram for the two-step photoionization of lithium isotopes. For $\lambda < 350$ nm the lithium atom will be ionized from its previous excited state. The selectivity is achieved by the diode laser. The $2p^2P_{1/2}$–$2p^2P_{3/2}$ spacing of 0.015 nm is on a greatly exaggerated scale in this figure compared to the energy levels.

$2s$–$2p$ transitions for ^{6}Li D_2 and for ^{6}Li D_1 lines were assigned to 670.7922 nm and 670.8073 nm, respectively [9].

As the energy level of these excited states is approximately 1.84 eV and the ionization potential is approximately 5.39 eV, the energy required to ionize the lithium atoms from the $2p$ level corresponds to wavelengths shorter than 350 nm, thus 266 nm will reach the ionization from any previously selectively excited 2p level [29–31].

11.8.2 Estimate of the Laser-Produced Ions at the End of a Laser Pulse

The number of ions at the end of a laser pulse can be estimated from density-matrix calculations for the ground-excited-ionization continuum system. The following rate equation is obtained in a two-step photoionization system where no collisions occur [30, 31].

$$\begin{aligned}
\dot{\rho}_{00} &= W(\rho_{11} - \rho_{00}) + \gamma\rho_{11} \\
\dot{\rho}_{11} &= W(\rho_{00} - \rho_{11}) - \gamma\rho_{11} - \Gamma_i\rho_{11} \\
W &= \frac{\frac{1}{2}\Omega^2\Gamma}{\Gamma^2 + ((\omega - \omega_0) - \mathbf{k}\cdot\mathbf{v})^2}
\end{aligned} \tag{11.22}$$

ρ_{00} and ρ_{11} are the populations of the ground and each excited state of the considered isotope respectively, $\gamma = 1/\tau$ is the spontaneous decay rate, where τ is the lifetime of the excited state, which is 27 ns for lithium, W is the transition rate from the ground to the excited state, $\Gamma_i = \sigma_i I_i(h\nu_i)$ is the ionization transition rate, I_i is the intensity of the ionizing laser in W/m^2, ν_i is its frequency in Hz, σ_i is the cross-section for ionization in m^2, ω is the angular frequency in Hz of the laser used for excitation, ω_0 is the angular transition frequency in Hz, $\mathbf{k}$ is the wave vector of the excitation radiation in m^{-1}, $\mathbf{v}$ is the velocity of the atoms in m/s, Γ is the total homogeneous broadening in Hz, and Ω is the Rabi frequency in Hz. The homogeneous broadening is a function of the transition rates and other broadening effects [32] according to $\Gamma = \gamma/2 + \Gamma_i/2 + \Gamma_L$ where Γ_L is the linewidth of the exciting laser. This system of homogeneous linear (rate) equations with constant coefficients was solved neglecting the hyperfine structure of the ground level. The solution of Equation 11.22 is given by

$$\begin{aligned}
\rho_{00}(t) &= Ae^{\lambda_1 t} + Be^{\lambda_2 t} \\
\rho_{11}(t) &= Ce^{\lambda_1 t} + De^{\lambda_2 t} \\
\lambda_{1,2} &= -b \pm \sqrt{b^2 - c} \\
b &= W + \frac{1}{2\tau} + \frac{\Gamma_i}{2} \\
c &= W\Gamma_i
\end{aligned} \tag{11.23}$$

where

$$\begin{aligned}
A &= \frac{1}{\lambda_1 - \lambda_2}\left[-(W + \lambda_2) + \rho_{11}(0)(2W + \gamma + \lambda_2)\right] \\
B &= \frac{1}{\lambda_1 - \lambda_2}\left[(W + \lambda_1) - \rho_{11}(0)(2W + \gamma + \lambda_1)\right] \\
C &= \frac{1}{\lambda_1 - \lambda_2}\left[W - \rho_{11}(0)(2W + \lambda_1)\right] \\
D &= \frac{1}{\lambda_1 - \lambda_2}\left[-W - \rho_{11}(0)\lambda_2)\right]
\end{aligned} \tag{11.24}$$

and

$$\rho_{00}(0) + \rho_{11}(0) = 1$$

The ionization probability (number of ions/total number of atoms) at a time t is obtained, when averaging over the velocity distribution as

$$P_i(t) = <1 - \rho_{00}(t) - \rho_{11}(t)> \tag{11.25}$$

Thus the number of ions obtained in a volume V with length x perpendicular to the direction of the laser beam after an irradiation pulse with duration t is given by

$$N_i = \rho V \frac{1}{X} \int_0^X \left(\int_0^t P_i(t')dt' \right) dx \tag{11.26}$$

where ρ is the initial density of neutral atoms inside this region.

Here we considered that t is sufficiently short such that no atoms enter or leave the region with length X. This condition applies when $t \ll$ Tt, where Tt is the transit time, typically 500 ns for a 1 mm path. As the neutral lithium beam is moving at thermal velocities, the laser beams are disposed perpendicular to the lithium beam direction, and the repetition rate of the laser pulses is low enough in our experiments that the ionized atoms will leave the ionization region before the next ionizing pulse arrives. Integrating Equation 11.22 and inserting Equations 11.25 and 11.26 we obtain

$$N_i = \rho V \Gamma_i \frac{1}{X} \int_0^X \left(\int_0^t \left\langle \rho_{11}(t') \right\rangle dt' \right) dx \tag{11.27}$$

If the laser used for excitation is a CW laser and the ionizing laser pulse has low power, we can assume that the number of excited atoms $\langle \rho_{11} \rangle$ remains nearly constant in time.

$$N_i = \rho V \Gamma_i t \frac{1}{X} \int_0^X \left\langle \rho_{11}(t) \right\rangle dx \tag{11.28}$$

The loss of excitation power along the irradiation path X is given by Equation 11.12

$$dI = -h\nu\rho \frac{1}{\tau} < \rho_{11} > dx \tag{11.29}$$

The absorption of the ionization laser power was neglected (as the ionization cross-section is low).

Integrating Equation 11.29 and using Equation 11.28 and the definition of Γ_i we have

$$N_i = \frac{A\tau\sigma_i I_i (I_0 - I)}{h^2 \nu_e \nu_i} \tag{11.30}$$

where A is the coincidence area normal to the two lasers when they are parallel, I_0 is the incident intensity, and I is the transmitted intensity of the exciting laser.

Then the number N_i of ions collected at the end of a laser ionizing pulse for low UV laser intensity is given by

$$N_i = \alpha P_i P_e (1-T)/A \tag{11.31}$$

where $\alpha = \sigma_i \tau T_{UV}/(h^2 \nu_e \nu_i) = 17100\ \text{m}^2/\text{w}^2$ for $T_{UV} = 200\ \mu\text{s}$ and $c/\nu_i = 266$ nm, P_i is the average UV laser power, P_e is the exciting laser power, T is the transmittance of the exciting laser at the coincidence area A of both lasers in the interaction region, $\sigma_i = 7 \times 10^{-22}\ \text{m}^2$ is the ionization cross-section [30], T_{UV} is the period of the UV laser pulses of the ionizing laser, h is Planck's constant, and ν_e, *and* ν_i are the excitation and ionization frequencies, respectively.

The transmittance is given approximately by Beer's law $T \approx e^{-\sigma n x}$ where n is the lithium density, x is the length of the lithium beam path, and σ is the absorption cross-section given by

$$\sigma \approx \frac{\sigma_0}{\sqrt{1+S_0}} \tag{11.32}$$

where S_0 is the saturation parameter, and σ_0 is the cross-section at low laser intensity, which is a Gaussian function due to Doppler broadening. Considering the dependence of S_0 with A in Equation 11.20 and Equations 11.31 and 11.32 and Beer's law, a high-saturation parameter and high transmittance is $N \propto 1\sqrt{A}$, where A is the focusing area. Thus the number of ions increases with better focus of the lasers. However, it is not convenient to focus more than the saturation intensity for ionization, which for UV is 50 GW/m^2. The value of the saturation ionizing intensity was obtained solving Equations 11.22 through 11.24, where the excitation and stimulated emission transition probabilities are considered a function of the atom velocity and laser frequency.

11.8.3 Resonance Ionization Spectrometer

The resonance ionization spectrometer is depicted in Figure 11.8.

A beam of lithium atoms was formed by evaporating metallic lithium from a molybdenum crucible in a Knudsen cell (Comstock, Mod. KMB237/6). The vapor was passed through a 1 mm collimator, and the beam was collimated again at 5 cm from the crucible aperture. The Knudsen cell has a shutter to interrupt the beam when necessary. The Knudsen cell can reach 630 °C with a stability of about 1 °C/min.

For excitation with a narrowband laser, we used a CW external-cavity tunable diode laser (New Focus, Mod. 6202) with a central wavelength of 671 nm, tunable over 12 nm and a linewidth of <5 MHz. This laser was focused into the lithium beam, while for ionization we focused the fourth harmonic of a Nd:YAG laser (LeeLaser, Mod. 815TQ) deployed in the counterpropagating direction.

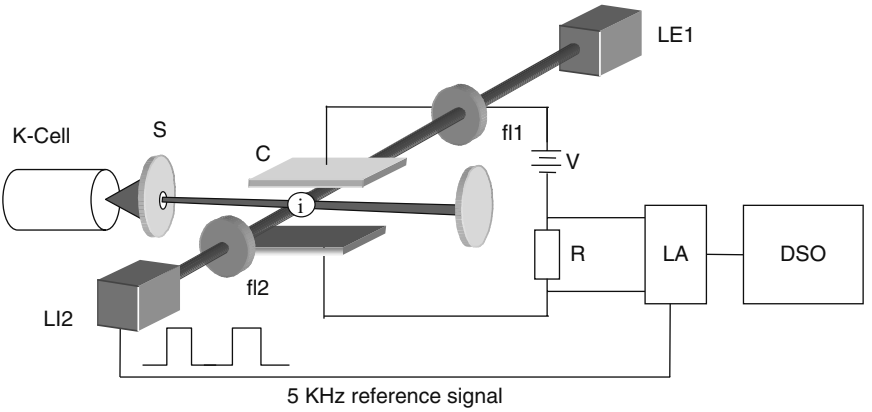

FIGURE 11.8 Apparatus diagram for the resonance ionization spectroscopy of lithium isotopes. K-cell is the Knudsen cell, S the collimation slit, LE1 the diode laser, LI2 the Nd:YAG laser, fl1 and fl2 the focusing lenses, i the interaction region, C the collector plate, V the applied acceleration voltage, R the resistance, LA the lock-in amplifier, and DSO the digital storage oscilloscope.

Typical power densities of the exciting and ionizing lasers are 60 kW/m^2 at 671 nm and 1 GW/m^2 at 266 nm, respectively. The Nd:YAG laser has a 5 kHz repetition rate and 120 ns pulse width with a KTP* crystal intracavity to produce the green output. We used a temperature-stabilized KD*P crystal (Inrad, Model 5-301) to produce the FHG at 266 nm, and a dispersive quartz prism to separate the green from the UV radiation. Laser-produced ions were deflected and collected by means of a plane parallel capacitor inside the vacuum chamber at the irradiation zone, which was polarized by 7V. For voltages over 4V all ions are collected. The photoion current was measured using the AM-lock-in technique. The voltage signal in a 47 kΩ load was amplified by the Lock-In Amplifier (Standford Research, Model SR510) and the amplified signal measured by a digital storage oscilloscope (LeCroy, Mod. 9310A). As a reference signal we used a square 5 kHz function from the Nd:YAG trigger. The diode laser wavelength was scanned slowly over the lithium transitions at 1 GHz/s by means of a function generator (Tektronix, Model CFG100).

The collected number of ions N measured after each ionizing laser UV pulse is given by

$$N \approx kT_{UV}V_M/eR_c \tag{11.33}$$

where k is a proportionality constant, T_{UV} is the period of the Nd:YAG laser pulses, V_M is the voltage measured at the load R_c by the lock-in amplifier when the phase was optimized, and e is the electron charge. The approximation and value of k were obtained considering the lock-in specifications and the signal conditions. The length of the ionization pulse after R_c distortion was of the order 30 μs.

To measure transmittance it is necessary to open the shutter at the Knudsen cell for absorption and to close it to obtain the baseline for the zero-absorption case.

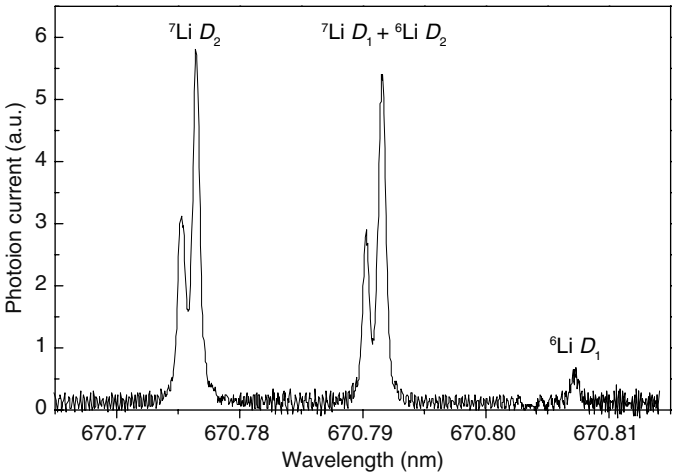

FIGURE 11.9 Typical RIS trace for the ^{6}Li and ^{7}Li isotopes.

11.8.4 Resonance Ionization Spectra

A typical recorded RIS spectrum is shown in Figure 11.9.

This spectrum shows saturation effects on the ^{7}Li D_2 line due to optical pumping between ground states produced by the diode laser. This effect can be observed as a diminishment of the photoion current. The hyperfine structure can also be seen in Figure 11.9 because of the narrow linewidth of the diode laser and the collimation of the lithium beam.

The lithium beam flux is given by $F = n\phi\upsilon$ where the density n is calculated from the absorption spectra, ϕ is the cross-section of the lithium beam, which can be calculated from fluorescence measurements, and υ was calculated from the temperature using kinetic gas theory. We have estimated a flux of 10^{15} atoms/s and confirmed the estimate with the measurements obtained with a quartz film thickness meter (Bal. Tec, Mod. QSG060).

We measured the transmittance of the ^{7}Li D_2 spectral line at 670.7764 nm as a function of the intensity of the excitation light (we used a well-collimated laser beam). In this case the diode laser wavelength was fixed and the Nd:YAG was off. The saturation curve obtained is shown in Figure 11.10, adjusted by the numerical procedure described previously.

The fit parameter is the transit time relaxation rate γ_T. We obtained $\gamma_T = 5 \times 10^5\ s^{-1}$ from the fitting. This value agrees with the inverse of the transit time calculated as x/υ, where x is the length of the atom path across the laser beam, which is the beam diameter considered as 3 mm, and υ is the velocity of the lithium atoms, which was 1800 m/s. The saturation parameter is approximately 10 times larger than in the case of a two-level atom, which can be explained by the various ground sublevels in lithium, where additional pumping can occur. The optical pumping could be altered by collisions between atoms, but in our case the collisions are

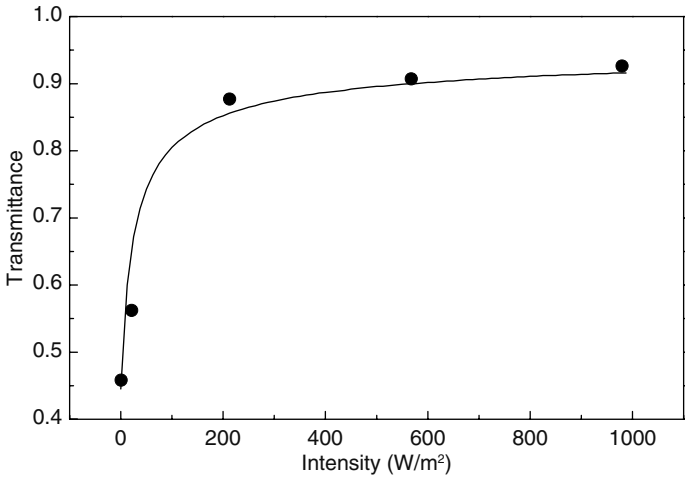

FIGURE 11.10 Saturation curve for the absorption of the ^{7}Li D_2 line at 670.7764 nm.

negligible due to a large mean-free path of 3 m, obtained using a high vacuum and a low lithium density. For this reason other relaxation mechanisms were also neglected.

For the RIS measurements the temperature of the Knudsen cell was set at T = 633 °C, the incoming power of the diode laser was P_e = 2360 μW, and at the exit we measured P_e = 2220 μW with an optical power meter (Newport, Mod. 818). The resolution determined experimentally for this power meter was better than 0.75% at the microwatt level.

The ionizing UV power P_i averaged 15 mW, which was focused at an area A = 7.5×10^{-9} m^2. The red light was focused with an f = 0.25 m lens and the UV light with an f = 0.58 m lens. As the shape of the diode laser light is elliptical and larger than the circular UV laser spot, the coincidence of the two lasers is not complete. So we used only the 0.25 part of the red light power. The proportionality constant of Equation 11.33 is k = 1.9 and V_M = 17.8 μV. Using Equation 11.33 and these values of k and V_M we obtained the measured ions/pulse $N = (9 \pm 1) \times 10^5$ and the estimated number of ions/pulse was $N = (12 \pm 3) \times 10^5$ considering Equation 11.31 and the values of P_e incident, P_e transmitted, A, and the fraction of the red light in the ionization zone. The total error of the value of N in each case was obtained by means of the error propagation theory and the given standard deviation error of each variable.

In a second case involving an incident diode laser power of P_e = 3750 μW and a transmitted power of P_e = 3550 μW we determined $N = (1.9 \pm 0.5) \times 10^5$ ions/pulse via Equation 11.31. This value should be compared with $N = (1.5 \pm 0.2) \times 10^5$ ions/pulse derived from the measurement and Equation 11.33.

11.8.5 Discussion and Conclusion

The method to measure the RIS spectra of lithium isotopes using a narrow-linewidth tunable diode laser for excitation is simple. There is agreement between the

estimation of the produced ions starting from transmittance measurements and the measurement of the photoion current. The intensity of the diode laser is high enough to produce saturation on the recorded photoion spectra.

The saturation was investigated measuring the transmittance at different laser intensities and fitted with the numerical procedure explained previously. This procedure considers the hyperfine structure of the levels and the optical pumping and takes the transit time relaxation rate as a fit parameter.

11.9 LITHIUM ISOTOPE SEPARATION USING TUNABLE DIODE LASERS

A laser isotope separation study of lithium has been performed using two-step excitation involving UV laser radiation and a visible tunable diode laser. The method yields a high degree of selectivity by tuning the narrow-linewidth diode laser to the D_1 or D_2 levels of the lithium atom. Selective laser excitation is simplified by the use of the tunable diode laser, and the overall approach benefits from the application of a compact mass selector that includes a precision magnetic sector and an ion beam designed specifically for light atoms such as lithium.

The laser isotope separation (LIS) method is considered, in the literature, to be very attractive owing to the high selectivity that can be achieved [27–30]. This approach applies a two-step selective photoionization method, and it can be used for nearly all elements of the periodic table using commercial tunable lasers. It can also be used for ultrasensitive trace element analysis [33].

Here we present a study of LIS in lithium using simple, compact, and inexpensive tunable diode lasers, which offer excellent spectral characteristics. The overall method allows complete separation of the different isotopes, even where the lines of the different isotopes overlap.

An integral component of the experimental method is a mass selector that includes a magnetic sector. A fairly detailed description of this relatively simple, compact, and inexpensive apparatus for separating lithium isotopes is given.

Tunable lasers useful to this type of application include the CW dye lasers [18] and narrow-linewidth CVL laser-pumped dye lasers [19–23]. CW dye lasers are relatively complex and require fairly sophisticated engineering for building and maintenance. One advantage is relatively high CW powers in a single-longitudinal mode. Even higher average powers are available from narrow-linewidth CVL laser-pumped pulsed dye lasers. However, this class of laser, although very desirable for this type of application, has been demonstrated and operated only in a handful of laboratories around the world [19–23]. An alternative is tunable external-cavity semiconductor lasers [16–17]. These lasers are relatively inexpensive and compact, and yield very narrow linewidth single-longitudinal-mode emission. Given our limited resources and the exploratory nature of the experiments, these compact coherent sources are very well suited.

It should be made clear that this experimental approach was specifically designed for selective excitation of light atoms for spectroscopic applications. Scaling the method using high-power tunable lasers was beyond the scope of this study.

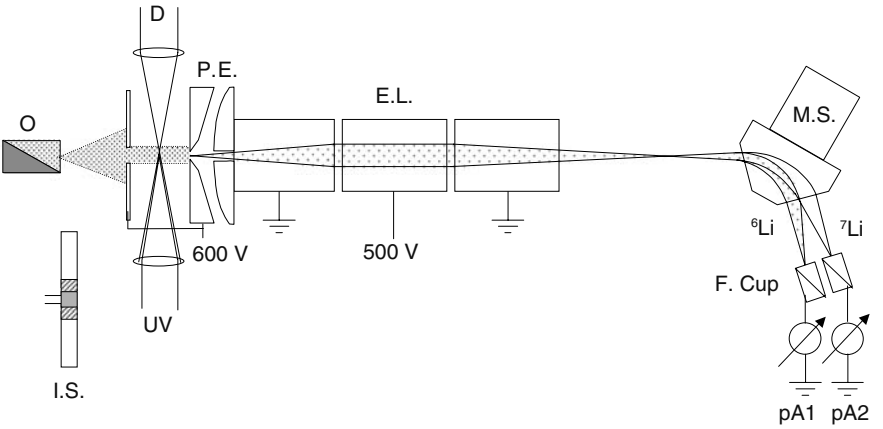

FIGURE 11.11 Diagram of the mass separator: O, molybdenum crucible with lithium; P. E., Pierce extractor; E. L., Einzel lenses; M. S., magnetic sector; FC1, FC2, Faraday cups; pA1, pA2, picoamperemeters; I. S., lithium ion source. The lithium ion source can be placed behind the Pierce extractor for nonselective ion production and calibration of the mass separator.

11.9.1 Experimental Details

The schematic for this lithium isotope separation is depicted in Figure 11.11.

A collimated beam of lithium atoms enters an optical cell. The lithium beam is illuminated by a focused UV laser beam and a spatially coincident counterpropagating focused tunable diode laser. By this means the neutral lithium atoms were selectively photoionized by the two-step excitation described previously. The lithium ions enter a Pierce extractor [34] and follow on to a set of Einzel lenses. The lithium ion beam is then focused into the entrance of a magnetic sector. At this stage the ion beam is separated into two subbeams corresponding to the ^{6}Li and ^{7}Li isotopes. Each of the isotopic ionic subbeams continue on to a separate Faraday cup where the picocurrent is measured.

11.9.2 Laser System

The CW tunable diode laser used in these experiments was a commercial device (EOSI, Model 2010) configured in a Littrow grating cavity [18, 19]. The tuning range of this laser is 25 nm without mode hops and is centered at 672 nm. This laser emits in a single-longitudinal mode at a linewidth of <100 kHz. The beam divergence is diffraction limited at an output power of 9 mW. This laser was tuned using an electronically controlled servomechanism that rotates the grating. This servomechanism includes a PZT driven by a slow triangular wave generator (HP, Model 3310B). The time to scan one complete spectrum was about 15 minutes, in order to get enough resolution at the ionization spectra. The emission wavelength was monitored with an optical wave meter (Burleigh, Model WA4500).

The tunable diode laser was focused into the neutral lithium beam with an $f = 0.25$ m lens, while for ionization of the excited atoms we focused the fourth harmonic of a Nd:YAG laser (Lee Laser, Model 815TQ) deployed in the counterpropagating direction with a fused silica $f = 0.58$ m lens. Typical average-power densities of the exciter and ionizer at the focus were 35 W/cm^2 at 671 nm and 125 W/cm^2 at 266 nm, respectively. The Nd:YAG laser has a 5 kHz repetition rate with a KTP* intracavity crystal to produce the green output. We used a temperature-stabilized KD*P crystal (Inrad, Model 5-301) to produce the FHG at 266 nm and a dispersive quartz prism to separate the green from the UV radiation. To increase the UV power density we used an $f = 0.2$ m lens to focus the green into the KD*P crystal and an $f = 0.2$ m fused silica lens to recollimate the beam. We measured the UV pulse length with a photodiode (EGG Model FND100Q) obtaining 80 ns (FWHM). We measured the focusing area of the red and UV laser using a ICCD (Princeton Instruments, Model 576EMG/RB) at different positions near the focal point. We obtained $A = (11.8 \pm 1.3) \times 10^{-9}$ m^2 for the red laser and $A = (16.8 \pm 0.7) \times 10^{-9}$ m^2 for the UV, respectively. In this case we are using only 71% of the UV light for ionization.

11.9.3 Isotope Separation Apparatus

The beam of lithium atoms (Fig. 11.11) was produced by evaporating metallic lithium from a heat pipe cell (Comstock, Model HP-802). The heat pipe used can reach a temperature of 800 °C with a stability better than 1 °C/min. A detailed description is given elsewhere [35, 36]. One end of the heat pipe was closed, and the other end was opened and connected to a vacuum chamber containing a mass selector. The aperture used to collimate the beam has a 0.5 cm diameter. The collimator and Pierce extractor were held at the same positive potential. The region between them is used as the laser excitation volume region. The Pierce extractor yields a divergent ion beam, which is focused with an Einzel lens system into the entrance of a mass selector. This mass selector was made in-house and is comprised of an ion gun and a magnetic sector.

11.9.3.1 Calibration of the Magnetic Sector

To calibrate the mass selector we used a lithium ion cell (Heat-Wave, Model Std.250x), which is a ceramic beta eucryptite source containing a 30%/70% mixture of ^{6}Li and ^{7}Li isotopes. The construction and performance of these cells have been discussed elsewhere [37]. We also tested our system with pure ^{6}Li and ^{7}Li cells. The Pierce voltage determines the ion beam energy. Using the relationship that mass is proportional to the inverse of the applied voltage at a given magnetic field strength and geometry we can estimate the required Pierce voltage. The most convenient value was obtained experimentally at 572 ± 1 V using a stabilized high-voltage power supply (Glassman, Model EH05P20) after focusing the beam at the entrance of the sector. To obtain a well-focused beam we used a beam profile monitor (National Electrostatics Corporation, Model BPM80) and adapted the length of the vacuum chamber to the position of the optimum focus. This focal point is 15 cm from the exit of the ion gun. The best focusing voltage V_f was held at 464 ± 1 V, and was determined experimentally by the position of the entrance slit of the magnetic sector.

To measure the mass spectrum we employed a 2.5 mm copper wire moved by a gear system connected to rotary motion feedthrough with a stepper motor (MDC, Model BRM275-03). The ion current reaching the wire was measured by a picoamperemeter (Keithley, Model 485) and recorded with a digital storage oscilloscope (LeCroy, Model 9314). By using a mixed cell it was possible to obtain a mass spectrum at one scan of the wire. The position of the isotopes and resolution were obtained from the barrel graduation.

With this result we could replace the wire at the exit of the sector by two 9-mm-wide copper plates separated by 1 mm. The size and position of the plates was determined from the mass spectrum. We adjusted the position of the plates by measuring the current using the ion cell again. In this manner we obtained a collector suitable for mass 6 and mass 7 isotopes.

In the experiments, where the ions were produced by the lasers, the ion cell was removed and replaced by the neutral beam and collimator described previously. The lasers were focused just behind the Pierce element. The root mean square value of the current at the ^{7}Li collector was measured with a picoamperemeter (Keithley, Model 485) connected with a GPIB interface to a personal computer and recorded with a Labview5.0 application. The current of the ^{6}Li isotope was recorded simultaneously with the same software and interface using a more sensitive picoamperemeter (Keithley, Model 595). The time required by our system to take the data for each pair of current values was 652 ms. The total number of ions produced at the ionization area were obtained from an absorption measurement and compared with the ions collected at both plates behind the magnetic sector. In this case the transmittance was measured at saturation with the same laser intensity used at the current measurement. This was done at resonance and slightly off resonance to avoid étalon effects.

To determine the density of neutral lithium atoms we removed the focusing lens and reduced further the intensity by means of a neutral density filter. The spectrum was recorded using an optical power meter (Newport, Model 1815C) and a digital storage oscilloscope (LeCroy, Model 9314A). The background light was subtracted. The absorption path length was determined from fluorescence measurements [38].

11.9.4 Experimental Overview

The overall experimental setup described in the previous two subsections fits on two 1.21 m × 2.43 m commercial optical tables with a total utilized surface area of approximately 4.5 m^2. The main two items contributing to this reduced area are the tunable diode laser and the in-house mass separator. The tunable diode laser is only a fraction of the size of an alternative CW dye laser or a CVL laser-pumped dye laser. The high-stability precision magnet comprising the mass selector was specifically designed for applications involving light atoms such as lithium. As such, it is only a small fraction of the size of a conventional commercial mass spectrometer. Ease of operation is a further experimental advantage.

In these experiments a beam of lithium atoms is produced and illuminated by a two-step selective laser excitation process. Following passage through a mass-selection apparatus, two detectors (Faraday cup 1 and Faraday cup 2) collect the spatially separated isotopes ^{7}Li and ^{6}Li, respectively. Spatial separation is shown, via a mass spectrum, in Figure 11.12.

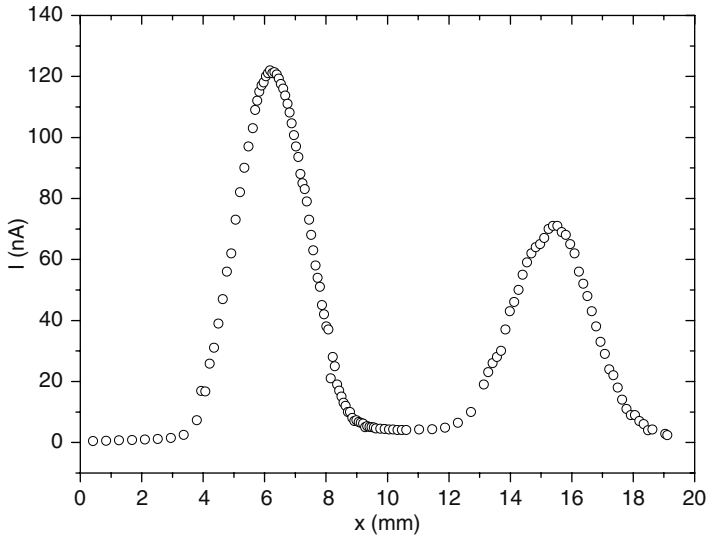

FIGURE 11.12 Mass spectrum of mixed ^{7}Li/^{6}Li beta-eucryptite source. For our experimental conditions we have a resolution of $\Delta M/M = 3$, which is enough to separate the isotopes of interest.

11.9.5 Lithium Laser Isotope Separation

The isotopic beam detected in Faraday cup 1 gives origin to the resonance ionization mass spectrum of ^{7}Li D_1 and ^{7}Li D_2 resolved in doublets (Fig. 11.13).

Note that this spectrum is clear, well resolved, and typical of this isotope alone. The isotopic beam detected in Faraday cup 2 gives origin to the resonance ionization mass spectrum of the ^{6}Li D_1 and ^{6}Li D_2 lines (Fig. 11.14).

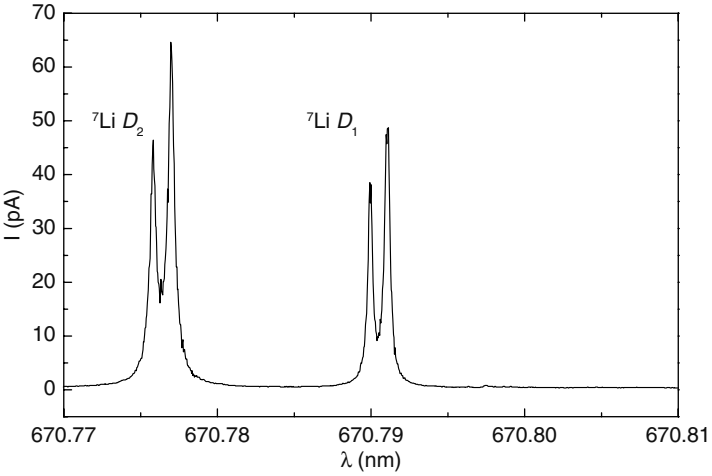

FIGURE 11.13 Resonance ionization mass hyperfine spectrum recorded at the FC1.

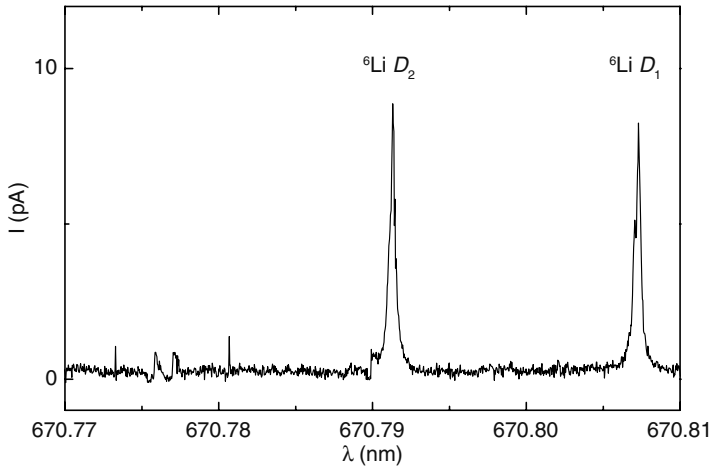

FIGURE 11.14 Resonance ionization mass hyperfine spectrum recorded at the FC2.

Note that this spectrum is characterized by the lower intensity peaks, which correspond to this particular isotope exclusively. For comparison purposes the reader can observe the mixed, or combined, high-resolution spectrum of ^{7}Li and ^{6}Li in Figure 11.9.

Albeit rather insignificant, the average value for the background signal was subtracted in each case from the measured spectra. This average background level was measured when the lithium was cold (heat pipe cell off), obtaining 0.87 pA and 0.12 pA at the ^{7}Li and ^{6}Li collector plate, respectively. This background level is deemed to have a negligible effect on the overall signal.

The hyperfine structure of the isotopes can be distinguished due to a reduction in the Doppler width produced by the collimation and expansion of the vapor [39]. The transmittance T of each hyperfine line of the ^{7}Li D_2 line was 0.991 and 0.996, respectively, and the ionization laser power was $P_i = (15 \pm 1)$ mW. In each case we considered the losses at the windows. For these parameters Equation 11.30 can be used to estimate the upper limit for the number of ions. In this case those upper limits are estimated to be $N_1 = 8.56 \times 10^5$ and $N_2 = 3.83 \times 10^5$, at the peaks of the lines, respectively.

The density of the neutral lithium beam was determined from the absorption spectra. In this measurement the intensity of the laser used for excitation was kept low enough to avoid saturation effects and optical pumping (1 W/cm^2 is convenient). At 780 °C the density of the beam was $n = 2.5 \times 10^{16}$ m^{-3} with a lithium beam diameter of 0.005 m. The collimator installed behind the Pierce has the important function of efficiently repelling the thermal ions arriving from the heat pipe cell, which could contribute to an increase of the background signal at the spectra giving a loss of selectivity. Selectivity could also be reduced by collision effects among atoms or ions as excitation transfer, but these effects are quite negligible due to the low lithium density, which gives a mean-free path $\lambda = 1/n\sigma$ of the order 10 m or more, depending on the cross-section value of each collision process. The ionization by electrons can also affect the selectivity, but this effect is absent because the Pierce

repels the electrons of the beam. An additional nonselective effect is the direct ionization of the lithium clusters produced by the UV; this effect can be measured with the experimental arrangement of Figure 11.8. This corresponds to 10^4 clusters/pulse or less. These clusters are filtered by the mass selector and do not contribute to the picocurrent signal.

In these experiments we observe a negligible background signal and the spectral lines ^{7}Li D_2 depicted in Figure 11.13 and ^{6}Li D_1 depicted in Figure 11.14, appear free of the simultaneous signal from the other isotope. This indicates high selectivity during the resonant ionization process.

11.9.6 Discussion and Conclusion

In these experiments we have recorded a high-resolution spectrum corresponding to ^{7}Li in one Faraday cup detector while the spectrum corresponding to ^{6}Li was recorded in a second Faraday cup detector. These two detectors were spatially separated from each other. This spatial mass-separation resulted from the selective two-step laser excitation, using a UV laser beam and a visible tunable diode laser, of an atomic beam of lithium that propagated via a relatively simple mass selector. The intensity ratio and wavelength characteristics of the two separated hyperfine spectra are consistent with known spectroscopic data.

To our knowledge this is the first report of laser isotope separation of lithium utilizing a tunable diode laser. The application of this tunable diode laser in conjunction with a simple, and compact, mass selector contributes significantly toward the ease of use and overall compactness of the experimental apparatus for LIS experiments in light atoms.

11.10 APPLICATION OF LITHIUM ISOTOPES

Lithium isotopes are important for fission and fusion reactors (see, for example, [40]). Solid breeder and liquid breeder blanket concepts are being developed for testing in the International Thermonuclear Experimental Reactor (ITER) [41]. Lithium is also considered in Tokamaks [42–43] as part of the breeder blanket that contains Li isotopes in ceramic or liquid for tritium production and release. Lithium ion clusters are used also for inertial confinement [44]. Lithium is also important in medicine for treating antidepressant-refractory depressed patients by successfully adding lithium to their antidepressant. Lithium-based compounds such as lithium carbonate (Li_2CO_3) are used as drugs to treat manic-depressive disorders [45–47]. Because of its high electrochemical potential, lithium is also used as battery anode material and lithium compounds are used in dry cells and storage batteries [48–50] and in rechargeable lithium batteries [51–52]. Lithium is alloyed with aluminum, copper, manganese, and cadmium to make high-perfomance alloys for aircraft that are approximately 10% lighter than aluminum [53]. Lithium metal has the highest specific heat of any solid element and so offers potential heat transfer applications.

ACKNOWLEDGMENTS

The experiments described in this chapter were performed in collaboration with Eduardo A. Saravia and Andrés E. Duarte, who performed many of the original

calculations. The author is grateful to Professor Edmund Wyndham for his valuable comments and corrections.

REFERENCES

1. Wieman, C., and L. Hollberg, Using diode lasers for atomic physics, *Rev. Sci. Instrum.* 62: 1–20 (1991).
2. MacAdam, K. B., A. Steinbach, and C. Wieman, A narrow-band tunable diode laser system with grating feedback and a saturated absorption spectrometer for Cs and Rb, *Am. J. Phys.* 60: 1098–1111 (1992).
3. Camparo, J. C., The diode laser in atomic physics, *Contemp. Phys.* 27: 443–477 (1985).
4. Hänsch, T. W., and H. Walther, Laser spectroscopy and quantum optics, *Rev. of Mod. Phys.* 71: 5242–5251 (1999).
5. Harris, S. E., Electromagnetically induced transparency, *Physics Today* 50: 36–42 (1997).
6. Hänsch, T. W., A. L. Schawlow, G. W. Series, The spectrum of atomic hydrogen, *Sci. Am.* 240: 94–98 (1979).
7. Feld, M. S., and V. S. Letokhov, Laser spectroscopy, *Sci. Am.* 229: 69–85 (1973).
8. Olivares, I. E., A. E. Duarte, T. Lokajczyk, A. Dinklage, and F. J. Duarte, Doppler-free spectroscopy and collisional studies with tunable diode lasers of lithium isotopes in a heat-pipe oven, *J. Opt. Soc. Am. B* 15: 1932–1939 (1998).
9. Sansonetti, C. J., B. Richou, R. Engleman, Jr., and L. J. Radziemski, Measurements of the resonance lines of ^{6}Li and ^{7}Li by Doppler-free frequency modulation spectroscopy, *Phys. Rev. A* 52: 2682–2688 (1995).
10. Camparo, J., The rubidium atomic clock and basic research, *Physics Today* 33–39 (2007).
11. Galbacs, G., Z. Galbacs, O. Axner, and Z. Geretovszky, Assessment and application of diode laser induced fluorescence spectrometry in an inductively coupled plasma to the determination of lithium, *Spectrochim. Acta B* 60: 299–306 (2005).
12. Olivares, I. E., and A. E. Duarte, Resonance ionization spectroscopy in a thermal lithium beam by means of diode lasers, *Appl. Opt.* 38: 7481–7485 (1999).
13. Olivares, I. E., A. E. Duarte, E. A. Saravia, and F. J. Duarte, Lithium isotope separation with tunable diode lasers, *Appl. Opt.* 41: 2973–2977 (2002).
14. Hojer, S., H. Ahlberg, and S. Lundqvist, Measurements of electric field strength in gas insulated high voltage components using infrared diode laser absorption spectroscopy, *Appl. Opt.* 25: 2984–2987 (1986).
15. Franzke, J., A. Schnell, and K. Niemax, Spectroscopic properties of commercial laser diodes, *Spectrochim. Acta Rev.* 15: 379–395 (1993).
16. Zorabedian, P., Tunable external-cavity semiconductor lasers, in *Tunable Lasers Handbook*, edited by F. J. Duarte, Academic, New York, 1995.
17. Duarte, F. J. (Ed.), *Tunable Laser Applications*, Marcel Dekker, New York, 1995.
18. Hollberg, L., CW dye lasers, in *Dye Laser Principles*, F. J. Duarte and L. W. Hillman, eds., Academic, New York, 1990, pp. 185–238.
19. Duarte, F. J., and J. A. Piper, Comparison of prism-expander and grazing-incidence grating cavities for copper laser pumped dye lasers, *Appl. Opt.* 21: 2782–2786 (1982).
20. Duarte, F. J., and J. A. Piper, Narrow linewidth high prf copper laser-pumped dye-laser oscillators, *Appl. Opt.* 23: 1391–1394 (1984).
21. Bass, I. L., R. E. Bonanno, R. P. Hackel, and P. R. Hammond, High-average-power dye laser at Lawrence Livermore National Laboratory, *Appl. Opt.* 31: 6993–7006 (1992).
22. Singh, S., K. Dasgupta, S. Kumar, K. G. Manohar, L. G. Nair, and U. K. Chatterjee, High-power high-repetition-rate copper-vapor-pumped dye laser, *Opt. Eng.* 33: 1894–1904 (1994).

23. Maruyama, Y., M. Kato, T. Arizawa, Effects of excited-state absorption and amplified spontaneous emission in a high-average-power dye laser amplifier pumped by copper vapor lasers, *Opt. Eng.* 35: 1084–1087 (1996).
24. Sugiyama, A., T. Nakayama, M. Kato, Y. Maruyama, T. Arisawa, Characteristics of a pressure-tuned single-mode dye laser pumped by a copper vapor laser, *Opt. Eng.* 35: 1093–1097 (1996).
25. Bokhan, P. A., V. V. Buchanov, N. V. Fateev, M. M. Kalugin, M. A. Kazaryan, A. M. Prokhorov, and D. E. Kakrevskii, *Laser Isotope Separation in Atomic Vapor*, Wiley-VCH, Weinheim, 2006.
26. Happer, W., Optical pumping, *Rev. Mod. Phys.* 44: 169–249 (1972).
27. Payne, M. G., L. Deng, and N. Thonnard, Applications of resonance ionization mass spectroscopy, *Rev. Sci. Instrum.* 65: 2433–2459 (1994).
28. Ackerhalt, J. R., and B. W. Shore, Rate equations versus Bloch equations in multiphoton ionization, *Phys. Rev. A* 16: 277–282 (1977).
29. Arisawa, T., Y. Maruyama, Y. Suzuki, and K. Shiba, Lithium isotope separation by laser, *Appl. Phys. B* 28: 73–76 (1982).
30. Karlov, N. V., B. B. Krynetskii, and O. M. Stel'makh, Measurement of the photoionization cross section of the Li atom at the 2P level, *Sov. J. Quantum Electron.* 7: 1305–1306 (1977).
31. Yamashita, M., and H. Kashiwagi, Method for separation and enrichment of lithium isotopes by laser, U.S. Patent 4149077 (April 10, 1979).
32. Hurst, G. S., M. G. Payne, S. D. Kramer, and J. P. Young, Resonance ionization spectroscopy and one-atom detection, *Rev. Mod. Phys.* 51: 767–819 (1979).
33. Bekov, G. I., V. S. Letokhov, and V. N. Radaev, Laser photoionization spectroscopy for ultrasensitive trace element analysis, *Fresenius Z. Anal. Chem.* 335: 19–24 (1989).
34. Pierce, J. R., Rectilinear electron flows in beams, *J. Appl. Phys.* II, 548–554 (1940).
35. Vidal, C. R., Spectroscopic observations of subsonic and sonic vapor inside an open-ended heat pipe, *J. Appl. Phys.* 44: 2225–2232 (1973).
36. Vidal, C. R., and J. Cooper, Heat-pipe oven: a new, well defined metal vapor device for spectroscopic measurements, *J. Appl. Phys.* 40: 3370–3374 (1969).
37. Heinz, O., and R. T. Reaves, Lithium ion emitter for low energy beam experiments, *Rev. Sci. Instrum.* 38: 1129–1130 (1968).
38. Dinklage, A., T. Lokajczyk, H. J. Kunze, B. Schweer, and I. E. Olivares, *In situ* density measurement for a thermal lithium beam employing diode lasers, *Rev. Sci. Instrum.* 69: 321–322 (1998).
39. Demtröder, W., *Laser Spectroscopy Basic Concepts and Instrumentation*, 2nd ed., Springer, New York, 1996.
40. Little, E. A., Development of radiation resistant materials for advanced nuclear power plant, *Mat. Sci. and Tech.* 22: 491–518 (2006).
41. Wong, C. P. C., V. Chernov, A. Kimura, Y. Katoh, N. Morley, T. Muroga, K. W. Song, Y. C. Wu, and M. Zmitko, ITER-Test blanket module functional materials, *Journal of Nuclear Materials* 367: 1287–1292 (2007).
42. Mansfield, D. K., K. W. Hill, J. D. Strachan, et al., Enhancement of Tokamak Fusion Test Reactor performance by lithium conditioning, *Physics of Plasmas* 3: 1892–1897 (1996).
43. Kapyshev, V. K., M. Y Chernetsov, S. I. Zhevotov, A. Y. Kersnovskij, B. N. Kolbasov, V. G. Kovalenko, N. P. Paltusov, G. A Sernyaev, J. S. Sterebkov, and A. P. Zyryanov, Lithium ceramic blankets for Russian fusion reactors and influence of breeding operation mode on parameters of reactor tritium systems, *Fusion Science and Technology* 48: 642–645 (2005).
44. Deutsch, C., and N. A. Tahir, Fragmentation and stopping of heavy cluster ions in a lithium target-application to target implosion, *Physics of Fluids B-Plasma Physics* 4: 3735–3746 (1992).

45. Freeman, M. P., and S. A. Freeman, Lithium: Clinical considerations in internal medicine, *The American Journal of Medicine* 119: 478–481 (2006).
46. Bschor, T., U. Lewitzka, A. Pfennig, and M. Bauer, Twenty-five years of lithium augmentation, *Nervenarzt* 78: 1237 (2007).
47. Bschor, T., U. Lewitzka, J. Sasse, et al., Lithium augmentation in treatment-resistant depression: Clinical evidence, serotonergic and endocrine mechanisms, *Pharmacopsychiatry* 36: 230–234 (2003).
48. Bates, J. B., N. J. Dudney, B. Neudecker, A. Ueda, and C. D. Evans, Thin-film lithium and lithium-ion batteries, *Journal of Power Sources* 54: 155–162 (1995).
49. Bates, J. B., N. J. Dudney, B. Neudecker et al., Thin-film lithium and lithium-ion batteries, *Solid State Ionics* 135: 33–45 (2000).
50. Thackeray, M. M., Manganese oxides for lithium batteries, *Progress in Solid State Chemistry* 25: 1–71 (1997).
51. Tarascon, J. M., M. Armand, Issues and challenges facing rechargeable lithium batteries, *Nature* 414: 359–367 (2001).
52. Rossouw, M. H., and M. M. Thackeray, Lithium manganese oxides from Li_2MnO_3 for rechargeable lithium battery applications, *Materials Research Bulletin* 26: 463–473 (1991).
53. Ishihara, K. N., F. Kubo, K. Irie, K. Shichi, E. Yamasue, and H. Okumura, Mechanical alloying of lithium-base systems, *Journal of Alloys and Compounds* 434: 542–545 (2007).

12 Interferometric Imaging

F. J. Duarte

CONTENTS

12.1 Introduction 341
12.2 Tunable Lasers 342
12.3 The Interferometer 344
12.4 Interferometric Theory 348
12.5 Interferometric Calculations 352
12.6 Applications 357
12.6.1 Densitometry in the Macroscopic Domain 357
12.6.2 Detection of Surface Microdefects 359
12.6.3 Photographic Film Grain Structure 361
12.6.4 Assessment of Transmission Gratings and MTF 363
12.6.5 Theoretical Enhancement of the Resolution of Photodiode Arrays 364
12.6.6 Laser Printing 365
12.6.7 Wavelength Measurements 366
12.6.8 Secure Interferometric Communications in Free Space 366
12.6.9 Interferometry in Textiles 367
12.6.10 Applications to Biomedicine 369
12.7 Conclusions 371
Acknowledgments 371
References 372

12.1 INTRODUCTION

Traditional measurements in imaging science include densitometry, spectrophotometry, and image structure. In densitometry, macroscopic optical densities are measured as a function of wavelength either in the transmission or reflection domain. In image structure, measurements include microdensitometry, also known as granularity measurements, and determination of the modulation transfer function (MTF). Microdensitometry provides statistical information on the distributions of microscopic crystal structures in photographic film. MTF measurements determine modulation as a function of spatial frequency in transmission gratings manufactured either with atomic or molecular films. All of these imaging measurements, as related to molecular structures, are described in detail by Dainty and Shaw [1].

Traditionally, these measurements have been performed using instrumentation based on incoherent sources of illumination. This is due to the strong and historical

link of imaging science and photography. Nevertheless, the use of coherent sources of illumination, in conjunction with digital detectors, was demonstrated in photographic imaging measurements in 1986 [2]. In particular, the use of lasers and photodiode detector arrays, and/or charge-coupled devices (CCDs) was investigated in detail [2–7].

In this chapter, the use of a laser-based interferometer capable of performing a plethora of imaging measurements is described. This *N*-slit laser interferometer (NSLI) introduced digital detection technology, in the form of photodiode-detector arrays, to molecular imaging diagnostics [2–7]. For instance, it can be used as a straightforward optical densitometer or as a microdensitometer. The use of a laser source, or tunable laser source, provides a long depth of focus and enhances its dynamic range considerably, thus enabling the characterization of high-optical density surfaces. Further, the photodiode-detector array introduces a feature of spatial discrimination that enables the same instrument to be used as a microdensitometer collecting hundreds, or even thousands, of data points simultaneously. Transmission characteristics from metallic or photographic gratings, as a function of spatial frequency, can also be measured. Further applications not possible with conventional instruments include the assessment of surface structure characteristics in clear film substrates and the detection of microdefects in thin metallic films. Here, in addition to imaging, applications in secure optical communications, textiles, and biomedical areas are discussed.

An important and distinct characteristic of this interferometer is that measurements can be described using the Dirac formalism [8]. As such, in typical quantum fashion, the researcher is allowed to predict an output intensity distribution only with knowledge of the input distribution, and the geometry of the interferometer, but without access to the intermediate propagation of the radiation. This approach enables the use of a powerful computer analysis to quantify and predict measurements [2–7]. It is this dual approach that enhances the applicability of the *N*-slit laser interferometer and method.

12.2 TUNABLE LASERS

The illumination in the NSLI is provided by a laser. Although a fixed frequency laser provides the most basic version of the instrument, its applicability is greatly enhanced by a tunable laser. The most important requirement on the tunable laser being used as an illumination source in these measurements is a TEM_{00} transverse-mode beam structure with a Gaussian or near-Gaussian beam profile.

Tunable lasers can be categorized into two subclasses: line-tunable (or discretely tunable) lasers and broadly tunable lasers. Line-tunable lasers include the argon ion (Ar^+), krypton ion (Kr^+), helium cadmium (He–Cd), and helium neon (He–Ne) lasers. In this application, all of these lasers are used mostly in the CW mode of operation albeit the interferometer could also use pulsed lasers as a source of illumination. Broadly tunable sources of coherent radiation include optical parametric oscillators (Chapter 2), dye lasers (Chapters 3 and 4), diode lasers (Chapter 5), titanium sapphire lasers, and fiber lasers (Chapters 6 and 7).

Table 12.1 lists the transitions and wavelengths available from Ar^+, Kr^+, He–Cd, and He–Ne lasers. An advantage of the emission from these gas lasers is their low

TABLE 12.1
Line-Tunable CW Lasers[a]

Laser	Transition[b, c]	Wavelength (nm)
Ar^+	$4p\ ^4D^0_{3/2}–4s^2P_{1/2}$	528.69
	$4p\ ^4D^0_{5/2}–4s^2P_{3/2}$	514.53
	$4p'\ ^4D^0_{5/2}–3d^2D_{3/2}$	510.72
	$4p\ ^2D^0_{3/2}–4s^2P_{1/2}$	496.51
	$4p\ ^2D^0_{5/2}–4s^2P_{3/2}$	487.99
	$4p\ ^2P^0_{3/2}–4s^2P_{1/2}$	476.49
	$4p\ ^2D^0_{3/2}–4s^2P_{3/2}$	472.69
	$4p\ ^2P^0_{1/2}–4s^2P_{3/2}$	465.79
	$4p\ ^2S^0_{1/2}–4s^2P_{1/2}$	457.93
	$4p\ ^2P^0_{3/2}–4s^2P_{3/2}$	454.50
Kr^+	$5p\ ^4P^0_{3/3}–4d^4D_{1/2}$	799.32
	$5p\ ^4P^0_{3/2}–5s^2P_{1/2}$	752.55
	$5p\ ^4P^0_{5/2}–5s^2P_{3/2}$	647.09
	$5p\ ^4D^0_{5/2}–5s^2P_{3/2}$	568.19
	$5p\ ^4P^0_{5/2}–5s^4P_{3/2}$	530.87
	$5p\ ^4P^0_{3/2}–5s^4P_{3/2}$	520.83
He–Ne	$3s_2–2p_4$	632.82
	$3s_2–2p_6$	611.80
	$3s_2–2p_7$	604.61
	$3s_2–2p_8$	593.93
	$3s_2–2p_{10}$	543.30
He–Cd	$5s^2\ ^2D_{3/2}–5p\ ^2P^0_{3/2}$	441.56
	$6p\ ^2P_{3/2}–5s^2\ ^2D_{3/2}$	488.20
	$4f\ ^2F–5d\ ^2D$	502.50
	$4f\ ^2F^0_{5/2}–5d\ ^2D_{3/2}$	533.75
	$4f\ ^2F_{7/2}–5d\ ^2D_{5/2}$	537.80
	$6g\ ^2G_{7/2}–4f\ ^2F^0_{5/2}$	635.48
	$6g\ ^2G_{9/2}–4f\ ^2F^0_{7/2}$	636.00

[a] Further transitions are available from these lasers. Here, emphasis is given to transitions in the visible spectrum.

[b] Transition assignment has been done following Willett [9].

[c] The laser linewidths of these transitions, in gas lasers, are usually below the few GHz range in the absence of intracavity line-narrowing optics.

TABLE 12.2
Broadly Tunable Dye Lasers in the Yellow-Orange-Red Region of the Spectrum

Laser	Laser linewidth	Continuous tuning range	Ref.
CW dye laser[a]	$\Delta\nu \approx 1$ MHz	575 nm $\leq \lambda \leq$ 639 nm[b]	11
Solid-state dye laser[c]	$\Delta\nu \approx 350$ MHz	550 nm $\leq \lambda \leq$ 603 nm	13

[a] Gain medium is Rhodamine 6G in a water-based solvent [11].
[b] Boundary wavelength values are approximate.
[c] Single-longitudinal-mode emission. Pulse duration is $\Delta t \approx 3$ ns. Gain medium is Rhodamine 6G-doped MPMMA [13].

divergence, exquisite TEM_{00} beam profiles, and long-term spectral stability. For details on gas lasers, the reader should refer to [9]. Table 1.4 of Chapter 1 indicates the approximate wavelength coverage available from various broadly tunable CW lasers.

Table 12.2 includes the tuning range for CW dye lasers, and narrow-linewidth pulsed dye lasers, emitting in the yellow-orange-red region of the spectrum. For a detailed description of CW dye lasers, the reader should refer to [10, 11]. Tunable narrow-linewidth pulsed dye lasers are described in [12–14]. Solid-state dye lasers are described in detail in Chapters 3 and 4.

Table 12.3 includes some of the wavelength characteristics of broadly tunable external-cavity semiconductor (ECS) lasers also known as tunable diode lasers. These lasers are described in detail in Chapter 5.

12.3 THE INTERFEROMETER

The interferometer is shown schematically in Figure 12.1. The TEM_{00} tunable laser is followed by a variable neutral density filter. The Gaussian beam is then expanded in two dimensions by a Galilean telescope. Following the telescope, there is an optional convex lens whose function is to focus the expanded beam from the telescope. As will

TABLE 12.3
Broadly Tunable External-Cavity Semiconductor Lasers[a]

Laser	Laser linewidth	Tuning range	Ref.
GaN	$\Delta\nu \approx 1$ MHz	394.40 nm $\leq \lambda \leq$ 396.15 nm[b, c]	15
Index-guided	$\Delta\nu \approx 100$ kHz	660 nm $\leq \lambda \leq$ 684 nm[b]	16
InGaAsP/InP	$\Delta\nu \approx 100$ kHz	1255 nm $\leq \lambda \leq$ 1335 nm	17

[a] These lasers emit in the CW regime.
[b] Obtained with a commercial ECS laser.
[c] The overall tuning range of these lasers is approximately 373 nm $\leq \lambda \leq$ 472 nm, which includes several gaps.

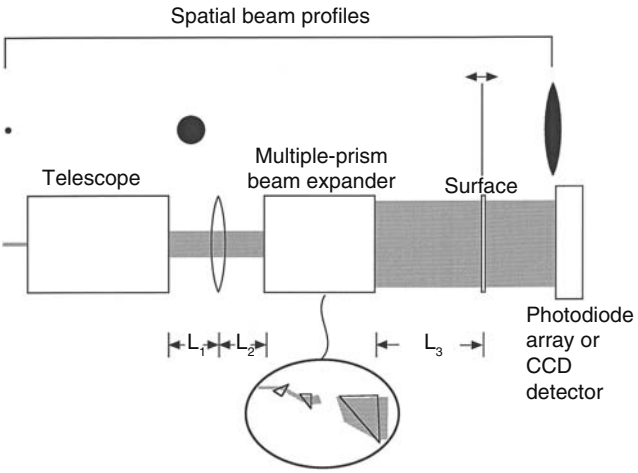

FIGURE 12.1 Schematic of the interferometer. The TEM_{00} beam from the tunable laser source is attenuated by a variable neutral density filter prior to two-dimensional expansion in a Galilean telescope. Following the telescope there is a convex lens that is followed by a multiple-prism beam expander that provides one-dimensional expansion in the plane of propagation. The surface to be measured that gives origin to the interference is located at the focal plane between the multiple-prism array and the photodiode-detector array. The use of the convex lens is optional and depends on whether an extremely elongated Gaussian beam is required.

be explained later, this lens is optional and its use depends on the interferometer's mode of application. The focusing TEM_{00} beam is then expanded again, in one dimension only, by an achromatic multiple-prism beam expander [4, 5, 18].

In the first mode of operation, the convex lens is part of the optical system and hence yields a well-focused beam at the focal plane. However, because the beam undergoes an additional one-dimensional expansion, the beam thus produced is very focused in the vertical plane and very wide in the horizontal plane (or plane of propagation). As a result, extremely elongated Gaussian beams are produced [4–7, 18]. In practice, the beam can be 10–30 μm in the vertical plane and 35–50 mm in the plane of propagation.

The alternative mode of operation does not require the presence of a convex lens and the beam thus produced is ~10 mm in the vertical plane and 35–50 mm in the plane of propagation. Of course, in both modes of propagation the resulting beam has a Gaussian beam profile.

The extremely elongated Gaussian beam is generally used when the detector is a linear photodiode array, and the unfocused beam is used in conjunction with two-dimensional CCD detectors. The signal from the detector is processed and displayed in an optical multichannel analyzer [5–7].

The surface to be examined is deployed on the vertical plane orthogonal to the plane of propagation between the multiple-prism beam expander and the photodiode-detector array. When the convex lens is used, the surface to be examined is positioned at the focal plane.

The ray transfer matrix for a multiple-prism beam expander composed of r prisms is given by [5, 7, 14, 19]

$$\begin{pmatrix} A & B \\ C & D \end{pmatrix} = \begin{pmatrix} M_1 M_2 & B \\ 0 & (M_1 M_2)^{-1} \end{pmatrix} \tag{12.1}$$

where

$$B = M_1 M_2 \sum_{m=1}^{r-1} L_m \left(\prod_{j=1}^{m} k_{1,j} \prod_{j=1}^{m} k_{2,j} \right)^{-2} + \left(\frac{M_1}{M_2} \right) \sum_{m=1}^{r} (l_m / n_m) \left(\prod_{j=1}^{m} k_{1,j} \right)^{-2} \left(\prod_{j=m}^{r} k_{2,j} \right)^{2} \tag{12.2}$$

$$M_1 = \prod_{m=1}^{r} k_{1,m} \tag{12.3}$$

$$M_2 = \prod_{m=1}^{r} k_{2,m} \tag{12.4}$$

Here the individual beam expansion terms for the mth prism are

$$k_{1,m} = \frac{\cos \psi_{1,m}}{\cos \phi_{1,m}} \tag{12.5}$$

$$k_{2,m} = \frac{\cos \phi_{2,m}}{\cos \psi_{2,m}} \tag{12.6}$$

where $\phi_{1,m}$ and $\phi_{2,m}$ are the angles of incidence and emergence, respectively. $\phi_{1,m}$ and $\phi_{2,m}$ are related to $\psi_{1,m}$ and $\psi_{2,m}$ via n_m and Snell's law. In Equation 12.2, L_m is the distance separating the prisms and l_m is the path length at the mth prism.

The overall ray transfer matrix at the plane of propagation is given by [5, 7]

$$\begin{pmatrix} M_t \left[M - \left(\frac{\zeta}{f} \right) \right] & B_t \left[M - \left(\frac{\zeta}{f} \right) \right] + L_1 \left(\frac{M}{M_t} \right) + \left(\frac{\zeta}{M_t} \right) \left[1 - \left(\frac{L_1}{f} \right) \right] \\ -\left(\frac{M_t}{Mf} \right) & (MM_t)^{-1} \left[1 - \left(\frac{L_1}{f} \right) - \left(\frac{B_t}{Mf} \right) \right] \end{pmatrix} \tag{12.7}$$

where $M = M_1 M_2$, and M_t and B_t refer to the A and B terms of the transfer matrix for the Galilean telescope. Also,

$$\zeta = ML_2 + B + \frac{L_3}{M} \tag{12.8}$$

For the vertical component, the corresponding ray transfer matrix becomes

$$\begin{pmatrix} M_t\left[1-\left(\frac{L_2'}{f}\right)\right] & \left[1-\left(\frac{L_2'}{f}\right)\right]\left[B_t+\left(\frac{L_1}{M_t}\right)\right]+\left(\frac{L_2'}{M_t}\right) \\ -\frac{M_t}{f} & M_t^{-1}\left[1-\left(\frac{L_1}{f}\right)\right]-\left(\frac{B_t}{f}\right) \end{pmatrix} \tag{12.9}$$

Note that in the absence of the convex lens, Equations 12.7 and 12.9 simplify to

$$\begin{pmatrix} (M_t M) & B_t M + L_1\left(\frac{M}{M_t}\right)+\frac{\zeta}{M_t} \\ 0 & (M_t M)^{-1} \end{pmatrix} \tag{12.10}$$

and

$$\begin{pmatrix} M_t & B_t+\left(\frac{L_1}{M_t}\right)+\left(\frac{L_2'}{M_t}\right) \\ 0 & M_t^{-1} \end{pmatrix} \tag{12.11}$$

To calculate the width of a Gaussian beam, the following expression is used [20]:

$$w(B') = w_0\left[(A')^2+\left(\frac{B'}{L_R}\right)^2\right]^{1/2} \tag{12.12}$$

where A' and B' are given by Equations 12.7 and 12.9, or 12.10 and 12.11. Here

$$L_R = \pi w_0^2/\lambda \tag{12.13}$$

is known as the Rayleigh length. For a description of relevant 2×2 and 4×4 propagation matrices, the reader is referred to [4]. Duarte [19] gives the generalized 4×4 matrix for multiple-prism arrays.

Using Equations 12.7 through 12.9 and 12.12, it can be shown that for the optical system incorporating the lens, a 0.5-mm TEM_{00} beam from a He–Ne laser (at $\lambda = 632.8$ nm) becomes 53.4 mm wide by 32.26 μm high at the focal plane for $M = 5.75$ and $M_t = 20$. It should also be mentioned that the depth of focus of this Gaussian beam is better than 2 mm. For microscopy applications this enormous depth of focus is one of the advantages that this coherent N-slit laser interferometer offers over traditional instrumentation. The ray matrix approach can also be applied to consider the question of astigmatism [20].

The overall dispersion of the system is determined by characterizing the multiple-prism beam expander. Here the overall generalized dispersion equation is given by [4, 12, 14]

$$\frac{\partial \phi_{2,r}}{\partial \lambda} = (M_1 M_2)^{-1} \sum_{m=1}^{r} (\pm 1) \mathcal{H}_{2,m} \left(\prod_{j=1}^{m} k_{1,j} \prod_{j=1}^{m} k_{2,j} \right) \left(\frac{\partial n_m}{\partial \lambda} \right) + \sum_{m=1}^{r} (\pm 1) \mathcal{H}_{1,m} \left(\prod_{j=m}^{r} k_{1,j} \prod_{j=m}^{r} k_{2,j} \right)^{-1} \left(\frac{\partial n_m}{\partial \lambda} \right) \tag{12.14}$$

where

$$\mathcal{H}_{1,m} = (\tan \phi_{1,m})/n_m \tag{12.15}$$

$$\mathcal{H}_{2,m} = (\tan \phi_{2,m})/n_m \tag{12.16}$$

Note that by making $\partial \phi_{2,r}/\partial \lambda = 0$, a zero-dispersion beam expander can be designed at a given wavelength [4, 12]. This enables a significant reduction in thermal deviations because [12]

$$\frac{\partial \phi_{2,r}}{\partial T} = \left(\frac{\partial \phi_{2,r}}{\partial \lambda} \right) \left(\frac{\partial n_m}{\partial \lambda} \right)^{-1} \left(\frac{\partial n_m}{\partial T} \right) \tag{12.17}$$

For a detailed discussion on the design of multiple-prism beam expanders, the reader should consult [4, 12, 14].

12.4 INTERFEROMETRIC THEORY

In the interferometer schematics shown in Figure 12.2, there is a source (s), an intermediate surface (j), and a detection plane (x). A generalized one-dimensional representation of this optical system is given in Figure 12.2a where the intermediate surface is represented by a generalized grating (j). Hence, using the Dirac formalism [8], the probability amplitude for photon propagation from the source (s) via the grating (j) to the screen (x) is given by

$$\langle x | s \rangle = \sum_{j=1}^{N} \langle x | j \rangle \langle j | s \rangle \tag{12.18}$$

Using

$$\langle j | s \rangle = \Psi(r_{s,j}) e^{-i\theta_j} \tag{12.19}$$

$$\langle x | j \rangle = \Psi(r_{j,x}) e^{-i\phi_j} \tag{12.20}$$

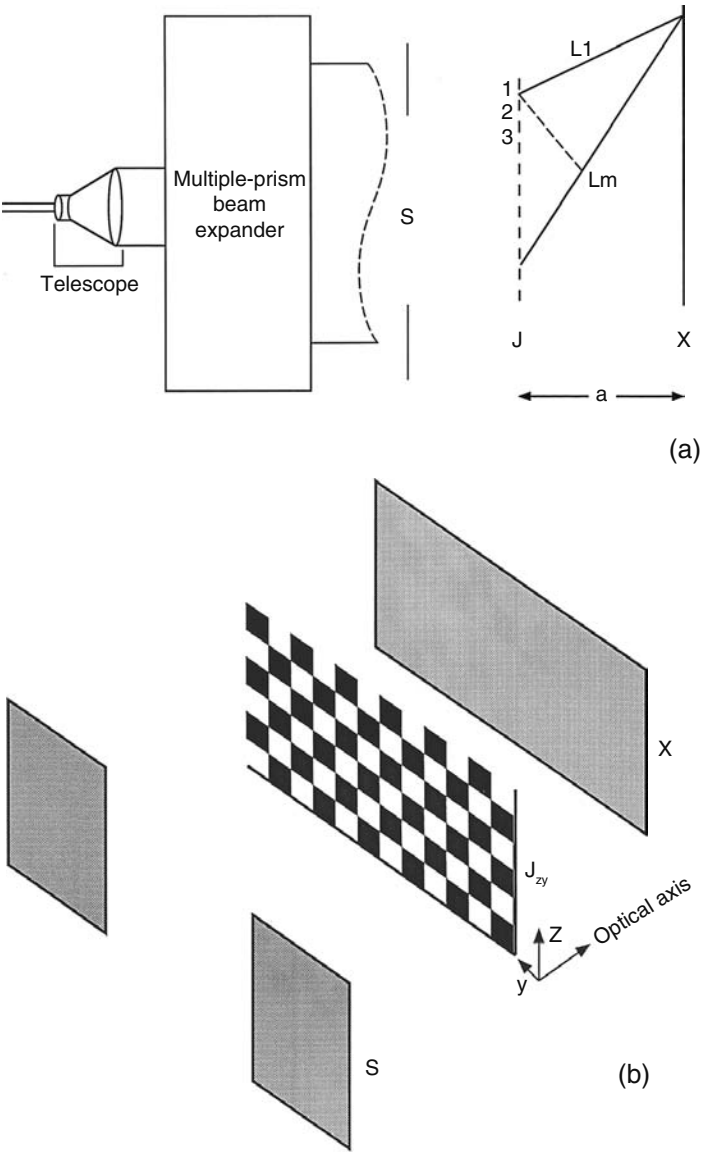

FIGURE 12.2 (a) Generalized one-dimensional geometrical representation of the interferometric measurement. A source (s) is generated at the aperture, and light propagates toward the detection screen (x) via the grating (j) (from Duarte, F. J., On a generalized interference equation and interferometric measurements, *Opt. Commun.* 103: 8–14 (1993)). (b) Two-dimensional representation showing the zy plane that is orthogonal to the plane of propagation.

we can write

$$\langle x|s\rangle = \sum_{j=1}^{N} \Psi(r_j) e^{-i\Omega_j} \tag{12.21}$$

where

$$\Psi(r_j) = \Psi(r_{s,j})\Psi(r_{j,x}) \tag{12.22}$$

and

$$\Omega_j = \theta_j + \phi_j \tag{12.23}$$

Here $\Psi(r_j)$, $\Psi(r_{s,j})$, $\Psi(r_{j,x})$ are the amplitudes of "wave functions of ordinary wave optics" [8]. Thus, the probability distribution at the detector screen is given by [4, 6, 14]

$$\left|\langle x|s\rangle\right|^2 = \sum_{j=1}^{N}\Psi(r_j)^2 + 2\sum_{j=1}^{N}\Psi(r_j)\left(\sum_{j=m+1}^{N}\Psi(r_m)\cos(\Omega_m - \Omega_j)\right) \tag{12.24}$$

In this equation the interference term is evaluated using

$$\cos(\phi_m - \phi_j) = \cos\left(\frac{2\pi}{\lambda}\right)\left|L_m - L_{m-1}\right| \tag{12.25}$$

where the path differences are expressed in terms of the geometry [6]

$$\left|L_m - L_{m-1}\right| = \frac{2\xi_m d_m}{\left|L_m + L_{m-1}\right|} \tag{12.26}$$

$$L_m^2 = a^2 + \left[\xi_m + \left(\frac{d_m}{2}\right)\right]^2 \tag{12.27}$$

$$L_{m-1}^2 = a^2 + \left[\xi_m - \left(\frac{d_m}{2}\right)\right]^2 \tag{12.28}$$

where a is the j-to-x distance (see Fig. 12.2a), d_m is the center-to-center distance of the slits, and ξ_m is the displacement on x from the projected medium of d_m to the point of calculation.

The approach just described for the generalized N-slit one-dimensional grating can be extended to two-dimensional grating as illustrated in Figure 12.2b. Propagation occurs from s to x via a two-dimensional grating j_{zy}. The plane zy is orthogonal to the plane of propagation. Under these conditions the probability amplitude for photon propagation from s to x, via j_{zy} is given by [7]

$$\langle x|s\rangle = \sum_{z=1}^{N}\sum_{y=1}^{N}\langle x|j_{zy}\rangle\langle j_{zy}|s\rangle \tag{12.29}$$

which can be written as

$$\langle x|s\rangle = \sum_{z=1}^{N}\sum_{y=1}^{N}\Psi(r_{j_{zy}})e^{-i\Omega_{zy}} \tag{12.30}$$

Hence, the corresponding probability equation can be expressed as [7]

$$\left|\langle x|s\rangle\right|^2 = \sum_{z=1}^{N}\sum_{y=1}^{N}\Psi(r_{j_{zy}})\sum_{q=1}^{N}\sum_{p=1}^{N}\Psi(r_{j_{qp}})e^{i(\Omega_{qp}-\Omega_{zy})}. \tag{12.31}$$

For one dimension,

$$\Psi(r_{j_{zy}}) = \Psi(r_j) \tag{12.32}$$

and

$$\Psi(r_{j_{qp}}) = \Psi(r_m) \tag{12.33}$$

so that Equation 12.31 reduces to

$$\left|\langle x|s\rangle\right|^2 = \sum_{j=1}^{N}\Psi(r_j)\sum_{m=1}^{N}\Psi(r_m)e^{i(\Omega_m-\Omega_j)} \tag{12.34}$$

This equation can be expanded and rearranged to yield the generalized one-dimensional Equation 12.24.

At this stage, it should be mentioned that, in the past, physicists have applied quantum mechanics to describe interference and diffraction. For instance, the contribution of Feynman in this area is well known [21, 22]. However, it is interesting to note that Feynman used the path integral method to describe single-slit diffraction [21] and the Dirac formalism to describe the famous two-slit interference experiment for electrons [22]. The method described here, which is based on the Dirac formalism, is a unified approach to describe interference and diffraction phenomena. Further, in the interference domain, the description is general and applies to any number of slits. Explicitly, from the interference term of Equation 12.24 and the geometry of Figure 12.2, a generalized diffraction equation follows [23]

$$L\pi = d_m(n_1\sin\Theta_m \pm n_2\sin\Phi_m)(2\pi/\lambda) \tag{12.35}$$

where $L = 0, 2, 4\ldots$. For $n_1 = n_2$ this equation reduces to the well-known diffraction grating equation [23]

$$m\lambda = d_m(\sin\Theta_m \pm \sin\Phi_m) \tag{12.36}$$

where Θ_m is the angle of incidence and Φ_m is the angle of diffraction [14, 23]. Note that the m in $m\lambda$ is the order of diffraction ($m = 1, 2, 3 \ldots$) and is unrelated to the subscript in d_m and the angular quantities. For a grating coated over an optical glass substrate as the dimensions of the slits, and the distance separating them decrease well below the wavelength λ, then diffraction ceases to occur [23]. Under those circumstances Equation 12.35 can only be solved for $L = 0$, thus giving rise to the law of refraction, also known as Snell's law,

$$n_1 \sin \Theta_m = n_2 \sin \Phi_m \tag{12.37}$$

where Θ_m is the angle of incidence and Φ_m becomes the angle of refraction [14, 23]. Hence, the Dirac description of N-slit interference leads to a succinct unified hierarchical description of optics in the sequential order of interference, diffraction, refraction, and reflection [14, 23]. Other alternative descriptions of optics have been recently discussed [24].

One further aspect of the approach leading to the derivation of Equations 12.24, 12.31, and 12.34 is that they are derived using a particle approach applicable to single-photon propagation. However, as explained in [25] the resulting interferometric equations are also applicable to describe the interference of a distribution of indistinguishable photons as available from narrow-linewidth lasers. The use of quantum mechanical methods with the description of "macroscopic phenomena, which are not disturbed by observation," has previously been eloquently discussed by van Kampen [26].

12.5 INTERFEROMETRIC CALCULATIONS

To illustrate the application of the theory, a number of dual measurements/calculations are considered using a variety of transmission gratings. The gratings used in these measurements are made of metallic coatings on high-quality glass substrates. The dimensions of the slits are uniform within 2%. In these measurements, the detection screen (x) is a photodiode array of 1024 pixels, each 25 μm wide [6, 7].

The first case is that of the classical double-slit experiment. Each slit is 50 μm wide separated by 50 μm; that is, the center-to-center distance is 100 μm and the grating-to-screen distance is 10 cm. The measured and calculated interference signals, using Equation 12.24, are shown in Figure 12.3.

For transmission gratings with a large number of slits, the comparison between measurement and theory is performed using gratings with center-to-center distances of 200 and 60 μm [7]. In the first case, 23 slits of a grating with 100-μm-wide slits, separated by 100 μm, is illuminated for a grating-to-screen distance of 1.5 cm. The resulting near-field interferograms are shown in Figure 12.4. Next, 25 slits of the same grating are illuminated and the interference signals are measured and predicted for a grating-to-screen distance of 25 cm. The resulting interferograms are shown in Figure 12.5.

For the grating with 30-μm-wide slits, separated by 30 μm, the grating-to-screen distance is 75 cm. The measured and predicted interferograms are shown in Figure 12.6.

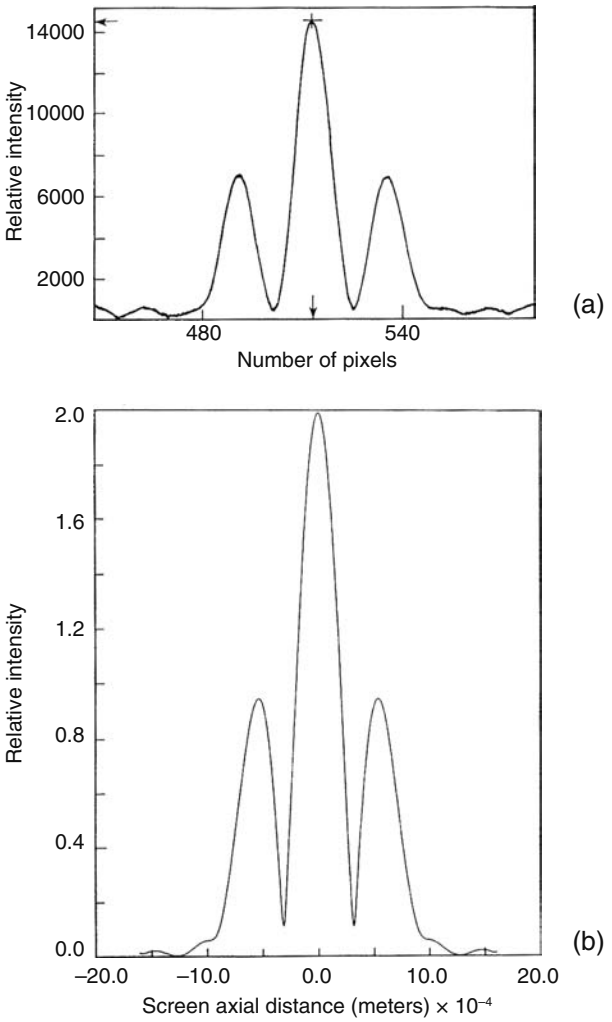

FIGURE 12.3 (a) Measurement of classical double-slit interference. Each slit is 50 μm separated by 50 μm. Each pixel is 25 μm wide. (b) Predicted interference pattern for the double-slit experiment using 50-μm-wide slits separated by 50 μm. (From Duarte, F. J., Dispersive dye lasers, in *High Power Dye Lasers*, edited by F. J. Duarte, Springer-Verlag, Berlin, 1991, Chap. 2.)

At this stage, it should be observed that the calculations have been performed using Equation 12.24 assuming plane-wave illumination of the grating. Under these idealized circumstances there is excellent agreement between theory and experiment in the spatial frequency domain. Criteria for agreement involve the number of ripples (or peaks) predicted by Equation 12.24 and the number of ripples measured. Also, predicted and measured distances agree to within 1%.

Note that the theory has not been modified to accommodate for the background noise of the instrument nor for the spatial resolution limitations of the detector. Further, beam propagation distortions are not included in the interferometric theory [7].

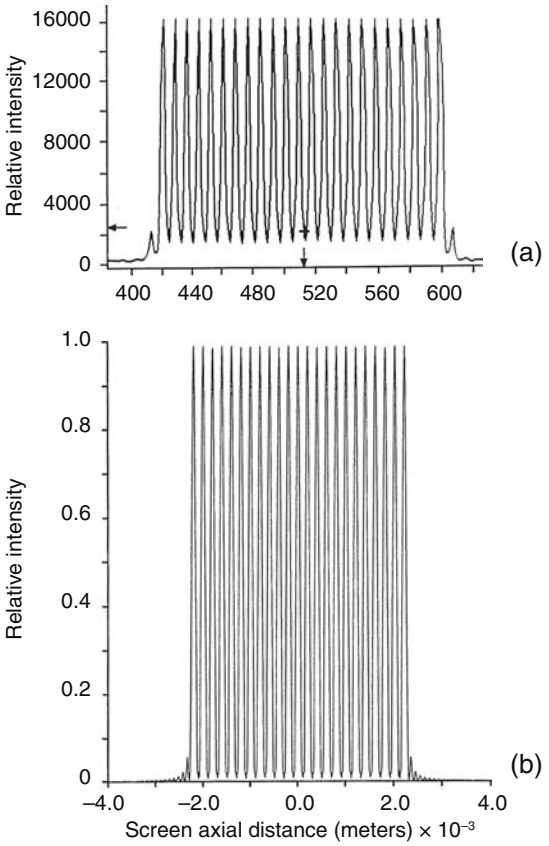

FIGURE 12.4 (a) Measured interferogram originating from a grating with 23 slits each 100 μm wide separated by 100 μm (center-to-center distance of 200 μm). The grating-to-screen distance is 1.5 cm. Each pixel is 25 μm wide. (b) Theoretical reconstruction using the generalized interference equation. (From Duarte, F. J., On a generalized interference equation and interferometric measurements, *Opt. Commun.* 103: 8–14 (1993).)

As mentioned earlier, the gratings utilized in these experiments have an intrinsic uncertainty in the dimensions of the slits of ~2%. Incorporating a ≤2% uncertainty in the dimensions of the grating yields a calculated interferogram as illustrated in Figure 12.7 for the 30-μm grating at a grating-to-screen distance of 75 cm. Note that the symmetry of the calculation without uncertainty (shown in Fig. 12.6) has deteriorated and the predicted signal yields a closer resemblance to the measurement.

A further refinement can be achieved by considering the edge effects of illumination on the grating. This occurs because a set of wide slits are used to determine the width of the beam illuminating the grating. In essence, this is a near-field diffraction phenomenon that can also be calculated using Equation 12.24. This time the wide slit or aperture is represented by hundreds of subslits. For the case of a 4-mm-wide aperture, the diffraction illumination pattern with a distance of 10 cm is shown in Figure 12.8. Here, the 4-mm aperture was represented by 800 slits, 4 μm

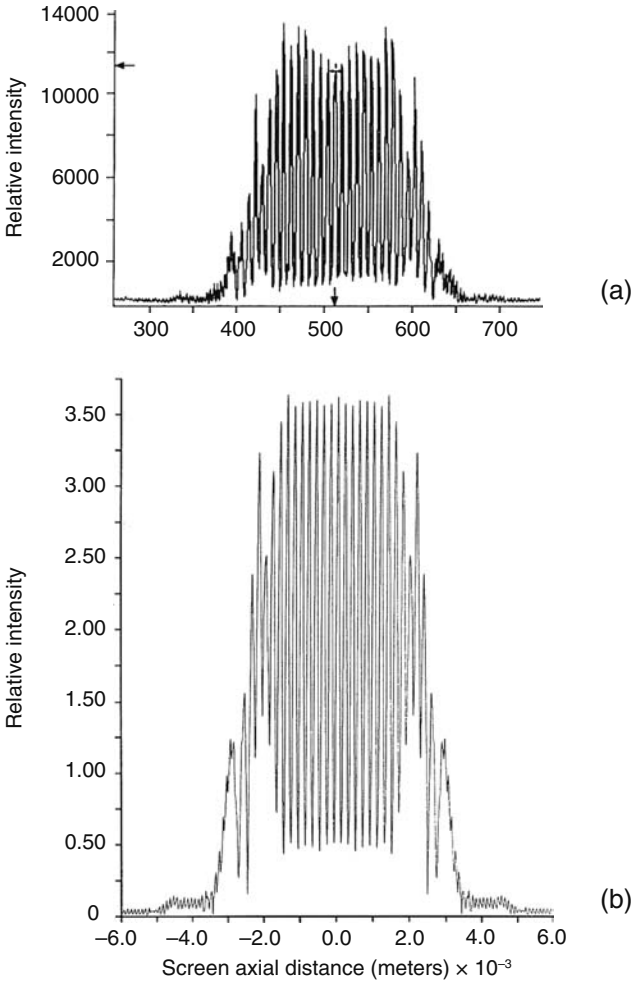

FIGURE 12.5 (a) Measured interferogram originating from a grating with 25 slits each 100 μm wide separated by 100 μm (center-to-center distance of 200 μm). The grating-to-screen distance is 25 cm. (b) Theoretical reconstruction using the generalized interference equation. (From Duarte, F. J., On a generalized interference equation and interferometric measurements, *Opt. Commun.* 103: 8–14 (1993).)

wide separated by a 1-μm interslit distance [7]. For this case, the Fresnel number ($N = w^2/L\lambda$) is 63.21.

Incorporation of the diffraction pattern, in the incidence wave, modifies the calculated interferograms from those predicted for the plane wave idealization. For the case of the 100-μm and 30-μm gratings at a grating-to-screen distance of 25 cm and 75 cm, respectively, the predicted interferograms are shown in Figure 12.9. In both cases there is a deterioration of the symmetry and a small increase in the magnitude of the oscillation at the central order [7].

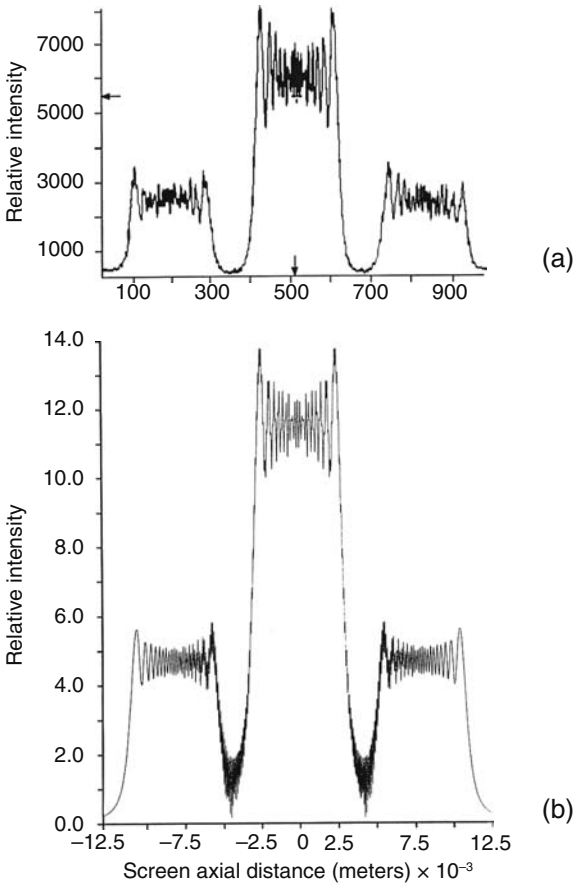

FIGURE 12.6 (a) Measured interferogram originating from a grating with 100 slits 30 μm wide separated by 30 μm (center-to-center distance of 60 μm). The grating-to-screen distance is 75 cm. (b) Corresponding theoretical reconstruction using the generalized interference equation. (From Duarte, F. J., On a generalized interference equation and interferometric measurements, *Opt. Commun.,* 103: 8–14 (1993).)

The prediction of diffraction patterns resulting from single-wide slits, or apertures, enable the application of Equation 12.24 to the calculation of transverse-mode structures in stable laser resonators [7].

The examples illustrated here indicate that the application of the Dirac formalism to beam propagation, via a generalized grating, in classical optics has yielded a unified approach to interference and/or diffraction. This is achieved by the use of a single and elegant equation.

Initially, the numerical cases considered here were analyzed using a program, written in Fortran 77, in an IBM 3090 mainframe computer. Subsequently Visual Fortran was used in a PC environment. A variety of gratings have been analyzed in the $2 \leq N \leq 2000$ slit range.

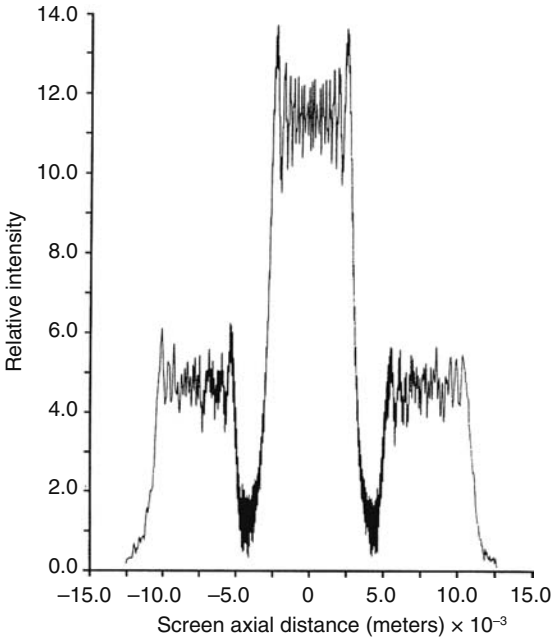

FIGURE 12.7 Theoretical interferogram for the grating composed of 100 slits 30 μm wide separated by 30 μm (center-to-center distance of 60 μm) and assuming a ≤2% uncertainty in the width of the slits. Note a deterioration of the symmetry relative to the calculation shown in the previous figure. (From Duarte, F. J., On a generalized interference equation and interferometric measurements, *Opt. Commun.* 103: 8–14 (1993).)

12.6 APPLICATIONS

The *N*-slit laser interferometer (NSLI) described here has found various applications in imaging, has been proposed for uses in secure interferometric communications, and has further uses in textiles, and biomedicine. The electro-optical interferometer described here can be used in two different modes, depending on the application. The first mode of application is the straightforward measurement of optical densities in the macroscopic domain for smooth surfaces. Also, transmission modulations can be determined in a classical noninterferometric domain where the detector screen is at a very close distance from the surface being examined and the slit dimensions are sufficiently wide. The second mode of application is in the interferometric domain.

12.6.1 Densitometry in the Macroscopic Domain

Using the linear photodiode array, the elongated Gaussian beam intensity profile, following propagation in air exclusively, is shown in Figure 12.10a. Insertion of an optically smooth surface, such as a thin microscope slide, yields little if no alterations to the beam profile, as illustrated in Figure 12.10b. As expected, the only difference is observed in the intensity domain.

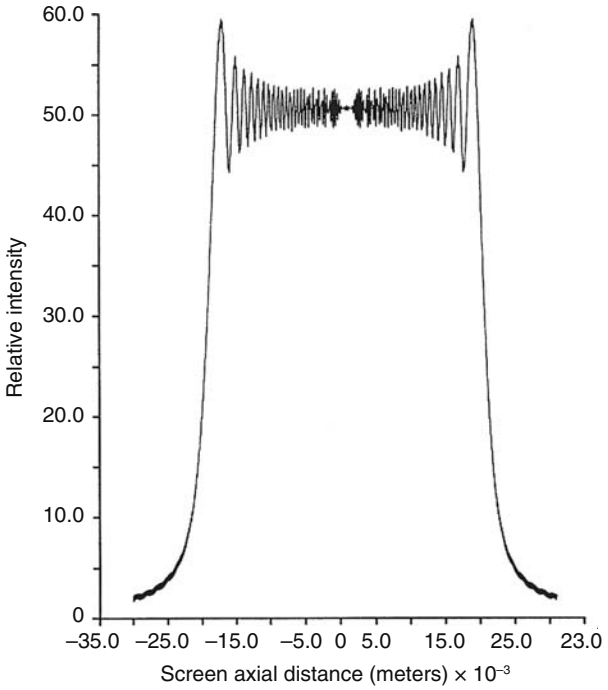

FIGURE 12.8 Theoretical diffraction near-field pattern originating from a 4-mm-wide aperture. The calculation distance is 10 cm, and the corresponding Fresnel number is 63.21. (From Duarte, F. J., On a generalized interference equation and interferometric measurements, *Opt. Commun.* 103: 8–14 (1993).)

This simple exercise illustrates that for optically smooth surfaces, such as neutral density filters, the instrument can be used as a straightforward densitometer. This is accomplished by integrating the area under the intensity curve due to the substrate alone $[I_s(\lambda, x)]$ and then by repeating the measurement with a coated substrate. The simple expression

$$D(\lambda, x) \approx \log_{10} \frac{\int I_S(\lambda, x)dx}{\int I_{s+c}(\lambda, x)dx} \tag{12.38}$$

yields the optical density D of the coating at a given wavelength. Here, I_{s+c} (λ, x) is the spatial intensity distribution measured at the wavelength λ. The advantage of this measurement over traditional density measurements is that any spatially dependent nonuniformity becomes immediately apparent. The spectral distribution of the optical density for a given surface can be obtained by tuning the laser to different wavelengths and evaluating $D(\lambda, x)$. Note that the use of the neutral-density filter prior to the telescope indicates that there is a significant intensity surplus for most measurements. This abundance of intensity enables the instrument to be applied to characterize surfaces with high-optical densities. The dynamic range of the instrument can be as high as 10^9.

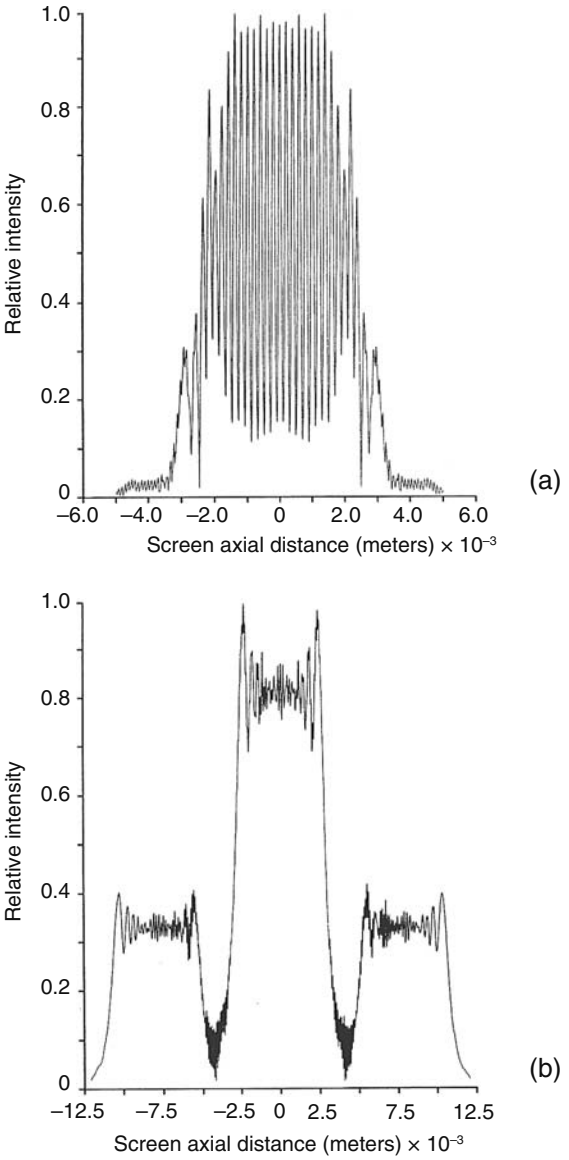

FIGURE 12.9 Theoretical interference patterns for the (a) grating with 25 slits 100 μm wide (at a grating-to-screen distance of 25 cm) and (b) the grating with 100 slits 30 μm wide (at a grating-to-slit distance of 75 cm). This time the diffraction edge effects from the wide illumination slit are incorporated into the calculation. The aperture grating distance is 10 cm. (From Duarte, F. J., On a generalized interference equation and interferometric measurements, *Opt. Commun.* 103: 8–14 (1993).)

12.6.2 Detection of Surface Microdefects

The interferometer described here is ideally suited for the detection of surface microdefects. This is illustrated in Figure 12.11a where dust particles deposited on

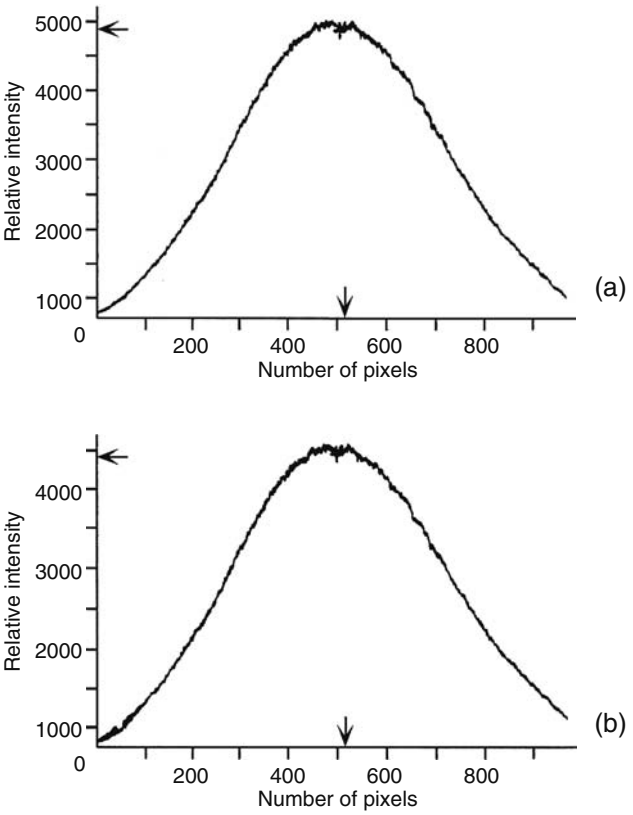

FIGURE 12.10 (a) Intensity profile, as a function of radial distance along the expanded axis, of the elongated Gaussian beam following propagation in air. (b) Intensity profile of the elongated Gaussian beam following propagation via a thin microscope slide. Note that the expanded axis is parallel to the plane of incidence. Each pixel is 25 μm wide.

the microscope slide are easily detected. On the other hand, for a high-optical-density thin metallic film, a microhole causes a strong diffraction signal. Again spatial information is easily available from the measurement (Fig. 12.11b).

As illustrated previously, a simple and inexpensive thin microscope slide yields high-fidelity transmission of the intrinsic elongated Gaussian beam intensity profile. Replacement of the glass substrate by a polymeric photographic film substrate yields an interferometric response as illustrated in a sequence of measurements recorded and displayed in the next figure. In Figure 12.12a the expanded beam intensity profile following propagation through a smooth glass substrate is displayed with no indication of interference. Replacement of the glass substrate by a high-quality polymeric photographic film substrate yields an interferometric signature as illustrated in Figure 12.12b. By contrast, a far more pronounced interferometric profile, following propagation via a lesser quality polymeric film substrate, is shown in Figure 12.12c.

It should be noted that the instrument described here provides a fast and unique avenue to quantify defects in clear polymeric film substrates that is not otherwise

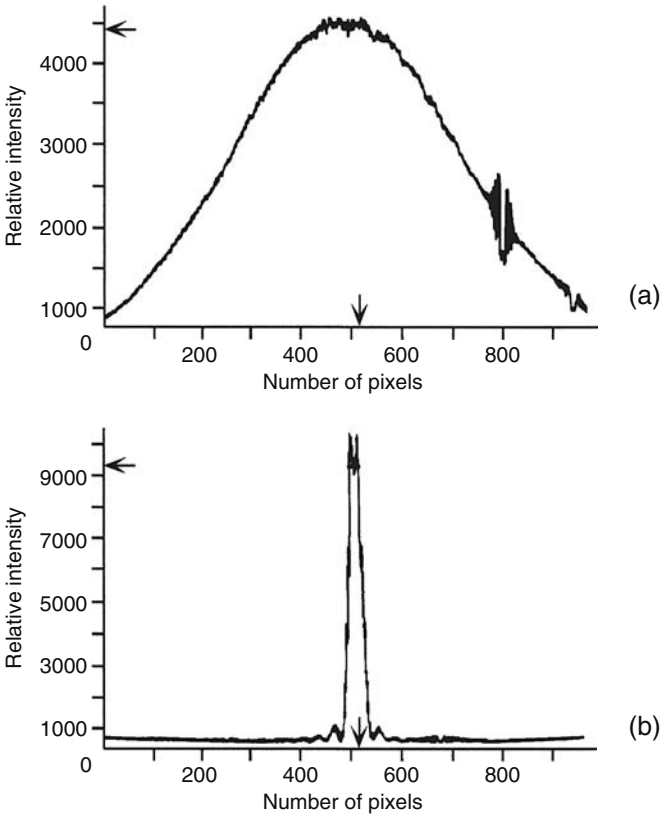

FIGURE 12.11 (a) Intensity profile of the elongated Gaussian beam following propagation via a thin microscope slide with some dust particles deposited on it. (b) Intensity profile of a neutral density filter with an optical density of 4. The diffraction pattern is caused by a microhole on the metallic film. Note that, due to Heisenberg's uncertainty principle (see Chapter 5 and [14]), the smaller the dimensions of the orifice the wider the diffraction pattern. Each pixel is 25 μm wide.

available. This is due to the fact that at these low-optical densities, traditional microdensitometers, using incoherent illumination sources, encounter serious noise limitations. In order to quantify the information provided in Figure 12.12, the log ratio of the signal is taken, relative to the intensity transmitted in air, and the standard of deviation is calculated. For the spatial profiles shown in Figures 12.12b and 12.12c, the standard of deviation is $\sigma = 0.009$ and $\sigma = 0.024$, respectively.

12.6.3 Photographic Film Grain Structure

A further application in the interferometric domain is the characterization of film grain structure in molecular imaging, as described in detail in [5]. For example, the grain structures of black-and-white silver-halide photographic film, and various other color films, have been characterized in detail. At this stage, it should be mentioned that the granularity measurement is performed by recording the microspatial intensity distribution that is the result of the interaction of the expanded laser beam with

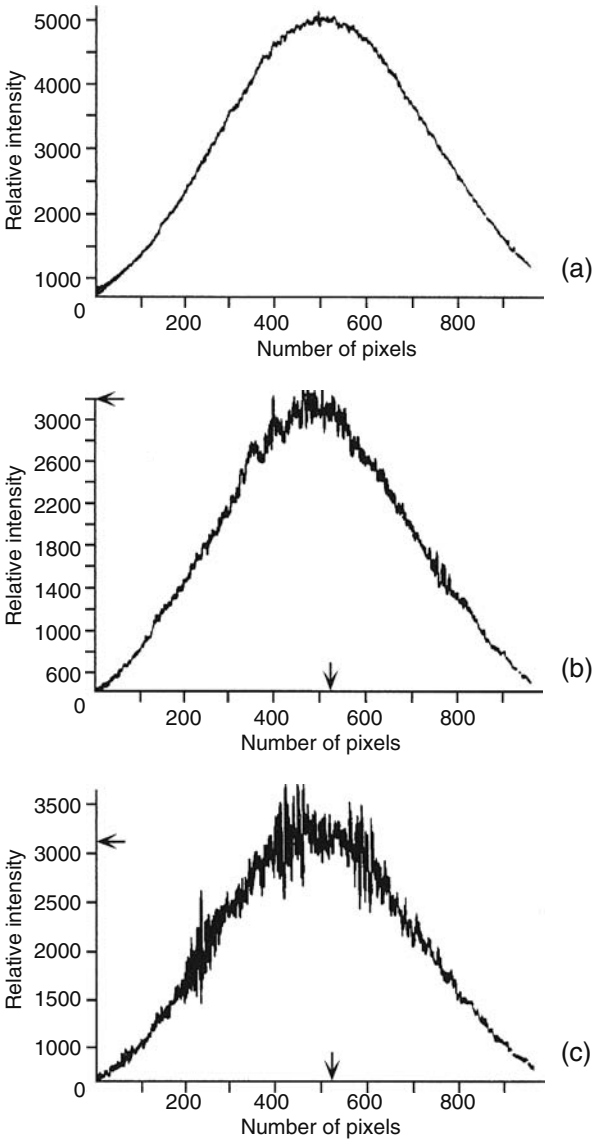

FIGURE 12.12 (a) Elongated Gaussian beam profile transmitted via a smooth thin glass substrate. (b) Interferometric profile of a high-quality clear polymeric film substrate. (c) Interferometric profile of a lesser-quality clear polymeric film substrate showing the effect of surface irregularities.

the nanodimensioned silver-halide crystals of the film and using this distribution to calculate an average microdensity and its standard of deviation according to [14]

$$D(x,\lambda) = \left(\sum_{x=1}^{N} I_i(x,\lambda)/I_t(x,\lambda) \right) N^{-1} \tag{12.39}$$

where $I_i(x, \lambda)$ is the incidence intensity, $I_t(x, \lambda)$ is the transmission intensity, and N is the total number of micro measurements. The standard of deviation of this quantity is a measure of the granularity σ of the molecular film or imaging surface.

Using an automated version of the NSLI, where the surface being illuminated is translated perpendicularly to the plane of propagation, extensive crossover measurements with conventional microdensitometers have been performed. Agreement is excellent in regard to macrodensities and similar behavior of σ as a function of D was established [14]. However, the absolute values of σ derived from the NSLI are higher than those from traditional microdensitometers given the enhanced sensitivity of the interferometric measurement. These measurements were performed at various wavelengths of interest throughout the visible range. Other advantages of the NSLI include a dynamic range of 10^9, a signal-to-noise ratio of 10^7, a depth of focus greater than 1 mm, and the simultaneous collection of a large number of data points [14].

Finally, from a mathematical perspective it should be mentioned that the form of Equation 12.34 is similar to the equation for power spectrum widely applied in traditional studies of microdensitometry [14].

The NSLI has also been used in the reflection domain, in a 45-degree configuration, to assess and quantify surface roughness in photographic, and digital imaging, papers [14].

12.6.4 Assessment of Transmission Gratings and MTF

In addition to the calculations and comparisons presented in the section on interferometric calculations, a straightforward application of the present interferometer, and the theoretical approach previously illustrated, is the assessment of transmission grating characteristics. For instance, one of the features observed in that section is that uncertainty in the dimensions of the slits cause a loss of symmetry in the interferometric/diffraction signal.

An important application is the assessment of transmission interferometric and diffractive properties of gratings coated, on transparent flexible substrates, with silver halide crystals. These gratings are compared against gratings of equal spatial specifications coated with metallic thin films. The interferometric and diffraction characteristics are measured as a function of the spatial frequency of the grating. The modulation is assessed using the usual definition due to Michelson [27]

$$\mathcal{V} = \frac{I_1 - I_2}{I_1 + I_2} \tag{12.40}$$

In the imaging community the visibility $\mathcal{V}$ is referred to as the modulation $\mathcal{M}$ while I_1 corresponds to the maximum intensity and I_2 to the minimum intensity. At the same time, the overall measured modulation patterns are compared with the corresponding theoretical prediction. Here it should be clarified that in the very near field, for an array of sufficiently wide slits, the measured patterns correspond to straightforward classical modulations similar to the distributions shown in Figure 12.4. These modulation measurements, or modulation transfer function (MTF) measurements, are

important since the higher the modulation the higher the spatial resolution, or image sharpness, offered by the imaging medium under examination.

These modulation comparisons between photographic and metallic gratings, at the same spatial frequency, are particularly useful to assist in the engineering of crystal-based imaging materials.

For example, at a spatial frequency of $f = 20$ lines/mm, the modulation of a particular set of photographic gratings is measured to be in the $0.6 \leq \mathcal{M} \leq 0.8$ range. This compares with $\mathcal{M} \approx 1$ registered from a metallic grating at the same frequency. Also, as the spatial frequency approaches 80 lines/mm and beyond, the spatial definition of the silver-halide coatings is adversely affected due to the crystalline grain structure of the photographic film. The dual theoretical/measurement approach described in the fourth and fifth sections is particularly suitable to quantify the deterioration in spatial characteristics of photographic gratings at higher spatial frequencies.

More recently this technique was extended to assess and compare the spatial resolution, via modulation measurements, of inkjet images using grating patterns of frequencies in the 0.25 lines/mm $\leq f \leq$ 5 lines/mm range. For a range of printers, at $f = 5$ lines/mm, the modulations were measured to be in the $0.71 \leq \mathcal{M} \leq 0.87$ range. All these measurements were made at $\lambda = 632.8$ nm.

It should be noted that the applicability of the NSLI extends to any grating-like array and is not just limited to imaging applications. For instance, for micromachining, microdrilling, and similar applications, one can rapidly examine and quantify the uniformity of an array of microscopic orifices or an array of microscopic nozzles.

12.6.5 Theoretical Enhancement of the Resolution of Photodiode Arrays

The interferometric theory in conjunction with the interferometric measurements can be applied to enhance the resolutions of photodiode arrays, CCD detectors, CMOS detectors, and digital detectors in general.

At present, individual diodes and/or pixels in a detector array have dimensions in the micrometer range. This size limitation, plus the need to use several diodes or pixels to resolve a given feature, introduces a serious physical limitation to the resolution of these optoelectronic detectors. A solution to this problem is outlined in [5] and rests on the use of the interferometric equations described here.

Assume that a grating with micrometer or submicrometer features needs to be characterized. For instance, this characterization may require the determination of the width of the slits of a uniform grating. For this case, positioning of the photodiode array right next to the grating provides no useful information, as the features are beyond the spatial resolution of the detector. Fortunately, as a consequence of the uncertainty principle the narrow slits, with dimensions in the micrometer or nanometer regimes, induce significant spatial spread in the far field so that the light emergent from a single slit can illuminate several individual diodes and/or pixels. For a large number of slits, the photodiode array captures the interferometric image resulting from the multiple-slit interference. Hence, a sequence of measurements in the far field can be used, in conjunction with Equation 12.24 (for the one-dimensional case, for example), to establish the dimensions and the number of slits generating the

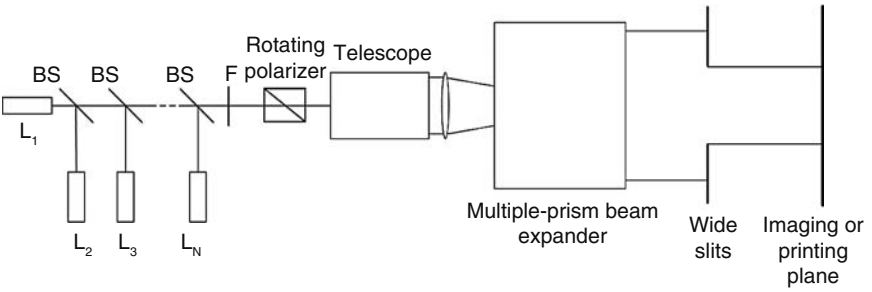

FIGURE 12.13 Schematics of the polarizer multiple-prism multiple laser (PMPML) printer. A multiple-prism expander in conjunction with a wide aperture produces a nearly constant intensity laser narrow line in the spatial domain [14]. The narrow line propagates parallel to the plane of propagation. The intensity of this narrow line can be varied continuously by rotating the Glan–Thompson polarizer. High-precision movable beam splitters determine if the exposure is single or multiple wavelength. Various lasers are designated by L_1, L_2, L_3, … L_N. (Adapted from Duarte, F. J., Laser sensitometer using multiple-prism beam expansion and polarizer, US Patent 6236461 B1 (2001).)

signal. Then the generalized interference equation can be applied to calculate the interference signals in the near field where the detector array was unable to provide a measurement.

12.6.6 Laser Printing

A multiwavelength laser instrument designed to print a series of lines, at varying intensity levels, was designed, built, and disclosed as a laser sensitometer [28]. A schematic of this optical system is shown in Figure 12.13. In essence, this is a laser printer that records a line, on a light-sensitive paper, without the need to scan a fast laser beam, with a circular cross-section, as done in alternative optical systems for this type of application [29]. In this instrument, linear polarization is used to vary the intensity of the combined laser beam using a rotating high-extinction coefficient Glan–Thompson polarizer [14, 28]. This instrument can be described as a polarizer multiple-prism multiple laser (PMPML) sensitometer or as a PMPML printer.

The collinear laser beams, usually corresponding to a blue, green, and red laser, first encounter a broadband filter to attenuate any excessive intensity. Then the multiple-wavelength beam propagates through the Glan–Thompson polarizer where high-precision rotation is used to adjust the intensity of the beam in fine increments [14, 28]. The two-dimensional telescope-lens combination yields a tightly focused beam, which is expanded in one dimension by the multiple-prism expander. This optical assembly can routinely yield an extremely elongated near-Gaussian beam 30–50 mm wide by a maximum height of 25 μm. As illustrated in [14], deployment of a wide aperture following the multiple-prism beam expander can yield a nearly constant intensity, or nearly flat, beam in the spatial domain that closely approaches a line. Displacement of a light-sensitive imaging surface, or photographic paper, perpendicular to the plane of propagation renders a series of exposures, at different wavelengths and intensity levels. For a detailed description of this instrument, the

reader should refer to [28]. An additional laser printing method utilizing a rotating polygon, in conjunction with a double-mirror arrangement, to produce high-speed displacement of a traditionally highly focused laser beam is described in [29]. This method produces a displacement of the focal point of a combined laser beam to linear speeds of ~4000 m/s.

12.6.7 Wavelength Measurements

One further application of the interferometer described here is its use as a wavelength meter. For instance, the intrinsic dependence of the measurement on wavelength is explicitly illustrated by Equations 12.24 and 12.25 because the interferometric term depends on $2\pi/\lambda$. In this regard, for a given grating and a fixed grating-to-screen distance, the interferogram becomes dependent on the wavelength alone. Hence, changes in wavelength produce changes in the interferogram. Examples of using the NSLI, and the interferometric equations, as a wavelength meter are given in [14].

A natural extension of this approach is to determine interferometrically the linewidth of the emission source [30, 31]. This development follows from the observation that interferograms from narrow-linewidth laser sources yield sharp, well-defined interferograms with a high-visibility figure ($\mathcal{V} \approx 1.0$). Broadband sources, on the other hand, produce broader, less-defined interferograms with a lower-visibility figure ($\mathcal{V} \leq 0.8$). Thus, for the same emission wavelength, and identical geometrical parameters, the interferogram from the narrow-linewidth laser source is used as a reference while Equation 12.24 is applied to generate a series of interferograms for different wavelengths departing from the central wavelength. Thus, a graphical representation of the difference of the spatial width, as a function of linewidth, is generated. This graphical representation is then used to estimate the linewidth of the unknown broader source [30, 31].

12.6.8 Secure Interferometric Communications in Free Space

The NSLI has also been shown to be applicable as an avenue of secure interferometric communications in free space [32, 33]. Security is provided by the quantum mechanical nature of the interferometric propagation. In other words, any attempt to intercept the intermediate signal, in order to extract information, distorts the signal thus alerting the receiver and subsequently the emitter. The advantage of this approach over other methods is that it works either in a single-photon mode or with a large population of indistinguishable photons as provided by a narrow-linewidth laser. So far this method has been demonstrated in the laboratory over short distances and should work well over long distances, via vacuum, in outer space. Nevertheless, preliminary measurements in the laboratory indicate that distortions in the signal due to turbulence induce a different class of distortions than those observed from interception attempts.

For this application the NSLI is divided into two parts. The laser-beam expander-grating assembly of the interferometer comprises the transmitter while the detector becomes the receiver. Configurationally, in reference to Figures 12.1 and 12.2 all stays the same, albeit the distance between the grating and the detector is allowed to become arbitrarily large. In the experiment reported in [33], the j to x distance is 723.5 cm.

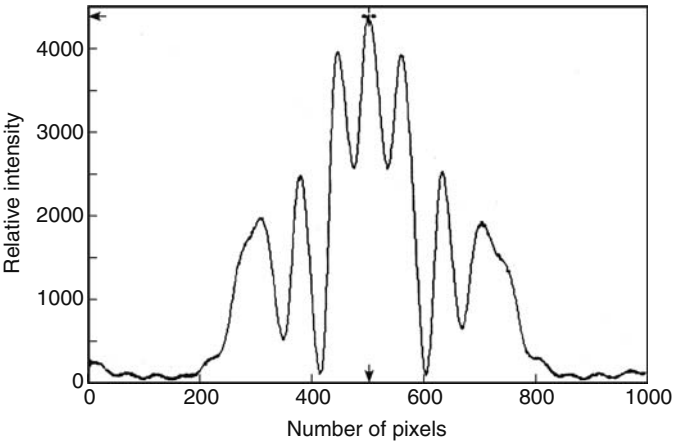

FIGURE 12.14 Interferometric character "c" generated by the interaction of an expanded TEM_{00} laser beam with four equidistant slits. Each slit is 570 μm wide and $\lambda = 632.82$ nm. The distance from the slits to the digital detector is 723.5 cm and the small cross indicates the position of the central pixel, each 25 m wide, in the digital detector. (From Duarte, F. J., Secure interferometric communications in free space: enhanced sensitivity for propagation in the metre range, *J. Opt. A: Pure Appl. Opt.* 7: 73–75 (2005).)

The concept of secure interferometric communications can be described with the following example, which uses the interferometric character "c" created by the interaction of an expanded laser beam with four slits in a grating [33]. In Figure 12.14 the initial undisturbed signal being emitted, transmitted, and received is displayed. In Figure 12.15 the effect, on the received interferometric signal, due to the partial insertion of a thin beam splitter is shown. In Figure 12.16 the effect on the received interferometric signal due to the complete insertion of the thin beam splitter is illustrated. In Figure 12.17 the interferometric signal is displayed as fully restored due to the withdrawal of the thin beam splitter.

The effect of atmospheric turbulence, simulated by the insertion of a thermal source in the path of the interferometric signal, is illustrated in Figure 12.18. As previously mentioned the pattern of these distortions is different from the violent effect due to the insertion of a thin beam splitter as depicted in Figure 12.15.

For further details on the generation of interferometric characters, the reader is referred to [32, 33]. In a discussion on conceptual countermeasures given in [33] it is underlined that the security of this method of communications is guaranteed by the principle of interference. Also, it is mentioned that Feynman [22] considered interference a fundamental principle of quantum mechanics. It is also relevant to mention that the principles of *N*-slit interferometry as described via Dirac's notation [8] can be used to provide an approximate derivation of Heisenberg's uncertainty principle [14].

12.6.9 Interferometry in Textiles

A semiorderly single-layer textile fabric looks like a grid or a two-dimensional grating as shown in Figure 12.19. Higher-quality fabrics present a more compact network

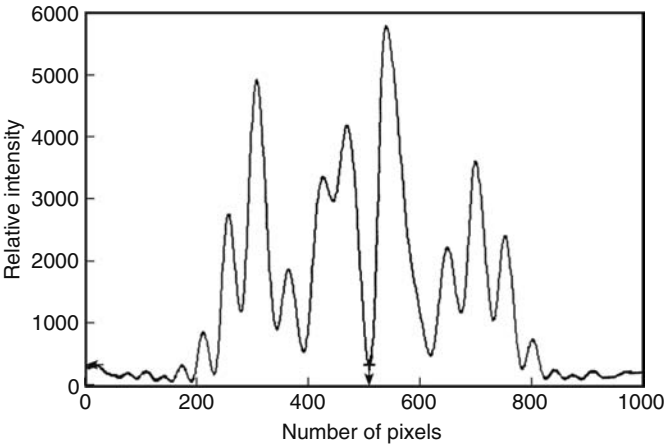

FIGURE 12.15 Severe spatial distortions induced in the interferometric character c by introducing a thin beam splitter at an angle near the Brewster angle relative to the axis of propagation. The laser beam is polarized parallel to the plane of propagation. (From Duarte, F. J., Secure interferometric communications in free space: enhanced sensitivity for propagation in the metre range, *J. Opt. A: Pure Appl. Opt.* 7: 73–75 (2005).)

of finer fibers. From an optics and interferometric perspective this means that a particular class of single-layered fabric corresponds to a particular grating structure and as such is applicable to an interferometric classification. An interferogram using the NSLI on the type of single-layer cotton fabric in Figure 12.19 yields an interferometric signature as shown in Figure 12.20.

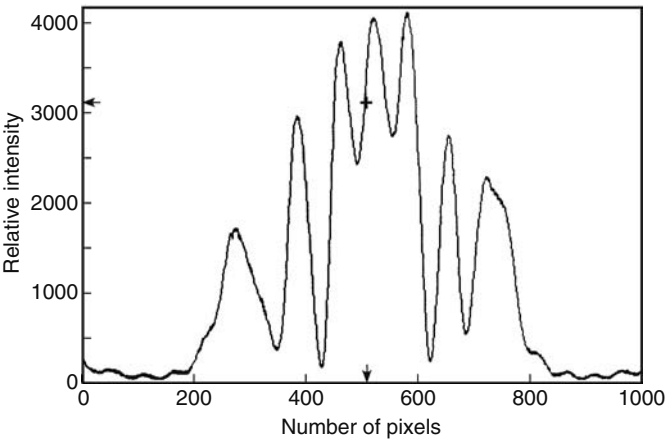

FIGURE 12.16 Spatial distortions in the interferometric character c with the thin beam splitter in place. The intercepted character does not display its original symmetry and is displaced ~300 μm to the right. (From Duarte, F. J., Secure interferometric communications in free space: enhanced sensitivity for propagation in the metre range, *J. Opt. A: Pure Appl. Opt.* 7: 73–75 (2005).)

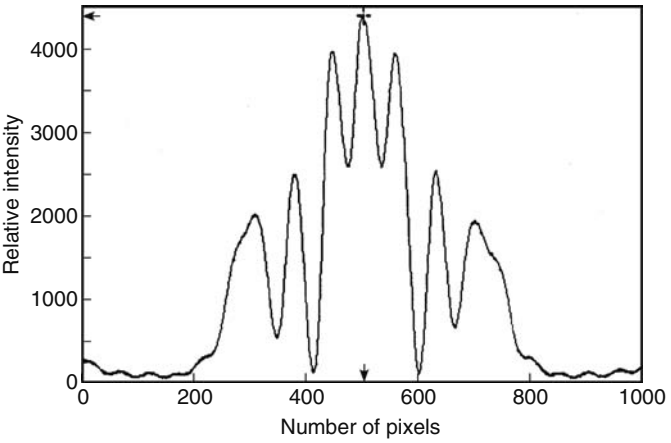

FIGURE 12.17 Removal of the beam splitter restores the original interferometric character c. (From Duarte, F. J., Secure interferometric communications in free space: enhanced sensitivity for propagation in the metre range, *J. Opt. A: Pure Appl. Opt.* 7: 73–75 (2005).)

In the same way a molecular coating, of given characteristics, yields a unique interferometric signature, it is not difficult to extrapolate to networks of fibers constituting textile fabrics. This technique could also be used as a forensic tool to determine the similarity, or differences, between two fabrics. This could be used to establish if a given fabric came from a particular region or epoch of interest.

12.6.10 Applications to Biomedicine

Early detection of certain cancers requires more sensitive and higher-resolution x-ray films. In this regard microdensitometry is an essential tool applied to determine the

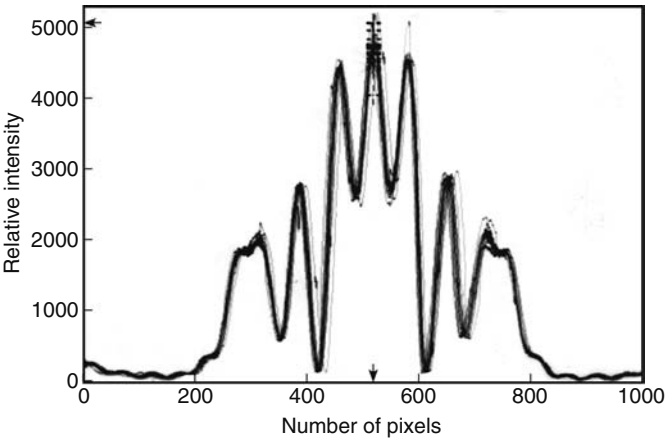

FIGURE 12.18 Cumulative spatial distortions in the interferometric character "c" caused by turbulence in the propagation air generated by a thermal source.

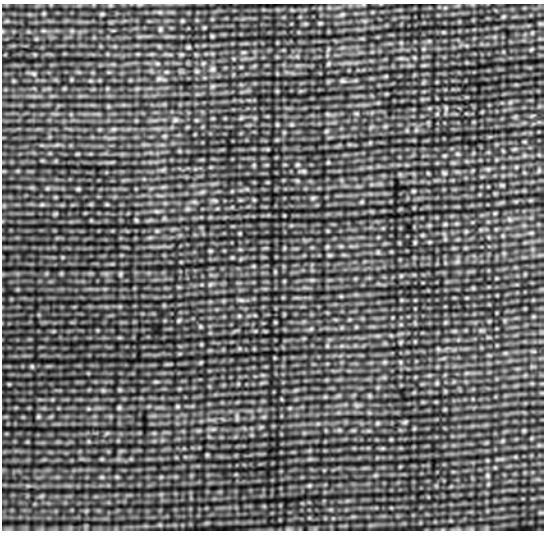

FIGURE 12.19 Single-layered textile 25 × 25 mm approximately.

granularity of the film. Modulation measurements are also important. As previously discussed the NSLI can be used to quantify both these parameters rapidly and with added sensitivity.

An additional way to think of the NSLI is as a laser microscope with a vastly extended field of observation and a vastly extended depth of focus. Microscopy has been used in biomedicine since the seventeenth century and, as we all know, today it continues to be used in a plethora of biomedical applications (see Chapter 9). The NSLI could also be used as a microdensitometer to observe, compare, and study biological samples in the transmission domain. Using a broadly tunable laser greatly enhances its information-gathering capabilities.

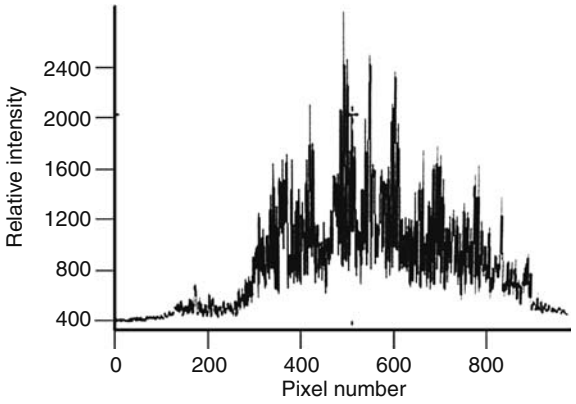

FIGURE 12.20 Interferometric signature of single-layered textile.

The illumination and wide microdetection capabilities of the NSLI have been found relevant by researchers and engineers working on instrumentation for structural analysis of organic compounds [34], cytological research [35], and x-ray imaging [36–38].

12.7 CONCLUSIONS

The *N*-slit laser interferometer has been discussed and analyzed. This instrument can be described as a tunable laser microscope with an extensive microillumination capability and a very long depth of focus. Alternatively, the NSLI can be thought of as a microdensitometer with wide illumination and extensive depth of focus. Beam propagation through the telescope and multiple-prism expander has been described using ray transfer matrices. This approach enables the prediction of the beam spatial characteristics at the focal plane. For one mode of operation, the optics yields an extremely elongated Gaussian spatial beam ~30 μm high by 35–50 mm wide. An alternative mode of operation is the generation of spatial Gaussian beams ~10 mm high by 35–50 mm wide.

Transmission surfaces can be assessed by positioning the surface of interest in the vertical plane, normal to the plane of propagation, between the multiple-prism expander and the digital detector array. For smooth optical surfaces the instrument can be used as a classical densitometer. For surfaces with micro and submicron features, such as transmission gratings, the instrument functions as an interferometer. However, in the near field, and for sufficiently wide slits, the instrument measures classical modulation patterns.

The Dirac formalism has been applied to describe the photon propagation from the source to the detection screen, via the intermediate grating. The resulting interferometric equations have been successfully applied to predict and quantify the measured interference/diffraction patterns. An important application of this method enables the prediction of interference signals in the near field where photodiode array detectors are unable to resolve. Thus, the resolution of these detectors can be enhanced.

Other applications include detection of microholes in thin metal films, detection of surface defects in clear transmission surfaces, characterization of grain structure in photographic film, assessment of transmission gratings, and wavelength measurements. The NSLI has also been applied to assess textile fabrics and to demonstrate secure interferometric communications in free space. Various biomedical applications have also been outlined.

The scope of applications is significantly enhanced by the availability of a variety of discretely tunable and broadly tunable laser sources. A requirement of the laser source is emission in a single-transverse mode.

ACKNOWLEDGMENTS

This work was made possible by the support of the former Photographic Research Laboratories of the Eastman Kodak Company and it was enthusiastically encouraged by J. Merrigan, in whose memory this work is dedicated. Also, the author is grateful to J. C. Kinard and J. P. Terwilliger. For software support, the author is thankful to D. J. Paine and F. J. Duarte, Jr.

REFERENCES

1. Dainty, J. C., and R. Shaw, *Image Science*, Academic, New York, 1974.
2. Duarte, F. J., Static multicolor laser system for microdensitometry: preliminary report, *Current Awareness Report*, Eastman Kodak Company, Rochester, New York, 1986 (unpublished).
3. Duarte, F. J., and D. J. Paine, Quantum mechanical description of N-slit interference phenomena, in *Proceedings of the International Conference on Lasers '88*, edited by R. C. Sze and F. J. Duarte, STS, McLean, Virginia, 1989, pp. 42–47.
4. Duarte, F. J., Dispersive dye lasers, in *High Power Dye Lasers*, edited by F. J. Duarte, Springer-Verlag, Berlin, 1991, Chap. 2.
5. Duarte, F. J., Electro-optical interferometric microdensitometer system, U.S. Patent 5255069 (1993).
6. Duarte, F. J., On a generalized interference equation and interferometric measurements, *Opt. Commun.* 103: 8–14 (1993).
7. Duarte, F. J., Interferometric imaging, in *Tunable Laser Applications*, 1st ed., Marcel Dekker, New York, 1995, Chap. 5.
8. Dirac, P. A. M., *The Principles of Quantum Mechanics*, 4th ed., Oxford, University, London, 1978.
9. Willett, C. S., *An Introduction to Gas Lasers: Population Inversion Mechanisms*, Pergamon, New York, 1974.
10. Hollberg, L., CW dye laser, in *Dye Laser Principles*, edited by F. J. Duarte and L. W. Hillman, Academic, New York, 1990, Chap. 5.
11. Johnston, T. F., and F. J. Duarte, Lasers, Dye, in *Encyclopedia of Physical Science and Technology,* 3rd ed., Volume 8, edited by R. A. Meyers, Academic, New York, 2002, pp. 315–359.
12. Duarte, F. J., Narrow linewidth pulsed dye laser oscillators, in *Dye Laser Principles*, edited by F. J. Duarte and L. W. Hillman, Academic, New York, 1990, Chap. 4.
13. Duarte, F. J., Multiple-prism grating solid-state dye laser oscillator: optimized architecture, *Appl. Opt.* 38: 6347–6349 (1999).
14. Duarte, F. J., *Tunable Laser Optics*, Elsevier-Academic, New York, 2003.
15. Olejnicek, J., H. T. Do, Z. Hubicka, R. Hippier, and L. Jastrabik, Blue diode laser absorption spectroscopy of pulse magnetron discharge, *Jpn. J. Appl. Phys.* 45: 8090–8094 (2006).
16. Olivares, I. E., A. E. Duarte, E. A. Saravia, and F. J. Duarte, Lithium isotope separation with tunable diode lasers, *Appl. Opt.* 41: 2973–2977 (2002).
17. Zorabedian, P., Characteristics of a grating-external-cavity semiconductor laser containing intracavity prism beam expanders, *J. Lightwave Technol.* 10: 330–335 (1992).
18. Duarte, F. J., Beam shaping with telescopes and multiple-prism beam expanders, *J. Opt. Soc. Am. A,* 4: P30 (1987).
19. Duarte, F. J., Multiple-prism dispersion and 4×4 ray transfer matrices, *Opt. Quantum Electron.* 24: 49–53 (1992).
20. Turunen, J., Astigmatism in laser beam optical systems, *Appl. Opt.* 25: 2908–2911 (1986).
21. Feynman, R. P., and A. R. Hibbs, *Quantum Mechanics and Path Integrals*, McGraw-Hill, New York, 1965.
22. Feynman, R. P., R. B. Leighton, and M. Sands, *The Feynman Lectures on Physics*, Addison-Wesley, Reading, MA, 1971, Vol. III.
23. Duarte, F. J., Interference, diffraction, and refraction, via Dirac's notation, *Am. J. Phys.* 65: 637–640 (1997).
24. Kurusingal, J., Law of normal scattering—a comprehensive law for wave propagation at an interface, *J. Opt. Soc. Am. A* 24: 98–108 (2007).

25. Duarte, F. J., Comment on "Reflection, refraction, and multislit interference," *Eur. J. Phys.* 25: L57–L58 (2004).
26. van Kampen, N. G., Ten theorems about quantum mechanical measurement, *Physica A* 153: 97–113 (1988).
27. Michelson, A. A., *Studies in Optics*, The University of Chicago, 1927.
28. Duarte, F. J., Laser sensitometer using multiple-prism beam expansion and polarizer, US Patent 6236461 B1 (2001).
29. Duarte, F. J., B. A. Reed, and C. J. Burak, Laser sensitometer, US Patent 6903824 B2 (2005).
30. Duarte, F. J., Coherent electrically-excited organic semiconductors: visibility of interferograms and emission linewidth, *Opt. Lett.* 32: 412–414 (2007).
31. Duarte, F. J., Coherent electrically-excited organic semiconductors: coherent or laser emission? *Appl. Phys. B*. 90: 101–108 (2008).
32. Duarte, F. J., Secure interferometric communications in free space, *Opt. Commun*. 205: 313–319 (2002).
33. Duarte, F. J., Secure interferometric communications in free space: enhanced sensitivity for propagation in the metre range, *J. Opt. A: Pure Appl. Opt*. 7: 73–75 (2005).
34. Chrastil, J., Spectrophotometric method for structural analysis of organic compounds, polymers, nucleotides, and peptides, US Patent 5550630 (1996).
35. Ortyn, W. E., L. R. Piloco, and J. W. Hayenga, Cytological system illumination integrity checking apparatus and method, US Patent 6011861 (2000).
36. Sliski, A. P., X-ray phantom apparatus, US Patent 5511107 (1996).
37. Sliski, A. P., CCD X-ray microdensitometer system, US Patent 5623139 (1997).
38. Kwok, C. S., and K. Y. Lee, Microdensitometer system with micrometer resolution for reading radiochromic films, US Patent 6927859 (2005).

13 Multiple-Prism Arrays and Multiple-Prism Beam Expanders: Laser Optics and Scientific Applications

F. J. Duarte

CONTENTS

13.1 Introduction 375
13.2 Dispersion Theory of Multiple-Prism Arrays 375
13.2.1 The Interferometric Origin of Dispersion 380
13.3 Applications to Laser Optics 383
13.4 Applications to Laser Spectroscopy and Sequential Laser Excitation 383
13.5 Applications to Guide Stars and Astronomy 384
13.6 Applications to Pulse Compression in Ultrashort Pulse Lasers 384
13.7 Applications to Microscopy and Ultrafast Spectroscopy 385
13.8 Applications to Interferometry and Optical Metrology 385
References 386

13.1 INTRODUCTION

Multiple-prism arrays were introduced by Newton's *Opticks* in 1704 [1]. In addition to introducing the reflection telescope, and providing a detailed qualitative description of multiple-prism arrays, the prophetic book also suggested using the prism as a beam expander [2]. A subsequent significant contribution was made by Brewster, who introduced prism pairs as beam expanders in 1813 [3].

13.2 DISPERSION THEORY OF MULTIPLE-PRISM ARRAYS

Multiple-prism wavelength tuners were introduced by Strome and Webb [4] in 1971. The introduction of a prism as an intracavity beam expansion element in tunable lasers by Hanna et al. [5] was followed by the introduction of multiple-prism beam expanders

to achieve efficient illumination of the diffraction grating in narrow-linewidth tunable laser oscillators [6–8]. Prismatic and multiple-prism intracavity beam expansion in oscillators using near grazing-incidence grating configurations was demonstrated shortly thereafter [9–11]. Comprehensive reviews on this subject are given in [12, 13].

The emission linewidth in a pulsed tunable laser oscillator is given by [4, 12–16]

$$\Delta\lambda \approx \Delta\theta(\nabla_\lambda \Theta)^{-1} \tag{13.1}$$

where

$$\nabla_\lambda \Theta = \partial\Theta/\partial\lambda \tag{13.2}$$

is the overall intracavity dispersion (see Chapter 4 for further details). This cavity linewidth equation was originally introduced from a classical perspective [4, 15] and was subsequently shown to be compatible with interferometric principles using Dirac's notation [13, 16].

Soon after the introduction of intracavity multiple-prism beam expanders it became necessary to develop a generalized multiple-prism dispersion theory. That was provided in 1982 by Duarte and Piper [17, 18]. For a generalized array of m prisms, as depicted in Figure 13.1, the cumulative dispersion at the mth prism is given by [17, 18]

$$\nabla_\lambda \phi_{2,m} = \mathcal{H}_{2,m} \nabla_\lambda n_m + (k_{1,m} k_{2,m})^{-1} \left(\mathcal{H}_{1,m} \nabla_\lambda n_m \pm \nabla_\lambda \phi_{2,(m-1)} \right) \tag{13.3}$$

where

$$\mathcal{H}_{1,m} = (\tan \phi_{1,m})/n_m \tag{13.4}$$

$$\mathcal{H}_{2,m} = (\tan \phi_{2,m})/n_m \tag{13.5}$$

are geometrical coefficients while

$$k_{1,m} = \frac{\cos \psi_{1,m}}{\cos \phi_{1,m}} \tag{13.6}$$

is the beam expansion experienced by the beam at the incidence surface of the mth prism and

$$k_{2,m} = \frac{\cos \phi_{2,m}}{\cos \psi_{2,m}} \tag{13.7}$$

is the corresponding term at the exit surface of the mth prism. Here $\phi_{1,m}$ and $\phi_{2,m}$ are the incidence and exit angles, respectively, at each individual prism, whereas

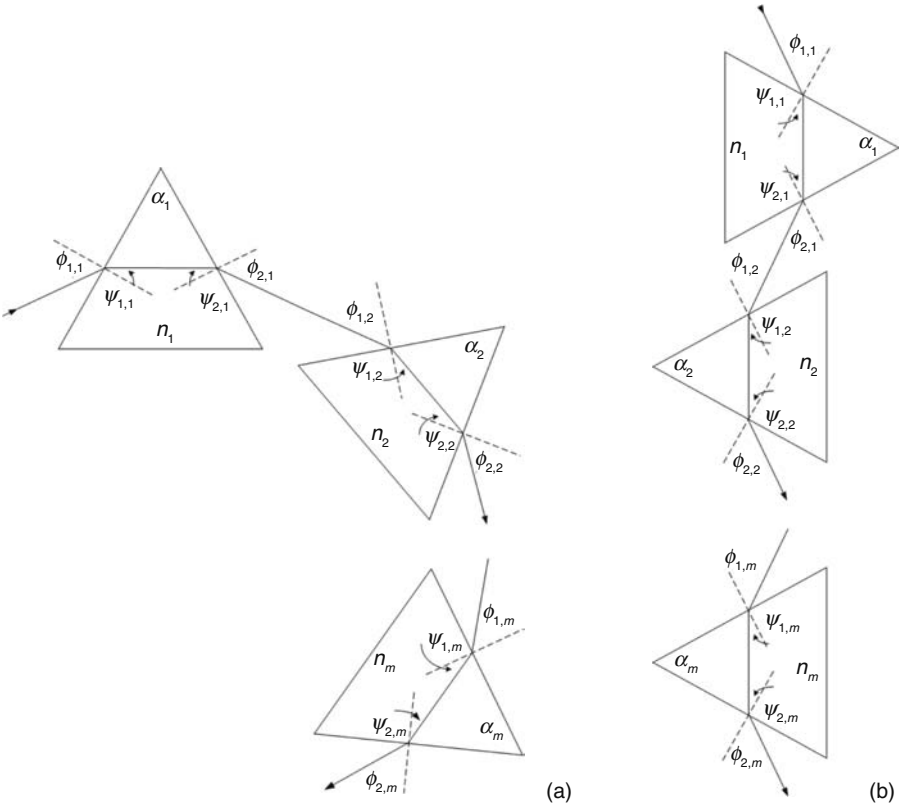

FIGURE 13.1 Generalized multiple-prism array deployed in (a) an additive configuration and (b) a compensating configuration. (This figure is a simplified version of the original generalized multiple-prism configurations illustrated by Duarte, F. J., and J. A. Piper, Dispersion theory of multiple-prism beam expander for pulsed dye lasers, *Opt. Commun.* 43: 303–307 (1982); and Duarte, F. J., and J. A. Piper, Generalized prism dispersion theory, *Am. J. Phys.* 51: 1132–1134 (1983).)

$\psi_{1,m}$ and $\psi_{2,m}$ are the corresponding angles of refraction as determined by Snell's law. In Equation 13.3 the term $\nabla_\lambda \phi_{2,(m-1)}$ refers to the cumulative dispersion up to the $(m-1)$ prism. Equations for the generalized double-pass dispersion are given in [12, 13, 17, 18]. In [12, 13] these double-pass equations are also expressed in explicit notation directly applicable to designs and calculations.

Using explicit notation, Equation 13.3 can be expressed as [12–14]

$$\nabla_\lambda \phi_{2,r} = \sum_{m=1}^{r} (\pm 1)\mathcal{H}_{1,m}\left(\prod_{j=m}^{r} k_{1,j} \prod_{j=m}^{r} k_{2,j}\right)^{-1} \nabla_\lambda n_m + (M_1 M_2)^{-1} \sum_{m=1}^{r} (\pm 1)\mathcal{H}_{2,m}\left(\prod_{j=1}^{m} k_{1,j} \prod_{j=1}^{m} k_{2,j}\right) \nabla_\lambda n_m \tag{13.8}$$

where

$$M_1 = \prod_{j=1}^{r} k_{1,j} \tag{13.9}$$

$$M_2 = \prod_{j=1}^{r} k_{2,j} \tag{13.10}$$

For the important practical case of an array of r right-angle prisms designed for orthogonal beam exit (that is, $\phi_{2,m} = \psi_{2,m} = 0$), Equation 13.8 reduces to [13]

$$\nabla_\lambda \phi_{2,r} = \sum_{m=1}^{r} (\pm 1)\mathcal{H}_{1,m} \left(\prod_{j=m}^{r} k_{1,j} \right)^{-1} \nabla_\lambda n_m \tag{13.11}$$

Furthermore, if the prisms in the array have identical apex angle ($\alpha_1 = \alpha_2 = \alpha_3 = \cdots = \alpha_m$) and are configured to have the same angle of incidence ($\phi_{1,1} = \phi_{1,2} = \phi_{1,3} = \cdots = \phi_{1,m}$) then Equation 13.11 reduces to [12–14]

$$\nabla_\lambda \phi_{2,r} = \tan \psi_{1,1} \sum_{m=1}^{r} (\pm 1)(1/k_{1,m})^{m-1} \nabla_\lambda n_m \tag{13.12}$$

This class of multiple-prism beam expander, for $r = 3$, is illustrated in Figure 13.2 for additive and compensating dispersion configurations.

For an array of r right-angle prisms, with identical apex angle ($\alpha_1 = \alpha_2 = \cdots = \alpha_m$) , deployed at the Brewster angle of incidence, and designed for orthogonal beam exit, Equation 13.8 assumes the rather elegant form of [12, 13]

$$\nabla_\lambda \phi_{2,r} = \sum_{m=1}^{r} (\pm 1)(1/n_m)^m \nabla_\lambda n_m \tag{13.13}$$

In this power series n_m is the refractive index of the mth prism. Under these special circumstances the overall beam expansion is given by [12]

$$M = n^r \tag{13.14}$$

One further case of practical significance is that of an array of r identical isosceles prisms, deployed symmetrically in additive configuration, so that $\phi_{1,m} = \phi_{2,m}$, then Equation 13.3 reduces to [12, 13]

$$\nabla_\lambda \phi_{2,r} = r \nabla_\lambda \phi_{2,1} \tag{13.15}$$

The use of the generalized dispersion equations to design multiple-prism beam expanders with zero dispersion at a given wavelength, that is,

$$\nabla_\lambda \phi_{2,m} \approx 0 \tag{13.16}$$

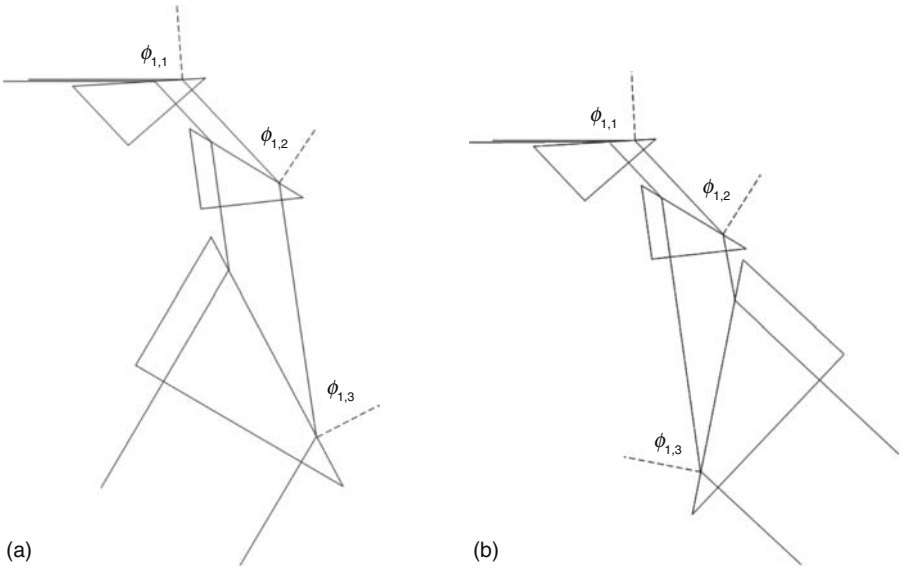

FIGURE 13.2 Multiple-prism expander, $r = 3$, designed for orthogonal beam exit. (a) Deployment in an additive configuration and (b) deployment in a compensating configuration yielding $\nabla_\lambda \phi_{2,3} \approx 0$. This particular depiction approximates a calculation suggested as a problem in [13] using crown glass at $\lambda = 590$ nm ($n \approx 1.5167$).

is described, and discussed, in [12, 13, 19]. Equations describing multiple-pass intracavity dispersion are given by Duarte and Piper [20] and also in [12, 13, 21].

For pulse compression it is necessary to use the identity

$$\nabla_n \phi_{2,m} = \nabla_\lambda \phi_{2,m} (\nabla_\lambda n_m)^{-1} \tag{13.17}$$

that allows re-expressing Equation 13.3 as [22]

$$\nabla_n \phi_{2,m} = \mathcal{H}_{2,m} + (k_{1,m} k_{2,m})^{-1} \left(\mathcal{H}_{1,m} \pm \nabla_n \phi_{2,(m-1)} \right) \tag{13.18}$$

Thus the derivative of the dispersion becomes [13, 22]

$$\begin{aligned} \nabla_n^2 \phi_{2,m} = {} & \mathcal{H}_{2,m} n_m (\nabla_n \phi_{2,m})^2 + (k_{1,m} k_{2,m})^{-1} \\ & \times \left\{ \left(\mathcal{H}_{1,m} \chi_{1,m} k_{1,m} n_m \nabla_n \phi_{1,m} \pm \nabla_n^2 \phi_{2,(m-1)} \right) + \left(\mathcal{H}_{1,m} \pm \nabla_n \phi_{2,(m-1)} \right) \right. \\ & \left. \left(\chi_{1,m} \nabla_n \psi_{1,m} - \mathcal{H}_{2,m} k_{2,m} \nabla_n \psi_{2,m} - \chi_{1,m} k_{1,m} n_m \nabla_n \phi_{1,m} \right) \right\} \\ & + (k_{2,m})^{-1} (\nabla_n \psi_{1,m} + \nabla_n \psi_{2,m}) \end{aligned} \tag{13.19}$$

where

$$\chi_{1,m} = \tan\psi_{1,m} \tag{13.20}$$

For the special case of four isosceles prisms [23], at minimum deviation, and deployed at the Brewster angle of incidence, the dispersion and its derivative become [13, 22]

$$\nabla_n \phi_{2,1} = \nabla_n \phi_{2,3} = 2 \tag{13.21}$$

$$\nabla_n \phi_{2,2} = \nabla_n \phi_{2,4} = 0 \tag{13.22}$$

$$\nabla_n^2 \phi_{2,1} = \nabla_n^2 \phi_{2,3} = 4n - (2/n^3) \tag{13.23}$$

$$\nabla_n^2 \phi_{2,2} = \nabla_n^2 \phi_{2,4} = 0 \tag{13.24}$$

13.2.1 The Interferometric Origin of Dispersion

In a paper published in 1997 a succinct derivation of refraction was given that established the following hierarchical description of optics: interference, diffraction, and refraction [24]. The next reductive step following refraction, namely reflection, was added in 2003 [13]. Apart from succinctness, the beauty of this interferometric approach, via Dirac's notation, is that it naturally opens further refractive avenues. A brief description of this approach is provided here from a slightly different perspective to that published in the recent literature [25].

Following the convention introduced in [25], and in reference to Figure 13.3, for incidence above the normal the sign of the angle is defined as positive (+). For diffraction below the normal the diffraction angle is defined as negative (–). In reference to Figure 13.4, for incidence below the normal the sign of the angle is defined as negative (–). For diffraction below the normal the diffraction angle is also defined as negative (–). Alternative cases of incidence and diffraction are illustrated in [25], and it is clear that there is a ± alternative associated with diffraction. The traditional description associated with incidence below the normal (–) and diffraction above the normal (+) is described in [25].

Interference associated with ± incidence and/or ± diffraction, as it occurs in nature, is accurately described by the generalized interferometric equation introduced in Chapter 12 [13, 26–28]

$$|\langle x \mid s\rangle|^2 = \sum_{j=1}^{N} \Psi(r_j)^2 + 2\sum_{j=1}^{N} \Psi(r_j)\left(\sum_{m=j+1}^{N} \Psi(r_m)\cos(\Omega_m - \Omega_j)\right) \tag{13.25}$$

The interferometric term of this equation, given in the inner parentheses, in conjunction with the detailed geometrical terms [13, 28], leads to the following diffraction equation allowing all the incidence and diffraction alternatives

$$d_m(\pm n_1 \sin\Theta_m \pm n_2 \sin\Phi_m)(2\pi/\lambda_v) = L\pi \tag{13.26}$$

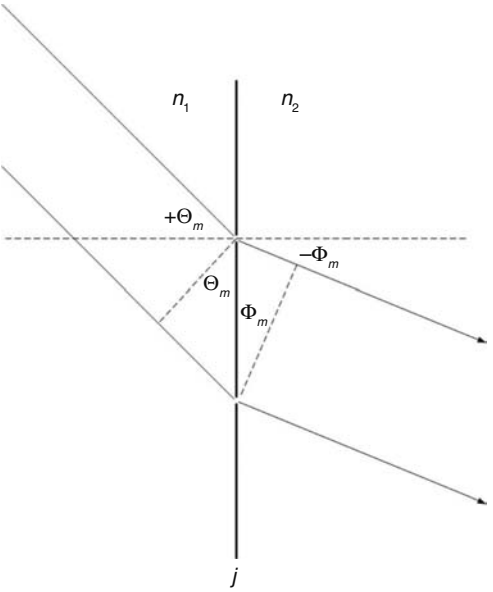

FIGURE 13.3 The plane of the slits (j) illustrating incidence above the normal $+\Theta_m$ and diffraction below the normal $-\Phi_m$ (see text).

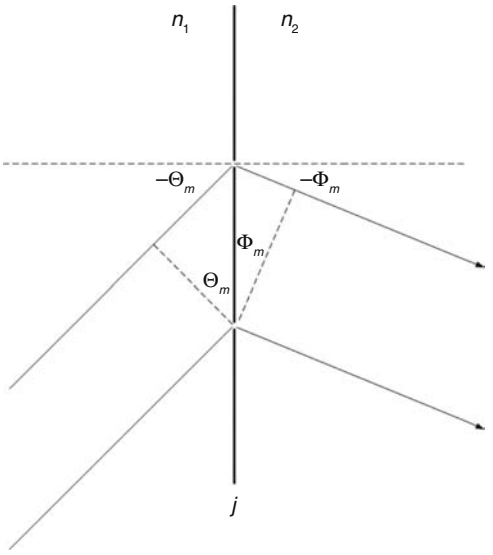

FIGURE 13.4 The plane of the slits (j) illustrating incidence below the normal $-\Theta_m$ and diffraction below the normal $-\Phi_m$ (see text).

This is a generalized form of the diffraction-grating equation where, in reference to Figures 13.3 and 13.4, n_1 and n_2 represent the refractive indices of two adjacent regions separated by the slit array comprising the diffraction grating, Θ_m is the angle of incidence, Φ_m is the angle of refraction, d_m is the sum of the dimensions of the mth slit plus the corresponding isle, and $L = 0, 2, 4, \ldots$. Also, in this equation, $(2\pi/\lambda_v)$ is related to the wave numbers associated with the two refractive index regions [25].

For incidence above the normal and diffraction below the normal (see Fig. 13.3), Equation 13.26 becomes

$$d_m(+n_1 \sin\Theta_m - n_2 \sin\Phi_m)(2\pi/\lambda_v) = L\pi \tag{13.27}$$

As explained in [13, 24] for the condition $d_m << \lambda$, diffraction ceases to occur and the equation can only be solved for $L = 0$ so that

$$(+n_1 \sin\Theta_m - n_2 \sin\Phi_m) = 0 \tag{13.28}$$

which leads directly to the well-known law of refraction also known as Snell's law

$$n_1 \sin\Theta_m = n_2 \sin\Phi_m \tag{13.29}$$

For incidence below the normal and diffraction below the normal (see Fig. 13.4), Equation 13.26 becomes

$$d_m(-n_1 \sin\Theta_m - n_2 \sin\Phi_m)(2\pi/\lambda_v) = L\pi \tag{13.30}$$

which again, for the condition $d_m << \lambda$, can only be solved for $L = 0$ so that

$$(-n_1 \sin\Theta_m - n_2 \sin\Phi_m) = 0 \tag{13.31}$$

leading directly to

$$-n_1 \sin\Theta_m = n_2 \sin\Phi_m \tag{13.32}$$

Using these results and the two alternative cases discussed in [25], a more general refraction equation emerges

$$\pm n_1 \sin\Theta_m \pm n_2 \sin\Phi_m = 0 \tag{13.33}$$

Thus, the equations describing propagation via a generalized hypothetical prism, exhibiting both positive and negative refraction, become [25]

$$\phi_{1,m} + \phi_{2,m} = \varepsilon_m \pm \alpha_m \tag{13.34}$$

$$\psi_{1,m} + \psi_{2,m} = \alpha_m \tag{13.35}$$

$$\sin\phi_{1,m} = \pm n_m \sin\psi_{1,m} \tag{13.36}$$

$$\sin \phi_{2,m} = \pm n_m \sin \psi_{2,m} \tag{13.37}$$

and the generalized single-pass multiple-prism dispersion equation is modified to [25]

$$\nabla_\lambda \phi_{2,m} = \pm \mathcal{H}_{2,m} \nabla_\lambda n_m \pm (k_{1,m} k_{2,m})^{-1} \left(\mathcal{H}_{1,m} \nabla_\lambda n_m (\pm) \nabla_\lambda \phi_{2,(m-1)} \right) \tag{13.38}$$

where the signs in parentheses refer to deployment at an either positive (+) or compensating (–) configuration, whereas the simple ± is indicative of either positive or negative refraction. Thus, the interferometric foundations for either positive or negative refraction have been established [25]. As discussed in this chapter, the geometrical implications of negative refraction, for a double-prism beam expansion alone, signify a potential increase of four times the number of possible geometrical permutations [25]. This chapter also discussed the use of a multiple-prism beam expander "in reverse," thus performing the function of a beam compressor. As in Figure 13.2, propagation toward the right results in spatial expansion, while propagation toward the left results in spatial compression.

13.3 APPLICATIONS TO LASER OPTICS

The application of multiple-prism beam expanders as intracavity elements in narrow-linewidth tunable lasers has been well documented in various reviews [2, 12, 13, 29]. Beam expansion factors provided by these prismatic expanders are approximately in the $25 \leq M \leq 100$ range [12], depending on the type of cavity configuration, although higher magnifications can be easily provided. Multiple-prism expanders in multiple-prism Littrow grating oscillators and hybrid multiple-prism grazing-incidence grating oscillators are depicted in Chapters 4 and 5.

In addition to the initial application of multiple-prism assemblies, in multiple-prism grating configurations for dye lasers [8–12], these prismatic beam expanders have also been applied to gas lasers [30–32], and semiconductor lasers [33, 34]. For gas lasers, single-longitudinal-mode oscillation has been reported, for cavity lengths of approximately 107 cm at $\Delta\nu \approx 140$ MHz [31]. This result is particularly relevant to contemporary fiber lasers where well-designed multiple-prism grating configurations should yield tunable single-longitudinal-mode lasing. A multiple-prism grating configuration for tunable fiber lasers is described in Chapter 6.

The use of prism pairs, as first outlined by Brewster [3], as extracavity components to correct the beam profile of semiconductor, or diode, lasers is also a well-known application [35].

13.4 APPLICATIONS TO LASER SPECTROSCOPY AND SEQUENTIAL LASER EXCITATION

One of the first applications of tunable lasers to incorporate intracavity multiple-prism beam expansion to illuminate the whole width of the tuning grating was laser spectroscopy [36–39], in particular, double-resonance spectroscopy, where one of the lasers was a tunable narrow-linewidth ultraviolet dye laser incorporating a multiple-prism

beam expander and a 3600 line/mm holographic grating [36, 37]. Recent interesting experiments performed with multiple-prism grating tunable lasers are those of time-resolved atomic spectroscopy in beryllium [39] and ionized iron [40].

An additional application for narrow-linewidth multiple-prism grating tunable lasers is the sequential excitation of atomic species and atomic vapor laser isotope separation [10, 11, 41–45]. Further references on this topic are given in Chapter 1.

13.5 APPLICATIONS TO GUIDE STARS AND ASTRONOMY

Copper-vapor-laser (CVL)-pumped narrow-linewidth dye lasers, incorporating multiple-prism grating cavity configurations, emit in the 565 nm $\leq \lambda \leq$ 605 nm range [11]. A high-average-power CVL laser-pumped dye laser system, utilizing multiple-prism beam expansion in its oscillator, was used in early experiments for *guide star* applications [43]. The guide star concept is used to correct for atmospheric turbulence, in conjunction with adaptive optics, at large terrestrial telescopes. This laser beacon principle [46] uses the sodium layer at the mesosphere, which is at an altitude of 80–100 km. Fugate [46] discussed pulse energy requirements and provides an historical introduction to the subject. The sodium transition utilized is the D_2 line, at $\lambda = 588.9963$ nm, which has an absorption linewidth of ~3 GHz. These requirements make high-power narrow-linewidth dye lasers, yielding laser linewidths in the 350 MHz $\leq \lambda \leq$ 700 MHz range, ideally suited for this application. The use of CW dye laser systems for this application is discussed in [47].

Multiple-prism beam expanders have also been found useful by researchers working in imaging systems for astronomy, in particular in the subfield of astrometry [48]. The imaging application discussed by these authors is related to the precise cataloguing of large numbers of stars [48].

13.6 APPLICATIONS TO PULSE COMPRESSION IN ULTRASHORT PULSE LASERS

The dispersive laser linewidth equation

$$\Delta\lambda = \Delta\theta(\nabla_\lambda \Theta)^{-1} \tag{13.39}$$

directly links laser linewidth to intracavity dispersion. This equation immediately suggests that minimizing the intracavity dispersion leads to broadband laser emission, that is, very large $\Delta\lambda$, and hence very large $\Delta\nu$. Heisenberg's uncertainty principle [49]

$$\Delta p \Delta x \approx h \tag{13.40}$$

leads directly to [13]

$$\Delta\nu\Delta t \approx 1 \tag{13.41}$$

Thus, for minimal intracavity dispersion, broad bandwidth emission is possible, which allows ultrashort pulse emission.

Prismatic pulse compression was first demonstrated by Dietel et al. [50]. Multiple-prism arrays in the form of double prisms [51], four prisms [23], double-prism pairs [52], and six prisms [53] have become widely used as pulse compressors in lasers yielding ultrashort pulses in the femtosecond domain.

The effect of minute beam deviations on the overall multiple-prism dispersion $\nabla_n \phi_{2,m}$ and its derivative $\nabla_n^2 \phi_{2,m}$ was calculated by Duarte [54]. In a series of experiments Osvay et al. [55–57] investigated the fine-tuning of intracavity dispersions in femtosecond lasers obtaining excellent agreement between theory [22, 54] and experiment in an 18 fs laser incorporating a prism pair pulse compressor [57].

An extensive review on prismatic pulse compression is given by Diels and Rudolph [58], and a recent study on pulse compression with prism pairs was reported in [59].

13.7 APPLICATIONS TO MICROSCOPY AND ULTRAFAST SPECTROSCOPY

Ultrashort pulse lasers emitting in the femtosecond regime have generated a renaissance in the field of microscopy. An introduction to this subject is given by Diels and Rudolph [58] and is treated in detail in Chapter 9 in reference to biology. Microscopy applied to the field of imaging is discussed in detail in Chapter 12.

Using a double-prism dispersion compensator, Nechay et al. [60] developed a femtosecond microscope with ~150 nm lateral resolution and ~250 fs temporal resolution. These authors applied their microscope to produce two-dimensional scans of GaAs/AlGaAs semiconductor structures [60]. The application of this type of instrument to characterize nanostructured materials, including single semiconductor quantum wires, with remarkable temporal and spatial resolution was reported by Siegner et al. [61].

Ultrafast dynamic studies of halogens in rare gas solids, using a laser system including prismatic compressors, have been performed by Gürh et al. [62].

13.8 APPLICATIONS TO INTERFEROMETRY AND OPTICAL METROLOGY

Multiple-prism beam expanders have become integral components of various improved, and some unique, optical instruments, including:

Densitometers
Digital microscopes
Interferometric wavelength meters
Laser printers
Microdensitometers
N-slit interferometers
Spectrometers

These optical instruments are described in detail in *Tunable Laser Optics* [13] and partly in Chapter 12.

REFERENCES

1. Newton, I., *Opticks*, Royal Society, London, 1704.
2. Duarte, F. J., Newton, prisms, and the *opticks* of tunable lasers, *Optics & Photonics News* 11 (5): 24–28 (2000).
3. Brewster, D., *A Treatise on New Philosophical Instruments for Various Purposes in the Arts and Sciences with Experiments on Light and Colours*, Murray and Blackwood, Edinburgh, 1813.
4. Strome, F. C., and J. P. Webb, Flashtube-pumped dye laser with multiple-prism tuning, *Appl. Opt.* 10: 1348–1353 (1971).
5. Hanna, D. C., P. A. Kärkkäinen, and R. Wyatt, A simple beam expander for frequency narrowing of dye lasers, *Opt. Quantum Electron.* 7: 115–119 (1975).
6. Klauminzer, G. K., Optical beam expander for dye laser, US Patent 4127828 (1978).
7. Kasuya, T., T. Suzuki, and K. Shimoda, A prism anamorphic system for Gaussian beam expander, *Appl. Phys.* 17: 131–136 (1978).
8. Duarte, F. J., and J. A. Piper, A double-prism beam expander for pulsed dye lasers, *Opt. Commun.* 35: 100–104 (1980).
9. Duarte, F. J., and J. A. Piper, Prism preexpanded grazing-incidence grating cavity for pulsed dye lasers, *Appl. Opt.* 20: 2113–2116 (1981).
10. Duarte, F. J., and J. A. Piper, Comparison of prism-expander and grazing-incidence grating cavities for copper laser pumped dye lasers, *Appl. Opt.* 21: 2782–2786 (1982).
11. Duarte, F. J., and J. A. Piper, Narrow-linewidth, high-prf copper laser-pumped dye-laser oscillators, *Appl. Opt.* 23: 1391–1394 (1984).
12. Duarte, F. J., Narrow linewidth pulsed dye laser oscillators, in *Dye Laser Principles,* edited by F. J. Duarte and L. W. Hillman, Academic, New York, 1990, Chap. 4.
13. Duarte, F. J., *Tunable Laser Optics*, Elsevier-Academic, New York, 2003.
14. Duarte, F. J., Transmission efficiency in achromatic nonorthogonal multiple-prism laser beam expanders. *Opt. Commun.* 71: 1–5 (1989).
15. Hänsch, T. W., Repetitively pulsed tunable dye laser for high resolution spectroscopy, *Appl. Opt.* 11: 895–898 (1972).
16. Duarte, F. J., Cavity dispersion equation $\Delta\lambda \approx \Delta\theta(\partial\theta/\partial\lambda)^{-1}$: a note on its origin, *Appl. Opt.* 31: 6979–6982 (1992).
17. Duarte, F. J., and J. A. Piper, Dispersion theory of multiple-prism beam expander for pulsed dye lasers, *Opt. Commun.* 43: 303–307 (1982).
18. Duarte, F. J., and J. A. Piper, Generalized prism dispersion theory, *Am. J. Phys.* 51: 1132–1134 (1983).
19. Duarte, F. J., Note on achromatic multiple-prism beam expanders, *Opt. Commun.* 53: 259–262 (1985).
20. Duarte, F. J., and J. A. Piper, Multi-pass dispersion theory of prismatic pulsed dye lasers, *Optica Acta* 31: 331–335 (1984).
21. Duarte, F. J., Multiple-return-pass beam divergence and the linewidth equation, *Appl. Opt.* 40: 3038–3041 (2001).
22. Duarte, F. J., Generalized multiple-prism dispersion theory for pulse compression in ultrafast dye lasers, *Opt. Quantum Electron.* 19: 223–229 (1987).
23. Fork, R. L., O. E. Martínez, and J. P. Gordon, Negative dispersion using pairs of prisms, *Opt. Lett.* 9: 150–152 (1984).
24. Duarte, F. J., Interference, diffraction, and refraction, via Dirac's notation. *Am. J. Phys.* 65: 637–640 (1997).
25. Duarte, F. J., Multiple-prism dispersion equations for positive and negative refraction, *Appl. Phys. B* 82: 35–38 (2006).
26. Duarte, F. J., and D. J. Paine, Quantum mechanical description of *N*-slit interference phenomena, in *Proceedings of the International Conference on Lasers'88*, edited by R. C. Sze and F. J. Duarte, STS Press, McLean, Virginia, 1989, pp. 42–247.

27. Duarte, F. J., Dispersive dye lasers, in *High Power Dye Lasers*, edited by F. J. Duarte, Springer, Berlin, 1991, Chap. 2.
28. Duarte, F. J., On a generalized interference equation and interferometric measurements. *Opt. Commun.* 103: 8–14 (1993).
29. Duarte, F. J., Multiple-prism arrays in laser optics, *Am. J. Phys.* 68: 162–166 (2000).
30. Duarte, F. J., Variable linewidth high-power TEA CO_2 laser, *Appl. Opt.* 24: 34–37 (1985).
31. Duarte, F. J., Multiple-prism Littrow and grazing-incidence pulsed CO_2 lasers, *Appl. Opt.* 24: 1244–1245 (1985).
32. Sze, R. C., and D. G. Harris, Tunable excimer lasers, in *Tunable Lasers Handbook*, edited by F. J. Duarte, Academic, New York, 1995, Chap. 3.
33. Duarte, F. J., Dispersive external-cavity semiconductor lasers, in *Tunable Laser Applications*, 1st ed., edited by F. J. Duarte, Marcel Dekker, New York, 1995, Chap. 3.
34. Zorabedian, P., Tunable external-cavity semiconductor lasers, in *Tunable Lasers Handbook*, edited by F. J. Duarte, Academic, New York, 1995, Chap. 8.
35. Hughes, D. W., and J. R. M. Barr, Laser diode pumped solid state lasers, *J. Phys. D: Appl. Phys.* 25: 563–586 (1992).
36. Duval, A. B., D. A. King, R. Haines, N. R. Isenor, and B. J. Orr, Fluorescence-detected Raman-optical double-resonance spectroscopy of glyoxal vapor, *J. Opt. Soc. Am. B* 2: 1570–1581 (1985).
37. Duarte, F. J., Technology of pulsed dye lasers, in *Dye Laser Principles,* edited by F. J. Duarte and L. W. Hillman, Academic, New York, 1990, Chap. 6.
38. Murray, J. R., Lasers for spectroscopy, in *Laser Spectroscopy and its Applications*, edited by L. J. Radziemski, R. W. Solarz, and J. A. Paisner, Marcel Dekker, New York, 1987, Chap. 2.
39. Schnabel, R., and M. Kock, *f*-value measurements of the Be I resonance line using a nonlinear time-resolved laser-induced-flourescence technique, *Phys. Rev. A* 61: 062506 (2000).
40. Schnabel, R., and M. Kock, Time-resolved nonlinear laser-induced fluorescence technique for a combined lifetime and branching-fraction measurement, *Phys. Rev. A* 63: 012519 (2000).
41. Broyer, M., and J. Chevaleyre, CVL-pumped dye laser for spectroscopic applications, *Appl. Phys. B* 35: 31–36 (1984).
42. Webb, C. E., High-power dye lasers pumped by copper-vapor lasers, in *High Power Dye Lasers*, edited by F. J. Duarte, Springer, Berlin, 1991, Chap. 5.
43. Bass, I. L., R. E. Bonanno, R. P. Hackel, and P. R. Hammond, High-average-power dye laser at Lawrence Livermore National Laboratory, *Appl. Opt.* 31: 6993–7006 (1992).
44. Singh, S., K. Dasgupta, S. Kumar, K. G. Manohar, L. G. Nair, and U. K. Chatterjee, High-power high-repetition-rate copper-vapor-pumped dye laser, *Opt. Eng.* 33: 1894–1904 (1994).
45. Sugiyama, A., T. Nakayama, M. Kato, Y. Maruyama, T. Arisawa, Characteristics of a pressure-tuned single-mode dye laser oscillator pumped by a copper vapor laser, *Opt. Eng.* 35: 1093–1097 (1996).
46. Fugate, R. Q., Laser beacon adaptive optics, *Opt. Photon. News* 4 (6): 14–19 (1993).
47. Pique, J.-P., and S. Farinotti, Efficient modeless laser for mesospheric sodium laser guide star, *J. Opt. Soc. Am. B* 20: 2093–2101 (2003).
48. Sirat, G. Y., K. Wilner, and D. Neuhauser, Uniaxial crystal interferometer: principles and forecasted applications to imaging astrometry, *Opt. Express* 13: 6310–6322 (2005).
49. Dirac, P. A. M., *The Principles of Quantum Mechanics*, 4th ed., Oxford University, London, 1978.
50. Dietel, W., J. J. Fontaine, and J.-C. Diels, Intracavity pulse compression, with glass: a new method of generating pulses shorter than 60 fsec, *Opt. Lett.* 8: 4–6 (1983).

51. Kafka, J. D., and T. Baer, Prism-pair delay lines in optical pulse compression, *Opt. Lett.* 12: 401–403 (1987).
52. Chou, Y-F., C-H. Lee, and J. Wang, Characteristics of a femtosecond transform-limited Kerr-lens mode-locked dye laser, *Opt. Lett.* 19: 975–977 (1994).
53. Pang, L. Y., J. G. Fujimoto, and E. S. Kintzer, Ultrashort-pulse generation from high-power diode arrays by using intracavity optical nonlinearities, *Opt. Lett.* 17: 1599–1601 (1992).
54. Duarte, F. J., Prismatic pulse compression: beam deviations and geometrical perturbations, *Opt. Quantum Electron.* 22: 467–471 (1990).
55. Osvay, K., P. Dombi, A. P. Kovács, and Z. Bor, Fine tuning of the higher-order dispersion of a prismatic pulse compressor, *Appl. Phys. B* 75: 649–654 (2002).
56. Osvay, K., A. P. Kovács, Z. Heiner, G. Kurdi, J. Klebniczki, and M. Csatári, Angular dispersion and temporal change of femtosecond pulses from misaligned pulse compressors, *IEEE J. Selec. Topics Quantum Electron.* 10: 213–220 (2004).
57. Osvay, K., A. P. Kovács, G. Kurdi, Z. Heiner, M. Divall, J. Klebniczki, and I. E. Ferincz, Measurement of non-compensated angular dispersion and the subsequent temporal lengthening of femtosecond pulses in a CPA laser, *Opt. Commun.* 248: 201–209 (2005).
58. Diels, J.-C., and W. Rudolph, *Ultrashort Laser Pulse Phenomena*, 2nd ed., Academic, New York, 2006.
59. Arissian, L., and J.-C. Diels, Carrier to envelope and dispersion control in a cavity with prism pairs, *Phys. Rev. A.* 75: 013814 (2007).
60. Nechay, B. A., U. Siegner, M. Achermann, H. Bielefeldt, and U. Keller, Femtosecond pump-probe near-field optical microscopy, *Rev. Sci. Instrum.* 70: 2758–2764 (1999).
61. Siegner, U., M. Achermann, and U. Keller, Spatially resolved femtosecond spectroscopy beyond the diffraction limit, *Meas. Sci. Technol.* 12: 1847–1857 (2001).
62. Gühr, M., M. Bargheer, M. Fushitani, T. Kiljunen, and N. Schwentner, Ultrafast dynamics of halogens in rare-gas solids, *Phys. Chem. Chem. Phys.* 9: 779–801 (2007).

14 Coherent Electrically Excited Organic Semiconductors

F. J. Duarte

CONTENTS

14.1 Introduction 389
14.2 Tunable Narrow-Linewidth Solid-State Organic Lasers 390
14.3 Spatial and Spectral Coherence 392
14.4 Electrically Excited Interferometric Emitter 393
14.5 Measured Beam Divergence and Interferograms 395
14.6 Energetics 396
14.7 Physical Interpretation of the Measurements 399
14.7.1 Interferometric Linewidth Estimate 400
14.8 Coherent Emission and Laser Emission 401
References 402

14.1 INTRODUCTION

Since the early days of organic tunable lasers, there has been an interest in solid-state tunable organic dye lasers [1, 2]. Early interest in the electrical excitation of these molecular species has been documented in the literature [3, 4].

The interest in solid-state tunable organic dye lasers was sporadic until the early 1990s when advances in solid-state organic dye gain media reenergized activity. For a general perspective on solid-state organic dye lasers, the reader can consult Chapters 3 and 4.

Despite the enormous success of broadly tunable optically pumped lasers, as evidenced by the various chapters on the subject included in this book, the issue of direct electrical excitation for organic gain media continues to interest scientists and researchers. Indeed, the possibility of direct electrical excitation has been considered in various recent reviews [5–7]. These review papers also describe work on optically pumped organic semiconductor gain media [8].

This chapter provides a succinct review of recent experiments [9–11] designed to produce coherent emission from direct electrical excitation of organic semiconductors. Relevant background necessary to the discussion is presented, and potential applications are also mentioned.

14.2 TUNABLE NARROW-LINEWIDTH SOLID-STATE ORGANIC LASERS

As discussed in Chapter 4, the availability of highly homogeneous dye-doped polymer gain media [12] led to the demonstration of broadly tunable narrow-linewidth emission in the yellow-red region of the spectrum [13–17]. One particular optimized tunable solid-state dye laser oscillator yielded single-longitudinal-mode lasing in the 550 nm $\leq \lambda \leq$ 603 nm portion of the spectrum with a laser linewidth of $\Delta\nu \approx$ 350 MHz (or $\Delta\lambda \approx 0.0004$ nm at $\lambda \approx 590$ nm) [17]. This emission was provided at a ~5% conversion efficiency with extremely low levels of ASE measured to be ~10^{-6}. The beam divergence of the single-transverse-mode emission was measured to be ~1.5 times the diffraction limit.

It should be mentioned that while using broadband emission cavity configurations these dye-doped polymer lasers have been *conservatively* reported to demonstrate conversion efficiencies in the 40–63% range [12, 13, 18].

As explained previously [17, 19], highly coherent emission from this class of oscillator is determined first of all by the emission of a single-transverse mode in the spatial domain, a smooth near-Gaussian profile in the temporal domain, and a single-longitudinal mode in the frequency domain. For the optimized multiple-prism grating solid-state dye laser depicted in Figure 14.1, the near-Gaussian temporal profile of the emission is shown in Figure 14.2, and the Fabry–Perot interferogram recording single-longitudinal-mode emission is shown in Figure 14.3.

As mentioned in Chapter 4 the measured laser linewidth ($\Delta\nu \approx 350$ MHz) from this optimized MPL grating laser oscillator appears to be approximately limited by the length of the temporal emission ($\Delta t \approx 3$ ns) according to

$$\Delta\nu\Delta t \approx 1 \tag{14.1}$$

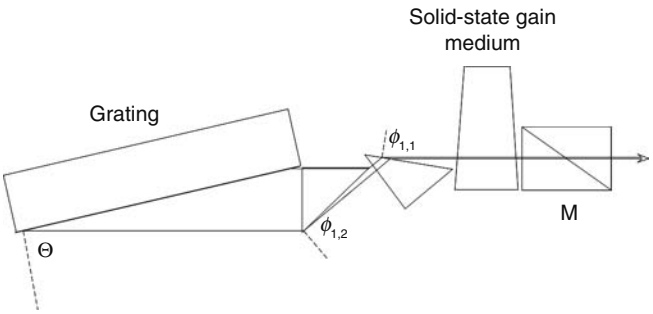

FIGURE 14.1 Optimized multiple-prism grating tunable laser oscillator incorporating an organic dye-doped polymer gain medium. This oscillator is of the multiple-prism Littrow (MPL) grating class with the added feature of a fully illuminated Littrow grating deployed at a relatively high angle of incidence. The excitation of this laser is accomplished in a longitudinal configuration. (From Duarte, F. J., Multiple-prism grating solid-state dye laser oscillator: Optimized architecture, *Appl. Opt.* 38: 6347–6349 (1999).)

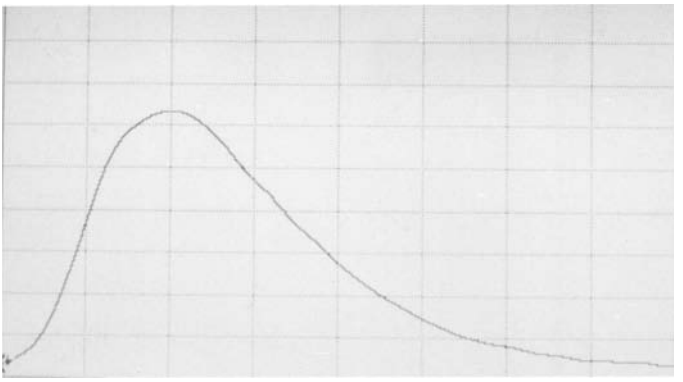

FIGURE 14.2 Smooth near-Gaussian temporal profile of the single-longitudinal-mode emission. Each division corresponds to 1 ns. (From Duarte, F. J., Multiple-prism grating solid-state dye laser oscillator: Optimized architecture, *Appl. Opt.* 38: 6347–6349 (1999).)

which, as explained in [19], is a direct consequence of Heisenberg's uncertainty principle [20]

$$\Delta p \Delta x \approx h \tag{14.2}$$

Hence, following [11] a description of the linewidth-narrowing process is provided here.

Multiple-prism grating oscillators benefit from an extraordinarily large intracavity dispersion illustrated by the dispersive linewidth equation [19]

$$\Delta\lambda \approx \Delta\theta_R \left(MR(\partial\Theta/\partial\lambda)_G\right)^{-1} \tag{14.3}$$

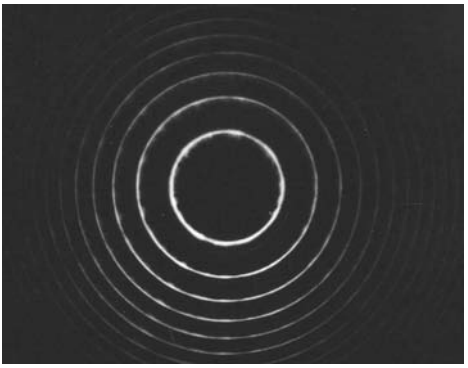

FIGURE 14.3 Silver-halide photograph of a Fabry–Perot interferogram showing single-longitudinal-mode emission at a laser linewidth of $\Delta\nu \approx 350$ MHz. (From Duarte, F. J., Multiple-prism grating solid-state dye laser oscillator: Optimized architecture, *Appl. Opt.* 38: 6347–6349 (1999).)

where M is the intracavity beam expansion, R is the number of return cavity passes necessary to achieve laser threshold, and $(\partial\Theta/\partial\lambda)_G$ is the dispersion of the grating deployed either in Littrow or near-grazing-incidence configuration. The multiple-pass beam divergence is given by [19, 21]

$$\Delta\theta_R \approx (\lambda/\pi w)\left(1 + (L/B_R)^2 + (LA_R/B_R)^2\right)^{-1} \tag{14.4}$$

where w is the beam waist, $L = (\pi w^2/\lambda)$ is known as the Rayleigh length, and A_R and B_R are the corresponding multiple-return-pass propagation matrix elements [19, 21]. In an optimized cavity configuration, using a liquid gain medium, often it is possible to reduce the terms in parentheses toward unity so that

$$\Delta\theta_R \approx (\lambda/\pi w) \tag{14.5}$$

is achieved, which is the diffraction-limited divergence allowed by Heisenberg's uncertainty principle [19]. For the solid-state gain matrices used in these oscillators, thermal lensing effects limit the reduction in beam divergence to

$$\Delta\theta_R \approx (3/2)(\lambda/\pi w) \tag{14.6}$$

In these highly dispersive oscillators, as the ASE photons leave the gain medium and encounter the entrance of the multiple-prism beam expander, which acts as the entrance of a highly discriminatory frequency filter, only photons highly resonant with the multiple-prism grating frequency band-pass return to the gain medium for further amplification [11].

14.3 SPATIAL AND SPECTRAL COHERENCE

This topic is discussed in detail in [11], but some basics are presented here. The link between spatial coherence, that is, low beam divergence, and laser emission is intimately entangled with the history of the laser. In fact, Siegman in his book *Lasers* reminds us of the "beam of heat" [22]. This link is justified since the first explicit observation of high-intensity emission in low-divergence beams was made by Maiman et al. [23]. More recently Wolf and Carter [24] have stated "a source with a high degree of spatial coherence, such as a laser, generates light that is highly directional."

In the spectral domain the highest form of coherence can be described using the Dirac's definition of interference [20] as a single-photon phenomenon. In practice the experimentalists observe that the sharpest interferograms are generated by sources of indistinguishable photons or narrow-linewidth lasers.

In [11] it was observed that a more accurate description of diffraction-limited beam divergence is given by

$$\Delta\theta \approx (\lambda \pm \Delta\lambda)/\pi w \tag{14.7}$$

which illustrates how spectral coherence influences spatial coherence. A broadband detector, such as a photographic plate, registers the larger value

$$\Delta\theta \approx (\lambda + \Delta\lambda)/\pi w \tag{14.8}$$

For narrow-linewidth, or spectrally coherent, emission, which can exhibit $\Delta\lambda \approx 0.0004$ nm at $\lambda \approx 590$ nm [17], this effect is negligible. However, in the case of broadband radiation the red end of the spectrum should give origin to some augmentation of the measurable beam divergence [11]. Thus, in principle, narrow-linewidth emission should be more likely to yield beams with a divergence close to the diffraction limit.

14.4 ELECTRICALLY EXCITED INTERFEROMETRIC EMITTER

An interferometric emitter was built [9–11] using an electrically excited organic semiconductor comprising a double-emitting region, in series (also described as a tandem organic light-emitting diode, or OLED). The active medium in both regions is a coumarin 545 tetramethyl (C545T) dye-doped Alq_3 matrix used in the engineering of high-brightness organic semiconductors [25, 26]. In addition, the C545T dye (see Fig. 14.4) was shown to oscillate as an efficient broadly tunable laser [27]. The cavity used in these experiments is shown in Figure 14.5 and the tuning curve for this laser, showing a useful tuning range of 501 nm $\leq \lambda \leq$ 574 nm, is shown in Figure 14.6. The emission linewidth of this laser was measured to be $\Delta\lambda \approx 3$ nm (FWHM) at $\lambda \approx 540$ nm [27].

The tandem dye-doped organic semiconductor was excited in the pulsed domain using nanosecond rise-time pulses up to ~100 V high [9]. The interferometric emitter is shown in Figure 14.7. A cavity, with a length of $l \approx 300$ nm, is configured with a high-reflectivity back mirror ($R_1 \approx 0.9$), which is also the cathode, and an output coupler mirror ($R_2 \approx 0.08$), which is also the anode. The output coupler mirror has a layer of ITO and a glass interface. The external surface of the output coupler is antireflection coated with MgF_2 to suppress possible intraglass interference. This interferometric emitter can be described as a doubly interferometrically confined organic semiconductor (DICOS) emitter where the emission medium is a laser dye-doped Alq_3 matrix [9–11].

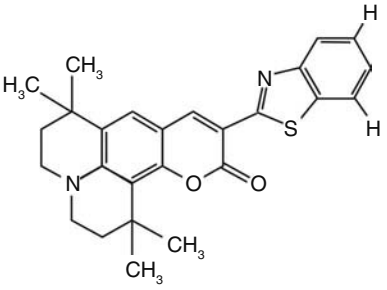

FIGURE 14.4 Molecular structure for the coumarin 545 tetramethyl (C545T) dye. (From Duarte, F. J., L. S. Liao, K. M. Vaeth, and A. M. Miller, Widely tunable green laser emission using the coumarin 545 tetramethyl dye as the gain medium, *J. Opt. A: Pure Appl. Opt.* 8: 172–174 (2006).)

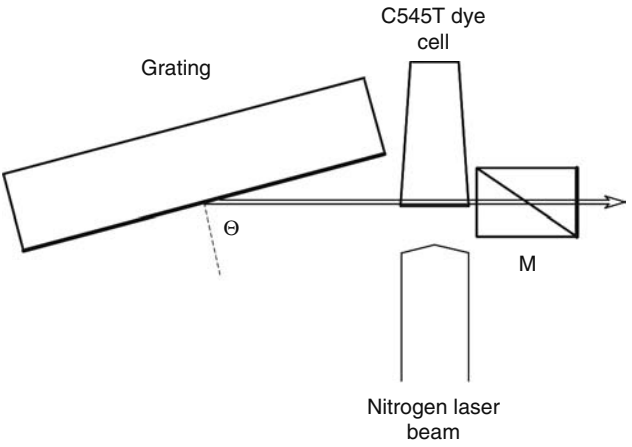

FIGURE 14.5 Transversely excited C545T dye laser. The output coupler is a Glan–Thompson polarizer with a ~20% reflectivity at its external surface. The tuning element is a 3000 lines/mm diffraction grating deployed in Littrow configuration. The excitation laser was a nitrogen laser emitting at $\lambda \approx 337$ nm. (From Duarte, F. J., L. S. Liao, K. M. Vaeth, and A. M. Miller, Widely tunable green laser emission using the coumarin 545 tetramethyl dye as the gain medium, *J. Opt. A: Pure Appl. Opt.* 8: 172–174 (2006).)

Excitation was also performed with the transmission line of a gas laser, which yielded nanosecond pulses at a voltage approaching 10 kV at the semiconductor load [11].

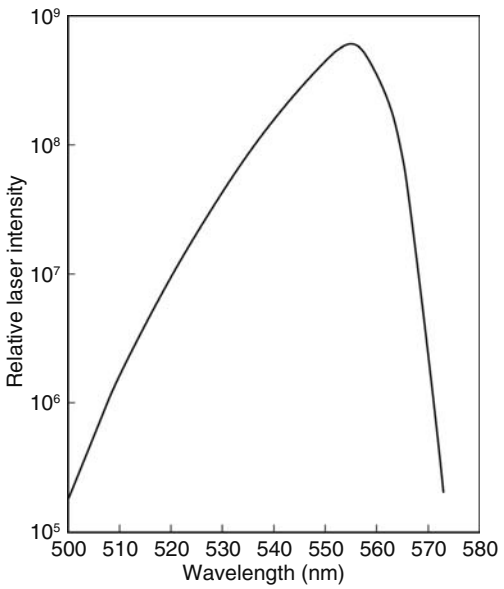

FIGURE 14.6 Laser tuning curve of the C545T laser at a concentration of 2 mM in ethanol. (From Duarte, F. J., L. S. Liao, K. M. Vaeth, and A. M. Miller, Widely tunable green laser emission using the coumarin 545 tetramethyl dye as the gain medium, *J. Opt. A: Pure Appl. Opt.* 8: 172–174 (2006).)

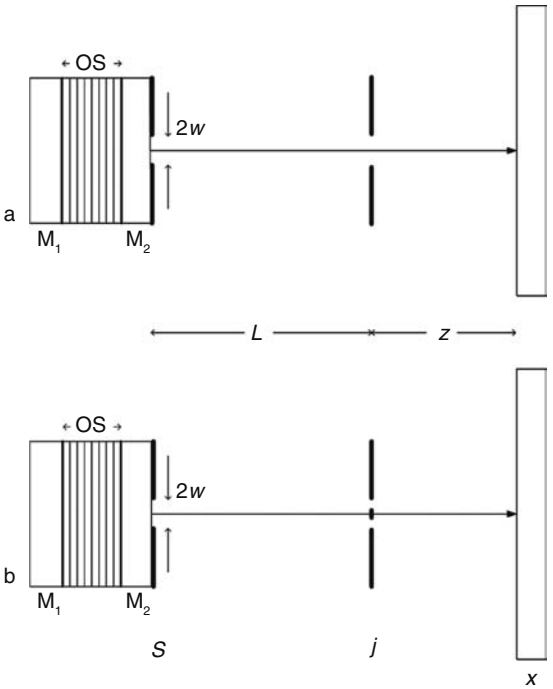

FIGURE 14.7 Schematics of the electrically excited DICOS emitter powered by a submicron cavity with a length of $l \approx 300$ nm. The back reflector (M_1) is also the cathode, and the output coupler mirror (M_2) is also the anode. The active region is labeled organic semiconductor (OS). (a) In its primary form the interferometric emitter is comprised of two sequential slits of width $2w$ separated by a distance L. (b) In its analytical version the secondary slit is replaced by a multiple-slit arrangement ($N = 2$, in these experiments) to perform interferometry of the emitted radiation. Detection occurs at position x either using a photographic silver-halide film or a digital detector. (Adapted from Duarte, F. J., Coherent electrically-excited organic semiconductors: coherent or laser emission? *Appl. Phys. B* 90: 101–108 (2008).)

The principle of operation of this interferometric emitter is as follows: The first aperture of width $2w$ induces divergence in the emission radiation. The second aperture, also of width $2w$, and positioned along the optical axis at a distance L from the first aperture, serves as the second spatial discriminator. This double-aperture arrangement ensures that only the emission precisely along the optical axis is allowed transmission by the second aperture. Because both of these apertures can be physically represented as an array of a large number of subapertures, they can be considered interferometric arrays. Subsequently interferometry of the emission is performed by replacing the second aperture by a double-slit arrangement also known as a Young-slit configuration [29]. In the present experiment $2w = 150$ μm, $L \approx 130$ mm, and the width of the slits of the interferometer (Fig. 14.7b) are 50 μm separated by 50 μm.

14.5 MEASURED BEAM DIVERGENCE AND INTERFEROGRAMS

The emission beam profile was measured both digitally and using archival black-and-white silver halide film. Digitally it was verified that the emission beam profile

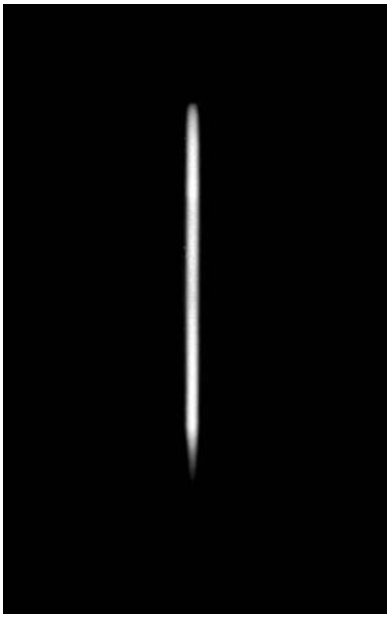

FIGURE 14.8 Beam profile recorded using black-and-white photographic film at a distance of $z \approx 340$ mm. The excitation voltage was ~100 V. The longitudinal profile is perpendicular to the plane of propagation. (From Duarte, F. J., L. S. Liao, and K. M. Vaeth, Coherence characteristics of electrically excited tandem organic light-emitting diodes, *Opt. Lett.* 30: 3072–3074 (2005).)

was near Gaussian [9]. A beam profile, at a distance of $z \approx 340$ mm, is shown in Figure 14.8. The beam profile measured while under the excitation of nanosecond pulses at voltages approaching 10 kV is shown in Figure 14.9.

Using the experimental arrangement depicted in Figure 14.7b, high-visibility interferograms were recorded as shown in Figure 14.10 for $z \approx 50$ mm. An interferometric comparison, using the same two-slit interferometer, and emission from a beam-expanded He–Ne laser emitting from its $3s_2$–$2p_{10}$ transition at $\lambda \approx 543.3$ nm is shown in Figure 14.11. A further interferometric comparison, this time with emission from the C545T high-power-pulsed dye laser, is shown in Figure 14.12.

The emission was determined to be in the nW regime [9, 10], and the measurements caused irreversible damage on the organic semiconductor. Damage was noticed as the emission intensity decreased with each voltage sweep up to 100 V. The experiments at ~10 kV caused visible irreversible damage after a few pulses as evidenced by the emission of red sparks from the semiconductor. Thus, after many attempts only a few beam profiles could be recorded and no interferometry could be performed at this excitation level.

14.6 ENERGETICS

For a discussion of energetic aspects of these experiments, please refer to [9–11]. Some points worth highlighting here include the fact that C545T under optical excitation offers tunable laser emission over a range of 60 nm and its intensity-dynamic range

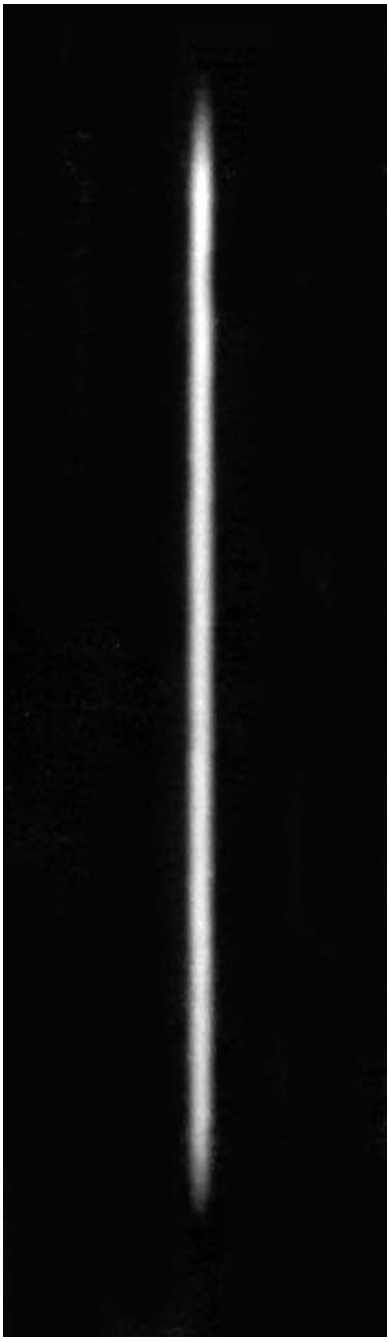

FIGURE 14.9 Beam profile from the DICOS emitter while under the excitation of nanosecond pulses at an amplitude of ~10 kV. (From Duarte, F. J., Coherent electrically-excited organic semiconductors: coherent or laser emission? *Appl. Phys. B* 90: 101–108 (2008).)

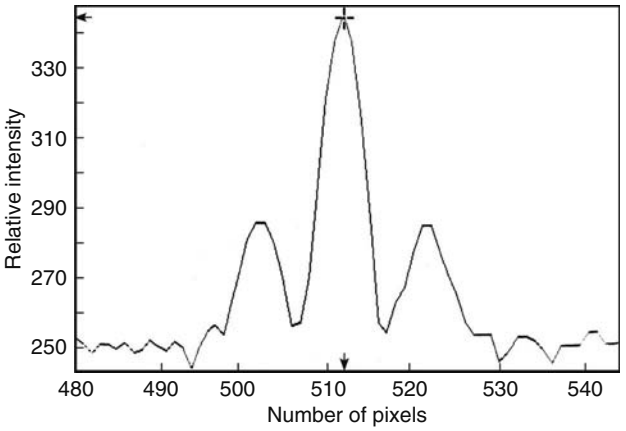

FIGURE 14.10 Interferogram of the radiation from the DICOS emitter, at $\lambda \approx 540$ nm, for $z \approx 50$ mm. (From Duarte, F. J., L. S. Liao, and K. M. Vaeth, Coherence characteristics of electrically excited tandem organic light-emitting diodes, *Opt. Lett.* 30: 3072–3074 (2005).)

spans nearly four orders of magnitude (see Fig. 14.6). The quoted laser efficiency in the diffraction grating-tuned cavity, under UV laser excitation, is ~14% [27]. This is consistent with previously published laser efficiencies for other coumarin tetramethyl dyes [28]. At this stage there are no published data that would enable a formal excitation analysis of the emission as done with other better-known laser dyes. Also, relevant information to perform an analysis under electrical excitation in a semiconductor matrix is not available.

The main issue that will be highlighted here is that the observed behavior of the output power, as a function of excitation current density, does indicate the presence of an emission discontinuity with a gradient ratio of $(\eta_2/\eta_1) \approx 2.33$. Comparison of

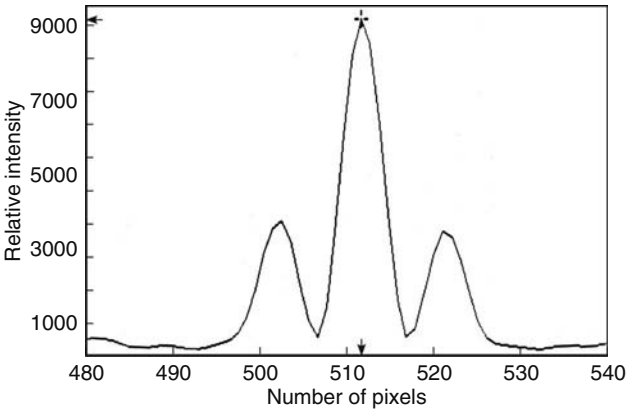

FIGURE 14.11 Interferogram using the identical interferometer of radiation from a He–Ne laser, at $\lambda \approx 543.3$ nm, for $z \approx 50$ mm. (From Duarte, F. J., L. S. Liao, and K. M. Vaeth, Coherence characteristics of electrically excited tandem organic light-emitting diodes, *Opt. Lett.* 30: 3072–3074 (2005).)

FIGURE 14.12 Interferometric comparison of the emission from the high-power C545T dye laser (a) and the emission from the DICOS emitter (b). Both measurements were performed at $z \approx 50$ mm. (From Duarte, F. J., L. S. Liao, and K. M. Vaeth, Coherence characteristics of electrically excited tandem organic light-emitting diodes, *Opt. Lett.* 30: 3072–3074 (2005).)

this ratio with existing laser data indicates that this ratio is at least compatible with soft threshold behavior observed in semiconductor lasers with asymmetrical cavities and some optically excited semiconductor lasers [11].

An additional point of interest is that the excitation experiments at high-pulsed voltages indicate that it only takes a few excitation pulses, in the nanosecond regime, to obliterate the organic semiconductor at ~10 kV. It is estimated that this excitation took place at current densities of $\rho \approx 190$ A/cm^2 [11].

14.7 PHYSICAL INTERPRETATION OF THE MEASUREMENTS

The divergence of the beam shown in Figure 14.8 was measured to be $\Delta\theta = 2.53 \pm 0.13$ mrad, which, for $2w \approx 150$ mm, is ~1.1 times the diffraction limit determined using the equation $\Delta\theta_R \approx (\lambda/\pi w)$. Also, the near-Gaussian profile of this beam [9] allows us to conclude that the emission is equivalent to what we know in laser development as single-transverse mode.

Using the visibility definition introduced by Michelson [29]

$$\mathcal{V} = (I_1 - I_2)/(I_1 + I_2) \tag{14.9}$$

it can be estimated that for the DICOS emitter $\mathcal{V} = 0.901 \pm 0.088$, while the visibility for the He–Ne laser emitting at $\lambda \approx 543.3$ nm is $\mathcal{V} = 0.952 \pm 0.031$ [10].

The literature tells us the visibility measurements for partially coherent emission, ASE, and emission from organic semiconductors is in the range of $0.40 \leq \mathcal{V} \leq 0.65$, corresponding to emission linewidths in the 17 nm $\leq \Delta\lambda \leq$ 100 nm range [30–32]. In this set of results the narrower linewidth corresponds to the ASE from a laser dye exhibiting a visibility of $\mathcal{V} \approx 0.65$ [31]. These results indicate, on a preliminary basis, that the visibility of the interferograms recorded with the radiation

from the DICOS emitter is higher than the visibility associated with ASE sources, and approaches the visibility values associated with laser emission as evident by the interferograms in Figures 14.10, 14.11, and 14.12.

14.7.1 Interferometric Linewidth Estimate

Strong evidence of highly spatially coherent emission plus interferograms showing high visibility might be sufficient to draw some conclusions on the nature of the emission being observed. However, this only suggests that the emission being observed should be somewhat narrow—at least narrower than amplified spontaneous emission (ASE). Thus, a question confronted [10] was how to use the available interferometric data and extract information about the linewidth of the emission. Given the low intensity of the emission, the possible use of conventional methods to perform this measurement had to be abandoned [11].

In order to elucidate this issue it must be realized that the generalized interferometric equation [19, 33]

$$|\langle x \mid s\rangle|^2 = \sum_{j=1}^{N} \Psi(r_j)^2 + 2\sum_{j=1}^{N} \Psi(r_j)\left(\sum_{m=j+1}^{N} \Psi(r_m)\cos(\Omega_m - \Omega_j)\right) \tag{14.10}$$

can be used, in conjunction with measured interferograms, to determine the wavelength of the emission under observation [19]. That is because, as explained in Chapter 12, the interferometric term (in parentheses) in Equation 14.10 depends on the exact geometry of the interferometer and the wavelength of the emission under observation. Thus, if the emission of different laser wavelengths is observed, under identical geometrical conditions, in an *N*-slit interferometer, then the interferograms thus recorded will be uniquely a function of emission wavelength [19]. It follows that if this interferometric method can yield information about the wavelength λ it should also yield information about the linewidth of the emission $\Delta\lambda$.

For completeness it should be mentioned that in Equation 14.10, $\Psi(r_j)$ are wave functions of "ordinary wave optics" [20] and the *j* index refers to the *j*th slit of the *N*-slit interferometer. Also the use of single-particle mechanics [20, 34] in a situation related to populations of indistinguishable photons is compatible with the approach of van Kampen to quantum mechanics [35].

Experimentally, it is observed that narrow-linewidth lasers yield sharp, well-defined *N*-slit interferograms while broadband sources yield broad, less-defined interferograms [9, 19]. This observation can be explained following the Dirac description of interference, as a single-photon phenomenon, or as a phenomenon that takes place between indistinguishable photons.

Thus, the sharpest and purest interferogram is provided by a single photon whose probability amplitudes, within the *N*-slit interferometer, are handled according to the mechanics described by Equation 14.10. As described in [10, 11], interference for broadband emission takes place in the same manner but now a multitude of interferograms are integrated at the detector, which is either a silver-halide photographic plate or a digital detector. Both methods of detection provide an integrated view of the interferometric event [10, 11, 36].

This description of interference is compatible with the link between sharp, well-defined interferograms with narrow-linewidth laser emission or the emission of populations of indistinguishable photons. It also allows the link between broad, less-defined interferograms with the emission of broadband radiation. Thus, for radiation at the same wavelength, and observation at the same N-slit interferometer, it is possible to use narrow-linewidth laser emission as a reference to estimate the bandwidth of broader emission.

The approximate spatial-graphical technique for estimating $\Delta\lambda$ has been described in [10, 11], and it is described briefly here. First, either the full width or half width of the interferogram under examination is defined. Once this definition is done, then the width of the narrow reference interferogram (W_r) and the width of the broader interferogram (W_m) are measured. Then the broadening factor Δb can be defined as

$$\Delta b = (W_m - W_r)/W_r \tag{14.11}$$

Using this definition, the broadening factor of the interferogram of the DICOS emitter (Fig. 14.10) relative to the interferogram generated with the $3s_2$–$2p_{10}$ transition, of the He–Ne laser (Fig. 14.11), was determined to be $\Delta b \approx 0.04$.

The second part consists of generating a calculated interferogram at the reference wavelength followed by a series of calculations at various wavelength increments above and below the reference wavelength. This approximate technique then uses graphical methods to relate the broadening factor Δb to $\Delta\lambda$. As reported in [10, 11], for the case at hand the linewidth related to $\Delta b \approx 0.04$ was $\Delta\lambda \approx 11$ nm.

Certainly the accuracy of this graphical approach is limited and it would be useful to extend the scope of the theory to provide equations which would make this task faster and improve accuracy.

14.8 COHERENT EMISSION AND LASER EMISSION

Following the previous exposition, the set of variables related to the radiation from the DICOS emitter are $\Delta\theta_R \approx (1.1) \times (\lambda/\pi w)$, $\mathcal{V} \approx 0.9$, and $\Delta\lambda \approx 11$ nm—all parameters that reaffirm the coherent nature of the emission. However, it is useful to reevaluate these parameters in light of what is known in the literature.

We already know, via Equations 14.3 and 14.7, that low-beam divergence is compatible with narrow-linewidth emission.

It has already been established that the visibility of the interferograms observed from the DICOS emitter radiation is superior to the visibility of both partially coherent and ASE sources. The question now is, how does a value of $\mathcal{V} \approx 0.9$ compare with visibilities of known laser emission? Some researchers that have turned to two-slit interferometry to determine the coherence of their lasers are those working on x-ray lasers. Scrutiny of the relevant literature [37–40] indicates that the spatial resolution and visibility of the interferometry recorded in these experiments is within range of the observed values for x-ray lasers. Furthermore, the visibility of the interferogram produced by the DICOS emitter approaches the visibility measured ($\mathcal{V} \approx 0.95$) with a relatively narrow linewidth ($\Delta\nu \approx 1$ GHz) He–Ne laser.

From the experimental results presented in Figure 14.12 it is evident that the interferogram produced with radiation from the DICOS emitter is almost identical to the interferogram recorded, in the same interferometer, with radiation from the high-power C545T dye lasers tuned at $\lambda \approx 540$ nm. In other words, the interferogram produced with radiation from the electrically excited organic interferometric emitter, doped with C545T, is nearly indistinguishable, in its spatial features, from the interferogram recorded with radiation from the high-power C545T dye laser.

Independent of the literature information presented thus far, the interferometric analysis, described in Section 14.7, indicates that the emission linewidth of the DICOS emitter is $\Delta\lambda \approx 11$ nm [10, 11], which is comparable to the linewidth reported for a broadband dye laser by Schäfer et al. [41].

The results presented thus far indicate that this electrically powered organic interferometric emitter yields a nearly diffraction-limited beam, with a Gaussian profile, compatible with single-transverse-mode emission. Also given the extremely short length of the cavity ($l \approx 300$ nm), an emission linewidth of $\Delta\lambda \approx 11$ nm is compatible with single-longitudinal-mode emission. That is, the emission is compatible with broadband laser emission, although it remains to perform the traditional laser cavity adjustments [11].

In summary, a new class of electrically powered coherent emitter has been demonstrated and its emission characterized. Avenues to improve emission intensity levels, and to reduce its dimensions by one order of magnitude, have been disclosed in the literature [11].

Electrically driven miniature tunable coherent devices yielding spatially well-defined low-divergence emission beams could find a number of applications in spectroscopy, interferometry, and other yet unimagined uses.

REFERENCES

1. Soffer, B. H., and B. B. McFarland, Continuously tunable narrow-band organic dye lasers, *Appl. Phys. Lett.* 10: 266–267 (1967).
2. Peterson, O. G., and B. B. Snavely, Stimulated emission from flashlamp-excited organic dyes in polymethyl methacrylate, *Appl. Phys. Lett.* 12: 238–240 (1968).
3. Steyer, B., and F. P. Schäfer, A vapor phase dye laser, *Opt. Commun.* 10: 219–220 (1974).
4. Marowsky, G., F. P. Schäfer, J. W. Keto, and F. K. Tittel, Fluorescence studies of electron beam pumped POPOP dye vapor, *Appl. Phys.* 9: 143–146 (1976).
5. Kranzelbinder, G., and G. Leising, Organic solid-state lasers, *Rep. Prog. Phys.* 63: 729–762 (2000).
6. Baldo, M. A., R. J. Holmes, and S. R. Forrest, Prospects for electrically pumped organic lasers, *Phys. Rev. B.* 66: 035321 (2002).
7. Samuel, I. D. W., and G. A. Turnbull, Organic semiconductor lasers, *Chem Rev.* 107: 1272–1295 (2007).
8. Holzer, W., A. Penzkofer, T. Pertsch, N. Danz, Abräuer, E. B. Kley, H. Tillmann, C. Bader, and H. H. Hörhold, Corrugated neat thin-film conjugated polymer distributed-feedback lasers, *Appl. Phys. B.* 74: 333–342 (2002).
9. Duarte, F. J., L. S. Liao, and K. M. Vaeth, Coherence characteristics of electrically excited tandem organic light-emitting diodes, *Opt. Lett.* 30: 3072–3074 (2005).
10. Duarte, F. J., Coherent electrically excited organic semiconductors: visibility of interferograms and emission linewidth, *Opt. Lett.* 32: 412–414 (2007).

11. Duarte, F. J., Coherent electrically-excited organic semiconductors: coherent or laser emission? *Appl. Phys. B* 90: 101–108 (2008).
12. Maslyukov, A., S. Solokov, M. Kaivola, K. Nyholm, and S. Popov, Solid-state dye laser with modified poly(methyl methacrylate)-doped active elements, *Appl. Opt.* 34: 1516–1518 (1995).
13. Duarte, F. J., Solid-state multiple-prism grating dye-laser oscillators, *Appl. Opt.* 33: 3857–3860 (1994).
14. Duarte, F. J., Solid-state dispersive dye laser oscillator: very compact cavity, *Opt. Commun.* 117: 480–484 (1995).
15. Duarte, F. J., Multiple-prism near-grazing-incidence grating solid-state dye laser oscillator, *Opt. Laser Technol.* 29: 513–516 (1997).
16. Duarte, F. J., T. S. Taylor, A. Costela, I. García-Moreno, and R. Sastre, Long-pulse narrow-linewidth dispersive solid-state dye laser oscillator, *Appl. Opt.* 37: 3987–3989 (1998).
17. Duarte, F. J., Multiple-prism grating solid-state dye laser oscillator: optimized architecture, *Appl. Opt.* 38: 6347–6349 (1999).
18. Duarte, F. J., and R. O. James, Tunable solid-state lasers incorporating dye-doped polymer-nanoparticle gain media, *Opt. Lett.* 28: 2088–2090 (2003).
19. Duarte, F. J., *Tunable Laser Optics*, Elsevier Academic, New York, 2003.
20. Dirac, P. A. M., *The Principles of Quantum Mechanics*, 4th ed., Oxford, London, 1978.
21. Duarte, F. J., Multiple-return-pass beam divergence and the linewidth equation, *Appl. Opt.* 40: 3038–3041 (2001).
22. Siegman, A. E., *Lasers*, University Science, Mill Valley, 1986, Chap. 1.
23. Maiman, T. H., R. H. Hoskins, I. J. D'Haenens, C. K. Asawa, and V. Evtuhov, Stimulated optical emission in fluorescent solids II: spectroscopy and stimulated emission in ruby, *Phys. Rev.* 123: 1151–1157 (1961).
24. Wolf, E., and W. H. Carter, Angular distribution of radiant intensity from sources of different degrees of spatial coherence, *Opt. Commun.* 13: 205–209 (1975).
25. Liao, L. S., K. P. Klubek, and C. W. Tang, High-efficiency tandem organic light-emitting diodes, *Appl. Phys. Lett.* 84: 167–169 (2004).
26. Chang, C-C., S. W. Hwang, C. H. Chen, and J-F. Chen, High-efficiency organic electroluminescent device with multiple-emitting units, *Jpn. J. Appl. Phys.* 43: 6418–6422 (2004).
27. Duarte, F. J., L. S. Liao, K. M. Vaeth, and A. M. Miller, Widely tunable green laser emission using the coumarin 545 tetramethyl dye as the gain medium, *J. Opt. A: Pure Appl. Opt.* 8: 172–174 (2006).
28. Chen, C. H., J. L. Fox, F. J. Duarte, and J. J. Ehrlich, Lasing characteristics of new coumarin-analog dyes: broadband and narrow-linewidth performance, *Appl. Opt.* 27: 443–445 (1988).
29. Michelson, A. A., *Studies in Optics*, The University of Chicago, Chicago, 1927.
30. Thompson, B. J., and E. Wolf, Two beam interference with partially coherent light, *J. Opt. Soc. Am.* 47: 895–902 (1957).
31. Saxena, K., D. S. Mehta, R. Srivastava, and M. N. Kamalasanan, Spatial coherence properties of electroluminescence from Alq_3–based organic light emitting diodes, *Appl. Phys. Lett.* 89: 061124 (2006).
32. Dharmadhikari, J. A., A. K. Dharmadhikari, and G. R. Kumar, High-contrast interference pattern of amplified spontaneous emission from dyes under transient grating excitation, *Opt. Lett.* 30: 765–767 (2005).
33. Duarte, F. J., On a generalized interference equation and interferometric measurements, *Opt. Commun.,* 103: 8–14 (1993).
34. Feynman, R. P., R. B. Leighton, and M. Sands, *The Feynman Lectures on Physics*, Addison-Wesley, Reading, 1965, Vol. III.

35. van Kampen, N. G., Ten theorems about quantum mechanical measurement, *Physica A* 153: 97–113 (1988).
36. Duarte, F. J., Comment on "Reflection, refraction, and multislit interference," *Eur. J. Phys.* 25: L57–L58 (2004).
37. Shimkaveg, G. M., M. R. Carter, R. S. Walling, J. M. Ticehurst, J. A. Koch, S. Mrowka, J. E. Trebes, B. J. MacGowan, L. B. Da Silva, D. L. Mathews, R. A. London, and R. E. Stewart, X-ray laser coherence experiments in neon-like yttrium, in *Proceedings of the International Conference on Lasers '91*, edited by F. J. Duarte and D. G. Harris, STS, Mc Lean, Virginia, 2002, pp. 84–92.
38. Trebes, J. E., K. A. Nugent, S. Mrowka, R. A. London, T. W. Barbee, M. R. Carter, J. A. Koch, B. J. MacGowan, D. L. Matthews, L. B. Da Silva, G. F. Stone, and M. D. Feit, Measurements of spatial coherence of a soft x-ray laser, *Phys. Rev. Lett.* 68: 588–591 (1992).
39. Ditmire, T., E. T. Gumbrell, R. A. Smith, J. W. G. Tisch, D. D. Meyerhofer, and M. H. R. Hutchison, Spatial coherence measurements of soft x-ray radiation produced by high-order harmonic generation, *Phys. Rev. Lett.* 77: 4756–4759 (1996).
40. Lucianetti, A., K. A. Janulewicz, R. Kroemer, G. Priebe, J. Tümmler, W. Sandner, P. V. Nickless, and V. I. Redkorechev, Transverse spatial coherence of a transient nickellike silver soft-x-ray laser pumped by a single picosecond laser pulse, *Opt. Lett.* 29: 881–883 (2004).
41. Schäfer, F. P., W. Schmidt, and J. Volze, Organic dye solution laser, *Appl. Phys. Lett.* 9: 306–309 (1966).

15 Appendix on Optical Quantities and Conversions of Units

F. J. Duarte

CONTENTS

15.1 Introduction 405
15.2 Linewidth Equivalence 406
15.3 Photon-Energy Wavelength Equivalence 407
References 407

15.1 INTRODUCTION

In this book electromagnetic radiation is described both in frequency and wavelength units. For the sake of completeness a brief description of the identities relating these units is provided here in addition to relevant physical constants commonly used throughout the book.

The basic relation between wavelength, λ, and frequency, ν, is given by

$$\lambda = c/\nu \tag{15.1}$$

where c is the speed of light. Here, c is given in ms^{-1}, λ in m, and ν in Hz. Standard physical constants, such as c, are given in Table 15.1. The values of these constants are those listed by the National Institute of Standards and Technology (NIST) available at the time of publication.

The Planck quantum energy is given by

$$E = h\nu \tag{15.2}$$

and the wave number, k, is defined as

$$k = 2\pi/\lambda \tag{15.3}$$

TABLE 15.1
Physical Constants

Name	Symbol	Value	Units
Elementary charge	e	$1.602176487 \times 10^{-19}$	C
Permeability of vacuum[a]	μ_0	$4\pi \times 10^{-7}$	NA^{-2}
Permittivity of vacuum	ε_0	$8.854187817 \times 10^{-12}$	Fm^{-1}
Planck constant	h	$6.62606896 \times 10^{-34}$	Js
Speed of light in vacuum	c	2.99792458×10^{8}	ms^{-1}

[a] $\pi \approx 3.141592653\ldots$

15.2 LINEWIDTH EQUIVALENCE

For laser emission at any particular wavelength λ it is important to estimate the purity, or bandwidth, of this radiation. This is quantified by the width of the laser line, or linewidth, $\Delta\lambda$. As explained in [1] starting from Heisenberg's uncertainty principle [2]

$$\Delta p \Delta x \approx h \tag{15.4}$$

one can write

$$\Delta\lambda \approx \lambda^2/\Delta x \tag{15.5}$$

which is an expression for linewidth in units of m. Its equivalent expression in the frequency domain is

$$\Delta\nu \approx c/\Delta x \tag{15.6}$$

which provides the linewidth in Hz. It should also be mentioned that in spectroscopy the reciprocal centimeter (cm^{-1}) is widely used as a unit of linewidth (see Chapter 2). This spectroscopist's linewidth can be obtained from Equation 15.6 in the form of

$$(\Delta\nu/c) \approx 1/\Delta x \tag{15.7}$$

TABLE 15.2
Linewidth Equivalence for $\Delta\lambda \approx 0.0004064$ nm at $\lambda \approx 590$ nm

Linewidth domain	Value
Wavelength	$\Delta\lambda \approx 0.0004064$ nm at $\lambda \approx 590$ nm
Frequency	$\Delta\nu \approx 350$ MHz
Spatial	$(1/\Delta x') \approx 0.0116747\ cm^{-1}$

TABLE 15.3
Photon-Energy Wavelength Equivalence

Photon energy	Wavelength (nm)[a]
1 eV	~1239.842
10 eV	~123.9842
100 eV	~12.39842
1 keV	~1.239842
10 keV	~0.123984

[a] Using $1\ \text{eV} = 1.602176487 \times 10^{-19}$ J

in units of 1/m. Conversion to units of cm^{-1} requires multiplication of Δx by 100 so that the spectroscopist's linewidth is calculated according to

$$1/\Delta x' \approx 1/(100\Delta x) \tag{15.8}$$

Thus, for a linewidth of $\Delta\nu \approx 30$ GHz we get $(1/\Delta x') \approx 1\ \text{cm}^{-1}$. To illustrate these conversions further, consider the laser linewidth of $\Delta\lambda \approx 0.0004064$ nm at $\lambda \approx 590$ nm given in its three versions in Table 15.2.

By definition, according to Equation 15.5, when a linewidth is quoted as $\Delta\lambda$ the wavelength at which it was measured, or calculated, must also be quoted. Linewidths in the frequency, or spatial, domain are not a function of wavelength. For an introduction to cm^{-1} units the reader is referred to Herzberg [3].

15.3 PHOTON-ENERGY WAVELENGTH EQUIVALENCE

In the x-ray field (see Chapter 10), as well as in spectroscopy [3] and semiconductor physics [4, 5], the absorption and emission spectra can be characterized in eV units. The equivalence between energy and frequency is established in Planck's quantum energy equation. Thus, using Equations 15.1 and 15.2

$$\lambda = (hc/E) \tag{15.9}$$

the equivalence is also made explicit for the wavelength domain. In Table 15.3 the equivalence of photon energy in eV and wavelength is given for a few spectral values of interest. A graphical equivalence between the two domains is given in [6].

REFERENCES

1. Duarte, F. J., *Tunable Laser Optics*, Elsevier-Academic, New York, 2003.
2. Dirac, P. A. M., *The Principles of Quantum Mechanics*, 4th ed., Oxford University, London, 1978.
3. Herzberg, G., *Spectra of Diatomic Molecules*, 2nd ed., Van Nostrand Reinhold, New York, 1950.

4. Kittel, C., *Introduction to Solid State Physics*, 4th ed., Wiley, New York, 1971.
5. Yariv, A., *Optical Electronics*, 3rd ed., Holt, Rinehart & Winston, New York, 1985.
6. Carroll, F., and C. A. Brau, Medical applications of the free electron laser, in *Tunable Laser Applications*, 1st ed., edited by F. J. Duarte, Marcel Dekker, New York, Chap. 6.

Index

Abbé diffraction limit, 253
ABCD ray transfer matrix. *See* Ray transfer matrix
Abdullin, U. A., 40
Ablation, 235
Absorption
  biological object image contrast, 248
  cross-section, 260
  doped silica fiber laser bands, 182
  Doppler-free saturation spectroscopy, 318–319
  dye laser process triplet, 98
  k-edge diagnostic imaging, 301–302
  laser dye triplet-triplet, 101
  lithium beam cross-section, 328
  monochromatic photo dynamic therapy, 236–237
  organic tissue response, 200
  phase contrast imaging, 302–304
  tattoo ink selective, 233
  tissue laser radiation resonance, 201–202
  two-photon, 259–260
  x-ray imaging information, 302–303
Absorption cross-sections, 253, 254
  laser intensity, 319
  two-photon, 260
Absorption spectra
  biomedicine fiber lasers, 198
  lithium beam density, 335
Absorption spectroscopy
  linear optical techniques, 56
  robust light-beam guides, 73
  saturated, 312–314
Acceleration driving frequency, 264
Accelerators, 285, 298, 306
Acceptance angle, single-mode fiber laser brightness, 180
Acetoxypolymethylene chains, 105
Achromatic design, nonlinear microscopy, 248
Acoustic waveforms, 250
Acousto-optic modulator (AOM), 47, 48
Acousto-optic tuning, 192
P-(acryloyloxypolymethylene) phenyl dyes (PA*rn*Ac), 105–107
Action cross-section, 260
Aesthetic medicine, 200
Affordability, 25
Ahmad, M., 102, 111, 117
Alexandrite lasers, 199
Alkoxides, 112, 113
Alq_3. *See* Aluminum tris(8-hydroxyquinoline) (Alq_3)
Aluminum tris(8-hydroxyquinoline) (Alq_3), 393
Aminonevulinic acid HCl, 236
Amplification, 19
  femtosecond laser pulse, 259
  hybrid tunable laser optical oscillators, 172
  injection seeded OPO systems, 50
  optical fiber hosts and dopants, 203
  parametric wave gain maximization, 36
Amplified spontaneous emissions (ASE)
  broadband light source, 211
  cavity configuration, 145
  supercontinuum fiber lasers, 218
Amplifiers
  erbium-doped fiber optical, 198
  optical, 197
  optical parametric, 5, 16
  pyrromethene dye, 110
  pyrromethene dyes efficiency, 110
  regenerative, 259
  Ti:sapphire regenerative, 71
  XeF laser, 4–5
Amplitude modulation, 318–319
Amplitude probability
  Dirac method, 150
  interferometric theory, 348–351
Anderson, R. R., 228, 233
Angiograms, 301–302
Angioplasty, 234–235
Angle of diffraction, ray transfer matrix, 156
Angle of divergence, 289
Angle of incidence
  dispersion derivatives, 380
  multiple-prism beam expansion, 378
  multiple-prism dispersion equation, 188
  ray transfer matrix, 156

Angle of refraction, multiple-prism beam expansion, 377
Angular frequency, resonance matrix, 316
Angular rotation
  closed cavity tuning, 147–148
  resonant wavelength changes, 158–159
Aniolek, K. W., 38
Antidepressants, 336
Anti-inflammatory agents, 302
Antireflection (AR) coatings, 145, 163–164, 166–167
Apertures
  DISCOS emitter, 395
  free-running OPO, 52
  Kerr-lens modelocked laser, 256–257
  single-mode fiber lasers, 180, 181
  waveguide excitation, 126
Application efficiency
  brightness, 218
  fiber lasers, 220
  linear energy transfer, 296
  photochemicals, 236
  turbines, 305
Applications, 383. *See also* Biomedical applications; Medical applications; Spectroscopic applications
  angioplasty, 234–235
  atomic spectroscopy, 46
  biological imaging, 249
  co-doped and ZBLAN fiber lasers, 216–217
  diode laser resonance ionization spectroscopy, 321–330
  dispersive external-cavity semiconductor lasers, 311–312
  dye-doped polymer/nanoparticle tunable lasers, 137–139
  dye lasers, 97
  erbium-doped fiber lasers, 209–212
  external-cavity semiconductor lasers, 167–170, 171
  fiber laser development, 197–198
  four-wave mixing microscopy, 270–271
  gain materials operational mode, 209–220
  harmonic microscopy, 264–270
  hemangioma treatment, 230–231
  holmium-doped fiber lasers, 215–216
  injection-seeding and high-resolution, 43
  interferometric imaging, 357–371
  laser development, 6
  laser optics, 383
  laser system design, 5
  lithium isotopes, 336
  lithotripsy, 234
  medical free-electron laser program, 283–289
  medical tool/instrument regulations, 220
  molecular spectroscopy, 46
  nonlinear microscopy imaging, 259–275
  optical heterodyne (OH) detection, 272–273
  orientation-patterned gallium arsenide, 70
  photodynamic therapy, 235
  polarization-sensitive detection, 271–272
  port-wine stain laser treatment, 229
  remote-sensing applications, 42
  safety in medical, 238–239
  scar/keloid treatment, 231–232
  second harmonic generation, 267–269
  solid-state dye lasers, 117–118
  spectroscopy, 33–34, 383–384
  supercontinuum fiber lasers, 217–220
  tattoo removal, 232–233
  thulium-doped fiber lasers, 214–215
  tunable diode laser, 330–336
  tunable lasers, 5–9
  tunable monochromatic x-ray devices, 289–306
  tunable optical parametric devices, 17
  two-photon fluorescence microscopy, 260–262
  vascular lesion treatment, 228–229
  ytterbium-doped fiber lasers, 213
Argon/dye laser photodynamic therapy, 237
Ar^+ (argon) lasers, 3, 199, 228, 229, 233, 237, 342, 343
Arissian, L., 155
Armstrong, D. J., 61
Ashworth, S. H., 59
Astronomy, 5, 384
Asymmetry
  cell membranes, 269
  chromophore imaging, 268–269
  electronic field orientation, 266
  elongated beam correction, 148–149
  emission beam, 147
  second harmonic and organic molecules, 265
Atmospheric sensing, 42, 59–61, 384
Atmospheric turbulence, 367
Atomic physics, 6, 336
Atomic resonance, 313
Atomic spectroscopy, 46, 57–64
Atoms, 312–315
Auger cascade radiotherapy (ACR), 282, 290–294, 297–298
Australian National University, 46
Autofluorescence, 262
Average power, 249
Axial rotation, 161

BaB_2O_4. *See* B-barium borate
Bacillus thuringiensis, 64
Backconversion, 49–50
Background suppression techniques
  nonresonant CARS, 67

optical heterodyne detection, 272–273
wave mismatch techniques, 273–274
Backscattered light, 246
Backscatter imaging, 304
Backward optical parametric oscillators, 70–71
Bacteria, 64
Ballistic light, 254–255
Ballistic photons, 304
Ballistic pulses, 255–256
Bandwidth
backward OPOs, 71
CARS microscopy design tradeoffs, 67–68
control and nanosecond-pulsed OPO, 34–50
free running OPO, 29
frequency range, 17
imitation and injection seeded tunable light pulses, 50
mode-hop-free injection seeding, 43
operational strategies, 33
OPO design, 29
ps-pulsed OPO, 70
pulse energy, 250
spectral emissions characteristics, 4
spectroscopic resolution, 34
tunability of nanosecond-pulsed OPO and, 35–38
tunable monochromatic x-ray machine, 289
β–barium borate, 20, 39
BBO optical parametric oscillators, 39, 40
injection seeded passive cavity, 59
passive cavity, 41
ring cavity pumped, 60
SFG crystal, 64
Beam. *See also* Gaussian beams; Intracavity beams; Laser beams; Output beam; TEM_{00} beam; X-ray beams
absorption cross-section, 328
absorption spectroscopy, 73
Auger cascade external radiation, 293–294
collinear laser printer, 365–366
diode-bar pump source, 64
divergence, 157
δn/δT characteristics, 124–125, 132–133
efficiency optimization, 61
electron, 283
external radiation, 290
fiber laser pump, 207
focus and image signal, 247
geometry of cone, 283, 289
grating, 356
high-performance narrowband, 44
monochromatic beam energies, 295–296
path, 180
plasmon excitation and laser, 251
pointing, 286–287
probe absorption spectroscopy, 313–314
probe Doppler-free saturated absorption, 314–315
propagation and fiber laser pumping, 207–208
proton therapy pediatric dose, 298
radiation energies, 292–293
Raman pumps, 41
self-adaptive tunable, 45
signal output, 46, 67, 68–69
single-transverse mode, 123
spectroscopic tailoring, 42
sub-Doppler, 57, 58
walkoff, 21
x-ray flux output counterpropagating, 286
Beam divergence
coherent/laser emissions, 401–402
diffraction-limited, 125–126
DISCOS emitter, 395–396
linewidth configuration, 187–188
multiple-pass, 392
spatial coherence, 392–393
Beam expanders, 123–124, 344–345. *See also* Multiple-prism beam expanders
Beam expansion
angle of incidence in multiple-prism, 376, 378
angle of refraction multiple-prism, 377
factor, 153
intracavity dispersive equation, 391–392
multiple-prism configuration equations, 188–189
multiple-prism grating configuration, 187–190
tuning grating correction, 148
Beam guides, absorption spectroscopy, 73
Beam profiles
DICOS emitter, 396, 397, 399, 402
dye-doped organic-inorganic gain medium emissions, 131–133
dye-doped polymer lasers, 390
fiber laser grating, 184
intracavity ray transfer matrix, 155–157
macroscopic interferometric imaging, 357–359
magnetic selector calibration, 332
multiple-prism grating linewidth configuration, 187–188
substrate interferometric response, 360–361
Beam quality
asymmetric emissions, 147
asymmetry correction, 148–149
free-running, pulsed OPO, 36
injection-seeding and high-resolution applications, 39, 43
lithium absorption spectra density, 335
ns-pulsed OPOs, 49
OPO performance and laser-like, 51

Beam quality *(continued)*
PPLN crystals, 44
twisting, 64
vertically elongated gain region, 147
Beat waveform information and frequency chirp, 47
Beer's law, 326
Biaxial crystals, 25–26
Bieske, E. J., 58
Bimolecular species spectroscopy, 34
Biological object staining and dyes, 248
Biomedical applications, 7, 8, 65–70, 199, 369–371
Biomembrane permeation, 265
Biomolecules, 64, 65, 67
Bioscience applications, 64, 198, 249, 256–259
Biosensing, 64, 74
Birefringence, 248
Birefringently phase-matched (BPM)
angled-scanned OPO systems, 53
crystals, 20, 22
Bisson, S. E., 62, 63
Bjorkholm, J. E., 38
Blood vessel thermal relaxation, 228
Blue dispersive lasers, 172
Blue dyes, 172
Blue-green region, 228, 233, 234
Blue pigments, 233
Blue region, 99, 143, 170, 171, 172, 206, 233, 237, 284, 365
Boltzmann velocity distribution, 313, 315
Bose–Einstein condensation, 6, 167, 169
Bosenberg, W. R., 31, 37, 51, 55
Bosenberg–Guyer type KTP OPO/NRO/OPA system, 51, 58, 59
Bragg grating
configuration, 164, 185
tunable fiber, 185–186, 190, 191, 203
tuned laser cavity, 184–185
tuning using, 163
Brain tumors, 296–297
Breast cancer, 298–301
Breast compression, 298–299, 299
Breast tissue, 302
Brewster, D., 383
Brewster angled crystals, 68
Brewster angle of incidence, 153–154, 368, 378, 380
Brightness
broadband light sources, 218
depth of uniform, 262
electron beam-normalized, 288
fiber laser configuration, 180–181
fluorescent imaging, 219
as glare, 284
LED array high, 126
medical dye lasers, 228
organic semiconductor Alq_3, 393
signal response and source high, 211
x-ray outputs, 305
Broadband amplification, optical coherence tomography, 210–211
Broadband capability
dye lasers, 198
OPO performance, 39, 51
photonics crystal fibers, 204, 208
Broadband detectors, 393
Broadband emissions
dye laser spatial coherence, 172
dye laser spatial homogeneity, 138
narrow-linewidth, 390
organic interferometric emitter yields, 402
Broadband filters, 365
Broadband fluorescence spectrum, 213
Broadband idler pulses, absorption spectroscopy, 73
Broadband output
femtosecond pulse cavity dispersion, 259
filtering to narrowband OPO, 38
free-running OPO, 37, 39
OPO spectroscopic tailoring, 41
solid-state dye laser, 110
Broadband radiation
interferogram, 401
OPO nonresonating waves, 44
single pulsed laser generation of Stokes, 66
x-ray production technology, 282
Broadband reflections, 191
Broadband resonances, CARS spectroscopy, 65
Broadband resonators, 126
Broadband sources
interferometers, 366
Michelson interferometer requirements, 201
supercontinuum fiber lasers, 218
tunable dye lasers, 131
Broadband spectroscopic OPO operational strategies, 33
Broadband tunability
dye and fiber lasers, 198
dye lasers, 227
ytterbium fiber lasers, 213
Broad bandwidth, free-running OPOs, 29, 36–37
Broadening
Doppler spectral line, 312, 313
Doppler width, 319, 326
extraction of homogeneous narrow bandwidth, 57
fluorescence emissions, 260
fluorescence spectra and line, 98
homogeneous linewidth/transit-time, 316, 324
linewidth and pressure, 62
steady-state pulse duration, 257

sub-Doppler inhomogeneous, 51, 58
sub-Doppler linewidth and pressure, 58
Broadly tunable sources
application scope, 371
external-cavity semiconductor, 143–172, 344
information-gathering, 370
interferogram quality, 400
lasers, 1–3, 342–344
OPO for CARS microscopy, 69
optically pumped lasers, 389
optical parametric devices, 16, 63
organic dye lasers, 343
organic semiconductors, 393
yellow-orange-red region dye, 344
Brookhaven National Laboratories, 299
Brosnan, S. J., 37
Browne, P. G., 72
Byer, R. L., 37, 52, 60

Calibration, magnetic selector, 332–333
Canalias, C., 70
Cancer, 170, 287, 289–297
CO_2 (carbon dioxide) lasers, 199, 214, 229
Carbon monoxide, 17
Cardiac imaging, 301–302
Cardiovascular surgery, 201
CARS. *See* Coherent anti-Stokes Raman scattering (CARS)
Carter, W. H., 392
Cassedy, E. S., 39, 40
Cassidy, D. T., 158
Cavities. *See also* Optical cavities; Oscillator cavities; Ring cavities
BBO OPO injection seeded passive, 41, 59
Bragg grating tuned, 184–185
closed, 145–146, 147–148, 170, 190
dispersive oscillator, 144–149
dumping in femtosecond pulse laser, 258
dye laser, 97
external fiber laser, 182
external tunable semiconductor, 144
Fabry–Perot, 164–165, 258–259
femtosecond pulse energy techniques, 258–259
fiber laser, 179
hybrid dye material optimized, 111
Kerr-lens modelocked femtosecond laser, 256
Littman–Metcalf, 183
miniature microelectromechanical system-driven, 159
optical fibers, 202–203
ORMOSIL glass, 111
passive seeded passive OPO performance characteristics, 52
Q-switching, 258
resonance injection seeding, 40
semiconductor laser external, 144, 164–166, 170–172, 311–312
single-mode fiber laser brightness, 180
tunable fiber lasers, 182
Cavity configuration. *See also* Littrow configuration
all-fiber rare-earth doped fiber lasers, 185–186
broadband emission, 390
broadband emission conversion efficiencies, 390
dispersion grating closed, 145–146
dispersive, 144–145
dispersive optical oscillators, 171
efficiency, 184
fiber laser diffraction grating, 182–183
fiber laser tuning, 182
fiber laser wavelength tuning, 182–183
grazing-incidence design, 190
linewidth dispersion, 187–188
linewidth equations, 187–190, 376
mirror-grating, 145
open, 145
open/closed, 170
Cavity control, 41, 44
Cavity design
four-quantum well laser antireflection coatings, 166–167
pulsed OPO design, 17
ultrashort-pulse external, 166–167
Cavity geometry, 72, 182
Cavity length
CARS microscopy, 68
double-pass dispersive linewidths, 158
dye laser linewidth, 157
fine-tuning, 161–163
for grazing-incidence grating, 161
longitudinal tuning, 160
multiple-prism grating configuration, 190
OPO, 19, 31, 39, 40, 41, 43
optimization, 44–45
resonator, 160
signal/idler pair resonance, 30
single longitudinal- mode, 188, 190
single-longitudinal-mode oscillation, 383
Cavity rotation, 161
Cavity tuning
angular rotation, 147–148
Bragg grating, 184–185
fiber laser configuration, 182
resonance approaches in optical, 30–31
Cells, 62, 69, 70, 269, 289–297
Centrosymmetric media, 18
Centrosymmetric systems, 266
Ceramics, 110
CHAPS. *See* Coherent heterodyne-assisted pulsed spectroscopy (CHAPS)

Chemical reactions, 201
Chemical sensing applications, 63, 65
Chemotherapy, 289–290, 292–293, 296
$X^{(3-)}$ nonlinear susceptibility, 268, 269, 270
  polarization-sensitive detection, 272
Children, 297–298
  hemangioma treatment, 230–231
  port-wine stain treatment, 229
  vascular lesion treatment, 228
Chirp, narrowband signal, 49–50
$X^{(2)}$ based optical parametric amplification, 22–25
$X^{(2)}$ based optical parametric gain, 22–25
$X^{(2)}$ nonlinear susceptibility, 20, 25
$X^{(2)}$ nonlinear susceptibility, 18
Choledochal stone lithotripsy, 234
Chromatic aberration, 248
Chromophores, 262, 268–269
  laser angioplasty, 234–235
  polymer dye covalent bonding, 101
  resonant second harmonic scatters, 265
  tattoo ink selective absorption, 233
Circular symmetry, photonics crystal fibers, 207–208
Cis-platinum, 292, 296–297
Cladding mode strippers, 182, 183, 186
Cladding pumped fiber lasers, 186
Clinical device design, 286–288
Closed cavities
  configuration, 145, 170
  dispersion grating, 145–146
  multiple-prism grating configuration, 190
  tuning, 147–148
Co-doped fiber lasers, 216–217
Coherence gating, 254
Coherence length
  femtosecond pulse gating, 254
  microscopy, 246
Coherent anti-Stokes Raman scattering (CARS), 22, 56–57, 247
  four-wave mixing microscopy, 270–271
  microscopy and imaging, biomedical application of OPOs, 65–70
  microscopy optimization, 66–67
  multiplex/multiwavelength seeded OPOs, 41
  nonlinear optical techniques, 56–57
  signals from vibrational resonance, 273
  spectroscopy, injection seeded instruments, 63–64
  techniques, 64
  vibrational resonance spectroscopy, 250
Coherent anti-Stokes resonance suppression, 274–275
Coherent control, vibrational resonances, 275
Coherent emissions, 401–402
Coherent heterodyne-assisted pulsed spectroscopy (CHAPS), 49, 57, 58
Coherent light
  full-wave-at-half-maximum (FWHM) duration pulse, 34
  high performance infrared spectroscopy, 73
  high-resolution laser spectroscopy sources, 50
  laser spectroscopic measurement, 33–34
  optical parametric devices, 18
  sources, 16
  source tunability and bandwidth factors, 35–38
Coherent local oscillator waves, background suppression techniques, 67
Coherent parametric emissions, stimulated parametric fluorescence (SPF), 271
Coherent quantum control, 252
Coherent radiation, 4–5, 9
  pulsed energetic characteristics, 3
  sources for optical parametric devices, 17–18
  sources of tunable, 6
  spectroscopic purposes, 16
  tunable pulse sources, 1–2
Coherent Raman spectroscopy, 56–57
Coherent sources, 3. *See also* Illumination sources; Light sources; Sources
  solid-state tunable, 6
Coherent sum
  emission directionality, 266–267
  harmonic radiators, 264–265
Coherent wavelength conversion, four-wave mixing processes, 21–22
Collimated light, diffraction grating, 183
Collimators, 149
Collinear geometry, phase-matching length, 265
Collisional relaxation, optical pumping relationship, 320–321
Collision-induced spectra, high-resolution OPO systems, 59
Commercial fiber Bragg gratings, 184
Commercial gain media, 127
  II–VI laser semiconductors, 171
Commercialization
  narrowband tunability, 37
  tuned monochromatic x-rays, 288, 305–306
Commercial laser-microscope, 250
Commercial PM dyes, 102–103
Commercial systems, 199, 228
  Bosenberg–Guyer-type KTP OPO/NRO/OPA, 58
  dye lasers, 237–238
  fiber lasers, 207
  high-quality laser beam, 218
  modelocked Nd:YVO_4 laser, 69
  1500 nm system, 212
  ns-pulsed OPOs, 37
  pulsed tunable OPO, 17
  reliable and cost-effective, 216

two-photon fluorescence microscopy, 260–261
ultrafast optical parametric systems, 32
Communications
free space security, 366–367
optical, 6
Complementarily, tunable laser, 4–5
Computed tomography (CT)
mammography without breast compression, 300
pediatric, 298
ps-pulsed image quality, 287
Conebeam geometry, 283, 289
Confocal fluorescent microscopy
spatial gating, 254–255
supercontinuum fiber lasers, 219
Confocal pinholes, 261, 263
Conservation conditions, nonlinear optics, 19
Conservation of brightness, single-mode fiber laser configurations, 180
Continuous tunability
ns-pulsed OPO application performance, 55–56
optical parametric processors, 50, 51
Continuous tuning
injection seeding, 39–40
instrument conditions, 50
spectral bandwidth, 40
Continuous wave (CW), 1, 2
dye laser operation, 227
fan-grating monitoring application, 62
fluorescence signal, 253
interferometer, 342
Kerr-lens modelocked femtosecond laser operation, 256–257
laser resolution limits, 248
OPO design, 30–31
optical parametric systems performance characteristics, 52–57
photodynamic therapy, 237
pumping, 24
scanning microscopy, 246
single-mode fiber laser configuration, 180
very narrow linewidth emission, 5
Continuous wave (CW) lasers
dispersive cavity configurations, 144–145
dye, 344
ionization pulse production estimates, 325
isotope separation, 330
linewidth, 157–158
lithium isotope separation, 331–332
medical applications, 199
thulium fiber, 214–215, 215
tissue laser radiation resonance, 201–202
tunable solid-state dye, 110
ytterbium fiber application characteristics, 213
Contrast
biological microscopy, 248
k-edge imaging and dye, 301–302
mammographic screening, 299
phase information imaging, 302–304
time gating and optimization of, 256
Contrast agents, 301–302
Conversion efficiency
broadband emission cavity configurations, 390
host material dielectric-oxide microparticles, 117
Copolymerization of dye matrix, 101
Copper anodes, 305
Copper photocathodes, 285
Copper-vapor lasers (CVL), 5, 110, 384
Core-pumped lasers
brightness configuration, 180
single-mode-fiber wavelength, 185–186
Coronary arteriography, 302
Cosmetic applications, 200, 211–212
Costs
application design, 5
medical application equipment switching, 209
Coumarin 545 tetramethyl (C545T) dye, 393–394, 396
Coumarin tetramethyl dyes, 102, 111, 124, 129, 130, 134–136, 398
Counterpropagating beams, 286
Counterpropagating optical waves, 70–71
COX-2 protein, 302
CPM. *See* Critical phase matching (CPM)
CRD spectroscopy, 56, 63
Critical phase matching (CPM), 20
Crystal fibers, 207, 208
Crystal laser replacement, 215
Crystallography, 304–305
Crystals
affordability and choice, 25
arrays of liquid, 250
beam waste and PPLN, 44
biaxial and uniaxial, 25–26
Brewster angled, 68
growth capacity, 25
Kerr-lens modelocked femtosecond laser, 256
LBO, 69
length and operating regimes, 27
medium choice, 25–27
nanodimensional silver-halide, 362–363
NLO, 72
noncentrosymmetric medium, 18, 20, 25
nonlinear optical, 20–21, 68
optical parametric oscillators, 64
phase contrast imaging, 303–304
photonic, 72–73, 73

Crystals *(continued)*
PPKTP, 69, 71
PPLN, 29–30
pump lasers, 25–26
structure microdensitometry, 341
CW. *See* Continuous waves (CW)

Dainty, J. C., 341
Damage
CARS microscopy, 70
diffraction grating design, 193
fluorescence, 249
medical laser safety, 238–239
optical, 17, 25–26
particle emitter adjacent cell, 296
photo, 69
polymer dye photodegradation, 100–101
reduction in multiphoton microscopy, 262
Danielmeyer, H. G., 38
Defense, 5
Degeneracy factor, parametric gain, 24
Degenerate four-wave mixing (DFWM) spectroscopy, 57
Delfyett, P. J., 166
Demtröder, W., 138
Densitometry, 341, 357–359
Density
emission wavelength tuning, 158–159
lithium beam absorption spectra, 335
oscillator spectral power, 126
radiographic image, 301
Zeeman multiplets and vapor, 316
Density-matrix, 323–326
Dentistry laser surgery, 202
DEOS. *See* Dimethyldiethoxysilane (DEOS)
Depth of focus
microscopy applications, 347
N-slit laser interferometer (NSLI), 371
Design
achromatic and pulse spectrum, 248
application requirements and laser systems, 5
applications and laser, 6
clinical machine beam pointing, 286–287
clinical monochromatic x-ray devices, 286–288
commercial laser microscopes, 250–251
dual-cladding fiber, 180–182
femtosecond pulse laser pulse energy, 258–259
injection-seeded pulsed OPO chirp control systems, 58
modular tunable OPO spectroscopic systems, 43
multiple-prism beam expanders, 378–379
narrow-linewidth long-pulse solid-state oscillating dye lasers, 124–126
OPO tuning elements, 37
optical parametric oscillators, 28–34
self-tuning ns-pulsed OPO, 44–46
synchronously pumped ps-pulsed OPOs, 69–70
thulium lasers, 214
tradeoffs in CARS microscopy, 67–68
tunable solid-state laser dye, 100–117
Destructive interference, 66–67
Detection
CARS microscopy *epi-*, 65
CARS optical heterodyne in CARS signals, 67
digital, 299–300, 342, 364–365
external-cavity semiconductor lasers, 168
femtosecond time gating, 256
fluorescent probes, 236
invisibility, 136
polarization-sensitive applications, 271–272
spectrometric, 73
wave mismatch techniques, 273–274
Detectors
gating imaging modalities, 246
linear photodiode array, 345
speed in biological image acquisition, 249
time-of-flight, 304
Detector screens, 350
DFG. *See* Difference-frequency generators (DFG)
DFWM spectroscopy
injection-seeding approach, 59
nonlinear optical techniques, 57
Diagnostic applications, 199, 200
coherent Raman spectroscopy, 65
imaging enabling technology, 289
imaging gating, 287
lasing wavelengths, 205
materials, 5
monochromatic x-ray device design, 286–288
tunable laser applications, 170
tunable monochromatic x-ray lasers, 298–305
1,4-diazobicyclo-2,2,2-octane, 102
Dielectric breakdown, third harmonic microscopy, 269
Diels, J. C., 155, 385
Dietel, W., 385
Difference-frequency generators (DFG), 18, 19, 29
input–output wave frequencies, 21
Differential absorption lidar (DIAL), 42
atmospheric remote sensing, 60–61
Diffraction
Gaussian pump beam limit, 253–254
geometry interferometric theory, 348–352
grating equation, 382

interference, 150
nanoparticulate distribution invisibility, 136
optical systems far-field limit, 251–252
pattern interferogram calculations, 355–357
Diffraction grating
collimated light incidence, 183
equation, 150, 152, 153, 158–159, 182–183
fiber laser tuning techniques, 190–193
Littrow configuration reflection, 148–149
properties, 363–364
supercontinuum fiber laser applications, 219
Digital detection, 342
interferometric theory, 364–365
mammographic monochromatic x-ray imaging, 299–300
Digital image processing techniques, stimulated parametric fluorescence (SPF), 275
Dimethyldiethoxysilane (DEOS), 112, 113
Diode laser pumps, 207
co-doping of semiconductor, 217
optical parametric device ethane sensing, 62
solid-state dye, 108
source peak power, 36
Diode lasers
dopants and high-intensity, 212
external-cavity tunable resonance ionization, 326–327
lithium spectroscopy with tunable, 311–337
medical applications, 199
pumped OPG/OPA systems, 38
resonance ionization spectroscopy, 321–330
single-mode fiber, 180
spectroscopy applications, 169, 170
tunable, 344
Diode pumped lasers
pulsed Nd:YAG, 29
YDFL optical pump radiation, 180–181
Diodes. *See also* Photodiode arrays
array waveguide excitation, 126
pump sources, 207
superluminescent light-emitting (SELD), 218–219
Dipole radiation, directionality, 266–267
Dipyrromethene dyes, 101, 102, 105, 106
Dipyrromethene dyes (PM. BF_2), 101, 102
Dirac, P. A. M., 376, 392
Dirac formalism, 342
beam grating, 356
dispersion interferometric, 380
photon propagation, 348, 351–352, 371
propagation amplitude, 150
Direct electrical excitation, 389
Directionality, emission geometry, 266–267
Discretely tunable lasers, 1
high-powered pulsed, 2, 4
spectral emission characteristics, 4
Dispersion
cavity linewidth configuration, 187–188
equations for double-pass, 377–378
generalized equation, 347–348
intracavity, 150–155
intracavity linewidth equation, 391–392
multiple-pass intracavity pulse compression, 379–380
multiple-prism arrays, 375–383
multiple-prism grating configuration, 187–190
optical laser oscillators, 171–172
silica nanoparticles in gain media, 126–129
Dispersion grating, closed cavity configuration, 145–146
Distributed-feedback (DFB) lasers, 71
solid-state dye lasers, 126
$\delta n/\delta T$ characteristics, 100, 116
DDPN/PN matrices laser beams, 132–133
hybrid organic-inorganic matrices, 122
multiple-prism beam expander, 124–125
PPMA-silica composite media, 128, 137
DNA, targeting of, 290–294
Dopants
coumarin 545 tetramethyl (C545T) dye, 393–394
dye lasing efficiency, 101
fiber laser rare-earth, 179
optical fiber, 197–198
optical fiber amplification, 203
Doping
fibers with rare earths, 205
organic-inorganic solid-state media dye, 116–117
ORMOSIL matrix-Perylene Red, 111
polymer gain media dye, 121–139
ZBLAN fiber and, 216–217
Doppler broadening, 326
Doppler-free saturation spectroscopy, 318–319
Doppler-free spectra
lithium vapor spectroscopic calculations, 320–321
two-level atoms, 314–315
Doppler linewidth
homogenous broadening, 319
isotope hyperfine structure imaging, 335
multilevel atoms, 314
Doppler shifting
inverse Compton process, 283
optical parametric oscillator performance, 51–54
saturated absorption spectroscopy linewidth, 312
Dose enhancement ratio (DER), 295
Double-clad pumping, 207–208
Double-pass dispersion equations, 377–378
Double-resonance spectroscopy, 383–384

Double resonant oscillators (DRO), continuous-wave design, 30
Double-slit interference experiment, 352–355
  Dirac formalism, 351
Doubly interferometrically confined organic semiconductor(DICOS) emitter, 393–402
Dougherty, T. J., 236
Driving waves, difference frequency generators, 19
Drugs, dye laser photodynamic therapy, 235
Dual-cladding fiber, 180–181
Dual-wavelength injection seeding, 41–42
Dual-wavelength passive ring-cavity optical parametric oscillators, 53
Dual-wavelength sources, 64
Duarte, F. J., 116, 122, 129, 133, 138, 145, 153, 158, 170, 376, 379, 385
Dunn, M. H., 72
Durability, optical parametric gain medium choice, 25
Duration
  FPDL vascular lesion treatment, 228
  port-wine stain treatment, 228
  short pulse emission, 1, 2
Dwell time, 248, 249
Dye amplification, frequency chirp, 50
Dye-doped polymer (DDP) mediums, 122
  synthesis and fabrication, 126–129
Dye laser oscillator
  hybrid systems, 4–5
  linewidth, 157
Dye lasers
  application domains, 5
  application requirements, 5
  broadly tunable, 344
  DICOS emitter, 402
  grazing-incidence cavity rotation, 161
  isotope separation, 330
  medical applications, 199, 227–239
  multiple-prism grating configuration applications, 384
  organic semiconductor broadband emissions, 172
  passive injection seeding, 40
  radiation look-up tables and diffraction gratings, 59
  seeded passive cavity OPOs performance characteristics, 52
  solid-state, 97–118
  solid-state media, 172
  solid-state tunable organic, 389
  spatial coherence, 172
  spectroscopy and tunable, 16–17
  tattoo removal, 233
  tunability, 198
  yellow-orange-red region, 344
Dyes
  biological objects, 248
  dipyrromethene, 102
  medical application risks, 227–228
  molecular imaging, 268
  organic polymer, 100–110
  performance and fluorine, 107–108
  solid matrix lasing host, 100–117
  x-ray diagnostic, 301–302

Ehret, G., 60
Eigenstates, 270
Electrical efficiency, 180
Electrical excitation, 389
  interferometric emitters, 393–395
Electrical shock, 239
Electromagnetic interference, 239
Electron beams, 283
Electron guns, 285
Electronic potential, harmonic frequency generation, 264
Electrons
  k-edge effect, 290–291
  x-ray beam interaction zone, 287
Ellipsoidal beams, vertically elongated gain region, 147
Emission characteristics
  broadly tunable sources, 3
  coherent and laser, 401–402
  DDP gain media laser, 129–133
  doped silica fiber laser bands, 181–182
  electrically excited interferometric emitter, 395–396
  FPDL penetration, 228–229
  lithotripsy, 234
Emission frequency, transition shifting, 1
Emissions
  geometric properties of harmonic, 265–267
  inorganic-organic matrices, 111
  nonlinear optical processes, 19
  visibility measurement, 399–401
Enabling technology, applications, 289
Endothelial cells, 230–231
Energetic characteristics, 3
  monochromatic x-rays, 284
  rare earth ions, 205–206
  x-ray production, 287
Energetics, DISCOS emitter, 396–397
Energies
  dye laser, 97, 227
  pump pulse quasi-phase matched (QPM) OPO, 36
  radiation beams, 292–293
Energy
  molecular transfer, 200–201
  nonlinear optic conservation, 19

optical efficiency, 259–260
photon excited state, 259–260
Energy conservation conditions
difference-frequency generators, 21
intensity-dip OPO cavity control, 44
three-wave optical parametric device, 20
Energy conversion, optimized pumping sources, 207–208
Energy levels
co-doped and ZBLAN glass fiber, 217
erbium lasers, 210
four-wave mixing microscopy, 270–271
holmium fiber lasers, 215
lithium isotopes, 322–323
organic dye, 97, 98
port-wine stain treatment, 230
thulium lasers, 214–215
vascular lesion treatment, 228
x-ray monochromaticity, 283
ytterbium lasers, 213
Energy-transfer dynamics, spectroscopic probing of, 59
Engines, 305–306
Environmental monitoring, OPO applications, 61–64
Epi-detection
CARS microscopy, 65
wave mismatch techniques, 273–274
Erbium (Er^{3+}), 179, 205, 216–217
Erbium-doped fiber amplifiers (EDFA), 198
Erbium-doped fiber lasers (EDFL), 179, 209–212
absorption/emissions wavelength, 182
applications, 210
cosmetic applications, 211–212
performance of tunable, 190–191
Er^{3+}:YAG solid-state lasers, 199, 212
Étalon-filtered sources, 63
Étalon tuning properties, 159
Ethane, 62
Excitation
beam plasmon, 251
confocal pinhole resolution, 263
coumarin 545 tetramethyl dye optical, 396, 398–399
electrical, 389, 393–395
femtosecond, 274–275, 295
fluorescent molecules, 253
infrared, 67
interferometric emitter electrical, 393–395
intracavity multiple-prism beam, 383–384
molecular, 263
molecular fluorescent, 253
multiphoton, 262, 263–264
plasmon, 251–252
two-photon, 57, 263, 264
waveguide, 126
Excited states
absorption technique, 206
dye-doped solid-state dye lasers, 126
multiphoton microscopy, 263–264
organic dye molecules, 97–98
photobleaching, 263
spectrographic resonance and broadening, 316
transitions (EST), 203
External beam radiation, 290
Auger cascades, 293–294
External cavities, 144
fiber laser gratings, 182
External-cavity semiconductor (ECS) lasers, 6, 344
antireflection coating, 163–164
applications, 167–170, 171, 311–312
Bose–Einstein condensation, 167
isotope separation, 330
linewidth, 170–172
neutral gas experiments, 312
performance characteristics, 164–166
performance of tunable, 163–164
power levels, 144
spectroscopy with dispersive, 311–312
External-cavity tunable diode laser, 326–327
External dispersive cavities, emissions linewidth, 158
External storage cavities, 258–259
Extracorporal shock wave lithotripsy (ESWL), 234
Eye protection, 238

Fabrication techniques, organic polymer dyes, 100
Fabry–Perot cavities (FPC), 258–259
resonators, 164–165
Fabry–Perot étalon, 51
Far-field diffraction, fluorescence microscopy, 253
Far infrared, 71
Favre, F., 159, 164
FDPL. *See* Flashlamp-pumped dye lasers (FDPL)
FEL. *See* Free electron lasers (FEL)
Femtosecond excitation, 295
CARS with transform-limited, 274–275
Femtosecond lasers
design techniques, 258–259
fiber, 257–258
pulse, 385
Femtosecond oscillators, 256–257
Ferroelectric domains, nonlinear optic media, 20
Fiber Bragg gratings (FBG), 203

Fiber lasers, 197–221. *See also* Erbium-doped fiber lasers (EDFL); Thulium-doped fiber lasers; Yb-doped fiber lasers (YDFL)
  Bragg grating tuning, 163
  cladding pumped, 186
  configuration of tunable, 182–190
  tunable, 179–194
Fiber loop mirrors, 204
Fiber optical amplifiers (FOA), erbium-doped, 198
Fiber optic technology
  co-doping, 217
  laser surgery, 202
Fiber photonic crystals, 73
Figure of merit (FOM), 24–25, 26, 27
Filters
  plasmon excitation, 251
  spectral, 252
  tuning element, 37
Fit parameters, 328–329
Fix, A., 39, 40, 60
Flashlamp-pumped dye lasers (FPDL), 5
  hemangioma treatment, 231
  lithotripsy, 234
  scar/keloid treatment, 232
  tattoo removal, 233
  vascular lesion therapy with pulsed, 228–229
Flashlamp-pumping, solid-state dye lasers, 98
Fleming, M. W., 146
Flow cytometry, supercontinuum fiber lasers, 217–218
Fluorescence
  biological object contrast, 248
  dye laser spectra lines, 98
  image signal, 246
  lithium beam absorption spectra, 328
  nonlinear optical processes, 19
  saturation and emission, 260
  two-photon (TPF), 247–248
Fluorescence microscopy
  multiphoton, 259–264
  resolution, 253
  supercontinuum fiber lasers, 217–218
Fluorescence spectroscopy, biomolecules, 64
Fluorescent molecules, 254
  organic dye, 97–98
  photobleaching, 254
Fluorescent wavelengths, coherent Raman spectroscopy, 65
Fluoride-based glasses, 203, 216
Fluorinated-modified polymers, 114
Fluorine, 107
Fluorophores, 262
  organic tissue laser response, 200
  saturation, 260, 264
  sinusoidal illumination pattern, 253
  two-photon absorption and organic, 259–260
Focal geometry, 27, 67–68
Focal spots
  inverse Compton scattering, 303
  mammography, 300
  radiological device design, 286
Focal volume, 264
Focus
  depth of, 347, 371
  free-electron laser, 283
FOM. *See* Figure of merit (FOM)
Forward-scattering, 289
Fourier processing, 253
Fourier transforms (FT), 34, 47, 48
Four-quantum well lasers, 166–167
Four-wave mixing, 21–22, 57
  microscope, 270–275
Free electron lasers (FEL), 1, 282, 283–289
Free-running optical parametric oscillators, 35, 36, 37
  idler frequency fluctuation, 73
  injection seeding, 39
  performance characteristics of aperture-selected, 52
  pump-pulse duration, 49
Frequency
  chirp-controlled OPO systems, 46–49
  chirp in narrowband signal output, 49–50
  nonlinear optical inelasticity, 19–20
  OPO output pulse profile, 47–48
  optical clockwork combs, 6
  parametric oscillator range, 17
  plasmon short-pulse laser beam, 251–252
  pump fields and persistent, 23
  quantities and unit conversion, 405–406
  stabilization and external storage cavities, 258–259
Frequency selectivity
  Bragg gratings, 184
  external-cavity lasers, 144
  tunable fiber lasers, 182
Frequency stabilization
  external reference cavities, 164–166
  spectroscopy applications, 169
Fresnel number, 150
Fuel biomolecules, 64
Full-wave-at-half-maximum (FWHM) duration, 34

GaAs. *See* Gallium arsenide (GaAs)
Gadolinium, 291, 301–302
Gadolinium-drugs, 293–294
Gain
  fiber Raman, 206
  Kerr-lens modelocked femtosecond laser, 256
  parametric wave maximization, 36

Gain media. *See also* Medium
application operational mode, 209–220
cross-sections, 128, 134
direct excitation of organic, 389
δn/δT values, 116
dye-doped hybrid solid state applications, 138–139
femtosecond laser pulse amplification, 259
fiber laser, 203–205
homogenous dye-doped polymer, 390
nanoparticulate distribution invisibility, 136–137
nanoparticulates in dye-doped polymer, 121–139
pyrromethene dye, 112
Rhodamine 6G-doped, 123
single-mode fiber laser configuration, 180
synthesis of dye-doped polymer, 126–129
Gain regions, 147, 150
Galilean telescopes, 344–347
GaAs (gallium arsenide), 27, 63, 70
GaA1As (gallium arsenide) lasers, 150, 158
Gases, 37, 57, 73
Gaussian beams
fiber laser grating, 184
intensity, 248
interferometer imaging device, 344–345
interferometer transfer matrix, 347
macroscopic interferometric imaging, 357–359
multiple-prism grating linewidth configuration, 187–188
pump diffraction limited, 253–254
substrate interferometric response, 360–361
third harmonic axial scattering, 266
Gaussian functions, 326
Gaussian–Laguerre doughnut mode, 253–254
Gaussian light pulse, 34
Gaussian pump beam, 253–254
Gaussian transform, 250
Gavrilovic, P. A., 158, 164
GEANT code Monte-Carlo simulations, 294
Generalized interference equation, 150, 152
Geometric length, 246, 254
Geometry
cavity, 72, 182
collinear phase-matching, 265
conebeam, 283, 289
dual-cladding fiber, 180–182, 181
focal, 27, 67–68
free-electron beam laser, 285
grazing-incidence cavity rotation, 161
harmonic sources/emissions, 265–267
interferometer, 342
interferometric measurement, 349
N-slit interferometer, 150
prism dispersion, 376–377
prisms, 251
pumping, 102–103
of samples, 266
solid dyes pumping, 102–103
surface plasmons, 252
Giffin, S. M., 101
Giordmaine, J. A., 35
Girls, 230
Glan–Thompson output coupler mirror, 190
Glan–Thompson polarizer, 189, 365–366
Glasses, 203, 216–217
Goldman, L., 138, 170
Göppert-Mayer, Maria, 259
Göppert-Mayer (GM) convention, 260
Gouy phase shift, 266, 269, 273
Granularity measurement, 341
Grating. *See also* Bragg grating; Diffraction grating; Littrow grating; Multiple-prism grating
backward OPO, 71
closed cavity configuration, 145–146
configuration of closed multiple cavity, 145–147
diagnostic imaging device design, 287
diffraction equation, 382
Dirac method generalization, 150
femtosecond time scale, 254
fiber laser external cavity, 182
interferometric calculation of silt, 352–357
mirror dispersion, 150–151
organic-inorganic gain media diffraction, 133
photodiode array resolution, 364–365
photon propagation in *N*-slit, 348–352
rotation wavelength tuning, 159
textile fabric interferometry, 368–369
transmission, 149, 341, 363–364
tuning illumination, 383
tuning in, 158–159
Grating/étalon-controlled optical parametric oscillators, 52
Grating-like arrays, *N*-slit laser interferometers (NSLI), 364
Grating-to-screen distance measurement, 355
Grating-tuned optical parametric oscillators, 37
Grazing-incidence (GI). *See also* Littrow configuration
cavity configurations, 145–146
cavity tuning, 170
fiber laser grating configuration, 182–183
grating cavity tuning, 160–161, 164
grating configuration near, 376
grating dispersion, 157
grating-tuned OPOs, 37, 53
hybrid multiple-prism, 383
hybrid multiple-prism near, 149
intracavity beam dispersion grating, 392

Grazing-incidence (GI) *(continued)*
multiple-prism grating configuration, 187–188, 190
solid-state dye laser near, 123–124
Green-blue region, 262
Green pigments, 233
Green region, 99, 108, 130, 201, 213, 284, 327, 332, 365, 394
Green-yellow region, 101
Grooves illumination, 183
Ground-excited ionization continuum system, 323–326
Ground states
injection-seeded passive-cavity OPO, 59
isotope ionization transition rate, 324
molecular photobleaching, 254
multilevel atoms resonance, 314–315, 316–317, 319, 321
optical pumping effect, 328
vibrational energy level, 275
Group velocity dispersion (GVD) constant, 154
Guide stars, 384
Guyer, D. R., 37, 51

Halide ions, 58
Hanna, D. C., 375
Hardness, 25
Hard x-rays, 284
Harmonic emission, 266–267
Harmonic generation, 35, 247, 264
Harmonic signals, 265
Harris, S E., 70
Health sciences, 64
Heat, 249
Heavy metals, 203
Heisenberg uncertainty principle, 259
diffraction-limited beam divergence, 125–126, 392
linewidth/wavelength equivalence, 406
MPL grating laser temporal emotions length, 391
tuning techniques, 160
ultrashort pulse emissions, 384–385
He–Cd (helium–cadmium) lasers, 342
He–Ne (helium–neon) lasers, 342, 347
HEMA. *See* Hydroxyethylmethacrylate
Hemangiomas, 230–231
Hematoporphyrin derivatives, 236
Herzberg, G., 406
High-average powers, application requirements, 5
High-energy radiation
hard x-ray production, 287
linear accelerator powered laser, 285
tissue thermal response, 202
High-gain
dye lasers, 145
optical damage threshold, 25
pulsed lasers, 157
single-pass power, 23–24
High-gain oscillators, cavity configurations, 145
High peak power
high-resolution laser spectroscopy, 50
microscopy, 246
multiple-prism grating configurations, 188
tunable solid-state laser technology, 172
ultrafast OPOs, 31–32
ytterbium-pulsed lasers, 213
High-resolution, signal beam tunability in CARS microscopy, 68–69
Hollberg, L., 164, 165, 169
Holmium (Ho^{3+}), 205
(Ho^{3+}-) doped fiber lasers, 210
applications, 215–216
Ho:YAG crystal lasers, 215
Homodyne terms, 273
Homogenous broadening
Doppler width, 319
linewidth/transit-time, 316, 324
narrow bandwidth extraction, 57
saturated absorption matrix, 316
Hospital device design characteristics, 287–288
Host materials, 203
co-doped and ZBLAN fiber lasers, 216–217
solid-state dye lasers, 98–99
Huisken, F., 52, 59
Hybrid laser systems, 4–5, 166, 172
Hybrid materials
$\delta n/\delta T$ gain media characteristics, 122
dye organic-inorganic gain, 110–114
nanoparticulate distribution invisibility, 136–137
photodynamic therapy, 238
polymer dyes, 99, 100
silicon-modified organic matrices, 114–116
synthesis of PMMA-silica nanoparticulate, 126–129
Hybrid multiple-prism near grazing-incidence (HMPGI)
grating laser cavities, 145–147
grating oscillators, 123–126
intracavity beam illumination, 149
Hydrogen bonds, 58
2-hydroxyethylmethacrylate (HEMA), 101, 103–104, 115
Hygroscopic properties, 25
Hyperfine hole-burning spectra, 58
Hypertrophy, 230

Idealized light pulses, 34
Idler fields, 23
Idler frequency, 73
Idler output
optical cavity resonance, 29
power parametric operating regimes, 27–28

single-longitudinal-mode tunable signal, 45
tetrahertz OPG/OPOs waves, 72
tunable narrowband OPO signal ranges, 44
Idler waves
fixed pump wavelength, 21
frequency chirp, 49
frequency control, 20
gain maximization, 35
high-gain devices, 25
infrared wavelength generation, 19
injection seeding, 36
injection-seeding approach, 59
monochromatic incident, 23
ns-pulsed OPO, 29
optical rectification, 72
oscillation threshold, 30, 32
output beam signal, 45
parametric gain, 27
pump waves and counterpropagating, 71
signal backconversion, 41
Illuminating beam
gratings and near-field diffraction, 354–355
multiphoton microscopy, 262
Illumination
diffraction grating, 376
diffraction grating and grooves, 183–184
N-slit laser interferometers, 342
Illumination intensity
fluorescence emissions, 260
multiphoton microscopy, 262
photobleaching, 263
Illumination lasers, repetition rates, 249
Illumination pattern, photobleaching, 253
Illumination response, spatial resolution and ultrashort pulse, 248
Illumination sources, 246
fiber lasers, 257–258
Kerr-lens modelocked femtosecond lasers, 256
nonlinear microscopy laser sources, 257
tunable lasers, 342
Image guided radiotherapy (IGRT), pediatric, 298
Image quality
fluorescent photons, 261
ps-pulses and motion artifacts, 287
Image science, photography, 341–342
Image signal
beam focus, 247
scanning microscopy, 246
Image structure, densitometry, 341
Imaging, 6
external-cavity semiconductor lasers, 167
interferometric, 341–371
k-edge diagnostic applications, 301–302
laser-based interferometry measurements, 342
lasing wavelengths, 205
measurement, 341–342
membrane, 268–269
multiple-prism beam expander applications, 384
optical parametric applications, 64
phase contrast, 302–304
pulse characteristics, 246
scattering lasers, 255
short-pulse laser, 276
supercontinuum fiber laser applications, 218–219
surface displacement and laser printing, 365–366
x-ray beam technology, 282–283
Incidental radiation, 264
Incident field, 251
Incoherent illumination, 361
Incoherent second harmonics, 266–267
Index of refraction. *See* Refractive index
Industrial monitoring applications, 61–64
Inelastic optical processes, 19
Information, beat waveform and frequency chirp, 47
Infrared absorption spectrum
carbon monoxide gas, 17
lidar techniques, 60
Infrared excitation, 67
Infrared fluorescence, 275
Infrared illumination
molecular excitation states, 263
photodynamic therapy sources, 237
Infrared laser beams, 283
Infrared lidar, 59–60
Infrared spectroscopy, 58, 63, 73
Injection-seeded pulsed optical parametric oscillators, 35, 38–42
atmospheric remote sensing, 61
CARS spectroscopy, 63–64
chirp-controlled systems, 46–49
high performance, 59
intensity cavity controlled, 44
OH chirp control system design, 58
self-adaptive tunable, 44–46
spectroscopic application performance, 51–56
Injection seeders, 48
Injection seeding
multiplex/multiwavelength, 41–42
narrowband OPO tuning, 59
OPO cavities and active, 42–43
passive, 40–41
rapid walk-off oscillation breakdown, 49–50
Inorganic compounds, 113
Input beams, 286
Input pulse duration, 250

Input waves
difference-frequency generators, 19
three-wave optical parametric device, 20
Instrumentation, CARS microscopy, 65–66
Instrument conditions, continuously tunable OPO, 50
Instrument development, nanosecond pulsed OPO, 34–35
Intensity
excitation of fluorescent molecules, 253
fiber lasers, 257–258
fluorophore excitation, 253
illumination, 260
incident pump radiation, 24
Kerr-lens modelocked femtosecond laser, 256
linear increase, 266–267
macroscopic interferometric imaging, 357–359
nonlinear optical processing, 247–248
optical parametric processors, 50
parametric generation and optical, 23
pulse profile, 47
pump laser, 25–26, 312–313
saturated absorption matrix, 316
second harmonic signals, 269
spectroscopic, 34, 39
spontaneous parametric processes, 19
threshold pump energy, 40
Intensity-dip, 44, 48
Interaction zone (IZ)
focal spot, 283
x-ray beams, 289
x-ray machine design, 286–287
Interference, 392
broadband light sources, 211
coherent quantum control phase, 252
definition, 392
destructive, 66–67
diffraction, 150
organic-inorganic gain media internal, 133–136
signal grating-to-screen distance measurement, 352, 355
Interferograms, 392, 400–401
near field and gratings, 352–357
Interferometers, 256, 344–348
Interferometric calculations
dispersion, 380–383
linewidth estimates, 400–401
organic-inorganic gain media diffraction, 134–136
Interferometric emitters, 393–395
Interferometric imaging, 341–371
Interferometric theory, dual measurement/calculation applications, 352–357
Interferometry, 6
dispersion analysis, 380–383
external-cavity semiconductor lasers, 167
laser-based, 341–371
multiple-prism beam expander applications, 385
phase contrast imaging, 303
propagation amplitude probability, 150
tissue volume and broadband light source, 211
International Thermonuclear Experimental Reactor, 336
Intracavity beam expanders, 383–385, 392
Intracavity beams
dispersion, 150–155, 157
multiple-prism expander applications, 383–385
narrowing/expansion process, 391–392
narrow-linewidth tunable laser, 123–124
output, 164
prismatic/multiprismatic expansion, 375–376
propagation theory, 148, 149–163
Intracavity dispersion, 150–155, 384–385
beam expansion equation, 391–392
multiple prism, 145, 379
Intracavity étalon
mirror grating, 147
monitoring application, 62
ns-pulsed SLM, 37–38
open cavities, 145, 146
sub-Doppler spectroscopy, 57–58
Intracavity fields, 72
Intracavity frequency-selective optics., 164
Intracavity grating grazing-incidence bandwidth tuning, 37
Intracavity optics, 7
crystals, 327, 332
electromechanical system, 164
nonlinearities, 167
prism separation, 166, 168
Intracavity prism separation, 168
Intracavity pulse
multiple-pass compression/dispersion, 379–380
peak power, 258–259
Intracavity ray transfer matrix, beam profiles, 155–157
Intracavity return passes, 124
Intracavity wavelength-selectivity elements, nanosecond-pulsed OPO, 36, 37
Intracellular structures, 290
Intrinsic signals, second harmonic generation, 267–268
Inverse Compton scattering, 283
mammographic monochromatic x-ray imaging, 299–300
monochromatic beam energies, 295–296
monochromatic x-ray source, 305
x-ray imaging information, 303–304
Iodinated deoxyuridine (IUdR), 295, 296

Iodine, 291, 295, 301–302
Ionization
  diode laser/Nd:YAG laser application, 312
  ground-excited continuum system density matrix, 323–326
  lithium isotopic spectroscopy, 321–322
  third harmonic microscopy, 269–270
Ionizing energy, 296
Ionizing power, 329
Ion production estimation, 323–326
Ions, 58
Isotope beam resonance, 334–335
Isotopes
  Auger cascades and iodine, 295
  hyperfine structure imaging, 335
  photoionization density matrix, 324
Isotope separation, 5, 6
  apparatus, 332–333
  diode laser and lithium, 312
  laser-pumped dye lasers, 330
  lithium, 331
  tunable diode laser, 330–336
  tunable external semiconductor laser applications, 169–170
Ito, H., 72

Jackson, S., 214
Jain, M., 39, 40
James, R. O., 116, 122
Johns, P. C., 299

K-edge
  diagnostic imaging applications, 301–302
  effect, 290–291
  platinum, 295
Keloids, 231–232
Kerr-lens modelocked lasers (KML), 256–257
King, T. A., 111, 214
Knudsen cell, 326, 327, 329
Kornaszewski, L. W., 73
Kovalchuk, E. V., 57–58
Kreuzer, L. B., 38
Kr^+ (krypton ion) lasers, 342
$KTiOPO_4$. *See* Potassium titanyl phosphate ($KTiOPO_4$)
KTP. *See* Potassium titanyl phosphate (KTP)
Kulp, T. J., 63
Kytina, I. G., 108–109

Lamb dip, 314, 315, 320
Lankard, J. R., 121
Laser-beam expander assembly, 366–367
Laser beams
  monochromatic x-rays, 284
  multilevel atoms resonance frequency, 314
  ns-pulsed, 45
  printer collinear, 365–366
  safety in medical applications, 238
  tunable dye-doped organic-inorganic gain medium, 129–133
Laser cooling, 6
  external-cavity semiconductor lasers, 167
  semiconductor tunable lasers, 169
Laser efficiency
  cascaded Raman laser, 206
  diffraction grating-tuned cavity, 397, 398
  doped-fiber and diode, 179
  dyes, 237–238
  Er-ZBLAN laser, 216–217
  fiber laser pumping, 180
  low brightness diode pump, 181
  pumping, 207–208
  silica-based host glasses, 216
  wavelength and, 201
Laser emissions, 401–402
  linewidth/wavelength equivalence, 406–407
  pulse compression, 384–385
Laser excitation, intracavity multiple-prism beam expansion, 383–384
Laser-induced fluorescence (LIF), 56
Laser isotope separation, 5
Laser lithotripsy, 234
Laser microscopes
  CARS microscopy, 66
  commercial applications, 250–251
Laser optics applications, 383
Laser performance, tunable fiber, 190–193
Laser power
  emission characteristics, 3
  FPDL vascular lesion treatment, 228–229
  image signal, 246
  ionization absorption, 325–326
  isotope hyperfine structure imaging, 335
  single-mode fiber laser configuration, 180
  solid-state dye, 108–110
  tunable fiber laser performance, 191–192
Laser printing, 365–366
Laser pulse
  CARS microscopy design tradeoffs, 67–68
  femtosecond, 246
  ionization region, 325
  Kerr-lens modelocked laser, 257
  lithium ion production estimates, 323–326
  sources of ultrashort, 276
Laser-pumped dye lasers, 330
Laser radiation
  angioplasty, 234–235
  dye material damage, 100
  hemangioma treatment, 231
  organic tissue interaction, 200–202
  saturated absorption matrix, 316
  second harmonic, 237
  tattoo removal, 233

Laser radiation *(continued)*
tunable coherent radiation, 5
wavelengths, 209
Laser repetition rate optimization, 249
Lasers. *See also* Ar^+ (argon) lasers; Continuous wave (CW) lasers; Diode laser pumps; Diode lasers; External-cavity semiconductor (ECS) lasers; Fiber lasers; Nd:YAG lasers; Yb-doped fiber lasers (YDFL)
alexandrite, 199
blue dispersive, 172
copper-vapor, 5, 110, 384
core-pumped, 180, 185–186
crystals, 215
nonlinear optics, 19
scanning microscopy, 246
spectroscopic measurement, 33–34
tabletop tetrawatt, 285
tunability, 1
Laser-spectroscopic techniques
industrial/environmental monitoring applications, 61–64
OPO system performance characterization, 51–57
Laser spectroscopy, 138
high-performance computer controlled, 58
Lasers (Siegman), 392
Laser suitability, criteria, 5
Laser surgery, 201–202, 228–231, 231–232
Lasing
dye laser intersystem crossing process, 98
nanoparticles, 122
narrow-linewidth long pulse, 123
Lasing efficiency
copper-vapor-lasers, 110
fluorinated-modified polymer silica aerogels, 114
fluorine polymer matrix content, 107–108
multiple-prism grating configuration, 190
organic-inorganic hybrid materials, 111
PA*rn*Ac/PA*rn*MA dyes, 105, 107
polymer host viscoelastic properties, 102
pyrromethene dyes, 112
Rhodamine dyes, 101
single-mode fiber lasers, 180
solid-state dye laser, 139
thulium lasers, 214
ytterbium lasers, 213
Lasing performance, PM dyes, 105
Lasing stability, TMOS-based hybrid matrices, 112
Lasing transitions, optical fiber host, 203
Lasing wavelengths, 205–206
Laue crystallography, 303–304, 305
Laurent, P., 165
Laurila, T., 147
Law of refraction, 346, 352
Layer transparency, 254
LBO crystals, 69
Length
femtosecond pulse gating, 254
microscopy and geometric, 246
Lenses, He–Ne laser TEM_{00} beam, 347
Lidar (light detection and ranging), 167–169
differential absorption, 42, 60–61
infrared atmospheric remote sensing, 60–61
LIF. *See* Laser-induced fluorescence (LIF)
Life sciences applications, 198–202
Lifetime imaging, 248
Light bullets, 246
Light-emitting diodes (LED), 126
tandem organic (OLED), 393
Light energy, organic tissue, 200
Light pulses, ultrashort, 246
Light scattering, infrared lidar techniques, 60
Light sources
broadband supercontinuum fiber lasers, 218
chemical sensing applications, 63
high-resolution laser spectroscopy, 50
photodynamic therapy, 236–237
PPLN-based coherent, 38
spectroscopy coherent, 50
tissue and broadband, 211
vacuum ultraviolet, 50
visibility and broadband, 211
Light therapy, 235–238
$LiNbO_3$. *See* Lithium niobate ($LiNbO_3$)
Linear absorption, 249
Linear accelerators, 285
CT imaging, 298
high-energy radiation powered laser, 285
Linear attenuation, 299
Linear energy transfer, 296
Linear optical spectroscopy, 56
Linear scanning microscopy, 246
Line-tunable lasers, 1, 342
Linewidth
external cavity semiconductor laser, 170–172
external-cavity semiconductor laser, 167
fiber amplifiers, 194
fiber laser grating, 184–185
interferometric estimates, 400–401
intracavity dispersion equations, 376–377, 384–385
intracavity narrowing, 4
isotope hyperfine structure imaging, 335
$LiNbO_3$ optical parametric oscillators, 17
lithium isotope separation laser, 331
longitudinal mode changes, 162–163
measurement, 126
measurement in interferometric imaging, 366
multilevel atoms Doppler, 314

multiple-prism beam expander, 376–389
multiple-prism grating, 157–158, 187–190
narrowing process, 391–392
narrowing strategies, 17
saturated absorption spectroscopy, 312
selectivity and Bragg gratings, 163
tunable fiber laser performance, 191–192
tunable laser applications, 170
very narrow, 5
wavelength equivalence, 406–407
Lipid peroxidation, 62
Liposomes, 266, 269
Liquid crystal arrays, 250
Liquid dye lasers, 98–99, 118
Lithium beam
experiments, 333–334
ionization, 325, 326
isotope separation, 332–333
resonance ionization spectra, 328–329
Lithium ion separation, 169–170
Lithium isotopes
applications, 336
energy level diagram, 322–323
resonance spectra measurement, 329–330
separation, 330–336
Zeeman multiplet state distribution, 316–318
$LiNbO_3$ (lithium niobate), 20, 26–27, 35
$LiNbO_3$ optical parametric oscillators, 17
DFG-seeded, 59
performance characteristics, 52, 53
Lithium spectroscopy, 311–337
LiB_3O_5 optical parametric oscillators, background suppression techniques, 67
Lithium vapor, 319–320
Lithotripsy, 234
Littman, M. G., 161
Littman–Metcalf cavities, 183
Littrow configuration
cavity grating tuning, 161
dispersive oscillator cavity, 145
dispersive oscillator optimization, 147–149
dye-doped organic-inorganic gain medium emissions, 132
fiber laser cavity configuration, 182
grating dispersion, 392
grating tuning, 158
intracavity dispersion, 151
linewidth, 157
multiple-prism grating dispersion, 124–125
multiple-prism grating linewidth configuration, 187–190
ray transfer matrix, 156
Littrow grating. *See also* Multiple-prism Littrow (MPL) grating
lithium isotope separation laser, 331
mounted, 167
tunable laser applications, 170
tuned fiber laser cavity, 184
Littrow grating lasers, 169
Lìu, K., 161
Lock-in amplifier technique, 327
Logical oscillators, 272–273
Long cavities, 258
Longitudinal tuning, 160
Lorentzian absorption profile, 315

Machine specifications, 288
Macquarie University, 17, 34–35, 39, 40, 46, 59, 63–64
$MgO:LiNbO_3$ optical parametric systems, 58, 72
Magnetic selector, 330
Magnetic selector calibration, 332–333
Maiman, T. H., 392
Mammography, 282–283, 284, 298–301, 302
Management guidelines, application design, 5
Margaritondo, Giorgio, 302
Marking requirements, 220
Maslyukov, A., 101
Mass selectors, 330, 331
Mass spectrometers, 312
Mass spectrum, 333, 334–335
Material processing, 5
Materials
harmonic generation/radiation, 264–265
solid-state dye lasers, 100–117
Materials sciences, 336
diagnostic applications, 5
free-electron laser program, 283
tuned monochromatic x-ray laser applications, 306
ultrashort pulse laser applications, 385
McFarland, B. B., 98, 121
Measurement
grating modulation transfer function, 363–364
imaging, 341–342
interferometric geometry, 349
interferometric theory, 352–357
laser-based interferometry, 342
laser spectroscopic, 33–34
linewidth, 126, 366
lithium ion resonance spectra, 328–330
metallic gratings modulation, 364
optical heterodyne techniques, 46–48
optical pulse solid-state lasers, 6
optical source density, 342
photographic grating modulation, 364
pulse duration, 126
resolution modulation, 363–364
signal grating-to-screen distance, 352, 355
spectroscopic, 33–34, 50–70
vapor cross-section lidar, 60
visibility, 363–364, 399–401

Media. *See* Gain media
Medical applications, 7, 8, 64, 198–202
  alexandrite lasers, 199
  dye lasers, 227–239
  Er^{3+} fiber laser power, 216–217
  fiber lasers, 197–221
  free electron laser (FEL) program, 283–289
  free electron lasers (FEL), 283–289
  pulsed/tunable monochromatic x-rays, 281–306
  solid-state dye lasers, 117–118
  solid-state tunable dye laser, 138–139
  tunable external cavity systems, 170
  ytterbium fiber lasers, 213
Medical devices
  regulations, 220
  safety, 287
Medical imaging, x-ray technology, 281–283
Medical laboratories, 256–259
Medical tool/instrument regulations, 220
Medicine, 5
  fiber laser wavelengths, 198
Medium
  β–BaB_2O_4, 35
  dye solid-state, 98
  nonlinear optical device, 20
  optical parametric gain choice, 25–27
  polarization and plan-wave radiation fields, 22
  Q-switching of active, 258
Membrane-binding chromophores, 265
Membrane imaging, second harmonic generation, 268–269
Membrane potential sensing, 268
Metallic coatings
  interferometric transmission gratings, 352
  rare-earths ions, 197, 203, 205, 209, 210
Metallic films, 342
Metallic gratings, modulation measurements, 364
Metallic vapors
  dispersive external-cavity semiconductor lasers, 312
  lithium isotope separation, 332
Meteorology, 6, 385
Methacryloyloxypolymethylene dyes (P*n*MA), 105–107
P-(methacryloyloxypolymethylene) phenyl dyes (PA*rn*MA), 105–107
Methyl ethyl ketone (MEK), 127
Methyl methacrylate (MMA), 101, 103–104, 115
Methyltriethoxysilane (TRIEOS), 112, 113
Michelson, A. A., 399
Michelson interferometers, 201, 211
Microdefects, interferometric imaging, 359–361
Microdensitometers, 342
Microdensitometry, 341
  biomedical interferometric imaging applications, 369–371
Microelectromechanical systems (MEMS), tuning miniature, 159–163
Microillumination, *N*-slit laser interferometer (NSLI), 371
Micromechanical systems, tunable cavity configuration controls, 146
Microscopes
  four-wave mixing, 270–275
  four-wave mixing applications, 270–271
  N-slit laser interferometers, 370–371
  saturation, 253–254
Microscopic imaging
  cell and tissue, 69
  defect interferometric imaging, 359–361
Microscopy
  coherent, 7–8
  coherent quantum control, 252
  coherent Raman spectroscopy, 65
  depth of focus, 347
  harmonic, 264–270
  membrane potential sensing, 268
  multiphoton fluorescence, 259–264
  ps-pulsed optical parametric oscillators, 70
  scanning, 246, 247, 257–258
  stimulated emission depletion (STED), 253–254
  third harmonic generation, 269–270
  ultrashort pulse laser, 256, 385
Mid-infrared spectrum
  holmium fiber lasers, 215
  rare-earths metal dopants, 198
  spectroscopy, 63, 70
Military applications, 305–306
Miller, R. C., 35
Miller rule, 24
Milton, M. J., 60
Mirrorless optical parametric oscillators, 70–71
Mirrors, 203–205
  Glan–Thompson output coupler, 190
  grating cavity configuration, 145
  grating dispersion, 150–151
  output coupler, 164, 393
  resonator displacement and wavelength tuning, 162
  ring cavity, 37–38, 48
  saturated absorption semiconductor, 203
MMA. *See* Methyl methacrylate
Mode hopping, 160, 163
Modeling, pulsed OPO bandwidth factors, 36
Modelocked lasers, 204
  Kerr-lens aperture, 256–257
  multiple-quantum well (MQW), 168
  prism sequence configuration, 166
Modelocking
  external-cavity semiconductor laser oscillation, 166
  ultrafast interval, 32

Modular designs, 287–288
Modulation transfer function (MTF), 341
  transmission grating assessment, 363–364
Molecular footprints, vibrational energy levels, 270
Molecular imaging
  diagnostic, 342
  dyes, 268
  k-edge, 301–302
  photographic grain structure, 361–363
Molecular orientation, second harmonic (SH) signal, 265–266
Molecular potential, harmonic frequencies, 264
Molecular spectroscopic sensing, optical parametric processing, 57–64
Molecular spectroscopy
  chirp-controlled, injection seeded OPO systems, 46
  ns-pulsed mid-IR tunable OPOs, 37
  parametric oscillators, 17
  passive injection seeded OPOs, 40
Molecular targeting
  chemotherapy drugs, 291–292
  x-ray radiation, 293
Molecules, 100, 198, 200–201, 253
Momentum
  conservation conditions, 20, 21
  nonlinear optic conservation, 19–20
Monochromatic incident idler waves, 23
Monochromatic light, photodynamic therapy, 236–237
Monochromatic x-rays, 283–284
  tuning, 290–291
Mooradian, A., 146
Motion
  harmonic and oscillator classic, 264
  pediatric radiation therapy, 297–298
MPMMA. *See* Poly(methyl methacrylate)
Müller, F., 62
Multigrating PPLN, sub-Doppler spectroscopy, 57–58
Multimode (MM) lasers
  fiber lasers, 207
  high-performance narrowband, 44
  passive injection seeding, 40
Multimode operations, pump-pulse duration, 49
Multiphoton excitation, 262
Multiphoton fluorescence
  microscopy, 259–264
  resolution, 263–264
Multiple anomalous dispersion (MAD), 305
Multiple-prism arrays, 375–383
  pulse compression, 166
  ray transfer matrix, 156–157
Multiple-prism beam compressors, 153–154
Multiple-prism beam expanders, 375–385
  dispersion analysis, 152–153
  dispersion characterization, 347–348
  $\delta n/\delta T$ characteristics, 124–125
  frequency filtering, 392
  grating configuration parameters, 188
  interferometer imaging device, 345–348
  laser printing collinear beams, 365–366
Multiple-prism dispersion
  prism beam expanders, 378–379
  single-pass equations, 383
Multiple-prism grating
  copper-vapor-laser cavity configuration, 384
  dye laser configuration, 383
  fiber lasers, 383
  gas lasers, 383
  solid state dye-doped lasers, 390
  tunable fiber laser linewidth configuration, 187–190
Multiple-prism grating assemblies
  DDPN gain media, 138
  intracavity dispersion, 150, 151–152
  resonant wavelength changes, 159
Multiple-prism grating cavities, dispersion configuration, 145–146
Multiple-prism Littrow (MPL) grating
  laser cavities, 145–146
  linewidth, 390–391
  oscillators, 123
Multiple-quantum well (MQW)
  grating tuned passively modelocked, 168
  passive modelocking techniques, 166
Multiple wavelengths, injection seeding, 41–42
Multiplex spectroscopy, optical parametric oscillator design, 29
Multiwavelength lasers, printers, 365–366
Multiwave/multiplex OPO operation, atmospheric remote sensing, 60–61
Munitions testing, 306

Nachay, B. A., 385
Nanoparticulates, dye-doped polymer gain media, 121–139
ns-optical parametric optical devices, 60
ns-optical parametric oscillators, 29–30
  bandwidth control, 34–50
  chirp-controlled, injection seeded, 46–49
  injection seeding and narrowband operations, 42–43
  intracavity wavelengths, 36
  performance and operating conditions, 49–50
  performance characteristics, 52–56
ns-pulsed devices
  atmospheric remote sensing, 60–61
  critical phase matching, 20
ns-pulse pump lasers, self-adaptive tunable injection-seeded, 43
Nanostructures, 385

Narrowband output
frequency chirp, 47, 49–50
homogeneously broadened, 57
multiple-prism grating, 190–192, 194
picosecond optical pulses, 271
PPLN OPO systems, 44–45
tuning range of pulsed, 47
Narrowband pump sources, 61
Narrowband radiation
backward OPOs, 71
CARS and femtosecond excitation, 274–275
high-resolution laser spectroscopy, 34
injection seeding, 39–40
inverse Compton scattering, 305
output wavelength approaches, 37
seed frequency, 40
single-longitudinal-mode (SLM), 34, 37–38
tunable x-ray beam, 283
Narrowband sources
actively seeded OPO cavities, 42–43
all-solid-state, 58
applications, 276
laser-spectroscopic measurements, 33–34
nonlinear oscillator coherent, 72
OPOs, 39, 50–52
replacement, 218
tunable laser oscillators, 123–126, 129
tunable x-ray beams, 283, 305
tuning OPO, 59
Narrowband spectroscopic sensing, 61, 63
Narrowband tunability
injection seeding approach, 59
monochromatic x-rays, 301
nanosecond-pulsed OPO performance characteristics, 37
ns-pulsed OPOs, 60
OPO signal and idler output, 45–46
tuning range, 227
Narrowband tuning, 59, 152–155
Narrow-linewidth emissions
application requirements, 5
cavity configurations, 17, 145–147, 184
CO_2 laser tunable, 4
external-cavity semiconductor lasers, 167, 169, 170, 172
interferometer, 352
laser cavity wavelength-selective elements, 97
MPL grating configuration, 189
multiple-prism array deployment, 8
reflection, 187
ring cavity configuration, 186
single-transverse-mode beams, 122
single-transverse-mode emission, 131–133
solid-state dye lasers, 7
tuning range, 344
vibrational resonances, 274
visible spectrum, 117
Narrow-linewidth lasers
background superluminescence, 164
interferograms, 366
intensity, 365
interferometric linewidth estimates, 400–401
intracavity elements, 383
multiple-prism beam expanders, 383–384
performance, 139
pulsed dye, 344
selective excitation, 322
solid-state organic, 390–392
spectroscopy, 138
spectrum saturation, 328
superluminescence, 164
Narrow-linewidth oscillation, 148–149
Narrow-linewidth oscillators, 99, 190, 376
Narrow-linewidth sources, 312, 320, 329–330
NCPM. *See* Noncritical phase matching (NCPM)
Nd:YLF lasers, 108
Near-Gaussian beam
dye-doped polymer lasers, 390
laser printing, 365–366
Near grazing-incidence configuration
grating dispersion, 392
linewidth, 157
multiple-prism grating, 187–189
multiple-prism grating dispersion, 124–125
Near-infrared radiation (IR)
continuous tunability, 37
light sources, 246
multimode OPO systems, 44
rare-earth metal dopants, 198
seeding of self-tuning narrowband OPS, 45
Negligible pump-field losses, 23
Neodymium (Nd^{3+}), 205
Nd:YAG lasers, 69
background suppression techniques, 67
biosensing applications, 64
chirp control, 46
diode lasers combination, 312
hemangioma treatment, 231
high performance, 44, 47
industrial/environmental monitoring applications, 62
injection-locked single frequency, 30
intersecting cavity geometry, 72
lithium beam ionization, 326–327
lithium isotope separation, 332
medical applications, 199
multimode, 40
near-IR spectroscopic sensing, 31
photodynamic therapy, 237
port-wine stain laser treatment, 229
pulsed diode-pumped, 29
resonance ionization spectroscopy, 321

scar/keloid treatment, 232
self-adaptive approach, 45
signal and idler tuning, 38
single-longitudinal-mode (SLM), 38, 41
spectroscopic tailoring, 42, 43
ytterbium fiber laser applications, 213
Neodymium glass rods, 286
Neodymium laser applications, 210
Nd:vanadate lasers, 257
Nesbitt, D. J., 59
Neutral-density filters, macroscopic interferometric imaging, 358
Ngai, A. K. Y., 62
90-degree phase matching. *See* Noncritical phase matching (NCPM)
NLO. *See* Under nonlinear optical
Noise
nonlinear optical processes, 19
reduction and linewidth, 165
Noncentrosymmetric crystalline medium, 18
NLO susceptibility interaction, 22
optical parametric devices, 20
tensor components, 25
Noncritical phase matching (NCPM), 21
Nonlinear effects, high pump intensity lasers, 207
Nonlinearity, Abbé diffraction limit, 253
Nonlinear microscopes, 246
Nonlinear microscopy, 247–251, 259–275, 276
Nonlinear optical coefficients, 22
Nonlinear optical crystals
CARS microscopy, 68
noncritical phase matching, 20–21
tetrahertz OPG/OPOs, 72
Nonlinear optical fibers, supercontinuum sources, 218
Nonlinear optical interactions, four-wave mixing, 270
Nonlinear optical materials, optical damage threshold, 25–26
Nonlinear optical medium, singly resonant oscillator design, 31
Nonlinear optical processes
$\chi^{(3)}$ susceptibility, 66–67
$\chi^{(2)}$ susceptibility, 18, 20, 22–25
difference-frequency generators (DFG), 19
figure of merit, 24–25
microscopy, 247–248
optical coherence gating, 256
Nonlinear optical spectroscopy, OPO performance characterization, 56–57
Nonlinear optical susceptibility tensors, 19, 20, 21, 268
coherent Raman spectroscopy, 65
noncentrosymmetric medium interactions, 22
Nonlinear optical techniques, tunable ranges, 1
Nonlinear optics (NLO)
backward OPO, 71
optical parametric device radiation, 18
pulsed OPOs, 35
Raman parametric processes, 22
Nonlinear phenomenon, symmetry-broken double-clad crystal fiber pumping, 208
NSLI. *See N*-slit laser interferometers (NSLI)
Nuclear reactors, 336

Office of Naval Research, 285
OH chirp control systems, injection-seeded pulsed optical parametric oscillators, 58
OH detection, CARS signals, 67
Olejnicek, J., 170
Oncology, 235–236, 289–301
OPAs. *See* Optical parametric amplifiers (OPAs)
Open cavities, 145, 147, 170
Operating conditions
optical parametric processes, 27–28
single-longitudinal-mode (SLM), 49–50
synchronously pumped ps-pulsed OPOs, 69–70
Operational strategies, spectroscopic measurement, 33
OPGs. *See* Optical parametric generators (OPGs)
OPO. *See* Optical parametric oscillator (OPO)
Optical amplifiers, 48, 197
Optical-array detectors, optical parametric oscillator design, 29
Optical axis, noncritical phase matching, 21
Optical bandwidth. *See* Bandwidth
Optical birefringence, 248
Optical cavities
free-running OPP, 36
injection seeding control and passive, 40–41
intensity dip control, 44
parametric process operating regimes, 27
parasitic losses and OPO design, 28–29
resonance and CW design, 30–31
seed-frequency synchronicity, 40
$ZnGeP_2$ OPO, 38
Optical circulator configuration, 191, 192
Optical clockwork, frequency combs, 6
Optical coherence gating, contrast optimization, 256
Optical coherent tomography (OCT), 199, 201
supercontinuum fiber lasers, 217–219
Optical communications, 6
external-cavity semiconductor lasers, 167
Optical conversion efficiency, 207–208
Optical damage
NLO materials thresholds, 25–26
optical parametric gain medium threshold, 25
parametric oscillators and spectroscopy, 17
PPKTP OPO systems, 69

Optical densitometer, 342
Optical depth, probe laser beam, 314–315
Optical energy efficiency, 274
Optical excitation, coumarin 545 tetramethyl (C545T) dye, 396, 398–399
Optical feedback, reflectivity and cavity configurations, 145
Optical fibers, 202–203
  applications, 197–198
  port-wine stain treatment, 229
  single-mode, 180
Optical frequency combs, photonic crystals fibers, 73
Optical heterodyne (OH)
  chirp-control modules, 47–49
  detection, 272–273
Optical-heterodyne measurement, 46
Optical homogeneity, organic polymer dyes, 100
Optical instruments, 385
Optical length, of cavities and tuning, 160–161
Optically smooth surfaces, macroscopic interferometric imaging, 358
Optical measurement, pulse solid-state lasers, 6
Optical mediums, simulated Raman scattering (SRS), 21–22
Optical noise, cavity configuration, 145
Optical nonlinearity, magnitude, 25
Optical oscillators, hybrid tunable laser systems, 172
Optical parametric amplification, $X^{(2)}$–based, 22–25
Optical parametric amplifiers (OPAs), 16
Optical parametric applications, imaging applications market, 64
Optical parametric devices
  NLO crystal characteristics, 26
  operations, 17–28
  photonic crystals, 72–73
  spectroscopic applications, 33–34
Optical parametric gain
  $X^{(2)}$–based, 22–25
  medium choice, 25–27
  phase-matched conditions, 27–28
Optical parametric generators (OPGs), 16, 18–19
Optical parametric oscillators (OPO), 1, 5, 15–74
  $X^{(2)}$–based, 22–25
  design, 28–34
  membrane imaging, 270
  spectroscopic performance, 50–57
Optical parametric processes, 17–20, 27–28
Optical parametric radiation, 34
Optical path length, calculation, 154
Optical power, third harmonic microscopy, 269–270
Optical pumping
  collisional relaxation relationship, 320–321
  two-state approximations, 318–319
Optical quantities, 405–407
Optical radiation hazards, 238–239
Optical response, organic tissue-laser radiation interaction, 200–202
Optical sectioning
  multiphoton microscopy, 261
  one-photon fluorescence confocal microscopy, 262
Optical systems, far-field diffraction limit, 251–252
Optical tables, lithium isotope separation experiment, 333
Optical theory, intracavity beam propagation, 149–163
Optical-to-optical conversion, 181
Optical unit conversion, 405–407
Optical waves, nonlinear optics, 19–20
Optics, Dirac interferometric approach, 380
Orange pigments, 233
Organically modified ceramics (ORMOCERS), 110
Organically modified silanes (ORMOSILS), 110, 111
Organic dye lasers, 1
  dispersive cavity configurations, 144–145
  dye-doped, 172
Organic dyes, 97–98
Organic matrices, silicon-modified, 114–116
Organic polymers, 100–110
Organic semiconductors
  coherent electrically excited organic, 389–402
  interferometric emitters, 393–395
Organic tissue. *See* Tissue
Organosilane precursors, 110
Orientation-patterned gallium arsenide, 70
ORMOCERS. *See* Organically modified ceramics (ORMOCERS)
ORMOSILS. *See* Organically modified silanes (ORMOSILS)
Orr, B. J., 138
Oscillation, 19
  external-cavity semiconductor lasers, 166
  injection seeding threshold, 39
  intracavity frequency-selective optics, 164
  laser ring unidirectional, 187
Oscillator-amplifier systems, cancer diagnostics, 170
Oscillator architecture
  narrow-linewidth long pulse lasing, 123
  optimized dispersive cavity, 148–149
Oscillator cavities
  dispersive, 144–149
  frequency stabilization, 258–259
  optimized dispersive, 147–149
  thermal changes in dispersive, 153

Oscillators
Bragg grating of fiber tunable, 184–185
classic motion and harmonic driving force, 264
configuration, 144–149, 170–173
Doppler shift, 315
hybrid multiple-prism near grazing-incidence (HMPGI) grating, 123
hybrid system integration, 4–5
laser complementary integration stage, 4–5
multiple-prism Littrow (MPL) grating, 123–126
Output beam
cavity configuration, 145
single-mode fiber core, 180–181
transmission diffraction grating distortion, 147–148
Output coupler mirrors
tandem dye-doped organic semiconductor, 393
tunable laser oscillators, 164
Output couplers, 186
Output energies, high performance injection-seeded OPO systems, 59
Output intensity distribution, 342
Output light, bandwidth optimization, 34
Output power, DISCOS emitter, 398–399
Output pulse
instantaneous frequency profile, 47–48
seeding failure, 49
Output radiation
spectroscopic bandwidth factors, 36
tunability and spectroscopic verification, 51
Output wavelength, nanosecond pulsed OPO, 37
Output waves
difference-frequency generators, 19
optical parametric oscillator design, 29
synchronous pumped optical parametric system classification, 32
Oxygen, 236
Ozone, 61

Pancreatic stone lithotripsy, 234
Pang, L. Y., 166
Parametric gain, 19
coefficients, 23
degeneracy factor, 24
Parametric generation
CW pumping, 24
pump fields in, 23
Parametric waves, gain maximization, 36
PA*rn*Ac dyes. *See* Acryloyloxypolymethylene phenyl dyes (PA*rn*Ac)
PA*rn*MA dyes. *See* Methacryloyloxypolymethylene phenyl dyes (PA*rn*MA)
Parrish, A., 228, 233
Particle emitters, 296
Pasiškevcius, V., 70
PA spectra. *See* Photoacoustic absorption (PA) spectra
Passive cavities
injection seeded BBO optical parametric oscillators, 59
injection seeding, 40–41
Patients, 287, 293
Patient safety, 238
Peak power
CARS microscopy design tradeoffs, 68
diode-laser pump sources, 36
external cavity semiconductor laser oscillators, 172
Fabry–Perot cavity, 258–259
intracavity pulse, 258=259
microscopy, 246
organic tissue laser response, 200
ultrafast optical paramedic oscillators, 31–32
Pediatric therapeutic radiation, 297–298
Penetration, FPDL emissions, 228–229
Pentaerythritol tetraacrylate (PETRA), 103–104, 110
Pentaerythritol triacrylate (PETA), 103–104
Performance characteristics
CW optical parametric systems, 51–57
dyes and fluorine, 107–108
external cavity semiconductor lasers, 164–166
external-cavity ultrashort pulse lasers, 166–167
infrared spectroscopy, 73
injection-seeded OPO high-resolution applications, 43
medical monochromatic x-ray device design, 286–289
narrowband tunability, 37
OPO beam quality, 51
PPL OPO systems, 44
tunable erbium-doped fiber lasers, 190–191
ultrashort-pulse external-cavity semiconductor lasers, 169
x-ray production technology, 281–283
Periodically polled media, 20, 26–27
Periodic index variation, Bragg grating tuning elements, 184
Perylene Orange, 111
Perylene Red, 111
PETA. *See* Pentaerythritol triacrylate (PETA)
Petelski, T. R., 58
Peterson, O. G., 98, 121
PETRA. *See* Pentaerythritol tetraacrylate (PETRA)
Pharmaceuticals, 289–290, 336
Phase cancellation harmonics, 265
Phase contrast imaging, 302–304

Phase matching, 19–20
counterpropagating waves, 71
microscopy applications, 265
optical parametric gain medium choice, 25
Phase perturbation, pulsed optical fields, 47
Phosphate-based glasses, 203
Photoacoustic absorption (PA) spectra, 62
grating-tuned OPO, 37
linear optical techniques, 56
Photoacoustic spectroscopy, 56
Photoaging applications, 212
Photobleaching, 253
fluorescent molecules, 254
multiphoton illumination, 262–263
Photochemical interactions, 236
Photodegradation
inorganic dye components, 112
organic polymer dyes, 100–101
solid-state dye lasers, 98
Photodiode arrays, 342
interference signals, 371
interferometric theory, 364–365
linear, 345
macroscopic interferometric imaging, 357–359
transmission grating calculations, 352–356
Photodynamic therapy (PDT), 201
dye laser applications, 235–238
laser dye stability, 108
tunable external cavity lasers, 170
Photographic film, 341, 361–363
Photographic grating, 364
Photography, 341–342
Photoionization, 323–324, 330
Photon emission rates, 263
Photonic bank gap fibers (PBFs), 73
Photonic crystal fibers (PCFs), 218
beam quality, 207–208
cross-sections, 204–205
Photonic crystals, 72–73
Photonic structure, sub-μm periodicity, 70
Photon interference, 392
Photons
Auger cascade, 290–292
conversion from pump field, 23
energy state and absorption, 259–260
energy wavelength equivalence, 406
infrared conversion to x-ray, 283
k-shell binding energy, 291–292
scatter and gating, 255
splitting pump, 19
Photorefractive distributed feedback grating, 37
Photosensitizers, 200, 201, 235
Photostability
hybrid organic-inorganic dyes, 111–112
organic dyes, 100–110
silicon-modified organic matrices, 115–116
Photothermolysis, 228, 233
Physical constants, 405–406
Physics, 5, 6, 311–312
Pierce extractor, 331, 332
Piezoelectric controlled intensity dip, 48
Piezoelectric translators (PZT), 44
Piper, J. A., 145, 376, 379
Planck quantum energy, 405–406
Planck's constant, 326
Plane of incidence (find more), tuning and grating axial rotation, 161
Plan-wave radiation
$X^{(2)}$–based optical parametric gain/amplification, 22
forward-propagating, 265
Plasmon excitation, signals and resolution, 251–252
Platinum-based drugs, 291, 292–293, 296
Platinum k-edge, 295
PM567 dye, 101, 103, 104, 105, 111, 115
PM597 dye, 115
P*n*MA dyes. *See* Methacryloyloxypolymethylene) phenyl dyes (PA*rn*MA)(P*n*MA)
Pockels coefficient, 185
Poisson's ratio, 185
Polarization
fiber ring cavity elements, 187
multiple-prism grating configuration, 190
nonlinear optical, 32
transmitted light change, 246
Polarization-sensitive detection, 271–272
Polarized light, saturated absorption matrix, 316
Polarizer multiple-prism lasers (PMPML) printers, 365
Polymer dyes, 100
nano-/micro-particles, 116–117
Polymeric film substrates, 360–361
Polymeric media, solid-state dye laser, 99
Polymerization, organic-inorganic hybrid materials, 110
Polymer matrix gain media, 100, 107, 122, 128, 137
Polymers, fluorinated-modified, 114
Poly(methyl methacrylate) (PMMA), 101–104, 107, 110, 116, 117, 122, 137
synthesis and fabrication, 126–129
Pope, E. J. A., 129, 133
Population
beam intensity/absorption, 318–319
dye laser radiationless emissions, 97–98
photoionization density matrix, 324
Population inversion, 5
dye amplification frequency stability, 50
nonlinear optical polarization, 32
nonlinear optics, 19

Population rate equations
saturated absorption matrix elements, 315–319
spontaneous emissions, 315
Porphryin, 236
Port-wine stains (PWS), 201, 229–230
Potassium titanyl phosphate (KTP), 20
crystals, 69, 229, 237
$KTiOpO_4$ optical parametric oscillators, periodically pooled, 46–50, 69
KTP optical parametric oscillator system, spectroscopic verification, 51
Power amplification, injection seeding wavelength control, 42–43
Power characteristics, 1, 3
Power densities
exciting and ionizing lasers, 327
lithium isotope separation, 332
Power dissipation, laser efficiency, 207
Power levels, external cavity semiconductor lasers, 144
Power spectrum, microdensity equations, 363
PPKTP (periodically pooled $KTiOpO_4$)
flux grown crystals, 71
optical parametric oscillators, 46–50
optical parametric oscillators CARS microscopy, 69
PPLN, 35. *See* $LiNbO_3$ (lithium niobate)
CW singly resonant oscillators, 31
PPLN-based coherent light sources, tunability and bandwidth, 38
PPLN crystals, nanosecond-pulsed OPS, 29–30
PPLN optical parametric oscillators
high performance, 44
performance characteristics, 53
Praseodymium (Pr^{3+}), 205
Praseodymium laser applications, 210
Prism array dispersion, 376
Prismatic cavities, wavelength function, 159
Prism beam
hybrid multiple expansion, 146
interferometer imaging expander, 345–348
Prisms, 251
intracavity dispersion, 150–155
modelocked ECS laser configuration, 166
pulse compression configuration, 166
Probe beam
absorption spectroscopy propagation, 313–314
Doppler-free saturated absorption, 314–315
Probe pulse probes, 248
Probes, visibility and optical path, 211
Product performance testing, 305–306
Product quality, textile fabric interferometry, 367–369
Propagation
amplitude probability, 150
communication security and interferometric, 366–367
fiber laser pumping beam, 207–208
interferometer imaging device ray, 345–346
optical theory and intracavity beam, 149–163
radiation intermediate, 342
second harmonic (SH) signal, 248
Propagation direction, noncritical phase matching, 21
Protein crystallography, 304–305
Proteins, 260
Proton beam therapy, 298
Prototypes, tunable monochromatic x-ray machines, 284–286, 288–289
ps-pulsed optical parametric oscillators, design and operating features, 69–70
ps-pulse imaging, motion artifacts, 287
Psychotropic drugs, 336
Pulse amplification, femtosecond laser, 259
Pulse compression
multiple-pass intracavity dispersion, 379–380
multiple-prism array, 166
multiple-prism beam expander applications, 384–385
ray transfer matrix, 157
Pulsed capability
dye laser, 227
OPO performance, 51
Pulsed dye amplification, vacuum ultraviolet radiation generation, 50
Pulsed-dye lasers, lithotripsy, 234
Pulsed energies
application requirements, 5
OPO pump sources, 17
Pulsed lasers
dispersive cavity configurations, 144–145
flashlamp-pumped dye lasers, 228–229
linewidth, 157
medical applications, 199
requirement for, 254
solid-state dye, 98
tissue laser radiation resonance, 201–202
ytterbium fiber laser applications, 213
Pulsed light
bandwidth, 34
organic issue laser response, 200
Pulsed optical parametric oscillators, 16
injection seeding mechanism, 39–40
nanosecond, 29–30
nonlinear optical wavelength-extension schemes, 29
Pulsed regime, energetic characteristics, 3

Pulsed sources
tunable coherent radiation, 1–2
ultrashort, 276
Pulsed tunable monochromatic x-rays, 281–306
Pulsed tunable OPO, quasi-phase matched (QPM) nonlinear media, 36
Pulse duration
CARS microscopy, 66
commercial laser microscopes, 250–251
Gaussian transform-limited, 250
Kerr-lens modelocked laser, 257
linewidth measurement, 126
optimization, 249
tradeoffs, 67–68
Pulse energy
femtosecond laser design techniques, 258–259
fiber lasers, 258
signal size, 250
Pulse illumination, ultrashort laser, 247
Pulse peak intensity
critical values, 249–250
optimization, 249
Pulse power, multiphoton microscopy, 262
Pulse ranging, x-ray beam application, 304
Pulses
linear accelerator powered laser, 285
port-wine stain treatment, 230
Pulse shape, dependencies, 168
Pulse spectrum, liquid crystal arrays, 250
Pump beam
diffraction limited Gaussian, 253–254
fiber lasers, 207
polarization-sensitive detection, 272
Pump cladding, 186
Pump couplers
fiber ring cavity, 187
ring fiber cavities, 187
Pumped lasers
brightness configuration, 180
pulsed Nd:YAG diode, 29
single-mode-fiber wavelength, 185–186
tunable optically, 389
YDFL optical radiation from diode, 180–181
Pump enhancement, optical cavity resonance, 30–31
Pump fields, parametric generation, 23
Pumping
continuous wave, 24
double-clad, 207–208
efficiency in ytterbium lasers, 213
laser efficiency, 207–208
laser wavelengths, 206
synchronous, 32
Pumping geometry, solid dyes, 102–103
Pump intensity
nonlinear effects, 207
thulium fiber lasers, 206
Pump lasers
beam optical depth, 314–315
crystals and intensity, 25–26
high performance PPL OPO systems, 44
nanosecond-pulsed OPO, 36
probe in saturated absorption spectroscopy, 312–314
single-mode fiber laser configuration, 180, 181
ultrafast optical parametric oscillators, 32
Pump photon splitting, 19
Pump power
cladding, 181
dye microparticles, 117
operating regimes, 27
Pump-probe imaging, 248
Pump pulse, organic dye stability, 104–105
Pump pulses
dye microparticles, 117
hybrid organic-inorganic dye stability, 111
organic dye stability, 102, 106–109
silicon-modified organic matrices, 115–116
Pump radiation, 19
actively controlled ring cavity tunability, 44
injection seeding, 39
solid dyes, 102–103
YDFL optical diode pump, 180–181
Pumps
fiber lasers, 180–181
media phase-matching conditions, 20
Pump sources
diodes, 207
Kerr-lens modelocked laser, 257
OPO, 17
peak power diode-laser, 36
Pump wavelengths, noncritical phase matching, 21
Pump waves, nonlinear optical coefficients, 23
Purple pigments, 233
Pyrromethene dyes, 99, 110, 111, 112, 113, 122

Q-switched lasers
broadband, 35, 218
gain media, 204
high-resolution lidar systems, 61
intracavity, 64
medical applications, 199
modelocked operations, 198, 298
Nd:YAG, 38, 43, 47, 61, 63
Nd:YLF, 108
solid-state dye, 108
tissue laser radiation resonance, 201–202
ytterbium fiber application characteristics, 213

Q-switching, 27, 256, 258
Quality control
  mammographic screening, 299
  microdefect interferometric imaging, 359–361
Quantum control, microscopy and coherent, 252
Quantum efficiencies, diode lasers, 179
Quantum mechanics
  electronic oscillator resonant frequency, 264
  interference and diffraction, 351–352
Quartz-enhanced PA spectroscopy (QEPAS), 62
Quasi-phase matched (QPM) design, 21
  mirrorless OPO, 70–71
  modular tunable OPO spectroscopic system, 43
  singly resonant oscillator, 31
Quasi-phase matched (QPM) materials, 20, 26–27
  pulsed tunable OPO nonlinear, 36

Radiation
  femtosecond excitation, 295
  incidental, 264
  single pulse mode laser prototype, 285
  supercontinuum (SC), 218–220
Radiation beams
  chemotherapy drugs, 292–293
  nondestructive test applications, 306
Radiation dose
  child brain tumor therapy, 297–298
  lethal, 290, 294–297
  monochromatic x-rays, 284, 290
  x-ray technology, 282
Radiation exposure, 293
Radiation therapy
  Auger cascades, 290–294
  child sensitivity to, 297–298
  tunable monochromatic x-ray, 289–297
  x-ray beams, 282
Radiative depopulation, dye laser emission, 97–98
Radiological technologists, 286–288
Radiolytic process, 290, 291
Radiosensitizers, 293
Radiotherapy
  auger cascade, 290–291
  tunable monochromatic x-ray laser, 289–297
Radziemski, L. J., 138
Rahn, M. D., 111
Rakestraw, D. J., 58
Raman gain, 206
Raman microscopy, four-wave mixing applications, 270–271
Raman parametric processes, coherent wavelength conversion, 21–22
Raman-shifted transitions, 209
Raman spectroscopy, nonlinear optical techniques, 56–57
Raman Stokes beams, 41
Random radiolytic process, 290, 291
Range gating, imaging modalities, 246
Rare-earths metal ions, 197, 205, 209
  doped-silica fibers, 179
  medical application lasers, 210
  optical fiber amplification, 203
  ZBLAN and co-doped fiber lasers, 216–217
Raster-scanning, 246, 247
Rayleigh length, 347
  beam divergence, 124–125
  multiple-pass beam divergence, 392
Rayleigh ranges, x-ray generation optimization, 286–287
Ray transfer matrix, 345–347
Red dye, 111
Red pigments, 233
Red radiation, 322
Red region, 99, 101, 143, 170, 171, 201, 206, 233, 238, 329, 332, 365, 393, 396
Reference cavities, frequency stabilization, 165
Reference probes, accuracy and visibility, 211
Reflection
  laser beams, 238
  loss om intracavity multiple-prism, 155
Reflection diffraction grating, intracavity beam illumination, 148–149
Reflection grating, 149
Reflective index
  diffraction-grating equation, 382
  multiple-prism beam expansion, 378
Reflectivity
  dispersive cavity configuration, 145
  frequency-selective optics, 164
  output coupler mirrors, 164
Refraction, 380
  Snell's law of, 352
Refractive index
  fiber laser brightness configuration, 180
  harmonic radiators, 265
  media phase-matching conditions, 20
  momentum conservation, 19–20
  nanoparticulate distribution invisibility, 136
  optical parametric gain medium choice, 25
  organic-inorganic gain media internal, 133
  ray transfer matrix, 155–156
  selectivity and Bragg grating, 163
Regenerative amplifiers, 259
Regulations, medical tool/instrument, 220
Remote sensing, 5, 6
  external-cavity semiconductor lasers, 167
  industrial/environmental monitoring applications, 61–64
Remote-sensing, dual-wavelength injection seeding, 42

Repetition rates
illumination lasers, 249–250
pulse amplification, 259
pulse energy, 258
Resolution
Coherent anti-Stokes radiation signals spectral, 274–275
critical damage fluorescence, 249
enhancement and signal increase, 251–254
fluorescence microscopy, 253
laser scanning microscopy, 248
lithium ionization spectra, 331
mammographic monochromatic x-ray imaging, 299–300
modulation measurements, 363–364
multiphoton fluorescence microscopy, 263–264
photodiode array, 364–365
supercontinuum fiber lasers, 218–219
x-ray imaging information, 302–304
Resonance
absorption, 201–202
actively controlled ring cavity, 44
ionization spectra, 328–329
ionization spectrometer, 326–327
ionizing spectroscopy, 312
surface plasmon, 251
Resonator cavity length, 160
Resonator mirror, 162
Rhodamine, 111
Rhodamine dyes, 101–102, 108–109, 116–117, 123, 237
Rhodamine 6G-doped gain media, 123, 133–136, 138–139
Richman, B. A., 37–38
Ring cavities
four-mirror signal resonant, 48
intensity-dip feedback and actively controlled, 44
OPO dual-wavelength passive performance characteristics, 53
pumped BBO optical parametric oscillator, 60
three-mirror signal resonant, 37–38
tunable fiber laser performance, 191–192
tunable fiber lasers, 182, 186–187
Rovibrational spectra, 58
Ruby lasers, 199
Rudolph, W., 155, 385

Safety, 234, 238–239, 287
Salvatore, R. A., 166–167
Sample geometry, 266
Sample heating, 249
Saturated absorption
matrix elements, 315–319
modelocked ECS lasers, 166
semiconductor mirrors (SESAM), 203
spectrometers, 319–320
spectroscopy, 312–314
Saturation
fluorophore, 264
microscopes, 253–254
multiphoton illumination, 262–263
Saturation parameters
lithium resonance ionization spectra, 328–329
low-intensity cross-section, 326
optical depth, 315
Scaling
fiber laser efficiency, 207
spectroscopic application, 330
Scanning microscopy, 246, 247, 257–258
Scars, 231–232
Scattering. *See also* Coherent anti-Stokes Raman scattering (CARS); Inverse Compton scattering
angles in mammography, 301
emission intensity, 266–267
gating in microscopy, 254–255
harmonic radiation, 264–265
infrared lidar techniques, 60
lasing dye materials, 100
mammographic monochromatic x-ray imaging, 299–300
multiphoton microscopy, 261
organic tissue optical response, 201
pediatric radiation therapy, 298
Raman and four-wave mixing applications, 270–271
second harmonic geometry, 265–266
stimulated Brillouin, 207
stimulated Raman, 21–22, 29, 59, 206, 207
time/coherence gating, 254–255
x-ray ballistic photons, 304
x-ray production forward, 289
Schäfer, F. P., 121
Schawlow–Townes linewidth, 158
Scheibner, H., 170
Scherer, J. J. D., 37
Second harmonic generation (SHG), 29, 247, 248, 265–267
KTP crystal/Nd:YAG laser, 229, 237
Second harmonic (SH) signal, 248, 265–266
Seed beam, 45, 48, 49
Seeding. *See* Injection seeding
Seed lasers, 285
Selectivity, lithium laser isotope separation, 335–336
Self-adaptive tunable (SAT) optical parametric oscillators, 44–46
Semiconductor lasers
application domains, 6
broadly tunable external-cavity, 143–172

co-doping and diode, 217
gain regions, 150
oscillators, 5
spectral regions, 171–172
spectroscopy applications, 169
wavelength tuning, 158–159
wavelength tuning of microelectromechanical system-driven, 162–163
Semiconductors
coherent electrically excited organic, 389–402
internal facet antireflection coating, 163–164
types, 143–144
Semiconductor saturable absorbing mirrors (SESAM), 203
Sensing, 268
Sensitivity, 67, 312
Shaping of laser pulses, 252
Shaw, R., 341
Short-pulse emissions, 2
Short-pulse lasers
applications, 259–275
coherent anti-Stokes resonance suppression, 274–275
emissions, 1
optical clockwork frequency combs, 6
Siegman, A. E., 392
Signal beams, 67, 68–69
Signal detection, 65
Signal output
CARS microscopy, 68
injection seeding and sideband, 41
ns-pulsed OPO operations, 49–50
optical cavity resonance, 29
optical heterodyne detection systems, 47–48
sideband injection seeding, 41
Signals
coherent addition, 265
coherent anti-Stokes Raman scattering (CARS), 273
intrinsic, 267–268
loss evolution description, 23
parametric operating regime power, 27
plasmon mediated nonlinear generation, 251–252
resolution enhancement, 251–254
second harmonic (SH), 248, 265–266
Signal-to-noise ratio, detector speed, 249
Silica aerogels, 114
Silica-based glasses, 203, 216
Silica fiber lasers, absorption/emission bands, 182
Silica nanoparticulates, dispersed in PPMA, 126–129
Silicate-based hybrid polymers, 110, 135
Silicate gain media, 122
Silicon-modified organic matrices, 114–116
$AgGaS_2$ optical parametric oscillators, 53
Silver-halide photographic film, 361–363
Single-longitudinal-mode (SLM)
cavity resonance, 40
chirp-controlled OPO system, 47
continuous tunability, 42–43
dye-doped polymer lasers, 390
high-performance narrowband lasers, 44
multiple-prism grating configuration, 187–190
narrowband tuning, 45–46
narrow bandwidth radiation, 34, 37–38
Nd:YAG lasers, 41
pulsed OPO operation dynamics, 49–50
tunable signal and idler output, 45
Single-mode optical fibers, 179, 180–181
Single-pass dispersion, ray transfer matrix, 156–157
Single-pass gain bandwidth, idealization, 36
Single-pass power gain, 23–24
Single-photon fluorescence confocal microscopy, 262
Single-photon interference, 392
Single-prism cavity, configuration, 145
Single-pulse mode lasers, 66, 285–286
Single-transverse mode, 123, 390
Singly resonant oscillators (SRO), 29–30, 30–31
Sinusoidal illumination patterns, 253
Sinusoidal modulation, 273
Skin, 201, 211–212, 228–229, 231–232, 236, 238–239
Slit arrangements, DISCOS emitter, 395
Slit grating
interferometric calculations, 352–357
photon propagation, 348–352
N-slit interference equations, 135–136
N-slit laser interferometers (NSLI), 342, 400–401
biomedical applications, 370–371
communication security in free space, 366–367
depth of focus, 347
depth of focus of coherent, 347
geometry, 150
grating-like array application, 364
microillumination and depth of focus, 371
photographic film grain structure, 363
SLM. *See* Single-longitudinal-mode (SLM)
Slope efficiency
doped fiber lasers, 191, 193
dye laser, 110
holmium-doped fiber lasers, 215
Smith, A. V., 61
Snavely, B. B., 98, 122
Snell's law of diffraction, 153, 346, 352, 377
derivation, 152

Soffer, B. H., 98, 121
Soft x-rays, 284
Solid-state coherent sources
  application domains, 6
  optical pulsed oscillator devices, 16
Solid-state dye lasers (SSDL), 97–118
  applications, 138–139
  dye-doped gain media, 122
  dye oscillator, 5
  fiber laser advantages, 179
  hybrid tunable, 172
  medical applications and safety, 239
  narrow-linewidth performance, 124
  organic tunable, 147
  Q-switching, 258
  tattoo removal, 233
  tunable narrow-linewidth organic, 390–392
  tunable organic, 389
Solid-state nonlinear-optical (NLO) devices, 16, 18–19
Solutes, 58
Solvents, 58, 127–128
Sorokin, P. P., 121
Sources. *See also* Illumination sources; Light sources
  broadly tunable coherent, 2–3
  coherent radiation tunable pulse, 1–2
  copper anode x-ray, 305
  dual-wavelength, 64
  étalon-filtered, 63
  fiber supercontinuum, 218
  geometric properties of harmonic, 265–267
  inverse Compton scattering, 305
  microscopy lasers, 256–259
  OPO pump, 17
  optical density measurement, 342
  optical parametric devices coherent radiation, 17–18
  pump, 36, 207, 257
  solid-state coherent, 6
  tunable monochromatic x-ray, 288
  ultrashort pulse, 276
Spatial coherence, 172, 392–393
Spatial frequency, 341
Spatial homogeneity, 138
Spatial resolution
  broadband light source, 211
  mammography, 300
  modulation measurements, 364
  ultrashort pulse illumination response, 248
Spectra
  absorption, 198, 335
  coherent quantum control, 252
  collision-induced high-resolution OPO systems, 59
  Doppler-free, 314–315, 320–321
  hyperfine hole-burning, 58
  photoacoustic absorption, 37, 56, 62
  resonance ionization, 328–329
  rovibrational Bosenberg–Guyer type KTP systems, 58
  two-photon absorption, 259–260
Spectral coherence, 392–393
Spectral coverage, 143–144
Spectral emission characteristics, 2, 4
  short-pulse lasers and CARS, 274–275
Spectral power, density, 126
Spectral profiles, backward OPOs, 71
Spectral regions
  Rhodamine dyes, 101–102
  semiconductor laser, 171–172
  solid-state dye lasers, 99
Spectrometers, 319–320, 326–327
Spectroscopic applications
  free-running OPOs, 37
  multiline requirements, 41
  narrowband tunability, 37
  OPO design, 15–74, 28
  optical parametric devices, 33–34
  passively seeded OPO cavities, 40–41
Spectroscopic bandwidth, output radiation factors, 36
Spectroscopic measurement, optical parametric oscillators, 50–70
Spectroscopic performance, sub-Doppler, 58
Spectroscopic resolution, optical bandwidth, 34
Spectroscopic sensing
  gases and photonic bandgap fibers, 73
  gas-phase/airborne species, 64
  optical parametric processing, 57–64
Spectroscopic tailoring
  applications for multiwavelength, 42
  injection seeding, 41
  OPO biosensing, 64
Spectroscopic techniques, 17, 52–56
Spectroscopic verification, OPO performance, 50–57
Spectroscopy, 5, 6
  coherent light sources for high-resolution laser, 50
  dispersive external-cavity semiconductor lasers, 311–312
  Doppler-free saturated absorption, 314–315
  external-cavity semiconductor lasers, 167
  injection seeding and high resolution, 39
  multiple-prism beam expander applications, 383–384
  nanosecond pulsed OPO, 34
  narrow-linewidth tunable laser applications, 139
  optical pulsed oscillator devices, 16, 73–74
  optical pulsed oscillators, 70–74
  resonant ionizing experiments, 312
  saturated absorption, 312–314

tunable dye laser, 16–17
tunable semiconductor lasers, 169–170
ultrashort pulse laser applications, 385
Speed, biological image acquisition, 249
Splitting, pump photons, 19
Spontaneous emissions
parametric operating regimes, 27–28
population rate equations, 315
Spontaneous parametric processes, 19
SRO. *See* Singly resonant oscillators (SRO)
Staining, biological objects, 248
Steady-state population, CW fluoroscope signal, 253
Steady-state pulse, Kerr-lens modelocked laser, 257
Stimulated Brillouin scattering, 207
Stimulated emission depletion (STED), 253–254
Stimulated parametric fluorescence (SPF), 271, 275
Stimulated Raman scattering (SRS), 21–22, 29, 59, 206, 207
Strategic Defense Initiative Organization, 283
Strome, F. C., 375
Sub-Doppler conditions
ns-pulsed/CW tunable system characterization, 55–57
OPO performance, 51
spectroscopy, 57–59
Submillimeter waves, 71
Substrates
macroscopic interferometric imaging, 358
multiple-prism refraction architecture, 148–149
transmission interferometric and diffractive properties, 363–364
Sum-frequency generation (SFG), 29
Supercontinuum (SC) fiber lasers, 217–220
Superfluorescent parametric emissions, 23–24
Superluminescence, narrow-line tunable lasers, 164
Superluminescent light-emitting diodes (SELD), 218–219
Surface plasmon resonance, 251
Surgery, 199, 201, 214–215, 215
Svanberg, S., 61
Symmetry class, 25
Synchronously pumped ps-pulsed OPOs, 69–70
Synchronous pumped optical parametric systems, 32
Synchronous pumping, 32
Synchronous wavelength tuning, 159, 161

Tattoo removal, 232–233
TDL-seeded passive ring-cavity optical parametric oscillators, 64
atmospheric remote sensing, 60
performance characteristics, 52, 53, 55
TDL-seeded radiation, output pulse beat optical heterodyne technique, 47
Telecommunications
fiber optic networks, 198
microelectromechanical system tuning, 159
tunable fiber lasers, 179
Telescopes, 344–345, 384
TEM_{00} beam
dye-doped organic-inorganic gain media, 116–117
expansion, 345
He–Ne laser lens, 347
illumination source, 342
interferometer imaging device, 344–345
spatial beam characters, 126
TEM_{00} tunable lasers, 344–345
Temperature. *See also* $\Delta n/\delta T$ characteristics
Doppler width, 319
emission wavelength tuning, 158–159
lithium resonance ionization spectra, 329
semiconductor lasers, 144
tunable ps-pulsed OPOs, 69
Zeeman multiplets and vapor, 318
TEOS. *See* Tetraethoxysilane (TEOS)
Terawatt lasers, 285, 286
Tetraethoxysilane (TEOS), 111–112
Tetrahertz waves, 71–72
Tetramethoxysilane (TMOS), 112
Tetramethyl Rhodamine, 263
Textile fabrics, interferometry in, 367–369, 370
TFMA. *See* Trifluoroethyl methacrylate (TFMA)
Therapeutic applications, 200, 289–297
Thermal changes, intracavity beam deviations, 153
Thermal coefficient, optical parametric gain medium choice, 25
Thermal deviations, 348
Thermal expansion, fiber material coefficient, 185
Thermal response, 200, 201–202
Thin films, 342, 360
Third harmonic generation (THG), 247, 269–270
3D imaging, 247, 276, 282, 304–305
Three-wave processes
nonlinear optical, 22–23
nonlinear optics, 20
optical parametric device, 18
Thulium (Tm^{3+}), 179, 205, 206
Thulium-doped fiber lasers, 193, 210
absorption/emissions wavelength, 182
applications, 214–215
performance of tunable, 190–191
Thymidine, 295
Tiihonen, M., 64
Tilted étalon, 37

Time gating microscopy, 254
Time-of-flight imaging, 304
Tissue, 69, 70, 200–202, 211, 239, 261
Titanium lasers, 16–17
Ti:sapphire lasers, 16, 21, 69, 73
  Kerr-lens modelocked femtosecond, 256–257
  optical sectioning, 262
  singly resonant oscillator design, 31
  vacuum ultraviolet radiation, 50
Ti:sapphire regenerative amplifiers, 71
Tm-doped fiber lasers (TDFL), 179
TMOS. *See* Tetramethoxysilane (TMOS)
Tm^{3+}. *See* Thulium (Tm^{3+})
Tokamaks, 336
Toxic compounds, 239
Toxicity, 293
Trace element analysis, 330
Transitions, 97–98, 342–343
Transit time relaxation rate, lithium resonance ionization spectra, 328–329
Transit-times, saturated absorption matrix, 316
Transmission efficiency, intracavity multiple-prism, 155
Transmission grating, 149
  interferometric calculations, 352–357
  modulation transfer function measurement, 363–364
  spatial frequency, 341
Transmission surfaces, *N*-slit laser interferometer (NSLI), 371
Transmittance, 326, 328
Transparency
  lasing dye materials, 100
  optical parametric gain medium choice, 25
  wavelength division multiplexor, 185–186
  ZBLAN fiber, 203
Transverse-mode beam, illumination source, 342
Trapezoidal cross-section gain media, 128–129
TRIEOS. *See* Methyltriethoxysilane (TRIEOS)
2,2,2-trifluoroethyl methacrylate (TFMA), 103–104
Tropospheric ozone, 61
Tunability
  dye lasers, 198, 227
  fiber-based systems, 179
  fiber laser multiple-prism grating configuration, 188
  fiber lasers, 198, 257
  nanosecond-pulsed OPOs, 35–38
  nonlinear optical crystals, 69
  semiconductor lasers, 144
  thulium lasers, 214–215
  x-ray beams, 282
  ytterbium fiber lasers, 213
Tunable coherent radiation, 1
  application utility, 5
  medical dye laser applications, 227
  optimal operation modes, 4
Tunable diode lasers, 344
  isotope separation, 330–336
  lithium isotope separation, 331–334
  lithium spectroscopy, 311–337
Tunable external cavity systems, 170
Tunable fiber Bragg grating (TFBG), 185–186
  ring cavities, 186–187
Tunable fiber lasers, 179–194
Tunable laser emission, 129–133
  cavity linewidth equation, 376–377
Tunable laser oscillators
  output coupler mirrors, 164
  solid-state dye laser, 123–126
Tunable lasers
  application, 1, 5–9
  complementarity, 4–5
  DDPN gain media applications, 138–139
  dye-doped polymer gain media with nanoparticulates, 121–139
  free-electron, 283
  illumination in *N*-slit laser interferometers, 342–344
  intracavity multiple-prism beam expander applications, 383–384
  lithium isotope separation, 312
  organic, 389
  prismatic coumarin, 129–133
  solid-state dye, 99
  solid-state dye CW, 110
  tattoo removal, 233
  utilitarian ethos, 6
Tunable light pulses, injection seeded tunable, 50
Tunable monochromatic x-rays, 281–306
Tunable OPO systems, energy-transfer dynamics, 59
Tunable ranges. *See also* Broadly tunable sources
  narrowband emissions, 227
  narrowband OPO signal and idler output, 44
  nonlinear optical techniques, 1
  OPO multigrating design, 43
Tunable semiconductor lasers, 143
Tunable sources
  continuous wave, 3
  short-pulse emissions, 2
  tunable pulsed, 3
  ultrafast optical parametric systems, 32
Tunable x-rays, machine prototype, 285–286
Tuning
  acousto-optic, 192
  approaches, 30–31, 40–41
  Auger cascade k-shell dose, 295

Bragg grating use, 163
cavity configuration, 182
fiber oscillator laser configuration, 193–194
grating illumination, 383
k-edge, 302
laser surgery, 202
miniature microelectromechanical systems, 159–163
monochromatic x-rays, 290–291
OPO design, 37
OPO spectroscopic performance, 51
pump lasers in absorption spectroscopy, 313
ranges, 158, 185, 331
techniques, 160, 191–193
Turbine engines, 305–306
Two-photon absorption, 259
cross-sections, 260
helium transition, 50
nonlinear processing, 247–248
stimulated parametric fluorescence, 271, 275
Two-photon excitation (TPE)
focal volume, 264
photobleaching and resolution, 263
spectroscopy, 57
Two-photon fluorescence (TPF), 247–248, 275
Two-photon resonance, 263

Uenishi, Y., 162–163
Ultrafast fiber lasers, 204
Ultrafast optical paramedic oscillators, 31–32
Ultrafast pump beam, 21
Ultrashort-pulse external-cavity semiconductor lasers, performance characteristics, 169
Ultrashort-pulse lasers, 276
biological microscopy, 245–276
multiple-prism beam expander applications, 384–385
performance of external-cavity, 166–167
potential utilization, 250–251
Ultraviolet (UV) light, 64
ionizing power, 329
lithium isotope separation, 330
OPO-base biosensing, 64
photorefractive distributed feedback grating, 37
Uniaxial crystals, 25–26

Vacuum permittivity, 22
Vacuum ultraviolet (VUV) light sources, 50
Vanadium-doped cadmium telluride, 46
Vanderbilt University, 283, 285, 300
Vapor
Boltzmann velocity distribution, 313
Doppler-free saturated absorption, 314
ionization cross-section, 324, 325, 326
light absorption and Zeeman multiplets, 318
Vapor cross-sections
ionization rate, 324
laser ionization, 326
lidar measurement, 60
Raman spectroscopy, 65
Vaporization, 215, 239
Vascular abnormalities, 201, 301–302
dye laser applications, 228–231
hemangioma treatment, 230–231
laser dye stability, 108
port-wine stain laser treatment, 229–230
V:CdTe (vanadium-doped cadmium telluride), 46
Vectors, wave mismatch techniques, 273–274
Velocity, 313–315, 316
Verdaasdonk, R., 214
Veterinary medicine, 302
Vibrational energy, four-wave mixing microscopy, 270
Vibrational resonances
CARS, 250, 271, 273
coherent control, 275
Vibronic levels, two-photon absorption, 259–260
Video laser/optical disks, 127
Viscoelastic properties, 100–102
Visibility
DICOS emitter, 401
inverse Compton scattering, 299–300
k-edge imaging, 301–302
modulation measurements, 363–364
optical path probes, 211
phase contrast imaging, 303–304
x-ray phase contrast imaging, 302–304
Visible spectrum, 206
Vodopyanov, K. L., 37

Walenstein, R., 39, 40
Water, 60, 201, 214–215, 216
Waveforms, liquid crystal arrays, 250
Wave functions, 150
Wave generators, 331
Waveguides, 126, 180–181
Wavelength
Bragg grating reflection, 184–185
conversion nonlinear phenomena, 207
core-pumped lasers single-mode-fiber division multiplexor, 185–186
densitometry, 341
external-cavity semiconductor lasers, 167, 169, 170–173
fiber lasers, 179
FPDL vascular lesion treatment, 228–229
Heisenberg uncertainty principle, 160
injection seeding with fixed, 39
interference nanoparticle distribution, 22
interferometric imaging, 366

Wavelength *(continued)*
laser angioplasty, 234–235
lasing, 205–206
line-tunable CW lasers, 342–343
lithotripsy, 234
monochromatic photodynamic therapy, 236–237
multiphoton excitation, 263–264
organic issue laser response, 200
photon-energy equivalence, 406
quantities and unit conversion, 405–406
refractive index at vacuum, 19–20
shifting in backward OPOs, 71
single-transverse mode beams, 123
structuring of media, 20
supercontinuum fiber lasers, 218–219
tattoo removal selective absorption, 233
Wavelength control
dye laser, 97
injection seeding, 39–40
power amplification and injection seeding, 42–43
self-adaptive tunable injection-seeded, 42–43
Wavelength ranges, 1, 3
external cavity semiconductor laser, 172
optical parametric device radiation, 18
tunable semiconductor lasers, 143–144
Wavelength tuners, 375. *See also* Multiple-prism beam expanders
Wavelength tuning
fiber laser cavity configuration, 182–183
resonator mirror displacement, 162
semiconductor lasers, 158–159
Wave packet imaging modalities, 246
Wave vector mismatch techniques, 273–274
Webb, J. P., 375
Weidemuller, M., 169
Weiman, C. E., 164, 169
Widely tunable laser systems, 69
Wilson, A. L., 61
Wolf, E., 392
Women's medicine, 298–301
Wounds, 231–232
Wrinkles, 212

Xanthene dyes, 111
XeF, 2
Xenon fluoride lasers, 2
Xie, X. E., 69
X-ray beams
forward-scattering, 289
production technology, 281–283
protein crystallography imaging, 304–305
pulse ranging application, 304
X-ray imaging, 302–304
X-ray interferometry, 303
X-ray machines
design characteristics, 286–288
tunable monochromatic prototypes, 284–286, 288–289
X-rays, 283–284
X-ray tubes, 282, 284, 298–299

Yaffe, M. J., 299
Yellow, 228, 229, 284
Yellow-orange region, 238
Yellow-orange-red region, 344
Yellow pigments, 233
Yellow-red region, 101, 390
Yb^{3+} (ytterbium), 179, 205, 207
Yb-doped fiber lasers (YDFL), 179, 193, 210, 213
Bragg grating range, 185
multiple-prism grating linewidth configuration, 188
performance of tunable, 190–191
single-mode fiber beam, 180–181

Zayhowski, J. J., 61
ZBLAN fiber, 203, 206
ZBLAN fiber lasers, 216–217
Zeeman multiplets, 316–318
$ZnGeP_2$ (ZFP), 38, 63
Zorabedian, P., 158
Z-position, 286, 299

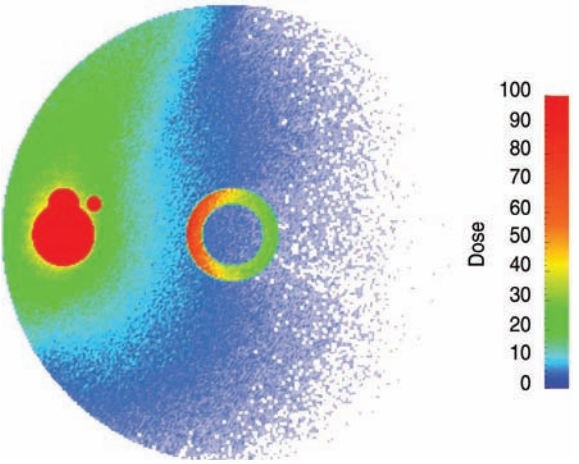

FIGURE 10.8 Percentage of lethal dose delivered to a tumor using a single rotating 50 keV monochromatic beam. The tumor is laced with an iodine-containing DNA drug. Radiation dose needed for lethality is 3 to 5 times less than that needed in standard radiotherapy. The irregular tumor, and the adjacent metastasis receive a lethal dose, yet the normal intervening tissues receive far less of a radiation dose. The monochromatic x-rays target the tumor, not the normal tissues. (Courtesy of Marcus H. Mendenhall, Ph.D. W.M. Keck Foundation Free-Electron Laser Facility, Vanderbilt University.)

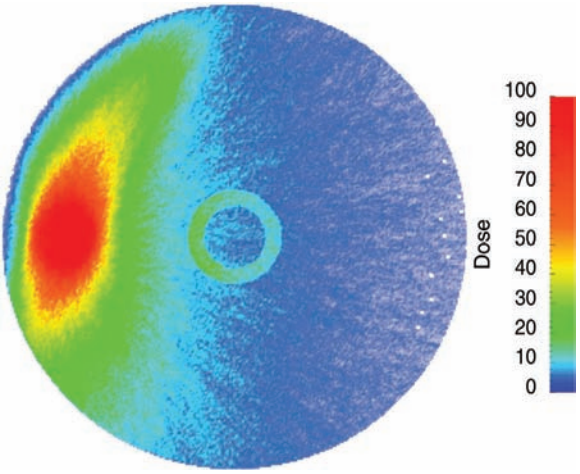

FIGURE 10.9 Distribution of the dosage of radiation to the tumor and satellite lesion with a 7 MeV rotating beam. The tumor contains the same iodine concentration as in the prior figure, and requires a dose of 60 Gy to kill the tumor.

Electrical Engineering

Tunable Laser Applications

Second Edition

Tunability has added an important dimension to a variety of laser devices and led to new systems and applications. From laser spectroscopy to Bose–Einstein condensation, the one nexus is the tunable laser.

Incorporating nine entirely new chapters, **Tunable Laser Applications, Second Edition** reflects the significant developments in tunable lasers that have taken place over the past decade. Internationally recognized experts describe the physics and architecture of widely applied tunable laser sources, emphasizing biomedical applications of fiber lasers and ultrashort pulsed lasers, such as laser isotope separation and cancer photodynamic therapy.

New to the **Second Edition**

- Advances in optical parametric oscillators
- Principles of tunable semiconductor lasers
- Solid-state dye lasers
- Interferometric imaging
- Large free-electron lasers

Outlining new applications in biology and medicine, this second edition offers a well-needed and up-to-date account of the most promising tunable laser applications.

60279

CRC Press
Taylor & Francis Group
an informa business
www.crcpress.com

6000 Broken Sound Parkway, NW
Suite 300, Boca Raton, FL 33487
270 Madison Avenue
New York, NY 10016
2 Park Square, Milton Park
Abingdon, Oxon OX14 4RN, UK

ISBN: 978-1-4200-6009-6
90000
9 781420 060096